frontiers | Research Topics

Experimental and computational aspects of bioactive proteins from animal venoms: An insight into pharmacological properties and drug discovery

Edited by
Michelle Yap, Cassandra M. Modahl
and Steven R. Hall

Published in
Frontiers in Pharmacology

ISSN 1664-8714
ISBN 978-2-8325-4523-2
DOI 10.3389/978-2-8325-4523-2

About Frontiers

Frontiers is more than just an open access publisher of scholarly articles: it is a pioneering approach to the world of academia, radically improving the way scholarly research is managed. The grand vision of Frontiers is a world where all people have an equal opportunity to seek, share and generate knowledge. Frontiers provides immediate and permanent online open access to all its publications, but this alone is not enough to realize our grand goals.

Frontiers journal series

The Frontiers journal series is a multi-tier and interdisciplinary set of open-access, online journals, promising a paradigm shift from the current review, selection and dissemination processes in academic publishing. All Frontiers journals are driven by researchers for researchers; therefore, they constitute a service to the scholarly community. At the same time, the *Frontiers journal series* operates on a revolutionary invention, the tiered publishing system, initially addressing specific communities of scholars, and gradually climbing up to broader public understanding, thus serving the interests of the lay society, too.

Dedication to quality

Each Frontiers article is a landmark of the highest quality, thanks to genuinely collaborative interactions between authors and review editors, who include some of the world's best academicians. Research must be certified by peers before entering a stream of knowledge that may eventually reach the public - and shape society; therefore, Frontiers only applies the most rigorous and unbiased reviews. Frontiers revolutionizes research publishing by freely delivering the most outstanding research, evaluated with no bias from both the academic and social point of view. By applying the most advanced information technologies, Frontiers is catapulting scholarly publishing into a new generation.

What are Frontiers Research Topics?

Frontiers Research Topics are very popular trademarks of the *Frontiers journals series*: they are collections of at least ten articles, all centered on a particular subject. With their unique mix of varied contributions from Original Research to Review Articles, Frontiers Research Topics unify the most influential researchers, the latest key findings and historical advances in a hot research area.

Find out more on how to host your own Frontiers Research Topic or contribute to one as an author by contacting the Frontiers editorial office: frontiersin.org/about/contact

Experimental and computational aspects of bioactive proteins from animal venoms: An insight into pharmacological properties and drug discovery

Topic editors

Michelle Yap — Monash University Malaysia, Malaysia

Cassandra M. Modahl — Department of Tropical Disease Biology, Liverpool School of Tropical Medicine, United Kingdom

Steven R. Hall — Lancaster University, United Kingdom

Citation

Yap, M., Modahl, C. M., Hall, S. R., eds. (2024). *Experimental and computational aspects of bioactive proteins from animal venoms: An insight into pharmacological properties and drug discovery*. Lausanne: Frontiers Media SA.

doi: 10.3389/978-2-8325-4523-2

Table of contents

frontiers | Frontiers in Pharmacology

TYPE Editorial
PUBLISHED 16 February 2024
DOI 10.3389/fphar.2024.1380193

OPEN ACCESS

EDITED AND REVIEWED BY
Filippo Drago,
University of Catania, Italy

*CORRESPONDENCE
Michelle Khai Khun Yap,
yap.michelle@monash.edu

RECEIVED 01 February 2024
ACCEPTED 13 February 2024
PUBLISHED 16 February 2024

CITATION
Yap MKK, Modahl CM and Hall SR (2024), Editorial: Experimental and computational aspects of bioactive proteins from animal venoms: an insight into pharmacological properties and drug discovery.
Front. Pharmacol. 15:1380193.
doi: 10.3389/fphar.2024.1380193

Editorial: Experimental and computational aspects of bioactive proteins from animal venoms: an insight into pharmacological properties and drug discovery

Michelle Khai Khun Yap[1]*, Cassandra M. Modahl[2] and Steven R. Hall[3]

[1]School of Science, Monash University Malaysia, Bandar Sunway, Malaysia, [2]Centre for Snakebite Research and Interventions, Liverpool School of Tropical Medicine, Liverpool, United Kingdom, [3]Lancaster Medical School and Biomedical and Life Sciences, Lancaster University, Lancaster, United Kingdom

KEYWORDS

animal toxins, therapeutics, bioinformatics, omics, molecular pharmacology

Editorial on the Research Topic
Experimental and computational aspects of bioactive proteins from animal venoms: an insight into pharmacological properties and drug discovery

The fascinating realm of animal venoms is a treasure trove of bioactive proteins, known as toxins, that are responsible for life-threatening pathological conditions in envenoming. Despite their deadly nature, they have promising potential to be developed into life-saving drugs. For example, an angiotensin-converting enzyme (ACE) inhibitor, captopril, from *Bothrops jararaca* venom has been developed for the treatment of life-threatening hypertension (Smith and Vane, 2003). To harness this potential, a comprehensive understanding of animal venom toxins (e.g., intricating their structures, functions, and mechanistic actions) is essential for therapeutic discovery and antivenom development (Kini, 2010). Recent advancements in biotechnologies have facilitated deeper insights into animal venoms. The use of omics (e.g., genomics, transcriptomics and proteomics) in venom research, termed venomics, seeks to describe the diversity and complexity of venoms, providing the foundation for toxin characterisation, and antivenom development (Modahl et al., 2020; Tan, 2022). These approaches characterise the pharmacological properties of toxins through the convergence of experimental and computational methods. Indispensable computational studies of toxins encompass molecular modelling, docking and simulations of molecular dynamics delineate structure-function relationships, especially interactions with cellular targets that drive pharmacological effects (Ojeda et al., 2017).

Our Research Topic collected 9 articles of new findings and perspectives to unravel the pharmacological and drug discovery potentials of venoms from spiders, snakes and bees.

Understanding the mechanistic actions of toxins on molecular targets is the first step towards the development of novel therapeutics. Li et al. expressed a novel toxin, LCTX-F2, identified from spider *Lycosa singoriensis* venom, and performed a series of characterisation experiments. LCTX-F2 is a 7.5 kDa peptide with 65 amino acids and belongs to the toxin 35 superfamily in spider venoms. Notably, this toxin possesses procoagulant activity with significant reduction in clotting times through interaction with coagulation factors FXIIa, Fxa, kallikrein, and thrombin. This study demonstrated a dose-dependent decrease in bleeding time in experimental mouse models with no cytotoxic or haemolytic activities. These findings suggest the potential of LCTX-F2 as a future procoagulant drug.

Badari et al. discovered a cysteine-rich secreted protein (CRISP) isoform they have named patagonin in the venom of a snake, *Philodryas patagoniensis*, by reverse-phase HPLC bioassay-guided fractionation. Patagonin exhibited significant antimicrobial effects against *Pseudomonas aeruginosa* and *Penicillium expansum*. Patagonin is also non-cytotoxic and non-haemolytic, highlighting snake venoms as promising sources of novel antimicrobial molecules.

Chan et al. discovered ZK002, a 30 kDa protein from *Deinagkistrodon acutus* venom with anti-angiogenic and anti-inflammatory effects. This protein targets VEGF signalling pathways and angiogenic-related proteins. It also suppresses pro-inflammatory cytokines which demonstrates the potential of ZK002 as dual-functional therapeutic agents for angiogenesis and inflammation-related diseases.

The scorpion venom toxin has also been found to exhibit anticancer properties. In a study by Mlayah-Bellalouna et al., P01 toxin from *Androctonus australis* possesses selective anticancer effects against glioblastoma cells, by targeting SK2 channels. Their findings proposed the potential therapeutic development of P01 for glioblastoma.

Shi et al. reviewed the pharmacological potentials of bee venoms. This review covers a comprehensive appraisal of the pharmacological effects of bee venoms and their principal components responsible for their anticancer, anti-inflammatory, anti-infective, analgesic and neuroprotective effects. The authors applied bioinformatic analyses, KEGG pathway analyses, and protein-protein interaction (PPI) analyses to predict mechanistic actions and signalling pathways which represent important molecular pharmacology of bee venoms. The review also provides a thorough overview of potential therapeutic applications of bee venoms through network pharmacology.

In addition to characterising toxin activities, it is of great importance to understand the structure-function relationship of toxins and their molecular targets. Dongol et al. investigated structure-function relationships of a spider venom toxin, Ssp1a, a selective sodium channel (Nav) subtype antagonist. They adopted molecular docking to design two promising Ssp1a analogues, S7R-E18K-rSsp1a and N14D-P27R-rSsp1, with enhanced potency and selectivity for NaV subtypes.

From here, they successfully developed S7R-E18K-rSsp1a and N14D-P27R-rSsp1, two promising analogues with improved efficacy and selectivity towards NaV subtypes, NaV1.3 and NaV1.2/1.7, respectively. These findings emphasise how computational approaches could be applied in rational drug design from toxins to achieve therapeutic outcomes for medical conditions associated with sodium channel subtypes.

Although we observe great therapeutic potentials in certain animal venom toxins, we also appreciate that it is the diversity of the animal venom toxins which can make the treatment of envenoming challenging. One of these challenges is the immunogenicity of venom toxins, which requires study to develop better antivenoms targeting specific toxins (Hiu et al., 2023) and exhibiting broader neutralising potency. In this regard, Chan et al. examined immunogenicity of α-neurotoxins from elapid venoms. Neurotoxins are lethal toxins found predominantly in elapid venoms which cause neuromuscular paralysis in envenomed victims. Current antivenoms exhibited low neutralisation efficacy for neurotoxins. Herein, the authors used a structure-based prediction model analysis and a DM-editing determinant screening algorithm to evaluate the immunogenicity of α-neurotoxins from five Asiatic elapid venoms - *Naja kaouthia*, *Ophiophagus hannah*, *Laticauda colubrina*, *Hydrophis schistosus*, and *Hydrophis curtus*. It was found that the low immunogenicity of neurotoxins could be attributed to the smaller size and amino acid compositions, hindering the effectiveness of existing antivenoms. The authors proposed the use of synthetic epitopes to develop more effective neurotoxin neutralising antivenoms.

Drug repurposing has also been an alternative, accessible and cost-effective treatment option for envenoming (Koh et al., 2020; Puzari et al., 2021; Hall et al., 2023). Herein, Clare et al. developed a high-throughput screening (HTS) panel on repurposed drug libraries and identified 14 repurposed drugs that can antagonise snake venom metalloproteinases (SVMPs), a known toxin family that causes haemorrhage and coagulopathy. In addition, a similar HTS pipeline was applied in parallel for another venom toxin, i.e., phospholipase A_2 (PLA_2) as discussed by Albulescu et al. These HTS pipeline methodologies offer automated and rapid strategies to discover drug "hits" from diverse chemical libraries as potential future envenoming therapeutics.

Overall, this Research Topic highlights the comprehensive investigations into experimental and computational facets within animal venom research, paving the way for profound insights and transformative drug discovery. The application of bioinformatics and computational tools enables holistic improvement in the identification of promising leads from animal venoms, forming a paradigm shift in drug discovery. Moving forward, artificial intelligence (AI) integration in animal venom research will likely revolutionise therapeutics discovery in a more streamlined and guided manner. Additionally, database curation of potential hits from animal venoms requires collation of diverse data, aiding in therapeutic development for venom research and promoting interdisciplinary collaboration.

Author contributions

MY: Writing–original draft, Writing–review and editing. CM: Writing–review and editing. SH: Writing–review and editing.

Funding

The author(s) declare that no financial support was received for the research, authorship, and/or publication of this article.

Acknowledgments

We would like to thank the contributions of authors, reviewers and editors to this Research Topic.

Conflict of interest

The authors declare that the research was conducted in the absence of any commercial or financial relationships that could be construed as a potential conflict of interest.

Publisher's note

References

Hall, S. R., Rasmussen, S. A., Crittenden, E., Dawson, C. A., Bartlett, K. E., Westhorpe, A. P., et al. (2023). Repurposed drugs and their combinations prevent morbidity-inducing dermonecrosis caused by diverse cytotoxic snake venoms. *Nat. Commun.* 14, 7812. doi:10.1038/s41467-023-43510

Hiu, J. J., Fung, J. K. Y., Tan, H. S., and Yap, M. K. K. (2023). Unveiling the functional epitopes of cobra venom cytotoxin by immunoinformatics and epitope-omic analyses. *Sci. Rep.* 13, 12271. doi:10.1038/s41598-023-39222-2

Kini, R. M. (2010). Toxin treasure in snake venoms: a protein biochemist's sandbox. *Biochem.* 1 32 (4), 24–28. doi:10.1042/BIO03204024

Koh, C. Y., Bendre, R., and Kini, R. M. (2020). Repurposed drug to the rescue of snakebite victims. *Sci. Transl. Med.* 12 (542), eabb6700. doi:10.1126/scitranslmed.abb6700

Modahl, C. M., Brahma, R. K., Koh, C. Y., Shioi, N., and Kini, R. M. (2020). Omics technologies for profiling toxin diversity and evolution in snake venom: impacts on the discovery of therapeutic and diagnostic agents. *Annu. Rev. Anim. Biosci.* 8, 91–116. doi:10.1146/annurev-animal-021419-083626

Ojeda, P. G., Ramírez, D., Alzate-Morales, J., Caballero, J., Kaas, Q., and González, W. (2017). Computational studies of snake venom toxins. *Toxins* 10 (1), 8. doi:10.3390/toxins10010008

Puzari, U., Fernandes, P. A., and Mukherjee, A. K. (2021). Advances in the therapeutic application of small-molecule inhibitors and repurposed drugs against snakebite. *J. Med. Chem.* 64 (19), 13938–13979. doi:10.1021/acs.jmedchem.1c00266

Smith, C. G., and Vane, J. R. (2003). *Discov. captopril. FASEB J* 17 (8), 788–789. doi:10.1096/fj.03-0093life

Tan, C. H. (2022). Snake venomics: fundamentals, recent updates, and a look to the next decade. *Toxins* 14 (4), 247. doi:10.3390/toxins14040247

frontiers in Pharmacology

ORIGINAL RESEARCH
published: 16 June 2020
doi: 10.3389/fphar.2020.00896

LCTX-F2, a Novel Potentiator of Coagulation Factors From the Spider Venom of *Lycosa singoriensis*

Pengpeng Li[1†], *Zhongzhe Zhang*[1†], *Qiong Liao*[1], *Er Meng*[2], *James Mwangi*[3], *Ren Lai*[3] *and Mingqiang Rong*[1*]

[1] The National & Local Joint Engineering Laboratory of Animal Peptide Drug Development, College of Life Sciences, Hunan Normal University, Changsha, China, [2] School of Life Sciences, Hunan University of Science and Technology, Xiangtan, China, [3] Key Laboratory of Animal Models and Human Disease Mechanisms of Chinese Academy of Sciences & Yunnan Province, Kunming Institute of Zoology, Kunming, China

OPEN ACCESS

Edited by:
Chiranjib Chakraborty,
Adamas University, India

Reviewed by:
Carla Cicala,
University of Naples Federico II, Italy
Claudiana Lameu,
University of São Paulo, Brazil
John Fanikos,
Brigham and Women's Hospital and Harvard Medical School, United States

***Correspondence:**
Mingqiang Rong
rongmq@hunnu.edu.cn

[†]These authors have contributed equally to this work

Specialty section:
This article was submitted to Experimental Pharmacology and Drug Discovery, a section of the journal Frontiers in Pharmacology

Received: 06 March 2020
Accepted: 02 June 2020
Published: 16 June 2020

Citation:
Li P, Zhang Z, Liao Q, Meng E, Mwangi J, Lai R and Rong M (2020) LCTX-F2, a Novel Potentiator of Coagulation Factors From the Spider Venom of Lycosa singoriensis. Front. Pharmacol. 11:896. doi: 10.3389/fphar.2020.00896

Spider venoms contain many functional proteins/peptides such as proteinases, serine/cysteine proteinase inhibitors, insecticidal toxins, and ion channel toxins. However, to date, no peptide toxin with procoagulant activities has been identified from spider venom. In this study, a novel toxin LCTX-F2 with coagulation-promoting activity was identified and characterized in the venom of the spider *Lycosa singoriensis* (*L. singoriensis*). LCTX-F2 significantly shortened activated partial thromboplastin time (APTT), clotting time, and plasma recalcification time. This toxin directly interacted with several coagulation factors such as FXIIa, kallikrein, thrombin, and FXa and increased their protease activities. In liver bleeding and tail bleeding mouse models, LCTX-F2 significantly decreased the number of blood cells and bleeding time in a dose-dependent manner. At the same dosage, LCTX-F2 exhibited a more significant procoagulant effect than epsilon aminocaproic acid (EACA). Moreover, LCTX-F2 showed no cytotoxic or hemolytic activity against either normal cells or red blood cells. Our results suggested that LCTX-F2 is a potentiator of coagulation factors with the potential for use in the development of procoagulant drugs.

Keywords: spider venom, peptide, coagulant, coagulation factors, toxin

INTRODUCTION

Excessive blood loss is a leading cause of the high mortality rate associated with surgical operations (Willner et al., 2016). Reducing blood loss and managing hemostasis are vital during surgery and hemorrhagic shock (Zakaria et al., 2005). In surgical operations, tranexamic acid (TXA), epsilon aminocaproic acid (EACA) (Alkjaersig et al., 1959), aprotinin, and recombinant activated factor VII (rFVIIa) are the most commonly used procoagulant drugs. The two antifibrinolytic agents, TXA

Abbreviations: APTT, activated partial thromboplastin time; PT, prothrombin time; FXIIa, activated factor XII; FXa, activated factor X; rFVIIa, recombinant activated factor VII; EACA, epsilon aminocaproic acid; TXA, tranexamic acid; HEK-293T, Human embryonic kidney 293T; CHO, Chinese Hamster Ovary 1; PBS, phosphate-buffered saline; PPP, platelet-poor plasma; IPTG, Isopropyl β-D-thiogalactoside; RBC, red blood cell.

and EACA, competitively inhibit the conversion of plasminogen to plasmin. Meanwhile, aprotinin is used to reduce bleeding during complex heart and liver surgery, and its main function is to slow down fibrinolysis so as to allow the breakdown of blood clots (Willner et al., 2016).

Several proteins that promote coagulation have been isolated from the venom of the snake *Pseudonaja textilis*. a factor Xa-like protein, Haempatch™, which exhibits potent procoagulant effects, has been developed as a haemostatic drug, and is used to reduce blood loss due to surgery or trauma. CoVase™ is regarded as a procoagulant cofactor. It is a systemic antibleeding medication used to treat noncompressible hemorrhage and internal bleeding (Fry et al., 2005). Textilinin-1, a selective plasmin inhibitor, can reduce blood loss associated with complex surgeries (Flight et al., 2009). Those procoagulant proteins affect multiple steps in the hemostatic process, ranging from activation of coagulation factors to platelet aggregation (Santos et al., 2000).

Abundant evidence has demonstrated that spider venoms contain many active peptide components (Meng et al., 2016). Most peptides identified in spider venom are small, disulfide-rich neurotoxins. Spiders of the genus *Loxosceles* (Tavares et al., 2011; Tavares et al., 2016), also known as brown spiders, are widely distributed in South America and their venom can cause a necrotizing-hemolytic syndrome in humans, as well as hemorrhagic problems, hemolysis, platelet aggregation, and renal failure (Tavares et al., 2004; Van Den Berg et al., 2007; Nguyen and Pandey, 2019); however, the mechanism underlying these venom-induced hemorrhagic disorders is poorly understood. *Lycosa singoriensis* (*L. singoriensis*) is distributed throughout the west of China and its venom causes severe illness, including pain, cutaneous necrosis, nausea, vomiting, and even dyspnea. In this study, a novel peptide with procoagulant activity, LCTX-F2, was identified in the venom of *L. singoriensis* and characterized. LCTX-F2 significantly shortened activated partial thromboplastin time (APTT), clotting time, and plasma recalcification time. We further employed *in vivo* mouse models of tail bleeding and liver bleeding to investigate the mechanism underlying the procoagulant activity of LCTX-F2.

MATERIALS AND METHODS

Animals and Cells

The BALB/c mice used in this experiment were purchased from Kunming Medical University. HEK-293T (Human embryonic kidney 293T) and CHO (Chinese hamster ovary 1) cells were purchased from the cell bank of the Kunming Institute of Zoology. All experiments were performed in accordance with national legislation and approved by the animal experimental ethics committee (SMKX-20170210) of the Kunming Institute of Zoology, Chinese Academy of Sciences.

cDNA Library Construction and Sequencing

The *L. singoriensis* sample was stored at the Kunming Museum of Zoology (Kunming City, Yunnan Province, China). The venom gland of *L. singoriensis* was dissected and used for the construction of a cDNA library (Yang et al., 2012). Total RNA was extracted from the venom glands of 20 spiders using TRIzol reagent (Life Technologies Ltd, Carlsbad, CA, USA) following the manufacturer's instructions. The cDNA library was constructed using the Creator SMART cDNA Library Construction Kit (Clontech, Palo Alto, CA, USA) according to manufacturer's instructions. A cDNA library with 3×10^6 independent colonies was produced. All the clones from the cDNA library were sequenced on an ABI PRISM 377 DNA sequencer (Applied Biosystems, Foster City, CA, USA). cDNA fragments longer than 200 bp were selected for further analyses. The LCTX-F2 sequence has been uploaded to GenBank of NCBI under the accession number BankIt 2321489 MT178457.

Expression and Purification of Recombinant LCTX-F2

The DNA sequence of LCTX-F2 was synthesized (Sangon Biotech, Co., Ltd, Shanghai, China) and a TEV enzyme cleavage site (ENLYFQG) was inserted immediately upstream of the sequence (Ma et al., 2016). For recombinant expression, an LCTX-F2/pET32a (+) prokaryotic expression vector was transformed into *Escherichia coli* strain BL-21 (DE3). LCTX-F2 was cleaved from the recombinant protein using the TEV enzyme (Beijing Solarbio Science & Technology Co., Ltd). The hydrolyzed LCTX-F2 was first separated by molecular exclusion using a Sephadex G-75 gel filtration column (2.6 cm × 100 cm; GE Healthcare Bio-Sciences AB, Uppsala, Sweden) with phosphate-buffered saline (PBS) (150 mM NaCl, 2.7 mM KCl, 1.5 mM KH_2PO_4, and 8 mM K_2HPO_4, pH 7.2). Then, LCTX-F2 was further eluted by reversed-phase high-performance liquid chromatography (RP-HPLC) using a C18 column (Unisil C18 column, 5-μm particle size, 10 × 250 mm). The gradient of high-performance liquid chromatography solution (0.1% trifluoroacetic acid/acetyl) increased by 1% per min. LCTX-F2 was dissolved in 0.1% trifluoroacetic acid/water (0.5 μl) and spotted onto a plate with 0.5-μl matrix (10 mg/ml α-cyano-4-hydroxycinnamic acid in 60% acetonitrile). The molecular weight of LCTX-F2 was determined using an UltraFlex I mass spectrometer (UltraFlex I, Bruker Daltonics, Billerica, MA, USA) in positive ion mode. The accuracy of mass determination was recorded according to the manufacturer's instructions. The purity of LCTX-F2 was approximately 95%.

Blood Coagulation Time Assay

Blood recalcification time was measured according to a previously described method (Gulliani et al., 1976). The platelet-poor plasma (PPP) negative control obtained from healthy human subjects was transferred to 96-well plates. LCTX-F2 (final concentration ranging from 0.0 to 3.0 μM) was

dissolved in 80 μl of HEPES buffer (10 mM HEPES, 150 mM NaCl, pH 7.4) and added to the plates with 20 μl of PPP. Two samples were incubated for 10 min at room temperature. Before recording clotting time, 50 μl of $CaCl_2$ (25 mM) was dispensed into the 96-well plates. The APTT was assayed as previously described (Jung and Kim, 2009). APTT reagent (50 μl), PPP (40 μl), and LCTX-F2 (10 μl) were incubated for 5 min at 37°C. The APTT was recorded after the addition of 50 μl of $CaCl_2$ (25 mM). The prothrombin time (PT) was assayed. PPP (40 μl) and LCTX-F2 (10 μl) were incubated for 5 min at 37°C. The PT was recorded after the addition of 50 μl of PT reagent. Three parallel tests were performed and the absorbance was recorded at 650 nm using a microplate spectrophotometer (BioTek Instrument, Inc., Winooski, VT, USA).

Determination of Serine Protease Activity

Serine protease activity was tested in Tris–HCl buffer (0.05 M, pH 7.8) at 37°C (Ma et al., 2016). The proteases factor Xa (HFXa 1011), trypsin (T4665), thrombin (T4393), plasmin (P1867), factor XIIa (HFXIIa1212a), and kallikrein (HPKa 1303) were preincubated with different doses of LCTX-F2 (0.0–3.0 μM) for 10 min at 37°C. Factor Xa, factor XIIa, and kallikrein were purchased from Enzyme Research Laboratories (South Bend, IN, USA). Thrombin, trypsin, and plasmin were purchased from Sigma (St. Louis, MO, USA). LCTX-F2 was mixed with the enzymes for 10 min, after which 0.5 mM of substrate was added to initiate each assay. The substrate for FXa, trypsin, thrombin, plasmin, and kallikrein/factor XIIa were F3301, B3133, H-D-Phe-Pip-Arg-pNa·2HCl, G8148, and H-D-Pro-Phe-ArgpNA·2HCl, respectively. All the substrates were purchased from Sigma, except H-D-Phe-Pip-Arg-pNa·2HCl and G8148 which were purchased from Hyphen Biomed (Neuville-sur-Oise, France). The LCTX-F2 enzyme reactions were continuously measured for 20 min at 405 nm.

Surface Plasmon Resonance Assay

The binding of LCTX-F2 to FXIIa, kallikrein, FXa, and thrombin was tested with a Biacore 3000 (GE Healthcare Bio-Sciences, Uppsala, Sweden) according to a previously described method (Konings et al., 2011; Zhang et al., 2012). The experiments were performed at 25°C using HBS-EP buffer as a running buffer (10 mM HEPES, pH 7.4, 3 mM EDTA, 150 mM NaCl, and 0.05% P20 surfactant). LCTX-F2 as a ligand was diluted with running buffer and coupled to CM5 by amine coupling, yielding a total of 2,000 response units. The running buffer flow rate was maintained at 30 μl/min. A series of twofold dilutions of FXIIa, kallikrein, FXa, and thrombin, as analytes, were generated using running buffer (0, 3.125, 6.25, 12.5, 25, 50, 100 μg/ml). Solutions of the different analytes were injected over the flow channel at a flow rate of 30 μl/min for 120 s, followed by dissociation for 300 s. The LCTX-F2/enzyme binding curve was acquired by subtracting the FL1 curve from the FL2 curve. All surface plasmon resonance (SPR) experiments were performed in triplicate and analyzed by BIA evaluation software.

Tail Bleeding Assay

Six BALB/c mice (20–25 g) were used in each group. The mice were anesthetized by intraperitoneal injection of 100 μl of a 0.3% pentobarbital sodium solution. Subsequently, saline, LCTX-F2 (0.625, 1.25, or 2.5 mg/kg), or EACA (5 mg/kg) was separately injected into the tail vein. After 10 min, a 7-mm tail-tip transection was made according to a previously described method (Schoenwaelder et al., 2011) to estimate the hemostatic effect. After transection, the bleeding tail was quickly steeped in saline solution at 37°C and the timing began. Bleeding time was recorded from the beginning of tail transection until 120 s after blood flow had stopped.

Liver Bleeding Assay

Seven BALB/c mice (20–25 g) were used in each group. The mice were anesthetized by intraperitoneal injection of 100 μl of a 0.3% pentobarbital sodium solution. Subsequently, saline, LCTX-F2 (1.25, 2.5, or 5 mg/kg), or EACA (5 mg/kg) were separately injected into the tail vein. After 10 min, scissors were used to open the thoracic cavity along the ventral white line. A piece (5.00 ± 0.15 mg) was cut from the lower edge of the right liver lobe (Tilly et al., 2014) and the thoracic cavity closed. After 20 min, the number of RBCs was calculated after peritoneal lavage with 4 ml of a 0.9% saline solution.

Cytotoxicity Assay

A cell counting kit-8 (CCK-8, HY-K0301; MedChemExpress, Monmouth Junction, NJ, USA) was used to evaluate the effect of LCTX-F2 on cell viability (Wang et al., 2010). HEK-293T and CHO cells were incubated with LCTX-F2 (0, 5, 10, 20, or 100 mg/ml) for 24 h. The cells were subsequently incubated with 0.2 ml of culture medium containing 10% CCK-8 reagent for 2 h. The absorbance was monitored at 450 nm using a microplate spectrophotometer.

Hemolysis Assay

A rabbit RBC suspension (2%) in PBS was obtained for subsequent experiments as previously described (Vives et al., 1997). Rabbit RBC suspensions were incubated with PBS, LCTX-F2 (5, 10, 20, or 100 mg/ml), or distilled water as positive control for 3 h at room temperature. After centrifugation at 10,050 rpm for 3 min, the absorbance of the supernatants was measured spectrophotometrically at 570 nm to calculate the hemolysis ratio.

Statistical Analysis

Data are presented as means ± SD from three independent experiments. Significance was determined by unpaired *t*-test; $P < 0.05$ was considered significant.

RESULTS

Identification of LCTX-F2

The *L. singoriensis* venom gland cDNA library comprised 3×10^6 independent clones. To obtain high-quality EST sequences, clones

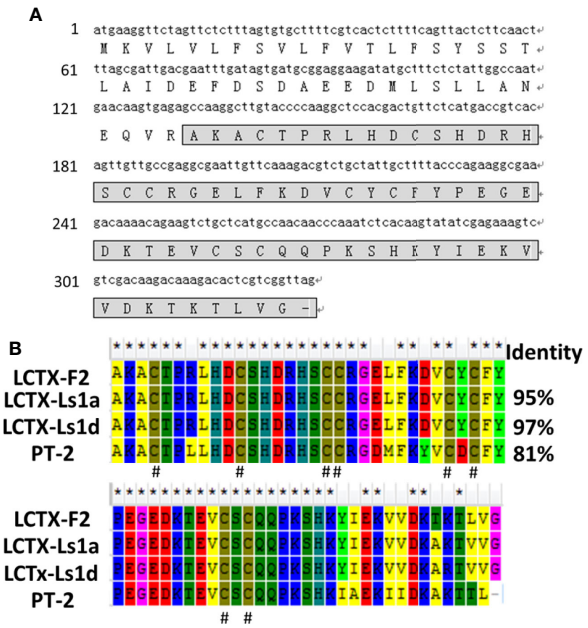

FIGURE 1 | Amino acid and cDNA sequence of LCTX-F2. **(A)** The cDNA sequence of LCTX-F2. The sequence of mature LCTX-F2 is boxed and the stop codon is indicated by a bar (–). **(B)** NCBI-BLAST sequence alignment of LCTX-F2 with other homologs. Identical amino acid residues are indicated by the symbol (*). Cysteine residues are indicated by the symbol (#).

shorter than 200 bp were excluded. A novel peptide named LCTX-F2 was identified from the cDNA library (**Figure 1A**). The open reading frame of LCTX-F2 was 315 bp long and encoded a 109-amino acid residue precursor containing a 44-residue signal peptide and a 65-residue mature peptide. A BLAST search indicated that LCTX-F2 belonged to the toxin 35 superfamily of spider toxins (**Figure 1B**), and the distribution of eight cysteines was the same as that observed in homologous toxins (LCTX-Ls1a, LCTX-Ls1d, and PT-2).

Expression and Purification of Recombinant LCTX-F2

The LCTX-F2/pET32a (+) prokaryotic expression vector was transformed into the *E. coli* strain BL-21 (DE3). LCTX-F2 was first induced by isopropyl β-D-thiogalactoside (IPTG, 1 mM) and then purified from soluble *E. coli* lysates. LCTX-F2 was separated using a Ni^{2+} affinity column (His-binding resin) and cleaved by the TEV enzyme. After cleavage, two bands were observed in SDS–PAGE, indicating that the fusion protein had been completely cleaved (**Figure S1A**). LCTX-F2 was first isolated using a Sephadex G-75 gel filtration column (**Figure S1A**), and then further separated by RP-HPLC on a C18 column with a linear gradient from 0–50% acetonitrile in 60 min. A single peak containing LCTX-F2 was detected at the 33.7% acetonitrile gradient (**Figure S1B**). The purified LCTX-F2 was subjected to mass spectrometric (MS) analysis. LCTX-F2 was found to have a molecular weight of 7,501.50 Da (**Figure S1C**), which was 8 Da less than the theoretical molecular weight (7,509.56 Da), implying the formation of four intramolecular disulfide bridges.

LCTX-F2 Shortened Blood Coagulation Time

The effects of LCTX-F2 on blood coagulation were tested by APTT and plasma recalcification time assays. In the APTT test, 0.03, 0.3, and 3 μM LCTX-F2 significantly reduced the APTT from 24.6 s to 23.9, 20.1, and 16.3 s, respectively (**Figures 2A, B**). The recalcification time of the control was 5.8 min. After the application of 0.75, 1.5, and 3 μM LCTX-F2, the plasma recalcification time was significantly reduced to 5.0, 3.3, and 2.9 min, respectively (**Figures 2C, D**). However, in the PT test, the clotting time of the negative control was 14.3 s. After the application of 0.3 and 3 μM LCTX-F2, the plasma recalcification time was reduced to 13.7 and 13.4 s, but the reductions were not significant (**Figures S2A, B**). As previously reported, the APTT test detects intrinsic coagulation pathways, whereas the PT test detects extrinsic coagulation pathways. Therefore, our results implied that LCTX-F2 had an effect on intrinsic coagulation pathways.

LCTX-F2 Increased Procoagulant Activity

Because we found that LCTX-F2 reduced the coagulation time, we further tested how LCTX-F2 affects coagulation factors and platelet aggregation. After LCTX-F2 application at 0.03, 0.3, and 3 μM, the relative protease activity of FXIIa was increased by 1.2%, 44.0%, and 96.0%, respectively. At 3

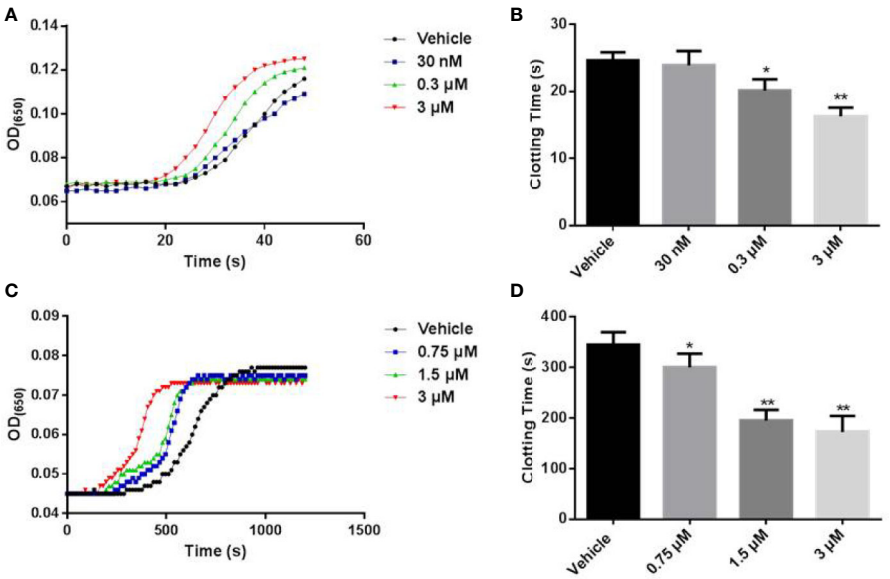

FIGURE 2 | The effect of LCTX-F2 on coagulation. **(A)** The effect of LCTX-F2 on APTT. LCTX-F2 was incubated with APTT reagent (50 μl) at 37°C for 3 min. **(B)** Histogram of APTT levels. **(C)** The effect of LCTX-F2 on recalcification time. **(D)** Histogram of recalcification time with different doses of LCTX-F2. Data are presented as means ± SD of three independent experiments. *$P < 0.05$, **$P < 0.01$ compared with vehicle as determined by the two-sample Student's *t*-test.

μM, LCTX-F2 increased the activity of thrombin, FXa, and kallikrein by approximately 36.9, 34.8, and 33.3%, respectively (**Figures 3A, B**). LCTX-F2 increased the activity of FXIIa significantly more than that of FXa and kallikrein. However, LCTX-F2 application had no effect on FVIIa, plasmin, and trypsin activity (**Figures S3A–C**). In the platelet aggregation assay, at 3 μM, no promotive effect of LCTX-F2 was observed (**Figures S3D, E**).

Interaction Kinetics Between LCTX-F2 and Coagulation Factors

As LCTX-F2 increased the activity of several coagulation factors, we tested whether LCTX-F2 directly interacts with these factors using a real-time SPR binding assay. The coagulation factors FXIIa, kallikrein, thrombin, and FXa were injected onto a chip containing immobilized LCTX-F2. Sensorgrams of the interactions between LCTX-F2 and the evaluated coagulation factors are shown in **Figure 4**. The binding affinity (K_D) of LCTX-F2 for FXIIa, kallikrein, thrombin, and FXa was 7.2, 4.6, 0.7, and 0.18 μM, respectively (**Figure 4**). LCTX-F2 showed stronger affinity for FXIIa and kallikrein than for FXa and thrombin. FXa and thrombin are reported to belong to the common coagulation pathway, whereas FXIIa and kallikrein belong to the intrinsic coagulation pathway. These results indicated that LCTX-F2 promoted blood coagulation through increasing the activity of the blood coagulation factors FXIIa, kallikrein, thrombin, and FXa.

LCTX-F2 Decreases Traumatic Hemorrhage

As shown in **Figure 5A**, the RBC count in the liver bleeding mouse model was 1.21×10^5/μl. After injection with 1.25, 2.5, or 5 mg/kg LCTX-F2 and 5 mg/kg EACA, the RBC count significantly decreased to 1.04×10^5, 0.99×10^5, 0.70×10^5, and 0.88×10^5/μl, respectively (**Figure 5A**). In the tail bleeding model, a 7-mm wound was made in the mouse tail to assess homeostasis. Compared with that of vehicle, tail vein injection of LCTX-F2 at 0.625, 1.25, or 2.5 mg/kg and EACA at 5 mg/kg significantly decreased the bleeding time from 171.5 to 139.3, 94.5, 68.5, and 114.3 s, respectively (**Figure 5B**). These results suggested that, at the same dose, LCTX-F2 had a better hemostatic effect than EACA.

LCTX-F2 Showed No Cytotoxic or Hemolytic Activities

Incubation with LCTX-F2 at concentrations ranging from 0 to 100 μg/ml for 24 h did not inhibit the viability of HEK-293T or CHO cells (**Figures 6A, B**). In the hemolysis assay (**Figure 6C**), LCTX-F2 did not exhibit hemolytic activity, even at the concentration of 100 μg/ml.

DISCUSSION

Peptides derived from spider venom are highly diverse, and include metalloproteinases, serine proteinases, hyaluronidases, serine/cysteine proteinase inhibitors, alkaline phosphatases, ATPases, and insecticidal toxins

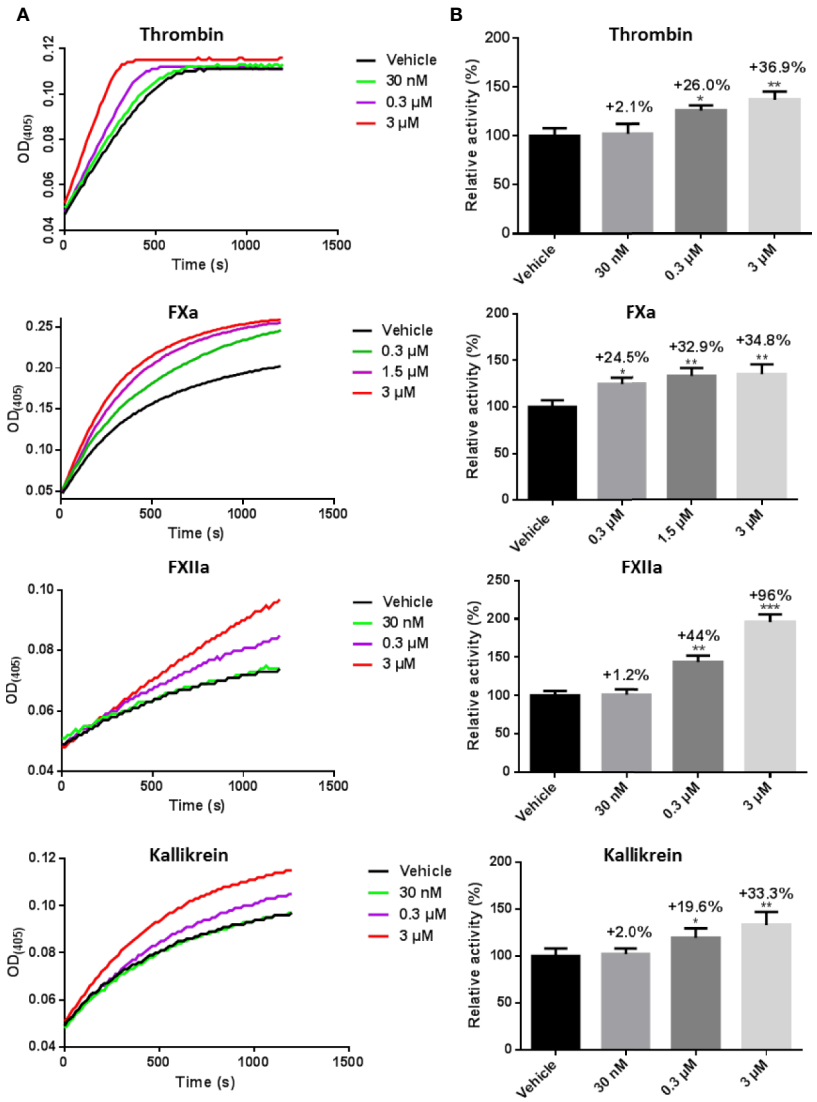

FIGURE 3 | LCTX-F2 increased the activity of coagulation factors. **(A)** After incubating with 0.03, 0.3, and 3 μM LCTX-F2, the activities of thrombin, FXa, FXIIa, and kallikrein were evaluated with the corresponding chromogenic substrates for 20 min. Relative activity was calculated through enzymatic reactions. **(B)** Histogram depicting the percent increases in coagulation factor activity stimulated by LCTX-F2. Data are presented as means ± SD of three independent experiments. $^{*}P < 0.05$, $^{**}P < 0.01$ compared with vehicle as determined by the two-sample Student's *t*-test.

(Machado et al., 2005; Chaim et al., 2011; Jin et al., 2017). LCTX-F2 consists of 65-amino acid residues, including four intramolecular disulfide bridges. The BLAST results showed that LCTX-F2 belongs to the toxin 35 family and shares high sequence identity with several known peptide toxins from wolf spiders. The number and positions of cysteines are highly conversed in the toxin 35 family, implying that LCTX-F2 also contains an ICK motif toxin (Zhang et al., 2010). The function of spider toxin 35 family members is not known, except that of purotoxin-2, which has been shown to act on ion channels (Liang, 2004; Liang, 2008; Kabanova et al., 2012).

In this study, LCTX-F2 significantly reduced the plasma recalcification time and APTT in a dose-dependent manner. Results of the SPR assay indicated that LCTX-F2 is a novel agonist that has affinity for, and directly interacts with, FXIIa, kallikrein, thrombin, and FXa. Moreover, LCTX-F2 did not enhance the activity of plasmin, trypsin, or FVIIa, or reduce platelet aggregation time. Evaluation of the effect of LCTX-F2 on traumatic hemorrhage in liver bleeding and tail bleeding mouse models showed that LCTX-F2 exhibited a more significant procoagulant effect than EACA at the same dosage. Furthermore, cytotoxicity and hemolysis assays

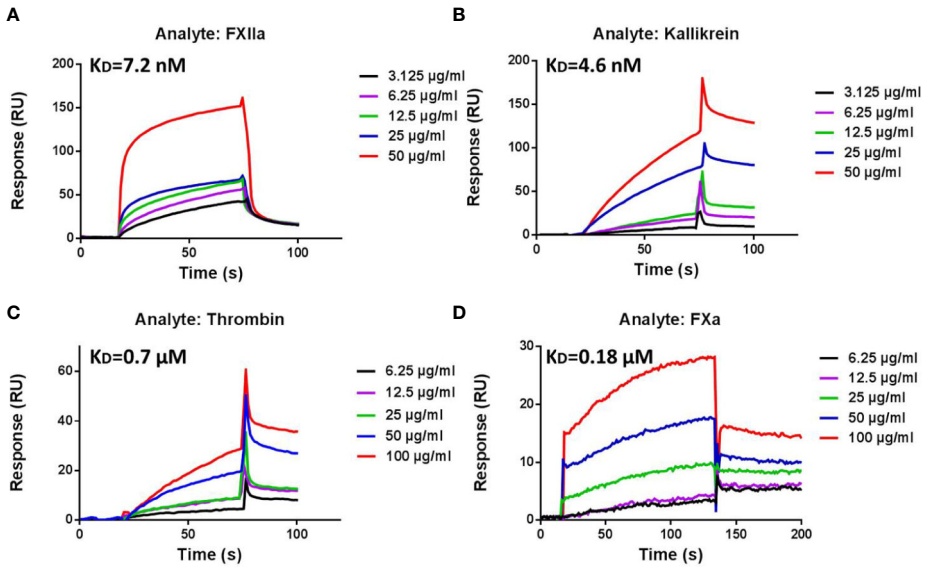

FIGURE 4 | Surface plasmon resonance (SPR) sensorgrams of interactions between LCTX-F2 and coagulation factors. The concentration of LCTX-F2 to FXIIa **(A)**, kallikrein **(B)**, thrombin **(C)**, and FXa **(D)** (from bottom to top) was 0, 3.125, 6.25, 12.5, 25, 50, and 100 μg/ml, respectively. Curves were analyzed with BIAevaluation software.

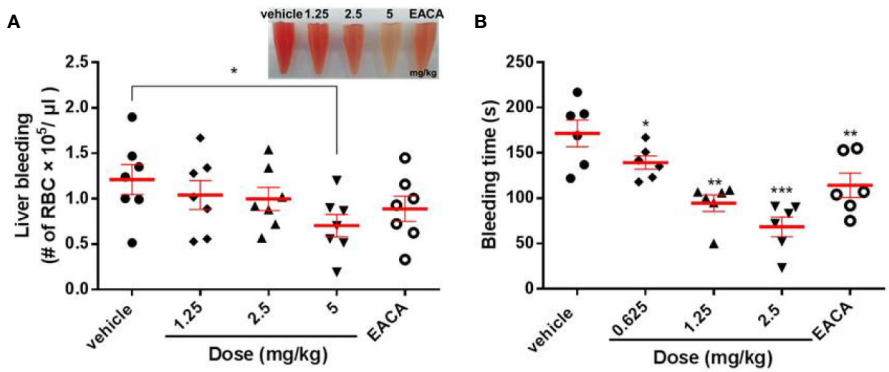

FIGURE 5 | The effect of LCTX-F2 on bleeding model *in vivo*. The hemostatic effect of LCTX-F2 (0.65, 1.25, and 2.5 mg/kg) and 5 mg/kg EACA were measured in liver bleeding **(A)** and tail bleeding **(B)** mouse models. **(A)** The number of red blood cells (RBCs) was counted to determine the effect of LCTX-F2 and EACA (n = 7). RBCs are shown in **(A)**. **(B)** Bleeding time was determined as the time from tail transection to the moment the blood flow stopped for 120 s (n = 6). Data are presented as means ± SD. $^{*}P < 0.05$, $^{**}P < 0.01$, $^{***}P < 0.001$ compared with vehicle as determined by the two-sample Student's t-test.

indicated that LCTX-F2 exerted no cytotoxic or hemolytic effects on normal cells.

Hemostasis is a complex physiological process encompassing initiation, amplification, propagation, and stabilization (Macfarlane, 1964). Hemostasis has also been traditionally classified into intrinsic and extrinsic pathways, and a further pathway common to both (Grover and Mackman, 2019). The intrinsic pathway is triggered by activation of FXII, followed by the sequential proteolytic activation of FXI and FIX. Formation of the intrinsic Xase (a complex of FVIIIa and FIXa) leads to the formation of the intrinsic FXa; in turn, FXa and FVa form the prothrombinase complex that catalyzes the cleavage of prothrombin (FII) to thrombin (FIIa). Thrombin is the terminal coagulation factor that cleaves soluble fibrinogen to insoluble fibrin. Procoagulant drugs such as factor-Xa like proteases, TXA, EACA, and kaolin have been used in clinical treatment. TXA and EACA, two antifibrinolytic agents, competitively inhibited the conversion of plasminogen to plasmin. Kaolin as an emergency trauma hemostatic agent could activate FXII

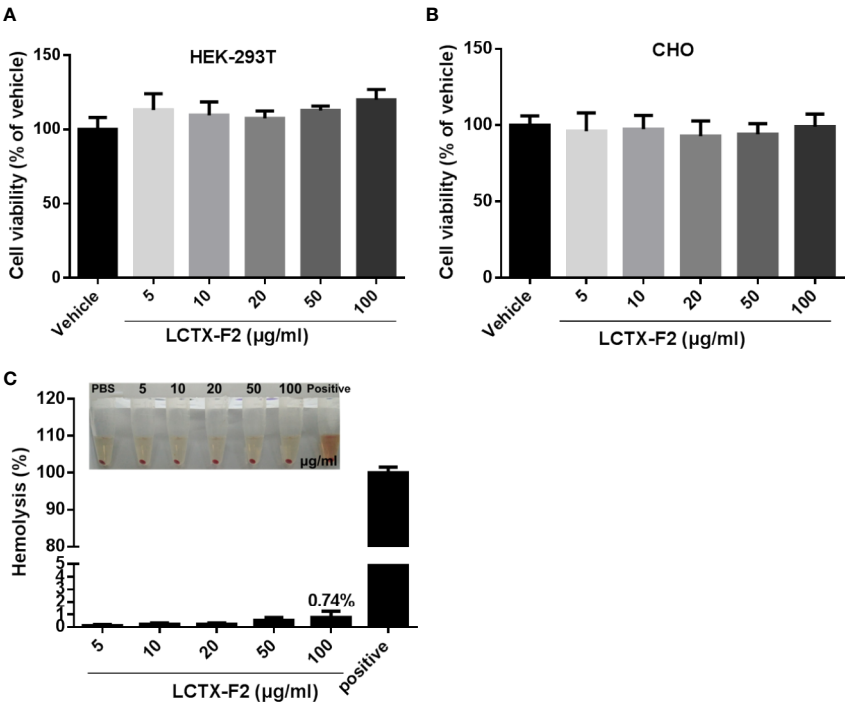

FIGURE 6 | The influence of LCTX-F2 on normal cells or cell lines. LCTX-F2 did not affect the viability of HEK-293T **(A)** or CHO **(B)** cells. **(C)** Incubation with LCTX-F2 (0–100 μg/ml) did not elicit hemolytic effects against red blood cells.

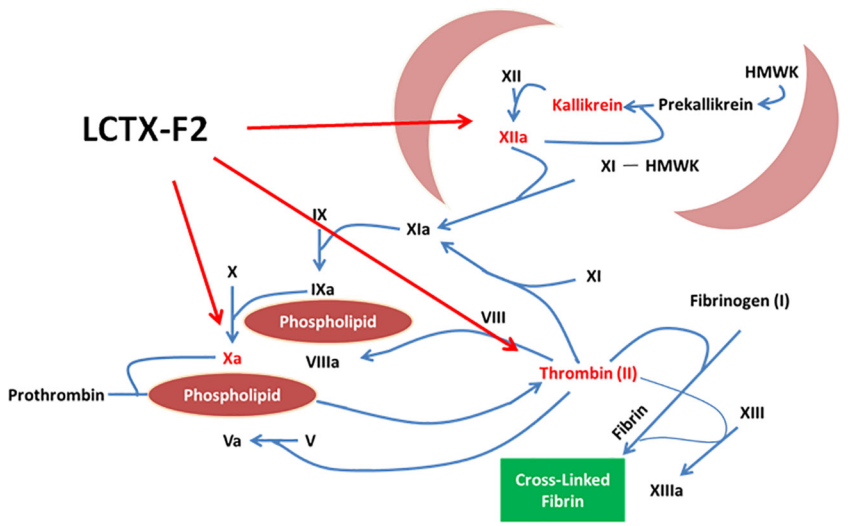

FIGURE 7 | LCTX-F2 promoted blood coagulation by increasing the activity of intrinsic blood coagulation factors, including FXIIa, kallikrein, thrombin, and FXa.

proenzyme into FXIIa. Factor X-like proteases from the venom of snakes (Siigur et al., 2001; Larreche et al., 2008; Sajevic et al., 2011; Khan and Al-Saleh, 2015) are either metalloproteases or serine proteases and could activate prothrombin to thrombin. In this study, LCTX-F2 promoted blood coagulation by increasing the activity of intrinsic blood coagulation factors, including FXIIa, kallikrein, thrombin, and FXa (**Figure 7**).To the best of our knowledge, LCTX-F2

is the first peptide activates coagulation factors and shortens blood coagulation time using mechanisms different from those previously reported for other proteins or drugs.

In summary, we identified LCTX-F2 as the first procoagulant peptide in spider venom. LCTX-F2 promoted coagulation by increasing the activity of blood coagulation factors. LCTX-F2 showed a better procoagulant activity than EACA and exhibited no cytotoxic or hemolytic activity against normal cells. LCTX-F2 may be a good candidate and/or template for the development of procoagulant drugs.

DATA AVAILABILITY STATEMENT

The LCTX-F2 sequence has been uploaded to GenBank of NCBI under the accession number BankIt 2321489 MT178457.

ETHICS STATEMENT

The animal study was reviewed and approved by the Animal Care and Use Committee at Kunming Institute of Zoology, Chinese Academy of Sciences (SMKX-20170210).

AUTHOR CONTRIBUTIONS

PL, ZZ, QL, and EM performed the experiments and analyzed the data. RL and MR conceived and supervised the project. PL, JM, RL, and MR prepared the manuscript. All authors contributed to the article and approved the submitted version.

FUNDING

This research was funded by the Education Department of Hunan Province (19A321), the National Natural Science Foundation of China (31971190, 81703400, 31801975), Huxiang High Level Talent Gathering Project (2018RS3071), Chinese Academy of Sciences (SAJC201606, ZSTH-034), and Science and Technology Department of Yunnan Province (2019ZF003, 2019FB040 and 2018ZF001).

SUPPLEMENTARY MATERIAL

The Supplementary Material for this article can be found online at: https://www.frontiersin.org/articles/10.3389/fphar.2020.00896/full#supplementary-material

REFERENCES

Alkjaersig, N., Fletcher, A. P., and Sherry, S. (1959). Epsilon Aminocaproic Acid - an Inhibitor of Plasminogen Activation. *Thromb. Et Diathesis Haemorrhag.* 3, 360–360.

Chaim, O. M., Da Silveira, R. B., Trevisan-Silva, D., Ferrer, V. P., Sade, Y. B., Boia-Ferreira, M., et al. (2011). Phospholipase-D activity and inflammatory response induced by brown spider dermonecrotic toxin: endothelial cell membrane phospholipids as targets for toxicity. *Biochim. Biophys. Acta* 1811, 84–96. doi: 10.1016/j.bbalip.2010.11.005

Flight, S. M., Johnson, L. A., Du, Q. S., Warner, R. L., Trabi, M., Gaffney, P. J., et al. (2009). Textilinin-1, an alternative anti-bleeding agent to aprotinin: Importance of plasmin inhibition in controlling blood loss. *Br. J. Haematol.* 145, 207–211. doi: 10.1111/j.1365-2141.2009.07605.x

Fry, B. G., Wickramaratana, J. C., Lemme, S., Beuve, A., Garbers, D., Hodgson, W. C., et al. (2005). Novel natriuretic peptides from the venom of the inland taipan (Oxyuranus microlepidotus): isolation, chemical and biological characterisation. *Biochem. Biophys. Res. Commun.* 327, 1011–1015. doi: 10.1016/j.bbrc.2004.11.171

Grover, S. P., and Mackman, N. (2019). Intrinsic Pathway of Coagulation and Thrombosis. *Arterioscler. Thromb. Vasc. Biol.* 39, 331–338. doi: 10.1161/ATVBAHA.107.155952

Gulliani, G. L., Hyun, B. H., and Litten, M. B. (1976). Blood recalcification time. A simple and reliable test to monitor heparin therapy. *Am. J. Clin. Pathol.* 65, 390–396. doi: 10.1093/ajcp/65.3.390

Jin, L., Fang, M., Chen, M., Zhou, C., Ombati, R., Hakim, M. A., et al. (2017). An insecticidal toxin from Nephila clavata spider venom. *Amino Acids* 49, 1237–1245. doi: 10.1007/s00726-017-2425-2

Jung, W.-K., and Kim, S.-K. (2009). Isolation and characterisation of an anticoagulant oligopeptide from blue mussel, Mytilus edulis. *Food Chem.* 117, 687–692. doi: 10.1016/j.foodchem.2009.04.077

Kabanova, N. V., Vassilevski, A. A., Rogachevskaja, O. A., Bystrova, M. F., Korolkova, Y. V., Pluzhnikov, K. A., et al. (2012). Modulation of P2X3 receptors by spider toxins. *Biochim. Biophys. Acta* 1818, 2868–2875. doi: 10.1016/j.bbamem.2012.07.016

Khan, S. U., and Al-Saleh, S. S. (2015). Biochemical characterization of a factor X activator protein purified from Walterinnesia aegyptia venom. *Blood Coagul. Fibrinolysis.* 26, 772–777. doi: 10.1097/MBC.0000000000000336

Konings, J., Govers-Riemslag, J. W. P., Philippou, H., Mutch, N. J., Borissoff, J. I., Allan, P., et al. (2011). Factor XIIa regulates the structure of the fibrin clot independently of thrombin generation through direct interaction with fibrin. *Blood* 118, 3942–3951. doi: 10.1182/blood-2011-03-339572

Larreche, S., Mion, G., and Goyffon, M. (2008). [Haemostasis disorders caused by snake venoms]. *Ann. Fr. Anesth. Reanim.* 27, 302–309. doi: 10.1016/j.annfar.2008.02.009

Liang, S. (2004). An overview of peptide toxins from the venom of the Chinese bird spider Selenocosmia huwena Wang [=Ornithoctonus huwena (Wang)]. *Toxicon* 43, 575–585. doi: 10.1016/j.toxicon.2004.02.005

Liang, S. (2008). Proteome and peptidome profiling of spider venoms. *Expert Rev. Proteom.* 5, 731–746. doi: 10.1586/14789450.5.5.731

Ma, H., Xiao-Peng, T., Yang, S. L., Lu, Q. M., and Lai, R. (2016). Protease inhibitor in scorpion (Mesobuthus eupeus) venom prolongs the biological activities of the crude venom. *Chin. J. Nat. Med.* 14, 607–614. doi: 10.1016/S1875-5364(16)30071-1

Macfarlane, R. G. (1964). An Enzyme Cascade in the Blood Clotting Mechanism, and Its Function as a Biochemical Amplifier. *Nature* 202, 498–499. doi: 10.1038/202498a0

Machado, L. F., Laugesen, S., Botelho, E. D., Ricart, C. A. O., Fontes, W., Barbaro, K. C., et al. (2005). Proteome analysis of brown spider venom: Identification of loxnecrogin isoforms in Loxosceles gaucho venom. *Proteomics* 5, 2167–2176. doi: 10.1002/pmic.200401096

Meng, P., Huang, H., Wang, G., Yang, S., Lu, Q., Liu, J., et al. (2016). A Novel Toxin from Haplopelma lividum Selectively Inhibits the NaV1.8 Channel and Possesses Potent Analgesic Efficacy. *Toxins (Basel)* 9, pii: E7. doi: 10.3390/toxins9010007

Nguyen, N., and Pandey, M. (2019). Loxoscelism: Cutaneous and Hematologic Manifestations. *Adv. Hematol.* 2019, 4091278. doi: 10.1155/2019/4091278

Sajevic, T., Leonardi, A., and Krizaj, I. (2011). Haemostatically active proteins in snake venoms. *Toxicon* 57, 627–645. doi: 10.1016/j.toxicon.2011.01.006

Santos, B. F., Serrano, S. M. T., Kuliopulos, A., and Niewiarowski, S. (2000). Interaction of viper venom serine peptidases with thrombin receptors on human platelets. *FEBS Lett.* 477, 199–202. doi: 10.1016/s0014-5793(00)01803-2

Schoenwaelder, S. M., Jarman, K. E., Gardiner, E. E., Hua, M., Qiao, J., White, M. J., et al. (2011). Bcl-xL-inhibitory BH3 mimetics can induce a transient thrombocytopathy that undermines the hemostatic function of platelets. *Blood* 118, 1663–1674. doi: 10.1182/blood-2011-04-347849

Siigur, E., Tonismagi, K., Trummal, K., Samel, M., Vija, H., Subbi, J., et al. (2001). Factor X activator from Vipera lebetina snake venom, molecular characterization and substrate specificity. *Biochim. Biophys. Acta* 1568, 90–98. doi: 10.1016/s0304-4165(01)00206-9

Tavares, F. L., Sousa-E-Silva, M. C., Santoro, M. L., Barbaro, K. C., Rebecchi, I. M., and Sano-Martins, I. S. (2004). Changes in hematological, hemostatic and biochemical parameters induced experimentally in rabbits by Loxosceles gaucho spider venom. *Hum. Exp. Toxicol.* 23, 477–486. doi: 10.1191/0960327104ht475oa

Tavares, F. L., Peichoto, M. E., Rangel Dde, M., Barbaro, K. C., Cirillo, M. C., Santoro, M. L., et al. (2011). Loxosceles gaucho spider venom and its sphingomyelinase fraction trigger the main functions of human and rabbit platelets. *Hum. Exp. Toxicol.* 30, 1567–1574. doi: 10.1177/0960327110393761

Tavares, F. L., Peichoto, M. E., Marcelino, J. R., Barbaro, K. C., Cirillo, M. C., Santoro, M. L., et al. (2016). Platelet participation in the pathogenesis of dermonecrosis induced by Loxosceles gaucho venom. *Hum. Exp. Toxicol.* 35, 666–676. doi: 10.1177/0960327115597983

Tilly, P., Charles, A. L., Ludwig, S., Slimani, F., Gross, S., Meilhac, O., et al. (2014). Blocking the EP3 receptor for PGE2 with DG-041 decreases thrombosis without impairing haemostatic competence. *Cardiovasc. Res.* 101, 482–491. doi: 10.1093/cvr/cvt276

Van Den Berg, C. W., Goncalves-De-Andrade, R. M., Magnoli, F. C., and Tambourgi, D. V. (2007). Loxosceles spider venom induces the release of thrombomodulin and endothelial protein C receptor: implications for the pathogenesis of intravascular coagulation as observed in loxoscelism. *J. Thromb. Haemost.* 5, 989–995. doi: 10.1111/j.1538-7836.2007.02382.x

Vives, M. A., Macian, M., Seguer, J., Infante, M. R., and Vinardell, M. P. (1997). Hemolytic action of anionic surfactants of the diacyl lysine type. *Comp. Biochem. Physiol. C. Pharmacol. Toxicol. Endocrinol.* 118, 71–74. doi: 10.1016/s0742-8413(97)00033-9

Wang, H., Ji, J., Zhang, W., Wang, W., Zhang, Y., Wu, Z., et al. (2010). Rat calvaria osteoblast behavior and antibacterial properties of O(2) and N(2) plasma-implanted biodegradable poly(butylene succinate). *Acta Biomater.* 6, 154–159. doi: 10.1016/j.actbio.2009.07.026

Willner, D., Spennati, V., Stohl, S., Tosti, G., Aloisio, S., and Bilotta, F. (2016). Spine Surgery and Blood Loss: Systematic Review of Clinical Evidence. *Anesth. Analg.* 123, 1307–1315. doi: 10.1213/ANE.0000000000001485

Yang, S., Liu, Z., Xiao, Y., Li, Y., Rong, M., Liang, S., et al. (2012). Chemical punch packed in venoms makes centipedes excellent predators. *Mol. Cell Proteom.* 11, 640–650. doi: 10.1074/mcp.M112.018853

Zakaria, E. R., Garrison, R. N., Kawabe, T., and Harris, P. D. (2005). Direct peritoneal resuscitation from hemorrhagic shock: Effect of time delay in therapy initiation. *J. Trauma.* 58, 499–507. doi: 10.1097/01.ta.0000152892.24841.54

Zhang, Y., Chen, J., Tang, X., Wang, F., Jiang, L., Xiong, X., et al. (2010). Transcriptome analysis of the venom glands of the Chinese wolf spider Lycosa singoriensis. *Zool. (Jena)* 113, 10–18. doi: 10.1016/j.zool.2009.04.001

Zhang, F. M., Liang, X. L., Pu, D., George, K. I., Holland, P. J., Walsh, S. T. R., et al. (2012). Biophysical characterization of glycosaminoglycan-IL-7 interactions using SPR. *Biochimie* 94, 242–249. doi: 10.1016/j.biochi.2011.10.015

Conflict of Interest: The authors declare that the research was conducted in the absence of any commercial or financial relationships that could be construed as a potential conflict of interest.

frontiers in Pharmacology

ORIGINAL RESEARCH
published: 02 February 2021
doi: 10.3389/fphar.2020.586705

Patagonin-CRISP: Antimicrobial Activity and Source of Antimicrobial Molecules in Duvernoy's Gland Secretion (*Philodryas patagoniensis* Snake)

Juliana Cuoco Badari[1], *Andrea Díaz-Roa*[2,3], *Marisa Maria Teixeira Rocha*[4], *Ronaldo Zucatelli Mendonça*[1] *and Pedro Ismael da Silva Junior*[2]*

[1]Laboratory of Parasitology, Butantan Institute, São Paulo, Brazil, [2]Laboratory for Applied Toxinology (LETA) - Center of Toxins, Immune-Response and Cell Signaling – CeTICS/CEPID Butantan Institute, São Paulo, Brazil, [3]Escuela de Ciencias Agrícolas, Pecuarias y del Medio Ambiente (ECAPMA), Universidad Nacional Abierta y a Distancia (UNAD), Bogotá, Colombia, [4]Laboratory of Herpetology, Butantan Institute, São Paulo, Brazil

OPEN ACCESS

Edited by:
Paula Gomes,
University of Porto, Portugal

Reviewed by:
Andreimar Martins Soares,
Fiocruz Rondonia, Brazil
Benjamin-Florian Hempel,
Charité Medical University of Berlin, Germany

***Correspondence:**
Pedro Ismael da Silva Junior
pisjr@butantan.gov.br

Specialty section:
This article was submitted to Experimental Pharmacology and Drug Discovery, a section of the journal Frontiers in Pharmacology

Received: 29 July 2020
Accepted: 16 December 2020
Published: 02 February 2021

Citation:
Badari JC, Díaz-Roa A, Teixeira Rocha MM, Mendonça RZ and Silva Junior PId (2021) Patagonin-CRISP: Antimicrobial Activity and Source of Antimicrobial Molecules in Duvernoy's Gland Secretion (Philodryas patagoniensis Snake). Front. Pharmacol. 11:586705. doi: 10.3389/fphar.2020.586705

Snake venom contains a variety of toxins with a range of biological activity, among these toxins cysteine-rich secreted proteins (CRISPs) can be found. The proteins of this family have masses of 20–30 kDa and display homologous amino acid sequences containing 16 cysteine residues, forming eight disulfide bonds. Some of these proteins have been explored, characterized, and described in terms of their activity; however, little is known about their range of activities. A search for new antimicrobial molecules is ongoing, as the number of microbial strains resistant to available antibiotics is increasing. We identified antimicrobial activity in the secretion of Duvernoy's gland of the rear-fanged *Philodryas patagoniensis*. Fractions of this venom were subjected to reverse-phase high performance liquid chromatography and analyzed to determine their antimicrobial activity with a liquid broth inhibition assay. One of the fractions presented activity against a Gram-negative bacterium and a filamentous fungus. This fraction was analyzed with LC-MS/MS, and a protein of 24,848.8 Da was identified. Database searches allowed us to identify it as a CRISP due to the presence of some unique fragments in the molecule. We called it patagonin-CRISP, as the same protein in the venom of *P. patagoniensis* had previously been characterized as having a different biological activity. Patagonin-CRISP presented activity at very low concentrations and showed no cytotoxic activity. This is the first time that antimicrobial activity has been identified for *P. patagoniensis* venom or for a CRISP family protein.

Keywords: CRISP, antimicrobial, bioprospecting, dipsadidae, snakes, toxin and patagonin-CRISP

INTRODUCTION

Microbial resistance is a major public health concern. Pathogenic microorganisms are responsible for countless deaths and generate huge financial losses worldwide. The increased resistance of microorganisms to antimicrobial agents is a serious public health problem that has aroused the attention of the pharmaceutical industry and led it to search for new types of antibiotics. The failure

of available antibiotics to contain certain pathogens indicates the need to develop more efficient and less toxic molecules from natural sources (Potron et al., 2015; Vassilara et al., 2017).

Brazil features a wealth of biomes that include a large part of the world's biodiversity; it is considered to have the highest number of endemic species (O'Driscoll et al., 2013), and one cannot deny its proliferation of natural products. These products have been extensively studied and much work have been done on different compounds of biological origin that may be usable in the development of new drugs and to improve existing diagnostic methodologies (Peichoto et al., 2007; Doley and Kini, 2009; Figueroa-Espinoza et al., 2015).

Studies have found antimicrobial activity in snake venom. This activity is linked to the need for self-protective mechanisms against pathogens present in their prey that are triggered by the innate immune system (Thomas and Pough, 1979; Osipov et al., 2005; Perumal Samy et al., 2017).

Venom from rear-fanged snakes, given their complexity and great pharmacological potential, is an interesting category to explore (Fry, 2005; Peichoto et al., 2011).

Philodryas patagoniensis is an opisthoglyphous snake, a member of the family Dipsadidae (Utkin, 2015). These snakes are distributed around all South America, inhabiting different environments, and they show high plasticity when adapting to places altered by man in addition to having an excellent ability to camouflage themselves due to their coloration (de Medeiros et al., 2010; Gouveia et al., 2017).

These snakes have a well-developed Duvernoy's gland, connected to their grooved teeth, which, although it is homologous to the venom glands of Solenoglyphous and Proteroglyphous snakes, are functionally and anatomically different (Kardong, 2002; Jackson and Vidal, 2019). Due to its musculature and lack of storage space, this gland produces a low amount of venom, which makes it challenging to study these materials, as it is difficult to obtain sufficient material to characterize it (Modahl and Mackessy, 2019).

Duvernoy's gland has an immediate function in feeding due to the presence of its serous cells, which, with the other components present in the toxic secretion, helps immobilize its prey, lubricates the food, and plays roles in digestive functions, antiputrefaction of the food, microbial neutralization, and oral hygiene (Taub, 1966; Serapicos and Merusse, 2006; Shivik and Carrion, 2009; Oliveira et al., 2016; Weinstein, 2016). The envenomation frame caused by *P. patagoniensis* includes local pain, swelling, erythema, ecchymosis, and regional lymphadenopathy with normal coagulation (Mosmann, 1983; Eberspaecher et al., 1995). These symptoms are often confused and treated as bothropic accidents (Silveira and Nishioka, 1992; Ribeiro et al., 1999).

The composition and biological activities of *P. patagoniensis* venom have previously been studied, and some of its components have been isolated and characterized (Hill and Mackessy, 2000; Peichoto et al., 2009; Peichoto et al., 2011; Peichoto et al., 2012).

One of these molecules is a cysteine-rich secretory protein (CRISP) called patagonin (Peichoto et al., 2012). CRISPs are a large family of single-chain bioactive polypeptides with a molecular mass between 20 and 30 kDa. The name of the group comes from the set of cysteine residues settled in its C-terminal region, establishing a compact domain (Eberspaecher et al., 1995). Cysteine-rich venom proteins (CRVPs) are widely distributed among lizard and snake venom (Adade et al., 2014).

The main characteristic here is the homology of the amino acid sequences, which contains 16 highly conserved cysteine residues, which form eight disulfide bonds; 10 of these Cys residues are in the C-terminal portion. In addition to the similarity of their molecular mass and the presence of Cys residues as distinctive structural features, they also have two distinct domains (PR-1 and CRD) (Tadokoro et al., 2020).

The C-terminal region includes the cysteine-rich domain (CRD), which is responsible for the interaction of CRISPs with the ionic channels. The sequence that makes up the N-terminal region is the most conserved among these proteins and belongs to the PR-1 domain. This domain promotes the interaction of these proteins with the target cell (Lima et al., 2006; Gibbs et al., 2008; Estrella et al., 2011; Tadokoro et al., 2020).

The biological activity of most snake venom CRISPs has not yet been described, and their role in envenomation is still uncertain; some studies suggest that they act as ion channel blockers (Silveira and Nishioka, 1992; Osipov et al., 2005; Utkin, 2015; Bernardes et al., 2019). Patagonin has already been characterized, and its biological activity has been described; it expresses necrotic activity in the murine gastrocnemius muscle when injected intramuscularly and has no effect on human platelet aggregation or proteolytic activity (Peichoto et al., 2009).

The CRISP Natrin, isolated from the venom of the snake *Naja atra*, promotes the regulation of the expression of adhesion molecules in endothelial cells that are involved in inflammation (Wang et al., 2010; Samy et al., 2014). Nk-CRISP is a CRVP isolated from the venom of another species of Naja that up regulates inflammatory gene expression in human macrophages (Deka et al., 2020).

Crovirin, isolated from *Crotalus viridis* venom, has been identified to have antiparasitic activity against different strains of Leishmania and Trypanosomes (Adade et al., 2014). The first CRISP from *Bothrops jararaca* has been isolated and denominated Bj-CRP, and it demonstrates possible action on the induction of inflammatory response (Levinskaite, 2012). A CRVP from the *Bothrops alternatus* venom was characterized as having effects on potassium channels and in inflammatory processes. This molecule was named BaltCRP (Bernardes et al., 2019).

The main objective of this study was to isolate, identify, and characterize at a primary structural level the antimicrobial molecules present in Duvernoy's gland secretion of *Philodryas patagoniensis*.

MATERIALS AND METHODS

Venom Samples

The venom was obtained from an adult female belonging to the Zoological Park Foundation of São Paulo. The extraction was performed using a pair of 100 μL microcapillary tubes placed in contact with the rear-fangs according to the procedure previously

described (Ferlan et al., 1983). During the extractions, the snake was not anesthetized, and no parasympathomimetic stimulants were used. In all, 16 extractions were performed, and each extraction had a variable yield between 30 and 60 µL.

Determination of Protein Concentration

The quantification of the samples was performed using Bradford's (1976) method, following the procedure described in the BIO-RAD protocol, with known concentrations of bovine albumin (Sigma) used as the standard.

Fractionation

Freeze-dried crude *P. patagoniensis* venom (~2 mg/ml) was homogenized in a 0.05% aqueous solution of TFA-trifluoroacetic acid and subjected to the reverse-phase high performance liquid chromatography (RP-HPLC) Shimadzu LC-10 system. In the first step, the sample was used for semipreparative Jupiter® RP-C18 LC-Column (10 µm, 300 Å, 10 mm × 129 250 mm, Phenomenex™) that had previously been balanced with A solvent (0.05% TFA). Elution was performed in a linear acetonitrile (ACN) gradient equilibrated in 0.05% TFA of 0–80% for 80 min at a flow rate of 2 ml/min. The absorbance was monitored at 225 and 280 nm, and the fractions were manually collected. Then, lyophilized fractions were suspended in 500 µL ultrapure water and an aseptically filtered in Millipore® 0.22 µm filters for antimicrobial assay.

The molecule here described (fraction 33) was submitted to a second step of fractionation in a linear gradient of ACN (20–55%) with 0.05% TFA for 80 min, at a flow rate of 1.0 ml/min and an analytic column Jupiter® C18 LC-Column (10 µm, 300 Å, 4.60 × 250 mm, Phenomenex™), with ACN equilibrated in 0.05% TFA. The hand-collected fractions were dried (Savant Instruments Inc.®) and suspended in 500 µL ultrapure water for MIC and MBC.

SDS-PAGE

Samples were submitted to 20% SDS-PAGE gel (sodium dodecyl sulfate-polyacrylamide gel electrophoresis). Then, 20 µg protein, solubilized in 20 µL ultrapure water and a sample buffer, was submitted to electrophoresis under reducing conditions. SeeBlue Prestained (Life Technologies R, 198–3 kDa) was used as a molecular mass marker. The proteins were stained with Coomassie Brilliant Blue R-250 (Laemmli, 1970) and Silver (Morrissey, 1981), and the gel images were captured with a photo documentation apparatus (UVITEC, Cambridge, United Kingdom). The protein band of interest was excised from the gel and eluted for antimicrobial activity and mass spectrometry analyses. The same band was digested with trypsin (Hanna et al., 2000) and analyzed by mass spectrometry.

Enzymatic In-Gel Digestion

The patagonin-CRISP bands were cut and stored separately in 1.5 ml microtubes. The band was destained in 0.5 ml 50% methanol/5% acetic acid overnight at room temperature before dehydration in 200 µL ACN, followed by complete drying in a vacuum centrifuge. The protein was reduced by adding 50 µL Dithiothreitol-DTT (10 mM) and alkylated by adding 50 µL iodoacetamide-IAA (100 mM) for 30 min at room temperature.

The bands underwent dehydration and rehydration using 200 µL ACN and 200 µL ammonium bicarbonate (100 mM), respectively. Finally, the bands were rehydrated in 50 µL with 20 ng μL^{-1} ice-cold porcine trypsin (Sigma-Aldrich®). Digestion was performed overnight at 37°C. The tryptic peptides produced were collected with successive extractions in 50 µL with 50 mM ammonium bicarbonate) and 50 µL with 50% ACN/5% formic acid (twice). The supernatant was concentrated in a vacuum centrifuge.

Mass Spectrometry

The samples were suspended in 10 µL 0.1% formic acid solution and analyzed by liquid chromatography coupled to tandem mass spectrometry (LC-MS/MS) using LTQ-Orbitrap Velos equipment (Thermo Fisher Scientific Inc.) coupled to the Easy-nLC II liquid nano-chromatography system (Thermo Fisher Scientific Inc.). A 5 µL sample was automatically injected into a C-18Jupiter C-18 (10 µm × 100 µm × 50 mm) precolumn (Phenomenex), coupled to an ACQUAC-18 analytical reverse phase column (5 µm × 75 µm × 100 mm) (Phenomenex). A linear gradient of 0–60% ACN for 60 min was used, with a flow rate of 200 nL/min. The ionization adopted was used in a positive mode that detects positively charged ions. The mass spectrometry proteomics data have been deposited to the ProteomeXchange Consortium via the PRIDE partner repository with the dataset identifier PXD022842.

Bioinformatics Analysis

The data were acquired by the Qual Browser program in XCalibur software (version 2.0; Thermo Fisher Scientific), using the default parameters, and the data were exported as text. The intact mass of protein was calculated with the deconvolution of m/z values from the MS spectra text file, performed with the software MagTran 1.02 (Zhang and Marshall,1998;Potron et al.,2015). The MagTran used a mass range of 3,000–30,000 and a charge range of 2–30. The raw data files were processed with a search on PEAKS Studio software (version 8.5, Bioinformatics Solutions Inc.). The analyses had a 10 ppm error tolerance for the precursor ions and a 0.6 Da tolerance for the fragment ions. Oxidation was considered a variable modification, and trypsin was considered to be enzyme-specific. The data were analyzed with cysteine carbamidomethylation as fixed modification and the oxidation of methionine as a variable modification. The MS/MS spectra were searched against the snakes, Dipsadidae, Colubridae, and CRVP databases (downloaded in FASTA format on October 20, 2019, from UniprotKB; http://www.uniprot.org/; 17,546, 3,867, 12,437, and 208 entries, respectively). The sequence obtained for the selected protein was subjected to similarity searches through the public NCBI (National Center for Biotechnology) database using the Basic Local Alignment Search Tool (Blast) to confirm the protein identity (Blast, 2020). To determine amino acid sequences, the LC-MS/MS files were loaded into PEAKS Studio software (Bioinformatics Solutions Inc.) and again subjected to analyses in the Uniprot databases.

Microorganisms and Antimicrobial Activity

Gram-positive and Gram-negative bacteria, fungi, and yeasts were tested for their sensitivity to the chromatographic fractions obtained from the *P. patagoniensis* secretion. The bacterial strains used for the tests were ATCC27853 *Pseudomonas aeruginosa* (Gram-negative) and ATCC6633 *Bacillus subitilis* (Gram-positive) from the American Type Culture Collection (ATCC), yeast MDM8 *Candida albicans* from the Department of Microbiology, University of São Paulo (USP), and the fungus *Penicillium expansum* (bread isolated). Microbial inoculum was prepared according to the method recommended by the standard M07-A9 from the Clinical and Laboratory Standards Institute (CLSI, 2012) in bacterial culture and described by NCCLS M38-P (NCCLS, 2002) for fungal inoculums.

The antimicrobial activity was monitored with a liquid growth inhibition assay (de Jesus Oliveira et al., 2019), performed on 96-well sterile microplates with a final volume of 100 µL. Aliquots of 20 µL fractions collected by HPLC were applied to each well, and 80 µL culture medium containing the suspension of a microorganism culture in log phase was added at a concentration of 1×10^5 CFU/ml. Ultrapure water was used as negative control, and the antibiotics Tetracycline and amphotericin B (10 mg/ml) were used as positive controls. Poor broth medium (1.0 g Peptone in 100 ml H_2O containing 86 mM NaCl, pH 7.2, 217mOsM) was used for bacterial strains, and poor dextrose potato broth (1.2 g potato dextrose in 100 ml H_2O, pH 5.0,79 mOsM) was used for fungus. Quality control was conducted for the water and the media with aliquots of 100 µL. The microplates were incubated at 30°C, and the bacteria were kept under stirring for 18 h, and the fungi were kept for 36 h without stirring. Microbial growth was evaluated according to the turbidity of the medium by measuring the optical density of the culture in a Victor^3 (1,420 Multilabel Counter/Victor^3, PerkinElmer) microplate reader at 595 nm.

The eluted fractions were placed in a liquid growth inhibition assay that inhibited the growth of the tested microorganisms and were screened based on the apparent expression of inhibition (turbidity reduction) and submitted to SDS-PAGE and subsequent mass spectrometry to verify homogeneity and purity.

MIC and MBC

MIC: After antimicrobial activity was confirmed for some fractions through the initial screening, they were submitted to a test of inhibition of microbial growth in liquid medium to determine the minimum inhibitory concentration (Antimicrobial-peptide-database, 2019). The MIC was performed using a sterile 96-well plate with a final volume of 100 µL. The purified fractions were serially diluted in ultrapure water, beginning with the same volume as the one where the sample showed activity (20 µL), and 80 µL inoculum with the medium solution was added. After 24 or 36 h incubation, the microplate was read at 595 nm absorbance, using a Victor^{3}microplate reader (1,420 Multilabel Counter/Victor3, PerkinElmer). MIC was defined as the minimum concentration of the peptide that causes 100% inhibition of the microorganism (Wiegand et al., 2008; Samy et al., 2014). The minimum inhibitory concentration (antimicrobial-peptide-database) is the concentration range between the maximum concentration of the tested peptide in which the microorganism is still growing and is the lowest concentration of the peptide that causes 100% microorganism death (Hetru and Bulet, 1997; Potron et al., 2015).

MBC: To determine the minimal bactericidal concentration (MBC), bacterial growth rates were measured after 96 h at 595 nm (Hancock, 1999; Yamamoto, 2003). The lowest concentration of the fractions that inhibited microbial growth was determined as MBC, indicating 99.5% of the initial inoculum. Microbial growth was monitored by increasing the optical density at 595 nm in a Victor^3 microplate reader (1,420 Multilabel Counter/Victor^3, PerkinElmer) modified from O'Driscoll et al. (2013). The assays were performed in triplicates.

MTT Assay in VERO Cells

The toxicity of patagonin-CRISP was evaluated in mammal cells, i.e., VERO cells (African green monkey kidney cells, *Cercopithecus aethiops*), using MTT assay (Molchanova et al., 2017). Cells were cultured at 37°C in T25 flasks containing 5 ml Leibovitz medium (L-15), supplemented with 10% fetal bovine serum, and kept in a CO_2 oven until reaching confluence. In the exponential phase, they were suspended in culture medium and counted in a hematocytometer to determine the cell concentration for plating. The cells were seeded in 96-well plates (2×10^5 cells/well) and cultured for 24 h. The molecule was tested with eight two-fold serial dilutions, starting from a concentration of 120 µg/ml, and cells were exposed to the varying concentrations of the molecule for 24 h. After this, 20 µL MTT (5 mg/ml in PBS) was added for another 4 h at 37°C. The formazan crystals were dissolved by adding 150 µL isopropanol, and the plate was incubated at room temperature until all crystals were dissolved. The cytotoxicity results were transformed into percentages in relation to the control (100% viability). For comparison between the treated and control groups, we used the ANOVA parametric.

Hemolytic Assay

Human red blood cells (hRBCs) were collected from a healthy donor in 0.15 M sodium citrate buffer pH 7.4, washed three times, and centrifuged (700× *g*, 15 min) in 0.15 M PBS (137 mM NaCl, 2.7 mMKCl, Na 2 HPO410 mM, 1.76 mM KH 2 PO 4, and pH 7.4). After the last centrifugation, the erythrocytes were suspended in PBS, pH 7.4.50 µL (120 µg/ml), and protein aliquots were tested in duplicate by adding 50 µL3% (v/v) solution of human erythrocytes in PBS on a U-bottom plate and incubated for 3 h at 37°C. The supernatant was transferred to a new flat-bottom microplate and used to determine the hemolytic activity of the protein with absorbance measurement at 405 nm in a Victor3 (1,420 Multilabel Counter/Victor3, PerkinElmer) plate reader. The percentage of hemolysis was expressed in relation to 100% of the lysis control (erythrocytes incubated with 0.1% triton X-100); PBS was used as a negative control.

TABLE 1 | Antimicrobial activity fractions from Duvernoy's gland secretion.

ACN%	Fraction	Microorganism			
		Pseudomanas aeruginosa ATCC27853	*Bacillus subitilis* ATCC6633	*Candida albicans* MDM8	*Penicillium expansum* (Bread isolated)
5	2	+	–	–	–
52	31	+	–	–	–
55	33	+	+	–	+

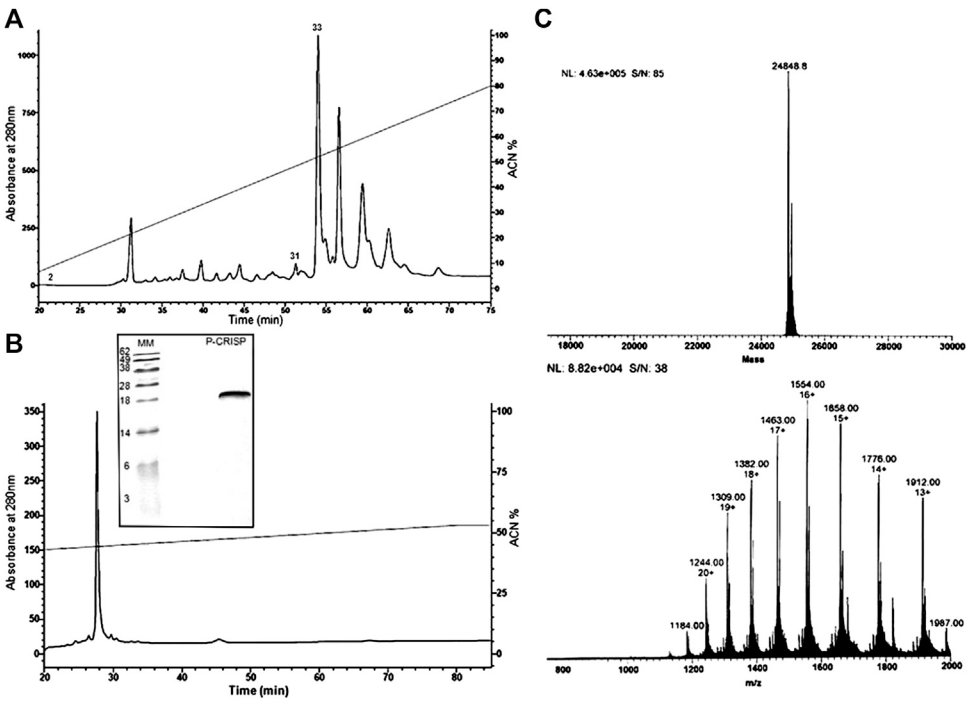

FIGURE 1 | Purification steps and molecular mass characterization. **(A)** Chromatographic profile of Duvernoy's gland secretion. Sample was subjected to a Jupiter® C18 semipreparative column (10 μm, 300 Å, 10 × 250 mm, Phenomenex™), with a 0–80% linear gradient of ACN in acidified water for 80 min at 2 ml/min flow rate. Absorbance was monitored at 280 and 225 nm. The fractions indicated by the numbers (2, 31 and 33) had antimicrobial activity. **(B)** Second step of purification by RP-HPLC. The chosen fraction (33) was subjected to an analytical column Jupiter® C18 (10 μm, 300 Å, 4.60 mm × 250, Phenomenex™) to check the homogeneity. The prominent peak was hand collected and submitted to a test of the inhibition of microbial growth in a liquid medium and mass analyzing. The SDS-PAGE analysis under reducing conditions shows a single band, with a mass of 25 kDa approximately, and confirms the fraction homogeneity. **(C)** Mass spectrometry analyses. The deconvolution of the ions revealed an m/z of 24,848.8 Da. The spectrum was submitted to the MagTran® software.

RESULTS

Fractionation of the Molecules from Durvenoy's Gland Secretion

After being extracted, Duvernoy's secretion was processed and submitted (2 mg/ml) to a fractionation step on a semipreparative C18 Júpiter® HPLC apparatus. In all, 80 fractions were eluted by the linear gradient of ACN (0–80%). All eluted molecules were tested against the microorganisms in a liquid growth inhibitory assay. Three fractions with antimicrobial activity were displayed (2, 31, and 33) (**Table 1**).

The fraction eluted with ≅55% CAN (fraction 33) was chosen for the characterization (**Figure 1A**). This fraction was active against *Pseudomonas aeruginosa* (ATCC27853), *Bacillus subitilis* (ATCC6633), and *Penicillium expansum* (isolated from bread) at a concentration of 240 μg/ml. Fraction homogeneity was assessed using RP-HPLC in an analytic column Júpiter® C18 LC-Column (**Figure 1B**). The fractions collected were retested, and the antimicrobial activity of the major peak was reconfirmed by the inhibition of microbial growth in a liquid medium.

The molecule was applied (20 μg) to SDS-PAGE 20% polyacrylamide under reducing conditions, where the mass was compared with the molecular weight marker (Life Technologies®). In the gel, the homogeneity of the sample was confirmed (**Figure 1B**), and the molecular mass obtained was between 28 and 18 kDa.

Protein Identification

Aliquots of molecules digested and not digested by trypsin were analyzed separately by mass spectrometry in an LC-MS/MS,

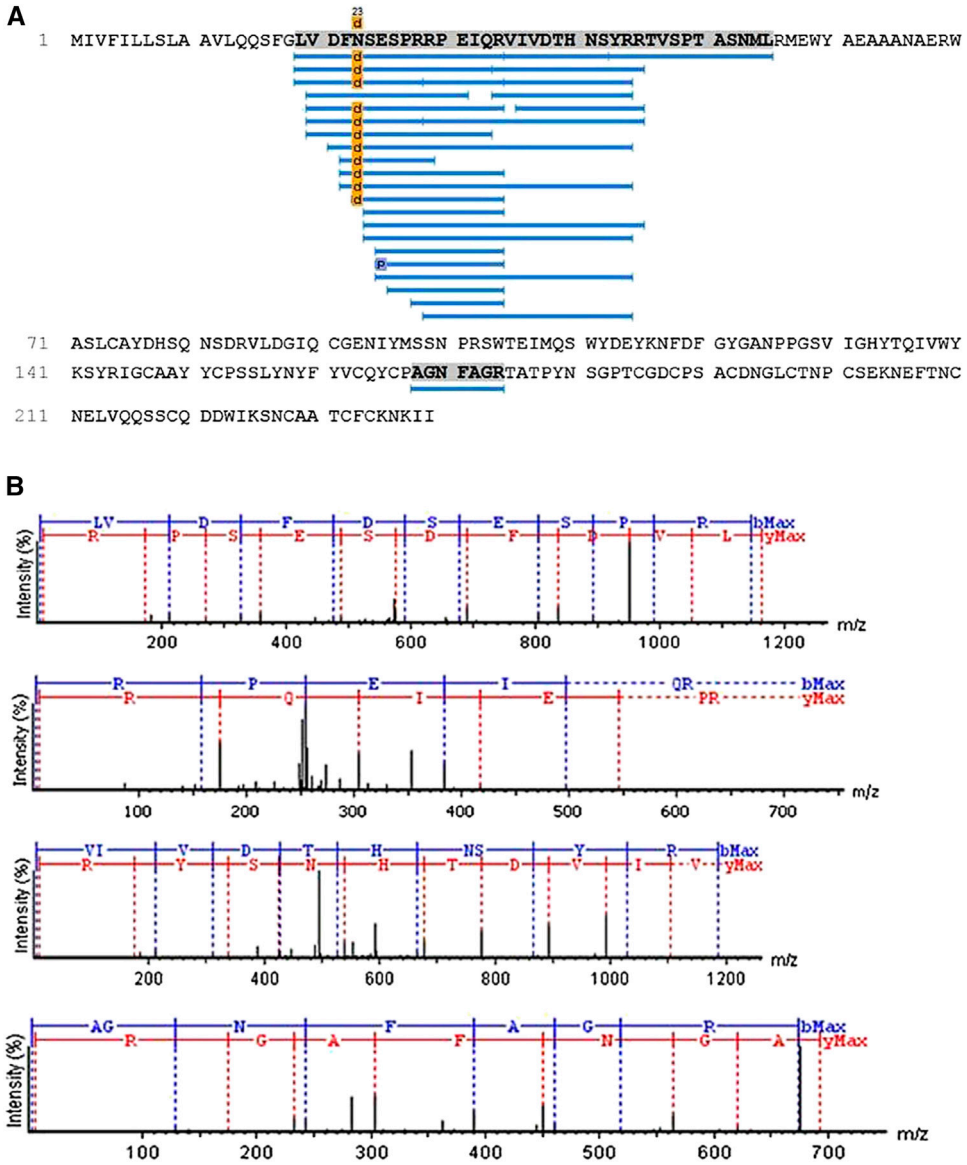

FIGURE 2 | Patagonin-CRISPidentification. **(A)** Through PEAKS Studio analyses with the Uniprot database, a cysteine-rich venom protein from *Philodryas olfersii* (AAZ75603.1) was identified by the presence of some unique fragments in our molecule. **(B)**The unique peptide fragments obtained with 99% ALC. The ions belonging to the y (red) and b (blue) series, indicated in the spectrum, correspond to the amino acid sequences of the peptide LVDFDSESPRRPEIQRVIVDTHNSYRR and AGNFAGR.

coupled with an LTQ-Orbitrap Velos. The analyses of the undigested molecule by MagTran® revealed a single protein with a mass (m/z) of 24,848.8 Da (**Figure 1A**), which corroborated the results obtained in SDS-PAGE analyses. Analyses of digested sample spectra with PEAKS Studio were used to compare the spectrum with Uniprot databases; keeping in mind that a unique peptide is defined as a peptide that exists only in one protein of interest, irrespective of length (Zhao and Lin, 2010), we identified a CRVP from *Philodryas olfersii* (AAZ75603.1) through the presence of unique fragments in our molecule (**Figure 2A**).

The analyses performed using PEAKS Studio allowed us to determine a peptide fragment of a primary structure of patagonin-CRISP, obtained with 99% average local confidence (ALC) from the N-terminal region, composed of 26 amino acids (LVDFDSESPRRPEIQRVIVDTHNSYRR). Another unique short fragment belonging to the C-terminal region has also been identified, and PEAKS Studio revealed a sequence composed of seven amino acids (AGNFAGR) (**Figure 2B**).

The N-terminal sequence was submitted to BLAST analyses using the BLAST protein function (BLASTp), which found a 100% identity and high reliability index with different fragments of CRVPs (sequence IDs: AJB84505.1, Q09GJ9.1, AAZ75604.1, P86537.1, P0MG5.1, and others). One of these is patagonin (P85099.1), a CRISP from Duvernoy's gland secretion of *P. patagoniensis* that was previously identified by Peichoto et al. (2009) and deposited in the database (Peichoto et al., 2009).

TABLE 2 | Minimum inhibitory concentration and minimum bactericidal concentration.

Microorganism	MIC (μg/ml)	μM	MBC (μg/ml)	μM
Pseudomanas aeruginosa (ATCC27853)	15–7.5	0.6–0.3	30–15	1.2–0.6
Penicillium expansum	7.5–3.7	0.3–0.15	30–15	1.2–0.6

MIC reports the minimum inhibitory concentration that is required to achieve 100% inhibition of microbial growth; MBC refers to the minimum inhibitory concentration that inhibits microbial growth after 96 h.

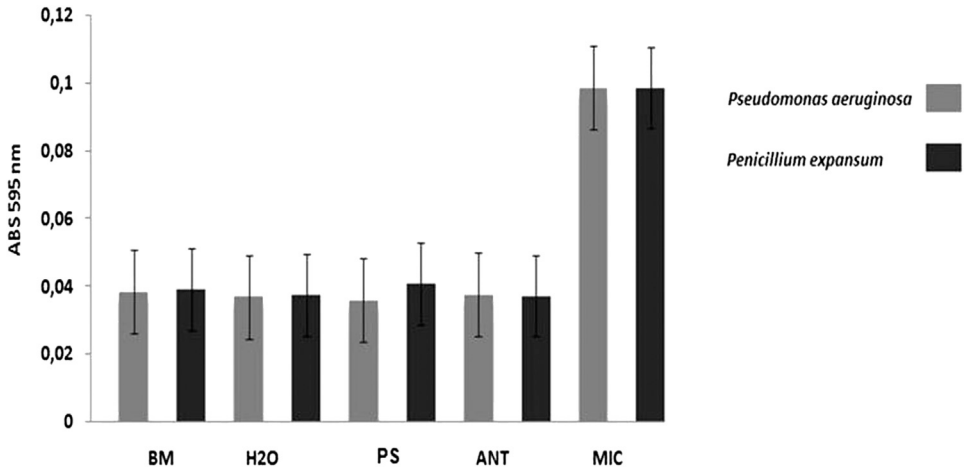

FIGURE 3 | Antimicrobial activity. In the graph it is possible to compare the results of the antimicrobial activity presented by the treatments with the samples in comparison to the controls. Result of antimicrobial assays against *Pseudomonas aeruginosa* ATCC27853 (MIC 1 –**in grey**) and *Penicillium expansum* (MIC2 –**in black**) by reading absorbance at 595 nm. **BM** –Broth medium (PB to bacteria and PDB to fungus): 100 μl; H2O –sterile ultrapure water: 100 μl; **MIC** –microorganism: 20 μl of sterile ultrapure water + culture medium with inoculums; **ANT** –antibiotics (Tetracycline to bacteriaand Anfotericin B to fungus): 20 μl ofantibiotic (10 mg/ml) + culture medium with inoculums; **PS** –protein sample (0.3 μM for **MIC 1** and 0.15 μM for **MIC 2**) in sterile ultrapure water: 20 μl of sample +culture medium with inoculums. **Obs.**: Microorganisms shown in sterile microplates with a lid. The bacteria, being aerobic organisms, were kept under agitation. The incubation period was 18 h for bacteria and 36 h for fungus, at 30°C (Orbital Shaker for Microplates).

Antimicrobial Assays

The antimicrobial activity of the native protein called patagonin-CRISP was screened against Gram-negative and Gram-positive bacteria, yeast, and fungus strains. The protein was active against *Pseudomonas aeruginosa* (ATCC27853) and *Penicillium expansum* (isolated from bread). The MIC of patagonin-CRISP was 15–7.5 μg/ml (0.6–0.3 μM) and 7.5–3.7 μg/ml (0.3–0.15 μM). The MBC was 30–15 μg/ml (1.2–0.6 μM) against both microorganisms (**Table 2**). The results of the absorbance readings of the plates are shown in **Figure 3**. To confirm the antimicrobial activity of patagonin-CRISP again, the eluted protein from the gel was retested at a certain concentration only against *Pseudomonas aeruginosa* (ATCC27853), and it exhibited its effects at 120 μg/ml (4.8 μM).

Cytotoxicity

Cells from the Vero line were used to test the cytotoxicity of patagonin-CRISP. Protein cytotoxicity was evaluated at the same concentration as the antimicrobial assay, and no sign of cytotoxicity was observed with patagonin-CRISP in the concentration range of 3–120 μg/ml. Viability was approximately 97% after treatment, and no morphological changes were observed. The obtained data were analyzed statistically with analyses of variance (Molchanova et al., 2017), followed by the Bonferroni post-test, executed in the Graph Pad Prism 5.0 software. The compiled results are presented in **Figure 4**.

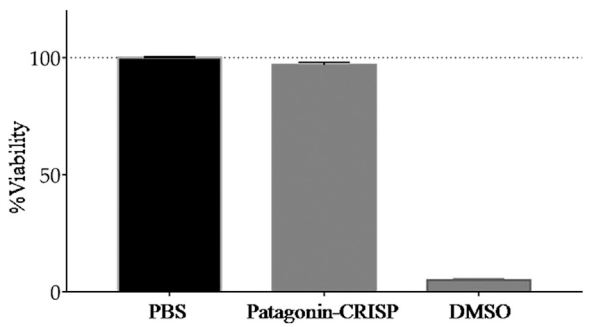

FIGURE 4 | Cytotoxicity analysis. MTT assay analysis of patagonin-CRISP against VERO cell line did not demonstrate significant cytotoxicity at <120 μg/ml concentrations.

Hemolytic activity was evaluated at a concentration of 120 μg/ml, the maximum concentration at which antimicrobial activity was tested, and no hemolytic activity was identified for human

red blood cells (results not shown); this suggests that at other concentrations (<120 μg/ml), it is not toxic.

Higher concentrations (>120 μg/ml) have not been tested due to the small amount of native protein available.

DISCUSSION

CRISPs are widely distributed in reptile venom (Mosmann, 1983; Utkin, 2015) and exhibit a wide range of activities. However, the biological activity of most CRVPs has not been described, and their roles in envenomation remain unknown (Osipov et al., 2005; Levinskaite, 2012; Adade et al., 2014; Samy et al., 2014). In this work, we found a CRISP with antimicrobial activity from Duvernoy's gland secretion of the *Philodryas patagoniensis* snake.

Using RP-HPLC and LC-MS/MS, we found a protein with a molecular mass of 24,848.8 Da or the mass range presented by CRISPs, which usually have weights of about 20–30 kDa (Eberspaecher et al., 1995; Osipov et al., 2005). CRISPs are a group of nonenzymatic, single-chain proteins with homologous amino acid sequences, containing 16 highly conserved cysteine residues in the C-terminal region, forming eight disulfide bridges. These features distinguish this family of proteins, which also has two distinct functional domains: C-terminal, that is, a cysteine-rich region, which includes an ion-channel regulation domain (Gibbs et al., 2008), and N-terminal region, which combines to form the CRISP, antigen 5, and PR-1domain (Gibbs et al., 2008).

The CRISP we identified using PEAKS Studio was found to be from *Philodryas olfersii* (AAZ75603.1) due to the presence of some unique fragments in our molecule. According to Zhao and Lin (2010), a fragment is defined as a single peptide that exists only in one protein of interest and that peptide may appear more than once in the protein's amino acid sequence. The analyses of patagonin-CRISP spectra obtained from PEAKS Studio led us to determine a peptide with 99% ALC. This peptide belongs to the N-terminal region of CRISP and is composed of 26 amino acids in the sequence LVDFDSESPRRPEIQRVIVDTHNSYRR. A unique short peptide belonging to the C-terminal region was also identified, and it is composed of seven amino acids (AGNFAGR). We decided to focus on the N-terminal peptide and submit it to BLAST protein analyses, which found 100% identity with other peptides unique to CRISPs. The application of the concept of unique peptides to the identification of proteins increases confidence in the results.

The amino acid sequence that makes up the N-terminal region characterizes the super-conserved domain of this protein group (Milne et al., 2003; Osipov et al., 2005; Modahl and Mackessy, 2019). One of the CRISPs found by BLASTp was patagonin (P85099.1), a CRVP purified from the venom of *P. patagoniensis*. Patagonin has a molecular mass of 24,858.64 Da and a peptide characterized by 14 amino acid residues (VDFDSESPRRPEIQ) (Peichoto et al., 2009). A subtle difference can be observed between the molecular masses of patagonin and patagonin-CRISP, probably due to a variation in the composition of the amino acids.

The composition and the biochemical and pharmacological properties of snake venom vary by species and even between individuals of the same species. Diet, season, age, sex, and habitat are directly related to these possible changes (Koh et al., 2006). Thus, locality differences can lead to species-specific variation in the genetic code and promoting minor changes in the amino acid sequence of proteins but without compromising conserved domains or their functions (Zamudio et al., 2016; Holding et al., 2018).

The domain belonging to the N-terminal is responsible for promoting interaction with the target cell (Milne et al., 2003; Osipov et al., 2005; Gibbs et al., 2008). It is also known that the PR-1 domain is related to antifungal activity and may also have antimicrobial activity, amplifying defense signals via sterols or effectors binding (Niderman et al., 1995; Tadokoro et al., 2020). However, this is the first time that antimicrobial activity has been reported for the CRISP family of proteins.

The toxins in snake venom have molecules of peptide and nonpeptide origin and with wide chemical and functional variability, and they have evident richness in bioactive compounds. Previous findings indicate that proteins isolated from snake venom can lead to the production of clinically and commercially viable drugs. For example, we have the antihypertensive Captopril, using a peptide extracted from *Bothrops jararaca* venom, and the antiplatelet agents Integrilin (eptifibatide) and Aggrastat (tirofiban), taken from the venom of *Sistrurus miliarius barbouri* and *Echis carinatus*, respectively (Cushman and Ondetti, 1991; Koh and Kini, 2012; Kini and Koh, 2020).

Other drugs are already under development, such as VRCTC-310-Onco, composed of two toxins, a crotoxin isolated from the poison of the *Crotalus durissus terrificus* and a cardiotoxin isolated from the poison of the *Naja atra* (Calderon et al., 2014).

Many studies have shown the antimicrobial potential of snake venom and their components (Perumalsamy et al., 2014). The venom of snakes from the families Viperidae and Elapidae has received the most exploration in the search for new antibiotics and exhibit a broad spectrum of activity against different microbial strains. At present, research is focused on combating resistant microorganisms that pose a threat to both public health and the economy (Bocian and Hus, 2020).

Patagonin-CRISP was screened against various strains of microorganisms with liquid growth inhibition assay. The microbial strains chosen are drawn from snakes' oral cavities or are of medical and economic relevance (Hetru and Bulet, 1997; Vassilara et al., 2017; Yin et al., 2017; Ghosh et al., 2018; Yadav et al., 2018).

The molecule acted against *Pseudomonas aeruginosa*, Gram-negative bacteria, and *Penicillium expansum*, a filamentous fungus. Four microbial strains were chosen to perform this screening to identify antimicrobial activity for the native protein. Because venom yields from rear-fangs snakes can be very low and we were using a native protein (Modahl and Mackessy, 2019), this provides a certain limitation on production until a synthetic protein is available.

The MIC obtained for patagonin-CRISP in this study suggested a potent activity with low concentrations (0.6–0.3 μM against *P.*

aeruginosa and 0.3–0.15 μM against *P. expansum*). The same was true for MBC, where the protein showed activity at concentrations below 1.2 μM, which means that a low quantity of the protein would be required to inhibit microbial growth; further, it does not show cytotoxicity and hemolytic activity at the concentrations tested. This result highlights the advantages of exploring the protein here identified, in view of the need for new effective substances, that can fight bacterial species that become resistant after a few days or even hours of exposure (Niderman et al., 1995; Overbeck et al., 2017; Gomes et al., 2018).

The identification of new antimicrobial agents originating from venom, which present different targets of action, together with the search for new routes of administration, makes this a very promising line of research (Bocian and Hus, 2020).

The mode of action of patagonin-CRISP remains unclear, but it is known that some CRVPs have already been characterized to inhibit several ion channels, which suggest that patagonin-CRISP might recognize and act on certain membrane targets (Martinac et al., 2008; Modahl and Mackessy, 2019). Our next step will be to express and obtain recombinant protein to allow it to be tested on a larger microbial spectrum so that we can investigate the mechanism of action of patagonin-CRISP.

Natural products are promising candidates against multidrug-resistant pathogens and for the suppression of biofilm formation due to their activities and low toxicity. They also can help the entry of other substances into cells, such as antibiotics, and act as antiresistance compounds to classic antibiotics (Dosler and Karaaslan, 2014).

CONCLUSION

These results indicate a new function of a CRVP and indicate a pharmacologically relevant substance for exploration. This article reports the identification of the first CRISP from *Philodryas patagoniensis* Duvernoy's gland secretion with antimicrobial activity against Gram-negative bacteria and filamentous fungus.

DATA AVAILABILITY STATEMENT

The datasets presented in this study can be found in online repositories. The names of the repository/repositories and accession number(s) can be found in the following: ProteomeXchange PRIDE repository, accession no: PXD022842.

ETHICS STATEMENT

The use of animals in this study was approved by the Butantan Institute Animal Ethics Committee, protocol number CEUA9997010416, Biodiversity Authorization and Information System (SISBIO) no 53845-1 and approved by the São Paulo Zoological Park Foundation through the craft number 181/2016/FPZSP, under the project registration no 385.

AUTHOR CONTRIBUTIONS

JB, PS, and RM were responsible for conceptualization; JB was responsible for data curation; JB, AD-R, and PS were involved in formal analysis; PS and RM were responsible for funding acquisition; JB performed investigation; JB, MT, PS, and RM were responsible for methodology; PS was involved in project administration; JB, AR, and PS were responsible for resources; PS and RM were involved in supervision; JB and PS were involved in validation; JB wrote the original draft; JB, AR, MT, PS, and RM wrote, reviewed, and edited the manuscript.

FUNDING

This research was funded by the Research Support Foundation of São Paulo (FAPESP), grant no. 2016/24867-1; FAPESP/CeTICS, grant no. 2013/07467-1; Brazilian National Technological and Scientific Development Council CNPq, grant no. 472744/2012-7.

ACKNOWLEDGMENTS

The authors would like to thank the Zoological Park of São Paulo, for ceding the specimen for extractions, especially to Cybele Sabino Lisboa and Junior Castro, for the assistance in the extractions. They also appreciate the referees for their critical review of the manuscript and to the colleagues of the laboratory who helped during the procedures.

REFERENCES

Adade, C. M., Carvalho, A. L., Tomaz, M. A., Costa, T. F., Godinho, J. L., Melo, P. A., et al. (2014). Crovirin, a snake venom cysteine-rich secretory protein (CRISP) with promising activity against Trypanosomes and Leishmania. *PLoS Negl. Trop. Dis.* 8 (10), e3252. doi:10.1371/journal.pntd.0003252

Antimicrobial-Peptide-Database. (2019). Available: http://aps.unmc.edu/AP/prediction/prediction_main.php. Accessed April 7th 2019].

Bernardes, C. P., Menaldo, D. L., Zoccal, K. F., Boldrini-França, J., Peigneur, S., Arantes, E. C., et al. (2019). First report on BaltCRP, a cysteine-rich secretory protein (CRISP) from Bothrops alternatus venom: effects on potassium channels and inflammatory processes. *Int. J. Biol. Macromol.* 140, 556–567. doi:10.1016/j.ijbiomac.2019.08.108

Blast. (2020). https://blast.ncbi.nlm.nih.gov/Blast.cgi (Accessed: 08 30, 2020). Available.

Bocian, A., and Hus, K. K. (2020). Antibacterial properties of snake venom components. *Chem. Pap.* 74 (2), 407–419. doi:10.1007/s11696-019-00939-y

Calderon, L. A., Sobrinho, J. C., Zaqueo, K. D., de Moura, A. A., Grabner, A. N., Mazzi, M. V., et al. (2014). Antitumoral activity of snake venom proteins: new trends in cancer therapy. *BioMed Res. Int.* 2014, 203639. doi:10.1155/2014/203639

CLSI (2012). Methods for dilution antimicrobial susceptibility tests for bacteria that grow aerobically, approved standard, 9th Edn., CLSI document M07-A9; Wayne, PA: USA, 2012. Clinical and Laboratory Standards Institute.

Cushman, D. W., and Ondetti, M. A. (1991). History of the design of captopril and related inhibitors of angiotensin converting enzyme. *Hypertension* 17 (4), 589–592. doi:10.1161/01.hyp.17.4.589

de Jesus Oliveira, T., Oliveira, U. C. D., and da Silva Junior, P. I. (2019). Serrulin: a Glycine-rich bioactive peptide from the Hemolymph of the Yellow Tityus serrulatus Scorpion. *Toxins* 11 (9), 517. doi:10.3390/toxins11090517

Deka, A., Sharma, M., Mukhopadhyay, R., Devi, A., and Doley, R. (2020). Naja kaouthia venom protein, Nk-CRISP, upregulates inflammatory gene expression in human macrophages. *Int. J. Biol. Macromol.* 160, 602–611. doi:10.1016/j.ijbiomac.2020.05.169

de Medeiros, C. R., Hess, P. L., Nicoleti, A. F., Sueiro, L. R., Duarte, M. R., de Almeida-Santos, S. M., et al. (2010). Bites by the colubrid snake *Philodryas patagoniensis*: a clinical and epidemiological study of 297 cases. *Toxicon* 56 (6), 1018–1024. doi:10.1016/j.toxicon.2010.07.006

Doley, R., and Kini, R. M. (2009). Protein complexes in snake venom. *Cell. Mol. Life Sci.* 66 (17), 2851–2871. doi:10.1007/s00018-009-0050-2

Dosler, S., and Karaaslan, E. (2014). Inhibition and destruction of *Pseudomonas aeruginosa* biofilms by antibiotics and antimicrobial peptides. *Peptides* 62, 32–37. doi:10.1016/j.peptides.2014.09.021

Eberspaecher, U., Roosterman, D., Kratzschmar, J., Haendler, B., Habenicht, U. F., Becker, A., et al. (1995). Mouse androgen-dependent epididymal glycoprotein CRISP-1 (DE/AEG): isolation, biochemical characterization, and expression in recombinant form. *Mol. Reprod. Dev.* 42 (2), 157–172. doi:10.1002/mrd.1080420205

Estrella, A., Sanchez, E. E., Galan, J. A., Tao, W. A., Guerrero, B., Navarrete, L. F., et al. (2011). Characterization of toxins from the broad-banded water snake Helicops angulatus (Linnaeus, 1758): isolation of a cysteine-rich secretory protein, Helicopsin. *Arch. Toxicol.* 85 (4), 305–313. doi:10.1007/s00204-010-0597-6

Ferlan, I., Ferlan, A., King, T., and Russell, F. E. (1983). Preliminary studies on the venom of the colubrid snake Rhabdophis subminatus (red-necked keelback). *Toxicon* 21 (4), 570–574. doi:10.1016/0041-0101(83)90137-x

Figueroa-Espinoza, M. C., Zafimahova, A., Alvarado, P. G. M., Dubreucq, E., and Poncet-Legrand, C. (2015). Grape seed and apple tannins: emulsifying and antioxidant properties. *Food Chem.* 178, 38–44. doi:10.1016/j.foodchem.2015.01.056

Fry, B. G. (2005). From genome to "venome": molecular origin and evolution of the snake venom proteome inferred from phylogenetic analysis of toxin sequences and related body proteins. *Genome Res.* 15 (3), 403–420. doi:10.1101/gr.3228405

Ghosh, T., Kumar Biswas, M., Roy, P., and Guin, C. (2018). Short review of different microflora from the oral cavity of snakes. *Applied Biological Chemistry*, 61 (1), 25–37. doi:10.1007/s13765-017-0333-5

Gibbs, G. M., Roelants, K., and O'Bryan, M. K. (2008). The CAP superfamily: cysteine-rich secretory proteins, antigen 5, and pathogenesis-related 1 proteins-roles in reproduction, cancer, and immune defense. *Endocr. Rev.* 29 (7), 865–897. doi:10.1210/er.2008-0032

Gomes, B., Augusto, M. T., Felicio, M. R., Hollmann, A., Franco, O. L., Goncalves, S., et al. (2018). Designing improved active peptides for therapeutic approaches against infectious diseases. *Biotechnol. Adv.* 36 (2), 415–429. doi:10.1016/j.biotechadv.2018.01.004

Gouveia, R. V., Novelli, I. A., Vieira, F. M., and Sousa, B. M. d. (2017). Morphological variation of Philodryas patagoniensis (Girard, 1858) (Serpentes, Dipsadidae) from Brazil, based on the study of pholidosis, coloration and morphometric features. *Biota Neotropica* 17, 256. doi:10.1590/1676-0611-bn-2016-0237

Hancock, R. E. W. (1999). Modifies MIC method for cationic antimicrobial peptides. Hancock Laboratory Methods. Department of Microbiology and Immunology, University of British Columbia. Available at: http://www.cmdr.ubc.ca/bobh/method/modified-mic-method-for-cationic-antimicrobial-peptides/

Hanna, S. L., Sherman, N. E., Kinter, M. T., and Goldberg, J. B. (2000). Comparison of proteins expressed by Pseudomonas aeruginosa strains representing initial and chronic isolates from a cystic fibrosis patient: an analysis by 2-D gel electrophoresis and capillary column liquid chromatography-tandem mass spectrometry. *Microbiology* 146, 2495–2508. doi:10.1099/00221287-146-10-2495

Hetru, C., and Bulet, P. (1997). Strategies for the isolation and characterization of antimicrobial peptides of invertebrates. *Methods Mol. Biol.* 78, 35–49. doi:10.1385/0-89603-408-9:35

Hill, R. E., and Mackessy, S. P. (2000). Characterization of venom (Duvernoy's secretion) from twelve species of colubrid snakes and partial sequence of four venom proteins. *Toxicon* 38 (12), 1663–1687. doi:10.1016/s0041-0101(00)00091-x

Holding, M. L., Margres, M. J., Rokyta, D. R., and Gibbs, H. L. (2018). Local prey community composition and genetic distance predict venom divergence among populations of the northern Pacific rattlesnake (Crotalus oreganus). *J. Evol. Biol.* 31 (10), 1513–1528. doi:10.1111/jeb.13347

Jackson, T., and Vidal, N. (2019). Snake venom in context: neglected clades and concepts. *Frontiers in Ecology and Evolution* 7, 332. doi:10.3389/fevo.2019.00332

Kardong, K. (2002). Colubrid snakes and Duvernoy's "venom" glands. *Toxin Rev.* 21, 1–19. doi:10.1081/TXR-120004739

Kini, R. M., and Koh, C. Y. (2020). Snake venom three-finger toxins and their potential in drug development targeting cardiovascular diseases. *Biochem. Pharmacol.* 181, 114105. doi:10.1016/j.bcp.2020.114105

Koh, C. Y., and Kini, R. M. (2012). From snake venom toxins to therapeutics--cardiovascular examples. *Toxicon* 59 (4), 497–506. doi:10.1016/j.toxicon.2011.03.017

Koh, D. C., Armugam, A., and Jeyaseelan, K. (2006). Snake venom components and their applications in biomedicine. *Cell. Mol. Life Sci.* 63 (24), 3030–3041. doi:10.1007/s00018-006-6315-0

Laemmli, U. K. (1970). Cleavage of structural proteins during the assembly of the head of bacteriophage T4. *Nature* 227 (5259), 680–685. doi:10.1038/227680a0

Levinskaite, L. (2012). Susceptibility of food-contaminating Penicillium genus fungi to some preservatives and disinfectants. *Ann. Agric. Environ. Med.* 19 (1), 85–89. doi:10.1111/jfq.12145

Lima, M. R., Ximenes, E. C., Luna, J. S., and Sant'Ana, A. E. G. (2006). The antibiotic activity of some Brazilian medicinal plants. *Revista Brasileira de Farmacognosia* 16, 300–306. doi:10.1590/s0102-695x2006000300004

Martinac, B., Saimi, Y., and Kung, C. (2008). Ion channels in microbes. *Physiol. Rev.* 88 (4), 1449–1490. doi:10.1152/physrev.00005.2008

Milne, T. J., Abbenante, G., Tyndall, J. D., Halliday, J., and Lewis, R. J. (2003). Isolation and characterization of a cone snail protease with homology to CRISP proteins of the pathogenesis-related protein superfamily. *J. Biol. Chem.* 278 (33), 31105–31110. doi:10.1074/jbc.M304843200

Modahl, C. M., and Mackessy, S. P. (2019). Venoms of rear-fanged snakes: new proteins and novel activities. *Front. Ecol. Evol.* 7 (279), 568. doi:10.3389/fevo.2019.00279

Molchanova, N., Hansen, P. R., and Franzyk, H. (2017). Advances in development of antimicrobial peptidomimetics as potential drugs. *Molecules* 22 (9). doi:10.3390/molecules22091430

Morrissey, J. H. (1981). Silver stain for proteins in polyacrylamide gels: a modified procedure with enhanced uniform sensitivity. *Anal. Biochem.* 117 (2), 307–310. doi:10.1016/0003-2697(81)90783-1

Mosmann, T. (1983). Rapid colorimetric assay for cellular growth and survival: application to proliferation and cytotoxicity assays. *J. Immunol. Methods* 65 (1-2), 55–63. doi:10.1016/0022-1759(83)90303-4

NCCLSM38-P (2002). Reference method for broth dilution antifungal susceptibility testing of filamentous fungi; approved standard, 2nd Edn. M38-A (ISBN 1-56238-470-8). Wayne, PA: NCCLS.

Niderman, T., Genetet, I., Bruyere, T., Gees, R., Stintzi, A., Legrand, M., et al. (1995). Pathogenesis-related PR-1 proteins are antifungal. Isolation and characterization of three 14-kilodalton proteins of tomato and of a basic PR-1 of tobacco with inhibitory activity against Phytophthora infestans. *Plant Physiol.* 108 (1), 17–27. doi:10.1104/pp.108.1.17

O'Driscoll, N. H., Labovitiadi, O., Cushnie, T. P., Matthews, K. H., Mercer, D. K., and Lamb, A. J. (2013). Production and evaluation of an antimicrobial peptide-containing wafer formulation for topical application. *Curr. Microbiol.* 66 (3), 271–278. doi:10.1007/s00284-012-0268-3

Oliveira, L., Scartozzoni, R., Almeida-Santos, S., Jared, C., Antoniazzi, M., and Salomão, M. D. (2016). Morphology of Duvernoy's glands and Maxillary teeth and a possible function of the Duvernoy's gland secretion in Helicops modestus Günther, 1861 (serpentes: Xenodontinae). *South American Journal of Herpetology* 11, 54–65. doi:10.2994/SAJH-D-16-00011.1

Osipov, A. V., Levashov, M. Y., Tsetlin, V. I., and Utkin, Y. N. (2005). Cobra venom contains a pool of cysteine-rich secretory proteins. *Biochem. Biophys. Res. Commun.* 328 (1), 177–182. doi:10.1016/j.bbrc.2004.12.154

Overbeck, G. E., Bergallo, H. G., Grelle, C. E. V., Akama, A., Bravo, F., Colli, G. R., et al. (2017). Global biodiversity Threatened by Science budget cuts in Brazil. *BioScience* 68 (1), 11–12. doi:10.1093/biosci/bix130

Peichoto, M. E., Mackessy, S. P., Teibler, P., Tavares, F. L., Burckhardt, P. L., Breno, M. C., et al. (2009). Purification and characterization of a cysteine-rich secretory protein from Philodryas patagoniensis snake venom. *Comp. Biochem. Physiol. C Toxicol. Pharmacol.* 150 (1), 79–84. doi:10.1016/j.cbpc.2009.03.002

Peichoto, M. E., Tavares, F. L., Santoro, M. L., and Mackessy, S. P. (2012). Venom proteomes of South and North American opisthoglyphous (Colubridae and Dipsadidae) snake species: a preliminary approach to understanding their biological roles. *Comp. Biochem. Physiol. Genom. Proteonomics* 7 (4), 361–369. doi:10.1016/j.cbd.2012.08.001

Peichoto, M. E., Teibler, P., Mackessy, S. P., Leiva, L., Acosta, O., Goncalves, L. R., et al. (2007). Purification and characterization of patagonfibrase, a metalloproteinase showing alpha-fibrinogenolytic and hemorrhagic activities, from Philodryas patagoniensis snake venom. *Biochim. Biophys. Acta* 1770 (5), 810–819. doi:10.1016/j.bbagen.2006.12.014

Peichoto, M., Zychar, B., Tavares, F., Gonçalves, L., Acosta, O., and Santoro, M. (2011). Inflammatory effects of patagonfibrase, a metalloproteinase from Philodryas patagoniensis (patagonia green Racer; Dipsadidae) venom. *Exp. Biol. Med.* 236, 1166–1172. doi:10.1258/ebm.2011.011125

Perumal Samy, R., Stiles, B. G., Franco, O. L., Sethi, G., and Lim, L. H. K. (2017). Animal venoms as antimicrobial agents. *Biochem. Pharmacol.* 134, 127–138. doi:10.1016/j.bcp.2017.03.005

Perumalsamy, R., Manikandan, J., Sethi, G., Franco, O., Okonkwo, J., Stiles, B., et al. (2014). Snake venom proteins: development into antimicrobial and Wound healing agents. *Mini-Reviews Org. Chem.* 11, 756. doi:10.2174/1570193X1101140402100131

Potron, A., Poirel, L., and Nordmann, P. (2015). Emerging broad-spectrum resistance in *Pseudomonas aeruginosa* and Acinetobacter baumannii: mechanisms and epidemiology. *Int. J. Antimicrob. Agents* 45 (6), 568–585. doi:10.1016/j.ijantimicag.2015.03.001

Ribeiro, L. A., Puorto, G., and Jorge, M. T. (1999). Bites by the colubrid snake Philodryas olfersii: a clinical and epidemiological study of 43 cases. *Toxicon* 37 (6), 943–948. doi:10.1016/s0041-0101(98)00191-3

Samy, R. P., Kandasamy, M., Gopalakrishnakone, P., Stiles, B. G., Rowan, E. G., Becker, D., et al. (2014). Wound healing activity and mechanisms of action of an antibacterial protein from the venom of the eastern diamondback rattlesnake (*Crotalus adamanteus*). *PloS One* 9 (2), e80199. doi:10.1371/journal.pone.0080199

Serapicos, E. O., and Merusse, J. L. B. (2006). Morfologia e histoquímica das glândulas de Duvernoy e supralabial de seis espécies de colubrídeos opistoglifodontes (serpentes, Colubridae). *Papéis Avulsos de Zoologia* 46, 187–195. doi:10.1590/s0031-10492006001500001

Shivik, J., and Carrion, C. (2009). Decomposition, PubMed, and CsaAre vultures birds, and do snakes have venom, because of Macro- and Microscavenger conflict?. *BioScience* 56, 819–823. doi:10.1641/0006-3568(2006)56[819:AVBADS]2.0.CO;2

Silveira, P. V. P., and Nishioka, S. d. A. (1992). Non-venomous snake bite and snake bite without envenoming in a brazilian teaching hospital: analysis of 91 cases. *Revista do Instituto de Medicina Tropical de São Paulo* 34, 499–503.

Tadokoro, T., Modahl, C. M., Maenaka, K., and Aoki-Shioi, N. (2020). Cysteine-rich secretory proteins (CRISPs) from venomous snakes: an overview of the functional Diversity in A large and underappreciated superfamily. *Toxins* 12 (3), 4569. doi:10.3390/toxins12030175

Taub, A. M. (1966). Ophidian cephalic glands. *J. Morphol.* 118 (4), 529–542. doi:10.1002/jmor.1051180406

Thomas, R. G., and Pough, F. H. (1979). The effect of rattlesnake venom on digestion of prey. *Toxicon* 17 (3), 221–228. doi:10.1016/0041-0101(79)90211-3

Utkin, Y. N. (2015). Animal venom studies: current benefits and future developments. *World Journal of Biological Chemistry* 6 (2), 28–33. doi:10.4331/wjbc.v6.i2.28

Vassilara, F., Galani, I., Souli, M., Papanikolaou, K., Giamarellou, H., and Papadopoulos, A. (2017). Mechanisms responsible for imipenem resistance among *Pseudomonas aeruginosa* clinical isolates exposed to imipenem concentrations within the mutant selection window. *Diagn. Microbiol. Infect. Dis.* 88 (3), 276–281. doi:10.1016/j.diagmicrobio.2017.04.005

Wang, Y. L., Kuo, J. H., Lee, S. C., Liu, J. S., Hsieh, Y. C., Shih, Y. T., et al. (2010). Cobra CRISP functions as an inflammatory modulator via a novel Zn2+- and heparan sulfate-dependent transcriptional regulation of endothelial cell adhesion molecules. *J. Biol. Chem.* 285 (48), 37872–37883. doi:10.1074/jbc.M110.146290

Weinstein, S. A. (2016). "Non-front-Fanged colubroid ("Rear-Fanged") snakes," in *Critical care toxicology*. Editors J. Brent, K. Burkhart, P. Dargan, B. Hatten, B. Megarbane, and R. Palmer (Cham: Springer International Publishing)), 1–41.

Wiegand, I., Hilpert, K., and Hancock, R. E. (2008). Agar and broth dilution methods to determine the minimal inhibitory concentration (MIC) of antimicrobial substances. *Nat. Protoc.* 3 (2), 163–175. doi:10.1038/nprot.2007.521

Yadav, A. K., Sirohi, P., Saraswat, S., Rani, M., Singh, M. P., Srivastava, S., et al. (2018). Inhibitory mechanism on combination of phytic acid with methanolic seed extract of Syzygium cumini and sodium chloride over Bacillus subtilis. *Curr. Microbiol.* 75 (7), 849–856. doi:10.1007/s00284-018-1457-5

Yamamoto, L. G. (2003). Inhibitory and bactericidal principles (MIC & MBC), in case based pediatrics for medical students and residents. *Chap. V. I.4*, University of Hawaii. John, A. Burns School of Medicine. Available at: www.hawaii.edu/medicine/pediatrics/pedtext/s06c04.html

Yin, G., Zhang, Y., Pennerman, K. K., Wu, G., Hua, S. S. T., Yu, J., et al. (2017). Characterization of blue Mold Penicillium species isolated from stored fruits using multiple highly conserved loci. *J Fungi (Basel)* 3 (1), 753. doi:10.3390/jof3010012

Zamudio, K. R., Bell, R. C., and Mason, N. A. (2016). Phenotypes in phylogeography: Species' traits, environmental variation, and vertebrate diversification. *Proc. Natl. Acad. Sci. USA* 113 (29), 8041–8048. doi:10.1073/pnas.1602237113

Zhang, Z., and Marshall, A. G. (1998). A universal algorithm for fast and automated charge state deconvolution of electrospray mass-to-charge ratio spectra. *J. Am. Soc. Mass Spectrom.* 9 (3), 225–233. doi:10.1016/s1044-0305(97)00284-5

Zhao, Y., and Lin, Y.-H. (2010). Whole-cell protein identification using the concept of unique peptides. *Dev. Reprod. Biol.* 8, 33–41. doi:10.1016/S1672-0229(10)60004-6

Conflict of Interest: The authors declare that the research was conducted in the absence of any commercial or financial relationships that could be construed as a potential conflict of interest.

frontiers | Frontiers in Pharmacology

TYPE Review
PUBLISHED 27 September 2022
DOI 10.3389/fphar.2022.1001553

OPEN ACCESS

EDITED BY
Michelle Yap,
Monash University Malaysia, Malaysia

REVIEWED BY
Goran Gajski,
Institute for Medical Research and Occupational Health, Croatia
Woojin Kim,
Kyung Hee University, South Korea

*CORRESPONDENCE
Peiying Shi,
peiyshi@126.com
Hong Yao,
hongyao@mail.fjmu.edu.cn

†These authors have contributed equally to this work

SPECIALTY SECTION
This article was submitted to Experimental Pharmacology and Drug Discovery, a section of the journal Frontiers in Pharmacology

RECEIVED 23 July 2022
ACCEPTED 29 August 2022
PUBLISHED 27 September 2022

CITATION
Shi P, Xie S, Yang J, Zhang Y, Han S, Su S and Yao H (2022), Pharmacological effects and mechanisms of bee venom and its main components: Recent progress and perspective. *Front. Pharmacol.* 13:1001553. doi: 10.3389/fphar.2022.1001553

Pharmacological effects and mechanisms of bee venom and its main components: Recent progress and perspective

Peiying Shi[1,2]*†, Shihui Xie[1†], Jiali Yang[1], Yi Zhang[1], Shuo Han[1], Songkun Su[1] and Hong Yao[3]*

[1]Department of Traditional Chinese Medicine Resource and Bee Products, College of Animal Sciences (College of Bee Science), Fujian Agriculture and Forestry University, Fuzhou, China, [2]State and Local Joint Engineering Laboratory of Natural Biotoxins, Fujian Agriculture and Forestry University, Fuzhou, China, [3]Department of Pharmaceutical Analysis, School of Pharmacy, Fujian Medical University, Fuzhou, China

Bee venom (BV), a type of defensive venom, has been confirmed to have favorable activities, such as anti-tumor, neuroprotective, anti-inflammatory, analgesic, anti-infectivity effects, etc. This study reviewed the recent progress on the pharmacological effects and mechanisms of BV and its main components against cancer, neurological disorders, inflammatory diseases, pain, microbial diseases, liver, kidney, lung and muscle injury, and other diseases in literature during the years 2018–2021. The related target proteins of BV and its main components against the diseases include Akt, mTOR, JNK, Wnt-5α, HIF-1α, NF-κB, JAK2, Nrf2, BDNF, Smad2/3, AMPK, and so on, which are referring to PI3K/Akt/mTOR, MAPK, Wnt/β-catenin, HIF-1α, NF-κB, JAK/STAT, Nrf2/HO-1, TrkB/CREB/BDNF, TGF-β/Smad2/3, and AMPK signaling pathways, etc. Further, with the reported targets, the potential effects and mechanisms on diseases were bioinformatically predicted via Kyoto Encyclopedia of Genes and Genomes (KEGG) pathway, disease ontology semantic and enrichment (DOSE) and protein-protein interaction (PPI) analyses. This review provides new insights into the therapeutic effects and mechanisms of BV and its main components on diseases.

KEYWORDS

bee venom, melittin, phospholipase A_2, pharmacological effect, effect mechanism, bioinformatic analysis

Introduction

Under the dual selection of natural selection and genetic evolution, the animal kingdom has long evolved a unique defensive venom system (Casewell et al., 2013). Bee venom (BV), a type of defensive venom, is generated in the bee's venom glands and stored in the abdominal poison sac. (e.g., *Apis mellifera*) (Aufschnaiter et al., 2020). BV is a clear liquid with bitter taste, strong fragrance, pH value at 4.5–5.5, and specific gravity of 1.13, which is prone to volatilize and crystallize in the air (Khalil et al., 2021). BV contains

smaller proteins, peptides and enzymes such as melittin (MEL), apamin, phospholipase A_2 (PLA_2) and other components referring to amines, sugars and minerals (Aufschnaiter et al., 2020; Khalil et al., 2021).

Based on these active components, BV has multiple diverse pharmacological effects. Some reviews have retrieved the pharmacological progress on one or a few aspects of BV, mainly referring to anti-tumor (Dutta et al., 2019; Mirzaei et al., 2021), neuroprotective (El-Seedi H. R. et al., 2020), anti-inflammatory (Dutta et al., 2019), analgesic (Kim and Han, 2020), anti-infectivity effects (El-Seedi H. et al., 2020), improving wound healing (Kurek-Gorecka et al., 2021), and other effects. Recently, Khalil et al. (2021) also summarized the therapeutic effects of BV in treatment of cancers, multiple sclerosis, dementia, osteoarthritis, rheumatoid arthritis (RA), and wounds, etc. These demonstrates that BV has a wide range of clinical applications could be attributed to its multi-target and multi-pathway characteristics. However, so far, there is still a lack of comprehensive and systematic pharmacological analysis of BV with multiple targets and pathways, which is unbeneficial to understanding the integrative pharmacological effect and mechanism of BV and its main components on diseases.

In the past 10 years, bioinformatic analyses, e.g., Encyclopedia of Genes and Genomes (KEGG) pathway, disease ontology semantic and enrichment (DOSE) and protein-protein interaction (PPI) analyses, etc., have been widely used in the investigation fields of genomics and proteomics, due to that they can comprehensively discover the biological mysteries of large and complex biological data accounting for physiological and pathological alternations of organism, or changes of organism in response to external stimuli (Yu et al., 2015; Wen et al., 2022). For the bioinformatic analyses, differentially expressed miRNAs (differentially expressed genes (DEGs) or differentially expressed proteins (DEPs) from omics experiments are screened firstly, and KEGG and disease ontology (DO) databases can then be called online by R language platform with the screened DEGs or DEPs to identify enriched pathways and related diseases usually using a two-tailed Fisher's exact test. Meanwhile, all DEGs or DEPs can be searched against the STRING database for protein-protein interactions and can be visualized in R package to predict the key hub targets (genes or proteins). At present, by means of these bioinformatic ideas and tools, the potential therapeutic effects and mechanisms of several natural active ingredients, such as ginsenoside Rb_1, Re and Tanshinone IIA have been analyzed systematically and deeply through mining their reported targets and pathways from literature, which indeed provide a lot of inspiration and clues for the future study of these ingredients (Zhong et al., 2021; Cai et al., 2022; Lin et al., 2022). Reasonably, with the help of bioinformatic tools, it should also be able to comprehensively understand the therapeutic effects and potential targets and mechanisms of the main ingredients in BV by mining their reported targets and pathways from previous reports.

Hence, in this paper, articles published from 2018 to 2021 and archived in Web of Science and PubMed databases were searched mainly using the keywords "bee venom and pharmacology," supplemented with the keywords "bee venom and cancer" and "melittin and cancer," and the duplicate articles were excluded. Based on these articles, we reviewed the current progress mainly from year 2018–2021 on the investigation of pharmacological effects and mechanisms of BV and its main components, mainly MEL, $bvPLA_2$ and apamin. The reported action targets and pathways of them against cancer, neurological disorders, inflammatory diseases, pain, microbial diseases, liver, kidney, lung and muscle injury, and other diseases were summarized. Further, the possible anti-ill mechanisms of BV and its main components were comprehensively and systematically studied through DOSE, KEGG pathway, and PPI analyses according to the reported targets. The present study has deeply understood the pharmacological effects and mechanisms of BV and its main components against ills, which will help to promote the development and clinical application for BV.

Main components of bee venom

MEL, $bvPLA_2$ and apamin are three main components in BV, which are the important material basis for BV to exert its pharmacological effects, and their structures are shown in Figure 1.

Melittin

MEL is the dominant component, which is consisting of 26-residue peptide and representing about 40%–60% BV's dry weight (Wehbe et al., 2019). The carboxyl terminal of MEL contains positively charged amino acids, while the amino terminal is hydrophobic. Therefore, it contains both hydrophilic and hydrophobic properties. Both the MEL molecules and the membrane-bound MEL are through α spirally connected (Raghuraman and Chattopadhyay, 2007). Apart from its non-specific biofilm dissolution characteristics (Carpena et al., 2020), it has significant antibacterial, anti-tumor, and other effects (Pashaei et al., 2019; Yu et al., 2020).

Bee venom phospholipase A_2

PLA_2 is a 128 amino acids single polypeptide chain containing four disulfide bridges. The $bvPLA_2$ pertains to the group III secretory PLA_2 ($sPLA_2$) enzymes, accounting for 12%–15% of BV's dry weight (Wehbe et al., 2019; Carpena et al., 2020).

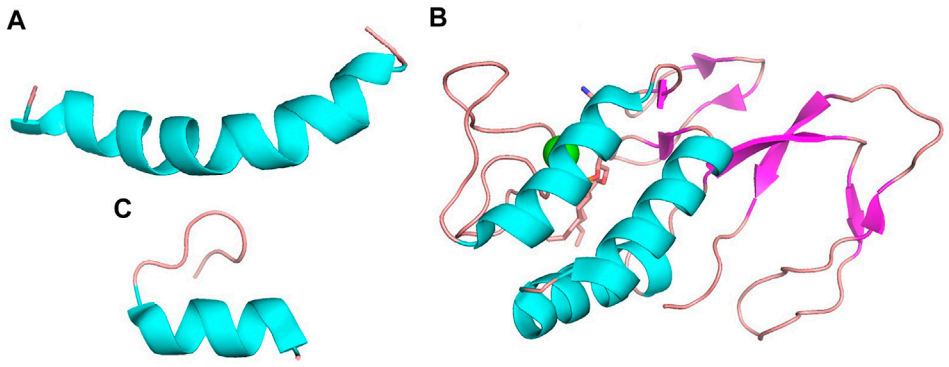

FIGURE 1
The structures of **(A)** MEL (PDB ID 6dst), **(B)** bvPLA$_2$ (PDB ID 1poc) and **(C)** apamin (PDB ID 7oxf). Structure **(A)** and **(C)** appear to be dominated by α-helix while structure **(B)** is dominated by a combination of α-helix and β-pleated sheet.

It hydrolyzes the sn-2 fatty acyl ester bond of membrane glycerol-3-phospholipids to liberate fatty acids and lysophospholipids, and this catalytic activity disrupts cell membranes, contributing to its anti-tumor, anti-infectivity, and other effects (Putz et al., 2007; Carpena et al., 2020). Besides, the abundant amino acids in bvPLA$_2$, leucine and lysine, promotes the phenomenon of neurotoxicity (Pattabhiramaiah et al., 2020).

Apamin

Apamin, an 18 amino acid peptide, makes up 2%–3% of its total dry weight (Gu et al., 2020). It is formed by a disulfide bond between two cysteines, which shapes its highly stable and compact chemical structure (Nguyen et al., 2015). Apamin has demonstrated the potential benefits in anti-atherosclerosis, anti-heart failure, and improvement of neurological disorders (Gu et al., 2020).

Anticancer effects

The incidence rate of cancer, the most serious cause of death, is constantly testing the global medical system's coping and resolving ability (Sung et al., 2021). The morbidity of many cancers, e.g., lung cancer, breast cancer, and colorectal cancer is still high, and the exploration of various forms, approaches and strategies of cancer treatment is still serious (Siegel et al., 2021). Animal-derived venoms are rich in a large number of active proteins and enzymes and have potential anticancer activities (Ejaz et al., 2018). As a promising natural product, BV and its main component MEL can regulate the cell cycle, change the permeability of cell membrane, inhibit the proliferation and migration, and promote endogenous/exogenous apoptosis and autophagy and other regulatory cell death modes to promote cell death (Mirzaei et al., 2021). Thus, it shows potential in strategies for inhibiting the occurrence and development of cancer and tumor (Wehbe et al., 2019; Carpena et al., 2020), as shown in Table 1, and the main affected targets and pathways in anticancer effects of BV is shown in Figure 2.

Anti-lung cancer research

In 2020, Lung cancer became the second most common malignancy worldwide with an incidence rate of 11.4% (Sung et al., 2021), mainly non-small cell lung cancer, occupying 80% of all new lung cancer cases (Sugarbaker and Dasilva, 2011). BV could inhibit epithelial-mesenchymal transition (EMT), increase the expression of vimentin, down-regulate the E-cadherin expression, and inhibit the recombination of F-actin related to the tumor metastasis in lung cancer A549, H1739 and H23 cells induced by epidermal growth factor (EGF). In A549 cells, BV decreased the phosphorylation of extracellular-regulated kinase (ERK), c-Jun N-terminal kinase (JNK), focal adhesion kinase (FAK) and mammalian target of rapamycin (mTOR), and eventually provoked the decrease of the transcription factors zinc finger E-box-binding homeobox 2 (ZEB2) and Slug in the EMT, suggesting its potential function in anti-cancer cell metastasis (Jeong et al., 2019). At the same time, as the main component of BV, MEL had a blockade effect on transforming growth factor-β (TGF-β), ERK and phosphorylated ERK in the ERK signaling pathway, resulting in the synthesis of Caspase-3 and Apaf-1 proteins that promoted apoptosis in A549 cells, and the cell growth, migration, invasion and other activities were blocked (Yu et al., 2020). Similarly, MEL also increased the apoptotic ratio in ChaGo-K1 of lung cancer, and the expression of mitogen activating protein-kinase activating

TABLE 1 Summary of the anti-cancer effects and mechanisms of BV and its main components.

BV and/or its components	Model	Cell/Animal (BV etc. administration)	Effects	Mechanisms	Reference
Lung cancer					
BV	Lung cancer	A549 (EGF induce; 0.1, 0.5, 1 and 2 μg/ml, for 1, 2, 12 and 24 h)	Inhibit cell migration and invasion; inhibit EMT	↓F-actin recombination; ↓EMT: ↑E-cadherin, ↓vimentin, ↓ZEB2, ↓Slug; ↓MARK pathway: ↓p-ERK, ↓p-JNK; ↓mTOR pathway: ↓p-FAK, ↓p-mTOR, ↓p-p70S6K, ↓p-4E-BP1	Jeong et al. (2019)
		H1739, H23 (EGF induce; 0.1, 0.5, 1 and 2 μg/ml, for 12 h)	Inhibit EMT	↓F-actin recombination; ↓EMT: ↑E-cadherin, ↓vimentin	
MEL	Lung cancer	A549, H358 (2 μg/ml, for 24, 48 and 72 h)	Inhibit cell growth, migration and invasion; induce apoptosis	↑Caspase-3, ↑Apaf-1; ↓ERK signaling pathway: ↓TGF-β, ↓ERK, ↓p-ERK	Yu et al. (2020)
		Male nude mice (5 mg/kg, local injection, once every 3 days for 21 days)	Inhibit tumor growth, prolong the survival time of mice	↓TGF-β, ↓ERK	
MEL	Lung cancer	ChaGo-K1 (0.7 and 2.5 μM, for 24 h)	Cell shrinkage and floating; inhibit cell proliferation and migration; promote apoptosis/necrosis; G0/G1 phase arrest	↑Bcl-2, ↓MADD	Tipgomut et al. (2018)
MEL	Lung cancer	A549/DDP (2, 4 and 8 μg/ml, for 48 h)	Inhibit the Warburg effect; inhibit cell growth and induce apoptosis	↓Tripartite motif-containing 8 (TRIM8); Akt pathway: ↓p-Akt	Zhang et al. (2021)
		Balb/c athymic nude mice (2 mg/kg, i.p., every 7 days for 3 weeks)	Inhibit tumor growth and reduce tumor size and mass; enhance the sensitivity of tumor and cells to cisplatin	—	
MEL	Lung cancer	NCI-H441 (0.5, 1, 2 and 4 μg/ml, for 24, 48 and 72 h)	Promote cell apoptosis, inhibit migration and invasion; inhibit cell growth	↓miR-183, ↓Bcl-2, ↑Caspase-2, ↑Bax	Gao et al. (2018)
		A549 (2 μg/ml, for 72 h)	Inhibit cell growth	—	
		Balb/c nu/nu mice (5 mg/kg, s.c., daily treated for 4 weeks)	Inhibit tumor growth	↑Caspase-2	
MLT@ZIF-8 NPs	Lung cancer, cervical carcinoma	A549 (2, 4 and 8 μg/ml, for 24 h)	Cells become smaller and round, chromatin condenses and nucleus shrinks; inhibit cell activity; promote apoptosis and reduce hemolysis	↑p53, ↑Bax, ↑Cyt C, ↑Caspase-3, ↑Caspase-9, ↓p-Akt, ↓PI3K, ↓Bcl-2	Li et al. (2018)
		HeLa (1, 2, 4, 6 and 8 μg/ml, for 24 h)	Inhibit cell activity	—	
		U14 tumor-bearing Kunming mice (MEL containing 1 mg/kg, i.v., daily treated for 3 days)	Inhibit tumor growth	—	
MpG@LPN	Lung cancer	A549 (5, 10, 15, 20 and 25 μg/ml, for 3, 24 and 48 h)	Induce apoptosis; reduce hemolysis and nonspecific cytotoxicity	↑Caspase-3	Ye et al. (2021)
		Female athymic nude mice (5 mg/kg, i.v., every other day for 5 times)	Inhibit tumor growth and reduce liver injury; improve tumor targeting ability	—	
Breast cancer					
BV, MEL, MEL and docetaxel	Breast cancer	SUM159 (2.5, 5, 5.58, 10, 15 and 20 ng/μL (BV), 2.5, 4.24, 5, 10, 15 and 20 ng/μL (MEL), for 1, 18 and 24 h)	The plasma membrane shrinks and is destroyed; reduce cell viability, induced cell death/apoptosis	PI3K/Akt and MAPK signaling pathway: ↑cleaved Capsase-3, ↑p-p44/42 MAPK, ↑p-Akt, ↓p-EGFR (BV). PI3K/Akt and MAPK signaling pathway: ↑cleaved Capsase-3, ↑p-p44/42 MAPK, ↑p-stress-activated protein kinase (SAPK)/JNK, ↑p-p38 MAPK, ↓p-EGFR, ↓p-Akt (MEL)	Duffy et al. (2020)
		SKBR3 (2.5, 5, 5.77, 10, 15 and 20 ng/μL (BV), 2.5, 5, 10, 15 and 20 ng/μL (MEL), for 1 and 24 h)	Reduce cell viability	PI3K/Akt and MAPK signaling pathway: ↓p-HER2, ↓p-EGFR,	

(Continued on following page)

TABLE 1 (*Continued*) Summary of the anti-cancer effects and mechanisms of BV and its main components.

BV and/or its components	Model	Cell/Animal (BV etc. administration)	Effects	Mechanisms	Reference
				↓p-p44/42 MAPK, ↓p-Akt, ↓p-SAPK/JNK, ↓p-p38 MAPK	
		MDA-MB-231 (2.5, 5, 10, 15 and 20 ng/μL (MEL), for 1 h)	—	↓p-EGFR, ↓p-MARK (MEL)	
		BALB/cJ female mice (5 mg/kg (MEL) and/or 7 mg/kg (docetaxel), intratumoral injection, on days 3, 5, 7, 9, 11, 13 and 15 post inoculation of T11 cells)	Reduce tumor cell proliferation; enhance cell sensitivity to docetaxel (MEL)	↓PD-L1, ↓p-EGFR, ↓p-HER2 (MEL)	
BV	Breast cancer, hepatocellular carcinoma	MDA-MB-231 (8, 12, 25, 50 and 100 μg/ml, for 45 min and 24 h)	Induce nuclear reduction; reduce cell viability; reduce mitochondrial membrane permeability; reduce 5meC and 5hmC; make 5 fC and 5caC increase first and then decrease	↓DNA methylation	Uzuner et al. (2021)
		HepG2 (8, 12, 25, 50 and 100 μg/ml, for 45 min and 24 h)	Reduce cell viability; reduce mitochondrial membrane permeability; increase mtDNA CNV; make 5meC, 5hmC, 5 fC and 5caC increase first and then decrease	↑DNA methylation	
BV	Breast cancer, lung cancer	MCF-7, A549 (for 24 h)	Inhibit cell proliferation; G1 phase arrest	↑H_2O_2; ↓Cyclin D1, ↓The nuclear translocation of NF-κB	Yoon et al. (2018)
MEL	Breast cancer	4T1, MCF-7 Mice (i.p.)	Inhibit cell viability Improve tumor radiosensitivity; inhibit tumor growth	↑Bax/Bcl-2 —	Chang et al. (2020)
MEL	Breast cancer	4T1 (0.125, 0.25, 0.5, 1, 2, 4, 8, 16 and 32 μg/ml, for 72 h)	Inhibit cell proliferation promote cell hemolysis and apoptosis	↑Mfn1, ↑Drp1	Moghaddam et al. (2020)
MEL	Breast cancer	MDA-MB-231 (5% O_2 induce; 1, 2 and 4 μg/ml, for 6 and 24 h)	Inhibit cell proliferation and induce apoptosis; adjust TME	↑Bax, ↑TNF-α ↓HIF-1α signaling pathway: ↓NF-κB, ↓HIF-1α, ↓LDHA, ↓VEGFA	Mir Hassani et al. (2021)
BV, MEL	Breast cancer	MCF-7 (0.1, 1, 10, 50 and 100 μg/ml (BV), 0.1, 1, 5, 10, 25 μg/ml (MEL), for 24 h)	Inhibit cell growth	—	Lischer et al. (2021)
BV (combined with hesperidin, piperine, tamoxifen)	Breast cancer	MCF-7, T47D (at a non-constant combination concentration, for 24 h)	Reduce cell viability and induce apoptosis; G2/M phase arrest	↑Bax, ↓Bcl-2, ↓ERα, ↓EGFR	Khamis et al. (2018)
BV, BV and *Annona muricata* fruit	Breast cancer	Wistar albino rats (N-methylnitrosourea induce; 75 μg/kg (BV), s.c., 2 dose of BV on the 4th and 16th day of gestation, 200 mg/kg (*A. muricata* fruit), from day 4 of pregnancy till weaning, 75 μg/kg (BV) and 200 mg/kg (*A. muricata* fruit))	Restore ovarian tissue structure and damage	↓MDA, ↑CAT, ↑SOD; ↓MMP-1, ↓NF-κB, ↓TNF-α, ↓p53, ↓Calretinin, ↑Caspase-3	El-Beltagy et al. (2021)
BV, BV and cisplatin	Breast cancer	4T1 (2, 4, 6, 8 and 10 μg/ml (BV), 5, 10, 15, 20, 25 and 30 μg/ml (cisplatin), 2, 4, 6, 8 and 10 μg/ml (BV) and 10 μg/ml (cisplatin), for 24 h)	Reduce cell viability and induce death; promote the cytotoxicity of cisplatin to cells	—	Arani et al. (2019)
MEL, MEL and plasma-treated phosphate buffered saline solution	Breast cancer, skin cancer (melanoma)	MCF-7, A375 (0.5, 1, 1.5 and 2 μg/ml (MEL), 0.5, 1, 1.5 and 2 μg/ml (MEL) and 10% (plasma-treated phosphate buffered saline solution), for 24 h)	Reduce cell viability; induce late apoptosis/necrosis and lipid peroxidation; inhibit tumor growth, reduce tumor size and mass	—	Shaw et al. (2019)

(Continued on following page)

TABLE 1 (*Continued*) Summary of the anti-cancer effects and mechanisms of BV and its main components.

BV and/or its components	Model	Cell/Animal (BV etc. administration)	Effects	Mechanisms	Reference
MEL loaded on FA-PENs	Breast cancer	MDA-MB-231 (15 μg/ml, for 24 and 48 h)	Lead to apoptosis and cell cycle arrest	↓Cyclin D1, ↓Bcl-2, ↓Caspase-8	Motiei et al. (2021)
MEL loaded on nGO, GN and ND	Breast cancer	MCF-7, MDA-MB-231 (10 mg/L (MEL), 20 mg/L (MEL) and 10 mg/L (GN), 20 mg/L (MEL) and 10 mg/L (nGO), 20 mg/L (MEL) and 10 mg/L (ND), for 24 h)	The cell bodies shriveled and cell protuberances were shortened; reduce cell metabolic activity; induce cell necrosis and apoptosis	↑ROS; ↑Bax, ↑high temperature requirement protease A (HTRA), ↑Caspase-3, ↑Caspase-8, ↓p21, ↓XIAP	Daniluk et al. (2020)
MEL loaded on niosome	Breast cancer	4T1 (72.42 μM (MEL), 97.41 μM (melittin-loaded niosome), for 72 h); SKBR3 (65.13 μM (MEL), 85.76 μM (melittin-loaded niosome), for 72 h)	Reduce cell viability; promote cell apoptosis, inhibit migration and wound healing	↑Caspase-3, ↑Caspase-9, ↑Bax, ↓MMP-2, ↓MMP-9, ↓Bcl-2	Moghaddam et al. (2021)
		Female BALB/c inbred mice (3 and 6 mg/kg (MEL), 1.5 and 3 mg/kg (melittin-loaded niosome), i.p., daily injection for 20 days)	Inhibit tumor growth, reduce tumor volume and the number of inflammatory cells in tumor; inhibit weight loss in mice	—	
MEL loaded on CA-MNPs	Breast cancer	MCF-7 (0.097, 0.195, 0.39, 0.781, 1.56, 3.125, 6.25 and 12.5 μg/ml, for 48 h)	Inhibit cell growth; improve the ability of magnetic targeting tumor	—	Hematyar et al. (2018)
MEL loaded on APNPs	Breast cancer	MDA-MB-231 (0.25, 0.5 and 1 μM, for 3 days)	Inhibit cell growth	—	Yu et al. (2018)
		Tumor-bearing mice (24 μg per mouse, i.v., 3 times a week for 2 weeks)	Promote tumor cell apoptosis; inhibit the tumor growth; improve tumor targeting ability	—	
MEL loaded on PIC	Breast cancer	MCF-7 (15 and 30 μg/ml, for 3, 7 days)	Enhance the uptake and the cytotoxicity of MEL; inhibit cell growth; reduce hemolysis and prevent MEL degradation; improve tumor targeting ability	—	Raveendran et al. (2020)
Cervical cancer					
BV	Cervical cancer	HeLa, Caski (1, 5 and 10 μg/ml, for 12, 24 and 48 h)	Reduce cell viability; inhibit cell proliferation, migration and wound healing; promote cell death and apoptosis	↑p21, ↑p27, ↑p53, ↑Rb, ↑Bax, ↑cleaved PARP, ↓Cyclin A, ↓Cyclin B, ↓Bcl-2, ↓Bcl-xL, ↓HPV E6, ↓HPV E7, ↓pro-Caspase-3, ↓pro-Caspase-9; ↓Mitotic signaling pathway: ↓Akt, ↓p-Akt, ↓JNK, ↓p-JNK, ↓p38, ↓p-p38, ↓p44/42, ↓p-p44/42	Da-Hyun Kim et al. (2020)
BV	Cervical cancer, lung cancer, breast cancer	HeLa (12.5 μg/ml, for 12 h); A549 (3.125 and 12.5 μg/ml, for 12 h); MDA-MB-231 (6.24 and 12.5 μg/ml, for 12 h)	Cell contraction, irregular character and cell membrane damage; reduce cell viability and induce apoptosis	—	Borojeni et al. (2020)
MEL	Cervical cancer	HeLa (1, 1.8 and 4 μg/ml, for 12 h)	Cell shrinkage, cytoplasm condensation, cell structure became disorder and lost shape; inhibit cell proliferation and induce apoptosis	—	Zarrinnahad et al. (2018)
MEL loaded on PEG-GO-Fe_3O_4	Cervical carcinoma	HeLa (13 μg/ml (PEG-GO-Fe_3O_4/MEL), containing 5 μg/ml (MEL), for 24, 48 and 72 h)	Prevent MEL from denaturation or degradation; induce cell contraction, deformation and membrane rupture; inhibit cell growth and promote apoptosis	—	Qi et al. (2020)
BV loaded on NFC	Cervical carcinoma	HeLa (500 μg/ml, for 24 and 48 h)	Cell contraction and cell membrane blistering; promote apoptosis	—	Alalawy et al. (2020)

(Continued on following page)

TABLE 1 (*Continued*) Summary of the anti-cancer effects and mechanisms of BV and its main components.

BV and/or its components	Model	Cell/Animal (BV etc. administration)	Effects	Mechanisms	Reference
Pancreatic cancer, gastric cancer, and colorectal cancer					
MEL	PDAC	PDAC cells (SW 1990, etc. 3 μg/ml, for 48 h)	Inhibit cell growth, migration, wound healing and EMT	↑NONHSAT105177; ↓EMT pathway: ↓Snail, ↓Slug, ↓vimentin, ↑E-cadherin	Wang et al. (2018)
MEL	Gastric cancer	AGS (0.05, 0.1 and 0.15 μM, for 24 h)	Reduce cell viability; inhibit cell migration, invasion and EMT; inhibit cell adhesion and colony formation	↓MMP-2, ↓MMP-9, ↓MMP-13; PI3K/Akt signaling pathway: ↓p-Akt, ↓PI3K; ↓Wnt/β-catenin signaling pathway: ↓Wnt-5α, ↓β-catenin, ↓vimentin, ↓N-cadherin, ↑E-cadherin; BMP/Smad signaling pathway: ↓Smad 1/5/8, ↓BMP, ↑glycogen synthase kinase 3α/β (GSK3 α/β)	Huang et al. (2021)
BV, MEL	Colorectal cancer	HCT-116, SW-480 (1, 5 μg/ml, for 24 h)	Reduce cell viability; induce early and late apoptosis; affect the biotransformation of cancer cell	↑Mitochondrial apoptosis pathway: ↑Fas, ↑Caspase-9; ↓CYP1A1, ↓GSTP1, ↓Bcl-2, ↓Bax (except HCT-116 with BV), ↑MRP-2 (HCT-116 with MEL), ↓MRP-2 (SW-480 with MEL)	Nikodijevic et al. (2021)
MEL	Colorectal cancer, gastric cancer	COLO205, HCT-15, AGS (5, 10 and 20 μg/ml, for 30 s, 1, 5, 10, 15 min and 4 h)	Cytoplasmic contraction and cell membrane damage; inhibit cell growth and induce cell death	—	Soliman et al. (2019)
BV, MEL, bvPLA$_2$	Colorectal cancer	HCT116 (14.05 μg/ml (MEL), 10 and 50 μg/ml (bvPLA$_2$), for 24 h)	Reduce cell viability and inhibit proliferation (BV, MEL); MEL and bvPLA$_2$ synergistically inhibited cell proliferation	—	Yaacoub et al. (2021)
BV	Colorectal cancer	HT-29 (7.5, 15 and 30 μg/ml, for 24 and 48 h)	Inhibit cell proliferation and promote apoptosis	↑15-lipoxygenase-1	Zare et al. (2019)
MEL loaded on oligopeptide alginate NPs	Human clonal colon adenocarcinoma	Caco-2 (2.5 and 5 μM, for 48 h)	Induce cell death	—	Wattanakul et al. (2019)
Hepatocellular carcinoma					
MEL	Hepatocellular carcinoma	HepG2 (3, 5 and 10 μg/ml, for 4, 8, 12, 24, 48 and 72 h)	Inhibit cell growth, induce apoptosis and autophagy	↓Bcl-2, ↓p62, ↑Beclin 1, ↑LC3; ↑Mitochondrial apoptotic pathway (When autophagy is inhibited): ↑Cyt C, ↑Caspase-3, ↑Caspase-9	Lv et al. (2019)
MEL	Hepatocellular carcinoma	SMMC-7721 ($CoCl_2$ induce; 2 and 4 μg/ml, for 24 h)	Inhibit the formation of EMT and VM; reduce cell viability; inhibit cell migration and invasion	↓N-cadherin, ↓vimentin, ↑E-cadherin, ↓VEGF, ↓MMP-2, ↓MMP-9; ↓Akt pathway: ↓HIF-1α, ↓p-Akt	Chen et al. (2019)
		Huh7, HepG2 (2 and 4 μg/ml, for 24 h)	Inhibit the formation of VM; reduce cell viability; inhibit cell migration and invasion	↓VEGF, ↓MMP-2, ↓MMP-9, ↓HIF-1α	
		BALB/c nude male mice (50 and 100 μg/kg, i.v., daily injection for 11 days)	Inhibit tumor growth and reduce tumor volume	↓HIF-1α	
BV, MEL, BV and sorafenib; MEL and sorafenib	Hepatocellular carcinoma	HepG2 (at a non-constant combination concentration, for 24 h)	Reduce cell viability and inhibit proliferation; G2/M phase arrest	↑MDA; ↑p53, ↑Bax, ↑Caspase-3, ↑Caspase-7, ↑PTEN, ↓Bcl-2, ↓Cyclin D1, ↓HIF-1α, ↓VEGF, ↓Rac1, ↓MMP-9, ↓NF-κB	Mansour et al. (2021)
Bladder cancer					
MEL	Bladder cancer	T24, 5637 (4 μg/ml, for 48 h)	Inhibit cell proliferation and migration	↓PI3K/Akt pathway: ↓LPAR1, ↓COL5A1, ↓COL6A2; ↓TNF	Jin et al. (2018)

(Continued on following page)

TABLE 1 (*Continued*) Summary of the anti-cancer effects and mechanisms of BV and its main components.

BV and/or its components	Model	Cell/Animal (BV etc. administration)	Effects	Mechanisms	Reference
MEL	Bladder cancer	UM-UC-3, 5637 (2, 4 and 6 μg/ml, for 24 h)	Inhibit cell proliferation, migration and invasion	pathway: ↓CXCL1, ↓CXCL2, ↓CXCL3 ↓MAPK pathway: ↓ERK5, ↓MEK5, ↓ERK1/2, ↓p-ERK1/2, ↓JNK, ↓p-JNK, ↓p-p38, ↓NRAS, ↓PAK1, ↓PAK2, ↓EGFR; ↓V-ATP: ↑ATP6V1F, ↓ATP6V0B, ↓ATP6V1C1, ↓ATP6V1E2, ↓ATP6V0C, ↓ATP6V0A2	Yao et al. (2020)
Skin cancer					
BV, MEL, MEL and temozolomide	Melanoma	A375SM (1, 2.5 and 5 μg/ml (BV, MEL), 50 μM (temozolomide), 1, 2.5 μg/ml (MEL) and 50 μM (temozolomide), for 24 and 72 h)	Inhibit cell growth, migration, invasion and promote apoptosis	↑cleaved Caspase-3, ↑cleaved Caspase-9, ↓MITF; ↓PI3K/Akt/mTOR pathway: ↓p-PI3K, ↓p-Akt, ↓p-mTOR; ↓MAPK signaling pathway: ↓ERK,↓p-ERK, ↓p38, ↓MMP-2	Lim et al. (2019)
		B16F10 (0.5, 1, 2.5 and 5 μg/ml (BV, MEL), for 24, 72 h); SK-MEL-28 (1, 2.5 and 5 μg/ml (BV, MEL), 50 μM (temozolomide), 1, 2.5 μg/ml (MEL) and 50 μM (temozolomide), for 24 and 72 h)	Inhibit cell growth, migration, invasion and promote apoptosis; inhibit melanin production	—	
MEL-AF	Melanoma	A375 (1, 2 and 3 μg/ml, for 2 and 24 h)	Inhibit cell proliferation, migration and invasion, and induce apoptosis	↑F-actin, ↓EGFR (MEL-AF); ↑Mitochondrial pathway: ↑Cyt C, ↑Caspase-3, ↑Caspase-9	Sangboonruang et al. (2020)
MEL, MEL and 5-fluorouracil	Skin squamous cell carcinomas	A431 (0.52 μM (MEL), 0.25 μM (5-fluorouracil), 0.52 μM (MEL) and 0.25 μM (5-fluorouracil), for 72 h)	Cell abscission and contraction, DNA fragmentation; inhibit cell proliferation and induce apoptosis/necrosis; S and G2/M phase arrest; enhance the sensitivity of cells to 5-fluorouracil	—	Ombredane et al. (2021)
BV, BV and cisplatin	HNSCC	UMSCC12, UMSCC29, UMSCC38, UMSCC47 (at a non-constant combination concentration, for 24 h)	Reduce cell viability and inhibit growth; G2/M phase arrest	↑Bax, ↓Bcl-2, ↓EGFR	Grawish et al. (2020)
Leukemia					
MEL	Leukemia	CCRF-CEM, K-562 (1, 10 and 100 μM, for 24 and 48 h)	Reduce cell viability and induce apoptosis	↑Caspase-3/7 pathway: ↑hydrolytic activity of Caspase-3/7	Ceremuga et al. (2020)
MEL	Leukemia	Jurkat (10^{-5} M, for 0.5 h)	Inhibit cell survival; increase permeability through the plasma membrane	—	Gasanoff et al. (2021)
Melectin	Leukemia	K562 (10, 20, 30 and 40 μM, for 0.5 and 4 h); K562/ADM, HL-60, Jurkat (10, 20, 30 and 40 μM, for 4 h)	Destroy cell membrane; inhibit cell proliferation	↑LDH	Liang et al. (2021)
Other tumors					
MEL	Hodgkin lymphoma	KM-H2 (0.5, 1 and 1.5 μM, for 24 and 72 h) L-428 (0.5, 1 and 1.5 μM, for 24 and 72 h)	Inhibit cell survival; Inhibit cell survival; enhance the sensitivity of cells to cisplatin	—	Kreinest et al. (2021)
MEL	Human osteosarcoma	143B (1, 2 and 4 μg/ml, for 24 and 48 h) Female BALB/$c^{nu/nu}$ nude mice (160, 320 and 640 μg/kg, intratumoral injection, each	Inhibit cell invasion; inhibit cell and tumor migration Reduce tumor size and mass; reduce the number of pulmonary metastatic nodules	↓Wnt/β-catenin signal pathway: ↓MMP-2, ↓MMP-9, ↓Cyclin D, ↓LRP5, ↓β-catenin, ↓C-myc, ↓survivin, ↓VEGF	Zhu et al. (2021)

(Continued on following page)

TABLE 1 (*Continued*) Summary of the anti-cancer effects and mechanisms of BV and its main components.

BV and/or its components	Model	Cell/Animal (BV etc. administration)	Effects	Mechanisms	Reference
		course lasted for 5 days and lasted for 4 courses, with an interval of 1 day between the 2 courses)			
BV, MEL	Glioblastoma multiforme	Hs683, T98G, U373 (2.5, 5 and 10 μg/ml, for 1, 4, 8 and 72 h)	Reduce cell viability; promote late apoptosis and necrosis	↑Bak, ↑Bax, ↓Caspase-3; Long non-coding RNAs: ↑RP11-838N2.4, ↑XIST	Lebel et al. (2021)
BV, MEL; BV and γ-radiation; MEL and γ-radiation	Ehrlich ascites carcinoma	EAC cell (30, 60, 120, 240, 480 and 960 μg/ml, for 24 h)	Inhibit cell viability	—	El Bakary et al. (2020)
		Female albino tumor-bearing mice (0.56 mg/kg (BV), 500 μg/kg (MEL), i.p., daily for 21 days, 0.5 Gy (γ-radiation) each time for 30 min)	Reduce tumor volume; destroy tumor tissue	↑CAT; ↓TNF-α, ↓VEGF-A, ↓MMP-2, ↓MMP-9, ↑Caspase-3	
MEL loaded on ^{9}G-A7R-Disk	Glioma	U87 (1, 2 and 4 μM, for 72 h)	Inhibit cell growth	—	Wang et al. (2019)
		Male BALB/c nude mice (total does of 18 mg/kg, i.v., at the 6th, 8th, 10th, 12th and 14th day)	Promote tumor cell apoptosis and inhibit angiogenesis; cause tissue damage		

Abbreviationsare as shown in the literature. (↓), down-regulation or inhibition; (↑), up-regulation or activation.

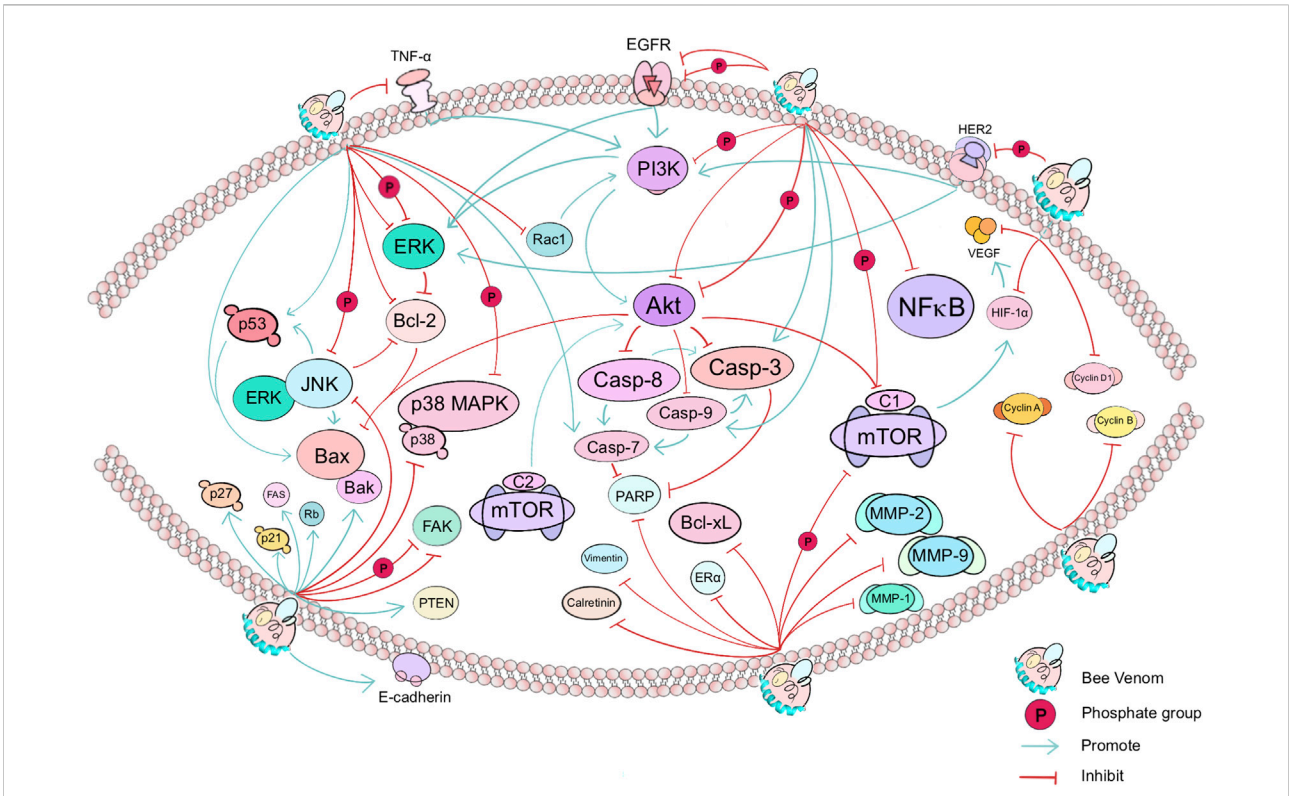

FIGURE 2
The main affected targets and pathways in anticancer effects of BV. In cancer, BV mainly affects the PI3K/Akt/mTOR pathway (e.g., PI3K, Akt, and mTOR), apoptosis signaling pathway (e.g., EGFR and TNF-α, including downstream effectors such as Casp-3, Casp-7, Casp-8, Casp-9, Bcl-2, Bax and Bcl-xL), p38 MAPK pathway, and thus affect the growth, differentiation, invasion, autophagy or migration of cancer cells in lung, breast, cervical and other cancers. Green arrows or red cut-off lines represent the "promote" or "inhibit" effect of the target (gene or protein) by the upstream target factor, respectively. Bee Venom, known as BV, is dispersed on the surface of a phospholipid bilayer. The text shows the direct or indirect targets of BV.

death domain (MADD) decreased, which further brought about cell cycle arrest in G0/G1 phase (Tipgomut et al., 2018).

After cisplatin-resistant lung cancer cells A549/DDP were cultured *in vitro* and treated with MEL, the Warburg effect as well as phosphorylated protein kinase B (Akt) were suppressed; after vaccinating A549/DDP into Balb/c athymic nude mice and treating them via intraperitoneal (i.p.) injection of MEL, their tumor and cell sensitivity to cisplatin was enhanced and tumor size and mass were controlled (Zhang et al., 2021). In addition, the miR-183 played a role as a tumor marker of lung cancer, and was inhibited by MEL in NCI-H441 cells. Its inhibition further increased the expression of Caspase-2 and Bcl-2-associated X protein (Bax), and reduced the Bcl-2 expression. Not only that, after subcutaneous (s.c.) injection of MEL in Balb/c nu/nu mice, Caspase-2 was elevated and tumor growth was restricted similarly (Gao et al., 2018).

Besides, MEL-carried nanoparticles (NPs) systems have considerably enhanced the security of MEL *in vivo* and its efficacy against tumors, offering the possibility of tumor elimination (Zhou et al., 2021). Such drug nano-delivery platforms have been observed in lung cancer research. MEL-carried zeolitic imidazolate framework-8 (MLT@ZIF-8) NPs (Li et al., 2018) and lipid-coated polymer NP (MpG@LPN) (Ye et al., 2021) increased apoptosis in A549 cells and inhibited tumor growth. In the meanwhile, the cellular hemolysis caused by piggybacking on these two nanomaterials was reduced to a certain extent compared with MEL alone.

Anti-breast cancer research

Breast cancer, as the most commonplace tumor in female population, has a very strong time variant tumor metastasis and spatial heterogeneity associated with genotype and phenotypic differences, leading to a continuous change in the evaluation and treatment process of breast cancer (Fumagalli and Barberis, 2021).

BV and MEL induced strongly selective cell death in triple-negative breast carcinoma and human epidermal growth factor receptor 2 (HER2) enriched breast cancer with little effect in routine cells, through interfering with growth factor-dependent receptor tyrosine kinase interactions critical for receptor phosphorylation and activation of phosphoinositide 3-kinase (PI3K)/Akt and mitogen-activated protein kinase (MAPK) signaling. Besides, in an allograft model, the effect of docetaxel in suppressing breast tumor growth was potentiated by the administration of MEL, and the programmed death ligand-1 (PD-L1) protein expression, phosphorylated HER2 and epidermal growth factor receptor (p-EGFR), were significantly reduced (Duffy et al., 2020). Researchers also investigated the effect of BV on epigenetic changes in cancer cells: after confirming that BV decreased the viability and mitochondrial membrane permeability of MDA-MB-231 cells, they further inspected epigenetic and mitochondrial DNA (mtDNA) Copy Number Variation (CNV). The experimental results revealed that BV generated morphological changes in the nucleus of MDA-MB-231 cells, and the exploration of cytosine modification in cancer cells showed that 5′-methylcytosine (5meC), 5′-hydroxymethylcytosine (5hmC) cells decreased rapidly after treatment with BV in MDA-MB-231 cells. And 5′-formlylcytosine (5 fC) and 5′-carboxycytosine (5caC) exhibited a similar increasing and then decreasing process (Uzuner et al., 2021).

BV reduced the expression of nuclear translocation of nuclear factor-κB (NF-κB) and Cyclin D1, enhanced H_2O_2 production, blocked G1 cycle and inhibited breast cancer proliferation in MCF-7 cells (Yoon et al., 2018). MEL reduced the viability of 4T1 and MCF-7 cell lines, and the addition of irradiation resulted in a significant increase of Bax/Bcl-2 value. Besides, MEL enhanced tumor radiosensitivity and inhibited the tumor growth in 4T1 tumor-bearing mice (Chang et al., 2020). MEL also showed the potential to promote mitofusin-1 (Mfn1) and dynamin-related protein 1 (Drp1) expression and apoptosis in 4T1 cells (Moghaddam et al., 2020). After 5% O_2 induction in MDA-MB-231 cells, the hypoxia-inducible factor-1α (HIF-1α) signaling pathway was inhibited by MEL and the expression of NF-κB, HIF-1α, vascular endothelial growth factor A (VEGFA) and lactate dehydrogenase A (LDHA) decreased, while the expression of Bax and tumor necrosis factor-α (TNF-α) was reversed, ultimately disrupting the tumor microenvironment (TME) of cancer cells and activating the phenomenon of apoptosis (Mir Hassani et al., 2021).

BV alone and in combination with other drugs or solutions had an anti-breast cancer impact (Khamis et al., 2018; Arani et al., 2019; El-Beltagy et al., 2021). *In vitro*, BV inhibited the growth of MCF7 and T47D cells, while blocking the cell cycle in the G2/M phase. BV alone or in combination with tamoxifen, hesperidin, and piperine resulted in reduced expression of Bcl-2, EGFR, and estrogen receptors α (ERα) receptors, and elevated expression of Bax, which eventually led to apoptosis. The anticancer and anti-drug resistance effects of tamoxifen were enhanced by the synergistic effect of BV (Khamis et al., 2018). *In vivo*, N-methylnitrosourea was able to induce breast cancer and ovarian complications in Wistar albino rats. After the combination of BV and *Annona muricata* fruit, serum levels of matrix metalloproteinase-1 (MMP-1), NF-κB, TNF-α, malondialdehyde (MDA), elevated Caspase-3, superoxide dismutase (SOD), catalase (CAT), and ovarian histopathological changes due to mammary carcinoma were improved in mothers and offspring rats. Additionally, calreticulin and p53 protein response in the ovarian stroma switched from positive to negative (El-Beltagy et al., 2021). In addition, the non-specific cytotoxicity of MEL in the clinical setting cannot be conveniently ignored. However, plasma-treated phosphate buffered saline solution can cause the death of MCF-7 and A375 melanoma cells on the one hand and circumvent the

non-specific cytotoxicity of MEL to a certain extent on the other, revealing the value of the combination therapy (Shaw et al., 2019).

The application of nanomaterials in combination with MEL has also yielded beneficial results in the treatment of breast carcinoma. The disruption of cell membrane by MEL was unaffected by loading in the NPs after carrying the MEL, and its effect on causing necrosis or apoptosis of the tumor or cancer cells remained undisturbed, such as folic acid (FA)-polyelectrolyte nanocarriers (PENs) (Motiei et al., 2021), nanographene oxide (nGO) and graphene (GN) (Daniluk et al., 2020), the niosome (Moghaddam et al., 2021), citrate functionalized Fe_3O_4 magnetic NPs (CA-MNPs) (Hematyar et al., 2018), and activatable protein NPs (APNPs) (Yu et al., 2018). Besides, after carrying MEL in poly-ion complex (PIC) added with estrone, it prevented the degradation of MEL in cells and increased the uptake of MEL and cytotoxicity (Raveendran et al., 2020).

Anti-cervical cancer research

Cervical cancer is one of the most common cancers in the global female population (Volkova et al., 2021). BV demonstrated the ability to inhibit the growth and migration of HPV-positive cervical cancer Caski and HeLa cells, and cell cycle protein Cyclin A and Cyclin B, Akt, JNK and p38/44/42 and their phosphorylated proteins associated with mitogenic signaling pathways were inhibited, and pro-Caspase-3, pro-Caspase-9, cleaved polyadenosine-diphosphate-ribose polymerase (PARP), Bcl-2 and Bcl-xL expression was reduced. On the contrary, proteins such as p53, p21, and retinoblastoma (Rb) were upregulated in expression with the utility of BV, and the number of dead and apoptotic cells was significantly promoted (Kim D. H. et al., 2020). It is worth noting that the main mode of death of HeLa cells after BV treatment is apoptosis, which causes severe cell membrane damage and cell shrinkage (Borojeni et al., 2020), while MEL can show the effect of inhibiting HeLa cell proliferation and inducing apoptosis such as cell shrinkage and structural disorganization (Zarrinnahad et al., 2018).

Graphene oxide magnetic nanocomposites (PEG-GO-Fe_3O_4)/MEL complexes caused time-dependent toxic effects on HeLa cells with deformation lysis, membrane breakage and other abnormal cellular states. The experimental results demonstrated that this material achieved the long-lasting release and effect enhancement of MEL, while preventing the degradation or denaturation of MEL, ensuring the anti-cervical cancer effect of MEL (Qi et al., 2020). BV loaded on nano-fungal chitosan (NFC) also showed effective anticancer activity in promoting apoptosis in HeLa cells (Alalawy et al., 2020).

Anti-pancreatic cancer, gastric cancer, and colorectal cancer research

BV and MEL have also been used to treat cancers of the digestive system, such as pancreatic cancer, gastric cancer, and colorectal cancer.

In pancreatic ductal adenocarcinoma (PDAC), overexpression of NONHSAT105177 in long non-coding RNAs is associated with activities such as cell proliferation and migration (Wang et al., 2018). This RNA is able to increase its expression under the regulation of MEL, further promoting its inhibitory effect on PDAC, which is related to EMT pathway-related proteins, such as causing the repressive expression of Snail, Slug and vimentin and the up-regulated expression of E-cadherin.

MEL exhibited inhibitory effects on human gastric cancer AGS cell viability, adhesion, colony-forming ability, EMT, and a limiting effect on MMP-2, MMP-9 and MMP-13 proteins related to cell migration and invasion ability. In addition, MEL tended to act more in a variety of signaling pathways, containing bone morphogenetic protein (BMP)/Smad, Wnt/β-catenin and PI3K/Akt pathways (Huang et al., 2021).

When BV and MEL were applied to HCT-116 and SW-480 of colorectal cancer cells, respectively, the mitochondrial apoptotic pathway was activated, cancer cell viability was reduced, chromatin was contracted, and apoptosis was induced in early and late colorectal cancer cells. The expression of Caspase-9 and Fas death receptor increased, however, CYP1A1 and GSTP1, Bcl-2 decreased in the same trend in both cells; while the mRNA expression of Bax and multidrug resistance protein-2 (MRP-2) increased when BV treated HCT-116 cells and decreased when BV treated SW-480 cells. After MEL treatment, the expression of Bax decreased and MRP-2 increased in HCT-116 cells, while the expression of Bax and MRP-2 decreased in SW-480 cells (Nikodijevic et al., 2021). Besides, the high concentration of MEL could directly and quickly cause membrane damage, content outflow and cell death to gastric cancer and colorectal cancer cell membranes within 15 min. This rapid dissolution effect appeared in AGS cells, COLO205 and HCT-15 cells in different ways (Soliman et al., 2019). In addition, MEL and $bvPLA_2$ inhibited HCT116 cell proliferation in a synergistic manner, demonstrating synergistic utility: MEL promoted the effect of $bvPLA_2$ on cell membranes, and pretreatment of cells with $bvPLA_2$ enhanced the inhibitory effect of MEL on cells (Yaacoub et al., 2021). Besides, the expression and activity of 15-lipoxygenase-1, a tumor suppressor in HT-29 cells, have elevated after being affected by BV, which in turn promoted apoptosis (Zare et al., 2019).

Meanwhile, the derivation of the side chain of oligopeptide-alginate NPs provided the basis for the specific binding of MEL, ultimately achieving potent killing ability on human cloned colon adenocarcinoma Caco-2 cells (Wattanakul et al., 2019).

Anti-liver cancer research

In the study of hepatocellular carcinoma, BV achieved the same breakthrough as MEL in anti-hepatocellular carcinoma growth with autophagy, which implied a possible anti-mutagenic effect on normal cells. The results showed that MEL down-regulated Bcl-2 and up-regulated cytochrome C (Cyt C), Caspase-3, and Caspase-9 expression, predicting that MEL may rely on the mitochondrial apoptotic pathway to induce tumor injury, and the ratio of apoptosis to necrosis in cancer cells was positively relative to the MEL concentration. On the other hand, MEL achieved its autophagy-inhibiting effect on HepG2 cells by downregulating p62 and upregulating Beclin 1 and LC3 expression. The anti-tumor effect of MEL was enhanced when the autophagy inhibitor chloroquine was applied; the enhanced autophagic effect of MEL on hepatocellular carcinoma cells was diminished after the application of the autophagy activator rapamycin (Lv et al., 2019). The shaping of hypoxic environment is strongly associated with tumor proliferation or angiogenesis, and the vasculogenic mimicry (VM) produced by SMMC-7721 cells induced by cobalt chloride ($CoCl_2$) with EMT can also be inhibited by applying MEL. The hypoxia model caused upregulation of the expression of HIF-1α, VEGF, MMP-2 and MMP-9 in SMMC-7721, Huh7, and HepG2 cells, and MEL reversed this trend. In addition, in the presence of MEL, it decreased SMMC-7721 cell viability, inhibited EMT induced by $CoCl_2$, upregulated E-cadherin, and downregulated p-Akt, vimentin and N-cadherin expression. An *in vivo* tumor treatment model of MEL was established by s.c. injecting SMMC-7721 cells into male BALB/c nude mice, which showed the significantly inhibited HIF-1α expression and tumor growth (Chen et al., 2019).

Sorafenib had unsatisfactory effects in the treatment of advanced hepatocellular carcinoma, while BV and MEL had certain efficacy in inhibiting hepatocellular carcinoma. Therefore, BV and MEL alone or in combination with sorafenib, respectively, showed synergistic effects in adjuvant inhibition of HepG2 cell proliferation. The expression of p53, Bax, Caspase-3, Caspase-7 and PTEN was elevated, meanwhile the expression of Bcl-2, Cyclin D1, HIF-1α, VEGF, Ras-related C3 botulinum toxin substrate 1 (Rac1), MMP-9 and NF-κB decreased in HepG2 cells. The promotion or suppression effects on the above genes were strengthened under the crosstalk conditions (Mansour et al., 2021).

Anti-bladder cancer and prostate cancer research

In an investigation of the Gene Expression Omnibus database of bladder cancer, MEL regulated and inhibited the expression of key module genes in the PI3K-Akt and TNF signaling pathways, referring to LPAR1, COL5A1, COL6A2, CXCL1, CXCL2 and CXCL3 in human bladder cancer cell lines T24 and 5637, and suppressed cell proliferation and migration activities, revealing the potential role of these genes as targets of MEL in bladder cancer (Jin et al., 2018). Similarly, bearing in mind the bioinformatics analysis of bladder cancer, the genes corresponding to two bladder cancer cells, UM-UC-3 and 5637, were selected for study. All these demonstrated that MEL could inhibit cell proliferation, migration and invasion by virtue of its effect on MAPK signaling pathway or V-ATPase (Yao et al., 2020).

Prostate cancer is divided into metastatic/non metastatic prostate cancer. As one of the familiar type diseases in masculinity, it faces several problems with drug resistance of cancer cells and inability to control the progress and spread of the disease. BV and MEL have certain effects on a variety of prostate cancer and xenotransplantation (Badawi, 2021). For example, BV produced selective antitumor effects on PC3 cells, reducing their cell viability (Viana et al., 2021).

Anti-skin cancer research

Melanoma stands out as one of the most lethal and invasive malignancies in skin cancer, yet it is highly resistant to drugs. BV and MEL can help to fight against the growth, migration and invasion of melanoma A375SM, B16F10 and SK-MEL-28 cells, causing apoptosis. Among them, MEL showed a more effective ability to inhibit migration and promote apoptosis. BV and MEL had similar inhibitory effects on PI3K/Akt/mTOR and MAPK signaling pathways in A375SM cells. At the same time, it elevated the cleaved Caspase-3 and Caspase-9 expression and reduced the microphthalmia-associated transcription factor (MITF) level. In addition, when MEL was combined with temozolomide, the growth and invasion inhibition of A375SM and SK-MEL-28 cells elevated (Lim et al., 2019). MEL from *Apis florea* (MEL-AF) similarly showed a proliferation inhibitory effect on A375 cells, where MEL-AF, upon binding to the cell membrane, caused an elevation of intracellular F-actin with a decrease in EGFR, ultimately resulting in apoptosis through the induced expression of Cyt C, Caspase-3 and Caspase-9 in the mitochondrial apoptotic pathway (Sangboonruang et al., 2020).

MEL alone or in combination with 5-fluorouracil was able to damage A431 cells of skin squamous cell carcinomas, causing morphological alternations, e.g., cell shedding, shrinkage, and plasma membrane damage. Besides, the combination of MEL and 5-fluorouracil caused a more significant decrease in terms of cell number and cell cycle arrest in both phases S and G2/M. More importantly, the drug combination re-sensitized A431 cells to 5-fluorouracil (Ombredane et al., 2021).

Head and neck squamous cell carcinoma (HNSCC) is also a type of skin cancer. Four types of HNSCC cells viability such as UMSCC12, UMSCC29, UMSCC38 and UMSCC47 were

inhibited by BV alone or combined with cisplatin. Besides, mitosis was blocked in G2/M phase, during which the Bcl-2 and EGFR expression was significantly reduced, while the expression of Bax was significantly elevated. It is worth noting that different drugs and ratios of treatment were shown to significantly reduce the number of the S-phase cells (Grawish et al., 2020).

Anti-leukemia research

MEL induced apoptosis while inhibiting cell viability in CCRF-CEM and K562 cells, relying on activation of the hydrolytic activity of Caspase-3/7 in the mitochondrial pathway and the hemiphilic aspartate pathway (Ceremuga et al., 2020). In addition to inhibiting cell viability, MEL had high permeability to the plasma membrane of cells in human acute T cell leukemia Jurkat cells, which enhanced the permeability of MEL through the plasma membrane and further caused cell death (Gasanoff et al., 2021). The anti-infectivity peptide melectin from *Melecta albifrons*, by virtue of its α-helical structure, inhibited cell proliferation by interfering with the cell membrane of leukemic cells K562, decreasing the viability of various cells such as K562, K562/ADM and HL-60 while enhancing LDH output (Liang et al., 2021).

Anti-other cancer research

In a study of Hodgkin lymphoma, MEL produced toxicity in lymphoma cells L-428 and KM-H2, while increasing the sensitivity of drug-resistant L-428 cells to cisplatin. And MEL preferentially acted on tumor cells, demonstrating prospect of Hodgkin lymphoma therapy in the future (Kreinest et al., 2021). Besides, Cyclin D, MMP-2, MMP-9, lipoprotein receptor related protein 5 (LRP5), β-catenin and other proteins associated with the Wnt/β-catenin pathway were downregulated after moderate and high concentrations of MEL on human osteosarcoma 143B cells, a malignant bone tumor. The s.c. injection of 143B cells and treatment with MEL in female BALB/$c^{nu/nu}$ nude mice showed a reduction in tumor size, mass and number of lung metastatic nodules, and inhibition of tumor metastatic behavior (Zhu et al., 2021). Glioblastoma multiforme is also a malignant tumor. BV and MEL reduced the viability of Hs683, T98G and U373 cells, elevated Bak and Bax expression, inhibited Caspase-3 expression as well as promoted late apoptosis and necrosis in glioblastoma multiforme. In addition, the expression of long-chain non-coding RNARP11-838N2.4 and X inactive-specific transcript (XIST) was significantly elevated in glioblastoma multiforme cells (Lebel et al., 2021). BV or MEL alone inhibited the growth of Ehrlich ascites carcinoma cells. Injection of BV or MEL into female albino tumor-bearing mice resulted in destruction of tumor tissue and suppression of tumor size. In addition, after combined treatment with γ-radiation, the tumor size inhibition was enhanced by re-enforcing the elevated levels of TNF-α, VEGF-A, serum MMP-2 and MMP-9, and CAT in liver caused by BV or MEL alone (El Bakary et al., 2020).

Lipodisk-based paclitaxel and MEL co-delivery system functionalized with glycopeptide ^{9}G-A7R (^{9}G-A7R-Disk/PTX/MEL) were used as an anti-degradation delivery system for MEL on U87 glioma cells cultured *in vitro* contributing to the growth inhibitory effect. Besides, inoculation of U87 cells in female BALB/c nude mice and intravenous (i.v.) administration of ^{9}G-A7R-Disk/PTX/MEL co-loaded liposomes resulted in increased apoptosis, tissue damage, and reduced angiogenesis at the glioma, demonstrating their targeted anti-tumor effects (Wang et al., 2019).

Effects on neurological disorders

Parkinson's disease (PD) and Alzheimer's disease (AD), belonging to neurodegenerative diseases, are caused by nervous system abnormalities, involving neurotransmitter abnormalities, the accumulation of false proteins, etc. (Guo and Ma, 2019). BV and its main component, $bvPLA_2$, showed neuroprotective effects and could postpone the progression of degenerative diseases. The effects mainly included enhancing motor performance or alleviating memory impairments, inhibiting oxidative stress, decreasing neuroinflammation, protecting neurons, preventing apoptosis, etc. Besides, BV and its main components also had neuroprotective effects against other neurological disorders, seen in Table 2, and the main affected targets and mechanism of BV and its main components in treating neurological disorders is shown in Figure 3.

Delaying the development of PD

BV was reported to have neuroprotective effect on dopaminergic neurons and alleviate PD symptoms. BV attenuated motor impairment, decreased oxidative/nitrosative stress, and TNF-α, Caspase-3, and monocyte chemoattractant protein-1 (MCP-1) expression, and increased dopamine (DA) content and butyrylcholinesterase (BuChE) activity in a rotenone-induced PD mice model (Badawi et al., 2020). Besides, BV restored the levels of DA, norepinephrine and serotonin (5-HT), balanced glutamate/γ-aminobutyric acid levels, prevented DNA fragmentation, reduced TNF-α and interleukin-1β (IL-1β), and increased the brain-derived

TABLE 2 Summary of the role and mechanism of BV and its main components in treating neurological disorders.

BV and/or its components	Model	Inducer/Method	Animal/Cell (BV etc. administration)	Effects	Mechanisms	References
PD						
BV	PD	Rotenone (s.c.)	Swiss albino male mice (0.065, 0.13, and 0.26 mg/kg, intradermal (i.d.), once a day every other day for 2 weeks)	Enhance motor performance; inhibit oxidative/nitrosative stress; decrease neuroinflammation; protect dopaminergic neurons	↓MDA, ↓NO, ↑GSH, ↑PON1 activity, ↑TAC; ↓MCP-1, ↓TNF-α, ↓Caspase-3, ↑BuChE activity, ↑DA	Badawi et al. (2020)
BV	PD	Rotenone (s.c.)	Swiss Albino male mice (1.0 mg/kg, i.p., for 6 consecutive days)	Recover motor strength and motor coordination; increase dopamine level and total antioxidant capacity; reinforce anti-inflammatory effect; restrict neuronal degeneration	↑DA, ↓IL-1β, ↓IL-6	Rakha et al. (2018)
BV	PD	Reserpine (i.p.)	Male rats (10 μL/kg, i.p., every other day for 30 days)	Increase monoamines neurotransmitters (norepinephrine, dopamine, 5-HT), elevate γ-aminobutyric acid and arginine, reduce glutamate, halt DNA fragmentation	↓acetylcholinesterase activity, ↓TNF-α, ↓IL-1β, ↑PON1 activity, ↑BDNF	Ahmed-Farid et al. (2021)
$bvPLA_2$	PD	1-Methyl-4-phenyl-1,2,3,6-tetrahydropyridine (MPTP) (i.p.)	C57BL/6J mice (0.5 mg/kg, s.c., for a consecutive 6 days)	Improve motor function; rescue loss of dopaminergic neurons	Activate Tregs; inhibit Th1 and Th17 cells	Kyung Hwa Kim et al. (2019a)
$bvPLA_2$	PD	MPTP (i.p.)	Male C57BL/6J mice (0.5 mg/kg, i.p., s.c., i.m., or i.v., for 6 days; 0.01–0.5 mg/kg, s.c., for six consecutive days)	Reverse motor deficits; inhibit loss of dopaminergic neurons; suppress microglial activation (↓Iba1-positive microglia, $ED1^+$ microglia)	Induce $CD4^+CD25^+Foxp3^+$ Tregs; inhibit Th1 and Th17 polarization (↓IFN-γ, ↓IL-17A)	Baek et al. (2018a), Kyung Hwa Kim et al. (2019b)
Fraternine (a novel Wasp peptide)	PD	6-Hydroxydopamine (Nigro-striatal pathway lesioned unilaterally)	Swiss male mice (0.01, 0.1, 1 and 10 μg/animal, i.c.v, on day 1, 3 and 5)	Trigger neuroprotective activity; improve motor coordination	—	Biolchi et al. (2020)
AD						
BV	AD	Aβ	U87MG (human glioblastoma cells) (10 μg/ml, for 120 h)	Increase cell viability; decrease Aβ accumulation; suppress inflammatory reaction; prevent apoptosis	↓COX-2, ↓TNF-α, ↓IL-1, ↓Caspase-3	Ku et al. (2020)
$bvPLA_2$	AD	Aβ1-42 peptide (s.c.)	AD model (3xTg-AD) mice (0.5 mg/kg, i.p., once a week for 3 months)	Alleviate memory impairments; reduce Aβ burdens in the hippocampal CA1 and cortex regions; high cerebral glucose uptake; eliminate central nervous system inflammation	↓IFN-γ, ↓TNF-α, ↑IL-10	Baek et al. (2018b)
		Aβ1-42 peptide (s.c.) and pertussis toxin (PT) (i.v.)	Male C57BL/6 mice (0.5 mg/kg, i.p., once a week for 3 months)	Eliminate central nervous system inflammation	—	

(Continued on following page)

TABLE 2 (*Continued*) Summary of the role and mechanism of BV and its main components in treating neurological disorders.

BV and/or its components	Model	Inducer/Method	Animal/Cell (BV etc. administration)	Effects	Mechanisms	References
BV $sPLA_2$	AD	LPS (i.p.)	Male ICR mice (0.02, 0.2, and 2 mg/kg, i.p., three times for 1 week)	Improve memory function; inhibit Aβ deposition; inhibit neuroinflammation and NF-κB activation; modulate Tregs infiltration	↓GFAP, ↓IBA-1, ↓iNOS, ↓COX-2, ↓p-IκB-α, ↓p50, ↓p65, ↑Foxp3	Ham et al. (2019a)
		LPS	Microglial BV-2 cells (0.01, 0.1, and 1 μg/ml, for 3 h)	Reduce amyloidogenesis and neuroinflammation	↓APP, ↓BACE1, ↓β-secretase activity, ↓iNOS, ↓COX-2, ↓IBA-1, ↓p-IκB-α, ↓p50, ↓p65, ↓TNF-α, ↓IL-1β, ↓IL-6	
$bvPLA_2$	AD	—	Tg2576 mice (1 mg/kg, i.p., twice per week for 4 weeks)	Alleviate genetically induced memory; inhibit accumulation of Aβ	↓APP, ↓BACE1, ↓$Aβ_{1–42}$, ↓$Aβ_{1–40}$, ↓β-secretase activity, ↓GFAP, ↓IBA-1, ↓iNOS, ↓COX-2, ↓TNF-α, ↓IL-1β, ↓IL-6, ↑IL-4, ↑TGF-β, ↓p-STAT3, ↓p-ERK	Ham et al. (2019b)
		LPS	BV-2 cells (0.01, 0.1, and 1 μg/ml, for 24 h)	Inhibit accumulation of Aβ, decrease nitric oxide concentration; directly binds to linker domain of STAT3	↓APP, ↓BACE1, ↓$Aβ_{1–42}$, ↓β-secretase, ↓iNOS, ↓COX-2, ↓IBA-1, ↓TNF-α, ↓IL-1β, ↓IL-6, ↑IL-4, ↑TGF-β, ↓p-STAT3	
		Aβ	BV-2 cells (0.01, 0.1, and 1 μg/ml, for 24 h)	—	↓iNOS, ↓COX-2, ↓p-STAT3, ↓TNF-α, ↓IL-1β, ↓IL-6	
Other neurological disorders						
BV	Epilepticus	Pilocarpine	Male Sprague Dawley rats (10 μg/animal, i.d., once every 3 days for four consecutive weeks)	Ameliorate disturbance of electrolytes and the interruption of electrolytes and ions, limit neuronal excitability via rapid repolarization of action potentials	↑SCN1A, ↑KCNJ2, ↑CLCNC, ↓CACNCL, ↓NMDAR, ↓IL-6, ↓IL-17, ↓TNF-α, ↓TGF-β, ↓FOXP3, ↓CTL4, ↑IL-10	Abd El-Hameed et al. (2021)
BV	Blood brain barrier damage and neurobehavioral changes	Methyl mercury chloride (gavaged)	Male Sprague–Dawley rats (0.5 mg/kg, s.c., for14 days)	Modulate methyl mercury chloride-induced behavioral alterations, increase pan neuron	↑GSH, ↑SOD, ↑CAT, ↑GST, ↑GPx, ↓MDA, ↓PCO, ↓8-hydroxy-2′-deoxyguanosine, ↑IL-10, ↓NO, ↓TNF-α, ↓IL-1β, ↓INF-γ, ↑occludin, ↑claudins-5, ↑Zonula occludens-1, ↓TGF-β, ↓IgG, ↓IBA-1	Abu-Zeid et al. (2021)
MEL	Memory-deficit	$Aβ_{25–35}$	HT22 mouse hippocampal cell (0.3, 1, and 3 μM, for 24 h)	Reduce apoptosis, decrease protein carbonyl levels	↓Bax/Bcl-2, ↓AIF, ↓Calpain, ↓Cyt C, ↓cleaved Caspase-3, ↓ROS, ↓MDA, ↓LDH, ↑Nrf2 nuclear/Nrf2 cytosolic ratio, ↑HO-1, ↑p-TrkB, ↑p-CREB, ↑BDNF	Cong Duc and Lee, (2021)
		$Aβ_{25–35}$ (intracerebroventricular)	Male ICR mice (0.15 and 1.5 mg/kg, s.c., on days 3, 5, 7, 9, and 11)	Improve memory impairment, increase neuron cell neurogenesis; reduce acetylcholinesterase activity, increase acetylcholine	↓ROS, ↓NO, ↓MDA, ↑p-CREB, ↑BDNF, ↓iNOS, ↑M1 muscarinic acetylcholine receptor	
Apamin	Laceration injury in cortical neurons	Laceration injury	Rat cerebral cortical neurons (1 and 10 μg/ml, for 24 and 48 h)	Enhance neurite outgrowth and axon regeneration, increase BDNF-positive and NGF-positive neurons	↑BDNF, ↑NGF	Aeyung Kim et al. (2021)

(Continued on following page)

TABLE 2 (*Continued*) Summary of the role and mechanism of BV and its main components in treating neurological disorders.

BV and/or its components	Model	Inducer/Method	Animal/Cell (BV etc. administration)	Effects	Mechanisms	References
		—	Rat cerebral cortical neurons (1 and 10 μg/ml, for 24 and 48 h)	—	↑BDNF, ↑NGF, ↑NF200, ↑GAP43	
BV, Wasp venom	Neuroinflammation	LPS	BV-2 murine microglial cells (0.5, 1, 2, and 4 μg/ml (BV), 5, 10, 20, and 40 μg/ml (Wasp venom), for 18 or 24 h)	Anti-inflammatory effect	↓NO, ↓TNF-α, ↓IL-6, ↓iNOS, ↓COX-2, ↓NF-κB	Yun et al. (2021)
Apamin	Neuroinflammation	LPS	BV-2 murine microglia cells (1 μg/ml, for 1 h)	Anti-neuroinflammatory effect	↓CD11b, ↓TNF-α, ↓IL1β, ↓IL6, ↓COX2, ↓K_{Ca}2.2, ↓pCaMKII, ↓TLR4, ↓pp65, ↓pSTAT3, ↓pERK, ↓pJNK	Park et al. (2020)
		LPS	Rat primary microglial cells (1 μg/ml, for 1 h)	Anti-neuroinflammatory effect	↓TNF-α, ↓IL1β, ↓CD11b, ↓K_{Ca}2.2, ↓pCaMKII, ↓TLR4, ↓pp65, ↓pSTAT3, ↓pERK	
Apamin	Multiple sclerosis	Cuprizone pellets (fed)	Male C57BL/6 mice (100 μg/kg/BW, i.p., during phase I (demyelination) or post-treatment phase II (remyelination) twice a week)	Increase Olig2+cells in phase I, show a decreasing trend in PDGFRa + cells after cuprizone withdrawal; stimulate oligodendrocyte progenitor cell proliferation in phase I, especially at the subventricular zone	—	Danesh-Seta et al. (2021)
$bvPLA_2$	Multiple sclerosis (experimental autoimmune encephalomyelitis)	MOG_{35-55} peptide in CFA containing *Mycobacterium tuberculosis* (s.c.) and pertussis toxin (i.p.)	C57BL/6 mice (0.2 mg/kg, i.p., daily for a period of 10 days)	Attenuate limb paralysis, decrease $CD4^+$ cell infiltration; the beneficial effects of $bvPLA_2$ disappeared when Tregs were depleted	—	Gihyun Lee et al. (2019)

Abbreviations are as shown in the literature. (↓), down-regulation or inhibition; (↑), up-regulation or activation.

neurotrophic factor (BDNF) and paraoxonase 1 (PON1) level in a reserpine-induced PD rat model (Ahmed-Farid et al., 2021). The above results implied that BV could be a potential adjuvant for PD treatment. The neuroprotective effects of $bvPLA_2$ against PD have also been studied. Purified $bvPLA_2$ showed dose-dependent neuroprotective effects on PD in mice, relating to the induction of $CD4^+CD25^+Foxp3^+$ regulatory T cells (Tregs), which to some extent suppressed the polarization of T helper 1 (Th1) and Th17, and the microglia activation (Kim et al., 2019b). Fraternine, a novel wasp peptide, also showed neuroprotective effects and ameliorated motor coordination in a 6-hydroxydopamine-induced PD mice model (Biolchi et al., 2020).

Besides, current evidence was summarized and supported the therapeutic effects of acupuncture in treating PD patients and animal models of PD (Guo and Ma, 2019). Therefore, BV combined with acupuncture could have great advantages in the treatment of PD.

Delaying the development of AD

BV increased cell viability, decreased amyloid β-protein (Aβ) accumulation in U87MG AD mimic cells, as well as suppressed inflammatory reaction through inhibiting the mRNA expression of IL-1, TNF-α and cyclooxygenase-2 (COX-2), and prevented apoptosis by reducing the expression level of Caspase-3, indicating that BV could be a potential AD therapeutic drug (Ku et al., 2020). Besides, $bvPLA_2$ also exerted neuroprotective effects against AD. It alleviated memory impairments, reduced

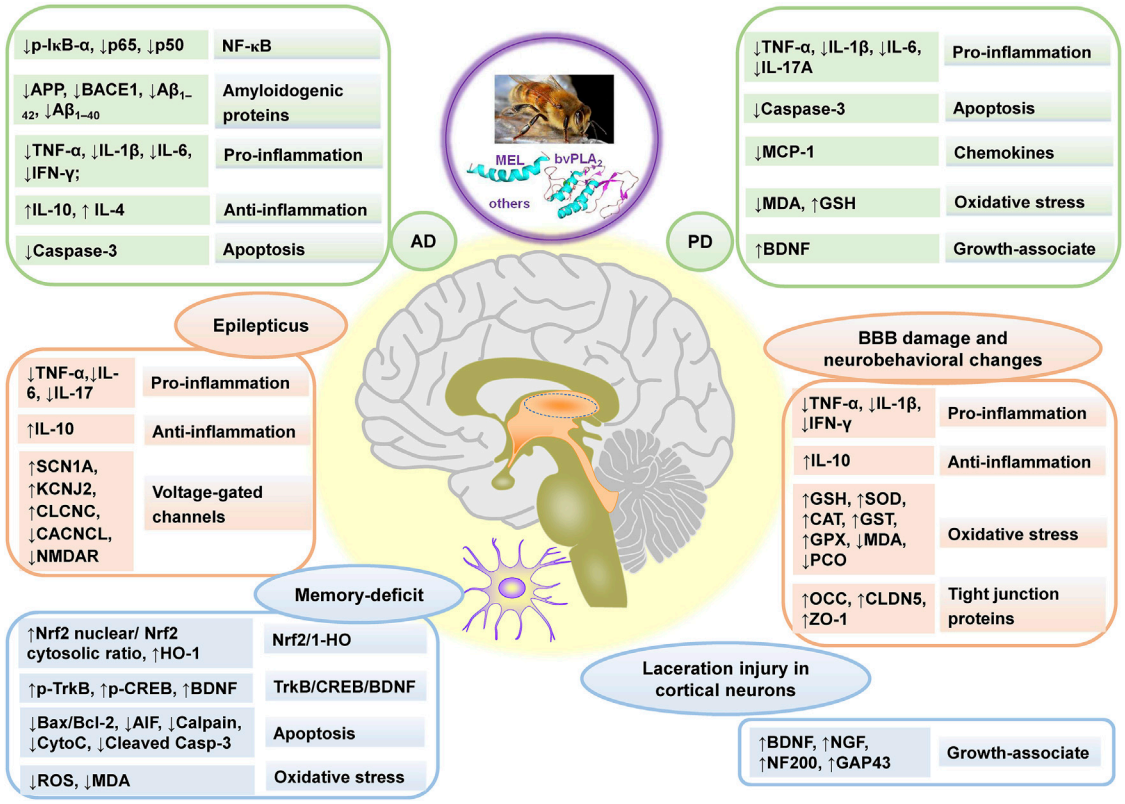

FIGURE 3
The main affected targets and mechanism of BV and its main components in treating neurological disorders, referring to Alzheimer's disease (AD), Parkinson's disease (PD), BBB damage and neurobehavioral changes, laceration injury in cortical neurons, memory-deficit, and epilepticus. "↑" and "↓" represent up-regulated and down-regulated targets (genes or proteins), respectively in the left column in each rounded rectangular box, and the texts demonstrate the effect and pathways in right column in each rounded rectangular box for BV and its main components.

Aβ burdens, showed high cerebral glucose uptake, and eliminate central nervous system inflammation through reducing TNF-α and interferon-γ (IFN-γ) level and elevating IL-10 level in a 3xTg-AD mouse model (Baek et al., 2018b). BV $sPLA_2$ improved memory function, suppressed Aβ deposition, inhibited neuroinflammation and NF-κB activation through the downregulation of glial fibrillary acidic protein (GFAP), ionised calcium binding adaptor molecule 1 (IBA-1), inducible nitric oxide synthase (iNOS), COX-2, p-IκB-α, p50 and p65, and modulated Tregs infiltration through the upregulation of Foxp3 in a lipopolysaccharide (LPS)-induced AD mouse model brain. Besides, it reduced amyloidogenesis and neuroinflammation by reducing the level of amyloid precursor protein (APP), β-amyloid precursor protein-cleaving enzyme-1 (BACE1), iNOS, COX-2, IBA-1, p-IκB-α, p50, p65, TNF-α, IL-6, IL-1β, and the activity of β-secretase in LPS-treated microglial BV-2 cells. The *in vivo* and *in vitro* results indicated that BV $sPLA_2$ inhibited inflammatory responses and amyloidogenesis via blockage of NF-κB signaling (Ham et al., 2019a). In addition, $bvPLA_2$ also exerted anti-inflammatory and anti-amyloidogenic effects via inhibiting signal transducer and activator of transcription 3 (STAT3) activity (Ham et al., 2019b).

Effects on other neurological disorders

BV and its main components, such as MEL and apamin, also had neuroprotective effects against other neurological disorders, including epilepticus, blood brain barrier damage and neurobehavioral changes, memory-deficit, laceration injury in cortical neurons, neuroinflammation and multiple sclerosis.

BV rebalanced neurotransmitters and blood electrolytes, ameliorated alterations of voltage-gated channels expression, and regulated pro- and anti-inflammatory cytokines levels in a pilocarpine-induced epilepticus rat model, which demonstrated that BV could slow down the development of epilepticus as a combined treatment with other antiepileptic drugs (Abd El-Hameed et al., 2021). Besides, Egyptian BV ameliorated blood-brain barrier dysfunction and neurobehavioral toxicity

TABLE 3 Summary of the effects and mechanisms of BV and its main components on inflammatory diseases.

BV and/or its components	Model	Inducer/Method	Animal/Cell (BV etc. administration)	Effects	Mechanisms	References
Atopic dermatitis						
BV	Atopic dermatitis	Chicken ovalbumin (i.p. inoculated)	Female BALB/c mice (1, 10, and 100 μg/kg, i.p., twice a week)	Decrease the extent of inflammatory cell infiltration and skin thickness, diminish the extent of mast cell infiltration and degranulation, increase filaggrin	↓IgE, ↓TNF-α, ↓TSLP, ↓CD4+, ↓CD11b+	Gu et al. (2018)
BV	Atopic dermatitis	Phthalic anhydride (topical application)	BALB/c mice (200 μL of a solution containing 0.1, 0.25, and 0.5 μg, topical application, 3 h)	Reduce atopic dermatitis clinical score, back and ear epidermal thickness, the weight of lymph node; decrease the number of eosinophil, neutrophil, monocytes, mast cells, F4/80-positive cells and Ly6G-positive cells	↓IgE, ↓IL-4, ↓IL-13, ↓TNF-α, ↓IL-1β, ↓IL-6, ↓p-ERK, ↓p-p38, ↓p-JNK, ↓p-IκB-α, ↓iNOS, ↓COX-2	Ji Hwan Lee et al. (2020)
		LPS	RAW 264.7 cells (1, 2.5, and 5 μg/ml, for 24 h)	Anti-inflammatory effect	↓NO, ↓NF-κB, ↓p-ERK, ↓p-p38, ↓p-JNK, ↓p-IκB-α, ↓iNOS, ↓COX-2, ↓p65, ↓p50	
		TNF-α/IFN-γ	HaCaT cells (1, 2.5, and 5 μg/ml, for 24 h)	Anti-inflammatory effect	↓NF-κB, ↓p-ERK, ↓p-p38, ↓p-JNK, ↓p-IκB-α, ↓p65, ↓p50	
BV and MEL	Atopic dermatitis	DNCB (topically to the shaved dorsal skin)	Female Balb/c mice (100, 200 and 500 μg, topical application, five times per week for 4 weeks)	Decrease dorsal skin thickness; inhibit pathological changes including the infiltration of inflammatory cells in skin lesions; decrease the levels of $CD4^+$ and $CD3^+$ T cells in the dorsal skin; improve abnormal epidermal differentiation	↓IFN-γ, ↓IL-4, ↓IgE, ↓TSLP	An et al. (2018)
		TNF-α/IFN-γ	Human keratinocyte HaCaT cell line (1, 10 and 100 ng/ml (BV), 0.1, 0.5 and 1 μg/ml (MEL), for 9 h)	Modulate chemokines expression via suppression of pro-inflammatory cytokines; inhibit JAK/STAT signal pathways; inhibit NF-κB pathways	↓CCL17, ↓CCL22, ↓IL-1β, ↓IL-6, ↓IFN-γ, ↓p-JAK2, ↓p-STAT1, ↓p-STAT3, ↓p-IκB, ↓p-NF-κB	
BV	Atopic dermatitis (Irritant contact dermatitis, ICD)	DNCB (topical application)	Male BALB/c mice (0.3 mg/kg, s.c., at 2-day intervals for 10 days)	Attenuate skin condition, decrease clinical skin score; inactivate complement system	↓C3C, ↓MAC, ↑CD55 (BV and MEL)	Yenny Kim et al. (2019)
		—	THP-1 cells (0–1 μg/ml, for 0–24 h or 0–120 min)	Inactivate complement system	↑CD55, ↑p-ERK1/2	
$bvPLA_2$	Atopic dermatitis	DNCB and house dust mite extract (*D. farinae* extract) (topically to the ear)	Male C57BL/6 mice (80 ng/ear, topical application, four times a week for 3 weeks)	Suppress atopic dermatitis-related skin swelling, improve ear thickness; decrease the expression of Th1 and Th2 cytokines; induce Treg; decrease epidermal and dermal thickness and macrophage infiltration; block mast cell infiltration	↓IgE, ↓IFN-γ, ↓IL-4, ↓IL-6, ↓IL-10, ↑Foxp3	Dasom Shin et al. (2018)

(Continued on following page)

TABLE 3 (*Continued*) Summary of the effects and mechanisms of BV and its main components on inflammatory diseases.

BV and/or its components	Model	Inducer/Method	Animal/Cell (BV etc. administration)	Effects	Mechanisms	References
BV	Atopic dermatitis	House dust mite (*D. farinae*) extract	HaCaT cells (0.1–10 μg/ml, for 24 h)	Anti-inflammatory effects	↓protease-activated receptor 2 (PAR2), ↓intercellular adhesion molecule-1 (ICAM-1), ↓IL-6	Han et al. (2018)
Arthritis						
BV	RA	Freund's complete adjuvant (sub-plantar, intra-dermally)	Male Wistar Albino rats (2, 4 and 20 mg/kg, s.c., every day for a period of 15 days)	Decrease paw volume and arthritis index; prevent DNA damage	↓total oxidant status, ↓oxidative stress index, ↑total antioxidant status, ↓MPO, ↓IL-1β, ↓IL-6, ↓TNF-α, ↓TGF-β1, ↓RF, ↓CRP, ↓ASO	Kocyigit et al. (2019)
BV and hesperidin	RA	Complete Freund's adjuvant (s.c., right hind paw)	Male Wistar rats (1 mg/kg b.w., s.c. (BV), 25 mg/kg b.w, oral gavage (hesperidin), daily for 3 weeks)	Decrease paw edema, the leukocytosis, lymphocyte, monocyte, neutrophil and eosinophil counts; counteract severe inflammatory changes and leukocytic infiltration in the periarticular tissue of the ankle joints (BV and/or hesperidin); amend the lymphoid hyperplasia in white pulps of spleen and the widening of the medulla and mononuclear cell infiltration found in thymus (BV and hesperidin)	↑GSH, ↑GPx, ↓IL-2, ↓IL-12, ↓TNF-α (BV); ↓LPO, ↑GSH, ↑SOD, ↑GPx, ↑IL-10, ↓IL-2, ↓IL-12, ↓TNF-α, ↑IL-4 (BV and hesperidin)	Ahmed et al. (2018)
Wasp venom	RA	—	MH7A cells (0, 12.5, 25, 50, and 100 μg/ml)	Inhibit viability, induce MH7A synovial cell apoptosis	↑Caspase-3, ↑Bax, ↓Bcl-2	Liu et al. (2021)
bvPLA$_2$	RA	Collagen-induced arthritis and incomplete Freund's adjuvant (s.c.)	Male DBA/1 mice (0.1, 0.5, 1.0 mg/kg, i.p., for 5 weeks)	Inhibit body weight loss, alleviate squeaking score, paw thickness, and arthritis index; alleviate histological signs of collagen-induced abnormalities in the knee joints; anti-arthritic effects were blocked by selective Treg depletion	—	Choi et al. (2021)
Polymeric microneedle-mediated transdermal delivery of MEL	RA	Freund's adjuvant (injected into hint foot pad)	Male SD rats (100 μg, transdermal, every other day for 8 times)	Decrease paw thickness, clinical score, suppress RA progression, preserve cartilage integrity, reduce infiltration of leukocytes and WBC level	—	Du et al. (2021)
			Male BALB/c mice (15 μg, transdermal, every other day for 6 times)	Decrease paw thickness, clinical score, reduce symptoms of RA, reduce infiltration of inflammatory cells, preserve integrity of cartilages; increase lymphocytes, decrease monocytes and granulocytes	↓TNF-α, ↓IL-17; increase CD3CD4CD25Foxp3$^+$ cells	

(Continued on following page)

TABLE 3 (*Continued*) Summary of the effects and mechanisms of BV and its main components on inflammatory diseases.

BV and/or its components	Model	Inducer/Method	Animal/Cell (BV etc. administration)	Effects	Mechanisms	References
MEL	Osteoarthritis	IL-1β	C518 cells (0, 0.1, 0.5, 1, and 10 μg/ml, for 24 h)	Inhibit NF-κB activation by preventing IκB degradation and NF-κB migration	↓iNOS, ↓NF-κB	Tang et al. (2021)
BV and apamin	Gouty arthritis	MSU (i.d. injection into the right paw)	C57BL/6 male mice (0.5 and 1 mg kg, i.p., once daily for 3 days)	Decrease paw edema, reverse the change in weight-bearing distribution; decrease MSU crystal formation	↓IL-1β, ↓IL-6, ↓TNF-α, ↓NLRP3, ↓ASC, ↓Caspase-1, ↓NF-κB	Yun Mi Lee et al. (2020)
		MSU	Murine macrophage RAW 264.7 cells (1–5 μg/ml, for 1 h)	–	↓TNF-α, ↓p-IκB-α	
BV	Gouty Arthritis	MSU (intra-articular injection)	Male SD rats (0.5 mg/kg, tibiotarsal intra-articular injection)	Mitigate paw edema and mechanical allodynia, suppress neutrophil infiltration, reduce progression of synovitis	↓MIP-1α, ↓MIP-1β, ↓MCP-1, ↓GRO-α, ↓MIP-2α, ↓iNOS, ↓COX-2	Goo et al. (2021)
Inflammation related digestive diseases						
BV	Gastric ulceration	Acetylsalicylic acid (oral administration)	Male Sprague-Dawley rats (2 mg/kg BW, i.p., for 7 days)	Gastric mucosa was nearly normal, with slight congestion; attenuate haematological, haemostatic, and histopathological alterations, reduce tissue eosinophil level; decrease ulcer index, fluid volumes, and pepsin concentrations	↓TNF-α, ↓MPO, ↓MDA, ↑SOD, ↑GSH, ↑Hsp70, ↓Bax, ↓Caspase-3	Mohamed et al. (2019)
BV	Nonalcoholic steatohepatitis	Fructose (drinking water)	Male Wistar albino rats (0.1 mg/kg, i.p., 3 times per week during the last 2 weeks)	Mitigate body weight and epididymal fat weight; increase blood glucose, decrease insulin concentration and HOMA; decrease serum and liver total lipids and TGs, total and LDL cholesterol, increase HDL cholesterol; normalize liver ODS, minute focal hepatocellular necrosis associated with inflammatory cell infiltration	↓SREBP1c, ↓SREBP2, ↑GCL, ↑Nrf2, ↓MDA, ↑intestinal tight junction proteins, ↓TNF-α, ↑LXRα, ↑FXR	Abd El-Haleim, (2020)
MEL	Ulcerative colitis	Acetic acid (intrarectal administration)	Swiss albino male mice (40 μg/kg, p.o., once per day for 5 days)	Increase body weight gain, decrease colon mass index; preserve colon mucosa and submucosa	↓TNF-α, ↓IL-6, ↓TLR4, ↓TRAF6, ↓p38 MAPK, ↓NF-κB, ↓PGE2, ↓COX-2, ↓$sPLA_2$, ↓MDA, ↑SOD, ↑GSH	Ahmedy et al. (2020)

(Continued on following page)

TABLE 3 (*Continued*) Summary of the effects and mechanisms of BV and its main components on inflammatory diseases.

BV and/or its components	Model	Inducer/Method	Animal/Cell (BV etc. administration)	Effects	Mechanisms	References
MEL	Acute liver failure	D-galactosamine/ LPS) (i.p.)	Male C57BL/6 mice (2, 4, and 8 mg/kg, i.p.)	Improve survival, hepatic functions, gross liver appearance and histological changes, decrease hepatocyte death, alleviate hepatic inflammation; induce no obvious *in vivo* toxicity; repress Warburg effect	↓Total bilirubin, ↓ALT, ↓AST, ↓TNF-α, ↓IL-1β, ↓p-Akt, ↓p-mTOR, ↓PKM2, ↓HIF-1α, ↓TNF-α, ↓IL-1β	Fan et al. (2020)
		LPS	RAW264.7 murine macrophages (0.35, 0.70, 1.40, and 2.80 μM, for 24 h)	Exert antioxidative effects; increase OCR, decrease ECAR, inhibit aerobic glycolysis; disrupt Warburg effect	↑SOD, ↑CAT, ↑GSH, ↓MDA, ↑acetyl-CoA, ↓LDH, ↓lactate, ↓glucose transporter 1 (GLUT-1), ↓LDHA, ↓p-Akt, ↓p-mTOR, ↓PKM2, ↓HIF-1α, ↓TNF-α, ↓IL-1β	
Inflammation related other diseases						
BV	Allergic chronic rhinosinusitis	Ovalbumin (i.p.) and *Staphylococcus aureus* enterotoxin B (intranasally)	Female BALB/c mice (0.5 and 5 ng/ml, intranasally, 3 times a week for 8 weeks)	Decrease neutrophils and eosinophils in nasal lavage fluid; decrease inflammatory cell infiltration and PAS-positive cells	↓INF-γ, ↓NF-κB, ↓AP-1	Seung-Heon Shin et al. (2018)
BV	Pleurisy	Carrageenan (injected into pleural cavity)	Male Balb/c mice (0.8 and 0.08 mg/kg, s.c. into the left Chize acupoint, LU-5, the first was 5 min before and a second was 12 h after carrageenan injection)	Suppress pleural exudate volume and leukocyte accumulation, increase the number of Fos-ir neurons	↓MPO, ↓IL-1β	Choi et al. (2018)
BV	Inflammatory periodontitis	*Porphyromonas gingivalis* (applied to gingival margin)	Male Balb/C mice (1, 10, and 100 μg/kg, once a week for 4 weeks)	Attenuate bone resorption and osteoclast formation	↓TNF-α, ↓IL-1β	Gu et al. (2019)
	Osteoclastogenesis	RANKL	Mouse monocyte/ macrophage RAW 264.7 cells (1, 10, and 100 ng/ml, for 5 days)	Show no cytotoxic effect; inhibit osteoclastogenic differentiation; attenuate F-actin ring formation and osteoclast resorptive activity	↓Nuclear factor of activated T cells 1 (NFATc1), ↓integrin αv, ↓integrin β3, ↓cathepsin K, ↓TNF-α, ↓IL-1β, ↓p-Akt, ↓p-ERK 1/2, ↓p-p38, ↓p-JNK	
MEL	Periodontitis	PgLPS	HaCaT cells (0.1, 0.5, and 1 μg/ml, for 8 h)	Anti-inflammatory effects	↓IFN-γ, ↓TNF-α, ↓TLR-4, ↓IL-8, ↓IL-6, ↓pIκB, ↓NF-κB p65, ↓pAkt, ↓pERK1/2	Woon-Hae Kim et al. (2018)
BV	Allergic inflammatory disorders	PMA and A23187 (PMACI)	HMC-1 cells (5 and 10 μg/ml, for 30 min-24 h)	Suppress histamine release	↓TNF-α, ↓IL-6, ↓IL-1β, ↓p-ERK, ↓p-JNK, ↓p-p38, ↓p-MEK1/2, ↓p-MAPK kinase 3/6 (p-MKK3/6), ↓p-MKK4, ↓p-STAT3 (Ser727), ↓p-Akt	Kang et al. (2018)
		Compound 48/80 (i.p., Anaphylactic shock)	ICR male mice (20 mg/kg, i.p.)	Reduce mortality rates	↓TNF-α, ↓IL-6, ↓IL-1β, ↓p-ERK, ↓p-JNK, ↓p-p38, ↓p-STAT3 (Tyr705)	

Abbreviations are as shown in the literature. (↓), down-regulation or inhibition; (↑), up-regulation or activation.

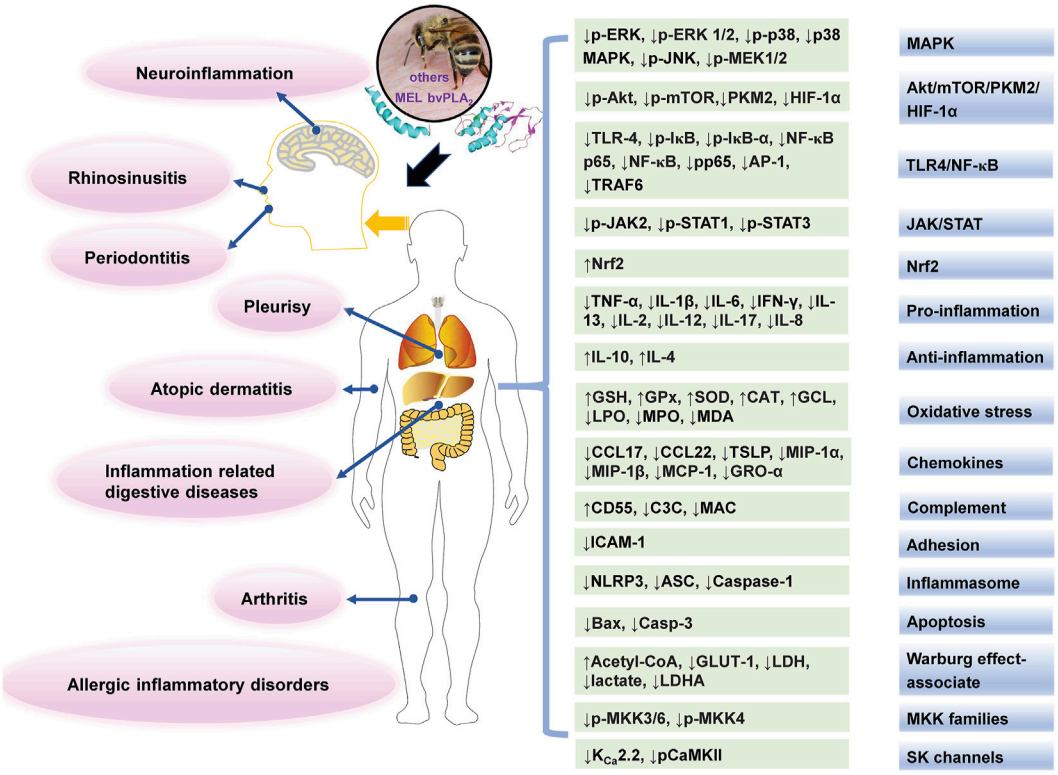

FIGURE 4
The main affected targets and mechanisms of BV and its main components in alleviating inflammatory diseases. The texts in pink oval boxes, light grey green boxes, and gradient grey blue boxes indicate related diseases, regulated targets and pathways (or mechanisms), respectively.

in rats induced by methyl mercury chloride through regulation of the methyl mercury chloride altered behavioral responses, gene expression of tight junction proteins, and immune-expression markers for specific neural cell types (Abu-Zeid et al., 2021).

MEL exerted neuroprotective effects on HT22 cells treated with $A\beta_{25-35}$ through activation of nuclear factor (erythroid-derived 2)-like 2 (Nrf2)/heme oxygenase-1 (HO-1), and tropomyosin-related kinase receptor B (TrkB)/cAMP response element-binding (CREB)/BDNF signaling pathways. Additionally, MEL restored exhausted learning and memory abilities in an $A\beta_{25-35}$-induced cognitive deficits mouse model. The above results showed that MEL could be a candidate agent for neurodegenerative disorders (Cong Duc and Lee, 2021). Apamin enhanced neurite outgrowth and axon regeneration after laceration injury, and increased the expression of BDNF, nerve growth factor (NGF) and regeneration-related genes in mature cortical neurons (Kim H. et al., 2021). Apamin inhibited LPS-induced neuroinflammatory responses in BV2 and rat primary microglial cells. It significantly inhibited proinflammatory cytokine production and microglial cell activation by downregulating the expression of pCaMKII and toll-like receptor 4 (TLR4) (Park et al., 2020). Especially, apamin inhibited the translocation of p65/STAT3 and MAPK-ERK signaling, which was verified through inhibitors (Park et al., 2020). The above findings suggested that apamin could be a potential adjuvant for treating a variety of neurological diseases. Besides, Apamin and $bvPLA_2$ contributed to the control of multiple sclerosis (Lee G. et al., 2019; Danesh-Seta et al., 2021).

Alleviating inflammatory diseases

Chronic inflammation could cause the development of many diseases, such as skin diseases and RA (Wehbe et al., 2019). In classical medicine, BV and its main components were used for treating chronic inflammatory disorders. Recent studies are shown in Table 3, and the main affected targets and mechanism of BV and its main components in alleviating inflammatory diseases is shown in Figure 4.

Effects on atopic dermatitis

As a chronic skin inflammatory disease, atopic dermatitis is caused by several genetic, inflammatory, and immunological abnormalities and characterized by recurrent eczema and

itching (Gu et al., 2018; Lee Y. J. et al., 2020). BV and its main components, MEL and bvPLA$_2$, have anti-inflammatory and atopic dermatitis effects *in vivo* and *in vitro*.

In vivo, BV treatment significantly reduced phthalic anhydride-induced atopic dermatitis clinical score, back and ear epidermal thickness, and the lymph node weight, decreased the level of IgE, IL-4, IL-13, TNF-α, IL-1β, and IL-6 and the number of eosinophil, neutrophil, monocytes, mast cells, F4/80-positive cells and Ly6G-positive cells, as well as inhibited the iNOS and COX-2 expression and activated MAPK and NF-κB in the skin tissues. *In vitro*, BV also suppressed MAPK and NF-κB pathway in RAW 264.7 murine macrophages treated with LPS and HaCaT human keratinocytes treated with TNF-α-/IFN-γ (Lee Y. J. et al., 2020). Besides MAPK and NF-κB pathways, Janus kinase (JAK)/STAT signal pathways were also blockaded by the treatment with BV or MEL in TNF-α/IFN-γ-treated HaCaT cells, and the chemokines CCL22 and CCL17 and pro-inflammatory cytokines IL-6, IL-1β, and IFN-γ decreased (An et al., 2018).

In addition, BV relieved atopic dermatitis by inactivating the complement system. *In vitro*, BV inhibited the complement system via the induction of CD55 by activating ERKs in THP-1 cells. *In vivo*, BV attenuated skin condition, and decreased clinical skin score in mice with atopic dermatitis-like lesions from 2.5% 2,4-dinitrochlorobenzene (DNCB) treatment; furthermore, BV and MEL inactivated the complement system, especially via the CD55 induction, which downregulated the membrane attack complex (MAC) and C3 convertase (C3C) levels (Kim Y. et al., 2019).

The bvPLA$_2$ treatment suppressed atopic dermatitis-related skin swelling, improved ear thickness, reduced IgE and the expression of Th1 and Th2 cytokines (IFN-γ, IL-4, IL-6 and IL-10), induced Treg, and decreased epidermal and dermal thickness and macrophage and mast cell infiltration in *Dermatophagoides farinae* extract/DNCB-treated mice. However, the effects were eliminated in CD206$^{-/-}$ mice after *D. farinae* extract/DNCB treatment. The above data suggested that bvPLA$_2$ could alleviate atopic skin inflammation through interaction with CD206 (Shin D. et al., 2018).

Effects on arthritis

Arthritis has a high incidence rate in the world and includes more than 100 forms, and the most common ones include RA, osteoarthritis, psoriatic arthritis and inflammatory arthritis (Tang, 2019). BV and its main components, MEL and apamin, and wasp venom, have anti-inflammatory, antioxidative, anti-apoptotic, and other effects on arthritis.

RA is a chronic inflammatory autoimmune disease, which is often affected by genetic, epigenetic, and environmental factors (Giannini et al., 2020). BV treatment decreased the paw volume and arthritis index in RA rats induced by Freund's complete adjuvant, and showed anti-oxidant, anti-inflammatory, anti-genotoxic, and immunomodulatory effects through decreasing total oxidant status, oxidative stress index, myeloperoxidase (MPO), IL-1β, IL-6, TNF-α, TGF-β1 and mononuclear leukocyte DNA damage levels, and increasing total antioxidant status level (Kocyigit et al., 2019). In addition, wasp venom dramatically inhibited the viability of MH7A human RA synovial fibroblasts *in vitro* and induced MH7A cell apoptosis through up-regulating the expression of Caspase-3 and Bax and down-regulating that of Bcl-2 (Liu et al., 2021). Besides, bvPLA$_2$ showed significant anti-inflammatory and arthritic effect on a RA mouse model though the induction of Tregs (Choi et al., 2021). Polymeric microneedle-mediated transdermal delivery of MEL inhibited the progression of RA in arthritis rat and mouse models, suppressed the levels of IL-17 and TNF-α, and raised the percentage of regulatory CD4 T cells, which suggested that polymeric microneedle-mediated MEL transdermal delivery could be used as a new treatment for RA and other autoimmune diseases (Du et al., 2021).

In addition, MEL showed anti-inflammatory effects on C518 rat knee joint cells induced by IL-1β *via* suppressing the expression of iNOS and preventing the degradation of IκB in cytoplasm and the migration of NF-κB from cytoplasm to nucleus, which suggested that MEL could be used as an anti-inflammatory candidate against osteoarthritis (Tang et al., 2021). BV and apamin treatment decreased the inflammatory paw edema, and reversed the alternation in weight-bearing distribution in monosodium urate (MSU)-administered mice by inhibiting proinflammatory cytokine production and inflammasome formation, as well as decreased MSU crystal formation, which suggested that BV and apamin could be potential novel agents for gouty arthritis (Lee Y. M. et al., 2020). Besides, BV also showed anti-inflammatory effect to alleviate pain and edema in gouty arthritis rats through reducing the expression of proinflammatory cytokines and chemokines (Goo et al., 2021).

Effects on inflammation related digestive diseases

BV and MEL exerted anti-inflammatory effects on inflammation related digestive diseases, such as gastric ulceration, nonalcoholic steatohepatitis, ulcerative colitis, acute liver failure, etc.

BV showed gastro-protective effects against rats gastric ulceration induced by acetylsalicylic acid. It attenuated the haematological, haemostatic, and histopathological alterations, reduced the tissue eosinophil level, as well as decreased the ulcer index, fluid volumes, and pepsin concentrations in acetylsalicylic acid-treated rats, which attributed to its anti-inflammatory and

antioxidant effects by decreasing TNF-α, MPO levels and MDA concentration, and increasing SOD activity and glutathione (GSH) concentration, its anti-apoptotic property by downregulating Bax and Caspase-3 levels, as well as protection of gastric tissue by upregulating Hsp70 (Mohamed et al., 2019). Besides, BV possessed antioxidant, anti-inflammatory, and anti-hyperlipidemic effects against rats nonalcoholic steatohepatitis induced by fructose, which may be due to the enhanced expression of nuclear receptors, liver X receptor α (LXRα) and farnesoid X receptor (FXR), the reduced liver sterol regulatory element-binding protein 1/2 (SREBP1/2) levels, and the improved intestine tight junction protein expression (Abd El-Haleim, 2020).

MEL showed antiulcerogenic effect in acetic acid-induced ulcerative colitis in mice. It increased the body weight gain, decreased colon mass index and preserved colon mucosa and submucosa, which could be via mitigating TLR4/TNF receptor associated factor 6 (TRAF6) mediated NF-κB and p38 MAPK signaling (Ahmedy et al., 2020). Besides, MEL improved survival rate, reduced serious symptoms and signs, and relieved hepatic inflammation by reducing total bilirubin, alanine transaminase (ALT), aspartate aminotransferase (AST), TNF-α and IL-1β levels in acute liver failure mice. In LPS-stimulated RAW264.7 macrophages, MEL exerted antioxidant and anti-inflammatory effects. Furthermore, MEL disrupted the Warburg effect by inhibiting the Akt/mTOR/pyruvate kinase M2 (PKM2)/HIF-1α pathway to alleviate inflammation *in vitro* and *in vivo*. Molecular docking analysis confirmed that MEL targeted PKM2, and knockout of PKM2 produced anti-inflammatory effects similar to MEL *in vitro*. The above findings highlighted a new strategy of MEL in treating acute liver failure (Fan et al., 2020).

Effects on inflammation related other diseases

BV and its main components, including MEL, $bvPLA_2$ and apamin, also exerted anti-inflammatory effects on other diseases, such as allergic chronic rhinosinusitis (Shin S. H. et al., 2018), pleurisy (Choi et al., 2018), inflammatory periodontitis (Kim W. H. et al., 2018; Gu et al., 2019), allergic inflammatory disorders (Kang et al., 2018), etc. For instance, BV showed anti-inflammatory effects in an allergic chronic rhinosinusitis mouse model. BV decreased neutrophil and eosinophil counts in nasal lavage fluid, reduced interferon-γ (INF-γ) level, inflammatory cell infiltration and PAS-positive cells, as well as suppressed NF-κB and activator protein-1 (AP-1) expressions in mouse nasal mucosa, which indicated that BV may possess potential value in treating allergic chronic rhinosinusitis (Shin S. H. et al., 2018).

Analgesic effect

BV is usually used to relieve pain, mainly by injecting it into acupoints, such as ST36 (Zusanli) (Li et al., 2020a). In recently 4 years, BV and its main components, including MEL and $bvPLA_2$, have been reported to attenuate neuropathic pain, osteoarthritis pain, and burn injury pain, etc., as shown in Table 4.

Effects on neuropathic pain

Neuropathic pain is a chronic pain, often caused by damaged or abnormally discharged neurons in the peripheral or central nervous systems (Hamad et al., 2018). Some anti-cancer agents, such as oxaliplatin, vincristine and paclitaxel, could induce neuropathic pain. BV acupuncture alleviated cold and mechanical allodynia induced by oxaliplatin through regulating the action potential threshold of A-fiber dorsal root ganglia neurons (Lee J. H. et al., 2020). Besides, s.c. injection of MEL at acupoint ST36 relieved the mechanical and cold allodynia, and inhibited hyperexcitated spinal wide dynamic range (WDR) neuronal activity, via activating the spinal $α_1$- and $α_2$-adrenergic receptors (Choi et al., 2019). BV acupuncture inhibited abnormal hyperexcitation of the spinal WDR neurons caused by cutaneous cold and mechanical stimulation in rats treated with vincristine, which was mediated by the descending noradrenergic pathway (Li et al., 2020a). Co-treatment of BV and venlafaxine produced a lasting and additive analgesic effects on paclitaxel-induced cold and mechanical allodynia in mice, through spinal $α_2$-adrenergic, 5-HT_1/5-HT_2, and 5-HT_3 receptors, providing a promising clinical strategy (Li et al., 2020b).

Effects on other pain

BV acupuncture improved the pain-related behavior in the rat model of collagenase-induced osteoarthritis resulting from the partial partaking of the δ-opioid and $α_2$-adrenergic receptors (Huh et al., 2018). Besides, BV biotherapy could sustainedly improve knee osteoarthritis pain and body function in a phase III clinical trial (Conrad et al., 2019).

Repeated BV treatment reduced the mechanical allodynia, recovered the ipsilateral paw print area and single stance, and reduced the tissue damage in a mice pain model induced by scalding burn. And BV stimulation inhibited the increase of Sub P expression in peripheral and central nervous systems. The above results suggested that BV treatment could effectively control the pain of burn patients (Kang et al., 2021).

TABLE 4 Summary of the analgesic effects and mechanisms of BV and its main components.

BV and/or its components	Model	Inducer/ Method	Animal/Cell (BV etc. administration)	Effects	Mechanisms	Reference
Neuropathic pain						
BV	Neuropathic pain	Oxaliplatin (i.p.)	SD rats (0.1 and 1 mg/kg, s.c., acupoint ST36 or LI11)	Alleviate cold and mechanical allodynia	Increase action potential and current threshold in acutely dissociated dorsal root ganglia neurons	Ji Hwan Lee et al. (2020)
MEL	Peripheral neuropathic pain	Oxaliplatin (i.p.)	SD rats (0.5 mg/kg, s.c., ipsilateral acupoint, Zusanli (ST 36) of right leg)	Alleviate mechanical and cold allodynia, inhibit hyperexcitated spinal WDR neuronal activity	Spinal α_1- and α_2-adrenergic receptors are involved in analgesic effects	Choi et al. (2019)
BV	Peripheral neuropathic pain	Vincristine (i.p.)	Male SD rats (1.0 mg/kg, s.c., right hind limb ST36 (Zusanli) acupoint)	Ameliorate cold and mechanical hypersensitivity, ameliorate hyperexcitation of spinal WDR neuron	Analgesia was mediated by descending noradrenergic pathway	Li et al. (2020a)
BV and venlafaxine (VLX)	Peripheral neuropathic pain	Paclitaxel (i.p.)	Male C57BL/6j mice (0.25, 1.0, and 2.5 mg/kg, s.c., ST36 (Zusanli acupoint) of right hind limb (BV); 1.0 mg/kg, s.c. (BV) and 40 mg/kg, i.p. (VLX))	Ameliorate cold and mechanical allodynia (co-administration > monotherapy)	Spinal α_2-adrenergic receptor, 5-HT_1, 5-HT_2, and 5-HT_3 receptors mediate analgesic effects (co-administration)	Li et al. (2020b)
$bvPLA_2$	Neuropathic Pain	Right L5 SNL surgery	SD rats (0.2 mg/kg/day, i.p., for 2 days)	Attenuate mechanical allodynia	Analgesic effects are mediated by activation of spinal α_1-adrenergic receptors	Woo et al. (2019)
Other pain						
BV	Osteoarthritis	Collagenase (intra-articularly injected)	Male Sprague-Dawley rats (1 and 2 mg/kg, ST-36 acupoint)	Improve pain-related behavior	Partial involvement of the δ-opioid and α_2-adrenergic receptors	Huh et al. (2018)
BV	Burn injury	Right hind paw immersed in hot water (65°C, 3 s)	Male ICR mice (0.01, 0.02, and 0.1 mg/kg, s.c., ipsilateral knee area, once daily for 14 days)	Reduce mechanical allodynia, recover ipsilateral paw print area and single stance, reduce tissue damage	↓Sub P (dorsal root ganglia and spinal cord)	Kang et al. (2021)

Abbreviations are as shown in the literature. (↓), down-regulation or inhibition; (↑), up-regulation or activation.

Anti-infectivity effect

In recent 4 years, BV and main components, MEL, $bvPLA_2$, melectin and MPX, have been reported to show anti-infectivity effects, as shown in Table 5. In particular, the effects on severe acute respiratory syndrome–coronavirus 2 (SARS-CoV-2) and drug resistant bacteria have attracted more and more attention.

Antiviral effect

Coronavirus disease (COVID-19), caused by SARS-CoV-2, has infected people in 210 countries and was declared a pandemic by WHO on 12 March 2020 (Al Naggar et al., 2021). BV has shown potent antiviral, anti-inflammatory and immunomodulatory effects, which suggested that BV treatment could be a promising complementary therapy to prevent SARS-CoV-2 (Kasozi et al., 2020; Al Naggar et al., 2021; Lima et al., 2021). In Hubei Province in China, the local beekeeper association investigated 5115 beekeepers (including 723 in Wuhan) from 23 February to 8 March in 2020. The results showed that no one had any symptoms related to COVID-19 (Yang et al., 2020). In addition, sitagliptin-MEL optimized nanoformula was repurposed, and showed antiviral potential against SARS-CoV-2 isolate with IC_{50} values of 8.439 μM and *in vitro* 3CL-protease inhibition with IC_{50} values of 7.216 μM. Sitagliptin-MEL could ensure improved delivery to target cells and cell uptaking, with anti-SARS-CoV-2 activity (Al-Rabia et al., 2021).

Human immunodeficiency virus (HIV) has been a major social and health problem for about 30 years. BV was safe and maybe therapeutic in a specified dose, owing to MEL uptake by HIV infected cells which resulted in reduced HIV gene expression and replication (Uzair et al., 2018). A recent study using bioinformatics tools indicated that in addition to envelope

TABLE 5 Summary of the anti-infectivity effects and mechanisms of BV and its main components.

BV and/or its components	Model	Inducer/Method	Animal/Cell (BV etc. administration)	Effects	Mechanisms	Reference
Antiviral effect						
MEL, Sitagliptin- MEL optimized nanoformula	SARS-CoV-2	SARS-CoV-2	Vero E6 cells (1 ng/ml-10 μg/ml)	Show antiviral activity and *in vitro* Mpro 3CL-protease inhibition	—	Al-Rabia et al. (2021)
BV	HCV	HCV (JFH1 strain of genotype 2a)	Huh7it-1 cells (0.01–1000 ng/ml)	Inhibit HCV	Act on HCV particles directly	Sarhan et al. (2020)
CH/AL-BV	PRRSV	PRRSV type II LMY strain (intramuscularly)	Pigs (2 mg, nasally)	Reduce lung lesion scores and microscopic lesion score, decrease viral genome levels, increase virus neutralization titers levels	↑Th cells, ↑IL-12, ↑IFN-γ, ↑PRRSV-specific IgG Ab, ↑$CD4^+$ T cells, ↑STAT4, ↑T-bet, ↓Treg cells, ↓IL-10, ↓TGF-β, ↓STAT5, ↓Foxp3, ↑IFN-γ secreting $CD4^+$ T cells, ↑Th/memory cells	Lee et al. (2018)
Antibacterial effect						
BV	MRSA pneumonia	—	ATCC 33591 (reference strain, HA-MRSA) (0.98, 1.95, 3.9, and 7.8 μg/ml, for 4 h)	Show antibacterial activity	↓*hla*, ↓*agrA*, ↓α-hemolysin	Kong et al. (2020)
		—	USA300 (wild-type LAC strain, CA-MRSA)	Show antibacterial activity	—	
		MRSA	264.7 RAW macrophages (0.98, 1.95, 3.9, and 7.8 μg/ml)	—	↓TNF-α, ↓IL-6	
		USA300	A549 cells (0.78–6.25 μg/ml)	—	↓LDH	
		USA300 (intranasal infection)	Balb/c mice (0.125, 0.25, and 0.5 mg/kg/day, i.p.)	Increase survival rates; no abscesses, less lung edema and fewer inflammatory cells; reduce the number of bacteria in the lungs	↓Serum amyloid A3 (Saa3), ↓chemokine (C–X–C motif) ligand 9 (Cxcl9), ↓orosomucoid 1 (Orm1), ↑PON1	
BV and MEL	MRSA	—	Enterotoxigenic *S. aureus* isolates (ATCC 13565, ATCC 14558, ATCC 19095, and ATCC 23235) (0.45–917 μg/ml)	Show antibacterial activity, do not interfere with staphylococcal enterotoxin production or release	—	Pereira et al. (2020)
			MRSA ATCC 33591 and 5 clinical isolates (0.45–917 μg/ml)	Show antibacterial activity, exhibit bactericidal synergism with oxacillin. Show cell distortion, cell disintegration with leakage of cytoplasmic content and loss of cytoplasm content (ATCC 33591)	—	
BV, MEL and PLA_2	*Escherichia coli*	—	*Escherichia coli* (ATCC® 25922™) (0–200 μg/ml (BV), 0–10 μg/ml (PLA_2))	Inhibit membrane-bound *E. coli.* F_1F_0-ATPase	—	Nehme et al. (2020)
BV	*Salmonella* strains	—	16 *Salmonella* strains (32–4096 μg/ml, for 24 h)	Show antibacterial activity, reduce biofilm formation	↑*rprA*, ↑*oxyS*, ↑*dsrA* (*S.* Newport Lhica N2 and *S.* Typhimurium T22)	Arteaga et al. (2019)
BV	Pathogenic Gram-positive and Gram-negative bacteria	—	*S. aureus* subsp. *aureus* (DSM 20231), *B. cereus* (DSM 6791), *S. enterica* subsp. *enterica* (DSM 14221), *L. innocua* (ATCC 3309) and *E. coli* (ATCC 25922) (12.5–800 μg/ml, for 24 or 48 h)	Show a broad spectrum of anti-infectivity properties	—	Tanuwidjaja et al. (2021)
		—			—	

(Continued on following page)

TABLE 5 (*Continued*) Summary of the anti-infectivity effects and mechanisms of BV and its main components.

BV and/or its components	Model	Inducer/Method	Animal/Cell (BV etc. administration)	Effects	Mechanisms	Reference
Crude BV in Thailand	Pathogenic Gram-positive and Gram-negative bacteria, a fungus		*B. subtilis*, *M. luteus*, *S. aureus*, *S. aureus* MRSA, *S. epidermidis*, *E. coli*, *K. pneuminiae*, *S. typhimurium* (3.12–400 μg/ml, for 24 h); *C. albicans* (3.12–400 μg/ml, for 48 h)	Show more robust antibacterial activities against Gram-positive than Gram-negative bacteria or a fungus		Maitip et al. (2021)
MEL	XDR *Acinetobacter* spp.	—	XDR *Acinetobacter* spp. (0.0625–8 μg/ml)	Show antibacterial activity, cause fluorescence release from XDR isolates, induce aggregation, cell lysis, membrane disruption, and vesicle	—	Pashaei et al. (2019)
		A. baumannii ATCC 19,606 (inoculated on burn wound area)	Mouse model of third degree burn (Balb/c mice) (8, 16, and 32 μg/ml, incubated on infected area, for 2 h)	Eradicate colonized XDR bacteria	—	
MEL and doripenem	MDR *A. baumannii*	—	MDR *A. baumannii* (for 24 h)	Show synergistic antibacterial activity	—	Akbari et al. (2019)
MEL-doripenem and MEL-ceftazidime	MDR *P. aeruginosa*	—	MDR *P. aeruginosa* (for 24 h)	Show synergistic antibacterial activity	—	
Melectin	Broad-spectrum	—	*S. aureus* ATCC 25923, *P. aeruginosa* KCTC 2004, *K. pneumoniae* KCTC 2008, *E. coli* ATCC 25922; drug resistant strains (0–32 μM)	Show antibacterial activity	Have an α-helical structure, bind to LPS or LTA and kill bacteria through bacterial membrane permeabilization (*S. aureus* ATCC 25923, and *P. aeruginosa* ATCC 27853)	Ko et al. (2020)
		S. aureus	Human dermal fibroblasts (5 μM, for 24 h)	—	↓TNF-α, ↓IL-8, ↓IL-6, ↓IL-1β	
Melectin	Broad-spectrum	—	Drug-sensitive bacterial strains (4, 8, and 16 μM, etc.)	Show antibacterial activity	Have an α-helix form, effect on the outer and inner membrane of bacteria (*E. coli*), interact with DNA	Liang et al. (2021)
MPX	*Actinobacillus pleuropneumoniae*	—	*A. pleuropneumoniae* (16, 32, and 64 μg/ml)	Show antibacterial activity, increase membrane permeability, release bacterial proteins and Ca^{2+}, Na^{+} and other cations, reduce biofilm formation	↑PurC, ↓ApxI, ↓ApxII, ↓Apa1, ↑Sap A	Wang et al. (2020)
		A. pleuropneumoniae serotype 5b L20 strain (inoculated intranasally)	Female BALB/c mice (20 mg/kg, i.p.)	Protect mice from a lethal dose of *A. pleuropneumoniae*, decrease the number of bacteria colonising the lung, relieve lung inflammation	↓TNF-α, ↓IL-6	
Antifungal effect						
BV	*Trichophyton rubrum*	—	*T. rubrum* (0.1, 10, and 40 mg/distilled water 100 μL)	Deliver a significant level of inhibition	—	Park et al. (2018)

Abbreviations are as shown in the literature. (↓), down-regulation or inhibition; (↑), up-regulation or activation.

and long terminal repeat, HIV capsid and proteases could have great potential as MEL targets (Dehghani et al., 2020).

Hepatitis C virus (HCV) infection is a worldwide health concern, which can lead to serious liver diseases. BV inhibited the entry stages of HCV infection cycle by interacting with virus particles, through a non-common peptide(s), which demonstrated that the BV could be a potential candidate for characterizing and developing new natural anti-HCV agents (Sarhan et al., 2020).

Besides, chitosan/alginate nanoparticle encapsulated BV (CH/AL-BV) was developed, and nasal administration of CH/AL-BV induced non-specific immune stimulating effects, and protected against porcine reproductive and respiratory syndrome virus (PRRSV) infection, suggesting that nasal-delivered CH/AL-BV could produce effective protective immunity against PPRSV infection (Lee et al., 2018).

Antibacterial effect

BV and MEL showed antibacterial activity against MRSA (Kong et al., 2020; Pereira et al., 2020). *In vitro*, BV showed strong anti-infectivity effects against two MRSA strains, ATCC 33591 and USA300, and decreased the *hla* and *agrA* genes expression and the α-hemolysin production in ATCC 33591. BV alleviated the secretion of TNF-α and IL-6 in MRSA-stimulated 264.7 RAW macrophage. Besides, BV protected A549 cells from MRSA. *In vivo*, BV increased mouse survival rates, decreased the bacteria number in the lungs and relived symptoms of pneumonia induced by MRSA in mice. The above results indicated that BV could be a candidate for treating pneumonia caused by MRSA infection (Kong et al., 2020). BV and mainly MEL and bvPLA$_2$, could inhibit *E. coli* F_1F_0-ATPase enzyme, a key molecular target for bacteria survival, which could be regarded as important candidate drugs against resistant bacteria (Nehme et al., 2020).

Besides, BV showed anti-infectivity activity against 16 *Salmonella* strains, and the minimum inhibitory concentrations (MIC) ranged from 256 to 1024 μg/ml. In addition, BV inhibited biofilm formation in 14 strains. The above findings indicated that BV was a potential anti-infectivity agent against food-borne pathogens (Arteaga et al., 2019).

Bacterial infection from antibiotic resistant bacteria has become a main cause of morbidity and mortality after burns. *In vitro*, MEL showed antibacterial activity against extensively drug-resistant (XDR) *Acinetobacter* spp., caused fluorescence release from XDR isolates which severed as a marker of membrane damage, and had membranolytic effect. *In vivo*, MEL eradicated the colonized XDR bacteria on infected mouse model with third-degree burn, and no toxicity at the therapeutic dose was observed (Pashaei et al., 2019). Furthermore, MEL-doripenem showed synergistic antibacterial activity against MDR *A. baumannii* isolates, while MEL-doripenem and MEL-ceftazidime showed synergistic antibacterial activity against multidrug-resistant (MDR) *P. aeruginosa* (Akbari et al., 2019). The above results showed that MEL, MEL-doripenem and MEL-ceftazidime could be regarded as topical drugs against burn infections from antibiotic resistant bacteria.

Melectin, from the venom of a bee, *Melecta albifrons*, showed broad-spectrum anti-infectivity activities against standard sensitive/clinical drug-resistant bacteria strains, and exhibited low or moderate cytotoxicity and no hemolytic activity. Besides, melectin reduced the release of TNF-α, IL-1β, IL-6, and IL-8 from *S. aureus*-stimulated human fibroblasts. These findings suggested that melectin could be considered as a new template against multidrug resistance (Ko et al., 2020; Liang et al., 2021).

MPX, from wasp venom, showed good antibacterial effect on *Actinobacillus pleuropneumoniae*, a causative agent of respiratory infections in pigs. MPX destroyed the bacterial cell membrane, blocked the bacterial biofilms formation, and modulated the expression of virulence factors of *A. pleuropneumoniae in vitro*, as well as protected mice from a lethal dose of *A. pleuropneumoniae* and relieved lung inflammation *in vivo*, which provided information for the clinical application of MPX (Wang et al., 2020).

Antifungal effect

The antifungal effects of BV components on *Trichophyton rubrum* have been evaluated, and the results showed that BV provided a significant level of inhibition in its overall form, and BV based products may play a potential antifungal therapeutic role (Park et al., 2018).

Protect effect on liver, kidney, lung and muscle injury

Protect effect on liver injury

BV and its main components, such as MEL and bvPLA$_2$, showed protect effects on liver diseases, including non-alcoholic fatty liver, hepatoxicity and cholestatic liver disease, as shown in Table 6.

The trend of elevated fasting glucose and insulin levels as well as lower levels of antioxidant parameters such as glutathione-S-transferase (GST), glutathione peroxidase (GPx), Nrf2 and GSH in rats induced by high-fat diet (HFD) was reversed by BV, and the levels of adiponectin and TNF-α were restored. The above results suggested that BV is a promising alternative treatment option for non-alcoholic fatty liver disease (Hanafi et al., 2018). BV and honey showed protective effects on hepatoxicity and lipid peroxidation in rats caused by LPS and

TABLE 6 Summary of the protect effects and mechanisms of BV and its main components on liver, kidney, lung and muscle injury.

BV and/or its components	Model	Inducer/ Method	Animal/Cell (BV etc. administration)	Effects	Mechanisms	Reference
Liver injury						
BV	Non-alcoholic fatty liver	HFD	Male Wistar rats (0.01, 0.05, 0.1 mg/kg, s.c.)	Normalize lipid profile values, decrease insulin resistance index, increase GSH/glutathione disulphide (GSSG) ratio; improve the architecture of liver cells showing normal sinusoids	↓ALT, ↓AST, ↓gamma-glutamyltransferase, ↓bilirubin, ↓FBG, ↓insulin, ↓TG, ↓TC, ↓LDL-C, ↓hepatic TGs, ↓hepatic TC, ↑HDL-C, ↑hepatic GSH, ↓serum GSSG, ↑glutathione reductase, ↑GST, ↑tGPx, ↑sGPx, ↑nsGPx, ↑Nrf2, ↓MDA, ↑adiponectin, ↓TNF-α	Hanafi et al. (2018)
BV and honey	Hepatoxicity	LPS and CCl_4 (i.p.)	Adult male albino rats (1 mg/kg bw, i.p. (BV); 1 mg/kg bw, i.p. and 25 mg/kg bw, orally (BV and honey); every day for 2 months)	Provide a protective effect on hepatotoxicity, reestablish disturbed hematological parameters and liver histopathology	↓ALT, ↓AST, ↓alpha-fetoprotein (AFP), ↓Plasma lipid peroxide, ↑GPx	Meligi et al. (2020)
MEL	Hepatotoxicity	Isoniazid and rifampicin (p.o.)	Male rats *Rattus rattus* (15 and 30 μg/kg, s.c., for 15 days)	Increase body weight and liver weight, decrease total protein content, show high hematological alterations, decrease severe histopathological lesions	↓Direct bilirubin, ↓total bilirubin, ↓alkaline phosphatase (ALP), ↓ALT, ↓AST, ↓LDH, ↑GSH	Naji et al. (2021)
$bvPLA_2$	Cholestatic liver disease	3,5-diethoxycarbonyl-1,4-dihydrocollidine diet	Male C57BL/6N mice (0.2 mg/kg, i.p., twice a week for 4 weeks)	Ameliorate cholestatic liver injury and fibrosis, attenuate apoptotic cell death, increase the number of Foxp3-positive cells, decrease the number of $F4/80^+$ macrophages and $CD4^+$ T-cells	↓AST, ↓ALT, ↓ALP, ↓total bilirubin, ↓collagen I, ↓fibronectin, ↓α-SMA, ↓TGF-β1, ↓p-Smad2/3, ↓cleaved Caspase-3, ↓cleaved PARP-1, ↓TNF-α, ↓IL-6, ↓p-NF-κB p65, ↑IL-10	Jung-Yeon Kim et al. (2021b)
Kidney injury						
BV	Sepsis-related acute kidney injury	LPS (i.p.)	C57BL/6N mice (100 μg/kg bw, i.p.)	Reverse renal dysfunction and structural injury, reduce the number of Mac-2 or CD4-positive cells, decrease the number of TUNEL-stained cells	↓creatinine, ↓blood urea nitrogen (BUN), ↓neutrophil gelatinase-associated lipocalin (NGAL), ↓kidney injury molecule-1 (Kim-1), ↓TNF-α, ↓IL-6, ↓4-hydroxynonenal (4-HNE), ↓MDA, ↓cleaved Caspase-3, ↓cleaved PARP1, ↓p53	Jung-Yeon Kim et al., (2020a)
MEL	Sepsis-related acute kidney injury	LPS (i.p.)	Male C57BL/6 N mice (0.01 mg/kg, i.p.)	Dampen renal dysfunction and structural damage, suppress NF-κB DNA-binding activity, reduce Mac-2-positive and CD4-positive cells, reduce 4-HNE-positive cells, reduce the number of TUNEL-stained cells, enhance survival rate	↓creatinine, ↓BUN, ↓NGAL, ↓Kim-1, ↓TNF-α, ↓IL-6, ↓p-IκB-α, ↑IκB-α, ↓p-NF-κB p65, ↓NF-κB p65, ↓MDA, ↓NOX4, ↑Nrf2, ↑HO-1, ↑quinone oxidoreductase 1 (NQO1), ↓cleaved Caspase-3, ↓cleaved PARP-1, ↓p53, ↓Bax, ↓receptor-interacting serine/threonine protein kinase 1 (RIPK1), ↓RIPK3, ↓p- mixed-lineage kinase domain-like protein (MLKL)	Jung-Yeon Kim et al. (2021a)

(Continued on following page)

TABLE 6 (*Continued*) Summary of the protect effects and mechanisms of BV and its main components on liver, kidney, lung and muscle injury.

BV and/or its components	Model	Inducer/ Method	Animal/Cell (BV etc. administration)	Effects	Mechanisms	Reference
Apamin	Sepsis-related acute kidney injury	LPS (i.p.)	Male C57BL/6N mice (0.1 mg/kg, i.p.)	Ameliorate renal dysfunction and histological injury, alleviate loss of brush borders in the proximal tubule, reduce 4-HNE-positive cells, increase GSH/GSSG ratio, decrease the number of TUNEL-stained cells, decrease number of galectin-3-stained and CD4-stained cells	↓creatinine, ↓BUN, ↓NGAL, ↓Kim-1, ↓MDA, ↓NOX4, ↑HO-1, ↓cleaved Caspase-3, ↓cleaved PARP-1, ↓TNF-α, ↓IL-6, ↓TLR4, ↓p-p65/p65, ↓E-selectin, ↓VCAM-1, ↓ICAM-1	Jung-Yeon Kim et al., (2020b)
MEL	Acute kidney injury	Cisplatin (i.p.)	Male C57/BL6 mice (10, 50, and 100 μg/kg, i.p., for 5 days)	Increase survival, ameliorate renal tubular damage, decrease CD16/32^{+} cells, increase Arg1^{+} cells, induce M2 macrophage infiltration into the kidney	↓creatinine, ↓BUN, ↓IL-6, ↓IL-1β, ↑IL-10, ↓COX-2, ↓macrophage receptor with collagenous structure (MARCO), ↑arginase 1	Hyunseong Kim et al. (2020)
Apamin	Renal fibrosis	Unilateral ureteral obstruction surgical procedure	Male C57BL/6 mice (0.5 mg/kg, i.p., twice a week)	Attenuate renal interstitial fibrosis, decrease F4/80^{+} macrophages	↑E-cadherin, ↓NGAL, ↓creatinine, ↓BUN, ↓TNF-α, ↓IL-1β, ↓cleaved-IL-1β, ↓IL-6, ↓MCP-1, ↓α-SMA, ↓vimentin, ↓fibronectin, ↓fibroblast-specific marker-1 (FSP-1), ↓TGF-β1, ↓p-STAT3, ↓p-Smad2, ↓p-Smad3, ↑Smad7	Gwon et al. (2021)
		TGF-β1	Rat renal interstitial fibroblast cells (NRK-49F) (0.5, 1, and 2 μg/ml, for 48 h)	Inhibit renal fibroblasts activation	↓collagen I, ↓fibronectin, ↓TGF-β1, ↓p-STAT3/t-STAT3, ↓p-Smad2, ↓p-Smad3, ↑Smad7	
Lung and muscle injury						
MEL	Lung injury	Paraquat (i.p.)	Male Swiss albino mice (0.1 and 0.5 mg/kg, i.p., twice per week for 4 weeks)	Reduce lung injuries	↑SOD, ↑CAT, ↑GPx, ↓MDA, ↓NO, ↑Bcl-2, ↑Survivin, ↓Ki-67	El-Aarag et al. (2019)
MEL	Muscle injury	Drop mass method	Male C57/BL6 mice (4, 20, and 100 μg/kg, i.m., for 7 days)	Increase locomotor activity in open field test and treadmill running activity, improve histological changes of damaged tissue	↓MCP-1, ↓TNF-α, ↓IL-6, ↑MyoD, ↑myogenin, ↑α-SMA, ↑MHC	Jae Eun Lee et al. (2019)
			C2C12 cells (1, 2.5, 5 ng/ml, for 16 h)	—	↑MHC	

Abbreviations are as shown in the literature. (↓), down-regulation or inhibition; (↑), up-regulation or activation.

carbon tetrachloride, while MEL possessed hepatoprotective activity on isoniazid- and rifampicin-induced liver hepatoxicity in rats, both of which suggested that a combination of BV and honey, or MEL could be beneficial for the prevention of hepatoxicity and could be used as potential therapeutic agents (Meligi et al., 2020; Naji et al., 2021). Besides, after treatment with bvPLA$_2$, the levels of cholestasis markers in the serum were attenuated, the abnormal state of liver fibrosis was restored, and hepatocyte inflammation and apoptosis were inhibited in mice with diet feeding 3,5-diethoxycarbonyl-1,4-dihydrocollidine (Kim J.-Y. et al., 2021b).

Protect effect on kidney injury

BV and its main components, such as MEL and apamin, showed protect effects on acute kidney injury and renal fibrosis, as listed in Table 6.

Acute kidney injury associated with sepsis is a worldwide health dilemma. Sepsis-related acute kidney injury is a global health issue. During sepsis, the endotoxin LPS mediates systemic inflammatory responses. BV, MEL and apamin ameliorated LPS-induced acute kidney injury *via* the suppression of oxidative stress, inflammation and cell death in mice (Kim J. Y. et al.,

2020a; Kim J. Y. et al., 2020b; Kim et al., 2021a). Take MEL as an example, it dampened renal dysfunction and structural damage, and at the same time, the levels of direct tubular injury markers were attenuated in LPS-treated mice. MEL decreased systemic and renal TNF-α and IL-6 levels, attenuated the accumulation of immune cells in the kidney, and suppressed NF-κB pathway. MEL reduced MDA level and inhibited the expression of nicotinamide adenine dinucleotide phosphate oxidase 4 (NOX4), and promoted Nrf2-mediated antioxidant defenses, as well as inhibited apoptosis and necrosis after LPS treatment. In addition, the survival duration of LPS-injected mice was significantly prolonged after MEL injection. The above results suggest that MEL could have a responsibility among the prospective options for the prevention and treatment of renal complications of sepsis (Kim J.Y. et al., 2021b). Besides, MEL alleviated mice acute kidney injury induced by cisplatin via regulating M2 macrophage expression (Kim H. et al., 2020).

With the chronic accumulation of progressive renal fibrosis, the kidneys continuously suffer one-way, irreversible damage, and end-stage diseases such as renal failure arrive as scheduled. *In vivo*, apamin inhibited renal fibrosis induced by unilateral ureteral obstruction; *in vitro*, it resisted renal fibroblasts activation induced by TGF-β1. This peptide suppressed TGF-β1/Smad2/3 and STAT3 pathways to inhibit inflammation response and tubular atrophy as well as reduce the activation of myofibroblast and the expression of fibrotic gene. These studies suggest that apamin may have a competitive advantage in the screening of therapeutic agent alternatives against renal fibrosis (Gwon et al., 2021).

Protect effect on lung and muscle injury

In addition, MEL reduced lung injuries induced by paraquat in mice. It increased SOD, CAT, and GPx activity, and decreased MDA and NO levels, as well as upregulated Bcl-2 and survivin expressions and downregulated Ki-67 expression, which demonstrated that MEL restored the pathological alternations of paraquat-induced lung injury in mice from the perspectives of enhancing antioxidant activity and reducing apoptosis (Table 6) (El-Aarag et al., 2019).

MEL ameliorated muscle function and histological changes of damaged tissue, and debilitated the production of pro-inflammatory factors, including IL-6, MCP-1, and TNF-α in muscle contusion mouse model. In addition, the expression of muscle recovery and regeneration-related biomarkers, such as myogenin, MyoD, α-smooth muscle actin (α-SMA) and myosin heavy chain (MHC), was elevated in mice. The results suggested that MEL could be a promising candidate for the muscle injury treatment (Table 6) (Lee J. E. et al., 2019).

Protect effect on other diseases

Anti-diabetic efficacy

Bee wax coated water-soluble fraction of BV (BWCBVA) and MEL-loaded NPs showed anti-diabetic efficacy in diabetic animal models, as shown in Table 7. BWCBVA decreased blood glucose level, normalized the serum biochemical parameters, and increased the body weight in streptozotocin-induced diabetic rats. Also, administration of BWCBVA reduced the expression of PI3K-p85 and enhanced the expression of glucokinase in liver, as well as increased the number of islet cells and decreased the damage of β-cell in pancreas. Furthermore, co-administering BWCBVA with nifedipine and nicorandil resulted in insulin secretion through enhancing the calcium ion influx and obstructing the potassium ion channel. The above results indicated that BWCBVA could be considered as an available mode to treat diabetes (Balamurugan et al., 2019). In addition, prolonged MEL release from polyelectrolyte-based nanocomplexes improved blood glycemic control in a type II diabetes mouse model (Gui et al., 2020).

Protective effect on cardiovascular system

Administration of BV decreased fasting blood glucose, serum total cholesterol (TC), triglycerides (TG), LDL-C, VLDL-C, creatine kinase (CK)-MB, LDH, troponin I, and heart MDA, NF-κB levels, and heart vascular cell adhesion molecule-1 (VCAM-1) and galectin-3 expression, as well as increased bodyweight, plasma insulin, serum HDL-C and heart total antioxidant capacity (TAC) levels in diabetic hyperlipidemic rats, which indicated that BV could reduce oxidative stress and downregulate NF-κB pathway to improve cardiac dysfunction (Zahran et al., 2021). Besides, bvPLA$_2$ could be a potential agent for atherosclerosis through inducing Treg cells (Kang et al., 2020). The above results are shown in Table 7.

Attenuating HFD-induced obesity

In vitro, BV suppressed lipid accumulation, and inhibited adipogenesis by reducing the expression of CCAAT/enhancer-binding proteins (C/EBPs), peroxisome proliferator-activated receptor γ (PPARγ), and p-p38, as well as by upregulating the expression of p-ERK, p-JNK, p-adenosine monophosphate–activated protein kinase (AMPK), and

TABLE 7 Summary of the protect effects and mechanisms of BV and its main components on other diseases.

BV and/or its components	Model	Inducer/ Method	Animal/Cell (BV etc. administration)	Effects	Mechanisms	Reference
Diabetes						
BWCBVA	Diabetes mellitus	Streptozotocin (i.p.)	Male Wister albino rats (0.125, 0.25 and 0.50 mg/kg, orally, once a day for 3 weeks)	Decrease glucose level, increase body weight, increase the islet cell numbers and decrease β-cell damage, result in insulin secretion by enhancing the calcium ion influx and obstructing the potassium ion channel when co-administered with nifedipine and nicorandil	↑insulin, ↓HbA1c, ↓TC, ↓TG, ↓SGOT, ↓SGPT, ↓PI3K-p85, ↑glucokinase	Balamurugan et al. (2019)
MEL-loaded nanoparticles	Type II diabetes	—	Male db/db mice (3 mg/kg, i.p.)	Decrease blood glucose level and body weight	—	Gui et al. (2020)
Cardiovascular system						
BV	Cardiac dysfunction	Streptozotocin (i.p.), a high-fat diet	Male albino rats (0.5 and 1.23 mg/kg, i.p., daily for 4 weeks)	Increase bodyweight, decrease fasting blood glucose levels	↑insulin, ↓TG, ↓TC, ↓LDL-C, ↓VLDL-C, ↑HDL-C, ↓CK-MB, ↓LDH, ↓troponin I, ↑TAC, ↓MDA, ↓NF-κB, ↓VCAM-1, ↓galectin-3	Zahran et al. (2021)
bvPLA$_2$	Atherosclerosis	Atherogenic high-cholesterol diet	ApoE$^{-/-}$ mice (0.2 mg/kg, i.p., every 2 days after a 4-week diet)	Increase in CD4$^+$ Foxp3$^+$ Treg cells in the lymph nodes, reduce atherosclerotic lesions and foam cell formation	↑HDL-C, ↓LDL-C, ↑HDL/LDL, ↓AST, ↓IFN-γ, ↓TNF-α	Kang et al. (2020)
HFD-induced obesity						
BV	HFD-induced obesity	Adipocyte differentiation	3T3-L1 preadipocytes (2.5, 5, and 10 μg/ml, for 3 or 9 days)	Suppress cell hyperplasia and lipid accumulation	↓C/EBPα, ↓C/EBPβ, ↓C/EBPδ, ↓PPARγ, ↑p-ERK, ↑p-JNK, ↓p-p38, ↑p-AMPK, ↑p-ACC	Cheon et al. (2018)
		HFD	C57BL/6 mice (0.1 and 1 mg/kg, i.p., during the last 4 weeks)	Suppress body weight, fat, and lipid accumulation	↓PPARγ, ↓C/EBPα, ↑p-AMPK, ↑p-ACC	
bvPLA$_2$	HFD-induced obesity	HFD	Male C57BL/6 mice (0.5 mg/kg, i.p., every 3 days for 11 weeks)	Reduce body weight and adipose tissue weight, decrease hepatotoxicity and nephrotoxicity, alleviate metabolic dysfunction; decrease macrophage infiltration and crown-like structures formation, decrease the M1/M2 ratio	↓ALT, ↓creatine, ↓glucose, ↓LDL-C, ↓insulin, ↓leptin, ↓TNF-α, ↓IL-12a, ↑IL-4, ↑CD206, ↓C/EBPα, ↑UCP-1	Jeong et al. (2021)
		LPS for M1 activation	Bone marrow cells (0–10 μg)	Inhibit M1 macrophage polarization	↓TNF-α, ↓IL-12a	
		IL-4 and IL-13 for M2 activation	Bone marrow cells (0–10 μg)	Stimulate M2 macrophage polarization	↑Ym1, ↑CD206	
		Adipocyte differentiation	3T3-L1 preadipocytes (0–10 μg)	Regulate lipid accumulation through macrophages	—	

(Continued on following page)

TABLE 7 (*Continued*) Summary of the protect effects and mechanisms of BV and its main components on other diseases.

BV and/or its components	Model	Inducer/ Method	Animal/Cell (BV etc. administration)	Effects	Mechanisms	Reference
BV	Obesity-associated inflammation	—	Differentiated 3 T3-L1 preadipocyte (0, 1, 5, and 10 μg/ml)	Inhibit lipid accumulation;	↓PPARγ, ↓C/EBPα	Hee-Yeon Kim et al. (2020)
		LPS	RAW264.7 macrophages (0, 1, 5, and 10 μg/ml)	—	↓TNF-α, ↓COX-2, ↓iNOS, ↓IL-1β	
		—	Differentiated 3 T3-L1 preadipocyte, RAW264.7 macrophages (0, 1, 5, and 10 μg/ml)	—	↓TNF-α, ↓COX-2, ↓iNOS, ↓IL-1β, ↓IL-6, ↓MCP-1, ↑AdipoQ, ↑GLUT4	
Wound healing						
BV	Impaired diabetic wound healing	Streptozotocin (i.p.), excising the skin and underlying panniculus carnosus	Male BALB/c mice (200 μg/kg/ wounded area/day, s.c., for 15 days)	Enhance wound closure, rescue wound tissue macrophages from apoptosis and restore impaired functional activity,	↑Collagen I, ↑Ang-1, ↑Nrf2, ↑phospho-tyrosine (pTyr) Tie-2, ↑peNOS, ↑pAkt, ↑pERK, ↑CD31, ↑GSH Px, ↑mitochondrial SOD, ↑CAT, ↑CCL2, ↑CCL3, ↑CXCL2, ↑BD-2	Hozzeinab et al. (2018)
$bvPLA_2$	Wound healing	Polyinosinic-polycytidylic acid [poly (I:C)]	HaCaT cells (0.05, 0.1, 0.5, 1 and 5 μg/ml)	Increase poly (I:C) localization in the lysosomes; increase the intracellular uptake of poly (I:C) and its enzymatic activity is essential	↑IL-8, ↑p-ERK, ↑p-JNK, ↑p-IKKαβ, ↑p-IκB-α	Nakashima et al. (2020)
Reproductive performance and growth performance						
BV	Reproductive performance	—	Male V-line rabbits (bucks) (0.1, 0.2, and 0.3 mg/rabbit, s.c., twice weekly over 20 weeks)	Show shorter reaction time (increased libido), increase viable sperm and concentration, total sperm output, live sperm, fertility percentage, testosterone concentration, and total protein, albumin, and glucose levels	↑TAC, ↑GST, ↑GSH, ↑IgA, ↑IgM	El-Hanoun et al. (2020)
BV	Reproductive performance	—	Spanish V-line mature does (primiparous) (0.1, 0.2 and 0.3 mg/rabbit, s.c., twice weekly for 1 week before mating and 4 weeks after mating)	Increase litter size at birth, litter weight, survival rate at weaning age, milk yield, conception and fertility rates, decrease plasma total lipids, cholesterol and urea	↑Estradiol 17-β (E2), ↓progesterone (P4), ↓AST, ↓ALT, ↑TAC, ↑GSH, ↑GST, ↑GPx, ↑SOD, ↓MDA, ↓TBARS, ↑IgG, ↑IgM, ↑IgA	Elkomy et al. (2021)
BV	Growth performance	—	Male broiler chicks (10, 50, 100, and 500 μg/kg of diet, for 5 weeks)	Improve feed conversion ratio, increase body weight gain; lower relative weight of spleen, bursa of Fabricius, and liver, increase relative breast meat yields; increase lightness (L*) value for meat decrease ileal villus height and narrowed width; reduce total in caecal digesta	↑Secretory IgA, ↓NO	Kim et al. (2018a)

(Continued on following page)

TABLE 7 (*Continued*) Summary of the protect effects and mechanisms of BV and its main components on other diseases.

BV and/or its components	Model	Inducer/ Method	Animal/Cell (BV etc. administration)	Effects	Mechanisms	Reference
Other aspects						
BV	Asthma	IL-13	A549 cells (0.1 and 1.0 μg/ml)	—	↓p-Akt/Akt, ↓SPDEF, ↑FOXA2, ↓MUC5AC	Sanga Kim et al. (2021)
BV	iPSCs	—	iPSCs (0–5 μg/ml)	Induce cell death, reduce cell membrane integrity; induce both apoptosis and necroptosis; enhance calcium influx, calpain activity, and ROS generation	↓F-Actin, ↓FAK, ↓Talin-1, ↓vinculin, ↑p-RIP, ↑p-MLKL, ↑cleaved Caspase-3, ↑cleaved PARP, ↑p-CaMKII, ↑p-cPLA$_2$	Aeyung Kim et al. (2020)
BV alongside CS	Radial bone defect	A 5 mm bone piece from the middle of the radius bone was removed to produce a non-union model	Male Wistar rats (0.1 mg, injected percutaneously into the defect site)	Show high radiographic outcomes, density of osseous tissue, and osteocytes and osteoblasts count	—	Meimandi-Parizi et al. (2018)
Natural extract eye drops containing BV, musk, and deer antlers	Dry eye disease	Scopolamine (s.c.)	Male Sprague-Dawley rats (4 times a day for 5 days)	Decrease corneal fluorescein staining scores	↓LDH, ↑MUC5AC	Choi et al. (2020)
		Lacrimal gland-excised	Male Sprague-Dawley rats (4 times a day for 5 days)	Decrease corneal fluorescein staining scores, increase tear volume	↓LDH, ↑MUC5AC	
bvPLA$_2$	Abortion	LPS (i.p.)	Mated female C57BL/6 mice (0.5 mg/kg, i.p., once a week for 2 weeks prior to mating)	Prevent fetal loss accompanied by growth restriction in the remaining viable fetus, increase CD4$^+$ T helper cells and uNK cells, decrease CD8$^+$ cytotoxic T cell populations	↓TNF-α, ↓IFN-γ, ↓IL-17A	Baek et al. (2019)

Abbreviations are as shown in the literature. (↓), down-regulation or inhibition; (↑), up-regulation or activation.

p-acetyl-coenzyme A carboxylase (ACC) during differentiation of 3T3-L1 preadipocytes. *In vivo*, BV inhibited fat and lipid accumulation and reduced body weight, through downregulating the expression of adipogenic markers, PPARγ and C/EBPα, and upregulating the expression of p-AMPK and p-ACC in HFD-induced obese mice, suggesting BV an effective preventive and therapeutic candidate for obesity (Cheon et al., 2018). Besides, bvPLA$_2$ also attenuated HFD-induced obesity in mice (Jeong et al., 2021). In addition, BV could attenuate adipocyte hypertrophy, as well as improve insulin resistance and obesity-related inflammation in obese adipose tissue (Kim H. Y. et al., 2020). The above results are shown in Table 7.

Improving wound healing

Diabetic wound formation is one of the serious complications of diabetes. BV treatment improved wound closure in streptozotocin-induced mice diabetic model through enhancing β-defensin-2 (BD-2) and collagen expression and restoring angiopoietin-1 (Ang-1) and Nrf2 levels, and thereby increasing the Tie-2 downstream signaling, including the phosphorylation of endothelial nitric oxide synthase (eNOS), Akt and ERK. Furthermore, BV restored wounded tissue antioxidant enzymes GSH Px, mitochondrial SOD and CAT activities, and the chemokines CCL2, CCL3 and CXCL2 levels, and then rescued wound macrophages from apoptosis induced by mitochondrial membrane potential. The above results provided a new example for BV treatment to stimulate angiogenesis and improve the wound healing process of diabetes (Hozzeinab et al., 2018). Besides, bvPLA$_2$ increased IL-8 production in HaCaT cells induced by poly (I:C), upregulated the expression of p-ERK, p-JNK, p-IKKαβ and p-IκB-α. It enhanced the intracellular poly (I:C) uptake, and the enzymatic activity was essential. These findings indicated that bvPLA$_2$ could ameliorate wound healing via the enhancement of TLR3 responses (Nakashima et al., 2020). The above results are shown in Table 7.

Improving reproductive performance and growth performance

BV could improve reproductive performance and growth performance, as shown in Table 7. BV improved reproduction and immune response of male and female rabbits, which demonstrated that BV could be used as an effective and safe substitute for artificial chemical drugs (sex stimulants) in rabbit breeding to improve some reproductive characteristics, immune response and health (El-Hanoun et al., 2020; Elkomy et al., 2021). Besides, dietary BV improved growth performance, the yield and quality of breast meat, and the concentration of secretory IgA on ileal mucosa in broiler chickens, and lowered internal organs including spleen, bursa, and liver, caecal short-chain fatty acids concentrations and ileal villus height, which demonstrated that BV could be regarded as a natural value-added substitute for antibiotics in feed to enhance growth and animal health (Kim D. H. et al., 2018).

Other aspects

Moreover, BV and $bvPLA_2$ had therapeutic and ameliorative effects on asthma, radial bone defect, dry eye disease and abortion, as well as eliminated teratogenic human induced pluripotent stem cells (iPSCs), as shown in Table 7.

BV prevented forkhead box A2 (FOXA2)-regulating mucin 5AC (MUC5AC) expression in IL-13-treated A549 cells not only through inhibiting Akt activation but also by suppressing enhanced SAM-pointed domain containing Ets-like factor (SPDEF), which demonstrated that BV could help prevent mucus metaplasia in asthma (Kim et al., 2021d). Although iPSCs is considerable practical in potential cell-based therapy, they remain confronted with problems such as teratoma formation. BV treatment resulted in impaired F-actin filaments within iPSCs, Ca^{2+} inward flow and accumulation to the cytoplasm, elevated calpain activity and reactive oxygen species (ROS) generation, selective induction and reduction of viability and adhesion capacity of undifferentiated stem cell iPSCs, and increased cell death. In addition, BV treatment before in ovo transplantation suppressed the formation of iPSC-derived teratoma. Moreover, BV was neither cytotoxic nor genotoxic to iPSC-derived differentiated cells. The above findings indicated that BV possessed anti-teratoma effect by getting rid of residual iPSCs, and could be a safe and effective cell preparation agent for stem cell therapy (Kim et al., 2020a).

BV alongside chitosan scaffold (CS) displayed high radiographic outcomes compared with the untreated and CS groups at day 56 postoperatively, and showed high osseous tissue density and high counts of osteocytes and osteoblasts compared with the CS and autograft groups, which highlighted the capability of CS-BV as a potential alternative and enhancer of bone graft substitute material (Meimandi-Parizi et al., 2018). The natural extract containing BV, deer antlers and musk as eye drops had therapeutic effects on scopolamine-injected dry eye disease rat models and lacrimal gland-excised dry eye disease rat models through repairing the damaged ocular surface, increasing the amount of tears, and restoring the tear mucin layer (Choi et al., 2020).

$bvPLA_2$ prevented fetal loss with growth restriction in the remaining live fetuses in abortion mouse model induced by LPS. It increased Treg cells, and decreased TNF-α and IFN-γ expression. The prophylactic effect of $bvPLA_2$ was not found in abortion prone mice lacking Treg. The above results indicated that $bvPLA_2$ might have effects on LPS-induced abortion mice through regulating Treg populations (Baek et al., 2019).

Safety and venom immunotherapy

An important concern with BV has been its safety. BV can cause anaphylaxis (Cherniack and Govorushko, 2018). It is reported that up to 3.4% of children and up to 7.5% of adults have systemic allergic sting reactions. Allergic reactions can be mild in skin; however, it can also be moderate to severe with a risk of life-threatening allergic reactions (Sturm et al., 2018). In an individual patient education, it addressed to correctly and timely use epinephrine auto-injectors, and recommend to stop physical exercise and adopt supine position during acute allergic attack (Stoevesandt et al., 2020).

Venom immunotherapy (VIT) could prevent severe allergic reactions in 80–100% subjects allergic to Hymenoptera venom. An immunological study on the early phase of VIT performed on forty individuals indicated that cytokines (CCL5/RANTES and IL-17E/IL-25) and eosinophils were conducive to the immune response (Palgan et al., 2020).

MEL could be used in adjuvant immunotherapy. MEL combined with LPS produced an increase of IL-1β and IL-6 levels and a decrease of IL-10 level in phorbol 12-myristate 13-acetate (PMA)-differentiated THP-1 cells. Besides, the response to MEL and LPS was characterized by metabolic profiling, and the clearest effects were on glycolysis, tricarboxylic acid cycle, oxidative phosphorylation, and purine, pyrimidine, and fatty acid metabolism (Alqarni et al., 2018). Similarly, the same research group also studied the metabolomic profiling for the immune stimulatory effect of a major constituent of BV, (Z)-11-eicosenol, and its derivations methyl cis-11-eicosenoate and cis-11-eicosenoic acid on PMA-differentiated THP-1 cells. The

results supported the proposed actions of the three components as immune system stimulators (Alqarni et al., 2019). Besides, bvPLA$_2$ has attenuated several immune system-related diseases. In a recent study, bvPLA$_2$ decreased apoptotic Treg cells, reduced early apoptosis in splenocytes and CD4$^+$CD25$^+$ Treg cells, and raised the expression of CTLA-4 and PD-1 on CD4$^+$CD25$^+$ Treg cells, which showed that bvPLA$_2$ could induce Treg expansion by changing apoptotic signal (Baek et al., 2020).

As experts have commented, if the venom is selected correctly, and adequate venom preparation and maintenance dose are used, VIT may be a treatment method of significant value in preventing the systemic reaction of Hymenoptera stings. Besides, the duration of VIT is usually 5 years, which can provide long-term protection from stinging after treatment interruption, but it recommends indefinite (possibly life-long) treatment for patients with mastocytosis or other high-risk patients (Incorvaia et al., 2018).

Toxicity, administration dose and new drug delivery system

Although BV and its main components often show good results towards cancerous cells, bacteria, viruses as well as other disorders and diseases, there are always open questions regarding their potential toxicity on normal non-target or host cells and tissues making this kind of toxicity one of the biggest obstacles for the possibility of applying such natural products as medications. A single high dose of 100 μg/ml of BV damaged the DNA molecule in human lymphocytes *in vitro*, resulting in cellular instability (Garaj-Vrhovac and Gajski, 2009). A further study suggested that the DNA damage effects of BV could be at least partially related to oxidative stress (Gajski et al., 2012). In addition, BV decreased cell viability, altered cell morphology, as well as induced cytogenotoxicity and dominantly necrotic type of cell death, in human peripheral blood lymphocytes with a dose- and time-dependent manner (Gajski and Garaj-Vrhovac, 2011). Similarly, MEL was also found to induce cytogenetic damage and oxidative stress in human peripheral blood lymphocytes (Gajski et al., 2016).

Therefore, the administration dose is of great noteworthy. Wi-38, a species of human lung fibroblast, was less sensitive to MEL and has higher colony formation capacity than ChaGo-K1 cells (IC_{50} = 0.6 μM), with an IC_{50} value of 2.35 μM at 48 h (Tipgomut et al., 2018). After 72 h incubation, the cell viability of BESA-2B (normal lung epithelial cells) remained unaffected at MEL concentrations ≤4 μg/ml with some reduction in activity, while the viability of NCI-H441 and A549 cells (lung cancer cells) was significantly affected at 2 μg/ml (Gao et al., 2018). Besides, the Selective Index of NIH3T3 (healthy mouse fibroblast cells) was higher than 3 compared to HepG2 and MDA-MB-231 cells, implying that BV was more selective for both types of cancer cells and that NIH3T3 showed altered cell morphology only when BV was 100 μg/ml (Uzuner et al., 2021). Moreover, Melectin at around 15 μM only slightly inhibited NIH3T3; Concentration below 50 μM caused only 20% erythrocyte lysis, with no significant hemolytic effect (Liang et al., 2021). Comparable results existed for MEL-AF treatment, where MEL-AF remained non-significantly cytotoxic at doses in the range of ≤10 μg/ml after 24 h of MEL-AF treatment (Sangboonruang et al., 2020). Besides, NRK-49F (rat renal interstitial fibroblast cells) cell viability with 48 h apamin treatment was reduced at 10 μg/ml of apamin. However, 0.1, 0.5, 1, 2, and 5 μg/ml did not affect NRK-49F cell viability (Gwon et al., 2021).

The effect of MEL on the viability of MCF 10A (human normal mammary epithelial cells), HDFa (human dermal fibroblasts), and MCF-12A (human mammary epithelial cells) cells was more delayed and attenuated, with an IC_{50} value of 22.17 μg/ml for HDFa cells at 24 h (Duffy et al., 2020).

When BV and MEL treated THLE-2 (normal human liver cell line) for 24 h, the IC_{50} values were 95.73 μg/ml in the BV group and 78.38 μg/ml in the MEL group, both of which were significantly higher than the IC_{50} values of treated HepG2 (1.4 and 2.8 μg/ml, respectively), which showed negligible effects of BV and MEL on hepatocytes (Mansour et al., 2021).

After treating HaCaT (normal human keratinocytes) with 0.1–10 μg/ml of BV and MEL for 24 and 72 h, the toxic effects possessed by BV were more pronounced, with IC_{50} values reaching 6.72 and 6.38 μg/ml for the two time periods, respectively; the IC_{50} values of MEL-treated HaCaT were greater than 10 μg/ml exceeding the maximum MEL concentration used in the experiment (Nikodijevic et al., 2021).

BV and Wasp venom were non-toxic to BV-2 murine microglial cells at concentrations of ≤12 μg/ml and ≤160 μg/ml for 24 h, respectively (Yun et al., 2021). And 1 μg/ml of apamin showed a 10% decrease in BV2 microglial cell proliferation for 12 h (Park et al., 2020). Cell viability of 0.1–30 μM of MEL on HT22 mouse hippocampal cells for 24 h was assessed and 3 μM was found to be the maximum safe concentration for further study (Cong Duc and Lee, 2021).

BV at 0.1 and 1 mg/kg was an effective concentration and had no side effects on rats (Lee et al., 2020a). Similarly, 0.5 and 1.23 mg/kg of BV were also taken as therapeutic dosages to rats (Zahran et al., 2021). Besides, i.p. administration of 1, 2, and 4 mg/kg of MEL leaded to no toxicity in mice. The LD_{50} of mice with i.p. injection of MEL was 7.4 mg/kg (PubChem Database. MEL, CID = 16129627) (Fan et al., 2020).

In order to decrease the toxic and side effects such as hemolysis of BV and MEL, and improve the characteristics of drug targets and release, besides of NPs mentioned above (Zhou et al., 2021), other new drug delivery system has also been developed and applied in clinics (Lyu et al., 2019). After the amino acid modification of MEL or the addition of specific functional groups, it can improve the ability of MEL to target recognition and prevent degradation of target cells while

reducing its toxicity to normal cells (Giribaldi et al., 2021). For example, after replacing valine at position 8 and proline at position 14 in MEL with lysine, MEL-pep had stronger ability to resist cell proliferation and inhibit tumor growth, reverse the drug resistance of cells to 5-fluorouracil, inhibit Akt pathway and P-glycoprotein (P-gp) of cells related to the exclusion of foreign bodies (Ke et al., 2018). Besides, a pH-sensitive amide bond was introduced between the 2,3-dimethyl maleimide and lysine of MEL to modify MEL, which could reduce the hemolytic status of MEL and maintain its low activity in the neutral or microalkaline environment, and show a stronger tumor targeting effect in the acidic microenvironment (Luo et al., 2018). The above investigations provided a feasible platform for improving the targeting and safety applications of BV and its main components, such as MEL.

Conclusion and perspectives

BV and its main constituents have multiple biological activities and applied to treat several diseases, such as cancer, neurological disorders, inflammatory diseases, pain, microbial diseases, liver, kidney, lung and muscle injury, etc. In this paper, we reviewed the recently published reports (2018–2021) on BV and its main constituents. These articles have indicated that BV and its main constituents exerted the above protections and were contained in a variety of signaling tranduction pathways (Figures 2–4).

BV played a vital role in cell proliferation, migration, invasion, inhibition of EMT and induction of apoptosis and autophagy by exerting multi-pathway and multi-target long-lasting effects on cells in lung cancer, breast cancer, cervical cancer, and many other cancers *in vitro* and *in vivo*. The mechanisms of action of BV were: upregulation of Caspase-3, Caspase-7, Caspase-9, Bax, p21, p27, p53, Rb, PTEN, and 15-lipoxygenase-1 expression, downregulation of MITF, PARP, Bcl-2, Bcl-xL, ERα, EGFR, VEGF, MMP-1, MMP-2, MMP-9, TNF-α, NF-κB, HIF-1α, Cyclin D1, Cyclin A, Cyclin B, and Rac1, etc. BV inhibited the mTOR pathway, PI3K/Akt and MAPK signaling pathway, and mitotic signaling pathway by reducing the expression of p-mTOR, Akt, p-Akt, p38, p-p38, JNK, p-JNK, ERK, p-ERK, p-PI3K, p-EGFR, and p-HER2, which in turn impaired cancer cell viability, reduced migration and invasion activities, and promoted cell death. BV activated the mitochondrial apoptotic pathway in cancer cells by increasing the expression of apoptosis signaling molecules such as Fas and Caspase-9. On the other hand, it inhibited EMT in cancer cells by decreasing the expression of vimentin, ZEB2, and Slug and elevating the expression of E-cadherin (Figure 2).

Except cancer, BV and its main components can treat a variety of other diseases, including neurological disorders, inflammatory diseases, liver, kidney, lung and muscle injury, etc., mainly via inhibiting the release of inflammatory cytokines and chemokines, regulating the redox balance in the body, modulating the expression of apoptosis related factors, and so on. The most common points were: first, BV and its main components reduced pro-inflammatory cytokines (TNF-α, IL-1β, IL-6, IFN-γ, IL-13, IL-2, IL-12, IL-17, etc.) and raiseed anti-inflammatory cytokines (IL-10 and IL-4); second, they improved antioxidant capacity by upregulating the levels of GSH, GPx, SOD, CAT, glutamate-cysteine ligase (GCL), GST, etc., and downregulating the levels of lipid peroxidation (LPO), MPO, MDA, protein carbonyl (PCO), ROS, etc.; third, they

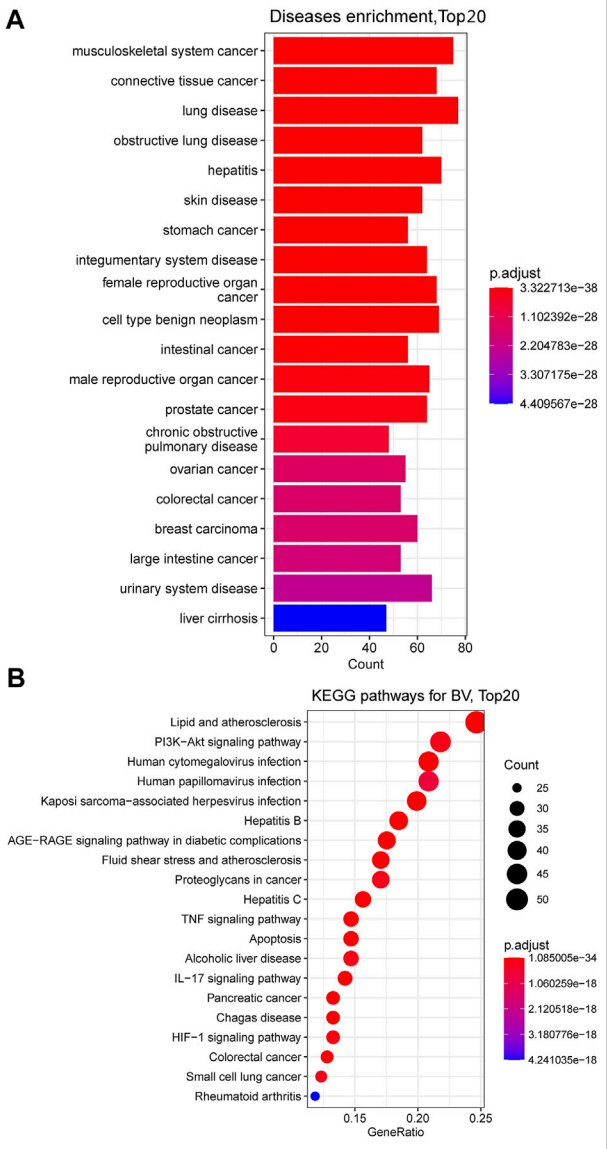

FIGURE 5
DOSE **(A)** and KEGG **(B)** analyses of proteins reported for BV and its main components in the literature. Top 20 diseases and KEGG pathways are enriched using R package "DOSE" and "topGO", respectively with *p*-value Cutoff = 0.01, q-value Cutoff = 0.01).

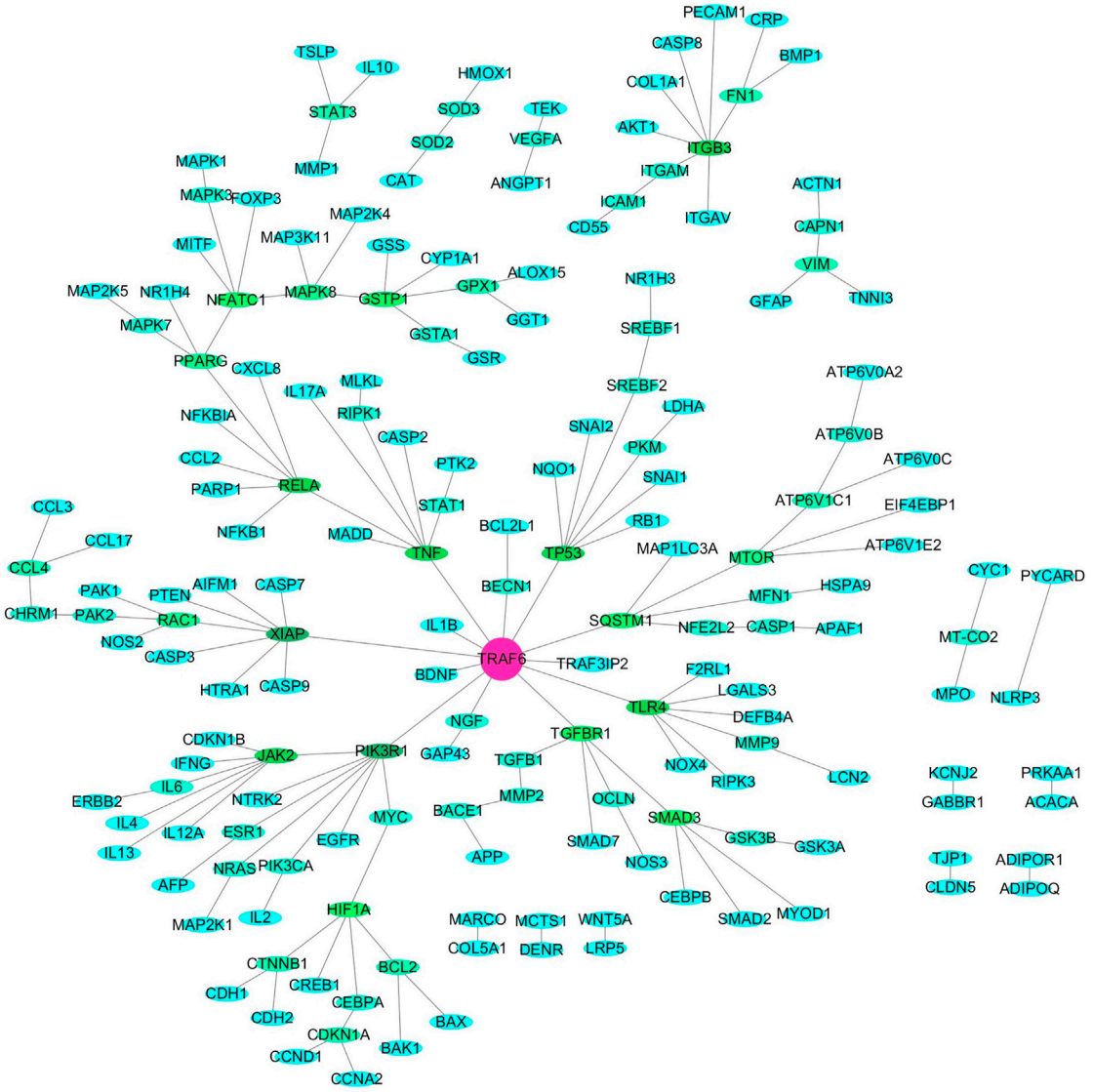

FIGURE 6
PPI analyses (confidence:0.4) of proteins and genes reported for BV and its main components in the literature visualized by Cytoscape 3.6.0 software. Texts in purple circle, green circle and light blue circle demonstrates the central hub target, secondary node target and the others node target.

downregulated pro-apoptotic factors (Caspase-3, cleaved Caspase-3, cleaved PARP-1, Bax, p53, apoptosis-inducing factor (AIF), Calpain, Cyt C, etc.) and upregulated anti-apoptotic factors (Bcl-2 and Survivin); fourth, they reduced chemokines, such as CCL17, CCL22, thymic stromal lymphopoietin (TSLP), macrophage inflammatory protein-1α (MIP-1α), MIP-1β, MCP-1, growth related oncogene-α (GRO-α), and so on; finally, they often downregulated MAPK, TLR4/NF-κB, Akt/mTOR and JAK/STAT signaling pathways, and upregulated Nrf2/HO-1 signaling pathway thereby producing corresponding pharmacological effects on different pathophysiological environments. Besides, BV and its main components upregulated TrkB/CREB/BDNF signaling pathway and the expression of growth-associated factors (BDNF, NGF, neurofilament 200 kDa (NF200) and growth-associated protein 43 (GAP43)), as well as downregulated the expression of amyloidogenic proteins (APP, BACE1, $A\beta_{1-42}$ and $A\beta_{1-40}$) in treating neurological disorders. They inhibited hepatic and renal fibrosis via suppressing TGF-β/Smad2/3 signaling pathway. They also downregulated the expression of C/EBPs and PPARγ, and activated AMPK signaling pathway in the treatment of obesity.

The potential effects of BV and its main components on ills and their potential mechanisms were predicted through bioinformatic analysis, referring to DOSE analysis and KEGG pathway enrichment of the targets reported using bioinformatics tools in the light of our previous methods (Zhong et al., 2021; Lin et al., 2022). As shown in Figure 5A**,** beside the reported diseases by literature, BV and its main components maybe have effect on the connective tissue cancer and obstructive lung disease. Meanwhile, KEGG pathway enrichment analysis (Figure 5B) shows that BV and its main components can mainly regulate the proteins involved in the pathways of lipid and atherosclerosis, PI3K–Akt, Human cytomegalovirus infection, Human papillomavirus infection, etc. To further screen the pivotal targets, PPI analysis was performed with the reported proteins for BV and its main components using the STRING on-line sever (https://www.string-db.org). As shown in Figure 6, a central protein, TRAF6 is highlighted in the PPI "tree" (located in purplish red circle). Indeed, according to the KEGG database, this protein is truly involved in the regulation of up to 34 pathways, including MAPK, NF-κB, Pathways in cancer, etc. Moreover, seven subcentral proteins, X-linked inhibitor of apoptosis protein (XIAP), TNF, phosphoinositide-3-kinase regulatory subunit1 (PIK3R1), tumor protein p53 (TP53), SQSTM1 (p62), TLR4 and TGF-β receptor 1 (TGFBR1), which can be attributed to different functional pathways, are displayed the direct interaction with the central protein TRAF6.

Ultimately, based on the previous results and the present bioinformatics and PPI analysis, it gives the following perspectives.

(1) First, although all the reported targets were proved to be correlated with the interfere effects of BV and its main components mainly on cancers, the DOSE analysis strongly suggest that BV and its main components could have an effect on lung disease and obstructive pulmonary disease, which could be worth exploring in the current COVID-19 epidemic. Therefore, next, it is suggested to further validate the effect of BV and its main components on lung disease and obstructive pulmonary disease for seeking hope for the treatment of lung diseases, especially COVID-19.
(2) Second, the present KEGG enrichment analysis suggests that lipid and atherosclerosis, Human cytomegalovirus infection and Human papillomavirus infection pathways could be involved in the disease intervention, but these pathways are not mentioned in the previous reports for BV and its main components. For integratively understanding the intervention and mechanisms of BV and its main components on diseases, proteomics or genomics investigations should be performed using *in vitro* and *in vivo* disease models to confirm the unreported pathways in the future study.
(3) Last, TRAF6 is predicted as one core target and XIAP, TNF, PIK3R1, TP53, SQSTM1, TLR4 and TGFBR1 are predicted as subcentral proteins for the therapeutic effects of BV and its main components. Accordingly, it will be very meaningful to validate the target roles of these proteins for the further drug development of BV and its main components by gene silencing, knockout experiments, etc.

In conclusion, these ideas provide valuable clues or perspectives to further study on the pharmacological effects and mechanisms of BV and its main components, so as to the promoting the drug development and clinical applications for BV.

Author contributions

Conceptualization, PS, SS, and HY; writing—original draft preparation, PS and SX; figures and tables, PS, SX, and HY; writing—reviewing and editing, HY; data curation, PS, SX, JY, YZ, and SH. All authors have read and agreed to the published version of the manuscript.

Funding

The authors gratefully acknowledge the financial supports of the National Natural Science Foundation of China (81973558).

Conflict of interest

The authors declare that the research was conducted in the absence of any commercial or financial relationships that could be construed as a potential conflict of interest.

Publisher's note

References

Abd El-Haleim, E. A. (2020). Molecular study on the potential protective effects of bee venom against fructose-induced nonalcoholic steatohepatitis in rats. *Pharmacology* 105 (11-12), 692–704. doi:10.1159/000508511

Abd El-Hameed, A. M., Abuelsaad, A. S. A., and Khalil, A. (2021). Bee venom acupuncture therapy ameliorates neuroinflammatory alterations in a pilocarpine-induced epilepticus model. *Metab. Brain Dis.* 36 (7), 2047–2058. doi:10.1007/s11011-021-00766-9

Abu-Zeid, E. H., Khalifa, B. A., Elewa, Y. H. A., Arisha, A. H., Ismail, T. A., Hendam, B. M., et al. (2021). Bee venom *Apis mellifera lamarckii* rescues blood brain barrier damage and neurobehavioral changes induced by methyl mercury via regulating tight junction proteins expression in rat cerebellum. *Food Chem. Toxicol.* 154, 112309. doi:10.1016/j.fct.2021.112309

Ahmed, O., Fahim, H., Mahmoud, A., and Ahmed, E. (2018). Bee venom and hesperidin effectively mitigate complete Freund's adjuvant-induced arthritis via immunomodulation and enhancement of antioxidant defense system. *Arch. Rheumatol.* 33 (2), 198–212. doi:10.5606/ArchRheumatol.2018.6519

Ahmed-Farid, O. A., Taha, M., Bakeer, R. M., Radwan, O. K., Hendawy, H. A. M., Soliman, A. S., et al. (2021). Effects of bee venom and dopamine-loaded nanoparticles on reserpine-induced Parkinson's disease rat model. *Sci. Rep.* 11 (1), 21141. doi:10.1038/s41598-021-00764-y

Ahmedy, O. A., Ibrahim, S. M., Salem, H. H., and Kandil, E. A. (2020). Antiulcerogenic effect of melittin via mitigating TLR4/TRAF6 mediated NF-κB and p38MAPK pathways in acetic acid-induced ulcerative colitis in mice. *Chem. Biol. Interact.* 331, 109276. doi:10.1016/j.cbi.2020.109276

Akbari, R., Hakemi-Vala, M., Pashaie, F., Bevalian, P., Hashemi, A., and Bagheri, K. P. (2019). Highly synergistic effects of melittin with conventional antibiotics against multidrug-resistant isolates of *Acinetobacter baumannii* and *Pseudomonas aeruginosa*. *Microb. Drug Resist.* 25 (2), 193–202. doi:10.1089/mdr.2018.0016

Al Naggar, Y., Giesy, J. P., Abdel-Daim, M. M., Ansari, M. J., Al-Kahtani, S. N., and Yahya, G. (2021). Fighting against the second wave of COVID-19: Can honeybee products help protect against the pandemic? *Saudi J. Biol. Sci.* 28 (3), 1519–1527. doi:10.1016/j.sjbs.2020.12.031

Al-Rabia, M. W., Alhakamy, N. A., Ahmed, O. A. A., Eljaaly, K., Aloafi, A. L., Mostafa, A., et al. (2021). Repurposing of sitagliptin- melittin optimized nanoformula against SARS-CoV-2; antiviral screening and molecular docking studies. *Pharmaceutics* 13 (3), 307. doi:10.3390/pharmaceutics13030307

Alalawy, A. I., El Rabey, H. A., Almutairi, F. M., Tayel, A. A., Al Duais, M. A., Zidan, N. S., et al. (2020). Effectual anticancer potentiality of loaded bee venom onto fungal chitosan nanoparticles. *Int. J. Polym. Sci.* 2020, 1–9. doi:10.1155/2020/2785304

Alqarni, A. M., Dissanayake, T., Nelson, D. J., Parkinson, J. A., Dufton, M. J., Ferro, V. A., et al. (2019). Metabolomic profiling of the immune stimulatory effect of eicosenoids on PMA-differentiated THP-1 cells. *Vaccines* 7 (4), 142. doi:10.3390/vaccines7040142

Alqarni, A. M., Ferro, V. A., Parkinson, J. A., Dufton, M. J., and Watson, D. G. (2018). Effect of melittin on metabolomic profile and cytokine production in PMA-differentiated THP-1 cells. *Vaccines* 6 (4), 72. doi:10.3390/vaccines6040072

An, H. J., Kim, J. Y., Kim, W. H., Gwon, M. G., Gu, H. M., Jeon, M. J., et al. (2018). Therapeutic effects of bee venom and its major component, melittin, on atopic dermatitis *in vivo* and *in vitro*. *Br. J. Pharmacol.* 175 (23), 4310–4324. doi:10.1111/bph.14487

Arani, F. S., Karimzadeh, L., Ghafoori, S. M., and Nabiuni, M. (2019). Antimutagenic and synergistic cytotoxic effect of cisplatin and honey bee venom on 4T1 invasive mammary carcinoma cell line. *Adv. Pharmacol. Sci.* 2019, 7581318. doi:10.1155/2019/7581318

Arteaga, V., Lamas, A., Regal, P., Vázquez, B., Miranda, J. M., Cepeda, A., et al. (2019). Antimicrobial activity of apitoxin from *Apis mellifera* in *Salmonella enterica* strains isolated from poultry and its effects on motility, biofilm formation and gene expression. *Microb. Pathog.* 137, 103771. doi:10.1016/j.micpath.2019.103771

Aufschnaiter, A., Kohler, V., Khalifa, S., Abd El-Wahed, A., Du, M., El-Seedi, H., et al. (2020). Apitoxin and its components against cancer, neurodegeneration and rheumatoid arthritis: Limitations and possibilities. *Toxins* 12 (2), 66. doi:10.3390/toxins12020066

Badawi, H. M. M., Abdelsalam, R. M., Abdel-Salam, O. M. E., Youness, E. R., Shaffie, N. M., and Eldenshary, E. E. S. (2020). Bee venom attenuates neurodegeneration and motor impairment and modulates the response to L-dopa or rasagiline in a mice model of Parkinson's disease. *Iran. J. Basic Med. Sci.* 23 (12), 1628–1638. doi:10.22038/ijbms.2020.46469.10731

Badawi, J. K. (2021). Bee venom components as therapeutic tools against prostate cancer. *Toxins* 13 (5), 337. doi:10.3390/toxins13050337

Baek, H., Jang, H. L., Jeon, H. N., and Bae, H. (2018a). Comparison of administration routes on the protective effects of bee venom phospholipase A2 in a mouse model of Parkinson's disease. *Front. Aging Neurosci.* 10, 179. doi:10.3389/fnagi.2018.00179

Baek, H., Lee, C. J., Choi, D. D., Kim, N. S., Kim, Y. S., Ye, Y. J., et al. (2018b). Bee venom phospholipase A2 ameliorates Alzheimer's disease pathology in Aβ vaccination treatment without inducing neuro-inflammation in a 3xTg-AD mouse model. *Sci. Rep.* 8, 17369. doi:10.1038/s41598-018-35030-1

Baek, H., Park, S. Y., Ku, S. J., Ryu, K., Kim, Y., Bae, H., et al. (2020). Bee venom phospholipase A2 induces regulatory T cell populations by suppressing apoptotic signaling pathway. *Toxins* 12 (3), 198. doi:10.3390/toxins12030198

Baek, H., Yang, H., Lee, J. H., Kang, N. H., Lee, J., Bae, H., et al. (2019). Prophylactic effects of bee venom phospholipase A2 in lipopolysaccharide-induced pregnancy loss. *Toxins* 11 (7), 404. doi:10.3390/toxins11070404

Balamurugan, R., Kim, J. H., Jo, M. N., Xue, C., Park, J. K., and Lee, J. K. (2019). Bee wax coated water-soluble fraction of bee venom improved altered glucose homeostasis in streptozotocin-induced diabetic rats. *J. Tradit. Chin. Med.* 39 (6), 842–852.

Biolchi, A. M., de Oliveira, D. G. R., Amaral, H. D., Campos, G. A. A., Goncalves, J. C., de Souza, A. C. B., et al. (2020). Fraternine, a novel wasp peptide, protects against motor impairments in 6-OHDA model of parkinsonism. *Toxins* 12 (9), 550. doi:10.3390/toxins12090550

Borojeni, S. K., Zolfagharian, H., Babaie, M., and Javadi, I. (2020). Cytotoxic effect of bee (*A. mellifera*) venom on cancer cell lines. *J. Pharmacopuncture* 23 (4), 212–219. doi:10.3831/KPI.2020.23.4.212

Cai, J. S., Huang, K. L., Han, S. N., Chen, R. C., Li, Z. J., Chen, Y., et al. (2022). A comprehensive system review of pharmacological effects and relative mechanisms of ginsenoside Re: Recent advances and future perspectives. *Phytomedicine.* 102, 154119. doi:10.1016/j.phymed.2022.154119

Carpena, M., Nunez-Estevez, B., Soria-Lopez, A., and Simal-Gandara, J. (2020). Bee venom: An updating review of its bioactive molecules and its health applications. *Nutrients* 12 (11), 3360. doi:10.3390/nu12113360

Casewell, N. R., Wüster, W., Vonk, F. J., Harrison, R. A., and Fry, B. G. (2013). Complex cocktails: The evolutionary novelty of venoms. *Trends Ecol. Evol.* 28 (4), 219–229. doi:10.1016/j.tree.2012.10.020

Ceremuga, M., Stela, M., Janik, E., Gorniak, L., Synowiec, E., Sliwinski, T., et al. (2020). Melittin-A natural peptide from bee venom which induces apoptosis in human leukaemia cells. *Biomolecules* 10 (2), 247. doi:10.3390/biom10020247

Chang, S. N., Kim, H. J., and Lee, K. C. (2020). Melittin, A major polypeptide of bee venom, increases radiosensitivity of breast cancer *in vitro* and *in vivo*. *Int. J. Radiat. Oncology*Biology*Physics* 108 (3), E527. doi:10.1016/j.ijrobp.2020.07.1649

Chen, Q., Lin, W., Yin, Z., Zou, Y., Liang, S., Ruan, S., et al. (2019). Melittin inhibits hypoxia-induced vasculogenic mimicry formation and epithelial-mesenchymal transition through suppression of HIF-1α/Akt pathway in liver cancer. *Evid. Based. Complement. Altern. Med.* 2019, 9602935. doi:10.1155/2019/9602935

Cheon, S. Y., Chung, K. S., Roh, S. S., Cha, Y. Y., and An, H. J. (2018). Bee venom suppresses the differentiation of preadipocytes and high fat diet-induced obesity by inhibiting adipogenesis. *Toxins* 10 (1), 9. doi:10.3390/toxins10010009

Cherniack, E. P., and Govorushko, S. (2018). To bee or not to bee: The potential efficacy and safety of bee venom acupuncture in humans. *Toxicon* 154, 74–78. doi:10.1016/j.toxicon.2018.09.013

Choi, G.-M., Lee, B., Hong, R., Park, S.-Y., Cho, D.-E., Yeom, M., et al. (2021). Bee venom phospholipase A2 alleviates collagen-induced polyarthritis by inducing Foxp3(+) regulatory T cell polarization in mice. *Sci. Rep.* 11 (1), 3511. doi:10.1038/s41598-021-82298-x

Choi, H. S., Kang, S. Y., Roh, D. H., Choi, S. R., Ryu, Y., and Lee, J. H. (2018). Bee venom stimulation of a lung meridian acupoint reduces inflammation in carrageenan-induced pleurisy: An alternative therapeutic approach for respiratory inflammation. *J. Vet. Sci.* 19 (5), 708–715. doi:10.4142/jvs.2018.19.5.708

Choi, S., Chae, H. K., Heo, H., Hahm, D. H., Kim, W., and Kim, S. K. (2019). Analgesic effect of melittin on oxaliplatin-induced peripheral neuropathy in rats. *Toxins* 11 (7), 396. doi:10.3390/toxins11070396

Choi, S. Y., Eom, Y., Kim, J. Y., Jang, D. H., Song, J. S., and Kim, H. M. (2020). Effect of natural extract eye drops in dry eye disease rats. *Int. J. Ophthalmol.* 13 (7), 1023–1030. doi:10.18240/ijo.2020.07.02

Cong Duc, N., and Lee, G. (2021). Neuroprotective activity of melittin-the main component of bee venom-against oxidative stress induced by aβ25-35 in *in vitro* and *in vivo* models. *Antioxidants* 10 (11), 1654. doi:10.3390/antiox10111654

Conrad, V. J., Hazan, L. L., Latorre, A. J., Jakubowska, A., and Kim, C. M. H. (2019). Efficacy and safety of honey bee venom (*Apis mellifera*) dermal injections to treat osteoarthritis knee pain and physical disability: A randomized controlled trial. *J. Altern. Complement. Med.* 25 (8), 845–855. doi:10.1089/acm.2019.0121

Danesh-Seta, T., Emami, F., Nasr-Esfahani, M. H., Ghaedi, K., and Aliomrani, M. (2021). Bee venom-derived BBB shuttle and its correlation with oligodendrocyte proliferation markers in mice model of multiple sclerosis. *Neurotox. Res.* 39 (4), 1181–1188. doi:10.1007/s12640-021-00361-x

Daniluk, K., Kutwin, M., Grodzik, M., Wierzbicki, M., Strojny, B., Szczepaniak, J., et al. (2020). Use of selected carbon nanoparticles as melittin carriers for MCF-7 and MDA-MB-231 human breast cancer cells. *Materials* 13 (1), 90. doi:10.3390/ma13010090

Dehghani, B., Hasanshahi, Z., and Hashempour, T. (2020). HIV capsid and protease, new targets of melittin. *Int. J. Pept. Res. Ther.* 26 (4), 2057–2065. doi:10.1007/s10989-019-10002-9

Du, G., He, P., Zhao, J., He, C., Jiang, M., Zhang, Z., et al. (2021). Polymeric microneedle-mediated transdermal delivery of melittin for rheumatoid arthritis treatment. *J. Control. Release* 336, 537–548. doi:10.1016/j.jconrel.2021.07.005

Duffy, C., Sorolla, A., Wang, E., Golden, E., Woodward, E., Davern, K., et al. (2020). Honeybee venom and melittin suppress growth factor receptor activation in HER2-enriched and triple-negative breast cancer. *NPJ Precis. Oncol.* 4 (1), 24. doi:10.1038/s41698-020-00129-0

Dutta, P., Sahu, R. K., Dey, T., Lahkar, M. D., Manna, P., and Kalita, J. (2019). Beneficial role of insect-derived bioactive components against inflammation and its associated complications (colitis and arthritis) and cancer. *Chem. Biol. Interact.* 313, 108824. doi:10.1016/j.cbi.2019.108824

Ejaz, S., Hashmi, F. B., Malik, W. N., Ashraf, M., Nasim, F. U. H., and Iqbal, M. (2018). Applications of venom proteins as potential anticancer agents. *Protein Pept. Lett.* 25 (7), 688–701. doi:10.2174/0929866524666180614102104

El Bakary, N. M., Alsharkawy, A. Z., Shouaib, Z. A., and Barakat, E. M. S. (2020). Role of bee venom and melittin on restraining angiogenesis and metastasis in γ-irradiated solid Ehrlich carcinoma-bearing mice. *Integr. Cancer Ther.* 19, 1534735420944476. doi:10.1177/1534735420944476

El-Aarag, B., Magdy, M., AlAjmi, M. F., Khalifa, S. A. M., and El-Seedi, H. R. (2019). Melittin exerts beneficial effects on paraquat-induced lung injuries in mice by modifying oxidative stress and apoptosis. *Molecules* 24 (8), 1498. doi:10.3390/molecules24081498

El-Beltagy, A. F. B. M., Elsyyad, H. I. H., Abdelaziz, K. K., Madany, A. S., and Elghazaly, M. M. (2021). Therapeutic role of *Annona muricata* fruit and bee venom against MNU-induced breast cancer in pregnant rats and its complications on the ovaries. *Breast Cancer* 13, 431–445. doi:10.2147/BCTT.S306971

El-Hanoun, A., El-Komy, A., El-Sabrout, K., and Abdella, M. (2020). Effect of bee venom on reproductive performance and immune response of male rabbits. *Physiol. Behav.* 223, 112987. doi:10.1016/j.physbeh.2020.112987

El-Seedi, H., Abd El-Wahed, A., Yosri, N., Musharraf, S. G., Chen, L., Moustafa, M., et al. (2020). Antimicrobial properties of *Apis mellifera*'s bee venom. *Toxins* 12 (7), 451. doi:10.3390/toxins12070451

El-Seedi, H. R., Khalifa, S. A. M., Abd El-Wahed, A., Gao, R. C., Guo, Z. M., Tahir, H. E., et al. (2020). Honeybee products: An updated review of neurological actions. *Trends Food Sci. Technol.* 101, 17–27. doi:10.1016/j.tifs.2020.04.026

Elkomy, A., El-Hanoun, A., Abdella, M., and El-Sabrout, K. (2021). Improving the reproductive, immunity and health status of rabbit does using honey bee venom. *J. Anim. Physiol. Anim. Nutr.* 105 (5), 975–983. doi:10.1111/jpn.13552

Fan, X. G., Pei, S. Y., Zhou, D., Zhou, P. C., Huang, Y., Hu, X. W., et al. (2020). Melittin ameliorates inflammation in mouse acute liver failure via inhibition of PKM2-mediated Warburg effect. *Acta Pharmacol. Sin.* 42 (8), 1256–1266. doi:10.1038/s41401-020-00516-0

Fumagalli, C., and Barberis, M. (2021). Breast cancer heterogeneity. *Diagnostics* 11 (9), 1555. doi:10.3390/diagnostics11091555

Gajski, G., Domijan, A. M., and Garaj-Vrhovac, V. (2012). Alterations of GSH and MDA levels and their association with bee venom-induced DNA damage in human peripheral blood leukocytes. *Environ. Mol. Mutagen.* 53 (6), 469–477. doi:10.1002/em.21708

Gajski, G., Domijan, A. M., Žegura, B., Štern, A., Gerić, M., Novak Jovanović, I., et al. (2016). Melittin induced cytogenetic damage, oxidative stress and changes in gene expression in human peripheral blood lymphocytes. *Toxicon* 110, 56–67. doi:10.1016/j.toxicon.2015.12.005

Gajski, G., and Garaj-Vrhovac, V. (2011). Bee venom induced cytogenetic damage and decreased cell viability in human white blood cells after treatment *in vitro*: A multi-biomarker approach. *Environ. Toxicol. Pharmacol.* 32 (2), 201–211. doi:10.1016/j.etap.2011.05.004

Gao, D. Q., Zhang, J. J., Bai, L., Li, F. B., Dong, Y., and Li, Q. S. (2018). Melittin induces NSCLC apoptosis via inhibition of miR-183. *Onco. Targets. Ther.* 11, 4511–4523. doi:10.2147/ott.s169806

Garaj-Vrhovac, V., and Gajski, G. (2009). Evaluation of the cytogenetic status of human lymphocytes after exposure to a high concentration of bee venom *in vitro*. *Arh. Hig. Rada Toksikol.* 60 (1), 27–34. doi:10.2478/10004-1254-60-2009-1896

Gasanoff, E., Liu, Y., Li, F., Hanlon, P., and Garab, G. (2021). Bee venom melittin disintegrates the respiration of mitochondria in healthy cells and lymphoblasts, and induces the formation of non-bilayer structures in model inner mitochondrial membranes. *Int. J. Mol. Sci.* 22 (20), 11122. doi:10.3390/ijms222011122

Giannini, D., Antonucci, M., Petrelli, F., Bilia, S., Alunno, A., and Puxeddu, I. (2020). One year in review 2020: Pathogenesis of rheumatoid arthritis. *Clin. Exp. Rheumatol.* 38 (3), 387–397.

Giribaldi, J., Smith, J. J., and Schroeder, C. I. (2021). Recent developments in animal venom peptide nanotherapeutics with improved selectivity for cancer cells. *Biotechnol. Adv.* 50, 107769. doi:10.1016/j.biotechadv.2021.107769

Goo, B., Lee, J., Park, C., Yune, T., and Park, Y. (2021). Bee venom alleviated edema and pain in monosodium urate crystals-induced gouty arthritis in rat by inhibiting inflammation. *Toxins* 13 (9), 661. doi:10.3390/toxins13090661

Grawish, M. E., Mourad, M. I., Esmaeil, D. A., Ahmed, R. A., Ateia, I. M., Hany, E., et al. (2020). Emerging therapeutic modality enhancing the efficiency of chemotherapeutic agents against head and neck squamous cell carcinoma cell lines. *Cancer Treat. Res. Commun.* 25, 100242. doi:10.1016/j.ctarc.2020.100242

Gu, H., An, H. J., Kim, J. Y., Kim, W. H., Gwon, M. G., Kim, H. J., et al. (2019). Bee venom attenuates *Porphyromonas gingivalis* and RANKL-induced bone resorption with osteoclastogenic differentiation. *Food Chem. Toxicol.* 129, 344–353. doi:10.1016/j.fct.2019.05.001

Gu, H., Han, S. M., and Park, K. K. (2020). Therapeutic effects of apamin as a bee venom component for non-neoplastic disease. *Toxins* 12 (3), 195. doi:10.3390/toxins12030195

Gu, H., Kim, W. H., An, H. J., Kim, J. Y., Gwon, M. G., Han, S. M., et al. (2018). Therapeutic effects of bee venom on experimental atopic dermatitis. *Mol. Med. Rep.* 18 (4), 3711–3718. doi:10.3892/mmr.2018.9398

Gui, Z. Z., Zhu, J. C., Ye, S., Ye, J., Chen, J., Ling, Y. Y., et al. (2020). Prolonged melittin release from polyelectrolyte-based nanocomplexes decreases acute toxicity and improves blood glycemic control in a mouse model of type II diabetes. *Int. J. Pharm.* 577, 119071. doi:10.1016/j.ijpharm.2020.119071

Guo, X. Y., and Ma, T. (2019). Effects of acupuncture on neurological disease in clinical- and animal-based research. *Front. Integr. Neurosci.* 13, 47. doi:10.3389/fnint.2019.00047

Gwon, M.-G., An, H.-J., Gu, H., Kim, Y.-A., Han, S. M., and Park, K.-K. (2021). Apamin inhibits renal fibrosis via suppressing TGF-β1 and STAT3 signaling *in vivo* and *in vitro*. *J. Mol. Med.* 99 (9), 1265–1277. doi:10.1007/s00109-021-02087-x

Ham, H. J., Han, J. H., Lee, Y. S., Kim, K. C., Yun, J., Kang, S. K., et al. (2019a). Bee venom soluble phospholipase A2 exerts neuroprotective effects in a lipopolysaccharide-induced mouse model of Alzheimer's disease via inhibition of nuclear factor-kappa B. *Front. Aging Neurosci.* 11, 287. doi:10.3389/fnagi.2019.00287

Ham, H. J., Han, S. B., Yun, J., Yeo, I. J., Ham, Y. W., Kim, S. H., et al. (2019b). Bee venom phospholipase A2 ameliorates amyloidogenesis and neuroinflammation through inhibition of signal transducer and activator of transcription-3 pathway in Tg2576 mice. *Transl. Neurodegener.* 8, 26. doi:10.1186/s40035-019-0167-7

Hamad, M. K., He, K., Abdulrazeq, H. F., Mustafa, A. M., Luceri, R., Kamal, N., et al. (2018). Potential uses of isolated toxin peptides in neuropathic pain relief: A literature review. *World Neurosurg.* 113, 333–347. e5. doi:10.1016/j.wneu.2018.01.116

Han, S. M., Kim, S. G., Jang, H. R., Woo, S. O., and Pak, S. C. (2018). Anti-atopic dermatitis of purified bee venom on keratinocytes via suppression of PAR2, ICAM-1, and IL-6 expression. *J. Apic. Sci.* 62 (2), 179–188. doi:10.2478/jas-2018-0016

Hanafi, M. Y., Zaher, E. L. M., El-Adely, S. E. M., Sakr, A., Ghobashi, A. H. M., Hemly, M. H., et al. (2018). The therapeutic effects of bee venom on some metabolic and antioxidant parameters associated with HFD-induced non-alcoholic fatty liver in rats. *Exp. Ther. Med.* 15 (6), 5091–5099. doi:10.3892/etm.2018.6028

Hematyar, M., Soleimani, M., Es-haghi, A., and Mokarram, A. R. (2018). Synergistic Co-delivery of doxorubicin and melittin using functionalized magnetic nanoparticles for cancer treatment: Loading and *in vitro* release study by LC-MS/MS. *Artif. Cells Nanomed. Biotechnol.* 46, S1226–S1235. doi:10.1080/21691401.2018.1536063

Hozzeinab, W. N., Badr, G., Badr, B. M., Allam, A., Al Ghamdi, A., Al-Wadaan, M. A., et al. (2018). Bee venom improves diabetic wound healing by protecting functional macrophages from apoptosis and enhancing Nrf2, ang-1 and tie-2 signaling. *Mol. Immunol.* 103, 322–335. doi:10.1016/j.molimm.2018.10.016

Huang, J.-Y., Peng, S.-F., Chueh, F.-S., Chen, P.-Y., Huang, Y.-P., Huang, W.-W., et al. (2021). Melittin suppresses epithelial-mesenchymal transition and metastasis in human gastric cancer AGS cells via regulating wnt/BMP associated pathway. *Biosci. Biotechnol. Biochem.* 85 (11), 2250–2262. doi:10.1093/bbb/zbab153

Huh, J. E., Seo, B. K., Lee, J. W., Kim, C., Park, Y. C., Lee, J. D., et al. (2018). Analgesic effects of diluted bee venom acupuncture mediated by δ-opioid and α_2-adrenergic receptors in osteoarthritic rats. *Altern. Ther. Health Med.* 24 (2), 28–35.

Incorvaia, C., Mauro, M., Gritti, B. L., Makri, E., and Ridolo, E. (2018). Venom immunotherapy in patients with allergic reactions to insect stings. *Expert Rev. Clin. Immunol.* 14 (1), 53–59. doi:10.1080/1744666x.2018.1413350

Jeong, H., Lee, C., Cheng, C., Chou, H. C., Yang, H., and Bae, H. (2021). Targeting of adipose tissue macrophages by bee venom phospholipase A2 attenuates high-fat diet-induced obesity. *Int. J. Obes.* 45 (8), 1656–1667. doi:10.1038/s41366-021-00823-4

Jeong, Y. J., Park, Y. Y., Park, K. K., Choi, Y. H., Kim, C. H., and Chang, Y. C. (2019). Bee venom suppresses EGF-induced epithelial-mesenchymal transition and tumor invasion in lung cancer cells. *Am. J. Chin. Med.* 47 (8), 1869–1883. doi:10.1142/s0192415x19500952

Jin, Z., Yao, J., Xie, N., Cai, L., Qi, S., Zhang, Z., et al. (2018). Melittin constrains the expression of identified key genes associated with bladder cancer. *J. Immunol. Res.* 2018, 5038172. doi:10.1155/2018/5038172

Kang, D. W., Choi, J. G., Kim, J., Park, J. B., Lee, J. H., and Kim, H. W. (2021). Bee venom reduces burn-induced pain via the suppression of peripheral and central substance P expression in mice. *J. Vet. Sci.* 22 (1), e9. doi:10.4142/jvs.2021.22.e9

Kang, G. H., Lee, S. J., Choi, D. B., Shin, D., Kim, J., Yang, H., et al. (2020). Bee venom phospholipase A2 ameliorates atherosclerosis by modulating regulatory T cells. *Toxins* 12 (10), 609. doi:10.3390/toxins12100609

Kang, Y. M., Chung, K. S., Kook, I. H., Kook, Y. B., Bae, H., Lee, M., et al. (2018). Inhibitory effects of bee venom on mast cell-mediated allergic inflammatory responses. *Int. J. Mol. Med.* 41 (6), 3717–3726. doi:10.3892/ijmm.2018.3558

Kasozi, K. I., Niedbala, G., Alqarni, M., Zirintunda, G., Ssempijja, F., Musinguzi, S. P., et al. (2020). Bee venom-A potential complementary medicine candidate for SARS-CoV-2 infections. *Front. Public Health* 8, 594458. doi:10.3389/fpubh.2020.594458

Ke, M., Dong, J., Wang, Y., Zhang, J., Zhang, M., Wu, Z., et al. (2018). MEL-pep, an analog of melittin, disrupts cell membranes and reverses 5-fluorouracil resistance in human hepatocellular carcinoma cells. *Int. J. Biochem. Cell. Biol.* 101, 39–48. doi:10.1016/j.biocel.2018.05.013

Khalil, A., Elesawy, B. H., Ali, T. M., and Ahmed, O. M. (2021). Bee venom: From venom to drug. *Molecules* 26 (16), 4941. doi:10.3390/molecules26164941

Khamis, A. A. A., Ali, E. M. M., Abd El-Moneim, M. A., Abd-Alhaseeb, M. M., Abu El-Magd, M., and Salim, E. I. (2018). Hesperidin, piperine and bee venom synergistically potentiate the anticancer effect of tamoxifen against breast cancer cells. *Biomed. Pharmacother.* 105, 1335–1343. doi:10.1016/j.biopha.2018.06.105

Kim, A., Lee, S. Y., Kim, B. Y., and Chung, S. K. (2020). Elimination of teratogenic human induced pluripotent stem cells by bee venom via calcium-calpain pathway. *Int. J. Mol. Sci.* 21 (9), 3265. doi:10.3390/ijms21093265

Kim, D. H., Han, S. M., Keum, M. C., Lee, S., An, B. K., Lee, S. R., et al. (2018). Evaluation of bee venom as a novel feed additive in fast-growing broilers. *Br. Poult. Sci.* 59 (4), 435–442. doi:10.1080/00071668.2018.1476675

Kim, D. H., Lee, H. W., Park, H. W., and Chun, K. H. (2020). Bee venom inhibits the proliferation and migration of cervical-cancer cells in an HPV E6/E7-dependent manner. *BMB Rep.* 53 (8), 419–424. doi:10.5483/BMBRep.2020.53.8.031

Kim, H., Hong, J. Y., Jeon, W. J., Baek, S. H., and Ha, I. H. (2020). Bee venom melittin protects against cisplatin-induced acute kidney injury in mice via the regulation of M2 macrophage activation. *Toxins* 12 (9), 574. doi:10.3390/toxins12090574

Kim, H., Hong, J. Y., Lee, J., Jeon, W.-J., and Ha, I.-H. (2021). Apamin enhances neurite outgrowth and regeneration after laceration injury in cortical neurons. *Toxins* 13 (9), 603. doi:10.3390/toxins13090603

Kim, H. Y., Jo, M. J., Nam, S. Y., Kim, K. M., Choi, M. B., and Lee, Y. H. (2020). Evaluating the effects of honey bee (*Apis mellifera* L.) venom on the expression of insulin sensitivity and inflammation-related genes in Co-culture of adipocytes and macrophages. *Entomol. Res.* 50 (5), 236–244. doi:10.1111/1748-5967.12431

Kim, J. Y., Jang, H.-J., Leem, J., and Kim, G.-M. (2021b). Protective effects of bee venom-derived phospholipase A_2 against cholestatic liver disease in mice. *Biomedicines* 9 (8), 992. doi:10.3390/biomedicines9080992

Kim, J. Y., Leem, J., and Hong, H. L. (2021a). Melittin ameliorates endotoxin-induced acute kidney injury by inhibiting inflammation, oxidative stress, and cell death in mice. *Oxid. Med. Cell. Longev.* 2021, 8843051. doi:10.1155/2021/8843051

Kim, J. Y., Lee, S. J., Maeng, Y. I., Leem, J., and Park, K. K. (2020a). Protective effects of bee venom against endotoxemia-related acute kidney injury in mice. *Biology* 9 (7), 154. doi:10.3390/biology9070154

Kim, J. Y., Leem, J., and Park, K. K. (2020b). Antioxidative, antiapoptotic, and anti-inflammatory effects of apamin in a murine model of lipopolysaccharide-induced acute kidney injury. *Molecules* 25 (23), 5717. doi:10.3390/molecules25235717

Kim, K. H., Kim, M., Lee, J., Jeon, H. N., Kim, S. H., and Bae, H. (2019a). Comparison of the protective effects of bee venom extracts with varying PLA_2 compositions in a mouse model of Parkinson's disease. *Toxins* 11 (6), 358. doi:10.3390/toxins11060358

Kim, K. H., Lee, S. Y., Shin, J., Hwang, J. T., Jeon, H. N., and Bae, H. (2019b). Dose-dependent neuroprotective effect of standardized bee venom phospholipase A_2 against MPTP-induced Parkinson's disease in mice. *Front. Aging Neurosci.* 11, 80. doi:10.3389/fnagi.2019.00080

Kim, M., and Han, C. H. (2020). Pharmacopuncture for stroke survivors: A systematic review of randomized controlled trials in South Korea. *Complement. Ther. Clin. Pract.* 40, 101179. doi:10.1016/j.ctcp.2020.101179

Kim, S., Kim, H.-W., Chang, S.-H., Leem, K.-H., and Park, H.-J. (2021). Bee venom prevents mucin 5AC production through inhibition of AKT and SPDEF activation in airway epithelia cells. *Toxins* 13 (11), 773. doi:10.3390/toxins13110773

Kim, W. H., An, H. J., Kim, J. Y., Gwon, M. G., Gu, H., Jeon, M., et al. (2018). Anti-inflammatory effect of melittin on *Porphyromonas gingivalis* LPS-stimulated human keratinocytes. *Molecules* 23 (2), 332. doi:10.3390/molecules23020332

Kim, Y., Lee, Y. W., Kim, H., and Chung, D. K. (2019). Bee venom alleviates atopic dermatitis symptoms through the upregulation of decay-accelerating factor (DAF/CD55). *Toxins* 11 (5), 239. doi:10.3390/toxins11050239

Ko, S. J., Park, E., Asandei, A., Choi, J. Y., Lee, S. C., Seo, C. H., et al. (2020). Bee venom-derived antimicrobial peptide melectin has broad-spectrum potency, cell selectivity, and salt-resistant properties. *Sci. Rep.* 10 (1), 10145. doi:10.1038/s41598-020-66995-7

Kocyigit, A., Guler, E. M., and Kaleli, S. (2019). Anti-inflammatory and antioxidative properties of honey bee venom on Freund's complete adjuvant-induced arthritis model in rats. *Toxicon* 161, 4–11. doi:10.1016/j.toxicon.2019.02.016

Kong, R., Lee, Y. S., Kang, D. H., Wang, S., Li, Q. Q., Kwon, D. Y., et al. (2020). The antibacterial activity and toxin production control of bee venom in mouse MRSA pneumonia model. *BMC Complement. Med. Ther.* 20 (1), 238. doi:10.1186/s12906-020-02991-8

Kreinest, T., Volkmer, I., and Staege, M. S. (2021). Melittin increases cisplatin sensitivity and kills KM-H2 and L-428 Hodgkin lymphoma cells. *Int. J. Mol. Sci.* 22 (1), 343. doi:10.3390/ijms22010343

Ku, Y. H., Kang, J. H., and Lee, H. (2020). Effect of bee venom on an experimental cellular model of Alzheimer's disease. *Am. J. Chin. Med.* 48 (8), 1803–1819. doi:10.1142/s0192415x20500901

Kurek-Gorecka, A., Komosinska-Vassev, K., Rzepecka-Stojko, A., and Olczyk, P. (2021). Bee venom in wound healing. *Molecules* 26 (1), 148. doi:10.3390/molecules26010148

Lebel, A. A., Kisembo, M. V., Soucy, M.-F. N., Hebert, M. P. A., Morin, P., Jr., and Boudreau, L. H. (2021). Molecular characterization of the anticancer properties associated with bee venom and its components in glioblastoma multiforme. *Chem. Biol. Interact.* 347, 109622. doi:10.1016/j.cbi.2021.109622

Lee, G., Kang, G. H., and Bae, H. (2019). Bee venom phospholipase A2 suppression of experimental autoimmune encephalomyelitis is dependent on its enzymatic activity. *Mol. Cell. Toxicol.* 15 (3), 307–313. doi:10.1007/s13273-019-0034-8

Lee, J. E., Shah, V. K., Lee, E. J., Oh, M. S., and Choi, J. J. (2019). Melittin - a bee venom component - enhances muscle regeneration factors expression in a mouse model of skeletal muscle contusion. *J. Pharmacol. Sci.* 140 (1), 26–32. doi:10.1016/j.jphs.2019.03.009

Lee, J. H., Gang, J., Yang, E., Kim, W., and Jin, Y. H. (2020). Bee venom acupuncture attenuates oxaliplatin-induced neuropathic pain by modulating action potential threshold in A-fiber dorsal root ganglia neurons. *Toxins* 12 (12), 737. doi:10.3390/toxins12120737

Lee, J., Kim, Y. M., Kim, J. H., Cho, C. W., Jeon, J. W., Park, J. K., et al. (2018). Nasal delivery of chitosan/alginate nanoparticle encapsulated bee (*Apis mellifera*) venom promotes antibody production and viral clearance during porcine reproductive and respiratory syndrome virus infection by modulating T cell related responses. *Vet. Immunol. Immunopathol.* 200, 40–51. doi:10.1016/j.vetimm.2018.04.006

Lee, Y. J., Oh, M. J., Lee, D. H., Lee, Y. S., Lee, J., Kim, D. H., et al. (2020). Anti-inflammatory effect of bee venom in phthalic anhydride-induced atopic dermatitis animal model. *Inflammopharmacology* 28 (1), 253–263. doi:10.1007/s10787-019-00646-w

Lee, Y. M., Cho, S. N., Son, E., Song, C. H., and Kim, D. S. (2020). Apamin from bee venom suppresses inflammation in a murine model of gouty arthritis. *J. Ethnopharmacol.* 257, 112860. doi:10.1016/j.jep.2020.112860

Li, D. X., Chung, G., and Kim, S. K. (2020a). The involvement of central noradrenergic pathway in the analgesic effect of bee venom acupuncture on vincristine-induced peripheral neuropathy in rats. *Toxins* 12 (12), 775. doi:10.3390/toxins12120775

Li, D. X., Yoo, J. H., and Kim, S. K. (2020b). Long-lasting and additive analgesic effects of combined treatment of bee venom acupuncture and venlafaxine on paclitaxel-induced allodynia in mice. *Toxins* 12 (10), 620. doi:10.3390/toxins12100620

Li, Y., Xu, N., Zhu, W., Wang, L., Liu, B., Zhang, J., et al. (2018). Nanoscale melittin@ zeolitic imidazolate frameworks for enhanced anticancer activity and mechanism analysis. *ACS Appl. Mat. Interfaces* 10 (27), 22974–22984. doi:10.1021/acsami.8b06125

Liang, X. L., Yan, J. X., Lu, Y. W., Liu, S., and Chai, X. J. (2021). The antimicrobial peptide melectin shows both antimicrobial and antitumor activity via membrane interference and DNA binding. *Drug Des. devel. Ther.* 15, 1261–1273. doi:10.2147/dddt.s288219

Lim, H. N., Baek, S. B., and Jung, H. J. (2019). Bee venom and its peptide component melittin suppress growth and migration of melanoma cells via inhibition of PI3K/AKT/mTOR and MAPK pathways. *Molecules* 24 (5), 929. doi:10.3390/molecules24050929

Lima, W. G., Brito, J. C. M., and Nizer, W. S. D. (2021). Bee products as a source of promising therapeutic and chemoprophylaxis strategies against COVID-19 (SARS-CoV-2). *Phytother. Res.* 35 (2), 743–750. doi:10.1002/ptr.6872

Lin, Z., Xie, R., Zhong, C., Huang, J., Shi, P., and Yao, H. (2022). Recent progress (2015-2020) in the investigation of the pharmacological effects and mechanisms of ginsenoside Rb_1, a main active ingredient in *Panax ginseng* meyer. *J. Ginseng Res.* 46 (1), 39–53. doi:10.1016/j.jgr.2021.07.008

Lischer, K., Sitorus, S. R. A., Guslianto, B. W., Avila, F., Khayrani, A. C., and Sahlan, M. (2021). Anti-breast cancer activity on MCF-7 cells of melittin from Indonesia's *Apis cerana*: An *in vitro* study. *Asian pac. J. Cancer Prev.* 22 (12), 3913–3919. doi:10.31557/APJCP.2021.22.12.3913

Liu, X. Q., Jin, J. R., Liu, G. M., Peng, F., Zhang, C. G., Guo, M. X., et al. (2021). Effect of wasp venom from vespa mandarinia smith on the proliferation and apoptosis of MH7A cells. *Lat. Am. J. Pharm.* 40 (2), 235–243.

Luo, L., Wu, W., Sun, D., Dai, H.-B., Wang, Y., Zhong, Y., et al. (2018). Acid-activated melittin for targeted and safe antitumor therapy. *Bioconjug. Chem.* 29 (9), 2936–2944. doi:10.1021/acs.bioconjchem.8b00352

Lv, C., Zhang, Z., Zhao, T., Han, M. F., Jia, D. P., Su, L. Z., et al. (2019). The anti-tumour effect of mel and its role in autophagy in human hepatocellular carcinoma cells. *Am. J. Transl. Res.* 11 (2), 931–941.

Lyu, C., Fang, F. F., and Li, B. (2019). Anti-tumor effects of melittin and its potential applications in clinic. *Curr. Protein Pept. Sci.* 20 (3), 240–250. doi:10.2174/1389203719666180612084615

Maitip, J., Mookhploy, W., Khorndork, S., and Chantawannakul, P. (2021). Comparative study of antimicrobial properties of bee venom extracts and melittins of honey bees. *Antibiotics* 10 (12), 1503. doi:10.3390/antibiotics10121503

Mansour, G. H., El-Magd, M. A., Mahfouz, D. H., Abdelhamid, I. A., Mohamed, M. F., Ibrahim, N. S., et al. (2021). Bee venom and its active component melittin synergistically potentiate the anticancer effect of sorafenib against HepG2 cells. *Bioorg. Chem.* 116, 105329. doi:10.1016/j.bioorg.2021.105329

Meimandi-Parizi, A., Oryan, A., Bigham-Sadegh, A., and Sayahi, E. (2018). Effects of chitosan scaffold along with royal jelly or bee venom in regeneration of critical sized radial bone defect in rat. *Iran. J. Vet. Res.* 19 (4), 246–254.

Meligi, N. M., Ismail, S. A., and Tawfik, N. S. (2020). Protective effects of honey and bee venom against lipopolysaccharide and carbon tetrachloride-induced hepatoxicity and lipid peroxidation in rats. *Toxicol. Res.* 9 (5), 693–705. doi:10.1093/toxres/tfaa077

Mir Hassani, Z., Nabiuni, M., Parivar, K., Abdirad, S., and Karimzadeh, L. (2021). Melittin inhibits the expression of key genes involved in tumor microenvironment formation by suppressing HIF-1α signaling in breast cancer cells. *Med. Oncol.* 38 (7), 77. doi:10.1007/s12032-021-01526-6

Mirzaei, S., Fekri, H. S., Hashemi, F., Hushmandi, K., Mohammadinejad, R., Ashrafizadeh, M., et al. (2021). Venom peptides in cancer therapy: An updated review on cellular and molecular aspects. *Pharmacol. Res.* 164, 105327. doi:10.1016/j.phrs.2020.105327

Moghaddam, F. D., Akbarzadeh, I., Marzbankia, E., Farid, M., Khaledi, L., Reihani, A. H., et al. (2021). Delivery of melittin-loaded niosomes for breast cancer treatment: An *in vitro* and *in vivo* evaluation of anti-cancer effect. *Cancer Nanotechnol.* 12 (1), 14. doi:10.1186/s12645-021-00085-9

Moghaddam, F. D., Mortazavi, P., Hamedi, S., Nabiuni, M., and Roodbari, N. H. (2020). Apoptotic effects of melittin on 4T1 breast cancer cell line is associated with up regulation of Mfn1 and Drp1 mRNA expression. *Anticancer. Agents Med. Chem.* 20 (7), 790–799. doi:10.2174/1871520620666200211091451

Mohamed, W. A., Abd-Elhakim, Y. M., and Ismail, S. A. A. (2019). Involvement of the anti-inflammatory, anti-apoptotic, and anti-secretory activity of bee venom in its therapeutic effects on acetylsalicylic acid-induced gastric ulceration in rats. *Toxicology* 419, 11–23. doi:10.1016/j.tox.2019.03.003

Motiei, M., Aboutalebi, F., Forouzanfar, M., Dormiani, K., Nasr-Esfahani, M. H., and Mirahmadi-Zare, S. Z. (2021). Smart Co-delivery of miR-34a and cytotoxic peptides (LTX-315 and melittin) by chitosan based polyelectrolyte nanocarriers for specific cancer cell death induction. *Mat. Sci. Eng. C Mat. Biol. Appl.* 128, 112258. doi:10.1016/j.msec.2021.112258

Naji, K. M., Al-Khatib, B. Y., Al-Haj, N. S., and D'Souza, M. R. (2021). Hepatoprotective activity of melittin on isoniazid- and rifampicin-induced liver injuries in male albino rats. *BMC Pharmacol. Toxicol.* 22 (1), 39. doi:10.1186/s40360-021-00507-9

Nakashima, A., Tomono, S., Yamazaki, T., Inui, M., Morita, N., Ichimonji, I., et al. (2020). Phospholipase A2 from bee venom increases poly(I:C)-Induced activation in human keratinocytes. *Int. Immunol.* 32 (6), 371–383. doi:10.1093/intimm/dxaa005

Nehme, H., Ayde, H., El Obeid, D., Sabatier, J. M., and Fajloun, Z. (2020). Potential inhibitory effect of *Apis mellifera*'s venom and of its two main components-melittin and PLA_2-on *Escherichia coli* F_1F_0-ATPase. *Antibiotics* 9 (11), 824. doi:10.3390/antibiotics9110824

Nguyen, H. V., Heger, Z., Kominkova, M., Michalek, P., Gumulec, J., Guran, R., et al. (2015). The electrochemical and statistical evaluation of isolation of mellitin and apamin from honey bee (*Apis mellifera*) venom. *Int. J. Electrochem. Sc.* 10, 1249–1260.

Nikodijevic, D. D., Milutinovic, M. G., Cvetkovic, D. M., Cupurdija, M. D., Jovanovic, M. M., Mrkic, I. V., et al. (2021). Impact of bee venom and melittin on apoptosis and biotransformation in colorectal carcinoma cell lines. *Toxin Rev.* 40 (4), 1272–1279. doi:10.1080/15569543.2019.1680564

Ombredane, A. S., de Andrade, L. R., Bonadio, R. S., Pinheiro, W. O., de Azevedo, R. B., and Joanitti, G. A. (2021). Melittin sensitizes skin squamous carcinoma cells to 5-fluorouracil by affecting cell proliferation and survival. *Exp. Dermatol.* 30 (5), 710–716. doi:10.1111/exd.14289

Palgan, K., Zbikowska-Gotz, M., and Bartuzi, Z. (2020). Expression of eosinophils, RANTES and IL-25 in the first phase of Hymenoptera venom immunotherapy. *Postepy Dermatol. Alergol.* 37 (4), 590–596. doi:10.5114/ada.2019.83655

Park, J., Jang, K. M., and Park, K. K. (2020). Apamin suppresses LPS-induced neuroinflammatory responses by regulating SK channels and TLR4-mediated signaling pathways. *Int. J. Mol. Sci.* 21 (12), 4319. doi:10.3390/ijms21124319

Park, J., Kwon, O., An, H. J., and Park, K. K. (2018). Antifungal effects of bee venom components on *Trichophyton rubrum*: A novel approach of bee venom study for possible emerging antifungal agent. *Ann. Dermatol.* 30 (2), 202–210. doi:10.5021/ad.2018.30.2.202

Pashaei, F., Bevalian, P., Akbari, R., and Bagheri, K. P. (2019). Single dose eradication of extensively drug resistant *Acinetobacter spp.* in a mouse model of burn infection by melittin antimicrobial peptide. *Microb. Pathog.* 127, 60–69. doi:10.1016/j.micpath.2018.11.055

Pattabhiramaiah, M., Ramesh, K., Vishwanath, K. V., and Reddy, S. M. (2020). Computational analysis of PhospholipaseA2 in the honey bee venom. *J. Apic. Res.* 59 (4), 706–721. doi:10.1080/00218839.2020.1754589

Pereira, A. F. M., Albano, M., Alves, F. C. B., Andrade, B. F. M. T., Furlanetto, A., Rall, V. L. M., et al. (2020). Influence of apitoxin and melittin from *Apis mellifera* bee on *Staphylococcus aureus* strains. *Microb. Pathog.* 141, 104011. doi:10.1016/j.micpath.2020.104011

Putz, T., Ramoner, R., Gander, H., Rahm, A., Bartsch, G., Bernardo, K., et al. (2007). Bee venom secretory phospholipase A2 and phosphatidylinositol-homologues cooperatively disrupt membrane integrity, abrogate signal transduction and inhibit proliferation of renal cancer cells. *Cancer Immunol. Immunother.* 56 (5), 627–640. doi:10.1007/s00262-006-0220-0

Qi, J. X., Chen, Y. H., Xue, T. T., Lin, Y., Huang, S. Y., Cao, S. Y., et al. (2020). Graphene oxide-based magnetic nanocomposites for the delivery of melittin to cervical cancer HeLa cells. *Nanotechnology* 31 (6), 065102. doi:10.1088/1361-6528/ab5084

Raghuraman, H., and Chattopadhyay, A. (2007). Melittin: A membrane-active peptide with diverse functions. *Biosci. Rep.* 27 (4-5), 189–223. doi:10.1007/s10540-006-9030-z

Rakha, M. K., Tawfiq, R. A., Sadek, M. M., Anwer, M. A., Salama, S. M., Mohamed, A. F., et al. (2018). Neurotherapeutic effects of bee venom in a rotenone-induced mouse model of Parkinson's disease. *Neurophysiology* 50 (6), 445–455. doi:10.1007/s11062-019-09777-w

Raveendran, R., Chen, F., Kent, B., and Stenzel, M. H. (2020). Estrone-decorated poly-ion complex micelles for targeted melittin delivery to hormone-responsive

breast cancer cells. *Biomacromolecules* 21 (3), 1222–1233. doi:10.1021/acs.biomac.9b01681

Sangboonruang, S., Kitidee, K., Chantawannakul, P., Tragoolpua, K., and Tragoolpua, Y. (2020). Melittin from *Apis florea* venom as a promising therapeutic agent for skin cancer treatment. *Antibiotics* 9 (8), 517. doi:10.3390/antibiotics9080517

Sarhan, M., El-Bitar, A. M. H., and Hotta, H. (2020). Potent virucidal activity of honeybee "*Apis mellifera*" venom against Hepatitis C Virus. *Toxicon* 188, 55–64. doi:10.1016/j.toxicon.2020.10.014

Shaw, P., Kumar, N., Hammerschmid, D., Privat-Maldonado, A., Dewilde, S., and Bogaerts, A. (2019). Synergistic effects of melittin and plasma treatment: A promising approach for cancer therapy. *Cancers* 11 (8), 1109. doi:10.3390/cancers11081109

Shin, D., Choi, W., and Bae, H. (2018). Bee venom phospholipase A2 alleviate house dust mite-induced atopic dermatitis-like skin lesions by the CD206 mannose receptor. *Toxins* 10 (4), 146. doi:10.3390/toxins10040146

Shin, S. H., Ye, M. K., Choi, S. Y., and Park, K. K. (2018). Anti-inflammatory effect of bee venom in an allergic chronic rhinosinusitis mouse model. *Mol. Med. Rep.* 17 (5), 6632–6638. doi:10.3892/mmr.2018.8720

Siegel, R. L., Miller, K. D., Fuchs, H. E., and Jemal, A. (2021). Cancer statistics, 2021. *Ca. Cancer J. Clin.* 71 (1), 7–33. doi:10.3322/caac.21654

Soliman, C., Eastwood, S., Truong, V. K., Ramsland, P. A., and Elbourne, A. (2019). The membrane effects of melittin on gastric and colorectal cancer. *PLoS One* 14 (10), e0224028. doi:10.1371/journal.pone.0224028

Stoevesandt, J., Sturm, G. J., Bonadonna, P., Elberink, J. N. G. O., and Trautmann, A. (2020). Risk factors and indicators of severe systemic insect sting reactions. *Allergy* 75 (3), 535–545. doi:10.1111/all.13945

Sturm, G. J., Varga, E.-M., Roberts, G., Mosbech, H., Bilò, M. B., Akdis, C. A., et al. (2018). EAACI guidelines on allergen immunotherapy: Hymenoptera venom allergy. *Allergy* 73 (4), 744–764. doi:10.1111/all.13262

Sugarbaker, D. J., and Dasilva, M. C. (2011). Diagnostic workup of lung cancer. *Surg. Oncol. Clin. N. Am.* 20 (4), 667–679. doi:10.1016/j.soc.2011.08.003

Sung, H., Ferlay, J., Siegel, R. L., Laversanne, M., Soerjomataram, I., Jemal, A., et al. (2021). Global cancer statistics 2020: GLOBOCAN estimates of incidence and mortality worldwide for 36 cancers in 185 countries. *Ca. Cancer J. Clin.* 71 (3), 209–249. doi:10.3322/caac.21660

Tang, C. H. (2019). Research of pathogenesis and novel therapeutics in arthritis. *Int. J. Mol. Sci.* 20 (7), 1646. doi:10.3390/ijms20071646

Tang, F. Q., Wu, H., Zheng, J. Z., Guo, H. L., Yan, L. P., Lin, Y. S., et al. (2021). Effect of melittin on iNOS and NF-κB expression induced by IL-1β in C518 cells. *Pak. J. Pharm. Sci.* 34 (1), 95–101. doi:10.36721/pjps.2021.34.1.reg.095-101.1

Tanuwidjaja, I., Svecnjak, L., Gugic, D., Levanic, M., Juric, S., Vincekovic, M., et al. (2021). Chemical profiling and antimicrobial properties of honey bee (*Apis mellifera* L.) venom. *Molecules* 26 (10), 3049. doi:10.3390/molecules26103049

Tipgomut, C., Wongprommoon, A., Takeo, E., Ittiudomrak, T., Puthong, S., and Chanchao, C. (2018). Melittin induced G1 cell cycle arrest and apoptosis in chago-K1 human bronchogenic carcinoma cells and inhibited the differentiation of THP-1 cells into tumour- associated macrophages. *Asian pac. J. Cancer Prev.* 19 (12), 3427–3434. doi:10.31557/APJCP.2018.19.12.3427

Uzair, B., Bushra, R., Khan, B. A., Zareen, S., and Fasim, F. (2018). Potential uses of venom proteins in treatment of HIV. *Protein Pept. Lett.* 25 (7), 619–625. doi:10.2174/0929866525666180628161107

Uzuner, S. C., Birinci, E., Tetikoglu, S., Birinci, C., and Kolayli, S. (2021). Distinct epigenetic reprogramming, mitochondrial patterns, cellular morphology, and cytotoxicity after bee venom treatment. *Recent Pat. anticancer. Drug Discov.* 16 (3), 377–392. doi:10.2174/1574892816666210422125058

Viana, G. A., Freitas, C. I. A., de Almeida, J. G. L., de Medeiros, G. V. D., Teofilo, T. D., Rodrigues, V. H. V., et al. (2021). Antioxidant, genotoxic, antigenotoxic, and antineoplastic activities of apitoxin produced by *Apis mellifera* in northeast, Brazil. *Cienc. Rural.* 51 (4), e20200545. doi:10.1590/0103-8478cr20200545

Volkova, L. V., Pashov, A. I., and Omelchuk, N. N. (2021). Cervical carcinoma: Oncobiology and biomarkers. *Int. J. Mol. Sci.* 22 (22), 12571. doi:10.3390/ijms222212571

Wang, H., Wang, S., Wang, R., Wang, X., Jiang, K., Xie, C., et al. (2019). Co-Delivery of paclitaxel and melittin by glycopeptide-modified lipodisks for synergistic anti-glioma therapy. *Nanoscale* 11 (27), 13069–13077. doi:10.1039/c9nr01820d

Wang, L., Zhao, X. Q., Zhu, C. L., Zhao, Y. Y., Liu, S. S., Xia, X. J., et al. (2020). The antimicrobial peptide MPX kills *Actinobacillus pleuropneumoniae* and reduces its pathogenicity in mice. *Vet. Microbiol.* 243, 108634. doi:10.1016/j.vetmic.2020.108634

Wang, X., Li, H., Lu, X., Wen, C., Huo, Z., Shi, M., et al. (2018). Melittin-induced long non-coding RNA NONHSAT105177 inhibits proliferation and migration of pancreatic ductal adenocarcinoma. *Cell. Death Dis.* 9 (10), 940. doi:10.1038/s41419-018-0965-3

Wattanakul, K., Imae, T., Chang, W. W., Chu, C. C., Nakahata, R., and Yusa, S. (2019). Oligopeptide-side chained alginate nanocarrier for melittin-targeted chemotherapy. *Polym. J.* 51 (8), 771–780. doi:10.1038/s41428-019-0191-6

Wehbe, R., Frangieh, J., Rima, M., El Obeid, D., Sabatier, J.-M., and Fajloun, Z. (2019). Bee venom: Overview of main compounds and bioactivities for therapeutic interests. *Molecules* 24 (16), 2997. doi:10.3390/molecules24162997

Wen, Y. J., Zhu, M. L., Zhang, X. R., Xiao, H. D., Wei, Y., and Zhao, P. Q. (2022). Integrated analysis of multiple bioinformatics studies to identify microRNA-target gene-transcription factor regulatory networks in retinoblastoma. *Transl. Cancer Res.* 11 (7), 2225–2237. doi:10.21037/tcr-21-1748

Woo, S., Chung, G., Bae, H., and Kim, S. K. (2019). Suppressive effects of bee venom-derived phospholipase A2 on mechanical allodynia in a rat model of neuropathic pain. *Toxins* 11 (8), 477. doi:10.3390/toxins11080477

Yaacoub, C., Rifi, M., El-Obeid, D., Mawlawi, H., Sabatier, J.-M., Coutard, B., et al. (2021). The cytotoxic effect of *Apis mellifera* venom with a synergistic potential of its two main components-melittin and PLA2-on colon cancer HCT116 cell lines. *Molecules* 26 (8), 2264. doi:10.3390/molecules26082264

Yang, W., Hu, F. L., and Xu, X. F. (2020). Bee venom and SARS-CoV-2. *Toxicon* 181, 69–70. doi:10.1016/j.toxicon.2020.04.105

Yao, J., Zhang, Z., Li, S., Li, B., and Wang, X. H. (2020). Melittin inhibits proliferation, migration and invasion of bladder cancer cells by regulating key genes based on bioinformatics and experimental assays. *J. Cell. Mol. Med.* 24 (1), 655–670. doi:10.1111/jcmm.14775

Ye, R., Zheng, Y., Chen, Y., Wei, X., Shi, S., Chen, Y., et al. (2021). Stable loading and delivery of melittin with lipid-coated polymeric nanoparticles for effective tumor therapy with negligible systemic toxicity. *ACS Appl. Mat. Interfaces* 13 (47), 55902–55912. doi:10.1021/acsami.1c17618

Yoon, J. E., Hong, K., and Han, S. G. (2018). Antiproliferative effects of bee venom in human lung and breast cancer cells by decreasing Cyclin D1 and NF-kappa B. *Curr. Top. Nutraceutical Res.* 16 (4), 235–244.

Yu, G. H., Wang, L. -G., Yan, G. -R., and He, Q. -Y. (2015). DOSE: An R/bioconductor package for disease ontology semantic and enrichment analysis. *Bioinformatics* 31 (4), 608–609. doi:10.1093/bioinformatics/btu684

Yu, R., Wang, M., Wang, M., and Han, L. (2020). Melittin suppresses growth and induces apoptosis of non-small-cell lung cancer cells via down-regulation of TGF-β-mediated ERK signal pathway. *Braz. J. Med. Biol. Res.* 54 (2), e9017. doi:10.1590/1414-431X20209017

Yu, X., Gou, X., Wu, P., Han, L., Tian, D., Du, F., et al. (2018). Activatable protein nanoparticles for targeted delivery of therapeutic peptides. *Adv. Mat.* 30 (7), 1705383. doi:10.1002/adma.201705383

Yun, H. S., Oh, J., Lim, J. S., Kim, H. J., and Kim, J.-S. (2021). Anti-inflammatory effect of wasp venom in BV-2 microglial cells in comparison with bee venom. *Insects* 12 (4), 297. doi:10.3390/insects12040297

Zahran, F., Mohamad, A., and Zein, N. (2021). Bee venom ameliorates cardiac dysfunction in diabetic hyperlipidemic rats. *Exp. Biol. Med.* 246 (24), 2630–2644. doi:10.1177/15353702211045924

Zare, M., Khayatzadeh, J., Nia, H. S., Mojarad, M., Baghbani, F., Sargolzaei, J., et al. (2019). Effects of bee venom on activity and expression of 15-lipoxygenase-1 in human HT29 colon cancer. *Acta Poloniae Pharm. - Drug Res.* 76 (1), 75–82. doi:10.32383/appdr/92651

Zarrinnahad, H., Mahmoodzadeh, A., Hamidi, M. P., Mahdavi, M., Moradi, A., Bagheri, K. P., et al. (2018). Apoptotic effect of melittin purified from Iranian honey bee venom on human cervical cancer HeLa cell line. *Int. J. Pept. Res. Ther.* 24 (4), 563–570. doi:10.1007/s10989-017-9641-1

Zhang, S., Lv, X., Li, L., Luo, Y., Xiang, H., Wang, L., et al. (2021). Melittin inhibited glycolysis and induced cell apoptosis in cisplatin-resistant lung adenocarcinoma cells via TRIM8. *Biocell* 45 (1), 167–175. doi:10.32604/biocell.2021.013636

Zhong, C., Lin, Z., Ke, L., Shi, P., Li, S., Huang, L., et al. (2021). Recent research progress (2015-2021) and perspectives on the pharmacological effects and mechanisms of Tanshinone IIA. *Front. Pharmacol.* 12, 778847. doi:10.3389/fphar.2021.778847

Zhou, J., Wan, C., Cheng, J., Huang, H., Lovell, J. F., and Jin, H. (2021). Delivery strategies for melittin-based cancer therapy. *Acs Appl. Mat. Interfaces* 13 (15), 17158–17173. doi:10.1021/acsami.1c03640

Zhu, H., Chen, D., Xie, X., Li, Y., and Fan, T. (2021). Melittin inhibits lung metastasis of human osteosarcoma: Evidence of wnt/β-Catenin signaling pathway participation. *Toxicon.* 198, 132–142. doi:10.1016/j.toxicon.2021.04.024

frontiers | Frontiers in Pharmacology

TYPE Original Research
PUBLISHED 10 April 2023
DOI 10.3389/fphar.2023.1143437

OPEN ACCESS

EDITED BY
Cassandra M. Modahl,
Liverpool School of Tropical Medicine,
United Kingdom

REVIEWED BY
Rohit Patel,
Liverpool School of Tropical Medicine,
United Kingdom
Iekhsan Bin Othman,
Monash University Malaysia, Malaysia

*CORRESPONDENCE
Kae Yi Tan,
kytan_kae@um.edu.my

SPECIALTY SECTION
This article was submitted to Experimental Pharmacology and Drug Discovery, a section of the journal Frontiers in Pharmacology

RECEIVED 13 January 2023
ACCEPTED 27 March 2023
PUBLISHED 10 April 2023

CITATION
Chan YW, Tan CH, Heh CH and Tan KY (2023), An immunoinformatic approach to assessing the immunogenic capacity of alpha-neurotoxins in elapid snake venoms.
Front. Pharmacol. 14:1143437.
doi: 10.3389/fphar.2023.1143437

An immunoinformatic approach to assessing the immunogenic capacity of alpha-neurotoxins in elapid snake venoms

Yi Wei Chan[1], Choo Hock Tan[2], Choon Han Heh[3] and Kae Yi Tan[1]*

[1]Protein and Interactomics Laboratory, Department of Molecular Medicine, Faculty of Medicine, University of Malaya, Kuala Lumpur, Malaysia, [2]Venom Research and Toxicology Laboratory, Department of Pharmacology, Faculty of Medicine, University of Malaya, Kuala Lumpur, Malaysia, [3]Department of Pharmaceutical Chemistry, Faculty of Pharmacy, University of Malaya, Kuala Lumpur, Malaysia

Introduction: Most elapid snakes produce venoms that contain alpha-neurotoxins (α-NTXs), which are proteins that cause post-synaptic blockade and paralysis in snakebite envenoming. However, existing elapid antivenoms are known for their low potency in neutralizing the neurotoxic activity of α-NTXs, while the immunological basis has not been elucidated.

Methods: In this study, a structure-based major histocompatibility complex II (MHCII) epitope predictor of horse (*Equus caballus*), complemented with DM-editing determinant screening algorithm was adopted to assess the immunogenicity of α-NTXs in the venoms of major Asiatic elapids (*Naja kaouthia, Ophiophagus hannah, Laticauda colubrina, Hydrophis schistosus, Hydrophis curtus*).

Results: The scoring metric M_2R, representing the relative immunogenic performance of respective α-NTXs, showed all α-NTXs have an overall low M_2R of <0.3, and most of the predicted binders feature non-optimal P1 anchor residues. The M_2R scores correlate strongly (R^2 = 0.82) with the potency scores (p-score) generated based on the relative abundances of α-NTXs and the neutralization potency of commercial antivenoms.

Discussion: The immunoinformatic analysis indicates that the inferior antigenicity of α-NTXs is not only due to their small molecular size but also the subpar immunogenicity affected by their amino acid composition. Structural modification with conjugation and synthetic epitope as immunogen may potentially enhance the immunogenicity for improved antivenom potency against α-NTXs of elapid snakes.

KEYWORDS

three-finger toxins, antivenom efficacy, bioinformatics, immunogenicity, antigenicity, molecular docking

1 Introduction

Alpha-neurotoxins (α-NTXs) belong to the three-finger toxins (3FTx) family and are commonly found in the venoms of most Asiatic elapid snakes, e.g., cobras (*Naja* spp.), sea snakes (*Hydrophis* spp.), King Cobra (*Ophiphagus hannah*) and kraits (*Bungarus* spp.) (Tan et al., 2015a; Tan et al., 2015b; Tan et al., 2015c; Leong et al., 2015; Oh et al., 2021). Depending on the amino acid composition, the α-NTXs are further classified into short neurotoxins

(SαNTX, 6–7 kDa) and long neurotoxins (LαNTX, 7–9 kDa) (Barber et al., 2013). As antagonists of post-synaptic nicotinic acetylcholine receptors (nAChR) of neuromuscular junctions, these non-enzymatic neurotoxins account for the neurotoxicity in most elapid envenomation, resulting in a fast onset of flaccid systemic paralysis, with death ensuing rapidly in the absence of proper treatment (Barber et al., 2013; Ranawaka et al., 2013).

Antivenoms, which contain animal immunoglobulins or derivatives raised against snake venoms, remain the definitive treatment for snakebite envenoming (World Health Organization, 2016). However, earlier studies consistently showed elapid antivenoms have low efficacy, with neutralization potency (P, expressed in the amount of venom neutralized completely per milliliter of antivenom) well below 1 mg/ml (Leong et al., 2012; Leong et al., 2015). In contrast, viperid antivenoms appear to have higher efficacy, with Potency (P) values up to 10 mg/ml (Leong et al., 2014). The lower efficacy of elapid antivenoms would inevitably lead to the need for a higher dose of antivenom treatment, resulting in higher medical expenses, curtail of antivenom stockpile, and at the same time exposing patients to a greater risk of hypersensitive reactions that can be fatal (World Health Organization, 2016; Patikorn et al., 2022). The elapid antivenom efficacy is particularly low in neutralizing venom lethality driven by α-NTXs (Ratanabanangkoon et al., 2016; Wong et al., 2016; Tan et al., 2017), suggesting inadequate immunogenic capacity of the α-NTX for the production of neurotoxin-specific antibodies. In this regard, factors such as the size, dose and foreignness of a molecule are known to affect its immunogenicity as an antigen during immunization (Clementi et al., 1991; Irais et al., 2020). The small size of α-NTX indicates a lower number of epitopes in eliciting an immune response, and the immunogenicity may be further compromised by other larger snake venom toxins present in an immunogen mixture. To overcome the current predicament, the concept of "diverse toxin repertoire" has been proposed and trialled whereby the pool of α-NTXs of various elapid species was used to enrich the venom immunogen mixture containing minimum high molecular weight (MW) components for hyperimmunization in horses (Ratanabanangkoon, 2021). The resultant antisera showed an exceptionally broad para-specificity of neutralization against diverse elapid venoms, while the strategy did not translate into a major improvement of neutralizing potency per individual snake species (Ratanabanangkoon et al., 2016; Ratanabanangkoon et al., 2020). Furthermore, even antivenoms raised against elapid venoms that contain abundant α-NTX (>40% of total venom proteins) showed generally low neutralizing potency, questioning if the "dose" of α-NTX is indeed the key determinant of eliciting good immunization response (Ratanabanangkoon et al., 2016; Palasuberniam et al., 2021; Tan et al., 2021). Hypothetically, there are other factors at play that intrinsically modulate the makeup of epitope(s) in the α-NTX, and this results in variable immunorecognition by the B-cell receptor (BCR) and/or T-cell receptor (TCR) for antibody production.

Conventionally, antivenom production exploits the adaptive immune system of host animals such as horses, in which venom proteins are used as specific antigens to strategically mount a humoral immune response. This entails the activation and maturation of naïve B-cells into antibody-producing plasma B-cells, under the regulation of helper T cells (also called $CD4^+$ cells). To produce specific venom-targeting antibodies, the venom antigens must first be recognized, bound and internalized by professional antigen-presenting cells (APC) which include the naïve B-cells (*via* the BCR), and other phagocytes, e.g., macrophages and dendritic cells. The endocytosed venom proteins are degraded in the endo-lysosomal compartments, yielding peptide fragments as antigens that will be loaded onto major histocompatibility complex II (MHCII) and displayed on the external cell membrane. The MCHII-loaded peptide antigens displayed on phagocytes, especially dendritic cells, will be recognized by naïve T helper cells (T_h cells) *via* the TCR, activating them into effector and memory T_h cells. The effector T_h cells recognize the particular antigen peptide displayed by the MCHII complex of B-cells, fully activating them to produce toxin-specific antibodies (immunoglobulin G) with longer half-life and higher affinity, while the same T_h cells also release cytokines that mediate proliferation of the activated B-cells (Hoogeboom and Tolar, 2016).

All in all, initiating the venom/toxin-specific humoral immunity requires proper loading of the toxin peptides onto MHCII membrane-bound proteins for subsequent antigen presentation to the T_h cells. The MHCII protein is composed of two subunits (α and β) chains, whose α_1 and β_1 domains of the extra-cellular segments form the antigen-binding groove with multiple pockets destined to bind antigenic peptides (of the exogenous toxins) in the endosomal compartment. From the endoplasmic reticulum where MHCII proteins are assembled, throughout their intracellular transport to the Golgi apparatus and finally to endosomes, the MHCII binding groove is blocked from endogenous peptide binding by the invariant (Ii) chain. In the endosomes, the drastic change in pH partially degrades the MHCII-bound Ii chain while leaving behind a short peptide named CLIP (class II MHC associated Ii peptide) that continues to shield the MHCII binding site. Here, the equine version of human leukocyte antigen-DM (HLA-DM) molecule plays a critical role for peptide exchange, where it accelerates the removal of CLIP and other peptides that lack appropriate anchor residues, thereby "editing" the repertoire of internalized peptides to make way for proper MHCII-peptide loading and subsequent antigen presentation on APCs (Morris et al., 1994; Denzin and Cresswell, 1995; Fung-Leung et al., 1996; Zhou et al., 2009; Schulze et al., 2013). The susceptibility to DM-mediated peptide editing is modulated by the dynamic conformation of MHCII bound with peptide. Previous studies highlighted the importance of the hydrogen bond network formed between peptide backbone and conserved residues in MHCII, especially those at the P1 and P2 pockets which are key sites of peptide binding (Stratikos et al., 2004; Anders et al., 2011; Yin et al., 2014). Accordingly, only strong-binding peptides with appropriate anchor residues for the pockets will succeed in the DM-mediated MHCII peptide exchange, demonstrating immunodominance of epitopes over others that favors their recognition by T_h cells in mounting a good humoral immune response. In this context, the understanding of the DM-editing susceptibility of various peptides display of α-NTXs to proper MHCII-peptide loading is important to elucidate the immunogenicity of these venom proteins, which has deep implication in antivenom production. Therefore, the present study aimed to assess immunogenic capacity of α-NTXs by using

the modified structure-based predictor in complement with the screening algorithm of DM-editing determinants. In addition, a scoring metric was configured to determine the relative immunogenicity of α-NTXs. It is hoped that this study will provide a deeper understanding about the poor efficacy of elapid antivenoms.

2 Materials and methods

2.1 Prediction of B-cell antigenic determinant

The full amino acid sequence of respective α-NTXs was acquired from UniProt and submitted to the input panel for B-cell epitope prediction with Kolaskar and Tongaonkar antigenicity scale (http://tools.iedb.org/bcell/) (Kolaskar and Tongaonkar, 1990). Selected α-NTXs for this study are: (i) LαNTXs, which include (a) α-cobratoxin (Nk_LαNTX-α-Cbtx, UniProt ID: P01391, *Naja kaouthia*); (b) long neurotoxin OH55 (Oh_LαNTX-OH55, UniProt ID: Q53B58, *O. hannah*); and (c) long neurotoxin 1 (Hc_LαNTX-1, UniProt ID: Q8UW29, *Hydrophis curtus*), and (ii) SαNTXs: (a) cobrotoxin-c (Nk_SαNTX-Cbtx-c, UniProt ID: P59276, *N. kaouthia*); (b) short neurotoxin 1 (Hs_SαNTX-1, UniProt ID: P68415, *Hydrophis schistosus*); and (c) short neurotoxin 2 (Lc_SαNTX-2, UniProt ID: P10457, *Laticauda colubrina*). Zinc metalloproteinase-disintegrin-like atragin (Na_SVMP, Uniprot ID: D3TTC2, *Naja atra*) was selected as a standard of high MW toxin.

2.2 Homology modeling of Eqca-DR MHCII models

The homology structures of horse (*Equus caballus*) major histocompatibility complex II (Eqca-DR) were modeled after human HLA-DR1 crystal structure [PDB_ID: 1HXY] obtained from Protein Data Bank (https://www.rcsb.org). With HLA-DR1 selected as a template, molecular modeling was carried out for the two allelic variants of Eqca-DR (Eqca-DRA*00103:DRB2*00201 and Eqca-DRA*00201:DRB2*00201; sequence obtained from EMBL's European Bioinformatics Institute (https://www.ebi.ac.uk) and modeled *via* webserver Swiss-Model (https://www.swissmodel.expasy.org). The 3D protein models were generated after transferring conserved atom coordinates as identified by the target-template alignment. To acquire a full-atom protein model, the construction of non-conserved amino acid side chains was performed with OpenStructure computational structural biology framework and ProMod3 modeling engine. Both models with the highest Global Model Quality Estimation (GMQE) and optimal QMEAN scores were submitted to Structural Analysis and Verification Server of UCLA (https://saves.mbi.ucla.edu/), and passed the Verify3D (at least 80% of the amino acids have scored ≥0.2 in the 3D/1D profile) and PROCHECK (Ramachandran plot: 92.4% residues in most favored regions, 6.9% residues in additional allowed regions, 0.3% residues in generously allowed regions and 0.3% residues in disallowed regions) assessments (Laskowski et al., 1993; Eisenberg et al., 1997).

2.3 Preparation of 15-mer α-NTXs peptide fragments

15-mer peptide sequences were generated automatically with an in-house Bash script that extracts 15 continuous amino acid residues from respective α-NTXs. Following that, the 3-dimensional structures of 15-mer were constructed with Pymol (Schrödinger and DeLano, 2020). Open Babel software was used to minimize the energy of the resulting 15-mer peptide structures with a conjugated algorithm for 100 cycles (O'Boyle et al., 2011).

2.4 Molecular docking simulation

The series of docking analyses were performed *via* the guru interface of the HADDOCK 2.2 webserver (https://alcazar.science.uu.nl/services/HADDOCK2.2/). The HADDOCK protocol encompasses three docking stages: (i) rigid body minimization (it0), (ii) semi-flexible annealing (it1), and (iii) explicit solvent refinement (water) (van Zundert et al., 2016). The decoys generated were clustered with Fraction of Common Contacts algorithm (FCC: 0.6) (Rodrigues et al., 2012; Takemura and Kitao, 2019). Cluster with the lowest HADDOCK scores of the top 4 models was ranked on top. By default, the HADDOCK scoring function settings are for protein-protein complexes that entail weighted sum of following terms:

$$HADDOCKscore - it0 = 0.01\,E_{vdw} + 1.0\,E_{elec} + 1.0\,E_{desol} + 0.01\,E_{air} - 0.01\,BSA$$

$$HADDOCKscore - it1 = 1.0\,E_{vdw} + 1.0\,E_{elec} + 1.0\,E_{desol} + 0.1\,E_{air} - 0.01\,BSA$$

$$HADDOCKscore - water = 1.0\,E_{vdw} + 0.2\,E_{elec} + 1.0\,E_{desol} + 0.1\,E_{air}$$

where E_{vdw} is the van der Waals energy, E_{elec} is the electrostatic energy, E_{desol} is the desolvation energy, E_{air} restraints (i.e., distance) violation energies, BSA is the buried surface area. More comprehensive HADDOCK protocol and different docking parameter settings were reported in de Vries et al. (2010).

2.4.1 Docking parameters optimization and validation of Eqca-DR MHCII models

To optimize input parameters of HADDOCK, hemagglutinin (HA) [PDB_ID: 1HXY] crystal structure was selected as the standard ligand (used in all quantitative analysis); endogenous peptide A2 (A2) [PDB_ID: 1AQD] crystal structure was selected as reference ligand (used to establish arbitrary binding threshold for binders classification). Both ligands were docked to both allelic variants of Eqca-DR due to their experimental proven MHCII binding (Stern et al., 1994; Murthy and Stern, 1997). The intermolecular interactions of the resulting Eqca-DR:HA and Eqca-DR:A2 complexes were assessed for hydrogen bonding interactions, *via* BIOVIA Discovery Studio Visualizer, between the main-chain peptide and conserved HLA-DR1 residues as reported earlier (Stern et al., 1994; Murthy and Stern, 1997). The sampling size across rigid body minimization (It0), semi-flexible annealing (It1) and explicit solvent refinement (water) stages was

optimized at 5000:300:300; random exclusion of ambiguous interaction restraints (AIRs) was disabled. The conserved residues of membrane-distal alpha-helices and whole peptides were selected as input for active residues; passive residues of receptor and ligand were defined automatically by HADDOCK. The computed linear combination of various energies and buried surface area of the Eqca-DR:HA and Eqca-DR:A2 complexes in the form of arbitrary HADDOCK scores were recorded.

2.4.2 Selection of 15-mer α-NTXs peptide fragments by docking with Eqca-DR

The energy-minimized 15-mer peptide fragments derived from α-NTXs were respectively docked onto Eqca-DRA*00103: DRB2*00201 and Eqca-DRA*00201:DRB2*00201 as per Section 2.4.1. The resulting Fraction of Common Contacts algorithm (FCC)-clustered decoys were screened and selected for susceptibility to DM-catalyzed peptide editing based on the defined algorithms in the present study:

1) The backbone atoms of P-1, P1, P2 anchor residues of the examined peptides must be hydrogen-bonded to Serα53-Asnβ82 of MHCII molecules.
2) The examined peptide N-terminus must extrude from the P1 pocket.
3) Bidentate hydrogen bonds must be formed between Asn82β and P2 anchor residue of the examined peptides.
4) The combined count of hydrogen bonds and salt bridges formed between membrane distal alpha-helices of MHCII molecules and the examined peptides must be ≥14. This is to enrich the pool of epitopes featuring binding stability and appropriate poses.

The lowest HADDOCK score of respective MHCII-peptide complexes was computed and inverted bars were plotted. The HADDOCK score of binders filtered *via* the algorithm outlined above was highlighted.

2.4.3 Determination of immunodominant regions of α-NTXs

Considering the immune response is elicited based on the binding strength and successful intermolecular interactions of a complex, the immunodominant regions of α-NTXs were estimated by HADDOCK score along with the scoring of amino acid residues of 15-mer α-NTXs peptides from immunogenic binders. The M_2R scoring metric, which represents the degree of computed immune response elicited by respective 15-mer peptides in the context of MHCII, was quantified as described in the formulation:

$$M_2R = \sum_{n=0}^{I'} S_{n+1} \tag{1}$$

$$S = \frac{\sum_{n=0}^{i} \mathrm{hr}_{n+1}}{\sum_{n=0}^{I} H'R'_{n+1}} \tag{2}$$

Where "*S*" is the score of individual residue constituting α-NTXs, "*I*'" is the total number of amino acid residues constituting α-NTXs, "r" is the frequency of individual amino acid residue that constitutes the filtered 15-mer peptides, "*R*'" represents the maximum frequency attainable for each residue, "*i*" is the total number of MHCII-bound 15-mer peptides, "*I*" is the total number of 15-mer peptides constructed from respective α-NTXs, "*h*" is the HADDOCK score ratio of respective algorithm-filtered decoys and standard ligand (HA), and "*H*'" is the maximum attainable HADDOCK score ratio.

The cumulative score of each residue was quantified, accumulated and plotted to quantify M_2R which represents the immunogenic spectrum of individual α-NTX.

3 Results and discussion

3.1 Molecular size and antigenicity of α-NTXs

In the present study, six different lethal elapid α-NTXs (Figure 1) belonging to short-chain and long-chain groups, and a snake venom metalloproteinase [SVMP, a higher molecular weight (MW) toxin] were analyzed for their antigenicity using the B-cell epitope prediction tool (Kolaskar and Tongaonkar, 1990). As shown in Figure 2, the sheer number of predicted antigenic sites of SVMP (MW~47 kDa, 15 antigenic sites identified) far exceeded that of the six α-NTXs (MW~7–8 kDa, 1–3 antigenic sites identified), consistent with previous findings of low MW toxins possessing less antigenic peptides (Tan et al., 2019b; Tan and Tan, 2021). The higher number of antigenic peptides in high MW proteins may provide greater exposures to BCRs, thus eliciting a higher antibody titer specific to these antigens, in comparison to the low MW proteins where α-NTXs are classified (MW~7–8 kDa). Moreover, the presence of high MW proteins in an immunogen mixture containing proteins with varying MW may dampen the antigenicity of low MW α-NTXs (<10 kDa) (Clementi et al., 1991; Irais et al., 2020) in eliciting immune responses amid the antigenic competition for BCRs (Hunt et al., 1995), consequently, the resulting neutralizing antibodies may be skewed toward high MW toxins. This is well exemplified by previous immunoprofiling studies applying microarrays (Engmark et al., 2016) and enzyme-linked immunosorbent assay (Lingam et al., 2020), as well as *in vivo* neutralization studies that showed viperid antivenoms are significantly more potent than elapid antivenoms (Calvete et al., 2016; Ratanabanangkoon et al., 2016; Bailon Calderon et al., 2020; Faisal et al., 2021). This is likely due to most viperid venoms are predominated with high MW toxins (MW > 25 kDa) (e.g., SVMP and snake venom serine protease, SVSP) (Offor et al., 2022), which are capable of eliciting stronger immune response for the production of neutralizing antibodies. However, given that venoms constituting neurotoxins of more than ~40% failed to raise antivenoms with major improvement in neutralization efficacy (Tan et al., 2015b; Tan et al., 2016a; Tan et al., 2019a; Palasuberniam et al., 2021), it is therefore suggested that the low neutralizing efficacy of elapid antivenom may be also attributed to other factors, such as amino acid composition, that intrinsically modulate the epitope configuration of α-NTXs to be recognized by T-cell receptor (TCR) to elicit a strong humoral response.

3.2 Screening of HLA-DM exchange determinant

The present study generated homolog models of Eqca-DR due to the absence of equine MHCII alleles binding data in the currently

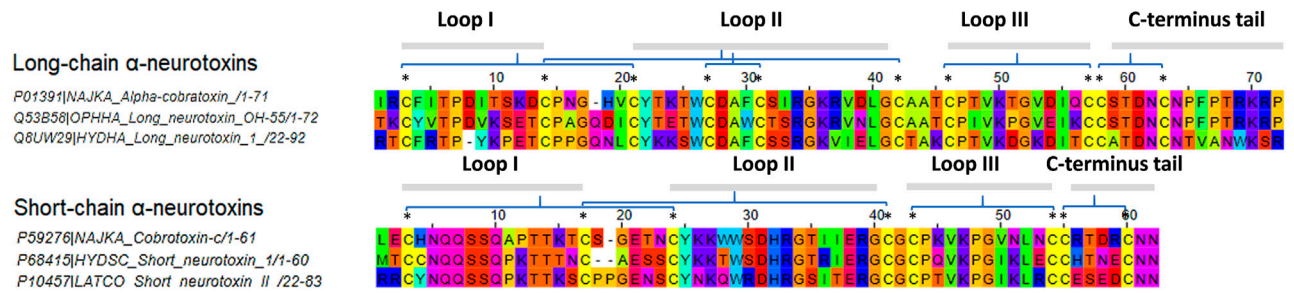

FIGURE 1
Multiple sequence alignment of selected elapids long-chain and short-chain alpha-neurotoxins. Sequences were acquired from the UniProt database. Abbreviations: *NAJKA*, *Naja kaouthia*; *OPHHA*, *Ophiophagus hannah*; *LATCO*, *Laticauda colubrina*; *HYDSC*, *Hydrophis schistosus*; *HYDHA*, *Hydrophis curtus*. Asterisk symbols indicate the location of disulfide bonds.

available databases. The immunogenicity of α-NTXs derived from the venoms of selected Asiatic elapids was examined by docking 15-mer peptides of α-NTXs generated to Eqca-DR, to assess for MHCII epitopes. The use of a structure-based approach in the present study is mainly due to the limitations of the existing range of bioinformatics tools (i.e., NetMHC-3.4, PSSM, SMM, TEPITOPE) in the provision of an accurate estimate on MHCII epitopes. Despite the availability of data-driven avenue, most of the data-driven machine-learning mediated predictors of MHC epitopes were trained with MHC-peptidome composed of synthetic sequences (Sidney et al., 2013) that sidestep proteasome cleavage and DM-editing selection. Although this method could narrow down the potential candidate of MHC epitopes, but it may not provide accurate prediction (Robbins et al., 2013; Yadav et al., 2014). Furthermore, although recent development entails the adoption of naturally processed and presented mass spectrometry (MS) derived MHC peptides to hone the accuracy of the existing predictors, the current MS-derived peptidome datasets still do not correlate well with predicted binding affinity (Zhao and Sher, 2018). Factors such as the indirect linear relationship between the kinetic stability of MHCII-peptide complexes and alignment issues due to peptide length varieties may have bugged the algorithm from performing at full capacity in predicting the MHCII binder (Belmares et al., 2002; Nielsen et al., 2010; ten Broeke et al., 2013). Thus, these limitations raise the need for an alternative avenue for immunogenicity study.

Contrary to the data-driven predictor, the structure-based approach does not rely on binding data. Adding to that, it provides visualization of atomic-resolution intermolecular interaction between the MHCII-peptide complex. Peptides are bound to MHCII *via* hydrogen bonding network between conserved MHCII side chains and peptide backbone and through interactions between MHCII pockets and peptide side-chain anchors. The complementing screening algorithm was customized based on the identification of multiple critical hydrogen bonds between conserved MHCII side-chains and peptide backbone (Figure 3) as a gauge to the susceptibility of DM-catalyzed peptide editing (McFarland et al., 2001; Stratikos et al., 2004; Zhou et al., 2009; Ferrante and Gorski, 2010; Anders et al., 2011; Painter et al., 2011). Following the same principle, MHC-loading enhancers (MLE) target P1 pocket as canonical MLE site to enhance T_h cells response, by maintaining the peptide-receptive conformation of MHCII which in turn expedited antigen-loading and ligand exchange on the cell surface (Gupta et al., 2008; Dickhaut et al., 2009). Validation of the MHCII homologs and optimization of docking simulation parameters were conducted by redocking standard (HA) and reference ligands (A2) with two allelic variants of Eqca-DR models (Figure 4). Two homologs examined feature critical intermolecular hydrogen bonding formed between MHCII residues with HA and A2 peptides (with side chains occupying major pockets, hence designated as P-1, P1 and P2 anchor residues), which verified the compatibility of the generated Eqca-DR models and the optimized docking simulation parameters for this study.

Herein, structure-based MHCII epitopes predictor augmented with DM-editing determinant algorithm, mimicry of humoral response, was adopted to assess the immunogenicity of α-NTXs derived from venoms of selected terrestrial, submarine and marine Asiatic elapids (Figure 1). The use of α-NTXs selected from cross-genus elapids was to validate the flexibility of the structural approach in determining the immunogenicity of α-NTXs, as well as for comparison to the previously reported data from neutralization studies (Tan et al., 2016b; Tan et al., 2018).

3.3 Algorithm clustering of MHCII binders

The arbitrary binding affinity threshold is commonly used as a gauge for the prediction of MHCII epitope ligands (Sette et al., 1994; Southwood et al., 1998). Table 1 showed the HADDOCK score of decoys of two allelic Eqca-DR models (Eqca-DRA*00103: DRB2*00201 and Eqca-DRA*00201:DRB2*00201) redocked with HA and A2 ligands that provide inference for a strong binder (Stern et al., 1994; Murthy and Stern, 1997). Applying the same approach, the inverted stacked HADDOCK scores of decoys of 15-mer peptides with respective allelic variants of Eqca-DR were shown in Figure 5. As delineated by Table 2, the 15-mer peptides were further benchmarked arbitrarily as strong (≤−230), moderate (−230 to −180) and weak binders (≥−180) based upon the HADDOCK score of HA and A2 ligand bindings (Table 1).

The present study showed none of these 15-mer peptides generated from all α-NTXs were considered as “strong binder.”

Nk_LαNTX-α-Cbtx

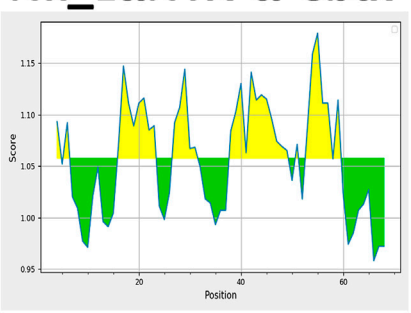

Predicted peptides:

No.	Start	End	Peptide	Length
1	16	23	NGHVCYTK	8
2	38	49	DLGCAATCPTVK	12

Oh_LαNTX-OH55

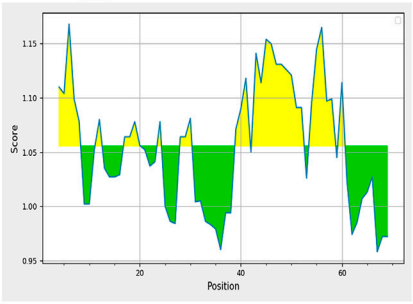

Predicted peptides:

No.	Start	End	Peptide	Length
1	43	52	AATCPIVKPG	10

Hc_LαNTX-1

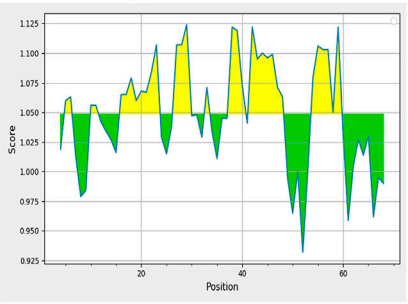

Predicted peptides:

No.	Start	End	Peptide	Length
1	16	23	GQNLCYKK	8
2	42	48	TAKCPTV	7
3	54	59	ITCCAT	6

Nk_SαNTX-Cbtx-c

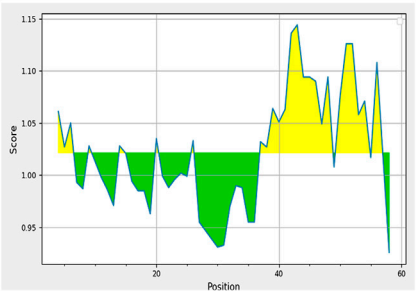

Predicted peptides:

No.	Start	End	Peptide	Length
1	37	48	ERGCGCPKVKPG	12

Hs_SαNTX-1

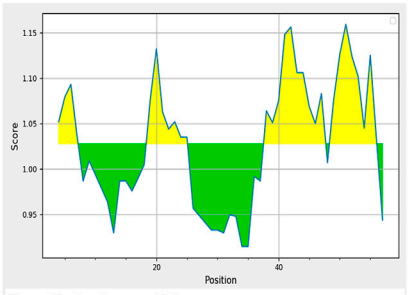

Predicted peptides:

No.	Start	End	Peptide	Length
1	19	25	ESSCYKK	7
2	38	47	GCGCPQVKPG	10
3	49	56	KLECCHTN	8

Lc_SαNTX-2

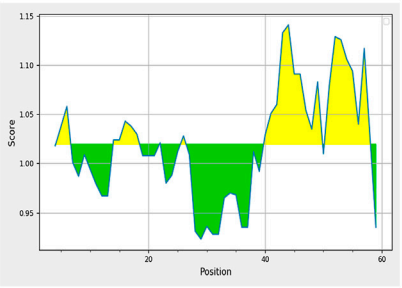

Predicted peptides:

No.	Start	End	Peptide	Length
1	40	49	GCGCPTVKPG	10
2	51	58	KLRCCESE	8

Na_SVMP

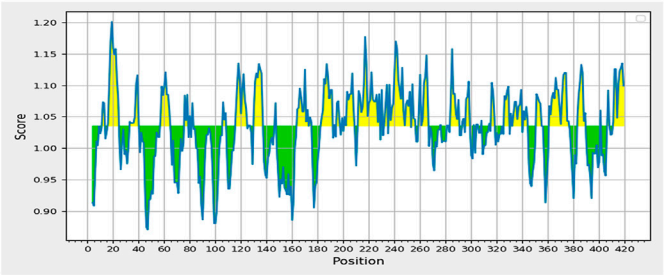

Predicted peptides:

No.	Start	End	Peptide	Length
1	16	24	IEFYVVVDN	9
2	33	40	DQPVIKRK	8
3	57	64	FHIALIGL	8
4	116	124	VGLAYIGSI	9
5	130	137	SAAVVQDY	8
6	164	172	FCTCGFNKC	9
7	183	191	YQFSSCSVR	9
8	201	208	RPQCILNK	8
9	212	228	TDIVSPPICGNYFVEVG	17
10	236	252	PADCQSACCNATTCKLQ	17
11	259	266	SEECCEKC	8
12	284	290	LPELCTG	7
13	333	339	GVKVSRD	7
14	361	376	KIPCAAKDVKCGRLFC	16
15	383	389	ICNCSIS	7

FIGURE 2
Prediction of antigenic determinants (B-cell epitope) of α-NTXs with Kolaskar and Tongaonkar antigenicity scale (Kolaskar and Tongaonkar, 1990). Abbreviations: Nk_LαNTX-α-Cbtx, α-cobratoxin (UniProt ID: P01391, *N. kaouthia*); Oh_LαNTX-OH55, long neurotoxin OH55 (UniProt ID: Q53B58, *O. hannah*); Hc_LαNTX-1, long neurotoxin 1 (UniProt ID: Q8UW29, *H. curtus*); Nk_SαNTX-Cbtx-c, cobrotoxin-c (UniProt: P59276, *N. kaouthia*); Hs_SαNTX-1, short neurotoxin 1 (UniProt ID: P68415, *H. schistosus*); Lc_SαNTX-2, short neurotoxin 2 (UniProt ID: P10457, *L. colubrina*); Na_SVMP, snake venom zinc metalloproteinase (Uniprot ID: D3TTC2, *Naja atra*) (high MW toxin). Yellow areas represent predicted B-cell epitopes with antigenicity scores above the dynamic threshold (~1.0).

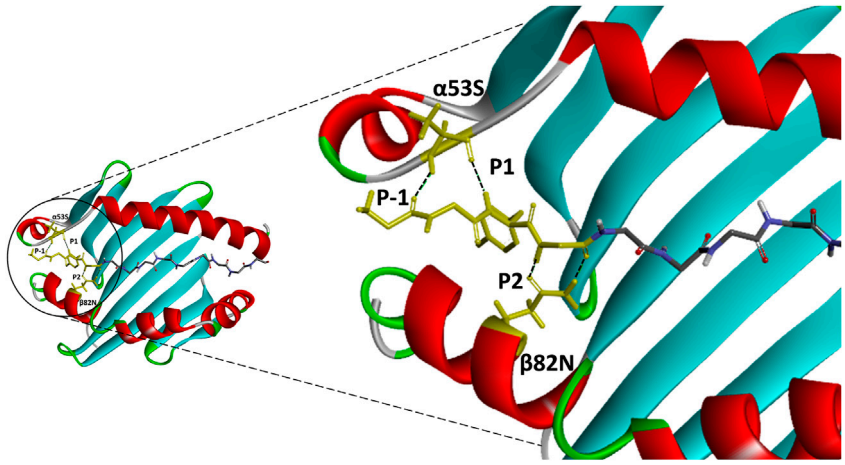

FIGURE 3
An atomic resolution of HLA-DR1:HA complex derived from PDB crystal structure (PDB:1HXY) with annotated critical intermolecular interactions between peptide ligand and the side chains of MHCII. Peptide backbone that formed conserved hydrogen bonds with MHCII residues (α53S and β82N) were denoted as P-1, P1 and P2 anchor residues and highlighted in yellow.

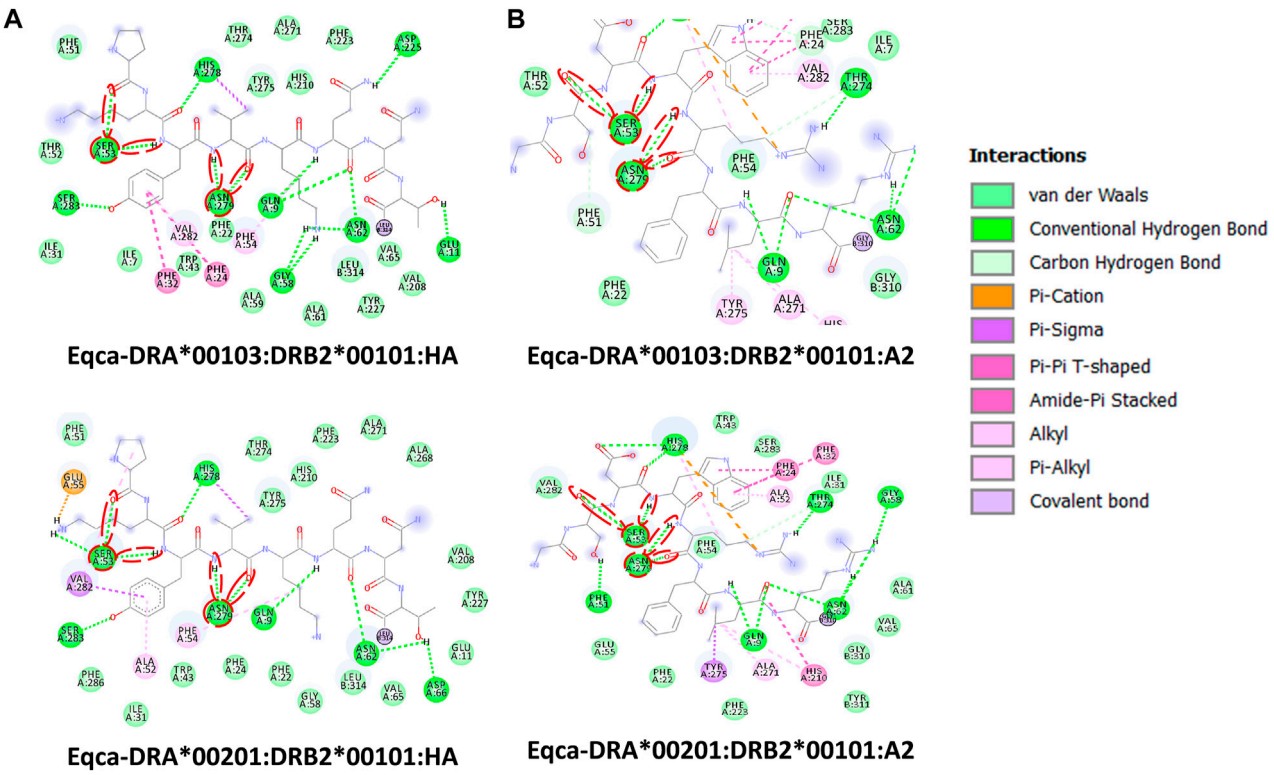

FIGURE 4
Molecular interactive illustration showing the interaction of redocked standard ligands with homology models of the two allelic Eqca-DR. **(A)** hemagglutinin (HA) and **(B)** endogenous peptide A2 (A2). 2D chemical structure represents the ligand surrounded by interactive MHCII binding groove residues. P-1, P1 and P2 anchor residues of HA and A2 and their hydrogen bonding interaction with residues of the binding grooves were circled in red. Two allelic Eqca-DR models examined were Eqca-DRA*00103:DRB2*00101 and Eqca-DRA*00201:DRB2*00101.

Out of the 57–58 15-mer peptides generated from the three LαNTXs, there were only 3–12 that were considered as "moderate binders" while the remaining were "weak binders." Similarly, the SαNTXs that are shorter in sequence length also showed no "strong binders" among the 46–48 15-mer peptides. At this point, the pool of low affinity 15-mer binding MHCII decoys already foreshadows weak immunogenicity, because it is suggested that the peptide that binds with a long half-life has the propensity to dominate the T_h cell

TABLE 1 HADDOCK scores of redocking of two allelic variants of Eqca-DR MHCII models with standard and reference ligand.

Ligand \ MHCII alleles	Eqca-DRA*00103:DRB2*00201	Eqca-DRA*00201:DRB2*00201
Hemagglutinin (HA)	−197.4 ± 6.7	−200.2 ± 3.9
Endogenous peptide A2 (A2)	−235.1 ± 0.6	−236.4 ± 2.5

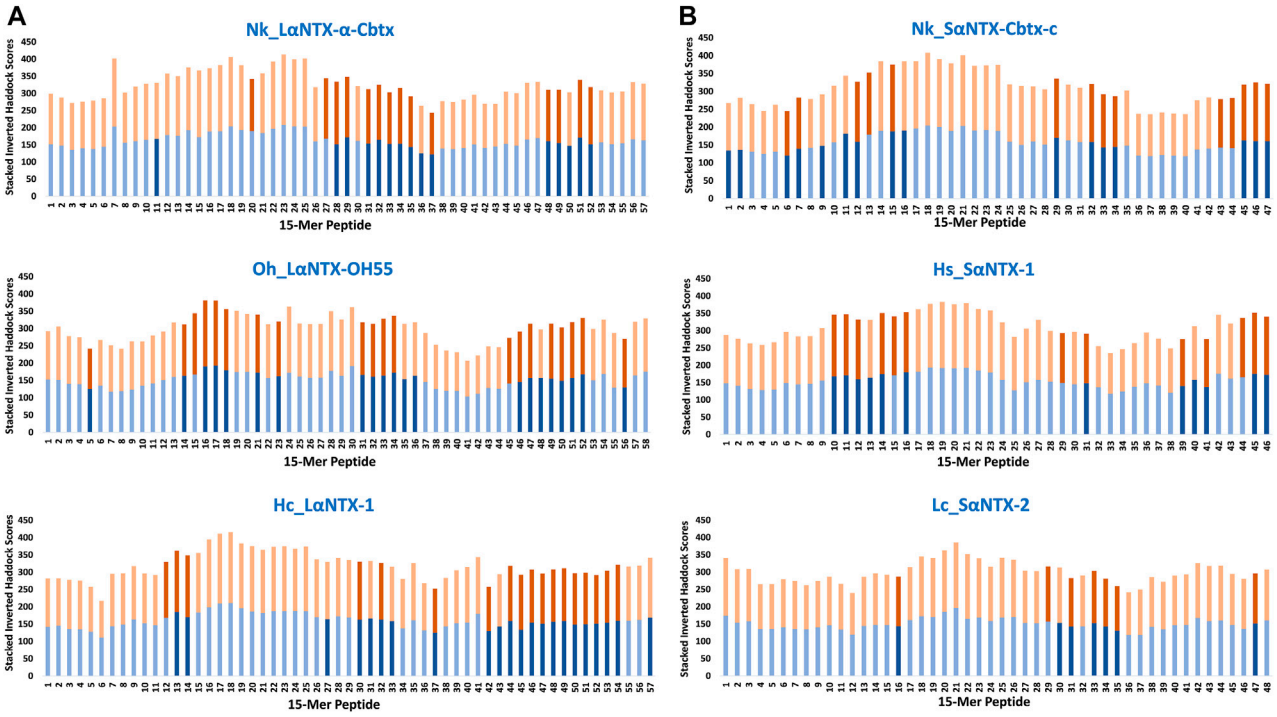

FIGURE 5
Accumulative inverted HADDOCK scores of 15-mer peptides binding decoys (Eqca-DR:15-mer) derived from docking of Eqca-DRA MHCII models to 15-mer peptides generated from α-neurotoxins. **(A)** Long-chain alpha-neurotoxins (LαNTX), and **(B)** Short-chain alpha-neurotoxins (SαNTX). Blue bars indicate Eqca-DRA*00103:DRB2*00201; and orange bars indicate Eqca-DRA*00201:DRB2*00201. Bars with dark blue/dark brown indicate the decoys (Eqca:15-mer) that fulfilled the defined algorithm in the present study. Abbreviations: Nk_LαNTX-α-Cbtx, α-cobratoxin (UniProt ID: P01391, *N. kaouthia*); Oh_LαNTX-OH55, long neurotoxin OH55 (UniProt ID: Q53B58, *O. hannah*); Hc_LαNTX-1, long neurotoxin 1 (UniProt ID: Q8UW29, *H. curtus*); Nk_SαNTX-Cbtx-c, cobrotoxin-c (UniProt: P59276, *N. kaouthia*); Hs_SαNTX-1, short neurotoxin 1 (UniProt ID: P68415, *H. schistosus*); and Lc_SαNTX-2, short neurotoxin 2 (UniProt ID: P10457, *L. colubrina*).

response (Pos et al., 2013). Although previous studies suggested that MHCII binders with higher affinity may not be translated to MHCII binding *in vivo* (Zhao and Sher, 2018), this may be a result of excluding the importance of peptide-editing role of DM molecules in the prediction or study performed (Belmares et al., 2002).

With the DM-editing determinant screening algorithm used in this study, the filtered 15-mer peptides were selected as predicted MHCII epitopes (Table 2). In comparison, LαNTXs generally feature a higher percentage of predicted MHCII binders (24%–38%) than SαNTXs (12%–34%) (Table 2). Of the LαNTXs derived 15-mer peptides, only 14–22 were predicted as MHCII epitopes, with the lowest binder proportion shown in Nk_LαNTX-α-Cbtx (24%–26%), followed by Oh_LαNTX-OH55 (~34–36%), and Hc_LαNTX-1 (31%–38%). For SαNTXs, the MHCII binder proportion was ranging from 12% to 34%, with the lowest shown in Lc_SαNTX-2 (~12%), followed by Hs_SαNTX-1 (26%–28%), and Nk_SαNTX-Cbtx-c (30%–34%). Unsurprisingly, most predicted MHCII binders were on the "weak binder" spectrum, with only a few classified as "moderate binders."

Binding affinity relative to algorithm-identified binders is suggested as a vital indicator that represents the degree of posing fit which indirectly reflects the importance of amino acid composition, and consequently dictates the dynamic conformation of MHCII-peptide that is least susceptible to DM-editing mechanism (Pos et al., 2013; Yin et al., 2014). Also, it relays information on the possible disposition of P9 leucine-binder in sidestepping the hydrogen bonding and pocket interaction at P1 (Yin et al., 2014), which may be a perk of strong MHCII binder (i.e., endogenous peptide A2). Ergo, it is suggested that the low amount of MHCII epitopes and their relatively weak affinity may

TABLE 2 Clustering of display and non-display decoys (Eqca-DR:15-mer) based on HADDOCK scores.

Peptide 15-mers	Eqca-DRA*00103:DRB2*00201			Eqca-DRA*00201:DRB2*00201		
	Binder classification[a]	Predicted MHCII epitope[b]	Predicted MHCII epitope (%)[c]	Binder classification[a]	Predicted MHCII epitope[b]	Predicted MHCII epitope (%)[c]
Long-chain alpha-neurotoxins (LαNTX)						
Nk_LαNTX-α-Cbtx	(S0:M12:W45)	W15	26.32	(S0:M12:W45)	M1W13	24.56
Oh_LαNTX-OH55	(S0:M3:W55)	M2W19	36.21	(S0:M3:W55)	M2W18	34.48
Hc_LαNTX-1	(S0:M12:W45)	W22	38.60	(S0:M9:W48)	W18	31.58
Short-chain alpha-neurotoxins (SαNTX)						
Nk_SαNTX-Cbtx-c	(S0:M12:W35)	M3W13	34.04	(S0:M11:W36)	M1W13	29.79
Hs_SαNTX-1	(S0:M6:W40)	W12	26.10	(S0:M5:W41)	W13	28.26
Lc_SαNTX-2	(S0:M2:W46)	W6	12.50	(S0:M2:W46)	W6	12.50

[a]15-mer peptides were classified into "strong binder" (S, HADDOCK score ≤−230), "moderate binder" (M, HADDOCK score −230 to −180), and "weak binder" (W, HADDOCK score ≥−180) based on the arbitrary binding thresholds. Thresholds are defined based on the HADDOCK scores of standard and reference ligands (hemagglutinin and endogenous peptide A2). The numerical values indicate the number of binders.

[b]15-mer peptides that fulfilled the defined algorithms outlined in the present study (Section 2.4.2). The numerical values indicate the number of binders.

[c]Relative percentage of 15-mer peptides with predicted MHCII epitopes over the total number of 15-mer peptides generated per examined α-NTX.

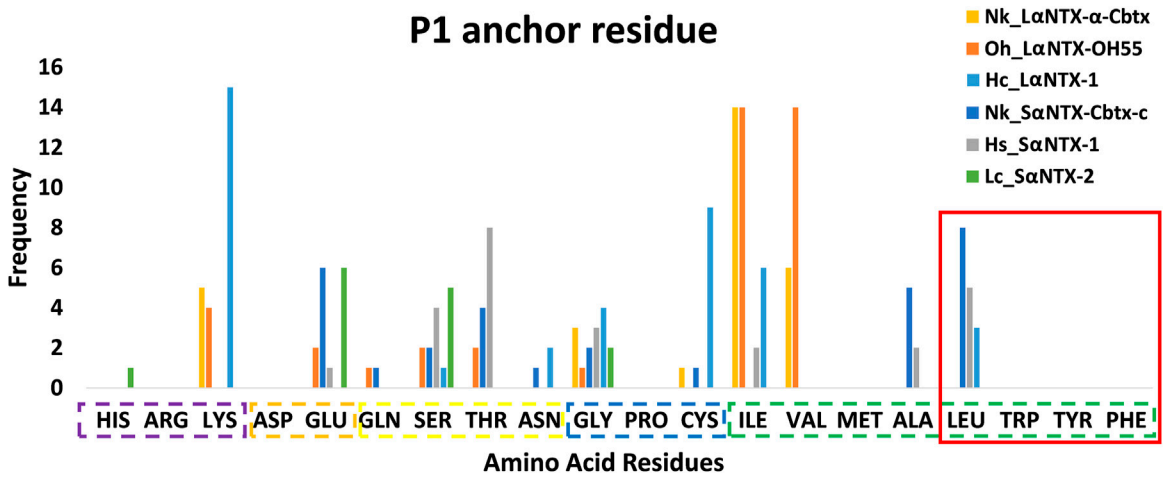

FIGURE 6
Anchor residue preferences of P1 pocket. Violet box: Positive side chain; Orange box: Negative side chain; Yellow box: Polar side chain; Blue box: Special cases; Green box: Non-polar side chain; Red square: Optimal P1 anchor residues. Abbreviations: Nk_LαNTX-α-Cbtx, α-cobratoxin (UniProt ID: P01391, *N. kaouthia*); Oh_LαNTX-OH55, long neurotoxin OH55 (UniProt ID: Q53B58, *O. hannah*); Hc_LαNTX-1, long neurotoxin 1 (UniProt ID: Q8UW29, *H. curtus*); Nk_SαNTX-Cbtx-c, cobrotoxin-c (UniProt: P59276, *N. kaouthia*); Hs_SαNTX-1, short neurotoxin 1 (UniProt ID: P68415, *H. schistosus*); and Lc_SαNTX-2, short neurotoxin 2 (UniProt ID: P10457, *L. colubrina*).

compromise the chances of α-NTXs to be processed for MHCII display by APCs that non-specifically uptake and process antigens for the activation of T_h cell in the context of humoral immunity (Hilhorst et al., 2014).

3.3.1 Binding specificity of major anchor sites of MHCII

Compositional analysis of α-NTXs was performed by profiling the amino acid residues of predicted MHCII binders derived from respective α-NTXs occupying P-1, P1 and P2 binding pockets of Eqca-MHCII. The known major anchor sites are P1, P4, P6 and P9 as evidenced by their substantial buried side chain solvent-exposed surface area (Murthy and Stern, 1997). However, we specifically look into the P1 pocket as the residue preference in this position plays a major role in dictating DM-catalyzed peptide editing susceptibility relative to other major pockets (Painter et al., 2011).

An earlier study showed tryptophan, tyrosine, phenylalanine and leucine that feature hydrophobic side chains are optimal

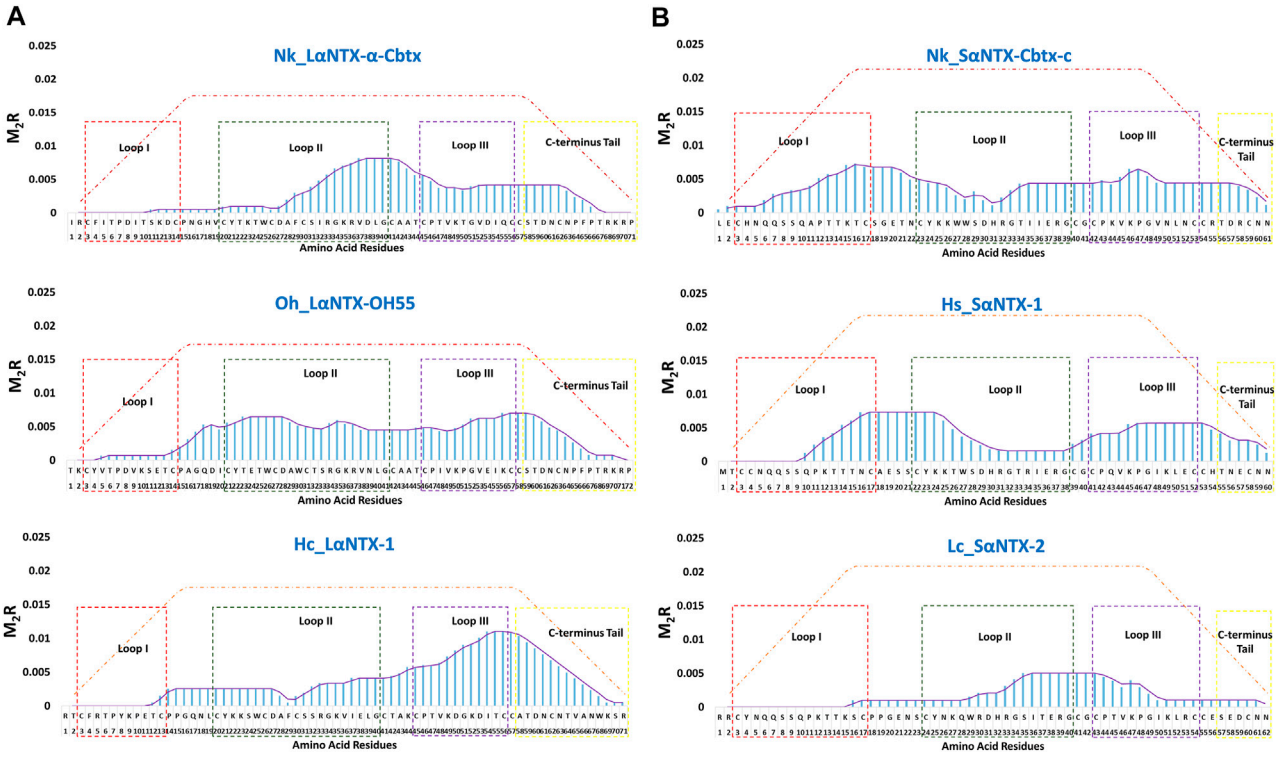

FIGURE 7
The immunodominant coverage across the amino acid sequences of α-neurotoxins. **(A)** Long-chain alpha-neurotoxins (LαNTX), and **(B)** Short-chain alpha-neurotoxins (SαNTX). Dashed squares in the figure represent the different loops and C-terminus tail of α-NTXs. The brown-dash dotted line indicates the maximum score of respective amino acid residues. Abbreviations: Nk_LαNTX-α-Cbtx, α-cobratoxin (UniProt ID: P01391, *N. kaouthia*); Oh_LαNTX-OH55, long neurotoxin OH55 (UniProt ID: Q53B58, *O. hannah*); Hc_LαNTX-1, long neurotoxin 1 (UniProt ID: Q8UW29, *H. curtus*); Nk_SαNTX-Cbtx-c, cobrotoxin-c (UniProt: P59276, *N. kaouthia*); Hs_SαNTX-1, short neurotoxin 1 (UniProt ID: P68415, *H. schistosus*); and Lc_SαNTX-2, short neurotoxin 2 (UniProt ID: P10457, *L. colubrina*). The details analyses were provided in Supplementary File S1.

P1 anchor residues (Yin et al., 2014). As depicted in Figure 6, only 16 out of 177 (<10%) identified predicted MHCII binders feature optimal P1 anchor amino acid residues mentioned above. These include Nk_SαNTX-Cbtx-c (8 binders), Hs_SαNTX-1 (5 binders), and Hc_LαNTX-1 (3 binders), and worth noting that all 16 binders consistently possess leucine as anchor residue. The lack of optimal P1 anchor residues may have culminated in binders with weak affinity to Eqca-DR which coincides with the predominant of weak MHCII binders as displayed in Table 2. Thus, this finding further validates that the amino acid composition of α-NTXs could be one of the major limiting factors in eliciting a strong humoral response, during the immunization process of antivenom production.

3.4 Immunodominance of α-neurotoxins

For ease of interpretation, scoring metric that reflects both binding affinity and proportion of predicted MHCII binders are vital for multilayered analysis. Based on the predicted MHCII epitopes, each amino acid composing α-NTXs was scored and cumulatively quantified as M_2R to enable elucidation of

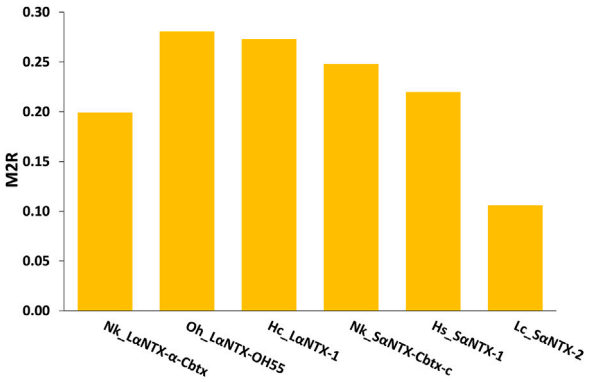

FIGURE 8
M_2R scoring of α-neurotoxins. Abbreviations: Nk_LαNTX-α-Cbtx, α-cobratoxin (UniProt ID: P01391, *N. kaouthia*); Oh_LαNTX-OH55, long neurotoxin OH55 (UniProt ID: Q53B58, *O. hannah*); Hc_LαNTX-1, long neurotoxin 1 (UniProt ID: Q8UW29, *H. curtus*); Nk_SαNTX-Cbtx-c, cobrotoxin-c (UniProt: P59276, *N. kaouthia*); Hs_SαNTX-1, short neurotoxin 1 (UniProt ID: P68415, *H. schistosus*); and Lc_SαNTX-2, short neurotoxin 2 (UniProt ID: P10457, *L. colubrina*). The details analyses were provided in Supplementary File S1.

TABLE 3 Correlation of neurotoxin abundance and neutralization efficacy of its homologous antivenom.

Elapid Antivenom	*Ophiophagus hannah* monovalent antivenom (OHMAV)	*Naja kaouthia* monovalent antivenom (NkMAV)		Sea snake antivenom (SSAV)	
α-NTXs	Oh_LαNTX-OH55	Nk_LαNTX-α-Cbtx	Nk_SαNTX-Cbtx-c	[@]Hc_LαNTX-1	Hs_SαNTX-1
Relative abundance of α-NTXs in venom (%)	~43.0[ł]	30.9[#]	4.6[#]	11.9[@]	52.2[@]
Normalized potency (mg/g)	26.75[&]	4.89[#]	1.33[#]	6.35[#]	1.61[#]
p-score	0.62	0.16	0.29	0.53	0.03

The values were acquired from previous studies reported from the same laboratories: [ł](Tan et al., 2015a); [&]unpublished; [#](Tan et al., 2016b); [@](Tan et al., 2015b). p-score: Normalized potency of the respective antivenom/relative abundances of α-neurotoxin in the venom. [@]LαNTX of *Hydrophis schistosus* was annotated to LαNTX of *Hydrophis curtus* (Hc_LαNTX-1) in the venom proteome study (Tan et al., 2015b).

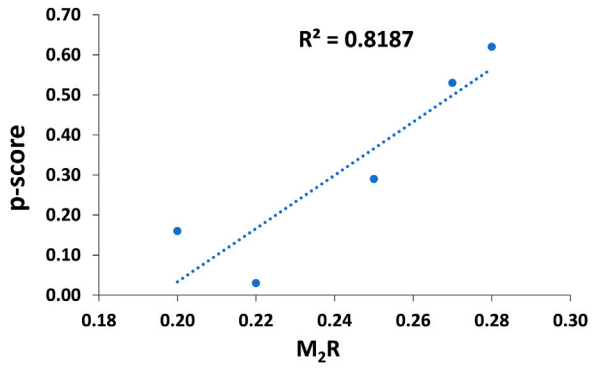

FIGURE 9
Coefficient of determination between empirical-based p-score and computed M_2R scoring.

immunodominance, in the context of T_h cell activation, across the entire sequence of α-NTXs (Figure 7; Supplementary File S1).

In general, the immunodominant amino acid sequences were noted to be skewed differently for all three LαNTXs from different species, where Nk_LαNTX-α-Cbtx and Oh_LαNTX-OH55 were shown to be more immunogenic at loop II, and to a lesser extent for Hc_LαNTX-1 that is more loop III dominant. All three α-NTXs feature minute responsiveness at loop I as indicated by their extremely low M_2R score. On the contrary, Nk_SαNTX-Cbtx-c, Hs_SαNTX-1 and Lc_SαNTX-2 are responsive across the three loops, except that Lc_SαNTX-2 featured a negligible response for loop I. Overall, all α-NTXs were predicted to be relatively responsive on loop II, which corroborates with a previous study that employed a data-driven MHCII epitope predictor utilizing human and mouse MHCII alleles binding data in predicting the immunogenicity of snake 3FTXs (Pruksaphon et al., 2022).

The general trend of M_2R scores for respective α-NTXs is shown to be less than 0.3 (Figure 8) while all predicted epitopes feature multiplier HADDOCK score ratio (h) ≤1 (Maximum M_2R = 1), suggesting α-NTXs are generally poor immunogens. The result is paralleled with the algorithm clustering of MHCII binders that showed the predomination of weak MHCII binders (Table 2). The accumulated overall M_2R scores for each α-NTX were also estimated and shown descending from Oh_LαNTX-OH55(0.28) > Hc_LαNTX-1(0.27) > Nk_SαNTX-Cbtx-c(0.25) > Hs_SαNTX-1(0.22) > Nk_LαNTX-α-Cbtx(0.2) > Lc_SαNTX-2(0.11) (Figure 8).

For comparative purposes, Table 3 illustrates the correlation study of reported commercial antivenoms on five selected α-NTXs examined in the present study. The p-score, defined as the relative potency of commercial antivenom for respective α-NTXs, is highly correlated (coefficient of determination, $R^2 = 0.82$) with M_2R scoring in the present study (Figure 9). The p-score trend showed as: Oh_LαNTX-OH55(0.62) > Hc_LαNTX-1(0.53) > Nk_SαNTX-Cbtx-c(0.29) > Nk_LαNTX-α-Cbtx(0.16) > Hs_SαNTX-1(0.03). Except for the slight swapping order between Nk_LαNTX-α-Cbtx and Hs_SαNTX-1, the p-score generated is consistent with the M_2R score in showing Hc_LαNTX-1 and Nk_SαNTX-Cbtx-c are more immunogenic compared to their homologous Hs_SαNTX-1 and Nk_LαNTX-α-Cbtx, respectively. The finding is however inconsistent with the earlier postulation where antigenicity and immunogenicity of LαNTXs are generally greater than SαNTXs, attributed to the slightly greater molecular size (Tan et al., 2016b; Wong et al., 2016; Tan et al., 2017). The present study showed a mixed observation that both LαNTXs and SαNTXs are generally low in antigenicity and immunogenicity, without clear distinction.

On the other hand, the p-score shown in Table 3 also highlights the disproportionate link between the relative abundance of α-NTXs and the neutralization efficacy of antivenoms. The poor neutralization potency of antivenom against α-NTXs could be multifactorial (e.g., molecular size, relative abundance, amino acid composition, and peptide binding recognition by MHCII), in particular the amino acid composition as highlighted in the present study, contributing to the inadequate immunogenic capacity of α-NTXs in eliciting a strong humoral response during the immunization in an animal host. Furthermore, the antigenicity could have been impacted by its small size when competing for B-cell receptors in the context of a heterogenous immunogen mixture (Hunt et al., 1995).

To date, a number of innovative strategies for new antivenom production have been reported, such as the use of synthetic peptide antigen (de la Rosa et al., 2018), multiepitopes string (Ramos et al., 2016) and virus-displayed epitopes (Menzies et al., 2022) as immunogens. These strategies selected the toxins mainly based on targeted snake species and showed that it is possible to produce elapid antivenoms by replacing crude venom immunogens. In the future exploration of

antivenom production, the immunoinformatic approach developed in this study can be applied to further strengthen the design of synthetic epitopes, thereby increasing the neutralization efficacy of antivenoms, especially in targeting the alpha-neurotoxins of elapid species.

4 Conclusion

In the present study, antigenicity tool and structure-based MHCII epitope predictor augmented with DM-editing determinant screening algorithm, collectively allude α-NTXs as poor antigen and immunogen. This is further supported by the relative immunogenicity of α-NTXs derived from the computed prediction that correlates strongly to the empirical data of *in vivo* neutralization efficacy of commercial antivenoms. Adding to that, most of the predicted binders feature non-optimal P1 anchor residues that greatly impede the formation of the MHCII-peptide complex with stronger affinity and stability. Overall, the outcome of this study suggests that both molecular size and amino acid composition are the main factors limiting the epitope configuration of α-NTXs as recognized by B-cell receptor (BCR) and T-cell receptor (TCR), resulting in a weaker humoral response in the animal host during immunization that applies a whole venom immunogen. The finding of the study provides insight into the low efficacy of elapid antivenoms against most elapid venoms which contain α-NTX as the principal toxins. Furthermore, DM-editing determinants could be incorporated as feature descriptors to the existing machine-learning-based predictors to enhance their accuracy in predicting MHCII epitopes while enabling the elucidation of immunodominant coverage of α-NTXs. This application has potential utility in the design and production of synthetic epitope immunogens for developing a better antivenom by applying various innovation strategies (Ramos et al., 2016; de la Rosa et al., 2018; Menzies et al., 2022).

Data availability statement

The original contributions presented in the study are included in the article/Supplementary Material, further inquiries can be directed to the corresponding author.

Author contributions

Conceptualization, KYT and CHT; methodology, KYT, CHH, and CHT; validation, KYT, CHH, and CHT; formal analysis, YWC; investigation, YWC; resources, KYT and CHT; data curation, KYT, CHH, and CHT; writing—original draft preparation, YWC; writing—review and editing, YWC, KYT, CHH, and CHT; visualization, YWC, KYT, CHH, and CHT; supervision, KYT, CHH, and CHT; funding acquisition, KYT. All authors have read and agreed to the published version of the manuscript.

Funding

This work was supported by the Fundamental Research Grant (FRGS/1/2019/SKK08/UM/02/2) from the Ministry of Higher Education, Malaysia.

Conflict of interest

The authors declare that the research was conducted in the absence of any commercial or financial relationships that could be construed as a potential conflict of interest.

Publisher's note

All claims expressed in this article are solely those of the authors and do not necessarily represent those of their affiliated organizations, or those of the publisher, the editors and the reviewers. Any product that may be evaluated in this article, or claim that may be made by its manufacturer, is not guaranteed or endorsed by the publisher.

Supplementary material

The Supplementary Material for this article can be found online at: https://www.frontiersin.org/articles/10.3389/fphar.2023.1143437/full#supplementary-material

References

Anders, A. K., Call, M. J., Schulze, M. S., Fowler, K. D., Schubert, D. A., Seth, N. P., et al. (2011). HLA-DM captures partially empty HLA-DR molecules for catalyzed removal of peptide. *Nat. Immunol.* 12, 54–61. doi:10.1038/ni.1967

Bailon Calderon, H., Yaniro Coronel, V. O., Caceres Rey, O. A., Colque Alave, E. G., Leiva Duran, W. J., Padilla Rojas, C., et al. (2020). Development of nanobodies against hemorrhagic and myotoxic components of *Bothrops atrox* snake venom. *Front. Immunol.* 11, 655. doi:10.3389/fimmu.2020.00655

Barber, C. M., Isbister, G. K., and Hodgson, W. C. (2013). Alpha neurotoxins. *Toxicon* 66, 47–58. doi:10.1016/j.toxicon.2013.01.019

Belmares, M. P., Busch, R., Wucherpfennig, K. W., Mcconnell, H. M., and Mellins, E. D. (2002). Structural factors contributing to DM susceptibility of MHC class II/peptide complexes. *J. Immunol.* 169, 5109–5117. doi:10.4049/jimmunol.169.9.5109

Calvete, J. J., Arias, A. S., Rodriguez, Y., Quesada-Bernat, S., Sanchez, L. V., Chippaux, J. P., et al. (2016). Preclinical evaluation of three polyspecific antivenoms against the venom of *Echis ocellatus*: Neutralization of toxic activities and antivenomics. *Toxicon* 119, 280–288. doi:10.1016/j.toxicon.2016.06.022

Clementi, M., Marini, S., Condo, S., and Giardina, B. (1991). Antibodies against small molecules. *Ann. dell'Istituto Super. sanitÃ* 27, 139–143.

De La Rosa, G., Corrales-García, L. L., Rodriguez-Ruiz, X., López-Vera, E., and Corzo, G. (2018). Short-chain consensus alpha-neurotoxin: A synthetic 60-mer peptide with generic traits and enhanced immunogenic properties. *Amino Acids* 50, 885–895. doi:10.1007/s00726-018-2556-0

De Vries, S. J., Van Dijk, M., and Bonvin, A. M. (2010). The HADDOCK web server for data-driven biomolecular docking. *Nat. Protoc.* 5, 883–897. doi:10.1038/nprot.2010.32

Denzin, L. K., and Cresswell, P. (1995). HLA-DM induces CLIP dissociation from MHC class II alpha beta dimers and facilitates peptide loading. *Cell* 82, 155–165. doi:10.1016/0092-8674(95)90061-6

Dickhaut, K., Hoepner, S., Eckhard, J., Wiesmueller, K. H., Schindler, L., Jung, G., et al. (2009). Enhancement of tumour-specific immune responses *in vivo* by 'MHC loading-enhancer' (MLE). *PLoS One* 4, e6811. doi:10.1371/journal.pone.0006811

Eisenberg, D., Luthy, R., and Bowie, J. U. (1997). VERIFY3D: Assessment of protein models with three-dimensional profiles. *Methods Enzymol.* 277, 396–404. doi:10.1016/s0076-6879(97)77022-8

Engmark, M., Andersen, M. R., Laustsen, A. H., Patel, J., Sullivan, E., De Masi, F., et al. (2016). High-throughput immuno-profiling of mamba (*Dendroaspis*) venom toxin epitopes using high-density peptide microarrays. *Sci. Rep.* 6, 36629. doi:10.1038/srep36629

Faisal, T., Tan, K. Y., Tan, N. H., Sim, S. M., Gnanathasan, C. A., and Tan, C. H. (2021). Proteomics, toxicity and antivenom neutralization of Sri Lankan and Indian Russell's viper (*Daboia russelii*) venoms. *J. Venom. Anim. Toxins Incl. Trop. Dis.* 27, e20200177. doi:10.1590/1678-9199-JVATITD-2020-0177

Ferrante, A., and Gorski, J. (2010). Cutting edge: HLA-DM-mediated peptide exchange functions normally on MHC class II-peptide complexes that have been weakened by elimination of a conserved hydrogen bond. *J. Immunol.* 184, 1153–1158. doi:10.4049/jimmunol.0902878

Fung-Leung, W. P., Surh, C. D., Liljedahl, M., Pang, J., Leturcq, D., Peterson, P. A., et al. (1996). Antigen presentation and T cell development in H2-M-deficient mice. *Science* 271, 1278–1281. doi:10.1126/science.271.5253.1278

Gupta, S., Hopner, S., Rupp, B., Gunther, S., Dickhaut, K., Agarwal, N., et al. (2008). Anchor side chains of short peptide fragments trigger ligand-exchange of class II MHC molecules. *PLoS One* 3, e1814. doi:10.1371/journal.pone.0001814

Hilhorst, M., Shirai, T., Berry, G., Goronzy, J. J., and Weyand, C. M. (2014). T cell-macrophage interactions and granuloma formation in vasculitis. *Front. Immunol.* 5, 432. doi:10.3389/fimmu.2014.00432

Hoogeboom, R., and Tolar, P. (2016). Molecular mechanisms of B cell antigen gathering and endocytosis. *Curr. Top. Microbiol. Immunol.* 393, 45–63. doi:10.1007/82_2015_476

Hunt, J. D., Jackson, D. C., Wood, P. R., Stewart, D. J., and Brown, L. E. (1995). Immunological parameters associated with antigenic competition in a multivalent footrot vaccine. *Vaccine* 13, 1649–1657. doi:10.1016/0264-410x(95)00145-q

Irais, C. M., Maria-De-La-Luz, S. G., Dealmy, D. G., Agustina, R. M., Nidia, C. H., Mario-Alberto, R. G., et al. (2020). Plant phenolics as pathogen-carrier immunogenicity modulator haptens. *Curr. Pharm. Biotechnol.* 21, 897–905. doi:10.2174/1389201021666200121130313

Kolaskar, A. S., and Tongaonkar, P. C. (1990). A semi-empirical method for prediction of antigenic determinants on protein antigens. *FEBS Lett.* 276, 172–174. doi:10.1016/0014-5793(90)80535-q

Laskowski, R. A., Macarthur, M. W., Moss, D. S., and Thornton, J. M. (1993). Procheck: A program to check the stereochemical quality of protein structures. *J. Appl. Crystallogr.* 26, 283–291. doi:10.1107/s0021889892009944

Leong, P. K., Fung, S. Y., Tan, C. H., Sim, S. M., and Tan, N. H. (2015). Immunological cross-reactivity and neutralization of the principal toxins of *Naja sumatrana* and related cobra venoms by a Thai polyvalent antivenom (Neuro Polyvalent Snake Antivenom). *Acta Trop.* 149, 86–93. doi:10.1016/j.actatropica.2015.05.020

Leong, P. K., Sim, S. M., Fung, S. Y., Sumana, K., Sitprija, V., and Tan, N. H. (2012). Cross neutralization of Afro-Asian cobra and Asian krait venoms by a Thai polyvalent snake antivenom (Neuro Polyvalent Snake Antivenom). *PLoS Negl. Trop. Dis.* 6, e1672. doi:10.1371/journal.pntd.0001672

Leong, P. K., Tan, C. H., Sim, S. M., Fung, S. Y., Sumana, K., Sitprija, V., et al. (2014). Cross neutralization of common Southeast Asian viperid venoms by a Thai polyvalent snake antivenom (Hemato Polyvalent Snake Antivenom). *Acta Trop.* 132, 7–14. doi:10.1016/j.actatropica.2013.12.015

Lingam, T. M. C., Tan, K. Y., and Tan, C. H. (2020). Proteomics and antivenom immunoprofiling of Russell's viper (*Daboia siamensis*) venoms from Thailand and Indonesia. *J. Venom. Anim. Toxins Incl. Trop. Dis.* 26, e20190048. doi:10.1590/1678-9199-JVATITD-2019-0048

Mcfarland, B. J., Katz, J. F., Beeson, C., and Sant, A. J. (2001). Energetic asymmetry among hydrogen bonds in MHC class II*peptide complexes. *Proc. Natl. Acad. Sci. U. S. A.* 98, 9231–9236. doi:10.1073/pnas.151131498

Menzies, S. K., Dawson, C. A., Crittenden, E., Edge, R. J., Hall, S. R., Alsolaiss, J., et al. (2022). Virus-like particles displaying conserved toxin epitopes stimulate polyspecific, murine antibody responses capable of snake venom recognition. *Sci. Rep.* 12, 11328. doi:10.1038/s41598-022-13376-x

Morris, P., Shaman, J., Attaya, M., Amaya, M., Goodman, S., Bergman, C., et al. (1994). An essential role for HLA-DM in antigen presentation by class II major histocompatibility molecules. *Nature* 368, 551–554. doi:10.1038/368551a0

Murthy, V. L., and Stern, L. J. (1997). The class II MHC protein HLA-DR1 in complex with an endogenous peptide: Implications for the structural basis of the specificity of peptide binding. *Structure* 5, 1385–1396. doi:10.1016/s0969-2126(97)00288-8

Nielsen, M., Lund, O., Buus, S., and Lundegaard, C. (2010). MHC class II epitope predictive algorithms. *Immunology* 130, 319–328. doi:10.1111/j.1365-2567.2010.03268.x

O'boyle, N. M., Banck, M., James, C. A., Morley, C., Vandermeersch, T., and Hutchison, G. R. (2011). Open Babel: An open chemical toolbox. *J. Cheminform* 3, 33. doi:10.1186/1758-2946-3-33

Offor, B. C., Muller, B., and Piater, L. A. (2022). A review of the proteomic profiling of african viperidae and elapidae snake venoms and their antivenom neutralisation. *Toxins* 14, 723. doi:10.3390/toxins14110723

Oh, A. M. F., Tan, K. Y., Tan, N. H., and Tan, C. H. (2021). Proteomics and neutralization of *Bungarus multicinctus* (Many-banded Krait) venom: Intra-specific comparisons between specimens from China and Taiwan. *Comp. Biochem. Physiology Part C Toxicol. Pharmacol.* 247, 109063. doi:10.1016/j.cbpc.2021.109063

Painter, C. A., Negroni, M. P., Kellersberger, K. A., Zavala-Ruiz, Z., Evans, J. E., and Stern, L. J. (2011). Conformational lability in the class II MHC 310 helix and adjacent extended strand dictate HLA-DM susceptibility and peptide exchange. *Proc. Natl. Acad. Sci. U. S. A.* 108, 19329–19334. doi:10.1073/pnas.1108074108

Palasuberniam, P., Chan, Y. W., Tan, K. Y., and Tan, C. H. (2021). Snake venom proteomics of samar cobra (*Naja samarensis*) from the southern Philippines: Short alpha-neurotoxins as the dominant lethal component weakly cross-neutralized by the philippine cobra antivenom. *Front. Pharmacol.* 12, 727756. doi:10.3389/fphar.2021.727756

Patikorn, C., Blessmann, J., Nwe, M. T., Tiglao, P. J. G., Vasaruchapong, T., Maharani, T., et al. (2022). Estimating economic and disease burden of snakebite in ASEAN countries using a decision analytic model. *PLoS neglected Trop. Dis.* 16, e0010775. doi:10.1371/journal.pntd.0010775

Pos, W., Sethi, D. K., and Wucherpfennig, K. W. (2013). Mechanisms of peptide repertoire selection by HLA-DM. *Trends Immunol.* 34, 495–501. doi:10.1016/j.it.2013.06.002

Pruksaphon, K., Yuvaniyama, J., and Ratanabanangkoon, K. (2022). Immunogenicity of snake alpha-neurotoxins and the CD4 T cell epitopes. *Toxicon* 214, 136–144. doi:10.1016/j.toxicon.2022.05.009

Ramos, H. R., Junqueira-De-Azevedo Ide, L., Novo, J. B., Castro, K., Duarte, C. G., Machado-De-Avila, R. A., et al. (2016). A heterologous multiepitope DNA prime/recombinant protein boost immunisation strategy for the development of an antiserum against Micrurus corallinus (coral snake) venom. *PLoS Negl. Trop. Dis.* 10, e0004484. doi:10.1371/journal.pntd.0004484

Ranawaka, U. K., Lalloo, D. G., and De Silva, H. J. (2013). Neurotoxicity in snakebite--the limits of our knowledge. *PLoS Negl. Trop. Dis.* 7, e2302. doi:10.1371/journal.pntd.0002302

Ratanabanangkoon, K. (2021). A quest for a universal plasma-derived antivenom against all elapid neurotoxic snake venoms. *Front. Immunol.* 12, 668328. doi:10.3389/fimmu.2021.668328

Ratanabanangkoon, K., Tan, K. Y., Eursakun, S., Tan, C. H., Simsiriwong, P., Pamornsakda, T., et al. (2016). A simple and novel strategy for the production of a pan-specific antiserum against elapid snakes of asia. *PLoS Negl. Trop. Dis.* 10, e0004565. doi:10.1371/journal.pntd.0004565

Ratanabanangkoon, K., Tan, K. Y., Pruksaphon, K., Klinpayom, C., Gutierrez, J. M., Quraishi, N. H., et al. (2020). A pan-specific antiserum produced by a novel immunization strategy shows a high spectrum of neutralization against neurotoxic snake venoms. *Sci. Rep.* 10, 11261. doi:10.1038/s41598-020-66657-8

Robbins, P. F., Lu, Y. C., El-Gamil, M., Li, Y. F., Gross, C., Gartner, J., et al. (2013). Mining exomic sequencing data to identify mutated antigens recognized by adoptively transferred tumor-reactive T cells. *Nat. Med.* 19, 747–752. doi:10.1038/nm.3161

Rodrigues, J. P., Trellet, M., Schmitz, C., Kastritis, P., Karaca, E., Melquiond, A. S., et al. (2012). Clustering biomolecular complexes by residue contacts similarity. *Proteins* 80, 1810–1817. doi:10.1002/prot.24078

Schrödinger, L., and Delano, W. (2020). *PyMOL*.

Schulze, M. S., Anders, A. K., Sethi, D. K., and Call, M. J. (2013). Disruption of hydrogen bonds between major histocompatibility complex class II and the peptide N-terminus is not sufficient to form a human leukocyte antigen-DM receptive state of major histocompatibility complex class II. *PLoS One* 8, e69228. doi:10.1371/journal.pone.0069228

Sette, A., Vitiello, A., Reherman, B., Fowler, P., Nayersina, R., Kast, W. M., et al. (1994). The relationship between class I binding affinity and immunogenicity of potential cytotoxic T cell epitopes. *J. Immunol.* 153, 5586–5592. doi:10.4049/jimmunol.153.12.5586

Sidney, J., Southwood, S., Moore, C., Oseroff, C., Pinilla, C., Grey, H. M., et al. (2013). Measurement of MHC/peptide interactions by gel filtration or monoclonal antibody capture. *Curr. Protoc. Immunol.* 18, doi:10.1002/0471142735.im1803s100

Southwood, S., Sidney, J., Kondo, A., Del Guercio, M. F., Appella, E., Hoffman, S., et al. (1998). Several common HLA-DR types share largely overlapping peptide binding repertoires. *J. Immunol.* 160, 3363–3373. doi:10.4049/jimmunol.160.7.3363

Stern, L. J., Brown, J. H., Jardetzky, T. S., Gorga, J. C., Urban, R. G., Strominger, J. L., et al. (1994). Crystal structure of the human class II MHC protein HLA-DR1 complexed with an influenza virus peptide. *Nature* 368, 215–221. doi:10.1038/368215a0

Stratikos, E., Wiley, D. C., and Stern, L. J. (2004). Enhanced catalytic action of HLA-DM on the exchange of peptides lacking backbone hydrogen bonds between their N-terminal region and the MHC class II alpha-chain. *J. Immunol.* 172, 1109–1117. doi:10.4049/jimmunol.172.2.1109

Takemura, K., and Kitao, A. (2019). More efficient screening of protein-protein complex model structures for reducing the number of candidates. *Biophys. Physicobiol* 16, 295–303. doi:10.2142/biophysico.16.0_295

Tan, C. H., Palasuberniam, P., Blanco, F. B., and Tan, K. Y. (2021). Immunoreactivity and neutralization capacity of Philippine cobra antivenom against *Naja philippinensis* and *Naja samarensis* venoms. *Trans. R. Soc. Trop. Med. Hyg.* 115, 78–84. doi:10.1093/trstmh/traa087

Tan, C. H., and Tan, K. Y. (2021). De novo venom-gland transcriptomics of spine-bellied sea snake (*Hydrophis curtus*) from penang, Malaysia—Next-generation sequencing, functional annotation and toxinological correlation. *Toxins* 13, 127. doi:10.3390/toxins13020127

Tan, C. H., Tan, K. Y., Fung, S. Y., and Tan, N. H. (2015a). Venom-gland transcriptome and venom proteome of the Malaysian king cobra (*Ophiophagus hannah*). *BMC Genomics* 16, 687. doi:10.1186/s12864-015-1828-2

Tan, C. H., Tan, K. Y., Lim, S. E., and Tan, N. H. (2015b). Venomics of the beaked sea snake, *Hydrophis schistosus*: A minimalist toxin arsenal and its cross-neutralization by heterologous antivenoms. *J. Proteomics* 126, 121–130. doi:10.1016/j.jprot.2015.05.035

Tan, C. H., Tan, K. Y., Ng, T. S., Sim, S. M., and Tan, N. H. (2018). Venom proteome of spine-bellied sea snake (*Hydrophis curtus*) from penang, Malaysia: Toxicity correlation, immunoprofiling and cross-neutralization by sea snake antivenom. *Toxins* 11, 3. doi:10.3390/toxins11010003

Tan, C. H., Tan, K. Y., and Tan, N. H. (2016a). Revisiting *Notechis scutatus* venom: On shotgun proteomics and neutralization by the "bivalent" sea snake antivenom. *J. Proteomics* 144, 33–38. doi:10.1016/j.jprot.2016.06.004

Tan, C. H., Wong, K. Y., Chong, H. P., Tan, N. H., and Tan, K. Y. (2019a). Proteomic insights into short neurotoxin-driven, highly neurotoxic venom of Philippine cobra (*Naja philippinensis*) and toxicity correlation of cobra envenomation in Asia. *J. Proteomics* 206, 103418. doi:10.1016/j.jprot.2019.103418

Tan, K. Y., Liew, J. L., Tan, N. H., Quah, E. S., Ismail, A. K., and Tan, C. H. (2019b). Unlocking the secrets of banded coral snake (*Calliophis intestinalis*, Malaysia): A venom with proteome novelty, low toxicity and distinct antigenicity. *J. proteomics* 192, 246–257. doi:10.1016/j.jprot.2018.09.006

Tan, K. Y., Tan, C. H., Fung, S. Y., and Tan, N. H. (2016b). Neutralization of the principal toxins from the venoms of Thai *Naja kaouthia* and Malaysian *Hydrophis schistosus*: Insights into toxin-specific neutralization by two different antivenoms. *Toxins (Basel)* 8, 86. doi:10.3390/toxins8040086

Tan, K. Y., Tan, C. H., Fung, S. Y., and Tan, N. H. (2015c). Venomics, lethality and neutralization of *Naja kaouthia* (monocled cobra) venoms from three different geographical regions of Southeast Asia. *J. Proteomics* 120, 105–125. doi:10.1016/j.jprot.2015.02.012

Tan, N. H., Wong, K. Y., and Tan, C. H. (2017). Venomics of *Naja sputatrix*, the javan spitting cobra: A short neurotoxin-driven venom needing improved antivenom neutralization. *J. proteomics* 157, 18–32. doi:10.1016/j.jprot.2017.01.018

Ten Broeke, T., Wubbolts, R., and Stoorvogel, W. (2013). MHC class II antigen presentation by dendritic cells regulated through endosomal sorting. *Cold Spring Harb. Perspect. Biol.* 5, a016873. doi:10.1101/cshperspect.a016873

Van Zundert, G. C. P., Rodrigues, J., Trellet, M., Schmitz, C., Kastritis, P. L., Karaca, E., et al. (2016). The HADDOCK2.2 web server: User-friendly integrative modeling of biomolecular complexes. *J. Mol. Biol.* 428, 720–725. doi:10.1016/j.jmb.2015.09.014

Wong, K. Y., Tan, C. H., and Tan, N. H. (2016). Venom and purified toxins of the spectacled cobra (*Naja naja*) from Pakistan: Insights into toxicity and antivenom neutralization. *Am. J. Trop. Med. Hyg.* 94, 1392–1399. doi:10.4269/ajtmh.15-0871

World Health Organization (2016). *Guidelines for the management of snakebites*. New Delhi: World Health Organization, Regional Office for South-East Asia.

Yadav, M., Jhunjhunwala, S., Phung, Q. T., Lupardus, P., Tanguay, J., Bumbaca, S., et al. (2014). Predicting immunogenic tumour mutations by combining mass spectrometry and exome sequencing. *Nature* 515, 572–576. doi:10.1038/nature14001

Yin, L., Trenh, P., Guce, A., Wieczorek, M., Lange, S., Sticht, J., et al. (2014). Susceptibility to HLA-DM protein is determined by a dynamic conformation of major histocompatibility complex class II molecule bound with peptide. *J. Biol. Chem.* 289, 23449–23464. doi:10.1074/jbc.M114.585539

Zhao, W., and Sher, X. (2018). Systematically benchmarking peptide-MHC binding predictors: From synthetic to naturally processed epitopes. *PLoS Comput. Biol.* 14, e1006457. doi:10.1371/journal.pcbi.1006457

Zhou, Z., Callaway, K. A., Weber, D. A., and Jensen, P. E. (2009). Cutting edge: HLA-DM functions through a mechanism that does not require specific conserved hydrogen bonds in class II MHC-peptide complexes. *J. Immunol.* 183, 4187–4191. doi:10.4049/jimmunol.0901663

frontiers | Frontiers in Pharmacology

TYPE Original Research
PUBLISHED 23 June 2023
DOI 10.3389/fphar.2023.1203247

OPEN ACCESS

EDITED BY
Manuela Berto Pucca,
Federal University of Roraima, Brazil

REVIEWED BY
Isadora Sousa de Oliveira,
University of São Paulo, Brazil
Isabela Gobbo Ferreira,
University of São Paulo, Brazil

*CORRESPONDENCE
Dorra Aissaoui-Zid,
aissaoui.dorra@yahoo.com

†These authors have contributed equally to this work

RECEIVED 10 April 2023
ACCEPTED 12 June 2023
PUBLISHED 23 June 2023

CITATION
Mlayah-Bellalouna S, Aissaoui-Zid D, Chantome A, Jebali J, Souid S, Ayedi E, Mejdoub H, Belghazi M, Marrakchi N, Essafi-Benkhadir K, Vandier C and Srairi-Abid N (2023), Insights into the mechanisms governing P01 scorpion toxin effect against U87 glioblastoma cells oncogenesis.
Front. Pharmacol. 14:1203247.
doi: 10.3389/fphar.2023.1203247

Insights into the mechanisms governing P01 scorpion toxin effect against U87 glioblastoma cells oncogenesis

Saoussen Mlayah-Bellalouna[1†], Dorra Aissaoui-Zid[1*†], Aurelie Chantome[2], Jed Jebali[1], Soumaya Souid[3], Emna Ayedi[1], Hafedh Mejdoub[4], Maya Belghazi[5], Naziha Marrakchi[1], Khadija Essafi-Benkhadir[3], Christophe Vandier[2] and Najet Srairi-Abid[1]

[1]LR20IPT01 Biomolécules, Venins et Application Théranostique, Institut Pasteur de Tunis, Université de Tunis El Manar, Tunis, Tunisia, [2]N2C UMR 1069, Institut national de la santé et de la recherche médicale, University of Tours, Tours, France, [3]LR16IPT04 Laboratoire d'Epidémiologie Moléculaire et Pathologie Expérimentale, Institut Pasteur de Tunis, Université de Tunis El Manar, Tunis, Tunisia, [4]USCR Séquenceur de Protéines, Faculté des Sciences de Sfax, Route de Soukra, Sfax, Tunisia, [5]Aix Marseille Université, CNRS, Plateforme Protéomique, IMM FR3479, Marseille Protéomique (MaP), Marseille, France

The emerging concept of small conductance Ca^{2+}-activated potassium channels (SK_{Ca}) as pharmacological target for cancer treatment has significantly increased in recent years. In this study, we isolated the P01 toxin from *Androctonus australis (Aa)* scorpion venom and investigated its effect on biological properties of glioblastoma U87, breast MDA-MB231 and colon adenocarcinoma LS174 cancer cell lines. Our results showed that P01 was active only on U87 glioblastoma cells. It inhibited their proliferation, adhesion and migration with IC_{50} values in the micromolar range. We have also shown that P01 reduced the amplitude of the currents recorded in HEK293 cells expressing SK2 channels with an IC_{50} value of 3 pM, while it had no effect on those expressing SK3 channels. The investigation of the SK_{Ca} channels expression pattern showed that SK2 transcripts were expressed differently in the three cancer cell lines. Particularly, we highlighted the presence of SK2 isoforms in U87 cells, which could explain and rely on the specific activity of P01 on this cell line. These experimental data highlighted the usefulness of scorpion peptides to decipher the role of SK_{Ca} channels in the tumorigenesis process, and develop potential therapeutic molecules targeting glioblastoma with high selectivity.

KEYWORDS

small conductance calcium activated potassium channel, SK2 channel subtype, glioblastoma, androctonus australis scorpion venom, P01 toxin

Abbreviations: Aa, *Androctonus australis*; CH3CN, acetonitrile; Coll-I, collagen-I; DMEM, dulbecco's modified eagle medium; DMSO, dimethylsulfoxyde; ECM, extracellular matrix; Fg, fibrinogen; Fn, fibornectin; FPLC, fast protein liquid chromatography; HPLC, high performance liquid chromatography; Lam, laminin; MTT. 3-(4, 5-dimethylthiazol-2-yl)-2,5-diphenyltetrazolium bromide; NR, Non retained AaG50 fraction; PBS, phosphate-buffered saline; PBS, phosphate-buffered saline; Pl, poly-L-lysine; SK_{Ca}, small conductance calcium-activated potassium channels; TFA, trifluoroacetic acid.

1 Introduction

Potassium (K^+) channels are the most diverse class of ion channels and are widely distributed in a variety of cells including cancer cells, where they are implicated in different stages of their development (Srairi-Abid et al., 2019). K^+ channel family described in tumor cells, includes Ca^{2+}-activated K^+ channels (K_{Ca}), Shaker-type voltage-gated K^+ channels, ether-a-go-go (EAG) K^+ channels, inward rectifier K^+ channels, ATP sensitive K^+ channels and swelling-activated K^+ channels (Wang, 2004). Particularly, the expression of K_{Ca} channels, including small-conductance K_{Ca} (SK_{Ca}) channels (consisting of SK1 ($K_{Ca}2.1$), SK2 ($K_{Ca}2.2$), and SK3 ($K_{Ca}2.3$) subtypes), intermediate-conductance (IK_{Ca}/SK4) and big-conductance (BKCa) channels in tumor cells has gained interest in the cancer field. They are associated with cell cycle progression, migration/invasion, cell volume control and apoptosis (Prevarskaya et al., 2010). SKCa channels are expressed in several cancer cell types and have been reported to be implicated in processes related to tumor cell survival (Krabbendam et al., 2020). Indeed, SK3 channels play a predominant role in melanoma and breast cancer cell migration (Potier et al., 2006; Chantome et al., 2009; Girault et al., 2012). On the other hand, SK4 channels have been involved in the migration potency of glioblastoma stem cells (Ruggieri et al., 2012). Thus, SKCa channels could be considered as biomarkers for carcinogenesis diagnosis and pharmacological targets for cancer treatment.

In this context, scorpion venom was shown to contain toxins and peptides which are specific blockers of these channels. Recently, the anticancer activities of some natural peptides/toxins attracted considerable attention in drug discovery and have been the object of several studies showing that they affect tumor growth, induce apoptosis and inhibit cancer metastasis and angiogenesis *in vitro* and *in vivo* (Ding et al., 2014; Majc et al., 2022). Several examples of the activity of these peptides/toxins as well as their effect on K^+ channels have been recently summarized in many reviews. These peptides/toxins allowed highlighting the implication of different ion channels in cancerogenesis (Srairi-Abid et al., 2019). For instance, charybdotoxin (from *Leiurus quinquestriatus*), a known blocker of IK_{Ca}/SK4, Kv1.3, and BK_{Ca} channels, inhibited proliferation and cell cycle progression in pancreatic and endometrial cancer cell lines (Wang, 2004). Moreover, tapamin, a toxin isolated from the *Mesobuthus tamulus* scorpion, blocked some cancer-related ion channels, such as SK_{Ca} and IK_{Ca}/SK4, and exerts a cytotoxic effect (Díaz-García et al., 2020).

In this work, we isolated and purified P01 from *Androctonus australis* (Aa) venom, previously reported as inhibiting binding of ^{125}I-apamin, a selective blocker of SK_{Ca} channels. P01 was used for studying its effects on the proliferation, migration and adhesion of three human cancer cell lines: U87 cells, derived from glioblastoma; MDA-MB231 cells, from breast cancer; and LS174 cells, from colon adenocarcinoma. Electrophysiological recordings, QPCR and Western blot studies were undertaken to highlight the involvement of SK2 channels in U87 glioblastoma tumorigenesis.

2 Experimental procedures

2.1 Scorpion venom and reagents

Venom of *Androctonus australis* scorpion from Beni Khedach (Tunisia) was collected by the veterinarian service of the Pasteur Institute of Tunisia (IPT) and kept frozen at −20°C in its crude form until use.

Chemicals (reagent grade) were purchased from Sigma Chemical Company, unless indicated otherwise.

Cell culture supplements and reagents were purchased from GIBCO (Cergy-Pontoise, France). Extracellular matrices were purchased from Sigma (St Louis, MO).

2.2 Cells lines and cellular culture

The ATCC (American Type Culture Collection, Rockville, MD, United States) cancer cell lines U87 (glioblastoma), MDA-MB231 (breast cancer) and LS174 (colon adenocarcinoma) were routinely cultured in DMEM supplemented with 10% fœtal bovine serum (FBS), 1% l-glutamine and 100 IU/mL penicillin/streptomycin. The fetal kidney HEK293 and HEK293T cell lines that do not express native SK_{Ca} channels were used for transfection experiments with plasmids encoding for the rat SK2 and human SK3. Rat SK2 cDNA cloned into pJA5 plasmid was a gift from Dr. Skolnik (university Langone Medical center, New York). Human SK3 cDNA cloned into Pipru vector was a king gift from Pr. Soriani (Université Côte d'Azur, CNRS, Inserm, Nice, France).

HEK293T-hSK3 and HEK293-rSK2 cells were selected using the puromycin and neomycin resistance gene respectively. HEK cells were routinely cultured in DMEM supplemented with 5% FBS and 1% l-glutamine. All cell lines were maintained at 37°C in a humid atmosphere of 5% CO_2 in air.

2.3 Purification of the scorpion venom

Crude venom was extracted with cold water (1:4 v/v), then centrifuged at 15,000 *g* for 15 min. The supernatant was loaded on Sephadex G-50 gel filtration chromatography column (K26/100) equilibrated with 0.1 M acetic acid as described by (Miranda et al., 1970). The major fraction was lyophilized and fractionated by FPLC (Dionex Ultimate 3,000, Germany). A Resource S column (HR 5/5, 6 mL 16 × 30 mm, GE Helthcare, Sweden) pre-equilibrated with 0.05 M ammonium acetate (pH 6.6) was used. Proteins were eluted with a 40 min linear gradient from 0.05 to 0.5 M ammonium acetate, (pH 6.6) at a flow rate of 0.8 mL/min. Absorbance was monitored at 280 nm, Elution was controlled by the software Chromeleon (version 6.80). High Performance Liquid Chromatography (HPLC) purification of the Non Retained (NR) AaG50 fraction (Srairi-Abid et al., 2005), was performed on a C18 reversed-phase HPLC column (5 µm 4.6 × 250 mm, Beckman Fullerton, CA, United States). The elution and detection were performed by Beckman Coulter Series125 pump and a Beckman diode array detector set, respectively and controlled by means of the 32 Karat software (Beckman Coulter Fulletrton CA United States). Proteins were eluted from the column at a flow rate of 0.8 mL/min, using a linear gradient (45 min) from 15% to 45% of buffer B (0.1% TFA in CH_3CN) in buffer A (0.1% TFA in water). The polypeptide concentration was determined using QuantiPro BCA Assay Kit (Sigma Aldrich).

2.4 Mass spectrometry and amino acid sequence determination

Samples were analyzed on an Ettan MALDI-Tof Pro (GE Healthcare Uppsala, Sweden) operating in positive reflectron mode with delayed extraction. The sample was co-crystallized with a 5 mg/mL solution of-cyano-4-hydroxy cinnamic acid (HCCA) on the MALDI target by the dry droplet method. MALDI spectra were acquired with an accelerating potential of 20 kV and a laser power set to the minimum level necessary to get a good signal. Mass calibration of the spectra was based on external calibration using appropriate peptide standards (Pepmix4, Laserbiolabs, Nice, France). Spectra acquired were analyzed on MoverZ software (Genomic Solutions,United States).

Reduction of 2 µg peptide with dithiothreitol and alkylation with 4-vinylpyridine, were performed as previously described (Srairi-Abid et al., 2000). The amino acid sequence was compared with those deposited in NCBI database, using FASTA (https://www.ebi.ac.uk/Tools/sss/fasta/) and BLAST program (https://blast.ncbi.nlm.nih.gov/Blast.cgi?PAGE=Proteins). Alignment was performed using CLUSTALW2 (https://www.ebi.ac.uk/Tools/msa/clustalw2/).

2.5 Cell viability assay

The human cell lines U87, MDA-MB231, or LS174 (10,000 cells per well) were treated with P01 peptide at different concentrations (25; 50; 100 and 200 µg/mL). After 24 h, the wells were washed with phosphate-buffered saline (PBS) and then the 3-(4,5-dimethylthiazol-2-yl)-2,5-diphenyltetrazolium bromide (MTT) (0.5 mg/mL) was added to the cells as previously described (Kouba et al., 2020). The crystals formed after the reduction of MTT by mitochondrial dehydrogenases were dissolved with dimethylsulfoxyde (DMSO). The quantification of live cells was achieved by measuring absorbance at 560 nm using a spectrophotometer (Thermo-Multiskan EX, Shanghai, China).

2.6 Cell proliferation test

The effect of the P01 peptide on cell proliferation was studied. The human cell lines U87, MDA-MB231 or LS174 (5,000 cells per well) were treated with 2; 5 and 10 µg/mL of P01 peptide. The plates were placed at 37°C for 72 h. Cellular proliferation was quantified at 560 nm by a spectrophotometer (Thermo-Multiskan EX, Shanghai, China) after treatment with 1% glutaraldehyde and staining with 0.1% crystal violet.

Every 24 h, a series of wells was washed with PBS, the cells were fixed with 1% glutaraldehyde, and preserved in PBS to follow the kinetics of proliferation. After 72 h, the cells were stained with crystal violet 0.1% and quantified by measuring the absorbance at 560 nm using a spectrophotometer (Thermo-Multiskan EX, Shanghai, China).

2.7 Cell migration assay

Cell migration assay was performed using modified Boyden chamber (NeuroProbe Inc., Bethesda, MD, United States) as previously described (Sarray et al., 2007). Membranes were coated with fibrinogen (Fg) (50 µg/mL), fibronectin (Fn) (10 µg/mL), collagen type I (Coll-I) (50 µg/mL) for U87, MDA-MB231 and LS174 cells respectively, for 2 h at 37°C. Cells were harvested as a single cell suspension (10^6 cells/mL) and treated with P01 at 50 µg/mL. Then added to pre-coated membranes and allowed to migrate for 5 h at 37°C in Boyden chamber. Cells were fixed on the underside of the membrane, stained by 0.1% crystal violet and migration was quantified by measuring the absorbance at 560 nm using a spectrophotometer (Thermo-Multiskan EX, Shanghai, China).

2.8 Cell adhesion assay

Adhesion assays were performed as previously described by (Sarray et al., 2007). Glioblastoma U87 cells in suspension (10^6 cells/mL) were treated with 50 µg/mL of P01 and deposited on wells coated with purified extracellular matrix (ECM): Fg at 50 µg/mL; Fn at 10 µg/mL; Coll-I at 50 µg/mL; laminin (Lam) at 15 µg/mL or poly-L-lysine (PL) at 20 µg/mL for U87. MDA-MB231 and LS174 cells were also used in their adequate ECM: Fg and Coll-I respectively. They were incubated to adhere to the substrate for 2 h or 24 h at 37°C. After washing, attached cells were fixed, stained by 0.1% crystal violet, lysed with 1% SDS and quantified by measuring absorbance at 560 nm. The specific adhesion is obtained by subtracting the absorbance obtained in the absence of adhesion substrate (no specific control). To study the dose-response effect, different concentrations of P01 were used (25–100 µg/mL) and the IC_{50} value was determined.

To study the implication of integrins in the P01 peptide activity, adhesion assays using anti-integrin blocking antibodies: anti- α1β1 (1/200), anti- αvβ3 (1/200), anti- α5 (1/200) and anti- β3 (1/200) were performed as described above, except that cells were pretreated with the active peptide P01 at 50 µg/mL.

2.9 PCR analysis

2.9.1 Total RNA extraction

RNA was extracted as previously described by (Jebali et al., 2014). Cells (1×10^6) were washed in ice-cold PBS and lysed in the Trizol buffer (Invitrogen) according to the manufacturer's instructions. The supernatant was cleared by centrifugation, Isopropanol-precipitated and resuspended in sterile Diethylpyrocarbonate (DEPC) 0.1%: nuclease inhibitor-water (Amersham-Pharmacia).

2.9.2 Reverse transcription (RT-PCR) and PCR amplification

Reverse transcription of total RNA was operated using the transcriptase reverse M-MLV RT (Moloney Murine Leukemia Virus-Reverse Transcriptase) according to the manufacturer's instructions. The reverse transcription reaction was performed with a mixture containing: 1 µL RNA (10 ng), 4 µL of First strand buffer (5X buffer) (Amersham-Pharmacia), 1 µL of dNTP (1 mM), 2 µL of oligo d (T) (0.1 mg/mL), 2 µL of DTT (100 mM) and 8.5 µL of DEPC H_2O for a final volume of 20 µL. The samples were mixed and incubated for 5 min at 65°C, then after a short centrifugation, a second incubation of 10 min at 37°C was

TABLE 1 The primer sequences used for PCR and qPCR reactions.

Primer	Sequence	Amplicon size (bp)
F-hGAPDH	5′CGCTCTCTGCTCCTCCTGTT 3′	310
R-hGAPDH	3′CCATGGTGTCTGAGCGATGT 5′	
F-SK1	5′AGGGAGACGTGGCTCATCTA3′	158
R-SK1	3′TTAGCCTGGTCGTTCAGCTT5′	
F-SK2	5′GACTTGGCAAAGACCCAGAA	230
R-SK2	3′CCGCTCAGCATTGTAAGTGA5′	
F-SK3	5′GTTTGGAATTGTTGTTAT GGTGA3′	130
R-SK3	3′GATGATCAAGCCCAAAAGGA5′	

performed. 1 µL of reverse transcriptase M-MLV RT (200 IU) and 0.5 µL of RNase inhibitor (RNasin (Ribonuclease inhibitor 40 IU) were then added and incubated for 1 h at 37°C. The inactivation of the reverse transcriptase is carried out for 5 min at 95°C.

The PCR reaction was performed in a final volume of 50 µL of the reaction mixture containing 0.5 µg of cDNA; 20 picomoles of each of the two primers corresponding at both ends of the target DNA (Table 1); 10 mM of each dNTP; 1x Taq buffer (50 mM KCl, 10 mM pH 8.3 and 1.5 mM $MgCl_2$) and 1 units of Taq polymerase (Amersham-Pharmacia). The PCR protocol included an initial denaturation step at 95°C for 5 min followed by 35 cycles of denaturation (30 s at 94°C), annealing (30 s at 55°C) and extension (30 s at 72°C), and a final extension for 7 min at 72°C. The amplified fragments were separated on 1% agarose gel electrophoresis. The Amplicon was visualized under UV light on a transilluminator to be photographed.

2.9.3 Quantitative-PCR

One-step quantitative real-time reverse transcription polymerase chain reaction (Q-PCR) was performed on a LightCycler®480 II System from Roche using the LightCycler480 SW 1.5 Software. Brilliant II SYBR_Green QPCR Master Mix was used for the Q-PCR reaction in a final volume of 25 µL of the reaction mixture. The experimental reaction was prepared as recommended by the manufacturer. The primer sequences used are presented in Table 1. The endogen control GAPDH was used as a housekeeping gene and was prepared in the same conditions. The alternative protocol with Three-Step Cycling, cited in the manufacturer instructions, was used with an initial denaturation step of 10 min at 95°C followed by 40 cycles. Each cycle comprises 3 steps: DNA denaturation at 95°C for 30 s, a specific hybridization of the SK1, SK2 and SK3 primers for 1 min at 58°C and a polymerization at 72°C for 30 s. Primer pair specificity was tested by amplification of the target using 10 ng of DNA.

2.10 Western blot analysis

Protein expression of the SK2 channel was assessed by Western blotting analysis using a polyclonal antibody raised against synthetic peptide ETQMENYDKHVTYNAERS corresponding to a region of SK2 (Clinisciences). U87, LS174 and MDA-MB-231 cells were plated at a density of 3.10^5 cells/well in 6-well culture plates in DMEM medium supplemented with 10% FBS (Fetal Bovine Serum) and allowed to adhere overnight. Cells were washed twice with PBS and subsequently lysed with Laemmli buffer (1X) at room temperature. About 50 µg of whole cell extracts were resolved in SDS-polyacrylamide gels (10%) and transferred onto a polyvinylidene difluoride (PVDF) membrane (Immobilon-P, Millipore). The immune-reactive proteins were visualized by the enhanced chemiluminescence detection system (ECL, Pierce, Rockford).

2.11 Patch-clamp experiments

Experiments were performed with cells seeded into 35-mm Petri dishes at 3,000 to 6,000 cells per cm^2. All experiments were performed using the conventional whole-cell recording configuration of the patch-clamp technique (Girault et al., 2011). For HEK cells expressing SK2 or SK3 channels, voltages clamp ramp protocols were used with a duration of 2 s, with varying voltages -100 to +100 mV, with a holding potential of 0 mV. This protocol is suitable for studying the channels whose activation (and inactivation) is independent of the voltage and the time, which is the case of SK_{Ca} channels. The compositions of extracellular solution (in mM: NaCl 140, KCl 4, $MgCl_2$ 1, NaH_2PO_4 0.33, $CaCl_2$2 HEPES 10, and D-glucose 11.5) and the intracellular pipette solution (KCl 145, $MgCl_2$ 1, Mg-ATP 1, $CaCl_2$ 0.87, EGTA 1, HEPES 10; the pCa is of 6 (10^{-6} M of calcium concentration) are such that predominantly visible currents, resulting from this imposed voltage protocol, are due to the activity of K^+ channels, particularly SK_{Ca}. Indeed, using these solutions, the equilibrium potential for chlorine (E_{Cl}-) in our conditions is zero, due to the presence of an identical amount of chloride ions on each side of the cell membrane (E_{Cl-} = 0 mV). To measure the amplitude of the currents in HEK cells overexpressing channels of interest, we positioned ourselves to this membrane voltage (Vm = 0 mV). Also, at 0 mV, the membrane potential currents will be recorded mainly K^+ currents and not Cl^- currents.

For U87 cells, whole-cell K^+ currents were generated by stepwise 8 mV depolarizing pulses from a constant holding potential of −90 up to +60 mV. The composition of extracellular solution is the same as that described above and the intracellular pipette solution is as follows in mM: K-glutamate 125, KCl 20, $MgCl_2$ 1, Mg-ATP 1, HEPES 10, $CaCl_2$ 0.7, EGTA 1, and pH was adjusted to 7.2 with KOH. The pCa is of 6.4 ($10^{-6.4}$ M of calcium concentration). Leidab-7 (Tocris, France) was used as reference peptide to selectively block SK2 currents in U87 cells.

2.12 Statistics

Statistical analysis, evaluated by one-way analysis of variance (ANOVA) done with GraphPad Prism 6 (GraphPad Softweare, San Diego, CA, United States), was made using Student t test. Data are reported as mean ± SD. Statistical comparisons between three or more sets of data were performed. Differences were considered significant when $p < 0.05$.

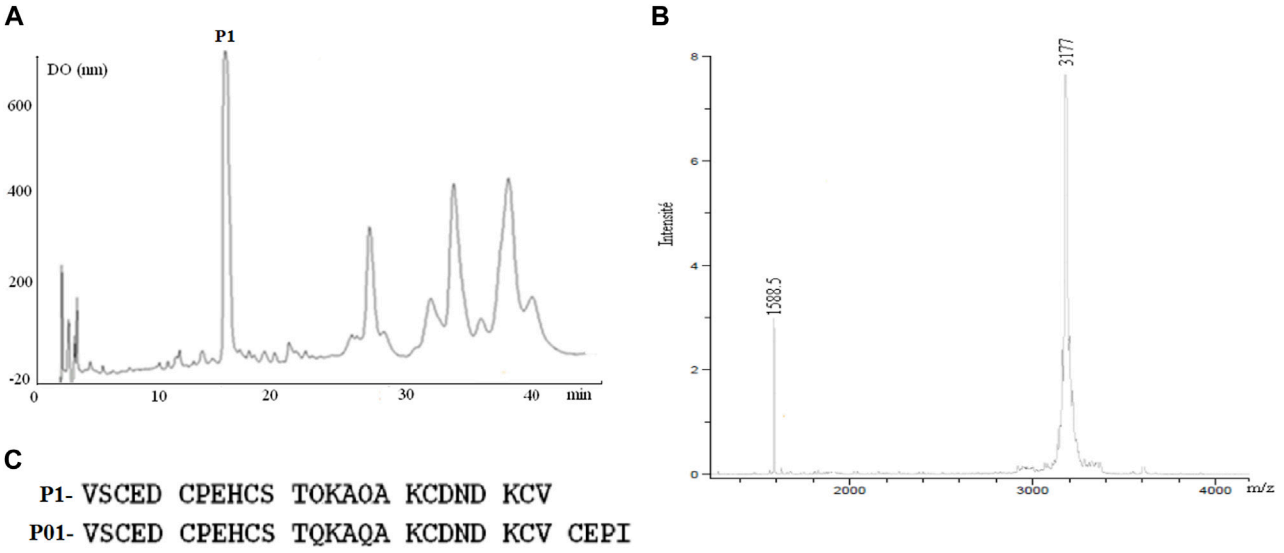

FIGURE 1
(A) Chromatogram of the HPLC purification of P01: C18 with a linear gradient from 15% to 45% buffer B (0.1% TFA in CH_3CN) in A (water 0.1% TFA) at a flow rate of 0.8 mL/min over 45 min. **(B)** the major fraction 1 has a mass of 3,177 Da. **(C)** Comparison of Amino acid sequence obtained by the Edman method of fraction P1 and sequence of the P01 toxin (Zerrouk et al., 1996).

3 Results

3.1 Purification and identification of P01

The toxic fraction AaHG50 representing 33% of the crude venom and containing peptides of 3–7 kDa (Miranda et al., 1970) was obtained by sephadex-G50 chromatography of Aa venom. FPLC of AahG50 has been performed as previously described by (Srairi-Abid et al., 2005). The non-retained AaG50 fraction was injected in an HPLC system using C18 column (Figure 1A). A mass spectrometry analysis of the first major peptide P1 gives a mass of 3,177 Da (Figure 1B).

The Edman degradation of 1 nmol of the native peptide allowed the identification of the 25 first amino acids of its sequence (Figure 1C). Comparison with protein sequences existing in the databases indicates that this peptide showed complete identity with the N-terminal sequence of P01 toxin (Figure 1C). Furthermore, fragmentation of our peptide and that of P01 (provided by Maya Belghazi), using ULTRAFLEX II mass spectrometer, showed a complete MSMS spectrum identity between the two peptides (data not shown).

3.2 P01 had a specific effect on U87 glioblastoma cells

Cell viability was investigated on the three cancer cell lines U87, MDA-MB231 and LS174 using MTT assay. Our results showed that after 24 h of treatment, P01 at different concentrations (25–200 µg/mL) did not have a cytotoxic effect (Figure 2A) on the tested tumor cells that maintained a normal morphology. Interestingly, after 72 h, P01 at 10 µg/mL (3 µM) inhibited about 50% of U87 cell proliferation with no effect on MDA-MB231 and LS174 cells (Figure 2B). The kinetic effect of P01 on U87 cells showed that the inhibition appeared after 48 h of treatment (Figure 2C).

When tested on the migration of the 3 cell lines, P01 (at 50 µg/mL) exhibited an anti-migratory effect only in U87 cells (48% of inhibition), while it had no effect neither on MDA-MB231 nor on LS174 cells (Figure 3).

Likewise, P01 inhibited the adhesion of only U87 cells (data not shown). As shown in Figure 4A, after 2 h of incubation, the best inhibitory effects were obtained with Fg and Fn, as ECM, with a rate of 41% and 38%, respectively. Moreover, no inhibition could be observed on the integrin-independent substratum, poly-L-lysine (Pl), suggesting that the effect of P01 involves the integrins family as adhesion receptors. Based on these results, we studied the dose-response effect of P01 on these two ECM (Fg and Fn). The IC_{50} values of P01 were 48.86 µg/mL and 62.04 µg/mL, respectively (Figure 4C). After 24 h of incubation, P01 stayed active on Fg and Fn, and an inhibition effect on Pl appeared (Figure 4B).

To identify the possible targeted integrins, we checked the effect of P01 on the adhesion of U87 cells on some integrins linked to glioblastoma malignancy. As illustrated in Figure 4D, P01 was not able to alter cell adhesion through β3 integrins, but reduced the adhesive function of α1β1, αvβ3 and α5 integrins. Thus, our results highlighted that P01 had an anti-tumoral effect specifically on U87 glioblastoma cells and integrins could be associated with this activity.

3.3 SK2 channel subtype is expressed in the three cancer cell lines

Since P01 is a peptide ligand of the apamin-sensitive receptor (Zerrouk et al., 1996), it is thought that its activity could be *via* the inhibition of the SK_{Ca} channels. Accordingly, we have investigated

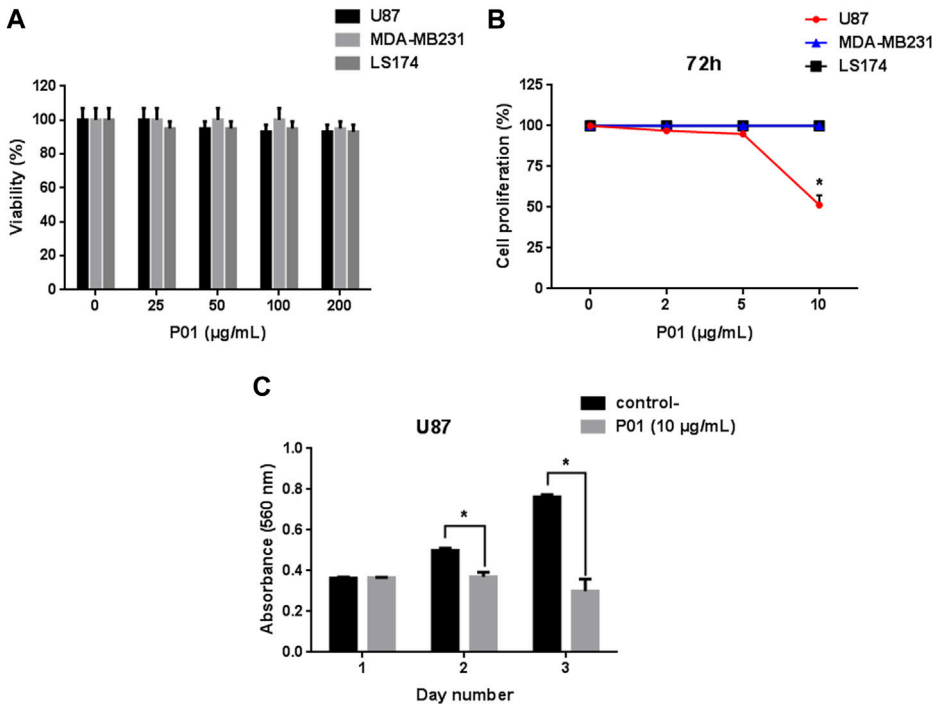

FIGURE 2
(A) Effect of P01 on the viability of cancer cell lines: U87, MDA-MB231, and LS174 cells were treated with 25–200 µg/mL of peptide for 24 h. **(B)** Dose-response effect of P01 on the proliferation of the three cancer cell lines after 72 h of incubation with 2–10 µg/mL of P01. **(C)** Kinetic effect of P01 at 10 µg/mL on U87 cell proliferation. The Mean, SD (n = 3). *p < 0.05, significantly different from control.

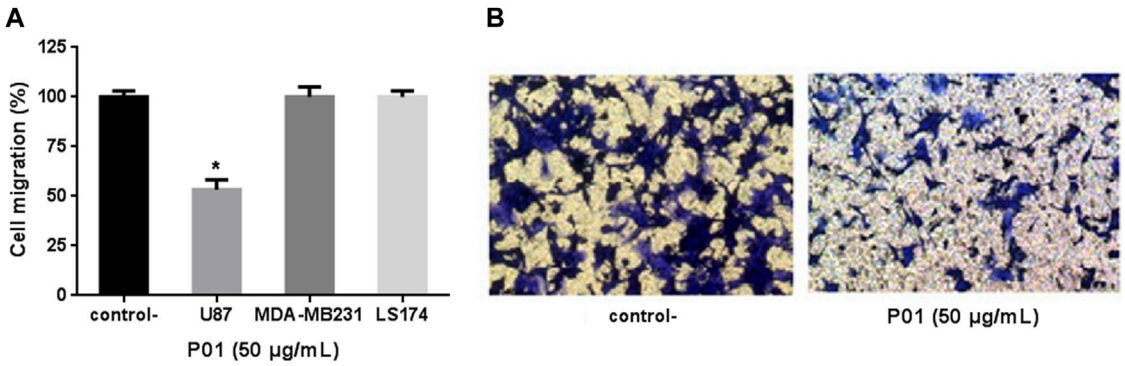

FIGURE 3
(A) Effect of P01 on U87, MDA-MB231, and LS174 cells migration. **(B)** Microscopic observation after migration, fixation and staining of U87 cells treated with 50 µg/mL of P01 compared to negative control. The Mean, SD (n = 3). *p < 0.05, significantly different from control.

the expression of SK channel subtypes in the three tested cancer cell lines.

First, we carried out PCR analysis to verify the expression of SK_{Ca} channel subtypes genes in the three cancer cell lines. GAPDH (glyceraldehyde-3-phosphate deshydrogenase) was used as a housekeeping gene. The Figure 5A showed that only the amplified product of 230 bp, corresponding to the SK2 subtype of SK_{Ca} channels transcript, is expressed in the 3 cells lines with a Cycle threshold_(Ct) value of 16.84 ± 0.58, while neither SK1 (Ct = 27.335 ± 2.605) nor SK3 (Ct = 26 ± 0.36) expressions were noticed in the 3 cell lines (Figure 5B). Since the set of primers, used, allowed us to highlight the expression of SK2 channels in the three cancer cell lines, they are also exploited to quantify this channel by Q-RT-PCR.

Due to gene regulation at different levels, the expression of mRNA transcripts does not necessarily exhibit the same pattern of protein expression resulting in production of functional channels. Therefore, the SK2 protein expression in the three cancer cell lines was investigated by Western blot.

Our result showed that SK2 encodes several protein isoforms of molecular weight (MW) ranging from 40–50 kDa to 100–140 kDa

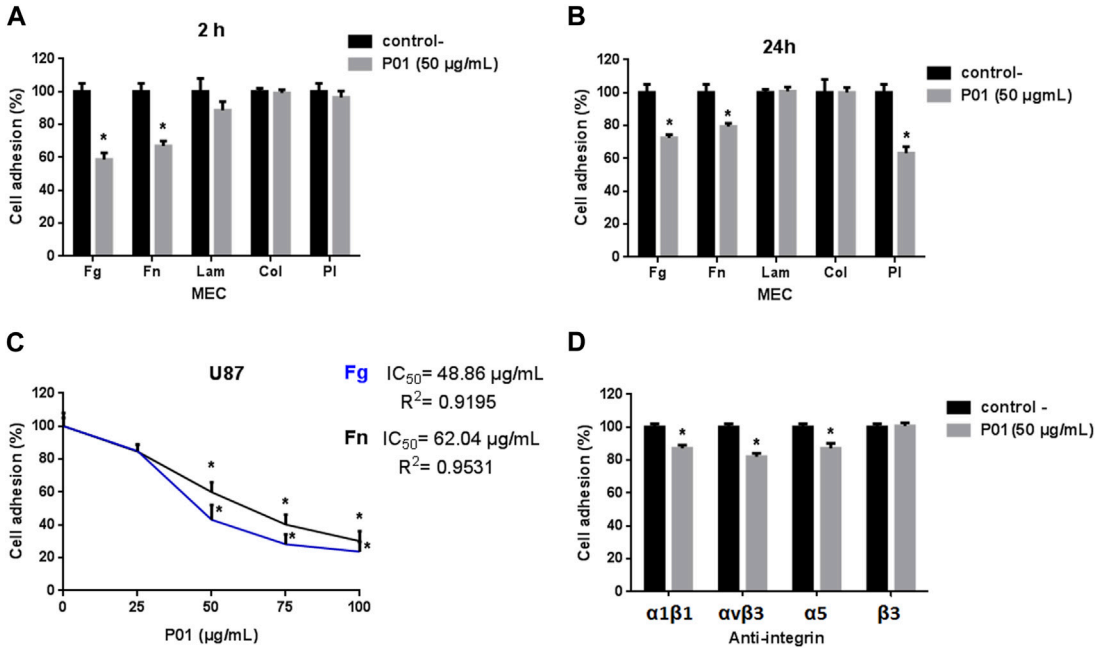

FIGURE 4
Effect of P01 on U87 cell adhesion **(A)** after 2 h, **(B)** after 24 h. Cells are treated with 50 µg/mL of P01 on Fg, Fn, Lam, Coll-I as ECM or Pl. **(C)** Dose-response effect of P01 on U87 cells adhesion to Fg and Fn, after 2 h of incubation. **(D)** Effect of P01 in the presence of anti-integrinic antibodies. Cells were pre-incubated in the absence (black bars) or in the presence (grey bars) of 50 µg/mL P01 for 30 min at room temperature and allowed to adhere for 2 h at 37°C in presence of anti-α1β1, -αvβ3, -α5, or -β3. The Mean, SD (n = 3). *$p < 0.05$, significantly different from control.

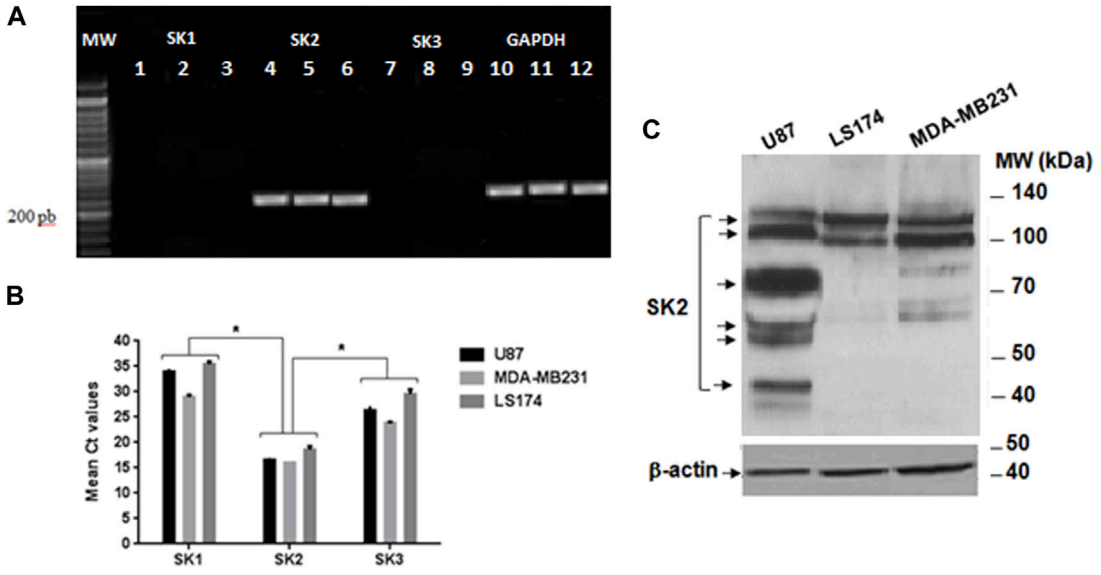

FIGURE 5
Expression of SK1, SK2, and SK3 channels on the three cancer cell lines. **(A)** Gel electrophoresis of the PCR products loaded on a BET agarose gel 1%. MW Molecular weight marker; Lanes 1, 2 et 3: expression of SK1 on U87, MDA-MB231 and LS72 cells lines respectively; Lane 4, 5, and 6: expression of SK2 on U87, MDA-MB231 and LS174 respectively; Lanes 7, 8, and 9 expression of SK3 on U87, MDA-MB231, and LS174; Lane 10, 11, and 12 expression of GADPH on U87, MDA-MB231, and LS174 respectively. **(B)** Cycle threshold (Ct) values of the SK1, SK2, and SK3 genes in U87, MDA-MB231, and LS174 cell lines, generated from the qPCR. **(C)** Western blot analysis with the specific SK2 antibody.

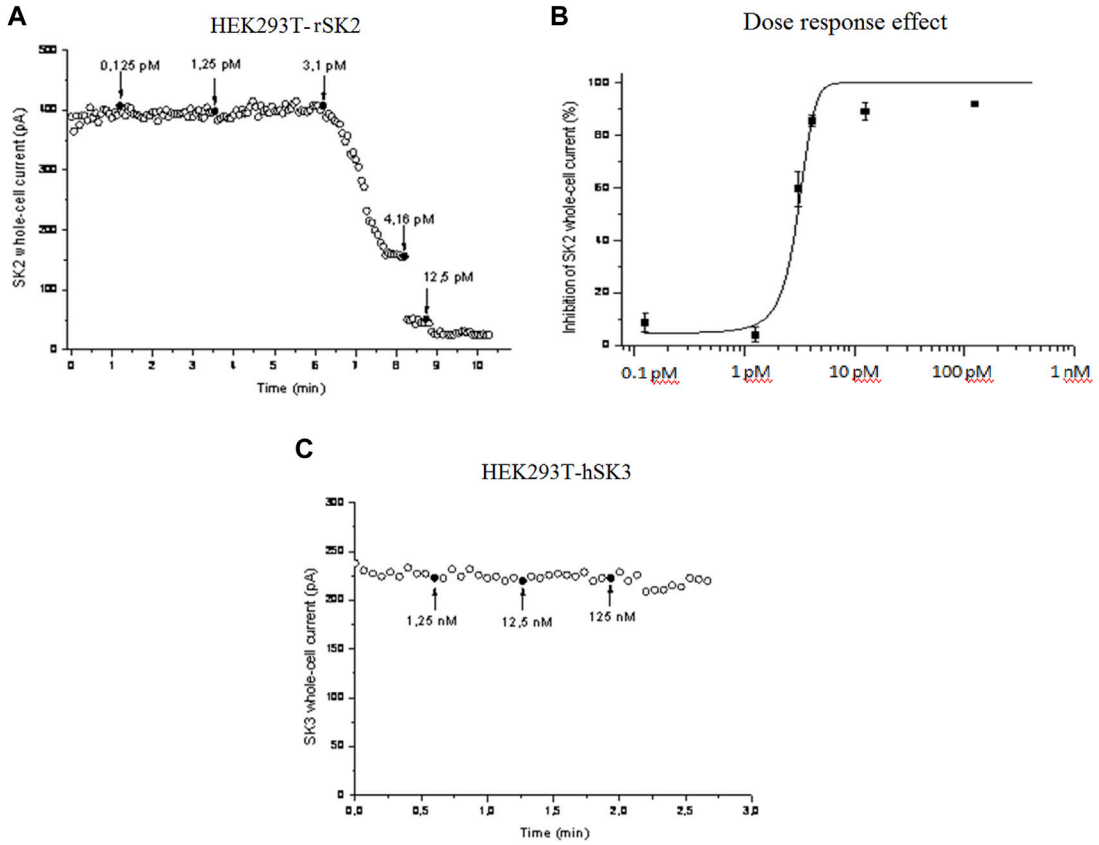

FIGURE 6
Effect of P01 on rat SK2 and human SK3 channels expressed in HEK293 cells. The inhibition of SK_{Ca} currents by P01 toxin were studied in dose-response experiments using whole-cell configuration of patch clamp (pCa 6). Voltages ramps were performed with a duration of 2 s, with varying voltages - 100 to +100 mV, with a holding potential of 0 mV. Amplitudes of SK2 **(A)** and Dose-response fit (n = 5) **(B)**. SK3 currents were recorded at 0 mV and plotted as a function of time. The bath solution was shifted to solutions with the indicated concentrations of P01 at the times marked by black arrows **(C)**. The solid curve was obtained after applying a Hill fitting procedure to the data-points.

and differentially expressed depending on the type of tumor cell line (Figure 5C). At a MW range from 100 to 140 kDa, while MDA-MB231 cells express two isoforms at the same level, U87 cells, in contrast, express high levels of a smaller one compared to LS174 cells showing increased expression of a larger molecular weight isoform (Figure 5C). Interestingly, four immuno positive protein bands (40–50 kDa; 50–70 kDa; 70–100 kDa) recognized by SK2 antibody were detected only in U87 cells (Figure 5C).

3.4 Effect of P01 on HEK cells expressing rSK2 and hSK3 channels

We then checked whether P01 could affect the activity of SK2 channel compared to SK3 channel. Electrophysiological records by voltage-clamp showed that P01 reduced SK2 currents (Figure 6A). The SK2 currents reduction was dose-dependent giving an IC_{50} of 3 pM (Figure 6B), while no effect was noticed on the current of the SK3 channel (Figure 6C).

3.5 Effect of P01 on SK2 currents of U87 cells

Finally, we inspected if SK2 currents were detected in U87 cells. As shown Figure 7A, application of Leidab-7, a selective SK2 channel blocker caused a large reduction of the outward K^+ currents compared to control condition (53% reduction at + 10 mV, Figure 7B) demonstrating the presence of SK2 channel conductance in the plasma membrane of U87 cells. As expected, current density-voltage relationships obtained with P01-treated cells and Leidab-7 treated cells were similar (Figures 7A, B) suggesting that P01 reduced endogenous SK2 conductance.

4 Discussion

Potassium channels have been implicated in many diseases, either in a primary etiologic role in channelopathies or as mediators in other pathogenesis. It is not surprising that roughly one third of all drugs used in modern therapies are ion channel modulators (Wickenden, 2002; Huang and Jan, 2014).

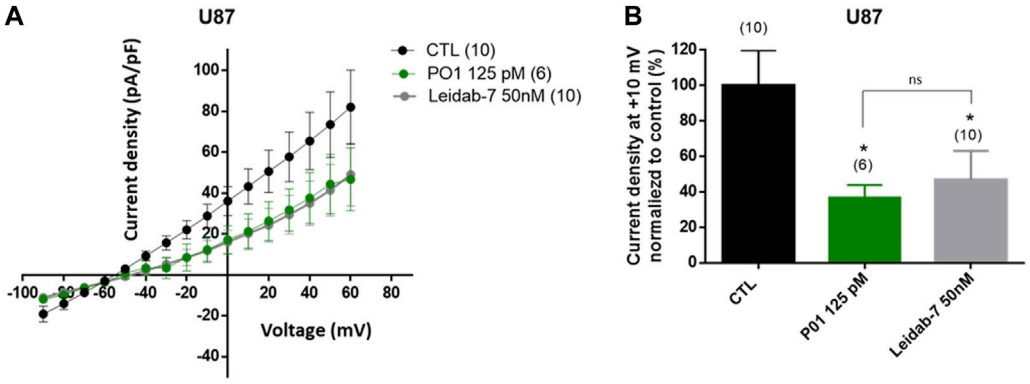

FIGURE 7
Effect of P01 on currents of U87 cells. The reduction of SK2 currents by P01 toxin were studied using whole-cell configuration of patch clamp (pCa6.5). Whole-cell currents were generated by stepwise 8 mV depolarizing pulses (400 ms duration; 5 s intervals) from a constant holding potential of −90 up to +60 mV. **(A)** Current density-voltage relationships obtained in control condition (CTL) and after application of P01 (125pM) or Leidab-7 (50 nM). Leidab-7 was used as reference peptide to selectively block SK2 currents. The current density−voltage relation was obtained by dividing the averaged steady-state currents elicited between −90 and +60 mV by the respective cell capacitance. **(B)** Current density at +10 mV normalized to control condition (%). Results represent the mean ± SEM. The Kruskal–Wallis test with Dunn's correction was used. *: Significantly different from control condition at $p < 0.05$. ns: no significant different between P01 and Leidab-7 treatment on current density. The numbers in brackets indicate the number of cells.

Fundamental studies have been accumulating evidence that tumor cells possess various types of K^+ channels playing important roles in regulating their development, increasing evidence that cancer constitutes a category of channelopathies. The K^+ channels involved in oncological processes belong to four main classes (Huang and Jan, 2014). Among these, KCa channels have gained interest in the cancer field. Indeed, they are associated with cell cycle progression, migration/invasion, cell volume control and apoptosis (Jäger et al., 2004; Wang, 2004). Interestingly, scorpion peptides, especially those blocking K^+ channels have been investigated, as they represent specific ligands, and shown promising anticancer effects, although purification and characterization of active components still remain a challenge for novel cancer therapies (Ding et al., 2014).

Our team has initiated the fractionation of *Aa* scorpion venom, in order to identify scorpion peptides targeting potassium channels involved in the oncological process. Thus, we succeeded to isolate one peptide well represented in this venom. Based on its N-terminal sequence and its mass fingerprint this peptide corresponded to the P01 toxin, previously described by (Zerrouk et al., 1996). P01, classified as a α-Ktx8.1 toxin, was reported to inhibit the binding of ^{125}I-apamin, a toxin from *Apis mellifera* bee venom that specifically blocked SK channel subtypes (Wei et al., 2005; Pedarzani and Stocker, 2008). In this work, we found that P01 exhibited a high inhibiting effect on the SK2 channel subtype expressed in HEK293 cells, with an IC_{50} value of 3 pM, whereas it has no effect on the SK3 channel subtype. P01 appeared to be more active than apamin, which blocked hSK1 and rSK2 channels in HEK 293 cells with IC_{50} values of 3.3 nM and 83 pM, respectively (Strobaek et al., 2000). P01 has also a higher effect than leiurotoxin I (also called scyllatoxin), the first toxin isolated from *Leiurus quintestriatus* scorpin, which blocked the rSK2, channels, expressed in HEK293 cells with an IC_{50} value of 0.28 nM (Hosseini et al., 2001).

It is worthy to note that the effects of P01 on SK_{Ca} channel subtypes, recorded in our work, were different from those obtained by Shakkottai (Shakkottai et al., 2001), which showed that P01 had little or no blocking activity on SK2 or SK3 expressed on Jurkat cells. This can be explained by the differential expression of either functional SK2 isoforms or other membrane receptors between HEK293 and Jurkat cells. Indeed, in their work Shah and Haylett (Shah and Haylett, 2000) showed that apamin blocked hSK1 expressed in HEK293 and COS-7 cells with IC_{50} values of 8 nM and 12 nM, respectively, which are also different from that recorded on hSK1 channels expressed in *Xenopus oocytes* (100 pM) (Shah and Haylett, 2000). Accordingly, they demonstrate that the properties of the channel may depend on the expression system.

This can also explain the specific effect of P01 on U87 cells. Indeed, we found that P01 inhibited the viability of only U87 cells after 72 h of incubation with IC_{50} of 10 μg/mL (3.14 μM) and had no effect on those of MDA-MB231 and LS174 cells. The effect of P01 is nearly 2.5 times more important than that of KAaH2, a scorpion peptide isolated from the same venom (Srairi-Abid et al., 2005; Aissaoui et al., 2018). In fact, like P01, KAaH2 has an inhibiting effect on U87 cells proliferation, with an IC_{50} value of 8 μM, without being active neither on MDA-MB231 nor on LS174 cells (Aissaoui et al., 2018). In fact P01 could be considered as a potent peptide, comparing to peptides from scorpion venoms. Indeed it is also 6 times more active than the tetrapeptide AaTs1 isolated from the same venom (Aissaoui-Zid et al., 2021). This later inhibited the proliferation of U87 cells with an IC_{50} of 0.5 mM by up regulating the p53 and FPRL-1 expression.

When tested on cell adhesion and migration, as key processes of metastasis, P01 showed also a specific effect on U87 cells whereas MDA-MB231 and LS174 cells were not affected. Indeed, P01 affected the adhesion of U87 cells on Fg and Fn with IC_{50} values of 48.86 μg/mL (15.3 μM) and 62.04 μg/mL (19.48 μM), respectively.

When compared to KAaH1, an isoform of KAaH2, active on Kv1.1 and Kv1.3 potassium channels, P01 showed a roughly comparable effect on U87 cell adhesion. Indeed, KAaH1 displayed IC_{50} values of 9.5 μM and 15 μM on Fg and Fn, respectively (Aissaoui et al., 2018). Besides, contrary to P01, at 2 h of adhesion, KAaH1 has an effect on the Pl and not with the anti-integrinic antibodies. The P01 effect on Pl significantly appeared when cells were treated for 24 h, showing that non-integrinic receptors could also be involved in the U87 cell adhesion.

For the cell migration, P01 exerted its effect on only U87 cells with an IC_{50} of 50 μg/mL (15.7 μM), while KAaH1 was active on the 3 cell lines (Aissaoui et al., 2018). Thus, P01 and KAaH1 inhibited the U87 cell migration with different mechanisms. These results brought to extent the list of substances from animal venomous reported to exhibit inhibition effects on U87 cells development, especially those from snake venoms, with other mechanism of action. For instance, PIVL, a Kunitz-type serine protease inhibitor, from the venom of the Tunisian snake *Macrovipera lebetina transmediterranea,* reduced the U87 cell adhesion, migration and invasion in the nanomoral range, by impairing the function of αvβ3 integrin (Morjen et al., 2013). Also the contortrostatin a disintegrin, that inhibited the tumor (induced by the stereotactically injection of U87 cells) progression, and prolongation of survival in a rodent glioma model (Pyrko et al., 2005). This protein specifically binds to certain integrins on the tumor cell and angiogenic endothelial cell surface and inhibits their interaction with the extracellular matrix, resulting in blockage of cell motility and invasiveness (Schmitmeier et al., 2005). On the other hand the CC-LAAO, an L-Amino Acid Oxidase from Cerastes cerastes Snake Venom, induced a dose-dependent apoptotic effect through the H_2O_2 generated during the enzymatic reaction (Abdelkafi-Koubaa et al., 2021).

Since P01 is highly active on SK2 channels and neither SK1 nor SK3 channels are expressed on U87 cells, we can suggest that SK2 channels are involved in the U87 cell tumorigenesis. This is in agreement with a recent paper demonstrating that SK2 channel, expressed in pancreatic ductal adenocarcinoma, increased invasiveness and metastasis formation, an effect that depends on cancer-associated fibroblasts (CAF) promoting SK2 phosphorylation through an integrin–epidermal growth factor receptor (EGFR)–AKT (Protein kinase B) axis (Rapetti-Mauss et al., 2022).

In addition, in our study, we found, in one hand, that the level of SK2 mRNA in the three cancer cells, was significantly higher than those of SK1 and SK3 (Figures 5A, B), which is in accordance with the study of (Abdullaev et al., 2010). On the other hand, we showed that the expression pattern of the SK2 isoforms was cell-type specific (Figure 5C). Indeed, while the three cancer cells express differently two isoforms at high molecular weight, only U87 cells express four SK2 isoforms at medium and smaller molecular weights. This result is in agreement with that of Strassmaier and its collaborators that highlighted the distribution and expression of four distinct SK2 channel isoforms in the human brain: the standard, the long and two short isoforms (Strassmaier et al., 2005). The shown expression of human SK2 isoforms in the brain could explain the variability of electrophysiological findings observed with SK2 channels (Willis et al., 2017).

Thus, based on the pharmacological results of P01, the specific antitumor effect of this latter on U87 cells, could be due to its interaction with these four isoforms expressed only in U87 cells, suggesting that their expression could rely on their functional activity, and their involvement in the U87 tumor mechanism.

Besides, it seems that the effect of P01 on U87 cell proliferation is not due only to its blocking activity of SK2 channels, but also by targeting a complex of membrane receptors and/or effectors expressed in U87 cells, including SK2. Indeed the use of the UCL1848 trifluoroacetate salt, which blocked SK2 channel expressed in HEK 293 cells with IC_{50} value of 0.12 nM (Hosseini et al., 2001), had no effect on U87 cell proliferation (Abdullaev et al., 2010). These authors noted that the concentrations necessary for blocking proliferation were higher than those necessary for blocking these ion channels, as we found in our study (Abdullaev et al., 2010; Abdallah et al., 2023). This suggests that the P01 and UCL1848 interact with different sites, generating different activity of SK2 channel and that the U87 cell proliferation needs the recruitment of other protein membranes to form an active complex.

Adhesion assays using blocking antibodies raised against some integrins known to be expressed in U87 and having affinity for Fg and Fn (Zhu et al., 2002; Morjen et al., 2013) indicated that P01 exerted its anti-adhesive effect by interacting with α1β1, αvβ3, α5 integrins. Thus, the specific effect of P01 on U87 cells could be due to the regulation of these integrins activity through a cross talk with the SK2 channel on the cell surface. In fact, it has been reported that K^+ channels can interact with integrins (especially with the β subunit) and constitute macromolecular complexes associated with different cell responses (Vira and Howard, 2002; Crottès et al., 2013; Becchetti et al., 2019). Indeed, the interaction between β3 integrin and SKCa channels has been reported to play an important role in the extra-telencephalic pyramidal neurons of layer V of the medial prefrontal cortex (mPFC) of KO mice, and that the ablation of this integrin leads to an alteration of their functional activity (Vitale Carmela Thesis, 2018). Particularly, in prostate cancer, the KCa/αvβ3 integrin complex stimulates cell proliferation (Du et al., 2016). More still, in other cases, complexes can be formed by three elements (channel-integrin-receptor). For instance, in acute myeloid leukemia (AML), the Kv11.1 (hERG1) associates with β1 integrin and the vascular endothelial growth factor (VEGF) receptor 1 (also known as Flt-1), to form a complex that modulates the cell proliferation and trans-endothelial migration signaling pathways (Pillozzi et al., 2007).

5 Conclusion

In the light of these results, P01 is obviously a potent and specific SK2 channel blocker that may be considered a promising tool to study and target this channel in many diseases, in which it is overexpressed. Interestingly, the present study advocated the implication of SK2 channel isoforms as well as α1β1, αvβ3, α5 integrins in the selective activity of the scorpion toxin P01 against U87 glioblastoma cells.

However, to gain more insight into the mechanisms of P01 activity, further investigations are needed, especially to decipher the interaction between the SK2 channel and these integrins. Thus, this study highlights the potential of this peptide

for the development of a new generation of anti-glioblastoma drugs and opens perspectives for more effective treatment strategies to handle these malignancies more successfully.

Data availability statement

The original contributions presented in the study are included in the article/supplementary materials, further inquiries can be directed to the corresponding author.

Author contributions

SM-B, purification of scorpion venom, SM-B, DA-Z, and EA: performed the cellular experiments; SM-B, DA-Z, and NS-A wrote the paper, AC: electrophysiology analysis, JJ: performed PCR and qPCR, SM-B and SS: performed Western blot analysis, HM: performed amino acid sequencing, MB: performed mass spectrometry, NM, KE-B, CV, and NS-A: analyzed the data and edited the manuscript; NS-A: conceived and designed the experiments. NS-A and CV: contributed reagents/materials/analysis tools. All authors contributed to the article and approved the submitted version.

Funding

This study was supported partly by the Tunisian Ministry of Higher Education and Scientific Research (LR 20 IPT 01), and by grants from the University of Tours, the "Région Centre-Val de Loire" "INSERM," the MOTIVHEALTH network, Canceropôle Grand Ouest, la Ligue Contre le Cancer de l'inter région Bretagne, Centre, Pays de la Loire, the Institut National du Cancer (INCa-PLBIO18-151), with financial support from Inserm Cancer and des "ministères de l'Europe et des affaires étrangères; et de l'enseignement supérieur, de la recherche et de l'innovation."

Acknowledgments

We would like to thank Pr. Hechmi Louzir the general director of Pasteur Institute in Tunis for his support. Thouraya Chagour (LBVAT, Pasteur Institute of Tunis) for her technical help.

Conflict of interest

The authors declare that the research was conducted in the absence of any commercial or financial relationships that could be construed as a potential conflict of interest.

Publisher's note

References

Abdallah, F., Elias, B. C., Lin, D., and Piggott, B. J. (2023). Ion channels in gliomas-from molecular basis to treatment. *Int. J. Mol. Sci.* 24, 2530. doi:10.3390/ijms24032530

Abdelkafi-Koubaa, Z., Elbini-Dhouib, I., Souid, S., Jebali, J., Doghri, R., Srairi-Abid, N., et al. (2021). Pharmacological investigation of CC-laao, an L-amino acid Oxidase from cerastes cerastes snake venom. *Toxins (Basel)* 13 (12), 904. doi:10.3390/toxins13120904

Abdullaev, I. F., Rudkouskaya, A., Mongin, A. A., and Kuo, Y. H. (2010). Calcium-activated potassium channels BK and Ik1 are functionally expressed in human gliomas but do not regulate cell proliferation. *PLoS One* 5 (8), 12304. doi:10.1371/journal.pone.0012304

Aissaoui, D., Mlayah-Bellalouna, S., Jebali, J., Abdelkefi-Koubaa Ze, S. S., Souid, S., Moslah, W., et al. (2018). Functional role of Kv1.1 and Kv1.3 channels in the neoplastic progression steps of three cancer cell lines, elucidated by scorpion peptides. *Int. J. Biol. Macromol.* 111, 1146–1155. doi:10.1016/j.ijbiomac.2018.01.144

Aissaoui-Zid, D., Saada, M. C., Moslah, W., Potier-Cartereau, M., Lemettre, A., Othman, H., et al. (2021). AaTs-1: A tetrapeptide from Androctonus australis scorpion venom, inhibiting U87 glioblastoma cells proliferation by p53 and FPRL-1 up-regulations. *Molecules* 26 (24), 7610. doi:10.3390/molecules26247610

Becchetti, A., Petroni, G., and Arcangeli, A. (2019). Ion Channel conformations regulate integrin-dependent signaling. *Trends Cell. Biol.* 29 (4), 298–307. doi:10.1016/j.tcb.2018.12.005

Chantome, A., Girault, A., Potier, M., and Pagès, J. C. (2009). KCa2.3 channel-dependent hyperpolarization increases melanoma cell motility. *Exp. Cell. Res.* 315 (20), 3620–3630. doi:10.1016/j.yexcr.2009.07.021

Crottès, D., Guizouarn, H., Martin, P., Borgese, F., and Soriani, O. (2013). The sigma-1 receptor: A regulator of cancer cell electrical plasticity? *Front. Physio* 4, 175. doi:10.3389/fphys.2013.00175

Díaz-García, A., VarelaVoltage-Gated K+/Na+ Channels, D., and Venom, S. (2020). Voltage-gated K+/Na+ channels and scorpion venom toxins in cancer. *Front. Pharmacol.* 11, 913. doi:10.3389/fphar.2020.00913

Ding, J., Chua, P. J., Bay, B. H., and Gopalakrishnakone, P. (2014). Scorpion venoms as a potential source of novel cancer therapeutic compounds. *Exp. Biol. Med. (Maywood)* 239 (4), 387–393. doi:10.1177/1535370213513991

Du, C., Zheng, Z., Li, D., Chen, L., Li, N., Yi, X., et al. (2016). BKCa promotes growth and metastasis of prostate cancer through facilitating the coupling between αvβ3 integrin and FAK. *Oncotarget* 7 (26), 40174–40188. doi:10.18632/oncotarget.9559

Girault, A., Haelters, J-P., Potier-Cartereau, M., Chantôme, A., Jaffrés, P-A., Bougnoux, P., et al. (2012). Targeting SKCa channels in cancer: Potential new therapeutic approaches. *Curr. Med. Chem.* 19 (5), 697–713. doi:10.2174/092986712798992039

Girault, A., Haelters, J-P., Potier-Cartereau, M., Chantome, A., Pinault, M., Marionneau-Lambot, S., et al. (2011). New alkyl-lipid blockers of SK3 channels reduce cancer cell migration and occurrence of metastasis. *Curr. Cancer Drug Targets* 11 (9), 1111–1125. doi:10.2174/156800911798073069

Hosseini, R., Benton, D. C., Dunn, P. M., Jenkinson, D. H., and Moss, G. W. (2001). SK3 is an important component of K(+) channels mediating the afterhyperpolarization in cultured rat SCG neurones. *J. Physiol.* 535 (2), 323–334. doi:10.1111/j.1469-7793.2001.00323.x

Huang, X., and Jan, L. Y. (2014). Targeting potassium channels in cancer. *J. Cell. Biol.* 206 (2), 151–162. doi:10.1083/jcb.201404136

Jäger, H., Dreker, T., Buck, A., Giehl, K., Gress, T., and Grissmer, S. (2004). Blockage of intermediate-conductance Ca^{2+}-activated K^+ channels inhibit human pancreatic cancer cell growth *in vitro*. *Mol. Pharmacol.* 65, 630–638. doi:10.1124/mol.65.3.630

Jebali, J., Fakhfekh, E., Morgen, M., Srairi-Abid, N., Majdoub, H., Gargouri, A., et al. (2014). Lebecin, a new C-type lectin like protein from *Macrovipera lebetina* venom with anti-tumor activity against the breast cancer cell line MDA-MB231. *Toxicon* 86, 16–27. doi:10.1016/j.toxicon.2014.04.010

Kouba, S., Braire, J., Félix, R., Chantôme, A., Jaffrès, P. A., Lebreton, J., et al. (2020). Lipidic synthetic alkaloids as SK3 channel modulators. Synthesis and biological evaluation of 2-substituted tetrahydropyridine derivatives with potential anti-metastatic activity. *Eur. J. Med. Chem.* 186, 111854. doi:10.1016/j.ejmech.2019.111854

Krabbendam, I. E., Honrath, B., Bothof, L., Silva-Pavez, E., Huerta, H., Peñaranda Fajardo, N. M., et al. (2020). SK channel activation potentiates auranofin-induced cell death in glio- and neuroblastoma cells. *Biochem. Pharmacol.* 171, 113714. doi:10.1016/j.bcp.2019.113714

Majc, B., Novak, M., Lah, T. T., and Križaj, I. (2022). Bioactive peptides from venoms against glioma progression. *Front. Oncol.* 12, 965882. doi:10.3389/fonc.2022.965882

Miranda, F., Kupeyan, C., Rochat, H., Rochat, C., and Lissitzky, S. (1970). Purification of animal neurotoxins. Isolation and characterization of eleven neurotoxins from the venoms of the scorpions Androctonus australis hector, Buthus occitanus tunetanus and Leiurus quinquestriatus quinquestriatus. *Eur. J. Biochem.* 16 (3), 514–523. doi:10.1111/j.1432-1033.1970.tb01111.x

Morjen, M., Kallech-Ziri, O., Bazaa, A., Othman, H., Mabrouk, K., Zouari-Kessentini, R., et al. (2013). PIVL, a new serine protease inhibitor from *Macrovipera lebetina* transmediterranea venom, impairs motility of human glioblastoma cells. *Matrix Biol.* 32 (1), 52–62. doi:10.1016/j.matbio.2012.11.015

Pedarzani, P., and Stocker, M. (2008). Molecular and cellular basis of small-and intermediate-conductance, calcium-activated potassium channel function in the brain. *Cell. mol. LifeSci.65* 65, 3196–3217. doi:10.1007/s00018-008-8216-x

Pillozzi, S., Brizzi, M. F., Bernabei, P. A., Bartolozzi, B., Caporale, R., Basile, V., et al. (2007). VEGFR-1 (FLT-1), beta1 integrin, and hERG K^+ channel for a macromolecular signaling complex in acute myeloid leukemia: Role in cell migration and clinical outcome. *Blood* 110 (4), 1238–1250. doi:10.1182/blood-2006-02-003772

Potier, M., Joulin, V., Roger, S., Besson, P., Jourdan, M. L., Leguennec, J. Y., et al. (2006). Identification of SK3 channel as a new mediator of breast cancer cell migration. *Mol. Cancer Ther.* 5 (11), 2946–2953. doi:10.1158/1535-7163.MCT-06-0194

Prevarskaya, N., Skryma, R., and Shuba, Y. (2010). Ion channels and the hallmarks of cancer. *Trends Mol. Med.* 16, 107–121. doi:10.1016/j.molmed.2010.01.005

Pyrko, P., Wang, W., Markland, F. S., Swenson, S. D., Schmitmeier, S., Schönthal, A. H., et al. (2005). The role of contortrostatin, a snake venom disintegrin, in the inhibition of tumor progression and prolongation of survival in a rodent glioma model. *J. Neurosurg.* 103 (3), 526–537. doi:10.3171/jns.2005.103.3.0526

Rapetti-Mauss, R., Nigri, J., Berenguier, C., Finetti, P., Tubiana, S. S., Labrum, B., et al. (2022). SK2 channels set a signalling hub bolstering CAF-triggered tumourigenic processes in pancreatic cancer. *Gut* 0, 722–735. doi:10.1136/gutjnl-2021-326610

Ruggieri, P., Mangino, G., Fioretti, B., Catacuzzeno, L., Puca, R., Ponti, D., et al. (2012). The inhibition of KCa3.1 channels activity reduces cell motility in glioblastoma derived cancer stem cells. *PLoS ONE* 7, 47825. doi:10.1371/journal.pone.0047825

Sarray, S., Delamarre, E., and Marvaldi, J. (2007). Lebectin and lebecetin, two C-type lectins from snake venom, inhibit alpha5beta1 and alphaV-containing integrins. *Matrix Biol.* 26 (4), 306–313. doi:10.1016/j.matbio.2007.01.001

Schmitmeier, S., Markland, F. S., Schönthal, A. H., and Chen, T. C. (2005). Potent mimicry of fibronectin-induced intracellular signaling in glioma cells by the homodimeric snake venom disintegrin contortrostatin. *Neurosurgery* 57 (1), 141–153. doi:10.1227/01.neu.0000163426.25227.56

Shah, M., and Haylett, D. G. (2000). The pharmacology of hSK1 Ca^{2+}-activated K^+ channels expressed in mammalian cell lines. *Br. J. Pharmacol.* 129 (4), 627–630. doi:10.1038/sj.bjp.0703111

Shakkottai, V. G., Regaya, I., Wulff, H., Fajloun, Z., Tomita, H., Fathallah, M., et al. (2001). Design and characterization of a highly selective peptide inhibitor of the small conductance calcium-activated K+ channel, SkCa2. *J. Biol. Chem.* 276, 43145–43151. doi:10.1074/jbc.M106981200

Srairi-Abid, N., Guijarro, J. I., Benkhalifa, R., Mantegazza, M., Cheikh, A., Ben Aissa, M., et al. (2005). A new type of scorpion Na^+-channel-toxin-like polypeptide active on K^+ channels. *Biochem. J.* 388 (2), 455–464. doi:10.1042/BJ20041407

Srairi-Abid, N., Mansuelle, P., Mejri, T., Karoui, H., Rochat, H., Sampieri, F., et al. (2000). El Ayeb M. Purification, characterization and molecular modelling of two toxin-like proteins from the *Androctonus australis Hector* venom. *Eur. J. Biochem.* 267 (17), 5614–5620. doi:10.1046/j.1432-1327.2000.01632.x

Srairi-Abid, N., Othman, H., Aissaoui, D., and Ben Aissa, R. (2019). Anti-tumoral effect of scorpion peptides: Emerging new cellular targets and signaling pathways. *Cell. Calcium* 80, 160–174. doi:10.1016/j.ceca.2019.05.003

Strassmaier, T., Bond, C. T., Sailer, C. S., Hans-Guenther Knaus, H. G., and Adelman, J. P. (2005). A novel isoform of SK2 assembles with other SK subunits in mouse brain. *J. Biol. Chem.* 280 (22), 21231–21236. doi:10.1074/jbc.M413125200

Strobaek, D., ørgensen, T. D. J., Christophersen, P., K Ahring, P., and P Olesen, S. (2000). Pharmacological characterization of small-conductance Ca(2+)-activated K(+) channels stably expressed in HEK 293 cells. *Br. J. Pharmacol.* 129 (5), 991–999. doi:10.1038/sj.bjp.0703120

Vira, V. A., and Howard, R. P. (2002). Molecular proximity of Kv1.3 voltage-gated potassium channels and beta1-integrins on the plasma membrane of melanoma cells: Effects of cell adherence and channel blockers. *J. Gen. Physiol.* 120, 29–37. doi:10.1085/jgp.20028607

Vitale Carmela Thesis (2018). β3 integrin-dependent regulation of SK channel-mediated Ca2+-activated K+ currents in intra- and extra-telencephalic cortical pyramidal neurons Dottorato di ricerca in neuroscienze. Universita degli studi di Genova. Avaliable At: https://hdl.handle.net/11567/996218.

Wang, Z. (2004). Roles of K^+ channels in regulating tumour cell proliferation and apoptosis. *Pflügers Arch.* 448, 274–286. doi:10.1007/s00424-004-1258-5

Wei, A. D., Gutman, G. A., Aldrich, R., Chandy, K. G., Grissmer, S., and Wulff, H. (2005). International Union of Pharmacology. LII. Nomenclature and molecular relationships of calcium activated potassium channels. *Pharmacol. Rev.* 57 (4), 463–472. doi:10.1124/pr.57.4.9

Wickenden, A. (2002). K(+) channels as therapeutic drug targets. *Pharmacol. Ther.* 94 (1-2), 157–182. doi:10.1016/s0163-7258(02)00201-2

Willis, M., Trieb, M., Leitner, I., Wietzorrek, G., Marksteiner, J., and Knaus, G. (2017). Small-conductance calcium-activated potassium type 2 channels (SK2, KCa2.2) in human brain. *Brain Struct. Funct.* 222, 973–979. doi:10.1007/s00429-016-1258-1

Zerrouk, H., Laraba-Djebari, F., Fremont, V., Meki, I. A., Darbon, I. H., Mansuelle, P., et al. (1996). Characterization of PO1, a new peptide ligand of the apamin-sensitive Ca2 + activated K+ channel. *Int. J. Pept. Protein Res.* 48 (6), 514–521. doi:10.1111/j.1399-3011.1996.tb00870.x

Zhu, Q., Liang, S., Martin, L., Gasparini, S., Ménez, A., and Vita, C. (2002). Role of disulfide bonds in folding and activity of leiurotoxin I: Just two disulfides suffice. *Biochemistry* 41 (38), 11488–11494. doi:10.1021/bi026136m

frontiers | Frontiers in Pharmacology

TYPE Original Research
PUBLISHED 29 September 2023
DOI 10.3389/fphar.2023.1227962

OPEN ACCESS

EDITED BY
C. James Chou,
Medical University of South Carolina, United States

REVIEWED BY
Bhargab Kalita,
Amrita Vishwa Vidyapeetham (Kochi campus), India
Sudhakaran P. R.,
University of Kerala, India

*CORRESPONDENCE
Karl Wah-Keung Tsim,
botsim@ust.hk
Wen-Luan Wendy Hsiao,
wlhsiao@must.edu.mo
Mandy Li,
mandy.li@zkoph.com
Xiao-Yi Li,
drli@leespharm.com
William Chi-Shing Tai,
william-cs.tai@polyu.edu.hk

†These authors have contributed equally to this work and share first authorship

RECEIVED 24 May 2023
ACCEPTED 19 September 2023
PUBLISHED 29 September 2023

CITATION
Chan BD, Wong W-Y, Lee MM-L, Yue PY-K, Dai X, Tsim KW-K, Hsiao W-LW, Li M, Li X-Y and Tai WC-S (2023), Isolation and characterization of ZK002, a novel dual function snake venom protein from *Deinagkistrodon acutus* with anti-angiogenic and anti-inflammatory properties. *Front. Pharmacol.* 14:1227962. doi: 10.3389/fphar.2023.1227962

Isolation and characterization of ZK002, a novel dual function snake venom protein from *Deinagkistrodon acutus* with anti-angiogenic and anti-inflammatory properties

Brandon Dow Chan[1†], Wing-Yan Wong[2†], Magnolia Muk-Lan Lee[1†], Patrick Ying-Kit Yue[3], Xiangrong Dai[4], Karl Wah-Keung Tsim[5*], Wen-Luan Wendy Hsiao[6*], Mandy Li[7*], Xiao-Yi Li[7*] and William Chi-Shing Tai[1,8*]

[1]Department of Applied Biology and Chemical Technology, The Hong Kong Polytechnic University, Kowloon, Hong Kong SAR, China, [2]Department of Food Science and Nutrition, The Hong Kong Polytechnic University, Kowloon, Hong Kong SAR, China, [3]Department of Biology, Hong Kong Baptist University, Kowloon, Hong Kong SAR, China, [4]Lee's Pharmaceutical (HK) Limited, Hong Kong Science Park, Shatin, Hong Kong SAR, China, [5]Division of Life Science and Center for Chinese Medicine, The Hong Kong University of Science and Technology, Kowloon, Hong Kong SAR, China, [6]State Key Laboratory of Quality Research in Chinese Medicine, Macau University of Science and Technology, Taipa, Hong Kong SAR, China, [7]Zhaoke (Hong Kong) Ophthalmology Pharmaceutical Limited, Hong Kong Science Park, Shatin, Hong Kong SAR, China, [8]State Key Laboratory of Chinese Medicine and Molecular Pharmacology (Incubation), Shenzhen Research Institute of the Hong Kong Polytechnic University, Shenzhen, Hong Kong SAR, China

Introduction: Pathological angiogenesis, the abnormal or excessive generation of blood vessels, plays an important role in many diseases including cancer, diabetic retinopathy, psoriasis, and arthritis. Additionally, increasing evidence supports the close linkage between angiogenesis and inflammation. Snake venoms are a rich natural source of biologically active molecules and carry rich potential for the discovery of anti-angiogenic and anti-inflammatory modulators.

Methods: Here, we isolated and purified a novel protein, ZK002, from the venom of the snake *Deinagkistrodon acutus*, and investigated its anti-angiogenic and anti-inflammatory activities and mechanisms.

Results: ZK002 was identified as a 30 kDa heterodimeric protein of α and β chains, which exhibited anti-angiogenic activity in various *in vitro* assays. Mechanistically, ZK002 inhibited activation of VEGF signaling and related mediators including eNOS, p38, LIMK, and HSP27. ZK002 also upregulated the metalloproteinase inhibitor TIMP3 and inhibited components of the VEGF-induced signaling cascade, PPP3R2 and SH2D2A. The anti-angiogenic activity of ZK002 was confirmed in multiple *in vivo* models. ZK002 could also inhibit the *in vitro* expression of pro-inflammatory cytokines, as well as *in vivo* inflammation in the carrageenin-induced edema rat model.

Conclusion: Our findings highlight the potential for further development of ZK002 as a dual function therapeutic against diseases with involvement of pathogenic angiogenesis and chronic inflammation.

KEYWORDS

ZK002, snake venom protein, anti-angiogenesis, anti-inflammation, dual-function

1 Introduction

Pathological angiogenesis, referring to the abnormal or excessive generation of blood vessels, has been shown to play an important role in many diseases including cancer, diabetic retinopathy, psoriasis, and arthritis (Carmeliet, 2003). A host of growth factors, cytokines, and lipid mediators can stimulate angiogenesis, most notably via vascular endothelial growth factor (VEGF) signaling, which is the key regulatory pathway of angiogenesis (Shibuya, 2011). In addition, increasing evidence supports a tight connection between angiogenesis and inflammation. On one hand, during inflammation, immune cells release pro-angiogenic factors, including VEGF, that induce neovascularization. On the other, increased vascularization contributes to the propagation of inflammation by facilitating the migration of immune cells and inflammatory mediators to affected sites (Waldner et al., 2010; Ribatti, 2017). Thus, the two processes are tightly linked, each inducing and advancing the other.

In recent years, there has been an increased focus on the development of anti-angiogenic modulators for the treatment of angiogenesis-related diseases (Ferrara and Adamis, 2016). Snake venoms are a rich natural source for the discovery of biologically active molecules with diverse effects. *Deinagkistrodon acutus,* also known as hundred-pace snake and Chinese moccasin, is a poisonous snake belonging to the viper family and is commonly found in southern China, Taiwan, and northern Vietnam. *D. acutus* has long been used in traditional Chinese medicines for the treatment of arthritis, and thus has significant medical and commercial value. Recent studies have shown that snake venoms contain a mixture of proteins and peptides including snake venom metalloproteinases, C-type lectins, phospholipase A2, and snake venom serine proteases, and possess a wide range of biological activities including anti-thrombosis, haemostasis, analgesia, anti-tumor, and anti-angiogenic effects (Chen et al., 2019; Mohamed Abd El-Aziz et al., 2019). Many anti-angiogenic snake venom molecules and snake venom protein mimetics are being studied for the treatment of various diseases (Munawar et al., 2018). In our work, we set out to mine the therapeutic potential of proteins isolated from the venom of *D. acutus*.

In this study, we first isolated and purified a novel protein, ZK002, from the venom of *D. acutus* and through *in vitro* and *in vivo* studies, we demonstrated its potent anti-angiogenic effects. Mechanistic investigations demonstrated that the anti-angiogenic activity of ZK002 potentially involved inhibition of the VEGF signaling pathway, upregulation of metalloproteinase inhibitors, and downregulation of components of VEGF-induced signaling. With the aim of expanding the therapeutic scope of ZK002, its effects in inflammation cell line and animal models were also examined. We found that in addition to its anti-angiogenic properties, ZK002 also exhibited strong anti-inflammatory activity, establishing it as a dual function snake venom protein.

2 Materials and methods

2.1 Materials

Deinagkistrodon acutus venom was purchased from Qimen Venom Supplies (Southern Anhui, China). DEAE Sepharose Fast Flow was from Pharmacia (Uppsala, Sweden) and Sephacryl S-100HR was from Cytiva (MA, United States). Protein-PAK DEAE 8HR column was from Waters (MA, United States). All other chemicals used were of analytical grade.

2.2 Preparation of ZK002 monoclonal antibody

Primarily isolated ZK002 protein was subjected to SDS-PAGE analysis. Protein of at least 85% purity was confirmed to possess *in vitro* anti-migration and anti-proliferation activity before being used as the antigen for monoclonal antibody production. 6–12 week-old BALB/c mice were used to generate the antibody. Hybridoma cell production was performed by fusing a spleen cell suspension from the immunized mice with myeloma cells at a 1: 5 ratio, using a standard polyethylene glycol (PEG) cell fusion protocol. The established hybridoma cell strain was named 1D9 and hybridoma cells were cultured in serum-free media. Hybridoma cell culture media was applied to a recombinant *Staphylococcus aureus* protein A coupled affinity column and monoclonal antibody recognizing ZK002 (purity ≥90%, SDS-PAGE) was purified.

2.3 Primary purification of ZK002

Crude *D. acutus* venom was weighed and dissolved in 0.02 M, pH 8.0 Tris-HCl buffer and centrifuged twice at 4,000 RPM for 10 min, with a buffer change between centrifugations. Supernatant was applied to an equilibrated anion-exchange DEAE-Sepharose Fast Flow (FF) column. The target fraction was identified via ELISA using ZK002 monoclonal antibody, and further purified through stepwise separation via cation-exchange chromatography with an equilibrated CM-Sepharose FF column. The resulting eluent was the primary purified ZK002.

2.4 ZK002 isolation by antibody affinity chromatography

ZK002 monoclonal antibodies were coupled with a Sepharose 4B column to produce a ZK002 antibody affinity chromatography column. The primary purified ZK002 was applied to the affinity chromatography column equilibrated with buffer (0.02 M Tris-HCl +0.15 M NaCl, pH 7.6). Target protein was eluted, concentrated, and further loaded onto an equilibrated gel-chromatography S-100 filtration column. The resulting eluent was the highly purified ZK002. The purity and molecular weight of the purified ZK002 protein was determined by MALDI-TOF-MS using an Autoflex III mass spectrometer (Bruker, Germany).

2.5 Mass spectrometry analysis and protein identification

ZK002 α and β chains were separated by SDS PAGE and the corresponding gel bands excised. Gel bands were dehydrated in

200 µL ACN at room temperature for 10 min, followed by removal using a SpeedVac Vacuum Concentrator. Peptides were then reduced by addition of 25 µL 200 mM DTT solution and incubation at room temperature for 45 min. Next, alkylation was performed by addition of 4 µL 1 M IAA solution and incubation in the dark at room temperature for 20 min. 671 µL 50 mM ammonium bicarbonate solution was added to dilute the urea concentration in the samples to 1 M. For trypsin digestion, 2 µL of trypsin gold solution was added to the samples and incubated at 37°C overnight. Afterwards, 200 µL MilliQ water and 7 µL 100% TFA were added to the samples. The digested peptide samples were cleaned up using a QASIS HLB 1CC Extraction cartridge with two washes of 0.5% TFA before eluting twice with 70% ACN. The eluates were dried with a SpeedVac. Finally, the samples were resuspended in 100 µL 0.1% FA and transferred to LC vials with inserts for Nano-LCMS analysis.

Proteomics analysis was carried out on an UltiMate™ 3,000 RSLCnano System (Thermo Scientific) and Acclaim™ PepMap™ 100 C18 Column 250 mm (Thermo Scientific) with an Orbitrap Fusion Lumos Mass Spectrometer (Thermo Scientific). The mobile phase included 0.1% formic acid in water as solvent A and 0.1% formic acid in acetonitrile as solvent B. The NanoLC program was set as follows: 0–10 min B 2%; 10–12 min B 2%–6%; 12–47 min B 6%–20%; 47–52 min B 20%–30%; 52–56 min B 30%–90%; 56–61 min B 90%; 61–61.1 min B 90%–2%; 61.1–66 min B 2%. Flow rate was set to 0.3 µL/min, and column temperature was 50°C. MS conditions were as follows: Mode of detection: positive mode; Scan range: 400–1,500 m/z; Ionization Source: NSI; Spray Voltage: Static; Positive ion source voltage: 2,300 V; Ion transfer tube temperature: 300°C. The mass spectrometer was operated in data-dependent acquisition mode.

Protein sequences uploaded to the Mascot Server (Matrix Science) and proteomics MS data was processed by Progenesis QI for Proteomics (Waters) with default settings. The peptide ions were identified by Mascot MS/MS ion search of the Uniprot database (Taxonomy: Chordata) using the following criteria: Peptide charge: 2+, 3+, 4+; Peptide tolerance: 10 Da (13C = 2); MS/MS tolerance: 0.1 Da; Fixed modification: Carbamidomethyl (C); Variable modification: Oxidation (M); Enzyme: No specific; Max missed cleavages: 2; Instrument type: ESI-FTICR. The novel ZK002 α-chain MS proteomics data have been deposited to the ProteomeXchange Consortium via the PRIDE (Perez-Riverol et al., 2022) partner repository with the dataset identifier PXD037093.

2.6 Crystallization, data collection, and refinement of ZK002

The ZK002 crystals formed rod-like crystals using the hanging drop vapor diffusion method and a Mosquito robot (TTP LabTech) at 19°C utilizing the precipitants 0.2 M $(NH_4)_2SO_4$, and 20% polyethylene glycol (PEG) 3,350 in 100 mM Tris pH 7.5. The ZK002 crystals formed in the monoclinic space group *P2*, with two copies per asymmetric unit of $(\alpha\beta)_2$ heterodimers arranged through 2-fold rotation symmetry. Data collection was performed under cryo conditions (100 K) using a Rigaku RU-H3R X-ray instrument. The crystals diffracted to 2.1 Å resolution and all diffraction images were indexed and integrated using the Mosflm program (Leslie and Powell, 2007), and the integrated reflections were scaled using the SCALA program (Evans, 2006). Structure factor amplitudes were calculated using TRUNCATE (French and Wilson, 1978) from the CCP4 program suite. The structure of ZK002 was solved by molecular replacement with the program PHASER (McCoy, 2007), using the refined structure of the α subunit (PDB code: 1WT9) with 100% sequence identity and the β subunit (PDB code: 3BX4) with 56% identity.

All steps of the atomic refinements were performed with the PHENIX.refine program (Afonine et al., 2012). The model was built

TABLE 1 X-ray data collection statistics for the ZK002 crystal.

	HG1
Data collection	
PDB code	7QAJ
Space group	P 1 2 1
Cell dimensions	
a, b, c (Å)	103.16, 54.29, 107.64
α, β, γ (°)	90, 100.56, 90
No. of copies in a.u	2
Resolution (Å)	27.45–2.10
Upper resolution shell (Å)	2.17–2.1
Unique reflections	68,733 (6,489)[a]
Completeness (%)	98.07 (94.81)
Average I/σ(I)	41.05 (5.19)
Rpim	0.2113 (0.3453)
CC1/2	0.75 (0.735)
Refinement	
Resolution range (Å)	27.45–2.10
No. of reflections [I/σ(I) > 0]	67,661
No. of reflections in test set	3,269
R-working/R-free	0.1990/0.2421
No. of protein atoms	8,334
No. of water molecules	550
Overall average B factor (Å^2)	38.62
Root mean square deviations	
- bond length (Å)	0.004
- bond angle (°)	0.59
Clashscore	3.1
Ramachandran plot	
Most favored (%)	96.35
Additionally allowed (%)	3.35
Disallowed (%)	0.3

[a]Values in parentheses refer to the data of the corresponding upper-resolution shell.

into 2mFobs—DFcalc, and mFobs—DFcalc maps using COOT (Emsley and Cowtan, 2004). Refinement movements were accepted only when they produced a decrease in the Rfree value. The model was optimized using PDB_REDO (Joosten et al., 2011), and was evaluated with MOLPROBIDITY (Chen et al., 2010). Details of the data collection and refinement statistics of the ZK002 structure are described in Table 1. The coordinates of ZK002 were deposited in the RCSB Protein Data Bank with accession code 7QAJ.

2.7 Cell culture

HUVECs and RAW264.7 murine macrophages were purchased from the American Type Culture Collection (ATCC) (Manassas, United States). HUVECs were cultured on 0.04% gelatin-coated (Sigma, MO, United States) plates in M199 medium supplemented with penicillin/streptomycin (50 U/mL), 2 mM L-glutamine (Invitrogen, CA, United States), 10% fetal bovine serum (FBS), and 25% EGM at 37°C, 5% CO_2. HUVECs underwent one passage weekly and were used throughout passages 2 to 4. RAW264.7 murine macrophages were maintained in Dulbecco's Modified Eagle Medium (DMEM) (Life Technologies, United States) supplemented with 10% heat inactivated FBS and penicillin/streptomycin (50 U/mL) at 37°C, 5% CO_2. Cell lines were regularly tested and confirmed to be free of *mycoplasma* contamination.

2.8 Tube formation assay

Matrigel (BD Biosciences) was plated in a 96-well plate at 37°C for 1 h to allow the matrix solution to solidify. 2×10^4 HUVECs in medium only (uninduced), medium containing 2% FBS, or medium containing 2% FBS and 5 μM ZK002 were then pipetted over the matrix solution and incubated at 37°C for 16 h. Capillary tube structures were photographed with a digital camera attached to an inverted light microscope (×40). Quantification was conducted using WimTube image analysis software.

2.9 *In vitro* wound-healing assay

HUVECs were seeded in gelatin coated 6-well plates at density of 3×10^5 cells per well for 24 h. Next, an overlapping double cross shape was scraped in each well using a pipette tip and cells were treated with vehicle (negative control), latrunculin, or ZK002 (5 or 10 μM) and incubated at 37°C for 3 or 6 h. Images were taken before and after drug treatment. Cell migration was analyzed by TScratch software by measuring the area void of cells.

2.10 Transwell migration assay

HUVECs were seeded at a density of 5×10^4 cells per well onto 8 μm transwell inserts (Costar, Corning, NY, United States). The lower chamber was filled with 500 μL low serum cell culture medium only, or low serum cell culture medium containing VEGF (10 ng/mL). Cells were then treated with 0, 1, or 5 μM ZK002. After 4 h at 37°C, non-migrated cells were removed with cotton buds and migrated cells were fixed with 4% formaldehyde and stained for 10 min with crystal violet. The magnitude of HUVEC migration was evaluated by counting migrated cells in six random high-power (×100) microscope fields.

2.11 Transwell invasion assay

The transwell invasion assay was conducted as the transwell migration assay above, except inserts were coated with 50 μL of matrigel and allowed to solidify in a 37°C incubator for 30 min to form a thin gel layer before the seeding of HUVECs.

2.12 Analysis of VEGF-associated protein activation

HUVECs were seeded overnight then serum starved for 3 h in culture medium alone or with ZK002 (5 μM), after which VEGF (100 ng/mL) was applied for 0, 2.5, 5, or 10 min. Cell pellets were collected and stored at −80°C before assessment of the phosphorylation of select molecules by Western blotting.

2.13 Western blot analysis

Cell pellets were lysed in RIPA buffer (50 mM Tris-HCl, pH 7.4, 150 mM NaCl, 1 mM EDTA, 1% Triton X-100, 1% sodium deoxycholate, 0.1% SDS) containing 1× Complete protease inhibitor (Roche, Germany) and 1× PhosSTOP phosphatase inhibitor (Roche), and then centrifuged to remove debris. Cell lysates (20 μg) were solubilized in Laemmli sample buffer (250 mM Tris-HCl, pH 6.8, 10% w/v SDS, 0.1% w/v bromophenol blue, 50% v/v glycerol, 10% v/v β-mercaptoethanol), electrophoresed through an SDS-PAGE gel and transferred onto PVDF membranes (Bio-Rad, CA, United States). Blots were then blocked in 5% nonfat skim milk in TBS-Tween20 (TBST) buffer (137 mM NaCl, 2.7 mM KCl, 25 mM Tris-HCl, pH 7.5, 0.1% Tween 20) and probed using the following antibodies in 5% BSA in TBST buffer overnight: p-VEGFR2, p-eNOS, p-p38, p-LIMK, p-cofilin, p-Hsp27, p-Erk1/2 and β-actin (Cell Signaling Technology, MA, United States). Expression was quantified using by scanning autoradiogram and densitometry (Quantity One, Bio-Rad).

2.14 Quantitative real-time polymerase chain reaction

HUVECs were treated with ZK002 (5 or 10 μM) for 24 h. RAW264.7 cells were pre-treated with or without ZK002 at 1 μM for 24 h, then stimulated with 0.1 μg/mL LPS for another 6 h. To detect changes in gene expression after ZK002 treatment, total RNA was isolated from cells using the E.Z.N.A.® Total RNA Kit I (Omega Bio-Tek, GA, United States) according to manufacturer's instructions. RNA integrity was assessed using a Nanodrop One spectrophotometer (Thermo Scientific, MA, United States). Single-

strand cDNA was synthesized from 1 μg of RNA using SuperScript® VILO™ MasterMix (Thermo Scientific) according to manufacturer's instructions. The mRNA levels of select genes were assessed by quantitative real-time polymerase chain reaction (qPCR). Primer sequences are listed in Supplementary Table S1. PCR was performed using PowerUp SYBR Green Master Mix (Applied Biosystems, MA, United States). Amplification and detection were performed using a QuantStudio 7 Real-Time PCR system (Applied Biosystems) at the following conditions: 2 min at 50°C, 10 min at 95°C, followed by 45 cycles of 15 s at 95°C, and 1 min at 60°C. Relative gene expression was calculated using the $2^{-\Delta\Delta CT}$ method. β-actin was used as a reference gene. Experiments were conducted in triplicate.

2.15 Chicken embryo chorioallantoic membrane (CAM) assay

VEGF was mixed with various doses of ZK002 (0.3, 0.8, 1.6, 3.3, or 16.4 μM) in 5 respective chicken embryos. Treatment with VEGF alone served as a positive control. An additional treatment (VEGF +1.6 μM ZK002 + excess ZK002 monoclonal antibody) was used to validate the anti-angiogenic effects of ZK002. Angiogenesis was assessed via observation and photography of blood vessel growth in embryos and quantified using IKOSA CAM Assay online software (Annese et al., 2023).

2.16 Animals

Male or female BALB/c nude mice (6–8 weeks) and SD rats (~200–220 g) were purchased from the Animal Centre of The Chinese University of Hong Kong. Animals were kept in individually ventilated cages in a barrier-sustained animal house, air-conditioned at 20°C ± 2°C and humidity at 55% ± 10%, under a 12 h light/dark cycle. Food and water were provided *ad libitum*, and mice were examined daily. All animal experiments were approved by the Animal Subjects Ethics Sub-Committee (ASESC) of The Hong Kong Polytechnic University and conducted in accordance with the Institutional Guidelines and Animal Ordinance of the Department of Health, HK S.A.R.

2.17 *In vivo* matrigel plug assay

8-week-old male BALB/c nude mice were subcutaneously injected at the abdominal midline with 0.4 mL matrigel alone, or matrigel supplemented with endothelial growth supplements (bFGF/heparin) with or without 3 μM ZK002. After 7 days, mice were killed, and vessels penetrating the matrigel were photographed. The matrigel plugs were then carefully extracted, with removal of surrounding connective tissue, and analyzed for hemoglobin levels. Plugs were weighed and homogenized for 5–10 min on ice, then supernatant or standard (50 μL) was added to a 96-well plate in duplicate, followed by 50 μL tetramethylbenzidine. The plate was allowed to develop at room temperature for 15–20 min with gentle shaking, and the reaction was stopped by adding 150 μL of 2 N H_2SO_4. Absorbance was read at 450 nm, and hemoglobin levels were normalized to the weight of the plugs.

2.18 Directed *in vivo* angiogenesis assay (DIVAA)

The DIVAA assay was performed according to manufacturer's protocols (Trevigen, MD, United States). Briefly, 8 week-old female nude mice were anesthetized and a 1 cm incision was made on both dorsal-lateral surfaces of the animal, into which two basement membrane extract (BME)-filled angioreactors were implanted on each side. Each angioreactor contained a total of 25 μL BME premixed with VEGF, bFGF, and heparin with or without 3 μM ZK002. Angioreactors containing no growth factors or ZK002 served as controls. After 7 days, mice were killed, and the angioreactors photographed and removed. Hemoglobin content was measured as detailed above.

2.19 Acute carrageenan-induced inflammation rat model

Male SD rats (200–220 g each) were used for acute carrageenan-induced paw edema inflammation experiments. Animals were divided into 4 groups: uninduced, vehicle, ZK002 (2.5 mg/kg), and indomethacin (positive control; 10 mg/kg). Drugs were administered via intraperitoneal injection (ZK002) or oral administration (indomethacin), 1 h before induction. Swelling was induced by subplantar injection of 100 μL of a 1% (w/v) suspension of carrageenan in the right hind paw. Paw volumes of each rat were measured with a plethysmometer every 2 h for up to 6 h post-induction. Degree of edema was calculated by the ratio a/b, where a = right hind paw volume post-carrageenan induction, and b = right hind paw volume pre-carrageenan induction.

2.20 Statistical analysis

Results are expressed as mean ± SD (*in vitro* experiments) or mean ± SEM (*in vivo* experiments) of at least three independent experiments. One-way ANOVA followed by Bonferroni post-test were used for statistical analysis. Values of $p < 0.05$ were considered as statistically significant.

3 Results

3.1 Isolation and purification of ZK002

In preliminary studies, we found that ZK002 isolated from the venom of *D. acutus* possessed potential anti-angiogenic activity. To facilitate further assessment, a partially purified fraction of ZK002 was extracted from crude *D. acutus* venom via stepwise separation using an anion-exchange column and cation-exchange column. As shown in Figure 1A, six peaks were identified in the eluate from anion-exchange columns, with the ZK002 target peak (identified by ELISA using ZK002 monoclonal antibodies) indicated by an arrow. The collected eluate was further purified by a cation-exchange column (Figure 1B). To obtain highly purified ZK002, the eluate was loaded onto an antibody affinity column (Figure 1C). The fraction was then concentrated on an equilibrated gel-chromatography S-100 column and the resulting eluent was the purified protein (Figure 1D). Gel electrophoresis profiles of the

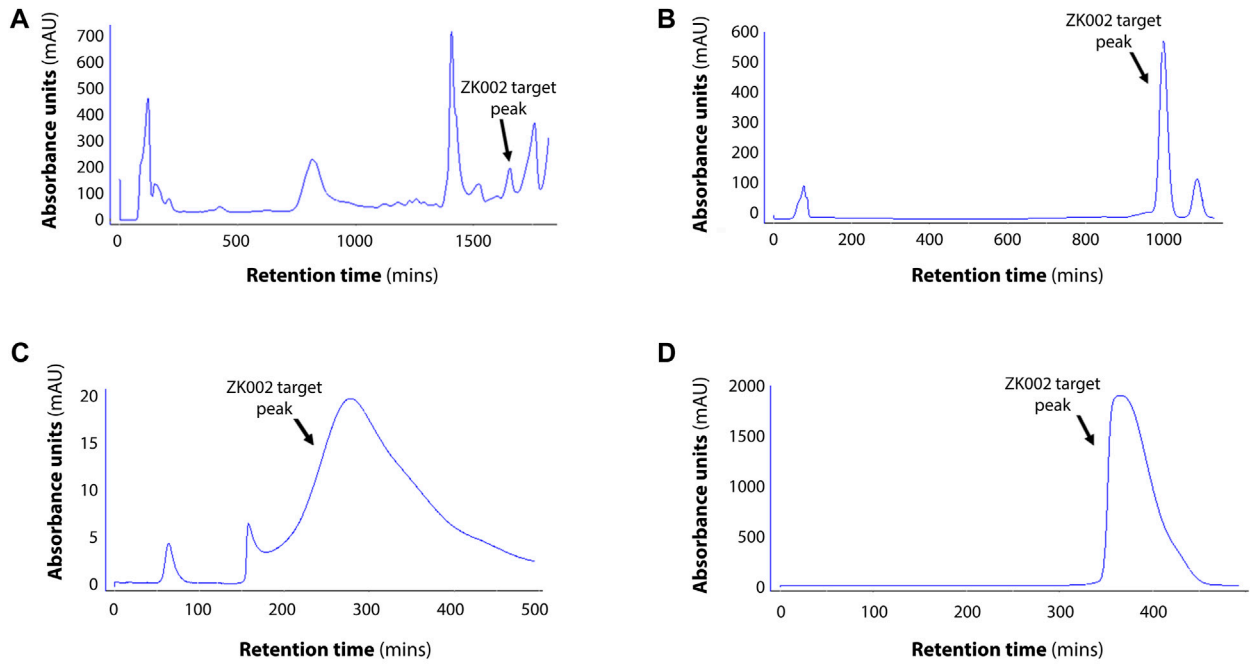

	Anion-exchange chromatography	Cation-exchange chromatography	Affinity chromatography	Gel chromatography
Yield (%)	2–6	0.25–0.50	0.08–0.13	0.05–0.08

FIGURE 1
Chromatographic profiles of the purification steps of ZK002. **(A)** Chromatogram of crude solution A from anion-exchange chromatography. **(B)** Chromatogram of crude product B from cation-exchange chromatography. **(C)** Chromatogram of product C from affinity chromatography. **(D)** Chromatogram of high-purity ZK002 from gel chromatography. ZK002 target peaks were identified and confirmed by ELISA with ZK002 monoclonal antibodies. Yields of each step, as a percentage of the initial crude protein amount, are indicated in the table below.

successive fractions indicated the removal of contaminating proteins and enrichment of target (Supplementary Figure S1). The yield of ZK002, as a percentage of total input venom, was 0.05%–0.08%. SDS-PAGE analysis showed a single band for the purified protein, indicating its high purity. Under non-reducing conditions, a band size of approximately 30 kDa was observed, while under reducing conditions, a band of around 15 kDa was seen (Figure 2). These results provided some insight into the structure of ZK002 as a protein of approximately 15 kDa dimers.

By MALDI-TOF mass spectrometry analysis, we identified the mass of purified ZK002 protein as 30,472.967 Da. The purified protein showed a molecular mass of 30 kDa, and two distinct peaks with a molecular mass of 15 kDa (α subunit) and 16 kDa (β subunit) (Figure 3A), results in line with our previous SDS-PAGE experiments indicating that ZK002 is a disulfide-linked heterodimer.

Through tandem mass spectrometry analysis, we identified the protein sequence of ZK002 α and β chains (Figure 3B; Supplementary Figure S2). Database search showed the sequence of the β-chain was a complete match to an existing snake venom C-type lectin protein (snaclec) of *D. actus* (UniProtKB: Q8JIV8). The sequence with highest similarity to the ZK002 α-chain was Snaclec stejaggregin-A subunit alpha (UniProtKB: Q71RQ1.1), to which it shared 76% identity, thus indicating that the α-chain was a novel sequence (Figures 3C, D). NCBI Conserved Domain Database (Marchler-Bauer et al., 2015) analysis indicated that both ZK002 α and β possessed C-type lectin-like domains, a prototypical domain featured in snaclecs.

The structure of ZK002 was determined via X-ray crystallography to a resolution of 2.1 Å. In agreement with the mass spectrometry results above, ZK002 exists as an αβ heterodimer. In line with previous reports on snaclecs (Zelensky and Gready, 2005; Eble, 2019), the structure of both α and β chain subunits of ZK002 comprised two β-sheets consisting of the β strands β0–β1–β5 and β2–β3–β4, connected by two orthogonally orientated α-helices, and a long loop was seen between β2 and β3 strands. Further, disulphide bridges between cysteine residues were seen between β0 and β1, α1 and β5, β3 and the loop region of β5, and between the two loop regions of the heterodimers (Figure 4A). The asymmetric crystallographic unit was made up of a tetramer of αβ heterodimers (Figure 4B).

Taken together, the sequence and structure of ZK002 were strongly consistent with that of the snaclecs class of proteins.

3.2 ZK002 exhibited anti-angiogenic activity in the HUVEC tube formation assay

The anti-angiogenic activity of ZK002 was first assessed using the HUVEC tube formation assay. Anti-angiogenic activity was

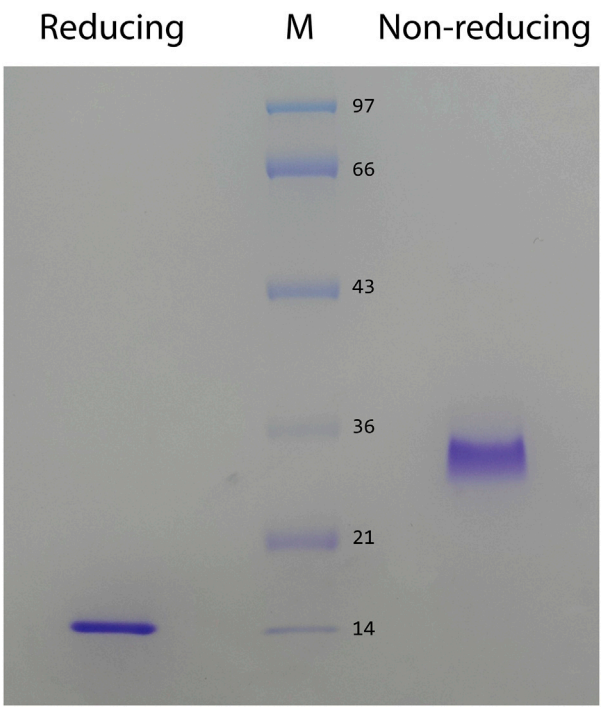

FIGURE 2
SDS PAGE of the purified protein, ZK002, was conducted under reducing (lane 1) and non-reducing (lane 2) conditions.

quantified based on HUVEC tube length, branching points, tube covered area, and total loops. Figure 5A shows the results of the tube formation assay for two batches of ZK002, of which there was no significant batch-to-batch variation. Both batches of ZK002 displayed comparable anti-angiogenic activity, reducing tube length by an average of 36.2%, branching points by an average of 54.2%, tube coverage by an average of 28.7%, and total loops by an average of 59.3% (Figure 5B).

3.3 ZK002 inhibited cell migration and invasion of HUVECs

Based on the above results, we further investigated the *in vitro* anti-angiogenic effects of ZK002. In the wound healing assay, after treatment with ZK002 (5 or 10 μM) for 3 or 6 h, HUVEC migration was analyzed. Results showed that ZK002 could significantly and dose-dependently inhibit the cell migration of HUVECs, up to a 26.4% reduction at 6 h under the 10 μM dose (Figures 6A, B).

We then looked to confirm the anti-cell migratory effect and investigate the anti-invasive effect of ZK002 in VEGF-induced HUVECs via the transwell migration and transwell invasion assays. As shown in Figure 7A, the results confirmed the inhibitory effect of ZK002 on cell migration, completely inhibiting VEGF-induced migration at doses of 1 and 5 μM. Cell invasion was also significantly and dose dependently inhibited by ZK002; there was a 20.5% and 45.6% decrease in invasion of VEGF-induced cells when treated with 1 and 5 μM ZK002 respectively (Figure 7B).

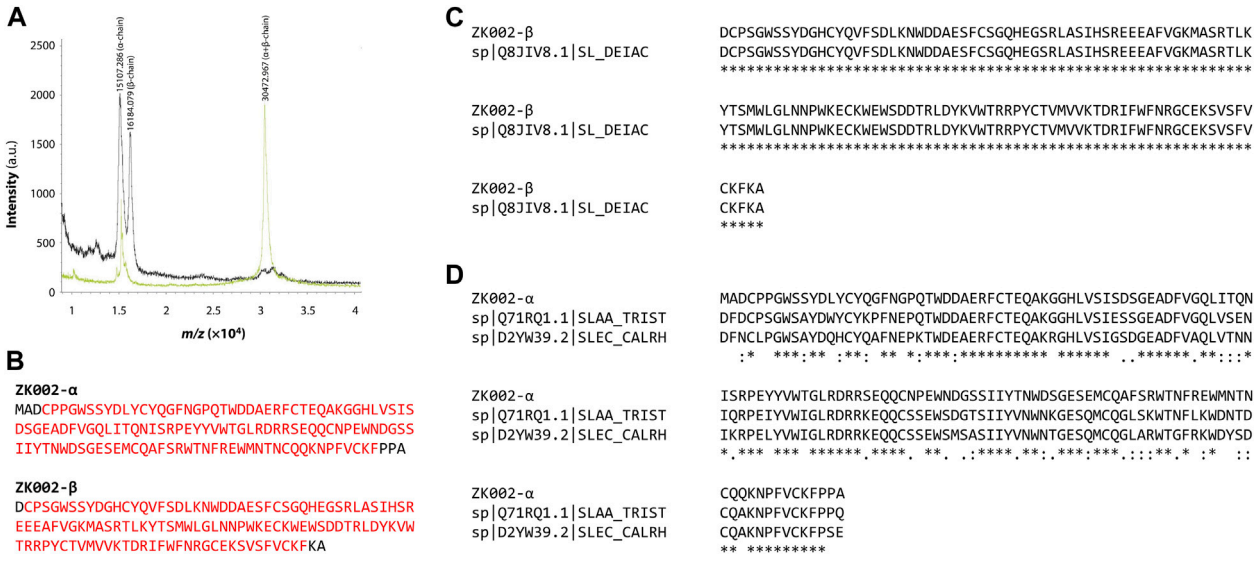

FIGURE 3
Sequence analysis of ZK002. **(A)** MALDI-TOF mass spectrometry results showing the respective masses of the α and β subunits, and the ZK002 heterodimer. **(B)** Sequence of the identified α and β chains of ZK002. NCBI Conserved Domain Search analysis indicated that both ZK002 α and β possessed C-type lectin-like domains characteristic of snaclecs (matching domain sequences highlighted in red). **(C)** The sequence of ZK002 β shared 100% identity with an existing snaclec (Snaclec clone 2100755, Uniprot Q8JIV8.1). **(D)** The sequence of ZK002 α was aligned with the α chain of stejaggregin-A, and the γ chain of rhodocetin.

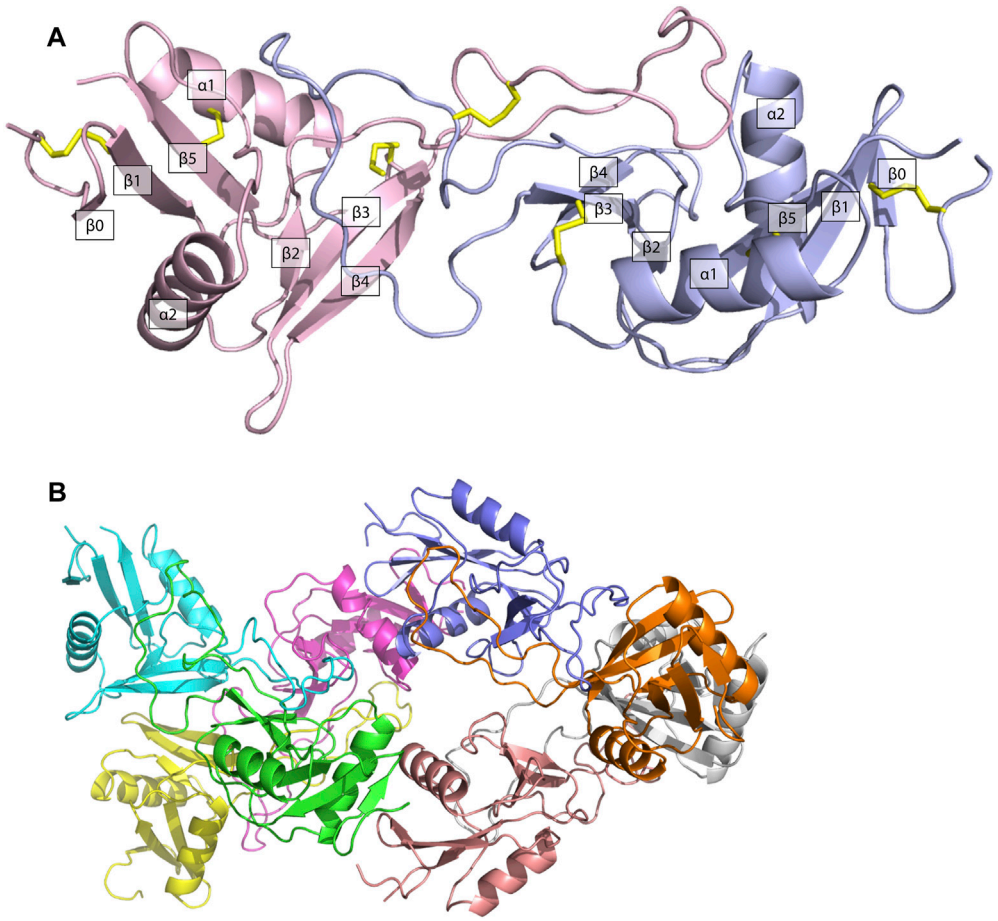

FIGURE 4
The structure of ZK002 was determined by X-ray crystallography. **(A)** Structure of the αβ chain heterodimer of ZK002. The α chain is displayed in light blue, while the β chain is displayed in pink. Disulphide-bonds formed between cysteine residues are indicated in yellow. **(B)** The crystallographic asymmetric unit of ZK002 containing four αβ heterodimers.

3.4 ZK002 exhibited anti-angiogenic effects in the chicken embryo chorioallantoic membrane assay

After demonstrating the *in vitro* anti-angiogenic efficacy of ZK002, we next examined its *in vivo* anti-angiogenic effects. In the chicken embryo CAM assay, ZK002 dose-dependently suppressed VEGF-induced angiogenesis. At the dose of 16.4 μM, vessel area was decreased by 32.6%, vessel length by 23.3%, and branch points by 52.2% when compared to control (Figures 8A, B). Notably, the ZK002 + ZK002 mAb group showed a similar extent of angiogenesis as the untreated control, confirming that the observed anti-angiogenic effects were due to ZK002 treatment.

3.5 *In vivo* anti-angiogeneic effects of ZK002 in the matrigel plug assay and directed *in vivo* angiogenesis assay models

We further investigated the anti-angiogenic effects of ZK002 by performing an *in vivo* matrigel plug assay in mice. 3 μM of ZK002 was mixed with matrigel and endothelial growth supplements (bFGF/heparin) and injected into the abdomens of mice. As shown in Figure 9A, neovascularization was seen in the matrigel plug upon induction with bFGF/heparin. In the presence of ZK002, the matrigel plugs were a light red or light yellow color compared with induction control, and neovascularization was almost completely attenuated. This observation was validated by measuring the hemoglobin content in each matrigel plug. As shown in Figure 9B, treatment with ZK002 dramatically reduced the hemoglobin content by 96.2%.

The above results were confirmed in the DIVAA assay, where in the presence of ZK002, again there was almost complete attenuation of neovascularization. Quantification of hemoglobin content showed an 88.6% reduction in ZK002 treated mice (Figure 10). The above results provide further support for the *in vivo* anti-angiogenic effects of ZK002.

3.6 ZK002 inhibited activation of VEGF and VEGF-induced signaling in HUVECs

After demonstrating the *in vitro* and *in vivo* anti-angiogenic activity of ZK002, we investigated the underlying molecular mechanisms involved. As VEGF signaling is the central modulatory pathway in

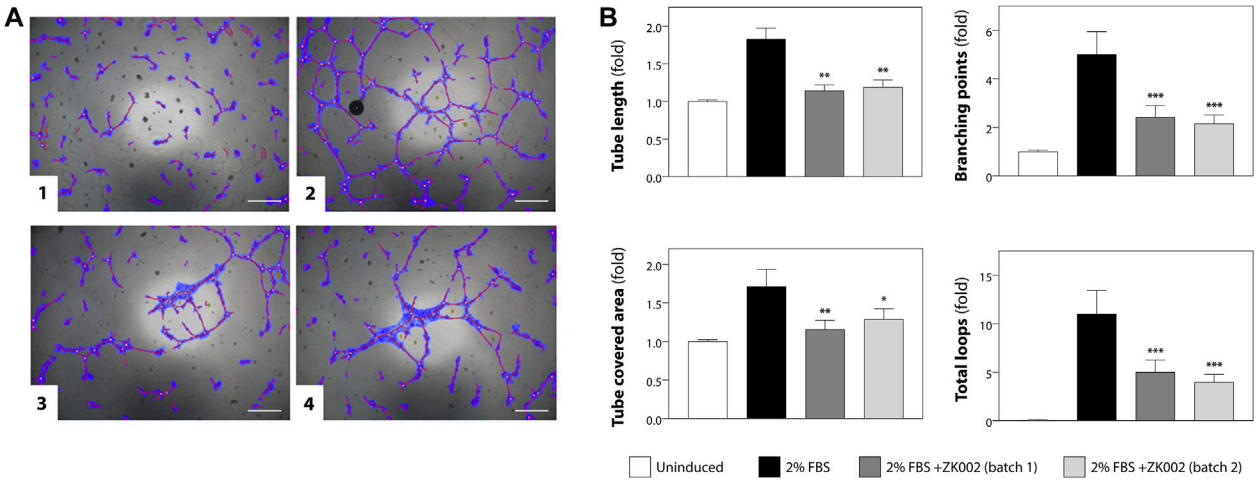

FIGURE 5
Analysis of anti-angiogenic activity of ZK002 by HUVEC tube formation assay. **(A)** HUVECs (2×10^4) were seeded in 96-well plates containing matrigel, and incubated with 1) Vehicle, 2) 2% FBS, 3) 2% FBS with batch 1 of ZK002 (5 μM), and 4) 2% FBS with batch 2 of ZK002 (5 μM). Capillary tube structures were photographed with a digital camera attached to a microscope (×40 magnification) and analyzed using WimTube software. Scale bar, 200 μm. **(B)** Quantification of the tube formation assays of the four experimental groups. Four aspects of tube formation: i) total tube length, ii) total branching points, iii) total tube covered area, and iv) total loops, were analyzed and scored. *$p < 0.05$, **$p < 0.005$, ***$p < 0.001$ vs. induction control.

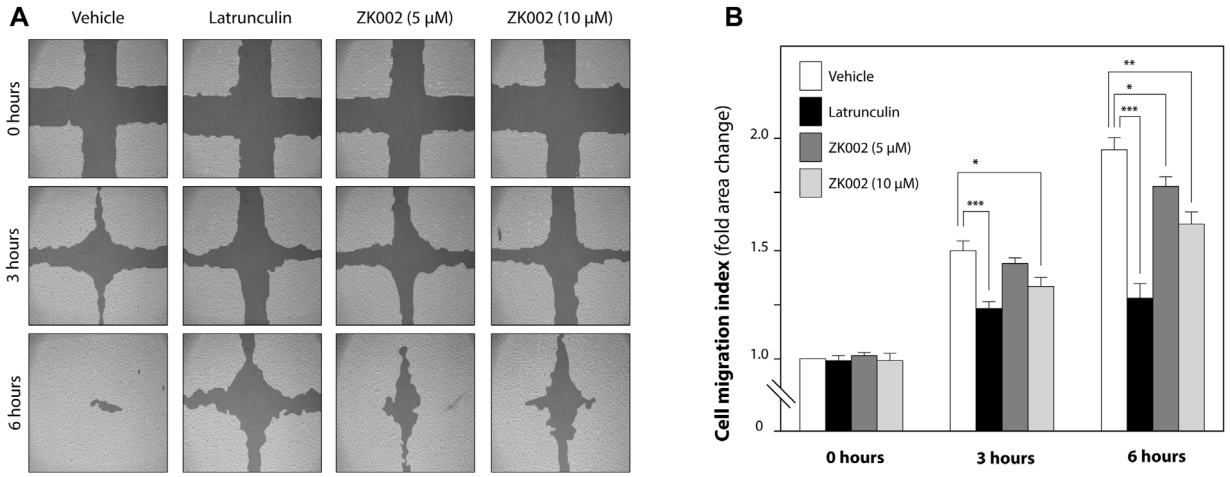

FIGURE 6
Inhibitory effect of ZK002 on HUVEC cell migration in the *in vitro* wound healing assay. **(A)** Representative photographs of cell migration 0, 3, and 6 h after treatment with ZK002 at 5 or 10 μM. Latrunculin was included as a positive control. **(B)** Cell migration quantification by TScratch software, expressed as cell migration index. *$p < 0.05$, **$p < 0.005$, ***$p < 0.001$ vs. vehicle control.

angiogenesis, we examined signaling molecules related to the VEGF signaling cascade and VEGF-induced cell proliferation and migration to see if treatment with ZK002 could affect their regulation.

Serum starved HUVECs were pre-treated with vehicle (negative control) or 5 μM ZK002 for 3 h, after which they were induced with VEGF (100 ng/mL) for 0, 2.5, 5, and 10 min. Western blot analysis was carried out to detect the phosphorylation status of select key proteins. Results showed that addition of VEGF indeed induced the phosphorylation of VEGF receptor 2 (VEGFR2), and pre-treatment with ZK002 (5 μM) significantly reduced the VEGF-induced phosphorylation of its receptor (Figures 11A, B). Next, several downstream mediators of VEGF-induced cell migration were examined, including eNOS, p38, LIMK, and HSP27. Pre-treatment with ZK002 could partially reduce the VEGF-induced phosphorylation of the aforementioned molecules. ZK002 also rescued the VEGF-induced decrease in phosphorylation of cofilin, a protein with actin depolymerization activity that is inhibited by LIMK-mediated phosphorylation. We also found that ZK002 treatment could inhibit VEGF-induced phosphorylation of the pro-cell proliferation mediator ERK1/2, suggesting its cell proliferation-inhibitory potential (Figures 11A, B).

Altogether, the above results clearly indicated that ZK002 could block VEGF-related signaling cascades, potentially leading to decreased cell migration and proliferation, and its anti-angiogenic effects.

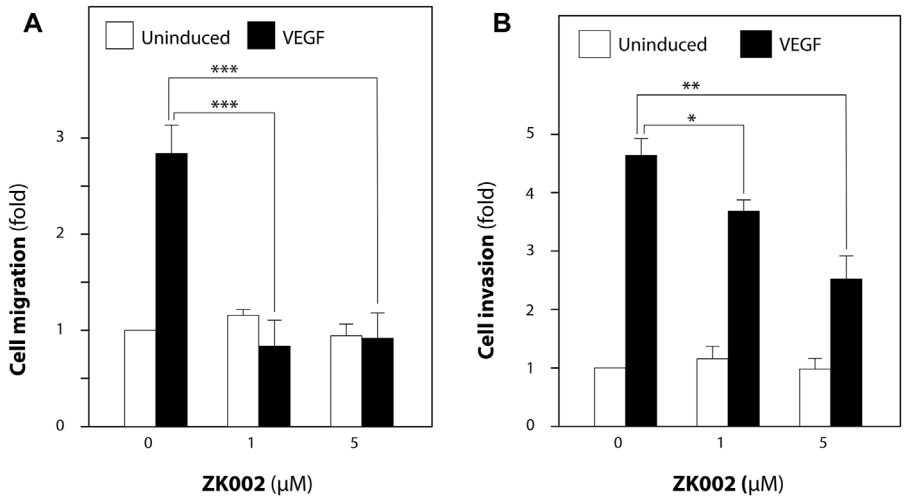

FIGURE 7
ZK002 inhibited migration and invasion of HUVECs. Effect of ZK002 on VEGF-induced (10 ng/mL) HUVEC migration and invasion in **(A)** Transwell migration assay and **(B)** Transwell invasion assay. *$p < 0.05$, **$p < 0.005$, ***$p < 0.001$ vs. induction control.

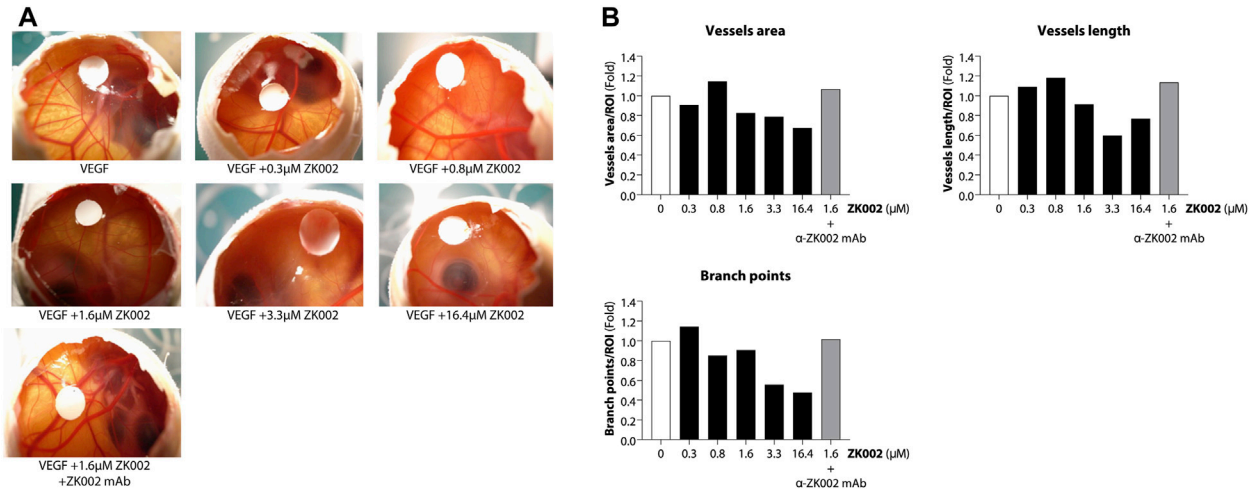

FIGURE 8
Anti-angiogenic effect of ZK002 in the chicken embryo chorioallantoic membrane (CAM) assay. Chicken embryos were induced with VEGF and treated with ZK002 at various doses from 0.3 to 16.4 μM. A VEGF-induced embryo treated with 1.64 μM ZK002 and an excess amount of anti-ZK002 monoclonal antibody was included as a control. **(A)** Representative photos show blood vessel growth at the experimental endpoint. **(B)** The effect of ZK002 on angiogenesis parameters were assessed using IKOSA CAM Assay software.

3.7 ZK002 upregulated metalloproteinase inhibitor gene expression and downregulated gene expression of components of VEGF-induced signaling in HUVECs

We further investigated the effect of ZK002 on the expression of angiogenesis-related genes, whether pro-angiogenic (MMP2/9/14, ANGPTL4, PECAM1, SERPINE1) or anti-angiogenic (TIMP1–3). 24 h of ZK002 treatment in HUVECs significantly and dose-dependently increased expression of the metalloproteinase inhibitor gene TIMP3 when compared to vehicle treated cells (5 μM, 1.34 fold; 10 μM, 1.76 fold; Figure 12A), suggesting that ZK002-mediated inhibition of angiogenesis potentially involved upregulation of metalloproteinase inhibitors. We then continued our analysis, investigating the inhibitory effects of ZK002 on a panel of VEGF-induced signaling cascade genes. We saw that ZK002 treatment could significantly and dose-dependently downregulate the expression of the VEGF-related genes PPP3R2 and SH2D2A (Figure 12B).

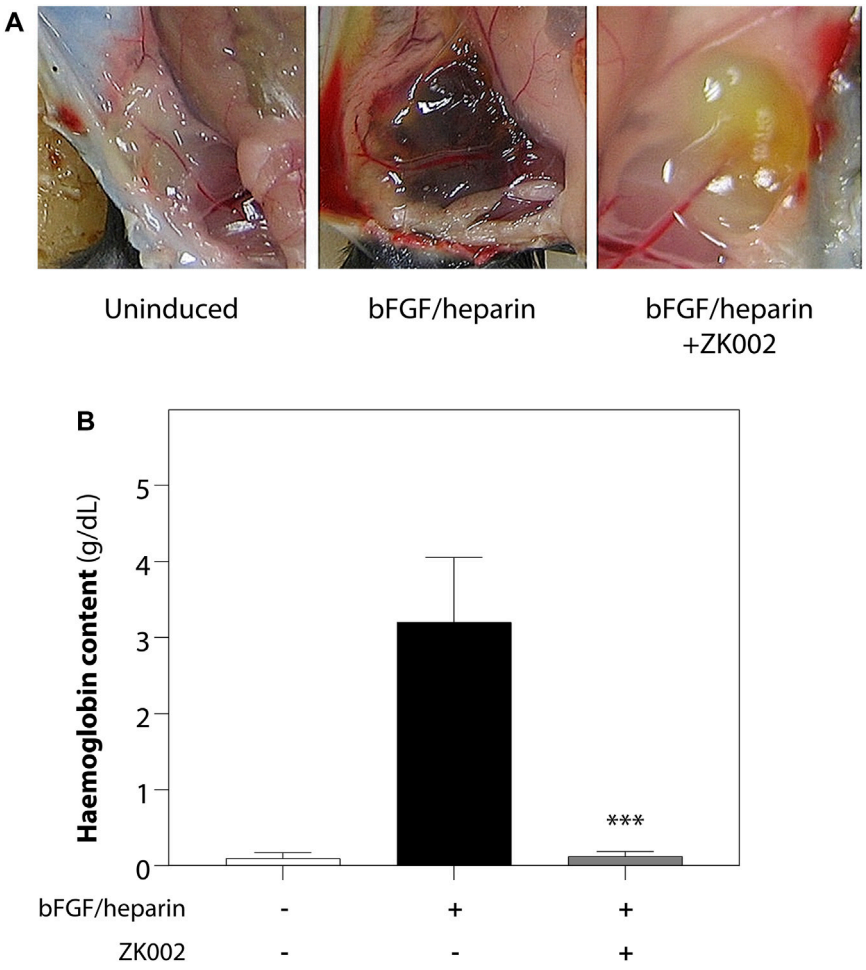

FIGURE 9
Inhibition of bFGF/heparin-induced *in vivo* angiogenesis by ZK002 in the matrigel plug assay. **(A)** Representative images showing gross morphology of gel plugs in uninduced (matrigel alone), induced (bFGF/heparin), and ZK002 (3 μM) treatment groups. **(B)** Extent of angiogenesis was quantified via measurement of hemoglobin content in matrigel plugs. ***$p < 0.001$ vs. induced group.

3.8 ZK002 reduced the gene expression of pro-inflammatory cytokines in LPS-induced macrophages

As angiogenesis and inflammation are co-occurrent in many diseases, to investigate whether the scope of the activity of ZK002 could be expanded, we also assessed its potential anti-inflammatory activity. The anti-inflammatory activity of ZK002 was first evaluated by assessment of pro-inflammatory cytokines in LPS-induced RAW264.7 macrophages. Results showed that treatment with ZK002 could significantly decrease gene expression of IL-6, IL-1β, and TNF-α. Notably, 1 μM ZK002 significantly reduced the gene expression levels of LPS-induced IL-6 by 53.8% when compared to vehicle treatment. Additionally, ZK002 significantly reduced the gene expression of IL-1β and TNF-α by 27.5% and 31.8% respectively (Figure 13). These results indicated the *in vitro* anti-inflammatory potential of ZK002.

3.9 *In vivo* anti-inflammatory effects of ZK002 in the acute carrageenan-induced inflammation rat model

Upon observing the *in vitro* anti-inflammatory effects of ZK002, we next assessed its *in vivo* anti-inflammatory potential in the acute carrageenan-induced inflammation rat model. Rats were pre-treated with the test compounds for 1 h before induction of edema by injection of hind paws with carrageenan. Paw volume was then measured every 2 h for 6 h in total. At 6 h, we found that 2.5 mg/kg ZK002 could attenuate paw swelling by 46% when compared to vehicle control. This reduction by ZK002 was similar in scale to the positive control, indomethacin, which reduced swelling by 56% but at a comparatively larger dose of 10 mg/kg, indicating the potent anti-inflammatory ability of ZK002 (Figure 14).

Based on these results we identified ZK002 as a dual function protein, exhibiting anti-angiogenic and anti-inflammatory activity, *in vitro* and *in vivo*.

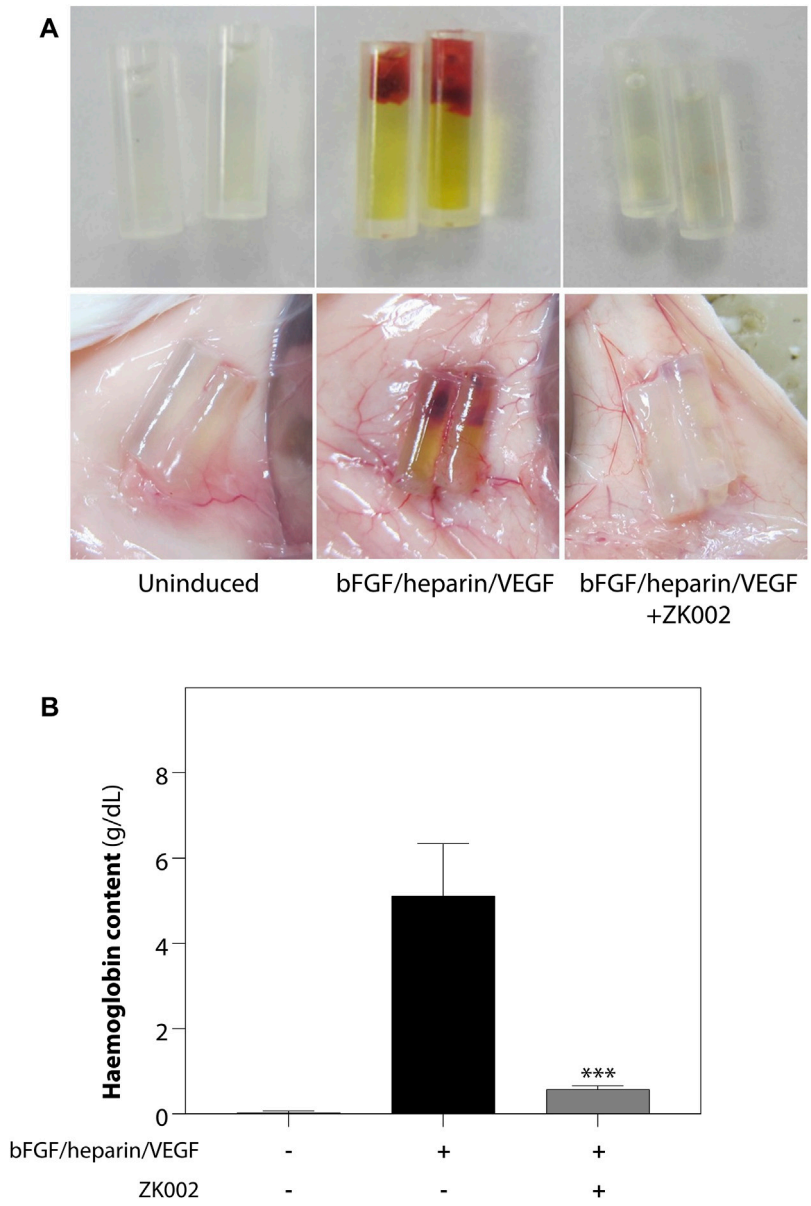

FIGURE 10
Inhibition of VEGF/bFGF/heparin-induced *in vivo* angiogenesis by ZK002 in the DIVAA assay. **(A)** Representative photographs showing the gross morphology of angioreactors of uninduced (basement membrane extract alone), induced (VEGF/bFGF/heparin), and ZK002 (3 μM) treatment groups. **(B)** Extent of angiogenesis was quantified by measurement of hemoglobin content in angioreactors. ***$p < 0.001$ vs. induced group.

4 Discussion

As pathogenic angiogenesis plays a key role in a multitude of diseases, development of novel agents with anti-angiogenic activity are much warranted. In this study, we demonstrated the isolation, purification, and characterization of a novel snake venom protein with anti-angiogenic and anti-inflammatory activity, ZK002.

Snake venoms are a rich natural source for the discovery of novel molecules with biological functions. The most well-studied anti-angiogenic snake venom compounds belong to the disintegrin family of proteins. First isolated from the Viperidae family of venomous snakes, disintegrins were initially identified as inhibitors of platelet aggregation, and several anti-thrombotic drugs have been developed using snake venom disintegrins as lead compounds (e.g., Eptifibatide from the snake venom protein Barbourin, and Tirofiban from the snake venom protein Echistatin). In addition to their anti-thrombotic function, further research has also demonstrated the strong anti-angiogenic activity of disintegrins (Calvete et al., 2005; Swenson et al., 2010; Lazarovici et al., 2019). Another group of proteins found in snake venom are snake venom C-type lectin-like proteins, also known as snaclecs (snake C-type lectins). Snaclecs are approximately 30 kDa in mass with heterodimeric structures comprised of homologous α and β subunits linked by a disulfide bond. Various studies have demonstrated the purification and characterization of snaclecs from the venom of *D. acutus*, with a wide range of biological

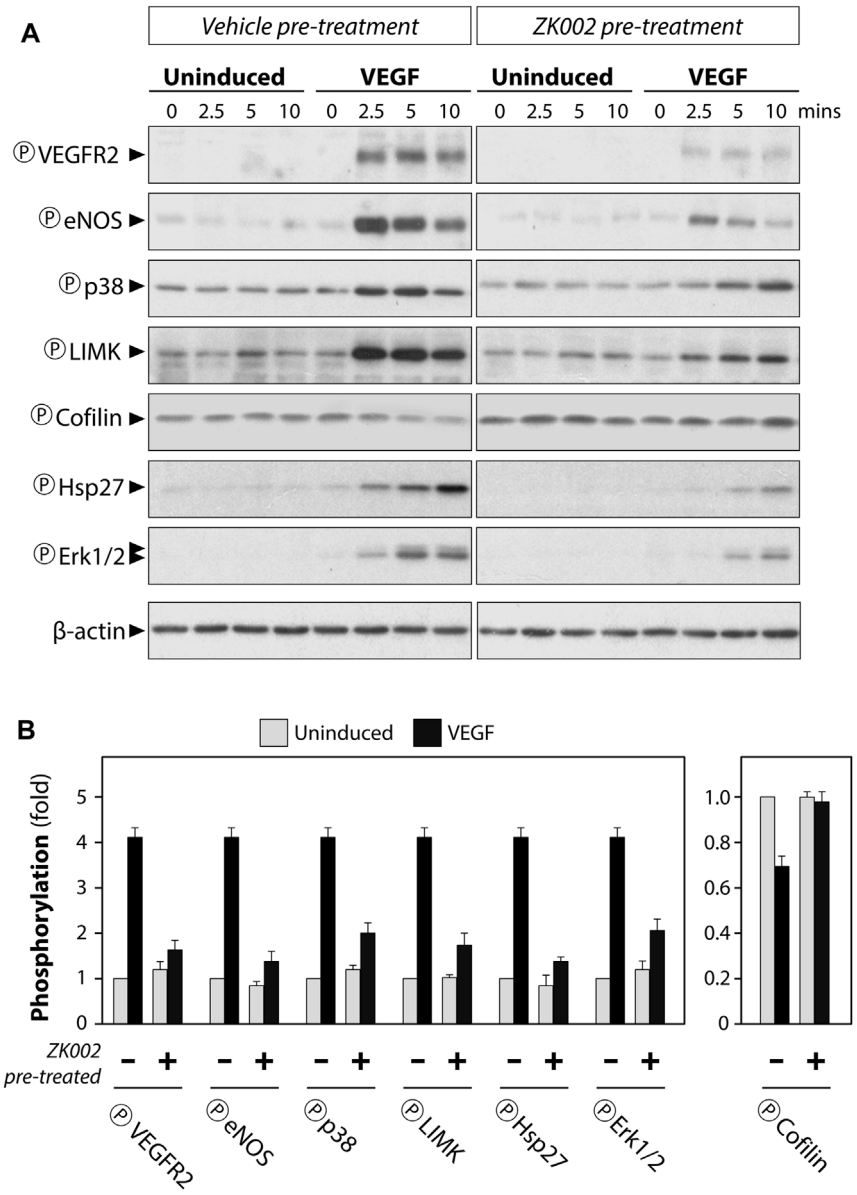

FIGURE 11
Attenuation of VEGF-induced phosphorylation in HUVECs by ZK002. Serum starved HUVECs were pre-treated with vehicle (water) or 5 μM ZK002 for 3 h, after which they were induced for 0, 2.5, 5, and 10 min with VEGF (100 ng/mL). **(A)** Western blotting results of the phosphorylated forms of select VEGF-related mediators. **(B)** Quantification of band density at the 5 min timepoint was conducted using QuantityOne software analysis from replicate results.

activities including platelet aggregation, inhibition of platelet aggregation, anti-coagulant activity, erythrocyte-targeting, endothelial adhesion, and angiogenesis (Liu et al., 2002; Xu et al., 2004; Li et al., 2005; Wang, 2008; Zhang et al., 2012). In other studies, snaclecs have been demonstrated to exert anti-angiogenic effects through their modulation of platelet agglutination and coagulation activities (Yeh et al., 2000; Morita, 2005).

In the first part of this paper, we described the isolation and purification of ZK002 and its identification as a 30 kDa heterodimer of α and β peptide chains of the snaclec class of proteins. In contrast to the classical C-type lectins, to which they share sequence homology, snaclecs lack carbohydrate and Ca^{2+} binding abilities and lectin activity. Snaclecs have been shown to act on membrane receptors, coagulation factors, and proteins essential to hemostasis to carry out anticoagulant and antithrombotic activities (Arlinghaus and Eble, 2012). Previous studies have demonstrated that snaclecs, including EMS16 from *Echis multisquamatus*, and Vixapatin from *Vipera xantina palestinae*, exhibit anti-angiogenic effects (Marcinkiewicz et al., 2000; Momic et al., 2012; Chung et al., 2017), indicating the potential for this class of protein as anti-angiogenic drugs.

Our results showed that ZK002 exhibited potent anti-angiogenic activity, with inhibition of tube formation, cell migration, and cell invasion in VEGF-induced HUVECs, and significant

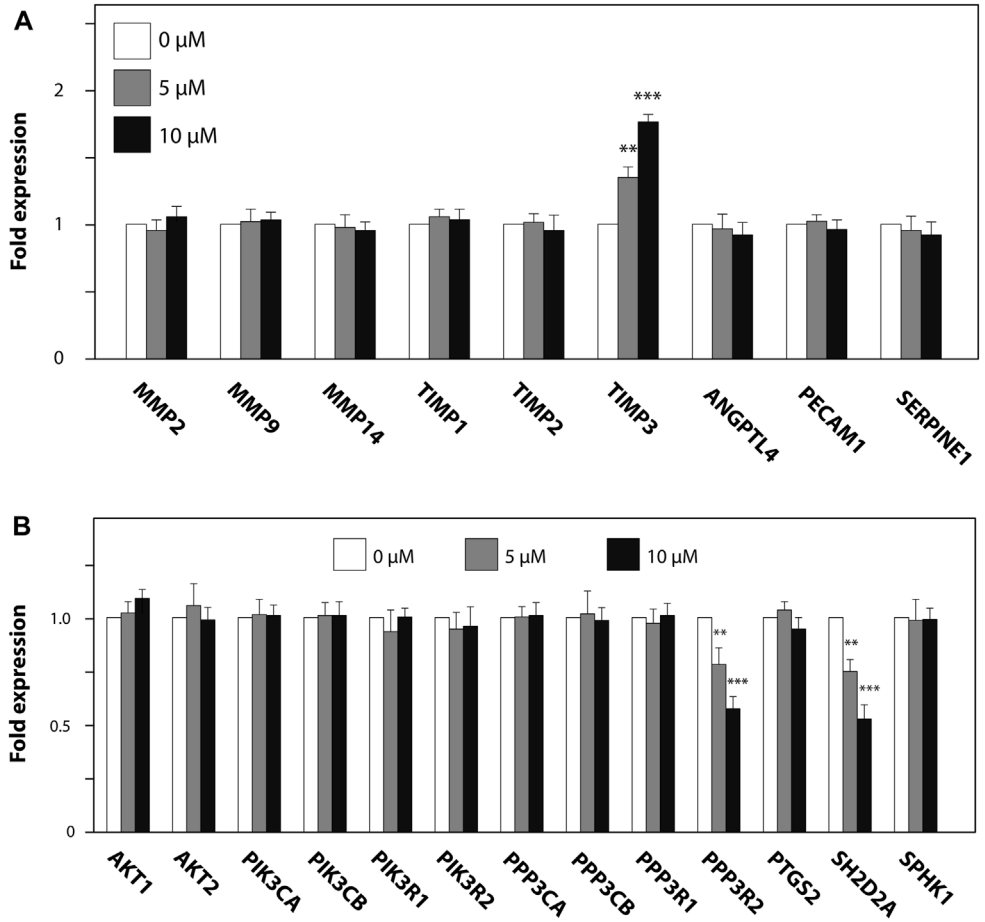

FIGURE 12
Modulation of metalloproteinase inhibitor and VEGF-induced signaling cascade genes in HUVECs by ZK002. HUVECs were treated for 24 h with 5 or 10 μM ZK002 before collection for qPCR analysis of **(A)** metalloproteinase inhibitor and **(B)** VEGF signaling-related genes. $^{**}p < 0.005$, $^{***}p < 0.001$ vs. untreated control.

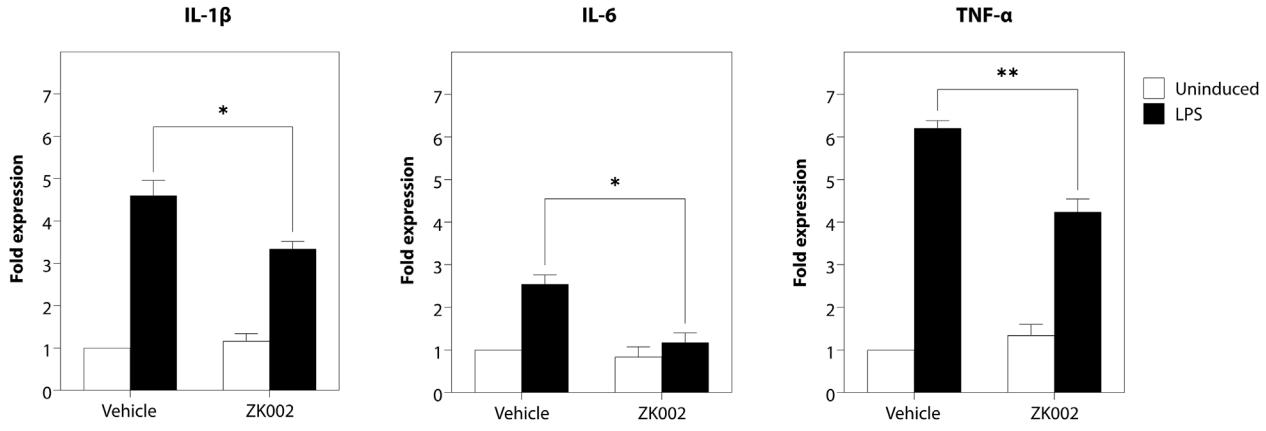

FIGURE 13
ZK002 inhibited pro-inflammatory cytokine gene expression in LPS-induced RAW264.7 cells. RAW264.7 macrophages (1×10^5) were seeded in each well of a 12 well plate for 24 h. Cells were pre-treated with or without 1 μM ZK002 for 24 h, then stimulated with 0.1 μg/mL LPS for another 6 h. The mRNA levels of IL-1β, IL-6, and TNF-α in cell lysates were measured by qPCR. $^{*}p < 0.05$, $^{**}p < 0.005$ vs. vehicle-treated control.

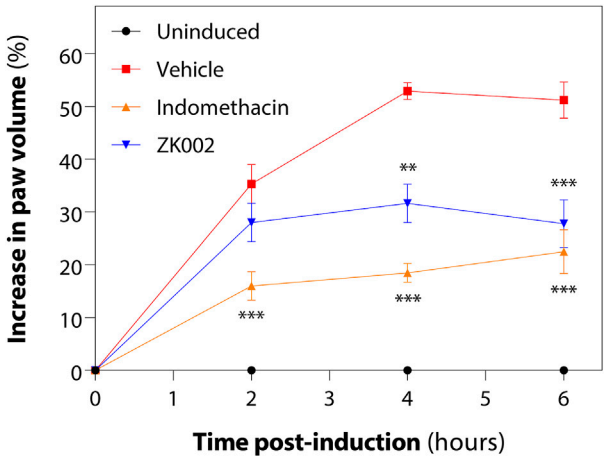

FIGURE 14
ZK002 inhibited rat paw inflammation in the carrageenan-induced rat model. SD rats were divided into 4 groups: uninduced, vehicle, 10 mg/kg indomethacin, and 2.5 mg/kg ZK002. Drugs were given by intraperitoneal injection (ZK002) or oral administration (indomethacin) 1 h before induction. Edema was induced in hind paws of by subcutaneous injection of carrageenan. Paw volume of each animal was measured with a plethysmometer every 2 h. $^{**}p < 0.01$, $^{***}p < 0.001$ vs. vehicle-treated control.

anti-angiogenic activity in multiple *in vivo* models. The VEGF proteins are key mediators of angiogenesis, with VEGF-A the prototype member of a family that also includes VEGF-B, VEGF-C, VEGF-D, VEGF-E, and PlGF. VEGF-A binds to two tyrosine kinase receptors, VEGFR-1 and VEGFR-2, VEGFR-2 being the major receptor involved in angiogenic signaling. During angiogenesis, activation of VEGFR-2 promotes cell proliferation, migration, and vascular permeabilization (Apte et al., 2019). In our study, we found that ZK002 treatment inhibited activation of VEGFR2, an event located at the proximal point of VEGF-mediated signaling (Abhinand et al., 2016; Abhinand et al., 2023).

As various studies have shown that VEGF-mediated signaling can trigger activation of MAPK, PI3K/AKT, and eNOS/NO pathways (Koch and Claesson-Welsh, 2012; Yang and Li, 2018), we examined the effects of ZK002 on key molecules of these pathways. Our results showed that ZK002 inhibited the activation of eNOS, p38, HSP27, and LIMK/cofilin activity, all of which have been shown to promote cell migration (Lamalice et al., 2007). We also found that ZK002 inhibited ERK1/2, which mediates cell proliferation during angiogenesis (Srinivasan et al., 2009). This inhibition of pathways implicated in VEGF-induced cell migration and proliferation by ZK002 may further contribute to its anti-angiogenic activity.

To further investigate the molecular mechanisms of ZK002, we examined its effect on angiogenesis-related genes, finding upregulated expression of TIMP3 after ZK002 treatment. Members of the matrix metalloproteinase (MMP) family of proteins are key players in the extracellular matrix (ECM) remodeling activity associated with angiogenesis (Rundhaug, 2005; Ma et al., 2020), and tissue inhibitor of metalloproteinases (TIMPs) are natural inhibitors of the MMP protein family. There exist 4 members of the TIMP family, TIMP 1 to 4, each possessing different specificities and efficacies of MMP inhibition and also exhibiting different activities outside of MMP inhibition. TIMP3 is the only TIMP family member with a high affinity for ECM proteoglycans, and it possesses the broadest range of substrates, including not only all MMPs, but also other ECM-remodeling enzymes from the ADAM (a disintegrin and metalloproteinases) and ADAMTS (ADAM with thrombospondin motifs) families (Brew and Nagase, 2010; Fan and Kassiri, 2020). The TIMP3 gene encodes metalloproteinase inhibitor 3, a potent inhibitor of angiogenesis, whose mechanism of action involves direct binding to VEGFR2, thereby blocking the activity of VEGF (Qi et al., 2003). Previous studies have shown that treatment of VEGF-induced HUVECs with TIMP3 could inhibit their proliferation, migration, and invasion, and also tube formation. Additional studies in the chicken CAM assay demonstrated that angiogenesis was also inhibited by TIMP3 treatment (Lafleur et al., 2003). In other work, silencing of TIMP3 increased expression of MMP2 and MMP9 and capillary network formation (Hu et al., 2016). Altogether, these findings highlight the anti-angiogenic activity of TIMP3, which we found was upregulated by ZK002.

We also found that ZK002 inhibited gene expression of components of the VEGF-induced signaling cascade, PPP3R2 and SH2D2A. PPP3R2 encodes calcineurin subunit B type 2, the calcium-binding regulatory subunit of calcineurin, a calcium-dependent serine/threonine phosphatase that plays a major role in coupling calcium signals to cellular responses (Li et al., 2011). Increased VEGF signaling leads to increased cytoplasmic calcium, activating calcineurin to dephosphorylate the nuclear factor of activated T cells (NFAT) family of transcription factors, which have been shown to be critical in VEGF-induced angiogenesis. Calcineurin-activated NFAT can then translocate to the nucleus to initiate expression of pro-angiogenic target genes (Okamura et al., 2000; Zaichuk et al., 2004; Minami et al., 2013). Previous studies have shown that treatment with various calcineurin inhibitors, including Down syndrome critical region-1 (DSCR1), plasma membrane calcium ATPase (PMCA4), and cyclosporin A could inhibit VEGF-induced *in vitro* and *in vivo* angiogenesis, indicating the relevance of calcineurin inhibition in anti-angiogenesis (Rafiee et al., 2004; Baek et al., 2009; Baggott et al., 2014).

SH2D2A encodes T cell specific adapter protein (TSAd) (Dai et al., 2000), which has been shown to be critical for VEGF-A/VEGFR2 mediated angiogenesis in tumors (Matsumoto et al., 2005). TSAd binds to phosphorylated Y951 on VEGFR2 via its SH2 domain and to the SH3 domain of c-Src via its proline-rich domain to regulate actin reorganization and endothelial cell migration. This VEGFR2-TSAd–c-Src pathway was found to be required for regulation of vascular permeability and angiogenic sprouting, indicating its potential for targeting in pathogenic angiogenesis (Matsumoto et al., 2005; Sun et al., 2012; Gordon et al., 2016). Thus, the inhibition of the two pro-angiogenic genes PPP3R2 and SH2D2A by ZK002 provides further insight into the potential mechanism of its anti-angiogenic activity.

Through the above results we demonstrated that ZK002 could inhibit VEGF -induced, and -downstream signaling. On the other

hand, findings from our matrigel plug assay showed that ZK002 could also inhibit FGF-induced angiogenesis, indicating that ZK002 may potentially also act via VEGF-independent mechanisms. The specific molecular target of the anti-angiogenic activity of ZK002 remains to be identified; to further our understanding of the molecular mechanism of ZK002, its direct binding partner is an important item that demands additional investigation.

We also investigated the potential anti-inflammatory effects of ZK002. Our *in vitro* assessments showed that ZK002 could inhibit the major proinflammatory cytokines IL-1β, IL-6, and TNF-α, while *in vivo* investigation demonstrated its potent anti-inflammatory activity in the carrageenin-induced inflammation rat model. Whether this anti-inflammatory activity of ZK002 is linked to, or independent, of its anti-angiogenic effect is of interest for exploration in further studies.

In this study, we demonstrated that the snake venom protein ZK002 exhibited dual anti-angiogenic and anti-inflammatory functions. Angiogenesis and inflammation play a key role in the pathogenesis of many diseases such as cancer, diabetic retinopathy, arthritis, atherosclerosis, obesity, etc. (Carmeliet, 2003; Ribatti, 2017). Based on its dual activity identified in this study, ZK002 would be able to target two pathological aspects at once–a strategic advantage for the treatment of these diseases, highlighting its promise for further development. On the other hand, previous studies have shown that snake venom proteins may also exhibit potential unwanted side effects (Yeh et al., 2000; Li et al., 2005). For future development of ZK002 as a dual functional anti-angiogenic and anti-inflammatory therapeutic protein, further research in the areas of its safety and toxicity are required.

5 Conclusion

In this study we isolated and purified a novel protein, ZK002, from venom of the snake *D. acutus*. We then demonstrated that this protein possesses anti-angiogenic and anti-inflammatory effects. In cell line studies, we showed that ZK002 could inhibit the migration and invasion of HUVECs. In *in vivo* models, we demonstrated and confirmed the anti-angiogenic activity of ZK002. Studies into the molecular mechanisms of ZK002 identified inhibition of VEGF-induced signaling components related to cell migration and proliferation, including eNOS, p38, HSP27, LIMK/cofilin, and ERK1/2. Gene expression analysis identified upregulation of the anti-angiogenic metalloproteinase gene TIMP3, and downregulation of the pro-angiogenic genes PPP3R2 and SH2D2A. Further, we also showed that ZK002 could decrease expression of the pro-inflammatory cytokines IL-6, IL-1β, and TNF-α, and inhibit inflammation in an animal model.

Altogether, the results of this study highlight the rich potential for further development of ZK002 as a novel anti-angiogenic and anti-inflammatory protein drug for the treatment of diseases with involvement of pathogenic angiogenesis and inflammation.

Data availability statement

The datasets presented in this study can be found in online repositories. The names of the repository/repositories and accession number(s) can be found below: http://www.wwpdb.org/, 7QAJ https://www.ebi.ac.uk/pride/archive/, PXD037093.

Ethics statement

The animal study was approved by The Animal Subjects Ethics Sub-Committee (ASESC) of The Hong Kong Polytechnic University. The study was conducted in accordance with the local legislation and institutional requirements.

Author contributions

BC, W-YW, and MM-LL: Investigation, Formal analysis, Writing–original draft, Writing–review and editing. XD and PY-KY: Investigation. KW-KT and W-LWH: Conceptualization, Supervision. ML and X-YL: Conceptualization, Resources. WC-ST: Conceptualization, Supervision, Validation, Project administration, Writing–review and editing. All authors contributed to the article and approved the submitted version.

Funding

This study was supported in part by the Innovation and Technology Fund (UIM/307 to WC-ST and UIM/208 to W-LWH) and The Hong Kong Polytechnic University (Internal grant #1-ZVTU to WC-ST).

Acknowledgments

The authors would like to thank Dr. So Pui Kin (University Research Facility in Life Sciences, The Hong Kong Polytechnic University), Dr. Sirius Tse (University Research Facility in Chemical and Environmental Analysis, The Hong Kong Polytechnic University), and Mr. Thomas Lam Ka Yam for their assistance with the mass spectrometry work. We would also like to thank the Israel Structural Proteomics Center of the Weizmann Institute of Science for their assistance with the X-ray crystallography, and the University Research Facility in Life Sciences of the Hong Kong Polytechnic University for technical and equipment support.

Conflict of interest

Author XD was employed by Lee's Pharmaceutical (HK) Limited. Authors ML and X-YL were employed by Zhaoke (Hong Kong) Ophthalmology Pharmaceutical Limited.

The remaining authors declare that the research was conducted in the absence of any commercial or financial relationships that could be construed as a potential conflict of interest.

Publisher's note

All claims expressed in this article are solely those of the authors and do not necessarily represent those of their affiliated organizations, or those of the publisher, the editors and the reviewers. Any product that may be evaluated in this article, or claim that may be made by its manufacturer, is not guaranteed or endorsed by the publisher.

Supplementary material

The Supplementary Material for this article can be found online at: https://www.frontiersin.org/articles/10.3389/fphar.2023.1227962/full#supplementary-material

References

Abhinand, C. S., Galipon, J., Mori, M., Ramesh, P., Prasad, T. S. K., Raju, R., et al. (2023). Temporal phosphoproteomic analysis of VEGF-A signaling in HUVECs: An insight into early signaling events associated with angiogenesis. *J. Cell. Commun. Signal* 17 (3), 1067–1079. doi:10.1007/s12079-023-00736-z

Abhinand, C. S., Raju, R., Soumya, S. J., Arya, P. S., and Sudhakaran, P. R. (2016). VEGF-A/VEGFR2 signaling network in endothelial cells relevant to angiogenesis. *J. Cell. Commun. Signal* 10 (4), 347–354. doi:10.1007/s12079-016-0352-8

Afonine, P. V., Grosse-Kunstleve, R. W., Echols, N., Headd, J. J., Moriarty, N. W., Mustyakimov, M., et al. (2012). Towards automated crystallographic structure refinement with phenix.refine. *Acta Crystallogr. Sect. D-Structural Biol.* 68, 352–367. doi:10.1107/S0907444912001308

Annese, T., Tamma, R., and Ribatti, D. (2023). IKOSA(®) CAM assay application to quantify blood vessels on chick chorioallantoic membrane (CAM). *Methods Mol. Biol.* 2572, 129–139. doi:10.1007/978-1-0716-2703-7_10

Apte, R. S., Chen, D. S., and Ferrara, N. (2019). VEGF in signaling and disease: Beyond discovery and development. *Cell.* 176 (6), 1248–1264. doi:10.1016/j.cell.2019.01.021

Arlinghaus, F. T., and Eble, J. A. (2012). C-type lectin-like proteins from snake venoms. *Toxicon* 60 (4), 512–519. doi:10.1016/j.toxicon.2012.03.001

Baek, K. H., Zaslavsky, A., Lynch, R. C., Britt, C., Okada, Y., Siarey, R. J., et al. (2009). Down's syndrome suppression of tumour growth and the role of the calcineurin inhibitor DSCR1. *Nature* 459 (7250), 1126–1130. doi:10.1038/nature08062

Baggott, R. R., Alfranca, A., López-Maderuelo, D., Mohamed, T. M., Escolano, A., Oller, J., et al. (2014). Plasma membrane calcium ATPase isoform 4 inhibits vascular endothelial growth factor-mediated angiogenesis through interaction with calcineurin. *Arterioscler. Thromb. Vasc. Biol.* 34 (10), 2310–2320. doi:10.1161/atvbaha.114.304363

Brew, K., and Nagase, H. (2010). The tissue inhibitors of metalloproteinases (TIMPs): An ancient family with structural and functional diversity. *Biochim. Biophys. Acta* 1803 (1), 55–71. doi:10.1016/j.bbamcr.2010.01.003

Calvete, J. J., Marcinkiewicz, C., Monleón, D., Esteve, V., Celda, B., Juárez, P., et al. (2005). Snake venom disintegrins: Evolution of structure and function. *Toxicon* 45 (8), 1063–1074. doi:10.1016/j.toxicon.2005.02.024

Carmeliet, P. (2003). Angiogenesis in health and disease. *Nat. Med.* 9 (6), 653–660. doi:10.1038/nm0603-653

Chen, P. C., Huang, M. N., Chang, J. F., Liu, C. C., Chen, C. K., and Hsieh, C. H. (2019). Snake venom proteome and immuno-profiling of the hundred-pace viper, Deinagkistrodon acutus, in Taiwan. *Acta Trop.* 189, 137–144. doi:10.1016/j.actatropica.2018.09.017

Chen, V. B., Arendall, W. B., Headd, J. J., Keedy, D. A., Immormino, R. M., Kapral, G. J., et al. (2010). MolProbity: All-atom structure validation for macromolecular crystallography. *Acta Crystallogr. Sect. D-Structural Biol.* 66, 12–21. doi:10.1107/S0907444909042073

Chung, C. H., Chang, C. H., Hsu, C. C., Lin, K. T., Peng, H. C., and Huang, T. F. (2017). Aggretin venom polypeptide as a novel anti-angiogenesis agent by targeting integrin alpha2beta1. *Sci. Rep.* 7, 43612. doi:10.1038/srep43612

Dai, K. Z., Vergnaud, G., Ando, A., Inoko, H., and Spurkland, A. (2000). The SH2D2A gene encoding the T-cell-specific adapter protein (TSAd) is localized centromeric to the CD1 gene cluster on human Chromosome 1. *Immunogenetics* 51 (3), 179–185. doi:10.1007/s002510050029

Eble, J. A. (2019). Structurally robust and functionally highly versatile-C-type lectin (-Related) proteins in snake venoms. *Toxins (Basel)* 11 (3), 136. doi:10.3390/toxins11030136

Emsley, P., and Cowtan, K. (2004). Coot: Model-building tools for molecular graphics. *Acta Crystallogr. Sect. D-Biological Crystallogr.* 60, 2126–2132. doi:10.1107/S0907444904019158

Evans, P. (2006). Scaling and assessment of data quality. *Acta Crystallogr. D. Biol. Crystallogr.* 62 (1), 72–82. doi:10.1107/S0907444905036693

Fan, D., and Kassiri, Z. (2020). Biology of tissue inhibitor of metalloproteinase 3 (TIMP3), and its therapeutic implications in cardiovascular pathology. *Front. Physiol.* 11, 661. doi:10.3389/fphys.2020.00661

Ferrara, N., and Adamis, A. P. (2016). Ten years of anti-vascular endothelial growth factor therapy. *Nat. Rev. Drug Discov.* 15 (6), 385–403. doi:10.1038/nrd.2015.17

French, S., and Wilson, K. (1978). On the treatment of negative intensity observations. *Acta Crystallogr. Sect. A* 34, 517–525. Doi doi:10.1107/S0567739478001114

Gordon, E. J., Fukuhara, D., Weström, S., Padhan, N., Sjöström, E. O., van Meeteren, L., et al. (2016). The endothelial adaptor molecule TSAd is required for VEGF-induced angiogenic sprouting through junctional c-Src activation. *Sci. Signal* 9 (437), ra72. doi:10.1126/scisignal.aad9256

Hu, J., Ni, S., Cao, Y., Zhang, T., Wu, T., Yin, X., et al. (2016). The angiogenic effect of microRNA-21 targeting TIMP3 through the regulation of MMP2 and MMP9. *PLoS One* 11 (2), e0149537. doi:10.1371/journal.pone.0149537

Joosten, R. P., Joosten, K., Cohen, S. X., Vriend, G., and Perrakis, A. (2011). Automatic rebuilding and optimization of crystallographic structures in the Protein Data Bank. *Bioinformatics* 27 (24), 3392–3398. doi:10.1093/bioinformatics/btr590

Koch, S., and Claesson-Welsh, L. (2012). Signal transduction by vascular endothelial growth factor receptors. *Cold Spring Harb. Perspect. Med.* 2 (7), a006502. doi:10.1101/cshperspect.a006502

Lafleur, M. A., Handsley, M. M., and Edwards, D. R. (2003). Metalloproteinases and their inhibitors in angiogenesis. *Expert Rev. Mol. Med.* 5 (23), 1–39. doi:10.1017/s1462399403006628

Lamalice, L., Le Boeuf, F., and Huot, J. (2007). Endothelial cell migration during angiogenesis. *Circ. Res.* 100 (6), 782–794. doi:10.1161/01.RES.0000259593.07661.1e

Lazarovici, P., Marcinkiewicz, C., and Lelkes, P. I. (2019). From snake venom's disintegrins and C-type lectins to anti-platelet drugs. *Toxins (Basel)* 11 (5), 303. doi:10.3390/toxins11050303

Leslie, A. G. W., and Powell, H. R. (2007). "Processing diffraction data with mosflm," in *Evolving methods for macromolecular crystallography*. Editors R. J. Read and J. L. Sussman (Netherlands: Springer Netherlands), 41–51.

Li, H., Rao, A., and Hogan, P. G. (2011). Interaction of calcineurin with substrates and targeting proteins. *Trends Cell. Biol.* 21 (2), 91–103. doi:10.1016/j.tcb.2010.09.011

Li, W. F., Chen, L., Li, X. M., and Liu, J. (2005). A C-type lectin-like protein from Agkistrodon acutus venom binds to both platelet glycoprotein Ib and coagulation factor IX/factor X. *Biochem. Biophys. Res. Commun.* 332 (3), 904–912. doi:10.1016/j.bbrc.2005.05.033

Liu, S., Zhu, Z., Sun, J., Zhu, Z., Huang, Q., Teng, M., et al. (2002). Purification, crystallization and preliminary X-ray crystallographic analysis of agkaggregin, a C-type lectin-like protein from Agkistrodon acutus venom. *Acta Crystallogr. D. Biol. Crystallogr.* 58 (4), 675–678. doi:10.1107/s0907444902001294

Ma, Z., Mao, C., Jia, Y., Fu, Y., and Kong, W. (2020). Extracellular matrix dynamics in vascular remodeling. *Am. J. Physiol. Cell. Physiol.* 319 (3), C481–C499. doi:10.1152/ajpcell.00147.2020

Marchler-Bauer, A., Derbyshire, M. K., Gonzales, N. R., Lu, S., Chitsaz, F., Geer, L. Y., et al. (2015). Cdd: NCBI's conserved domain database. *Nucleic Acids Res.* 43, D222–D226. doi:10.1093/nar/gku1221

Marcinkiewicz, C., Lobb, R. R., Marcinkiewicz, M. M., Daniel, J. L., Smith, J. B., Dangelmaier, C., et al. (2000). Isolation and characterization of EMS16, a C-lectin type protein from Echis multisquamatus venom, a potent and selective inhibitor of the alpha2beta1 integrin. *Biochemistry* 39 (32), 9859–9867. doi:10.1021/bi000428a

Matsumoto, T., Bohman, S., Dixelius, J., Berge, T., Dimberg, A., Magnusson, P., et al. (2005). VEGF receptor-2 Y951 signaling and a role for the adapter molecule TSAd in tumor angiogenesis. *Embo J.* 24 (13), 2342–2353. doi:10.1038/sj.emboj.7600709

McCoy, A. J. (2007). Solving structures of protein complexes by molecular replacement with Phaser. *Acta Crystallogr. Sect. D-Biological Crystallogr.* 63, 32–41. doi:10.1107/S0907444906045975

Minami, T., Jiang, S., Schadler, K., Suehiro, J., Osawa, T., Oike, Y., et al. (2013). The calcineurin-NFAT-angiopoietin-2 signaling axis in lung endothelium is critical for the establishment of lung metastases. *Cell. Rep.* 4 (4), 709–723. doi:10.1016/j.celrep.2013.07.021

Mohamed Abd El-Aziz, T., Garcia Soares, A., and Stockand, J. D. (2019). Snake venoms in drug discovery: Valuable therapeutic tools for Life saving. *Toxins (Basel)* 11 (10), 564. doi:10.3390/toxins11100564

Momic, T., Cohen, G., Reich, R., Arlinghaus, F. T., Eble, J. A., Marcinkiewicz, C., et al. (2012). Vixapatin (VP12), a c-type lectin-protein from Vipera xantina palestinae venom: Characterization as a novel anti-angiogenic compound. *Toxins (Basel)* 4 (10), 862–877. doi:10.3390/toxins4100862

Morita, T. (2005). Structures and functions of snake venom CLPs (C-type lectin-like proteins) with anticoagulant-procoagulant-and platelet-modulating activities. *Toxicon* 45 (8), 1099–1114. doi:10.1016/j.toxicon.2005.02.021

Munawar, A., Ali, S. A., Akrem, A., and Betzel, C. (2018). Snake venom peptides: Tools of biodiscovery. *Toxins (Basel)* 10 (11), 474. doi:10.3390/toxins10110474

Okamura, H., Aramburu, J., García-Rodríguez, C., Viola, J. P., Raghavan, A., Tahiliani, M., et al. (2000). Concerted dephosphorylation of the transcription factor NFAT1 induces a conformational switch that regulates transcriptional activity. *Mol. Cell.* 6 (3), 539–550. doi:10.1016/s1097-2765(00)00053-8

Perez-Riverol, Y., Bai, J., Bandla, C., García-Seisdedos, D., Hewapathirana, S., Kamatchinathan, S., et al. (2022). The PRIDE database resources in 2022: A hub for mass spectrometry-based proteomics evidences. *Nucleic Acids Res.* 50 (D1), D543–d552. doi:10.1093/nar/gkab1038

Qi, J. H., Ebrahem, Q., Moore, N., Murphy, G., Claesson-Welsh, L., Bond, M., et al. (2003). A novel function for tissue inhibitor of metalloproteinases-3 (TIMP3): Inhibition of angiogenesis by blockage of VEGF binding to VEGF receptor-2. *Nat. Med.* 9 (4), 407–415. doi:10.1038/nm846

Rafiee, P., Heidemann, J., Ogawa, H., Johnson, N. A., Fisher, P. J., Li, M. S., et al. (2004). Cyclosporin A differentially inhibits multiple steps in VEGF induced angiogenesis in human microvascular endothelial cells through altered intracellular signaling. *Cell. Commun. Signal* 2 (1), 3. doi:10.1186/1478-811x-2-3

Ribatti, D. (2017). "Inflammation and angiogenesis," in *Inflammation and angiogenesis* (Cham: Springer International Publishing), 25–26.

Rundhaug, J. E. (2005). Matrix metalloproteinases and angiogenesis. *J. Cell. Mol. Med.* 9 (2), 267–285. doi:10.1111/j.1582-4934.2005.tb00355.x

Shibuya, M. (2011). Vascular endothelial growth factor (VEGF) and its receptor (VEGFR) signaling in angiogenesis: A crucial target for anti- and pro-angiogenic therapies. *Genes. Cancer* 2 (12), 1097–1105. doi:10.1177/1947601911423031

Srinivasan, R., Zabuawala, T., Huang, H., Zhang, J., Gulati, P., Fernandez, S., et al. (2009). Erk1 and Erk2 regulate endothelial cell proliferation and migration during mouse embryonic angiogenesis. *PLoS One* 4 (12), e8283. doi:10.1371/journal.pone.0008283

Sun, Z., Li, X., Massena, S., Kutschera, S., Padhan, N., Gualandi, L., et al. (2012). VEGFR2 induces c-Src signaling and vascular permeability *in vivo* via the adaptor protein TSAd. *J. Exp. Med.* 209 (7), 1363–1377. doi:10.1084/jem.20111343

Swenson, S., Minea, R., Zidovetzki, S., Helchowski, C., Costa, F., and Markland, F. S. (2010). "Anti-angiogenesis and disintegrins," in *Toxins and hemostasis: From bench to bedside*. Editors R. M. Kini, K. J. Clemetson, F. S. Markland, M. A. McLane, and T. Morita (Dordrecht: Springer Netherlands), 301–329.

Waldner, M. J., Wirtz, S., Jefremow, A., Warntjen, M., Neufert, C., Atreya, R., et al. (2010). VEGF receptor signaling links inflammation and tumorigenesis in colitis-associated cancer. *J. Exp. Med.* 207 (13), 2855–2868. doi:10.1084/jem.20100438

Wang, W. J. (2008). Agglucetin, a tetrameric C-type lectin-like venom protein, regulates endothelial cell survival and promotes angiogenesis by activating integrin alphavbeta3 signaling. *Biochem. Biophys. Res. Commun.* 369 (2), 753–760. doi:10.1016/j.bbrc.2008.02.091

Xu, G., Teng, M., Niu, L., Liu, P., Dong, Y., Liu, Q., et al. (2004). Purification, characterization, crystallization and preliminary X-ray crystallographic analysis of two novel C-type lectin-like proteins: Aall-A and Aall-B from Deinagkistrodon acutus venom. *Acta Crystallogr. D. Biol. Crystallogr.* 60 (11), 2035–2037. doi:10.1107/s0907444904021110

Yang, G. L., and Li, L. Y. (2018). Counterbalance: Modulation of VEGF/VEGFR activities by TNFSF15. *Signal Transduct. Target Ther.* 3, 21. doi:10.1038/s41392-018-0023-8

Yeh, C. H., Wang, W. C., Hsieh, T. T., and Huang, T. F. (2000). Agkistin, a snake venom-derived glycoprotein Ib antagonist, disrupts von Willebrand factor-endothelial cell interaction and inhibits angiogenesis. *J. Biol. Chem.* 275 (25), 18615–18618. doi:10.1074/jbc.C000234200

Zaichuk, T. A., Shroff, E. H., Emmanuel, R., Filleur, S., Nelius, T., and Volpert, O. V. (2004). Nuclear factor of activated T cells balances angiogenesis activation and inhibition. *J. Exp. Med.* 199 (11), 1513–1522. doi:10.1084/jem.20040474

Zelensky, A. N., and Gready, J. E. (2005). The C-type lectin-like domain superfamily. *Febs J.* 272 (24), 6179–6217. doi:10.1111/j.1742-4658.2005.05031.x

Zhang, Y., Xu, X., Shen, D., Song, J., Guo, M., and Yan, X. (2012). Anticoagulation factor I, a snaclec (snake C-type lectin) from Agkistrodon acutus venom binds to FIX as well as FX: Ca2+ induced binding data. *Toxicon* 59 (7-8), 718–723. doi:10.1016/j.toxicon.2012.03.006

frontiers | Frontiers in Pharmacology

TYPE Original Research
PUBLISHED 13 November 2023
DOI 10.3389/fphar.2023.1277143

OPEN ACCESS

EDITED BY
Cassandra M. Modahl,
Liverpool School of Tropical Medicine,
United Kingdom

REVIEWED BY
Vladimir Yarov-Yarovoy,
University of California, Davis,
United States
Stephan Kellenberger,
Université de Lausanne, Switzerland

*CORRESPONDENCE
Richard J. Lewis,
r.lewis@uq.edu.au

RECEIVED 14 August 2023
ACCEPTED 23 October 2023
PUBLISHED 13 November 2023

CITATION
Dongol Y, Wilson DT, Daly NL, Cardoso FC and Lewis RJ (2023), Structure-function and rational design of a spider toxin Ssp1a at human voltage-gated sodium channel subtypes. *Front. Pharmacol.* 14:1277143. doi: 10.3389/fphar.2023.1277143

Structure-function and rational design of a spider toxin Ssp1a at human voltage-gated sodium channel subtypes

Yashad Dongol[1], David T. Wilson[2], Norelle L. Daly[2], Fernanda C. Cardoso[1] and Richard J. Lewis[1]*

[1]Centre for Chemistry and Drug Discovery, Institute for Molecular Bioscience, The University of Queensland, Brisbane, QLD, Australia, [2]Australian Institute of Tropical Health and Medicine, James Cook University, Cairns, QLD, Australia

The structure-function and optimization studies of Na_V-inhibiting spider toxins have focused on developing selective inhibitors for peripheral pain-sensing $Na_V1.7$. With several Na_V subtypes emerging as potential therapeutic targets, structure-function analysis of Na_V-inhibiting spider toxins at such subtypes is warranted. Using the recently discovered spider toxin Ssp1a, this study extends the structure-function relationships of Na_V-inhibiting spider toxins beyond $Na_V1.7$ to include the epilepsy target $Na_V1.2$ and the pain target $Na_V1.3$. Based on these results and docking studies, we designed analogues for improved potency and/or subtype-selectivity, with S7R-E18K-rSsp1a and N14D-P27R-rSsp1a identified as promising leads. S7R-E18K-rSsp1a increased the rSsp1a potency at these three Na_V subtypes, especially at $Na_V1.3$ (~10-fold), while N14D-P27R-rSsp1a enhanced $Na_V1.2/1.7$ selectivity over $Na_V1.3$. This study highlights the challenge of developing subtype-selective spider toxin inhibitors across multiple Na_V subtypes that might offer a more effective therapeutic approach. The findings of this study provide a basis for further rational design of Ssp1a and related NaSpTx1 homologs targeting $Na_V1.2$, $Na_V1.3$ and/or $Na_V1.7$ as research tools and therapeutic leads.

KEYWORDS

ICK toxins, rational design, spider toxin, Ssp1a, structure-function, voltage-gated sodium channels

1 Introduction

Voltage-gated sodium (Na_V) channels underpin electrical signaling by allowing passive and rapid influx of Na^+ ions necessary to control initiation and propagation of action potentials in electrically excitable cells, including neurons and muscles (Ahern et al., 2016). Accordingly, Na_V channel dysfunction is associated with various neuronal and neuromuscular disorders, including pain, epilepsy, arrythmia and myopathy (de Lera Ruiz and Kraus, 2015; Cardoso and Lewis, 2018; Dib-Hajj and Waxman, 2019; Cardoso, 2020; Menezes et al., 2020; Goodwin and McMahon, 2021). These channels can be pharmacologically modulated by neurotoxins that bind to different sites on the Na_V channel to alter the voltage-dependence of activation, inactivation, and conductance (Stevens et al., 2011; de Lera Ruiz and Kraus, 2015). Peptidic gating modifier toxins, including spider toxins, preferentially target the extracellular binding sites located in the domain II (DII) and domain IV (DIV) of the Na_V channels to modulate the channel gating.

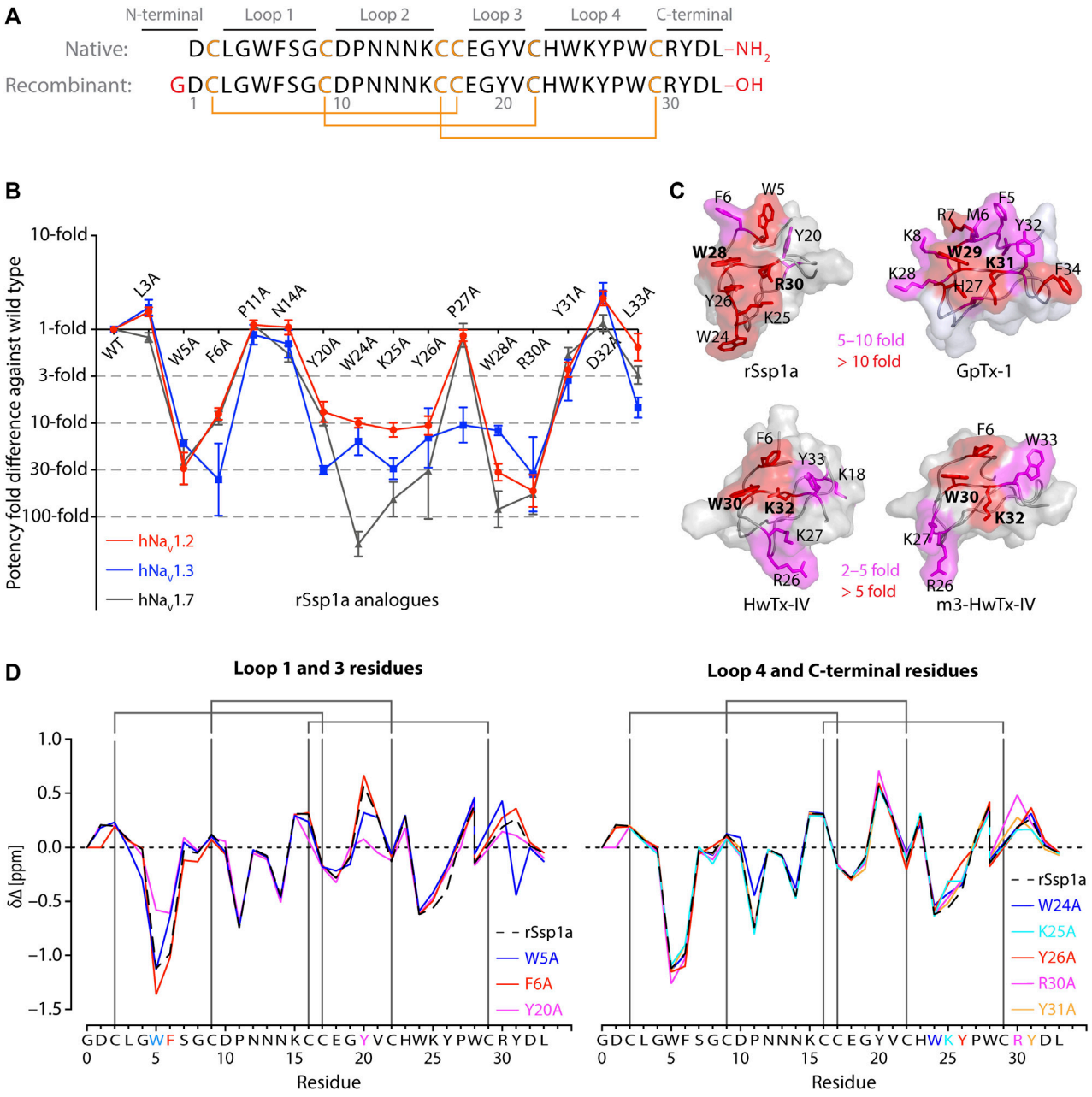

FIGURE 1
Structure-function of Ssp1a. **(A)** Primary structure of native Ssp1a and recombinant Ssp1a (rSsp1a) showing the disulfide bond connectivity. **(B)** Fold potency difference of rSsp1a alanine mutants vs. wild type (WT) rSsp1a at $hNa_V1.2$, $hNa_V1.3$ and $hNa_V1.7$. Data were presented as means ± SEM, with n = 3–12. The W5A, F6A, W24A, K25A, Y26A, W28A, R30A did not complete the dose-response curve at $hNa_V1.2$, $hNa_V1.3$, and $hNa_V1.7$ at the maximum concentration tested. Similarly, Y20A, P27A, Y31A and L33A at $hNa_V1.3$ also demonstrated incomplete dose-response. The IC_{50} values from the incomplete dose-response for these mutants were used to plot the panel for better comparison of rSsp1a residues key to $hNa_V1.2$, $hNa_V1.3$, and $hNa_V1.7$ activity. The readers are requested to follow Supplementary Table S1 for relative IC_{50} values and Supplementary Figures S1 for dose-response curves. **(C)** Active residues in the surface of rSsp1a (PDB: 7SKC) Dongol et al., 2021), GpTx-1 (modeled on engineered GPTX-1, PDB: 6MK5) (Murray et al., 2015), HwTx-IV (PDB: 2M4X) Revell et al., 2013) and m3-HwTx-IV (PDB: 5T3M) (Wisedchaisri et al., 2021) were compared to identify which alanine mutation reduced the toxin potency at $hNa_V1.7$ as indicated by the respective color code (red or pink). All four toxins were aligned at NaSpTx1 signature motif WCK/R (W and K/R bolded). **(D)** Secondary Hα chemical shift of rSsp1a and the alanine mutants. The secondary shifts were derived by subtracting the random coil Hα shift from the experimental Hα shifts for the eight alanine substitutions distributed across loop 1, loop 3, loop 4 and the C-terminal. The Hα for rSsp1a shifted in W5A, F6A and Y20A mutations.

The Na_V channel is structurally composed of four non-homologous domains (DI–DIV), which collectively forms the functional, pore-forming α-subunit (Shen et al., 2017; Dongol et al., 2019). There are nine known human Na_V isoforms ($hNa_V1.1$–1.9), each with distinct tissue localization, channel kinetics and physiological functions (de Lera Ruiz and Kraus, 2015). Modulating a specific isoform is key to avoiding side effects associated with the use of Na_V-inhibitor drugs; however,

the high structural homology between Na_V subtypes (Vetter et al., 2017) remains a challenge in obtaining subtype-selective inhibitors, which could be addressed by optimizing ligands, including venom peptides. Venoms evolved for prey capture and/or defense are rich in peptide Na_V-modulators (Kalia et al., 2015). Research in the 1980s first identified the Na_V-modulating effects of spider venom toxins (Fontana and Vital-Brazil, 1985; Adams et al., 1989), many of which are now used as research tools to help define the structure, function and pharmacology of Na_V channels (Escoubas et al., 2000; Stevens et al., 2011; Kalia et al., 2015; Wu et al., 2018) and their role in disease (Osteen et al., 2016). More recently, these complex venom peptide libraries have been exploited for potential drug leads (Saez et al., 2010; Pineda et al., 2014; Cardoso and Lewis, 2019; Saez and Herzig, 2019; Cardoso et al., 2022), including CcoTx-1 (Shcherbatko et al., 2016), GpTx-1 (Murray et al., 2015; Murray et al., 2016), ProTx-II (Flinspach et al., 2017) and Tap1a (Hu et al., 2021).

Ssp1a, a 33-residue inhibitor cystine knot (ICK) peptide (Figure 1A) belonging to the voltage-gated sodium channel modulator spider toxin family 1 (NaSpTx1), is a potent inhibitor of neuronal hNa_V subtypes 1.7, 1.6, 1.3, 1.2 and 1.1 (Dongol et al., 2021). The closest homologs with comprehensive structure-function data available are the distantly related GpTx-1 (44% identity) and HwTx-IV (40% identity), with HwTx-IV and recombinant Ssp1a (rSsp1a) showing similar pharmacology at $hNa_V1.7$ (Xiao et al., 2008; Dongol et al., 2021). While the NaSpTx1 toxin studies have focused on the development of $hNa_V1.7$-selective inhibitors (Minassian et al., 2013; Revell et al., 2013; Klint et al., 2015; Murray et al., 2015; Murray et al., 2016; Shcherbatko et al., 2016; Rahnama et al., 2017; Zhang et al., 2018; Neff et al., 2020), the determinants of NaSpTx1 pharmacology at the potential pain target $hNa_V1.3$ (Black et al., 1999; Kim et al., 2001; Hains et al., 2004; Hong et al., 2004; Garry et al., 2005; Lindia et al., 2005; Black et al., 2008; Chen et al., 2014; Tan et al., 2015; Xu et al., 2016) and epilepsy target $hNa_V1.2$ (Menezes et al., 2020) have been largely ignored. Therefore, the characterization of Ssp1a in this study could provide common structure-function information for several closer uncharacterized homologs and at targets $hNa_V1.2$ and $hNa_V1.3$, in addition to $hNa_V1.7$.

In this study, 15 alanine mutants of rSsp1a in the Na_V pharmacophore region of NaSpTx1 inhibitors (Li et al., 2004; Klint et al., 2012; Minassian et al., 2013; Revell et al., 2013; Murray et al., 2015; Murray et al., 2016; Shcherbatko et al., 2016) identified the Ssp1a-specific pharmacophore. Using these restraints, docking studies identified specific molecular interactions between rSsp1a and $hNa_V1.2$, $hNa_V1.3$ and $hNa_V1.7$. Through structure-function studies of rSsp1a activity at $hNa_V1.2$, $hNa_V1.3$ and $hNa_V1.7$ and previous optimization studies of NaSpTx1 peptides (Minassian et al., 2013; Revell et al., 2013; Murray et al., 2015; Zhang et al., 2015; Murray et al., 2016; Shcherbatko et al., 2016; Zhang et al., 2018; Neff et al., 2020), we designed rSsp1a analogues with significantly improved potency and subtype-selectivity for $hNa_V1.3$ and $hNa_V1.2$/$hNa_V1.7$, respectively. The findings of this study provide insight into rational design of rSsp1a and NaSpTx1 homologs targeting the $hNa_V1.2$, $hNa_V1.3$, and $hNa_V1.7$ subtypes, with single or multiple subtype-selectivity, with the aim of developing lead molecules that have high value as research tools and/or therapeutic agents.

2 Materials and methods

2.1 Cell culture

Human embryonic kidney 293 (HEK293) cells stably expressing recombinant $hNa_V1.2$, $hNa_V1.3$ and $hNa_V1.7$ and the β1 auxiliary subunit (Scottish Biomedical Drug Discovery, Glasgow, UK) were cultured in Minimal Essential medium (MEM) (Sigma-Aldrich, MO, United States) supplemented with 10% v/v FBS-New Zealand origin (Assay Matrix), 2 mM L-glutamine and selection antibiotics as per manufacturer's recommendation. The HEK293 cells heterologously expressing $mNa_V1.7$ and F813G-$mNa_V1.7$ were generously provided by Prof Irina Vetter and were cultured in Minimal Essential medium (MEM) (Sigma-Aldrich, MO, United States) supplemented with 10% v/v FBS-New Zealand origin (Assay Matrix), 2 mM L-glutamine and hygromycin 100 μg/mL.

2.2 Automated whole-cell patch-clamp electrophysiology

Na_V channel currents from HEK293 cells stably expressing Na_V subtypes and the β1 auxiliary subunit were recorded using an automated whole-cell patch clamp system QPatch 16X (Sophion Bioscience A/S, Ballerup, Denmark). As per the manufacturer's guidelines, the cells were cultured for 48 h to achieve ~80% confluency, detached using Detachin (Genlantis) and resuspended to 5×10^6 cells/mL in serum free media [CHO-cell SFM (Life Technologies), 25 mM HEPES and 100 U/mL penicillin/streptomycin]. The extracellular solution comprised (in mM) 1 $CaCl_2$, 1 $MgCl_2$, 5 HEPES, 3 KCl, 140 NaCl and 20 TEA-Cl, with the pH adjusted to 7.3 with NaOH. The intracellular solution comprised (in mM) 140 CsF, 1 EGTA, 5 CsOH, 10 HEPES and 10 NaCl, with the pH adjusted to 7.3 with CsOH. The osmolarity of both solutions were adjusted to 320 mOsm with sucrose. Compounds were prepared in extracellular solution containing 0.1% bovine serum albumin (Sigma-Aldrich). To obtain the dose-response curves, cells were maintained at a holding potential −80 mV and Na^+ currents were elicited by 20 m voltage steps to 0 mV from a −120 mV conditioning pulse applied for 200 m. Increasing concentrations of the peptide were incubated with the cells at the holding potential for 2 min before the voltage protocol was applied.

2.3 Nuclear magnetic resonance (NMR) structure determination of rSsp1a alanine mutants

Lyophilized peptide (500–1,000 μg) was resuspended in 90% H_2O:10%D_2O. Two-dimensional ^1H-^1H TOCSY and ^1H-^1H NOESY spectra were acquired at 290 K using a 600 MHz AVANCE III NMR spectrometer (Bruker, Karlsruhe, Germany) equipped with a cryogenically cooled probe. All spectra were recorded with an interscan delay of 1 s. NOESY spectra were acquired with mixing times of 200–250 ms and TOCSY spectra were acquired with isotropic mixing periods of 80 ms. Two-dimensional spectra were

collected over 4,096 data points in the f2 dimension and 512 increments in the f1 dimension over a spectral width of 12 ppm. Standard Bruker pulse sequences were used with an excitation sculpting scheme for solvent suppression. NMR assignments were made using established protocols (Wüthrich, 1983), and the secondary shifts derived by subtracting the random coil αH shift from the experimental αH shifts (Wishart et al., 1995). Spectra were recorded referenced to external 4,4-dimethyl-4-silapentane-1-sulfonic acid (DSS).

2.4 Alanine scanning and rational design of rSsp1a

Based on homology and earlier structure-function studies of NaSpTx1 toxins, 16 residues were selected for alanine substitution. The rSsp1a structure-function data across $hNa_V1.2$, $hNa_V1.3$, and $hNa_V1.7$ were then used along with the homology and structure-function information of other NaSpTx1 toxins to guide rational design of rSsp1a. Unfortunately, the docking model of rSsp1a at hNa_V subtypes were not used for rSsp1a rational design as the resting structure of $hNa_V1.7$ DII was published (Wisedchaisri et al., 2021) after the mutants were made. In total, sixteen positions in rSsp1a were mutated to recombinantly produce 38 rSsp1a-analogues, including 30 single mutants, five double mutants, one mutant with an N-terminal extension and two mutants with a C-terminal extension. A N-terminal extended version (GP-Ssp1a) was designed to mimic GP-HwTx-IV (Neff et al., 2020) and GP-ProTx-II (Flinspach et al., 2017), whereas a C-terminal extension (rSsp1a-GK) was designed to mimic the C-terminal amide version of HwTx-IV (Minassian et al., 2013; Neff et al., 2020). Double mutants were designed based on the activity of each single mutation at the three hNa_V subtypes.

The rSsp1a mutant plasmids were produced using a QuikChange Lightning Site-Directed Mutagenesis Kit (Agilent Technologies) and Ssp1a-pLicC plasmid construct (GeneArt Gene Synthesis, Life Technologies) comprising MalE signal sequence for periplasmic export, His_6 affinity tag, maltose binding protein (MBP) tag, a tobacco etch virus (TEV) recognition and cleavage sequence. Briefly, primers were designed using SnapGene software and purchased from Sigma-Aldrich, and the mutant strand was synthesized using polymerase chain reaction (PCR). The amplified PCR product was digested with Dpn I restriction enzyme to eliminate the parental rSsp1a construct and was transformed into Competent *E. coli* TOP10 cells. The transformed TOP10 cells were plated on Luria-Bertani (LB) agar plates containing 100 μg/mL ampicillin (Amp) and incubated overnight at 37°C. The isolated colonies were sub-cultured overnight at 37°C at 120 rpm, and the plasmid DNA was extracted using a QIAprep Spin Miniprep kit (QIAGEN) following manufacturer's protocol. The desired mutation in the extracted DNA was confirmed by Sanger sequencing at the Australian Genome Research Facility, Brisbane using Big Dye Terminator (BDT) chemistry version 3.1 (Applied Biosystem). Double mutant plasmids were made using rSsp1a single mutant plasmids as a base construct and a set of primers for the second mutation, and following site-directed mutagenesis, miniprep and Sanger sequencing as described above.

2.5 Recombinant production of rSsp1a analogues

rSsp1a analogues were recombinantly expressed in *E. coli* as a His_6 tagged-MBP fused peptide, harvested, and purified as described previously (Dongol et al., 2021). Briefly, the mutant plasmids were transformed into BL21 (λDE3) competent *E. coli* cells and cultured in LB-Amp medium at 37°C, 120 rpm until the optical density at 600 nm (OD600) reached 0.8–1.0. Peptide expression was induced with 500 μM isopropyl β-D-1-thiogalactopyranoside (IPTG) at 16°C and 120 rpm overnight and pelleted at 6,000 rpm for 10 min at 4°C. The pellet was resuspended in TN buffer (Tris 25 mM, NaCl 150 mM, pH 8.0) and lysed in a constant pressure cell disruptor at 25 kPa at 4°C–8°C. The fusion protein contained in the cell lysate was captured by passing the lysate supernatant through Ni-NTA resin (Hispur NiNTA, Thermo Scientific) and then eluted with TN buffer containing 500 mM imidazole. After desalting, the fusion protein was cleaved with TEV protease in the reducing environment provided by glutathione redox pair. The post-cleavage sample was filtered through a centrifuge filter to isolate the cleaved peptide from tag proteins and loaded onto a reversed-phase C_{18} column (30Å, 5μm, 4.6 × 250mm, Vydac 218TP, Grace) on an Agilent 1100 series HPLC for purification. The peptide was eluted using the following gradient of solvent B (90% ACN, 0.05% TFA in MilliQ water) in solvent A (0.05% TFA in MilliQ water): 5% solvent B over 0–5 min, 5%–10% solvent B over 5–10 min, 10%–50% solvent B over 10–40 min, 50%–80% solvent B over 40–45 min, wash at 80% solvent B over 45–50 min, 80%–5% solvent B over 50–55 min and a final wash with 5% solvent B over 55–65 min at a flow rate of 1 mL/min. Peak fractions at 214 nm were collected, checked the purity, analysed for the mass using MALDI-TOF/TOF (SCIEX 5800), lyophilized, quantitated using nanodrop, and stored at −20°C until use.

2.6 Molecular docking

The recently solved structure of $Na_VAb/Na_V1.7$ VS2A chimera (PDB: 7K48) (Wisedchaisri et al., 2021) provided the resting state structure of the $Na_V1.7$ DII, which was used as a template to build a homology model for $hNa_V1.2$ DII (UniProt: Q99250) and $hNa_V1.3$ DII (UniProt: Q9NY46) in the resting state using SWISS-MODEL (Waterhouse et al., 2018). HADDOCK2.2 webserver was used to perform data-driven docking studies under the Easy interface mode, which only requires the starting structures and the restraint definitions in the form of active and passive residues to drive the docking (de Vries et al., 2010; Van Zundert et al., 2016). Our NMR structure of rSsp1a, cryo-EM structure of the $Na_VAb/Na_V1.7$ VS2A chimera, and homology models of DII of $hNa_V1.2$ and $hNa_V1.3$ were uploaded with the structure and restraint definitions to generate putative ligand receptor complex. The rSsp1a active residues were defined based on our activity data of rSsp1a alanine mutants at $hNa_V1.2$, $hNa_V1.3$, and $hNa_V1.7$, whereas the active residues on DII of hNa_V subtypes were defined based on the previously published channel mutation data (Xiao et al., 2010; Xiao et al., 2011; Cai et al., 2015; Zeng et al., 2018; Xu et al., 2019). The docking program was allowed to define the passive residues automatically around the active residues.

For the rSsp1a–hNa$_V$1.2 docking, the rSsp1a active residues defined were W5, F6, W24, K25, Y26, W28, and R30. Similarly, the active residues in hNa$_V$1.2 DII S1–S2 loop were E779, Y781, T784, E785, F787, S788 whereas the active residues in the DII S3–S4 loop were E837, E844, and S847. Likewise, the rSsp1a–hNa$_V$1.3 docking was driven by defining the rSsp1a active residues W5, F6, Y20, W24, K25, Y26, P27, W28, R30 and L33, and hNa$_V$1.3 active residues in the DII S1–S2 loop (E780, Y782, T785, E786, F788, and S789) and DII S3–S4 loop (E838, S842, E845, and S848). Finally, to dock rSsp1a at hNa$_V$1.7, the active residues defined in rSsp1a were W5, F6, W24, K25, Y26, W28 and R30, while the active residues defined in the hNa$_V$1.7 DII S1–S2 loop were E753, E759, E760, F761 and K762, and active residues defined in the DII S3–S4 loop were E811, F813, D816 and E818. The docking results were displayed as a cluster of water-refined models, which were then downloaded and visualized using Pymol 2.4.1 (Schrodinger, 2018). Generally, the top 10 clusters were listed in the order of their HADDOCK score—the top position in the list occupied by the cluster with the lowest HADDOCK score. Further, each cluster contains the top four best scoring structures. A z-score was also determined for each cluster, indicating the number of standard deviations by which the HADDOCK score of a particular cluster differed from the mean score of all clusters. The top clusters in each list providing the lower z-score values are considered more reliable (de Vries et al., 2010; Van Zundert et al., 2016). Additionally, each of the top 10 generated models were evaluated to identify the docking pose that best supported the pharmacology for interactions. The 3D structure of rSsp1a analogues used for docking studies were obtained by introducing the mutation in the rSsp1a structure using Pymol. The docking of rSsp1a analogues were driven by defining the active residues at rSsp1a analogues and hNa$_V$ subtypes as described above for rSsp1a docking at each hNa$_V$ subtypes. The presence of key molecular interactions was determined by the distance separating the two specified interacting atoms participating in interactions between the toxin and the channel. Electrostatic interactions were categorized as hydrogen bonds (H-bonds) when an electronegative O-atom engaged with a H-atom covalently bonded either to an electronegative O- or N-atom within 2 Å. Conversely, electrostatic interactions were designated as salt bridges between positively charged N-atom (amino group) and the negatively charged O-atom (carboxyl group) within 3.3 Å. Similarly, hydrophobic interactions were defined interactions between hydrophobic residues of the toxin and channel (<5 Å), with the van der Waals radii represented as dots in the structural images. Dots representations were generated using the default parameters of the Pymol program for atom van der Waals radii, dot radius, width, and density. Additionally, aromatic amino acids from the toxin and the channel, located within a 5 Å distance, were considered to form π-π interactions.

2.7 Data analysis

The experimental data were analysed using QPatch Assay software v5.6.4 and GraphPad Prism 7.0 using a four-parameter Hill equation [Y = Bottom + (Top—Bottom)/(1 + 10(Log IC$_{50}$—X)* Hillslope)] to fit concentration response curves by non-linear regression analysis and Student's t-test. Data are presented as means ± standard error of mean (SEM) with number of independent experiments stated and $p < 0.05$ is considered statistically significant. Statistically insignificant shift in the activity is denoted by "little" while small but statistically significant shift in the activity is denoted by "slight" throughout the manuscript.

3 Results

3.1 Determining the active surface of rSsp1a

Fifteen rSsp1a alanine-analogues were produced via recombinant expression as previously described (Dongol et al., 2021), and their activity tested on hNa$_V$1.2, hNa$_V$1.3 and hNa$_V$1.7 as a function of varying concentration (Figure 1B; Supplementary Figure S1; Supplementary Table S1). The alanine mutations causing ≥10-fold loss in potency at all three hNa$_V$ subtypes included W5A, F6A, W24A, K25A, Y26A, W28A and R30A. Y20A was inactive at hNa$_V$1.3 but reduced hNa$_V$1.2 and hNa$_V$1.7 activity by nearly 10-fold. The P27A, Y31A and L33A mutations also preferentially impacted hNa$_V$1.3. Surprisingly, the conserved P11 played little role in rSsp1a activity, and little to slight effects were observed for the N14A mutant. Two mutants, L3A and D32A, slightly improved the rSsp1a potency at hNa$_V$1.2, but only D32A slightly enhanced rSsp1a potency at hNa$_V$1.3.

We compared the active surface of rSsp1a with GpTx-1, HwTx-IV, and the m3-HwTx-IV optimized variant, which revealed that the hydrophobic and basic residues that comprise the active surface in these toxins are distributed around a central WCK/R motif, with key residues aligned at corresponding positions in the 3D structure (Figure 1C). All active residues were solvent exposed and on the same face of these toxins, except Y20 in rSsp1a which was buried and K18 in HwTx-IV which was located on the opposite face. The loop 1, loop 4 and C-terminal region act in concert to form the active surface of these NaSpTx1 toxins as previously described for the spider peptide Tap1a (Hu et al., 2021).

Next, we determined whether alanine substitutions reducing rSsp1a activity were structural by assessing influences on the Hα secondary chemical shifts of rSsp1a alanine mutants with significant activity loss (Figure 1D). Mutant W5A produced a significant change in Hα chemical shift at Y20 and Y31, while F6A only affected the neighboring W5. The loop 3 mutant Y20A affected both W5 and F6 Hα chemical shifts likely due to their spatial proximity to the buried Y20, suggesting loop 3 residues play a structural role in these ICK peptides. The loop 4 mutations W24A, K25A and Y26A and C-terminal mutations R30A and Y31A had only minor local effects on the Hα chemical shifts, indicating that the activity losses attributed to these mutations are functional rather than structural. Unfortunately, W28A-rSsp1a analogue was obtained in insufficient yield for NMR analysis.

3.2 Molecular interaction of rSsp1a at hNa$_V$1.2, hNa$_V$1.3 and hNa$_V$1.7

Our previous work indicated that rSsp1a traps DII of hNa$_V$1.7 in the resting conformation (Dongol et al., 2021). The resting state

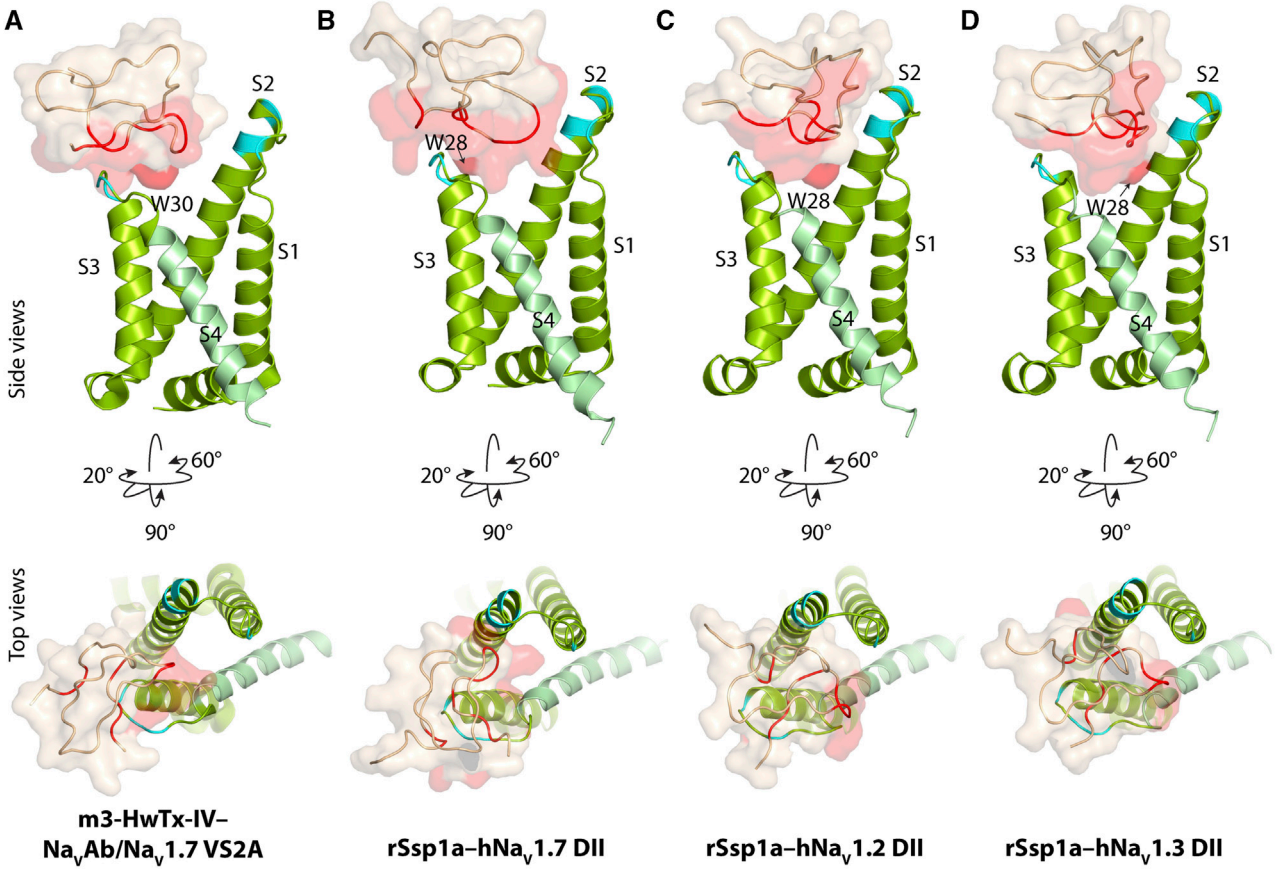

FIGURE 2
Docking pose of m3-HwTx-IV and rSsp1a. **(A)** Docking orientation of m3-HwTx-IV at $Na_VAb/Na_V1.7$ VS2A captured in cryo-EM and **(B–D)** docking orientation of rSsp1a at $hNa_V1.2$, $hNa_V1.3$, and $hNa_V1.7$ obtained using HADDOCK are shown with side and top views. The red surface indicates the activity surface of the corresponding toxin, with dark red indicating the Trp residue from the WCK/R motif. The cyan colour indicates non-identical residues among $hNa_V1.2$, $hNa_V1.3$, and $hNa_V1.7$. The recently published $Na_VAb/Na_V1.7$ VS2A structure (Wisedchaisri et al., 2021) provided the resting structure of DII that served as the $hNa_V1.7$ DII used to model the $hNa_V1.2$ and $hNa_V1.3$ DII resting state.

structure of $Na_V1.7$-DII trapped by m3-HwTx-IV was recently solved (Wisedchaisri et al., 2021), allowing predictive docking of rSsp1a using HADDOCK (Van Zundert et al., 2016). We validated the HADDOCK docking results by comparing the docking orientation and molecular interaction of m3-HwTx-IV at $Na_VAb/Na_V1.7$ VS2A between the HADDOCK-generated *in silico* structure and the cryo-EM structure captured by Wisedchaisri et al. (Wisedchaisri et al., 2021) (Supplementary Figure S2).

The docking results of rSsp1a to $hNa_V1.2$-, $hNa_V1.3$- and $hNa_V1.7$-DII illustrated that rSsp1a bound in the aqueous cleft formed between the S1–S2 and S3–S4 loops of each channel subtype, primarily targeting the S3–S4 loop as observed for m3-HwTx-IV (Figures 2A–D). rSsp1a docked at $hNa_V1.7$ similar to m3-HwTx-IV, with the key residue W28 (W30 in m3-HwTx-IV, Supplementary Figures S3A) positioned towards the S3–S4 loop in the aqueous cleft (Figures 2A, B) and interacting with hydrophobic residues in the S3–S4 loop to trap the S4 segment, as shown for m3-HwTx-IV in Supplementary Figures S3B. When compared to $hNa_V1.7$, the docking orientation of rSsp1a at $hNa_V1.2$ and $hNa_V1.3$ twisted, which allowed rSsp1a to occupy more space in the DII aqueous cleft with W28 occupying the center of the cleft (Figures 2C, D).

The docking orientation of rSsp1a at $hNa_V1.2$ revealed molecular interactions, including salt bridges, H-bonds and a series of hydrophobic interactions within the aqueous cleft (Figure 3A). Specifically, K25–E844 (2.8 Å, $-NH_3^+\bullet\bullet\bullet\bullet{}^-OOC-$) and R30–E837 (2.6 Å, $=NH_2^+\bullet\bullet\bullet\bullet{}^-OOC-$) salt bridges, and a H-bond between Y26 and E844 (1.8 Å, $-OH\bullet\bullet\bullet\bullet{}^-OOC-$) were observed. Additionally, W5 projects into the hydrophobic pocket formed by the LGLA residues in the DII S3–S4 loop and Y31 interacted with W5–LGLA complex, while F6 and W28 occupied the aqueous cleft and interacted with the neighboring hydrophobic residues in the DII S2 and S3–S4 loop. Further, an interaction was observed between W24, located on the edge of the hydrophobic patch in the rSsp1a, and Y781 from the DII S1–S2 loop.

Similar to the rSsp1a–$hNa_V1.2$ results, the rSsp1a–$hNa_V1.3$ docking orientation also showed K25 and R30 forming a salt bridge with E845 (3.0 Å, $-NH_3^+\bullet\bullet\bullet\bullet{}^-OOC-$) and E838 (2.6 Å, $=NH_2^+\bullet\bullet\bullet\bullet{}^-OOC-$), respectively, and Y26 forming a H-bond with S848 (1.7 Å, $-O\bullet\bullet\bullet\bullet HO-$) (Figure 3B). The bulky hydrophobic residue W5 fit within the hydrophobic pocket formed by LGL in the DII S3–S4 loop, with Y31and L33 positioned above the W5–LGL complex to hinder the upward transition of the S4, while F6 and V794 from S2 segment formed a hydrophobic

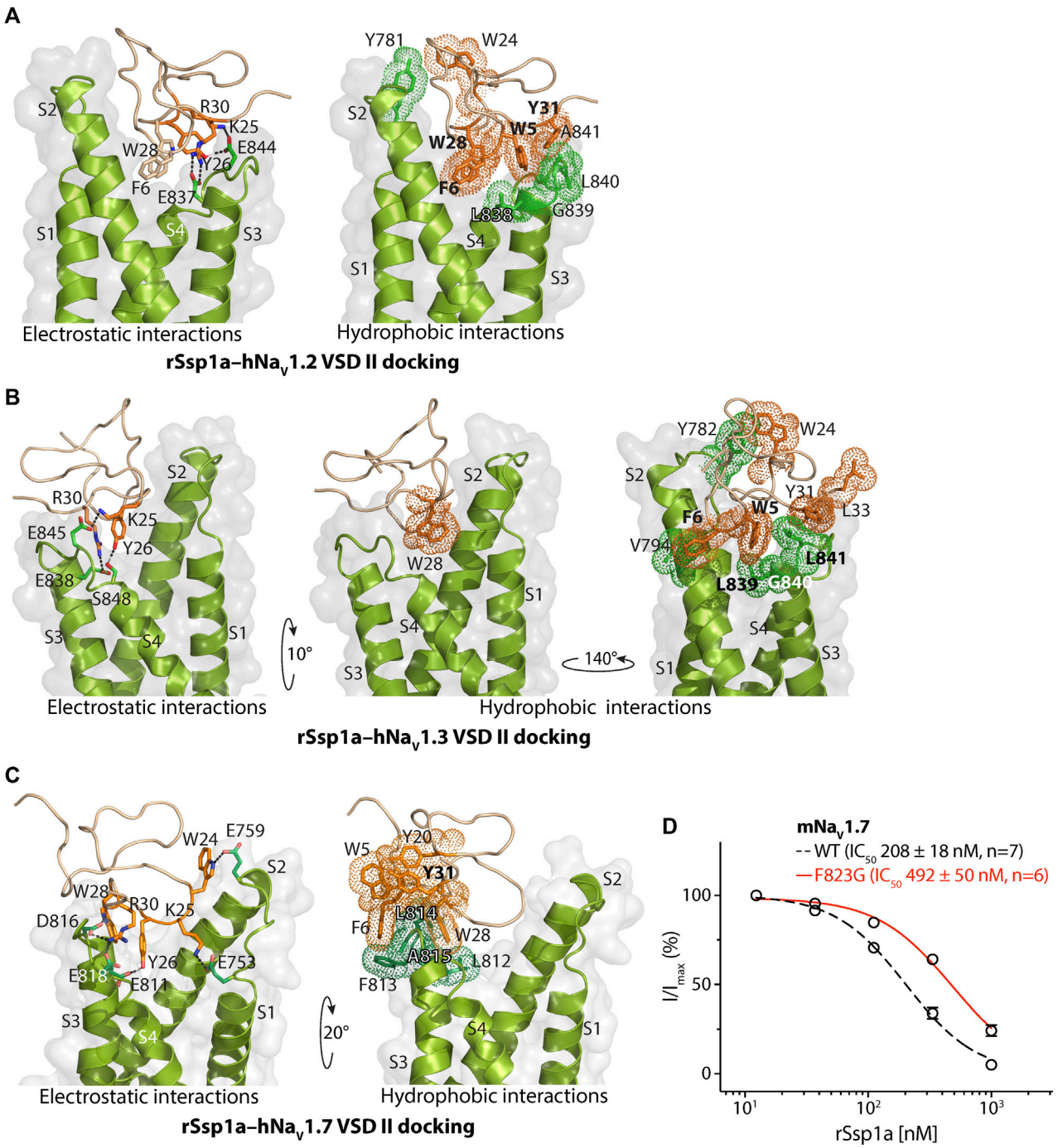

FIGURE 3
Molecular docking of rSsp1a. Molecular docking of rSsp1a at **(A)** hNa$_V$1.2 DII **(B)** hNa$_V$1.3 DII and **(C)** hNa$_V$1.3 DII illustrating electrostatic and hydrophobic interactions. The resting conformation of hNa$_V$1.2 and hNa$_V$1.3 DII was modelled on the resting state structure of Na$_V$Ab/Na$_V$1.7-VS2A chimera (PDB: 7K48) (Wisedchaisri et al., 2021). HADDOCK2.2 Easy interface (Van Zundert et al., 2016) was used for docking and the results were visualized using Pymol 2.4.1 (Schrodinger, 2018). The green and orange dots around the residues corresponds to the van der Waals radii. **(D)** Dose-response of rSsp1a at wild type (WT) and F823G-mNa$_V$1.7. Data presented as means ± SEM, with number of experiments (n) indicated in the legend.

interaction. The toxin penetrated deep into the channel where the bulky hydrophobic W28 occupied the aqueous cleft and interacted with the neighboring hydrophobic residues from DII S1 and S2 segments. Consistent with the hNa$_V$1.2 docking, the uniquely positioned W24 showed a hydrophobic interaction with Y782 in the DII S1–S2 loop to further stabilize rSsp1a interactions at the S3–S4 loop.

rSsp1a docked to hNa$_V$1.7 DII in a slightly altered orientation compared to hNa$_V$1.2 and hNa$_V$1.3. Salt bridges between K25–E753 (2.7 Å, -NH_3^+●●●●$^-$OOC-), R30–E818 (2.6 Å, =NH_2^+●●●●$^-$OOC-) and

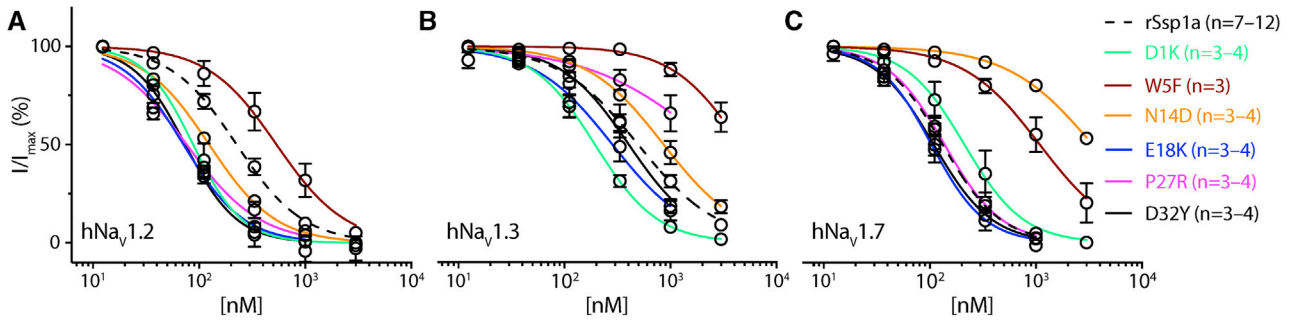

FIGURE 4
Dose-response of rSsp1a mutations. (**A–C**) Dose-response curve of selected rSsp1a analogues compared with rSsp1a at hNa$_V$1.2, hNa$_V$1.3, and hNa$_V$1.7 obtained using the whole-cell automated patch clamp electrophysiology (QPatch 16X) platform. Data presented as means ± SEM, with number of experiments (n) indicated in the legend.

R30–D816 (2.7 Å, =NH_2^+••••$^-$OOC-) were observed, with additional electrostatic interactions between W24–E759 (1.8 Å, >NH••••$^-$OOC-), W28–D816 (1.8 Å, >NH••••$^-$OOC-) and Y26–E810 (1.8 Å, -OH••••$^-$OOC-) (Figure 3C). The hydrophobic residues LFLA in the S3–S4 loop project into the hydrophobic groove in rSsp1a formed by W5, F6, Y20, Y31, and W28. This binding mode shifted W28 away from the aqueous cleft center towards the S3–S4 loop, with K25 expected to play a key role in restricting the upward movement of S4 upon depolarization to trap DII in the resting state. We also assessed the role of the non-conserved residue F813 from hNa$_V$1.7 DII S3–S4 in rSsp1a binding by using a F823G-mNa$_V$1.7 variant. The F823 in mNa$_V$1.7 DII corresponds to the F813 in the hNa$_V$1.7 DII. The F823G mutation slightly decreased the mNa$_V$1.7 sensitivity to rSsp1a (~2.5-fold) but was not critical for rSsp1a interaction (Figure 3D). Channel residues predicted by docking studies to interact with rSsp1a were highlighted in Supplementary Figure S4.

3.3 Optimizing rSsp1a

3.3.1 rSsp1a optimization through single residue substitution

Based on the active surface defined for rSsp1a through the alanine substitutions and evidence from earlier optimization studies of closely related homologs, we designed and tested several single residue substitutions for rSsp1a (Supplementary Figures S5A–E; Supplementary Figures S6A–F). A charge-reversing substitution of D1K, located away from the predicted interaction face (Supplementary Figures S6A), improved rSsp1a-activity at hNa$_V$1.2 and hNa$_V$1.3, but not at hNa$_V$1.7 (Figure 4; Supplementary Table S2). This suggests that the increased affinity of D1K-rSsp1a may be associated with lipid bilayer interactions that could facilitate interaction with hNa$_V$1.2 and hNa$_V$1.3. Substitution of the loop 1 hydrophobic residue W5 with a less bulky Phe was tolerated at hNa$_V$1.2 but not at hNa$_V$1.7 and hNa$_V$1.3 (Figure 4; Supplementary Table S2). Other substitutions at loop 1 had smaller effects on rSsp1a activity (Supplementary Table S2; Supplementary Figures S5A) and they surround the rSsp1a interaction face (Supplementary Figures S6B).

The surface exposed loop 2 variant N13G-rSsp1a (Supplementary Figures S6C) only slightly weakened activity at hNa$_V$1.7 (Supplementary Table S2; Supplementary Figures S5B). In contrast, introduction of an acidic residue Asp at the adjacent residue N14 slightly improved rSsp1a potency at hNa$_V$1.2, with little reduction of potency at hNa$_V$1.3 and >20-fold reduction of potency at hNa$_V$1.7. This provided N14D-rSsp1a variant hNa$_V$1.2-selectivity by >24-fold against hNa$_V$1.7 and by 7-fold against hNa$_V$1.3 (Figure 4; Supplementary Table S2). Reflecting the slight improvement observed at hNa$_V$1.2, the docking orientation of N14D-rSsp1a at hNa$_V$1.2 (Figure 5A) showed a small shift, which removed the Y26–E844 H-bond but favored a comparatively stronger π-stacking between W24 and Y781. However, in the docking orientation of N14D-rSsp1a at hNa$_V$1.7 (Supplementary Figures S7A), the major interaction D816–R30–E818 necessary to trap the DII S4 segment in its resting state was lost, contributing to the weaker toxin-channel interaction observed.

Of the five substitutions made in loop 3 (E18G, E18K, E18F, E18Y and Y20L), only the E18K substitution provided little or slight improvement in rSsp1a potency at all three hNa$_V$ subtypes (Figure 4; Supplementary Figures S5B; Supplementary Table S2), with the largest effect observed at hNa$_V$1.2 (>3-fold). E18 is spatially distant from the rSsp1a interaction face (Supplementary Figures S6D), suggesting that E18K-rSsp1a might allow longer-range dipole interactions with the lipid bilayer that enhance potency. Y20 is buried within the rSsp1a hydrophobic patch and contributes to rSsp1a activity (Figures 1B, D).

Loop 4 residues (residues 23–28) comprise the active surface of rSsp1a (Supplementary Figures S6E). To examine the role of loop 4, nine analogues mutating five residues from the loop 4 of rSsp1a were generated. Mutations of H23 caused a little increase in rSsp1a activity only for H23S at hNa$_V$1.2 (Supplementary Figures S5C; Supplementary Table S2). The W24R mutation partially inhibited hNa$_V$1.2 (~65%), and incompletely inhibited hNa$_V$1.7 (~50%) and hNa$_V$1.3 (~75%) at 3 μM (Supplementary Figures S8). In contrast, the Y26H mutation did not improve rSsp1a activity, while mutations reinstating conserved basic residues at position 27 (P27R and P27K) had opposing affinity at hNa$_V$1.3 and hNa$_V$1.2, providing >10-fold hNa$_V$1.2 selectivity (Figures 4A–C; Supplementary Figures S5C; Supplementary Table S2). However, the P27R and P27K analogues retained rSsp1a activity at hNa$_V$1.7 and the fold-potency differences of these two analogues between hNa$_V$1.2 and hNa$_V$1.7 is <2-fold. We then investigated the molecular basis for the improved selectivity of P27R-rSsp1a between hNa$_V$1.2 (Figure 5B) and hNa$_V$1.3

10.3389/fphar.2023.1277143

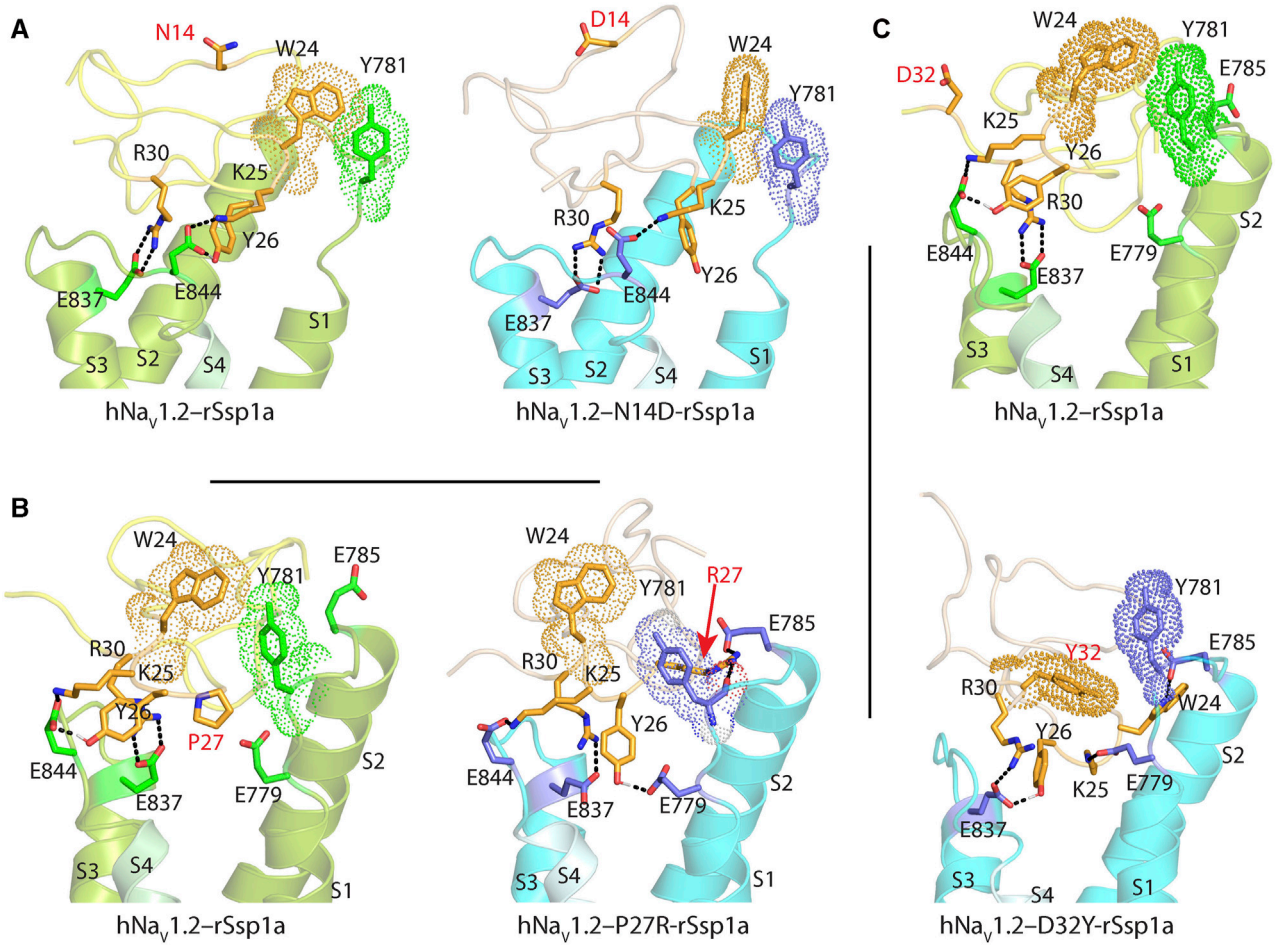

FIGURE 5
Molecular docking of rSsp1a single mutants. Visualization of molecular interactions of **(A)** N14D-rSsp1a, **(B)** P27R-rSsp1a and **(C)** D32Y-rSsp1a compared to rSsp1a at $hNa_V1.2$. Consistent with the activity data, rSsp1a and N14D-rSsp1a docked similarly at $hNa_V1.2$ while P27R-rSsp1a formed additional ionic interactions through the substituted R27 and E785 and Y781 (main chain). In addition, Y26–E779 engaged the S1–S2 loop to further strengthen the toxin–channel complex. Compared to rSsp1a, D32Y-rSsp1a formed a stronger interaction with $hNa_V1.2$, engaging both the S1–S2 and S3–S4 loops with ionic interactions, and consistent with the activity data.

(Supplementary Figures S7B). P27R-rSsp1a docked at $hNa_V1.2$ in a similar way to rSsp1a but included additional interactions with the S1–S2 loop. Specifically, in addition to the R30–E837 and K25–E844 ionic interactions in the S3–S4 loop, the substituted R27 formed a salt bridge with E785 and a H-bond with Y781 in the main chain, while Y26 interacted with E779 in the S1–S2 loop. These additional interactions at the S1–S2 loop stabilized the toxin-channel complex and improved the potency at $hNa_V1.2$. For the P27R-rSsp1a–$hNa_V1.3$ complex, the docking orientation most similar to the rSsp1a docking orientation was selected (Supplementary Figures S7B). These results revealed a spatial shift in the P27R-rSsp1a functional residues K25, Y26 and R30 that removed interactions between the active residues K25 and Y26 in rSsp1a and E838 and S848 in $hNa_V1.3$. These results are consistent with the reduced activity observed for P27R-rSsp1a at $hNa_V1.3$. The W28 residue of the WCK/R motif mutated to generate W28F and W28K analogues had a deleterious effect on hNa_V activity; however, the decrease in activity by W28F at $hNa_V1.7$ was only ~5-fold (Supplementary Figures S5C; Supplementary Table S2).

At the C-terminal, we mutated Y31 and D32 to generate six analogues. These two residues are close to the functional residues on the surface of rSsp1a, with Y31 forming the hydrophobic patch (Supplementary Figures S6F). Substitution of Y31 with bulky Trp significantly improved rSsp1a potency, while the Y31T mutation removed the activity (Supplementary Figures S5D; Supplementary Table S2). Substitutions made at D32, preferentially improved rSsp1a potency at $hNa_V1.2$ (up to 3-fold) and $hNa_V1.3$ (up to 6-fold). The D32F mutant significantly improved rSsp1a potency at $hNa_V1.3$ but not selectivity, while the D32Ymutant significantly improved rSsp1a potency (3-fold) and selectivity (~6-fold) for $hNa_V1.2$ against $hNa_V1.3$. The docking orientation of D32Y-rSsp1a at $hNa_V1.2$ (Figure 5C) differed compared to rSsp1a, allowing engagement of the S1–S2 loop with the ionic bond K25–E779. The DII S3–S4 loop key interactions, including R30–E837 and Y26–E837, were maintained while a new interaction (W24–E785) was formed. In addition, Y32 and Y781 showed the potential to engage through a π–π interaction based on their side chain flexibility; however, the orientation to support a π–π interaction was not evident in the molecular docking studies.

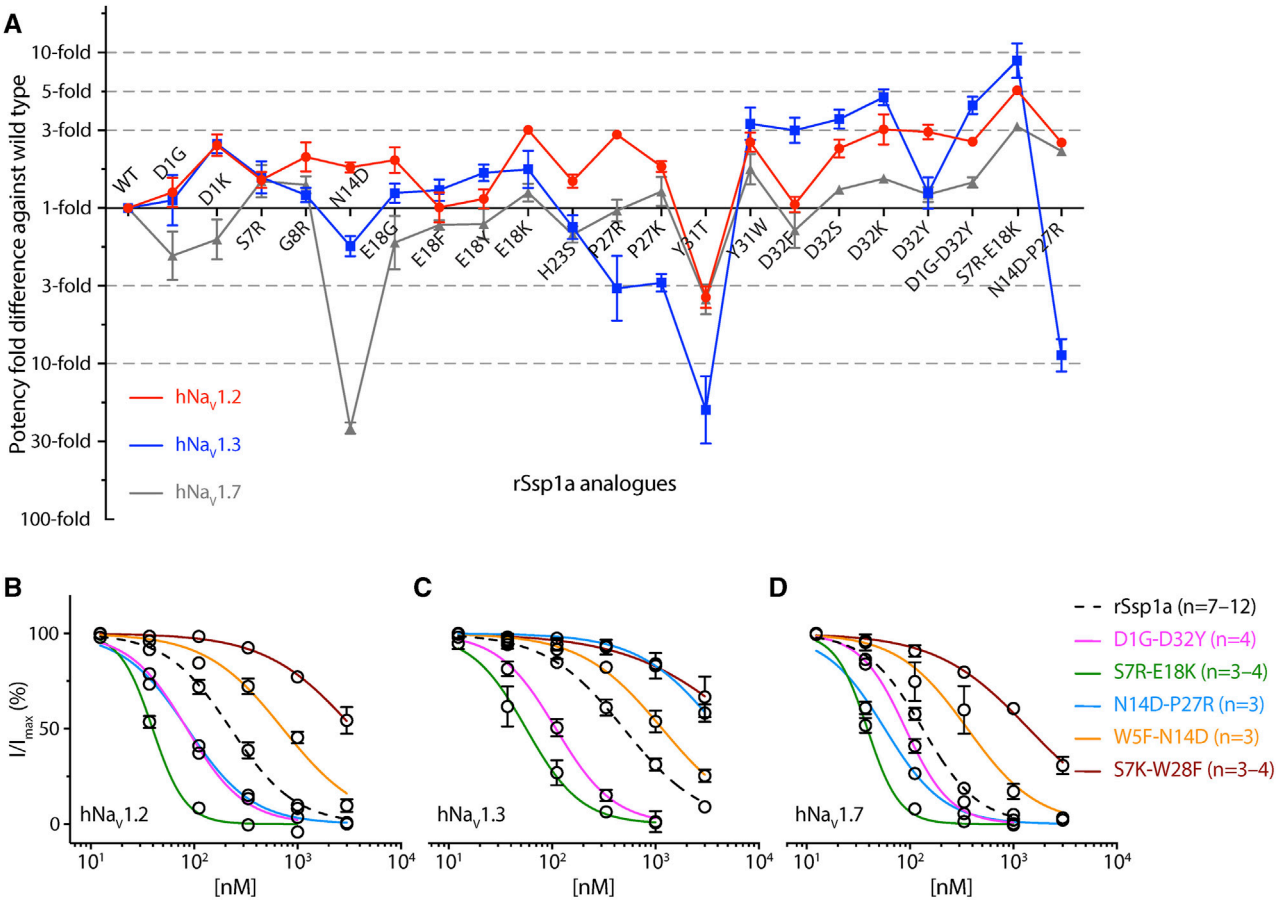

FIGURE 6
Potency and selectivity optimization of rSsp1a. **(A)** Potency fold-difference of selected rSsp1a analogues presented against the potency of wild type rSsp1a at $hNa_V1.2$, $hNa_V1.3$, and $hNa_V1.7$. Data were presented as means ± SEM (n = 3–12, except at $hNa_V1.2$ for E18F n = 2). **(B–D)** Dose-response curve of rSsp1a double mutants compared with rSsp1a at $hNa_V1.2$, $hNa_V1.3$ and $hNa_V1.7$, obtained using the whole-cell automated patch clamp electrophysiology (QPatch 16X) platform. Data presented as means ± SEM, with number of experiments (n) indicated in the legend.

TABLE 1 Double mutant designs for improved subtype-selectivity.

Mutant	Intended subtype-selectivity	Outcome
D1G-D32Y	$hNa_V1.2$	Enhanced affinity at $hNa_V1.3$ and $hNa_V1.7$, generating a non-selective inhibitor with nanomolar potency at the three hNa_V subtypes tested
W5F-N14D	$hNa_V1.2$	Predicted cumulative effects of single mutants that enhanced $hNa_V1.2$ selectivity were not realised
S7R-E18K	$hNa_V1.2$ and/or $hNa_V1.3$	Enhanced affinity at $hNa_V1.2$, $hNa_V1.3$ and $hNa_V1.7$, generating a non-selective inhibitor with nanomolar potency at the three hNa_V subtypes
S7K-W28F	$hNa_V1.7$	Reduced potency at $hNa_V1.7$
N14D-P27R	$hNa_V1.2$	Reverted the potency loss by N14D at $hNa_V1.7$ and provided $hNa_V1.2$/$hNa_V1.7$ selectivity against $hNa_V1.3$

3.3.2 rSsp1a optimization through combinatorial mutation

Guided by the potency and subtype-selectivity results of the single mutants, the double mutants D1G-D32Y, S7R-E18K, N14D-P27R, W5F-N14D and S7K-W28F were synthesised and tested (Figures 6A–D; Table 1). In contrast to the selectivity observed against $hNa_V1.3$ for the D32Y mutation, the D1G-D32Y mutation had significantly improved potency at $hNa_V1.3$ and $hNa_V1.7$ (Figure 6A). The S7R-E18K-rSsp1a analogue showed the greatest improvement in potency of the rSsp1a analogues tested, with $hNa_V1.2$ potency enhanced 6-fold, $hNa_V1.3$ enhanced ~10-fold, and $hNa_V1.7$ enhanced >3-fold. The N14D-P27R analogue

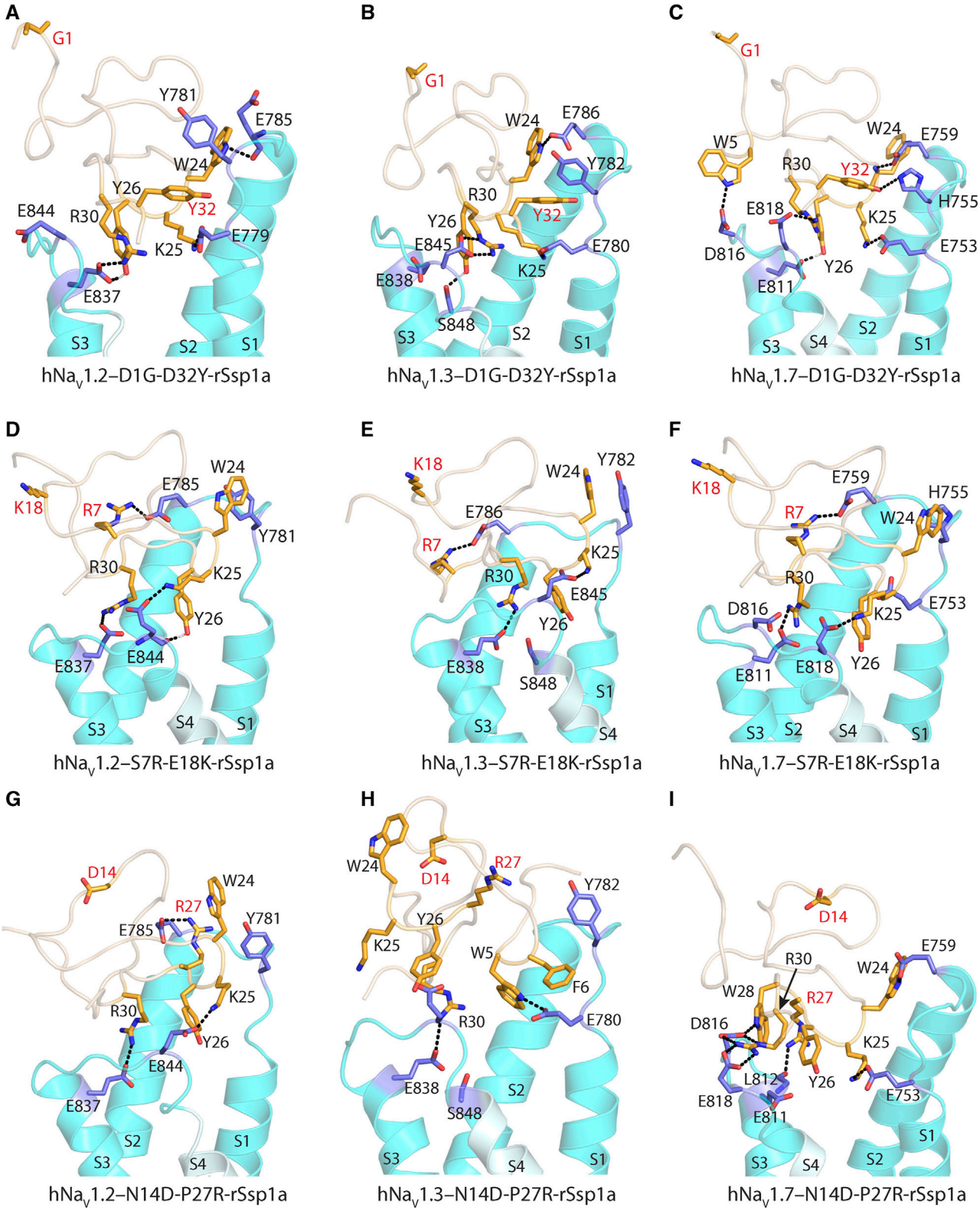

FIGURE 7
Molecular docking of rSsp1a double mutants. **(A)** D1G-D32Y-rSsp1a docked differently at hNa$_V$1.2 compared to rSsp1a (Supplementary Figures S9A) to form stronger ionic bonds, engaging both the S1–S2 and S3–S4 loops, as well as a possible π–π interaction between Y32–Y781, which was consistent with the activity data. **(B)** D1G-D32Y-rSsp1a docked at hNa$_V$1.3 similar to docking to hNa$_V$1.2, but in a different orientation compared to rSsp1a (Supplementary Figures S9B), which enabled stronger interactions that engaged both the S1–S2 and S3–S4 loops and a possible Y32–Y782 π–π interaction. **(C)** At hNa$_V$1.7, both rSsp1a (Supplementary Figures S9C) and D1G-D32Y-rSsp1a docked with a similar orientation, forming new interactions including W5–D816 and Y32–H755. **(D)** At hNa$_V$1.2, S7R-E18K-rSsp1a docked similar to rSsp1a (Supplementary Figures S9D) with R7 in S7R-E18K-rSsp1a
(*Continued*)

FIGURE 7 (Continued)
forming an ionic bond with E785 from the S1–S2 loop. In addition, a π–π interaction between W24–Y781 in a parallel displaced geometry was noted. These extra interactions engaging the S1–S2 loop are predicted to form a tighter toxin–channel complex, thus improving the toxin potency. **(E)** S7R-E18K-rSsp1a docked at $hNa_V1.3$ similar to docking to $hNa_V1.2$ and in an orientation similar to rSsp1a (Supplementary Figures S9E). An additional R7–E786 salt bridge engaging the S1–S2 loop is predicted to form a tighter toxin–channel complex. **(F)** At $hNa_V1.7$, S7R-E18K-rSsp1a docked differently to rSsp1a (Supplementary Figures S9F), but contained salt bridges K25–E818, R30–E811 and R7–E759 that tightly engaged the S1–S2 and S3–S4 loop. In addition to the extra R7–E759 salt bridge, a possible W24–H755 π–π interaction was observed. **(G)** At $hNa_V1.2$, N14D-P27R-rSsp1a docked similar to rSsp1a (Supplementary Figures S9G) with the R27 in N14D-P27R-rSsp1a forming an ionic bond with E785 from the S1–S2 loop. **(H)** The docking orientation for N14D-P27R-rSsp1a at $hNa_V1.3$ was chosen to resemble rSsp1a docking. The lack of activity of N14D-P27R-rSsp1a at $hNa_V1.3$ was consistent with the absence of major interactions. **(I)** At $hNa_V1.7$, N14D-P27R-rSsp1a docked similar to rSsp1a (Supplementary Figures S9I) with R27 interacting with the L812 carbonyl group. The substituted residues are highlighted in red.

decreased the rSsp1a potency at $hNa_V1.3$ (~40% block at 3μM) and reversed the potency reduction at $hNa_V1.7$ caused by the N14D mutation. The results reveal that the potency and subtype-selectivity at $hNa_V1.2$ conferred by the N14D and P27R mutations was not additive in the double mutant. The W5F-N14D and S7K-W28F mutants designed for $hNa_V1.2$- and $hNa_V1.7$-selectivity were unsuccessful.

Further, docking studies were performed to visualize the molecular basis of potency and subtype-selectivity on the D1G-D32Y-rSsp1a, S7R-E18K-rSsp1a and N14D-P27R-rSsp1a double mutants at the three hNa_V subtypes (Figures 7A–I; Supplementary Figures S9A–I). At $hNa_V1.2$, D1G-D32Y-rSsp1a docked differently to rSsp1a to form stronger ionic bonds that engaged both the S1–S2 and S3–S4 loops (Figure 7A; Supplementary Figures S9A). The R30–E837 and Y26–E837 interactions engaged the $hNa_V1.2$ DII S3–S4 loop, while the K25–E779 and W24–E785 interactions engaged with the S1–S2 loop. The proximity of Y32 to Y781 suggested π–π interactions were probable. Similar interactions were also observed for D1G-D32Y-rSsp1a docking with $hNa_V1.3$ (Figure 7B; Supplementary Figures S9B). When docked at $hNa_V1.7$, such π–π interaction with Y32 was not formed with the equivalent H755 in the $hNa_V1.7$ DII S1–S2 loop. However, interactions between Y32–H755 and W5–D816, in addition to R30–E818, Y26–E811, K25–E753 and W24–E759, predicted enhanced D1G-D32Y-rSsp1a potency compared to rSsp1a at $hNa_V1.7$ (Figure 7C; Supplementary Figures S9C).

S7R-E18K-rSsp1a docked at $hNa_V1.2$ (Figure 7D; Supplementary Figures S9D) and $hNa_V1.3$ (Figure 7E; Supplementary Figures S9E) in a similar way to rSsp1a, maintaining the major S3–S4 loop interactions. However, a new salt bridge was predicted to be formed between the substituted R7 and Glu from the S1–S2 loop in both hNa_V subtypes. In addition, the π–π interaction between W24 and Y781 (in $hNa_V1.2$) or Y782 (in $hNa_V1.3$) potentially stabilized the toxin–channel complex. At $hNa_V1.7$, the S7R-E18K-rSsp1a mutant docked in a different orientation to rSsp1a but retained the major R30–E811 and K25–E818 salt bridges, in addition to an extra R7–E759 salt bridge (Figure 7F; Supplementary Figures S9F). The closely oriented W24 and H755 were predicted to form a π–π interaction instead of the W24–E759 electrostatic interaction observed for rSsp1a.

The docking orientation of N14D-P27R-rSsp1a at $hNa_V1.2$ and $hNa_V1.7$ (Figures 7G, I; Supplementary Figures S9G, I) showed all major salt bridges were retained and the substituted R27 interacted with E785 from the S1–S2 loop in $hNa_V1.2$ and the L812 main chain carbonyl oxygen from the S3–S4 loop in $hNa_V1.7$. The docking of N14D-P27R-rSsp1a at $hNa_V1.3$ closely overlapped the rSsp1a docking orientation, with the loss of a major salt bridge formed by K25 and the substituted R27 did not engage with $hNa_V1.3$ DII residues (Figure 7H; Supplementary Figures S9H), contributing to its observed weaker binding at $hNa_V1.3$ (Figure 6).

3.3.3 rSsp1a optimization through N-terminal and C-terminal extension

Finally, we extended the rSsp1a N-terminal with GP- to mimic GP-HwTx-IV (Neff et al., 2020) and GP-ProTx-II (Flinspach et al., 2017), while the C-terminal was extended with -GK to mimic the C-terminal amides as previously designed for HwTx-IV (Minassian et al., 2013; Neff et al., 2020). Both GP-rSsp1a and rSsp1a-GK (Supplementary Table S3) did not improve rSsp1a activity or selectivity (Supplementary Figures S5E). Further, the Y26H-rSsp1a mutant with an extra two Leu at the C-terminal (Y26H-rSsp1a-LL) was made to assess the effect of the C-terminal extension with small, linear hydrophobic residues, however, the analogue did not improve the activity or selectivity.

4 Discussion

In recent decades, Na_V-modulating spider ICK toxins have generated significant interest in drug discovery (Dongol et al., 2019), with potential to target Na_V subtypes of therapeutic interest (Xie et al., 2015; Su et al., 2017; Salvatierra et al., 2018; Cardoso, 2020; Menezes et al., 2020). Despite the need to discover and develop subtype-selective Na_V-modulators, few comprehensive structure-function studies of NaSpTxs have been reported, with most focusing on $hNa_V1.7$ (Minassian et al., 2013; Revell et al., 2013; Murray et al., 2015; Hu et al., 2021). These findings have helped guide analogue development of NaSpTxs aimed at improving potency and subtype-selectivity for $hNa_V1.7$ (Revell et al., 2013; Klint et al., 2015; Murray et al., 2015; Murray et al., 2016; Shcherbatko et al., 2016; Agwa et al., 2017; Flinspach et al., 2017; Rahnama et al., 2017; Zhang et al., 2018; Mueller et al., 2020; Neff et al., 2020; Rupasinghe et al., 2020; Hu et al., 2021), while NaSpTx optimization at other subtypes have been overlooked. This study addresses the gap by investigating the structure-function relationships and optimization of Ssp1a at $hNa_V1.2$, $hNa_V1.3$ and $hNa_V1.7$.

4.1 Structure-function of rSsp1a at $hNa_V1.2$, $hNa_V1.3$ and $hNa_V1.7$

The active surface defined for rSsp1a and close homologs GpTx-1 (Murray et al., 2015), HwTx-IV (Revell et al., 2013), and m3-

HwTx-IV (Wisedchaisri et al., 2021) are similar, consistent with the concept of conservation in the interaction face of the peptides adopting the same fold with >30% sequence identity (Russell et al., 2004; Tuncbag et al., 2011). These comparisons reveal that the hydrophobic patch of rSsp1a forms the major binding face, with basic residues K25 (loop 4) and R30 (C-terminal) and the hydrophobic Y26 (loop 4) also expected to contribute to binding (Figure 1B; Figures 3A–C). Specifically, the hydrophobic residues W5, F6, W24 and W28 were predicted to be key to the rSsp1a activity. This is consistent with the conservation of Trp, Arg and Tyr in the binding site of peptides/proteins (Moreira et al., 2007), including the NaSpTx1 toxins (Klint et al., 2012; Minassian et al., 2013; Revell et al., 2013; Murray et al., 2015; Wisedchaisri et al., 2021). Although the structure-function of close homologs can be predicted, variations in the selectivity of analogs across Na_V subtypes provides an opportunity to optimize peptides to improve potency and selectivity towards a specific target. For example, P27A-rSsp1a only lost activity at $hNa_V1.3$, suggesting that the non-conserved Pro at this position likely played less of a structural role in rSsp1a and could be exploited to make designs non-selective to $hNa_V1.3$. This is supported by P27R mutation, which significantly improved rSsp1a activity at $hNa_V1.2$ while losing activity at $hNa_V1.3$ (Figure 4; Supplementary Table S2).

Based on the biophysical studies of rSsp1a (Dongol et al., 2021), we predicted that rSsp1a interacted with hNa_V subtypes similarly to HwTx-IV (Xiao et al., 2008) to trap the $hNa_V1.7$ DII in the resting state conformation. The available 3D structure of rSsp1a, activity data of rSsp1a alanine mutants, recently published cryo-EM structure of the resting state $hNa_V1.7$ DII (Wisedchaisri et al., 2021), previously published channel mutation data (Xiao et al., 2010; Xiao et al., 2011; Cai et al., 2015; Zeng et al., 2018; Xu et al., 2019), and the high sequence homology at the predicted interacting face encouraged data-driven docking of rSsp1a at $hNa_V1.2$, $hNa_V1.3$ and $hNa_V1.7$. Data-driven docking can often accurately predict the molecular interaction at the binding interface in the absence of high-resolution atomic structures to illustrate the molecular interactions (Rodrigues and Bonvin, 2014). The rSsp1a docking across hNa_V subtypes revealed the molecular mechanism of interaction is comparable to m3-HwTx-IV–$Na_V1.7$ (Wisedchaisri et al., 2021), while highlighting the subtle differences in rSsp1a binding mode across hNa_V subtypes (Figures 2, 3), as illustrated by the twisted docking orientation of rSsp1a at $hNa_V1.7$ compared to $hNa_V1.2$ and $hNa_V1.3$. The more hydrophobic LFLA stretch in $hNa_V1.7$ DII S3–S4, as compared to LGLA ($hNa_V1.2$) and LGLS ($hNa_V1.3$), potentially contributed to an observed twist and a shift in the docking of rSsp1a towards the S3–S4 loop in $hNa_V1.7$, and to a lesser extent in $hNa_V1.2$ and $hNa_V1.3$. This shift and twist likely facilitated stronger subtype-specific hydrophobic interactions in $hNa_V1.7$, with rSsp1a′s hydrophobic pocket locking the channel's LFLA stretch, as opposed to $hNa_V1.2$ and $hNa_V1.3$, where the channel's hydrophobic patch accommodated the hydrophobic residues of rSsp1a (Figures 3A–C). Additionally, the distinct binding pose of rSsp1a at $hNa_V1.7$ also enabled electrostatic interactions with DII S1–S2 loop, which are not observed in $hNa_V1.2$ and $hNa_V1.3$. Such differences in binding mode across hNa_V subtypes provide novel opportunities to optimize toxin-channel interactions across the hNa_V subtypes.

The key molecular interactions revealed by the docking studies involve strong salt bridges (≤3 Å) formed between rSsp1a basic residues and the channel subtype's acidic residues in DII S3–S4 loop (Figures 3A–C), including E753 in the DII S1–S2 loop in $hNa_V1.7$ that might allow the rational design of subtype-selective inhibitors. At $hNa_V1.7$, additional interactions between indole nitrogen (W24 and W28) and carboxylate (E759 and D816) were observed, possibly strengthening the rSsp1a binding. In contrast, hydrophobic interactions between rSsp1a residue W24 and a Tyr residue in DII S1–S2 loop of $hNa_V1.2$ and $hNa_V1.3$ were observed. These hydrophobic interactions represent another key molecular mechanism involved in trapping DII in the resting state. For example, prior research (Wisedchaisri et al., 2021) predicted that the hydrophobic interaction between the m3-HwTx-IV hydrophobic patch (I5, F6, W30, and W33) and the LFLA stretch in DII S3–S4 loop (Supplementary Figures S3B) hinders the upward movement of the S4 segment, effectively trapping DII in the resting state. A similar mechanism was observed in the docking of rSsp1a with $hNa_V1.7$, although distinct hydrophobic interactions were observed in the case of $hNa_V1.2$ and $hNa_V1.3$ (Figures 3A–C).

Despite the high sequence homology across Na_V subtypes, there is an important variation in the DII S3–S4 hydrophobic stretch in $Na_V1.7$ where a bulky hydrophobic Phe replaces the small, non-polar Gly prevalent across other Na_V subtypes except $Na_V1.6$ and $Na_V1.9$. Using the F823G-$mNa_V1.7$ variant (equivalent to F813 in $hNa_V1.7$) revealed that the Phe unique to $hNa_V1.7$ was not critical for rSsp1a interaction (Figure 3D), similarly to HwTx-IV (Xiao et al., 2010). In contrast, this mutation desensitized $mNa_V1.7$ binding to Pn3a from NaSpTx2 family by 28-fold (Mueller et al., 2020) and the binding to ProTx-II from NaSpTx3 family by 9–100 fold (Schmalhofer et al., 2008; Xiao et al., 2010). This pharmacology was verified by the structure of ProTx-II–DII-Na_VAb complex, where two hydrophobic residues W5 and M6 from ProTx-II flanked F813 to stabilize the DII S3–S4 helix (Xu et al., 2019). However, the docking orientation of rSsp1a (Figure 3C) and m3-HwTx-IV (Supplementary Figures S3B) (Wisedchaisri et al., 2021) at $hNa_V1.7$ DII revealed that these two toxins positioned themselves on top of the LFLA motif rather than surrounding F813, agreeing to small reduction of F813G-$hNa_V1.7$ or F823G-$mNa_V1.7$ affinity to HwTx-IV (Xiao et al., 2010) or rSsp1a, respectively.

4.2 Optimization of rSsp1a at $hNa_V1.2$, $hNa_V1.3$ and $hNa_V1.7$

Several optimization studies on NaSpTx toxins have indicated that removing the negative charge at the N-terminal by introducing pyroglutamate, 1-Nal (1-naphthylalanine), Gly, or GP- or simply substituting the acidic residue with Ala or Gly might contribute to toxin binding, potency, and/or selectivity (Minassian et al., 2013; Revell et al., 2013; Rong et al., 2013; Shcherbatko et al., 2016). Extra N-terminal Gly and GP- residues are remnants of TEV and HRV3C digestion of recombinantly expressed fusion proteins, respectively (Klint et al., 2013; Minassian et al., 2013; Flinspach et al., 2017). These non-native residues at the N-terminal are an advantage of the recombinant expression system, as replacing N-terminal acidic residue with Gly in HwTx-IV and HnTx-I has improved the toxin potency (Revell et al., 2013; Rahnama et al., 2017; Zhang et al., 2018). rSsp1a inclusion of a non-native Gly (G0) resulting from TEV digestion and the D1G mutation removed the N-terminal

negative charge. In contrast to HwTx-IV (Revell et al., 2013), the D1G-rSsp1a mutant reduced activity at $hNa_V1.7$, while no significant changes were observed at $hNa_V1.2$ and $hNa_V1.3$ (Supplementary Table S2). Instead, a charge reversal mutation (D1K) slightly improved $hNa_V1.2$ and $hNa_V1.3$ activity with little reduction in $hNa_V1.7$ activity, suggesting it could be used when combining mutations to achieve $hNa_V1.2$- and/or $hNa_V1.3$-selectivity. The D1K mutation is located outside the predicted interacting face of rSsp1a, suggesting this position plays an indirect role in binding, likely through longer-range charge effects. Previous studies have identified that the increased cationicity, as well as the presence of both native and substituted cationic residues (primarily Lys) contributes to the enhanced electrostatic interaction with anionic moieties within the lipid bilayer, including anionic lipid head groups, that can facilitate initial toxin-ion channel interactions (Henriques et al., 2016; Agwa et al., 2017; Agwa et al., 2018; Lawrence et al., 2019). Again, such toxin-membrane lipid binding can be subtype-specific, with D1K-rSsp1a showing reduced potency at $hNa_V1.7$ but not at $hNa_V1.2$ and $hNa_V1.3$.

In rSsp1a loop 1, reinstating cationic residue at position 7 had little effect on rSsp1a potency (Supplementary Figures S5A; Supplementary Table S2) contrasting to the key role played by R7 in GpTx-I activity (Murray et al., 2015; Murray et al., 2016) and K7 in HwTx-IV activity (Minassian et al., 2013) on $hNa_V1.7$. Interestingly, reinstating the predominant Lys did not improve rSsp1a potency while restoring the less predominant Arg showed little improvement in the rSsp1a potency, making it a prospective single mutation to combine with other mutations. Further, substituting key residue W5 with less hydrophobic Phe provided rSsp1a $hNa_V1.2$-selectivity with <3-fold reduction in potency.

Two mutations in loop 2, N13G and N14D, were anticipated to provide subtype-selectivity and improved potency at $hNa_V1.7$, respectively (Minassian et al., 2013; Neff et al., 2020). In contrast to N13G-HwTx-IV (Neff et al., 2020), N13G-rSsp1a lost the activity at $hNa_V1.7$. But surprisingly, N14D-rSsp1a significantly lost the $hNa_V1.7$ activity with slight improvement in $hNa_V1.2$ activity and little reduction in $hNa_V1.3$ activity, providing N14D-rSsp1a $hNa_V1.2$-selectivity (Figure 6A) and could be considered for combination with other mutations to achieve $hNa_V1.2$-selectivity.

Acidic residues in loop 3 are less frequent in NaSpTx1 family toxins (Klint et al., 2012). Therefore, E18 in rSsp1a was substituted to remove the negative charge, reverse the charge, or to introduce hydrophobicity. The charge reversal mutation E18K improved potency at all three hNa_V subtypes and its location away from the rSsp1a interaction face, like D1K mutation, suggested its indirect role in potency improvement, as discussed above.

Loop 4 in rSsp1a constitutes active residues, including P27 that was critical only for $hNa_V1.3$ activity (Figure 1B). Substituting the rare W24 with more conserved Arg or Ser did not improve rSsp1a activity at hNa_V subtypes. W24 was important for rSsp1a activity, contrasting with the equivalent Arg in HwTx-IV and GpTx-1, which was important for HwTx-IV activity at $hNa_V1.2$ (Minassian et al., 2013), and GpTx-1 (Murray et al., 2015) and HwTx-IV (Minassian et al., 2013) activity at $hNa_V1.7$. Y26H was designed to reinstate more common His, as the equivalent H27A-GpTx-1 decreased in potency at $hNa_V1.7$ by >10-fold (Murray et al., 2015; Murray et al., 2016), while D26H-HnTx-I improved $hNa_V1.7$ activity by >7-fold (Zhang et al., 2018). However, the design neither improved potency nor selectivity of rSsp1a (Supplementary Figures S5C; Supplementary Table S2), confirming the significance of Y26 as an active residue. The P27R that reinstated the more frequent basic residue in the position improved rSsp1a potency specifically at $hNa_V1.2$, suggesting incorporating it in a combined mutation to generate $hNa_V1.2$-selective analogues.

The comprehensive substitution of HwTx-IV residues suggested acidic residues at the C-terminal are not preferred to improve activity at $hNa_V1.2$ and $hNa_V1.7$ (Neff et al., 2020). Thus, D32, which also neighbors the rSsp1a interaction face, was substituted with several functionalities, including polar uncharged, basic, and hydrophobic entities, to evaluate their role in rSsp1a potency and selectivity (Figure 6A; Supplementary Table S2). D32S improved the rSsp1a potency at $hNa_V1.2$ (2.5-fold) and $hNa_V1.3$ (4-fold) compared to $hNa_V1.7$ (1.3-fold) but did not provide subtype-selectivity. In contrast, D32F improved rSsp1a potency only at $hNa_V1.3$ (~3.5-fold) but did not provide $hNa_V1.3$-selectivity, given the lower potency of rSsp1a at $hNa_V1.3$ compared to remaining two hNa_V subtypes. Similarly, the lack of $hNa_V1.3$-selectivity was also observed for D32K mutation despite improved $hNa_V1.3$ inhibition by 6-fold. Interestingly, D32Y provided $hNa_V1.2$-selectivity (5.5-fold) against $hNa_V1.3$ with improved potency (3-fold). This contrasts with $hNa_V1.3$-active CcoTx-2 which is a natural variant of $hNa_V1.3$-inactive CcoTx-1 with D32Y mutation (Bosmans et al., 2006). Thus, D32Y could be combined to generate $hNa_V1.2$-selective analogues. Optimization studies of CcoTx-1 (Shcherbatko et al., 2016), GpTx-1 (Murray et al., 2016) and HwTx-IV (Revell et al., 2013; Neff et al., 2020) suggested mutating Y31 in rSsp1a could improve potency and selectivity. Surprisingly, Y31T-rSsp1a did not contribute to $hNa_V1.7$-selectivity (Figure 6A), in contrast to the 10-fold $hNa_V1.7$-selectivity gained against $hNa_V1.2$ by equivalent Y33T-HwTx-IV (Neff et al., 2020). Instead, Y31W-rSsp1a improved the hNa_V activity between 1.5 and 3.5-fold, suggesting a preference of bulky hydrophobic in this position.

The potency and selectivity data from single-point mutations guided us to design five double mutants, from which only three designs improved rSsp1a activity (Figures 6A–D). The D1G-D32Y-rSsp1a designed for $hNa_V1.2$-selectivity instead improved potency at all three subtypes, showing that the effects of combining single mutations can be unpredictable. Of the 38 optimized rSsp1a analogues, the S7R-E18K-rSsp1a showed the most enhanced potency (up to 10-fold), with the effect of each single mutation being additive when combined and improved potency at all three hNa_V subtypes, thus minimising subtype-selectivity (Figure 6A). In contrast to the double mutant S7R-E18K-rSsp1a, the N14D-P27R-rSsp1a double mutant showed additive effects at $hNa_V1.3$ but not at $hNa_V1.7$, while the neutral effect at $hNa_V1.2$ helped it to achieve dual selectivity for $hNa_V1.2$ and hNav1.7. While the use of $hNa_V1.2$/hNav1.7-selective drugs is typically limited due to potential side effects (Eaton et al., 2021; Zhang et al., 2021; Echevarria-Cooper et al., 2022), this double mutant provides a new starting point for the design of $hNa_V1.2$-selective and hNav1.7-selective leads. Overall, rSsp1a optimization by combining two single-point mutations provided two major designs, S7R-E18K with improved potency and N14D-P27R with improved selectivity. Both S7R-E18K and N14D-P27R mutants represent promising starting points for further analogue studies to improve potency and/or subtype-

selectivity across hNa$_V$1.2, 1.3 and 1.7. Supporting these experimental findings, *in silico* docking studies of optimized rSsp1a analogues revealed key molecular interactions underpinning the improved potency and selectivity observed, including new or altered electrostatic, hydrophobic, π-π interactions, and interactions with the S1–S2 loop of hNa$_V$ channels.

In conclusion, we examined the pharmacology of 54 rSsp1a analogues to understand how this NaSpTx1 toxin can be modified to differentially alter interactions at hNa$_V$1.2, hNa$_V$1.3 and hNa$_V$1.7. The inclusion of hNa$_V$1.3 interactions provides the first view of NaSpTx1 pharmacology at this subtype. Given Ssp1a is distantly related to HwTx-IV (40% identity), which has comprehensive structure-function and optimization data and shares related pharmacology, the structure-function and optimization data of rSsp1a can be used to enrich the rational design of NaSpTx1 family toxins more broadly. Finally, this study reveals the complexities of moving from single to dual and triple mutations to develop improved research tools and/or potential therapeutic leads.

Data availability statement

The datasets presented in this study can be found in online repositories. The names of the repository/repositories and accession number(s) can be found in the article/Supplementary Material.

Ethics statement

Ethical approval was not required for the studies on animals in accordance with the local legislation and institutional requirements because only commercially available established cell lines were used.

Author contributions

YD: Conceptualization, Formal Analysis, Investigation, Methodology, Visualization, Writing–original draft, Writing–review and editing. DTW: Methodology, Writing–review and editing. NLD: Formal Analysis, Writing–review and editing, Funding acquisition. FCC: Supervision, Writing–review and editing, Funding acquisition. RJL: Conceptualization, Funding acquisition, Resources, Supervision, Visualization, Writing–review and editing, Project administration.

Funding

The authors declare financial support was received for the research, authorship, and/or publication of this article. This work was funded by the Australian National Health and Medical Research Council (NHMRC) Program Grant APP1072113 and Principal Research Fellowship APP1119056 (RJL); an NHMRC Ideas Grant APP1188959 (RJL, FCC); University of Queensland Research Training Scholarship (YD); and Australian Research Council LIEF Grants [LE120100015, LE160100218, (NLD)].

Acknowledgments

We thank Prof Irina Vetter and Jennifer Deuis from Vetter lab for providing HEK293 cells stably expressing mNa$_V$1.7 and F823G-mNa$_V$1.7.

Conflict of interest

The authors declare that the research was conducted in the absence of any commercial or financial relationships that could be construed as a potential conflict of interest.

The authors declared that they were an editorial board member of Frontiers, at the time of submission. This had no impact on the peer review process and the final decision.

Publisher's note

Supplementary material

The Supplementary Material for this article can be found online at: https://www.frontiersin.org/articles/10.3389/fphar.2023.1277143/full#supplementary-material

References

Adams, M. E., Herold, E. E., and Venema, V. J. (1989). Two classes of channel-specific toxins from funnel web spider venom. *J. Comp. Physiol. A* 164, 333–342. doi:10.1007/BF00612993

Agwa, A. J., Lawrence, N., Deplazes, E., Cheneval, O., Chen, R. M., Craik, D. J., et al. (2017). Spider peptide toxin HwTx-IV engineered to bind to lipid membranes has an increased inhibitory potency at human voltage-gated sodium channel hNa$_V$1.7. *Biochim. Biophys. Acta* 1859, 835–844. doi:10.1016/j.bbamem.2017.01.020

Agwa, A. J., Peigneur, S., Chow, C. Y., Lawrence, N., Craik, D. J., Tytgat, J., et al. (2018). Gating modifier toxins isolated from spider venom: modulation of voltage-gated sodium channels and the role of lipid membranes. *J. Biol. Chem.* 293, 9041–9052. doi:10.1074/jbc.RA118.002553

Ahern, C. A., Payandeh, J., Bosmans, F., and Chanda, B. (2016). The hitchhiker's guide to the voltage-gated sodium channel galaxy. *J. Gen. Physiol.* 147, 1–24. doi:10.1085/jgp.201511492

Black, J. A., Cummins, T. R., Plumpton, C., Chen, Y. H., Hormuzdiar, W., Clare, J. J., et al. (1999). Upregulation of a silent sodium channel after peripheral, but not central, nerve injury in DRG neurons. *J. Neurophysiol.* 82, 2776–2785. doi:10.1152/jn.1999.82.5.2776

Black, J. A., Nikolajsen, L., Kroner, K., Jensen, T. S., and Waxman, S. G. (2008). Multiple sodium channel isoforms and mitogen-activated protein kinases are present in painful human neuromas. *Ann. Neurol.* 64, 644–653. doi:10.1002/ana.21527

Bosmans, F., Rash, L., Zhu, S., Diochot, S., Lazdunski, M., Escoubas, P., et al. (2006). Four novel tarantula toxins as selective modulators of voltage-gated sodium channel subtypes. *Mol. Pharmacol.* 69, 419–429. doi:10.1124/mol.105.015941

Cai, T., Luo, J., Meng, E., Ding, J., Liang, S., Wang, S., et al. (2015). Mapping the interaction site for the tarantula toxin Hainantoxin-IV (β-TRTX-Hn2a) in the voltage sensor module of domain II of voltage-gated sodium channels. *Peptides* 68, 148–156. doi:10.1016/j.peptides.2014.09.005

Cardoso, F. C. (2020). Multi-targeting sodium and calcium channels using venom peptides for the treatment of complex ion channels-related diseases. *Biochem. Pharmacol.* 181, 114107. doi:10.1016/j.bcp.2020.114107

Cardoso, F. C., and Lewis, R. J. (2018). Sodium channels and pain: from toxins to therapies. *Br. J. Pharmacol.* 175, 2138–2157. doi:10.1111/bph.13962

Cardoso, F. C., and Lewis, R. J. (2019). Structure-function and therapeutic potential of spider venom-derived cysteine knot peptides targeting sodium channels. *Front. Pharmacol.* 10, 366. doi:10.3389/fphar.2019.00366

Cardoso, F. C., Servent, D., and de Lima, M. E. (2022). Editorial: venom peptides: a rich combinatorial library for drug development. *Front. Mol. Biosci.* 9, 924023. doi:10.3389/fmolb.2022.924023

Chen, H. P., Zhou, W., Kang, L. M., Yan, H., Zhang, L., Xu, B. H., et al. (2014). Intrathecal miR-96 inhibits $Na_V1.3$ expression and alleviates neuropathic pain in rat following chronic constriction injury. *Neurochem. Res.* 39, 76–83. doi:10.1007/s11064-013-1192-z

de Lera Ruiz, M., and Kraus, R. L. (2015). Voltage-gated sodium channels: structure, function, pharmacology, and clinical indications. *J. Med. Chem.* 58, 7093–7118. doi:10.1021/jm501981g

de Vries, S. J., Van Dijk, M., and Bonvin, A. M. (2010). The HADDOCK web server for data-driven biomolecular docking. *Nat. Protoc.* 5, 883–897. doi:10.1038/nprot.2010.32

Dib-Hajj, S. D., and Waxman, S. G. (2019). Sodium channels in human pain disorders: genetics and pharmacogenomics. *Annu. Rev. Neurosci.* 42, 87–106. doi:10.1146/annurev-neuro-070918-050144

Dongol, Y., Cardoso, F. C., and Lewis, R. J. (2019). Spider knottin pharmacology at voltage-gated sodium channels and their potential to modulate pain pathways. *Toxins (Basel)* 11, 626. doi:10.3390/toxins11110626

Dongol, Y., Choi, P. M., Wilson, D. T., Daly, N. L., Cardoso, F. C., and Lewis, R. J. (2021). Voltage-gated sodium channel modulation by a new spider toxin Ssp1a isolated from an Australian theraphosid. *Front. Pharmacol.* 12, 795455. doi:10.3389/fphar.2021.795455

Eaton, M., Zhang, J., Ma, Z., Park, A. C., Lietzke, E., Romero, C. M., et al. (2021). Generation and basic characterization of a gene-trap knockout mouse model of *Scn2a* with a substantial reduction of voltage-gated sodium channel $Na_V1.2$ expression. *Genes, Brain Behav* 20, e12725. doi:10.1111/gbb.12725

Echevarria-Cooper, D. M., Hawkins, N. A., Misra, S. N., Huffman, A. M., Thaxton, T., Thompson, C. H., et al. (2022). Cellular and behavioral effects of altered $Na_V1.2$ sodium channel ion permeability in $Scn2a^{K1422E}$ mice. *Hum. Mol. Genet.* 31, 2964–2988. doi:10.1093/hmg/ddac087

Escoubas, P., Diochot, S., and Corzo, G. (2000). Structure and pharmacology of spider venom neurotoxins. *Biochimie* 82, 893–907. doi:10.1016/S0300-9084(00)01166-4

Flinspach, M., Xu, Q., Piekarz, A., Fellows, R., Hagan, R., Gibbs, A., et al. (2017). Insensitivity to pain induced by a potent selective closed-state $Na_V1.7$ inhibitor. *Sci. Rep.* 7, 39662. doi:10.1038/srep39662

Fontana, M., Vital-Brazil, O., and Vital-Brasil, O. (1985). Mode of action of *Phoneutria nigriventer* spider venom at the isolated phrenic nerve-diaphragm of the rat. *Braz. J. Med. Biol. Res.* 18, 557–565. Available at:. https://pubmed.ncbi.nlm.nih.gov/2425876/.

Garry, E. M., Delaney, A., Anderson, H. A., Sirinathsinghji, E. C., Clapp, R. H., Martin, W. J., et al. (2005). Varicella zoster virus induces neuropathic changes in rat dorsal root ganglia and behavioral reflex sensitisation that is attenuated by gabapentin or sodium channel blocking drugs. *Pain* 118, 97–111. doi:10.1016/j.pain.2005.08.003

Goodwin, G., and McMahon, S. B. (2021). The physiological function of different voltage-gated sodium channels in pain. *Nat. Rev. Neurosci.* 22, 263–274. doi:10.1038/s41583-021-00444-w

Hains, B. C., Saab, C. Y., Klein, J. P., Craner, M. J., and Waxman, S. G. (2004). Altered sodium channel expression in second-order spinal sensory neurons contributes to pain after peripheral nerve injury. *J. Neurosci.* 24, 4832–4839. doi:10.1523/jneurosci.0300-04.2004

Henriques, S. T., Deplazes, E., Lawrence, N., Cheneval, O., Chaousis, S., Inserra, M., et al. (2016). Interaction of tarantula venom peptide ProTx-II with lipid membranes is a prerequisite for its inhibition of human voltage-gated sodium channel $Na_V1.7$. *J. Biol. Chem.* 291, 17049–17065. doi:10.1074/jbc.M116.729095

Hong, S., Morrow, T. J., Paulson, P. E., Isom, L. L., and Wiley, J. W. (2004). Early painful diabetic neuropathy is associated with differential changes in tetrodotoxin-sensitive and -resistant sodium channels in dorsal root ganglion neurons in the rat. *J. Biol. Chem.* 279, 29341–29350. doi:10.1074/jbc.M404167200

Hu, H., Mawlawi, S. E., Zhao, T., Deuis, J. R., Jami, S., Vetter, I., et al. (2021). Engineering of a spider peptide via conserved structure-function traits optimizes sodium channel inhibition *in vitro* and anti-nociception *in vivo*. *Front. Mol. Biosci.* 8, 742457. doi:10.3389/fmolb.2021.742457

Kalia, J., Milescu, M., Salvatierra, J., Wagner, J., Klint, J. K., King, G. F., et al. (2015). From foe to friend: using animal toxins to investigate ion channel function. *J. Mol. Biol.* 427, 158–175. doi:10.1016/j.jmb.2014.07.027

Kim, C. H., Oh, Y., Chung, J. M., and Chung, K. (2001). The changes in expression of three subtypes of TTX sensitive sodium channels in sensory neurons after spinal nerve ligation. *Mol. Brain Res.* 95, 153–161. doi:10.1016/s0169-328x(01)00226-1

Klint, J. K., Chin, Y. K., and Mobli, M. (2015). Rational engineering defines a molecular switch that is essential for activity of spider-venom peptides against the analgesics target $Na_V1.7$. *Mol. Pharmacol.* 88, 1002–1010. doi:10.1124/mol.115.100784

Klint, J. K., Senff, S., Rupasinghe, D. B., Er, S. Y., Herzig, V., Nicholson, G. M., et al. (2012). Spider-venom peptides that target voltage-gated sodium channels: pharmacological tools and potential therapeutic leads. *Toxicon* 60, 478–491. doi:10.1016/j.toxicon.2012.04.337

Klint, J. K., Senff, S., Saez, N. J., Seshadri, R., Lau, H. Y., Bende, N. S., et al. (2013). Production of recombinant disulfide-rich venom peptides for structural and functional analysis via expression in the periplasm of *E. coli*. *PLoS One* 8, e63865. doi:10.1371/journal.pone.0063865

Lawrence, N., Wu, B., Ligutti, J., Cheneval, O., Agwa, A. J., Benfield, A. H., et al. (2019). Peptide-membrane interactions affect the inhibitory potency and selectivity of spider toxins ProTx-II and GpTx-1. *ACS Chem. Biol.* 14, 118–130. doi:10.1021/acschembio.8b00989

Li, D., Xiao, Y., Xu, X., Xiong, X., Lu, S., Liu, Z., et al. (2004). Structure-activity relationships of Hainantoxin-IV and structure determination of active and inactive sodium channel blockers. *J. Biol. Chem.* 279, 37734–37740. doi:10.1074/jbc.M405765200

Lindia, J. A., Kohler, M. G., Martin, W. J., and Abbadie, C. (2005). Relationship between sodium channel $Na_V1.3$ expression and neuropathic pain behavior in rats. *Pain* 117, 145–153. doi:10.1016/j.pain.2005.05.027

Menezes, L. F. S., Sabiá Júnior, E. F., Tibery, D. V., Carneiro, L. d. A., and Schwartz, E. F. (2020). Epilepsy-related voltage-gated sodium channelopathies: a review. *Front. Pharmacol.* 11, 1276. doi:10.3389/fphar.2020.01276

Minassian, N. A., Gibbs, A., Shih, A. Y., Liu, Y., Neff, R. A., Sutton, S. W., et al. (2013). Analysis of the structural and molecular basis of voltage-sensitive sodium channel inhibition by the spider toxin Huwentoxin-IV (μ-TRTX-Hh2a). *J. Biol. Chem.* 288, 22707–22720. doi:10.1074/jbc.M113.461392

Moreira, I. S., Fernandes, P. A., and Ramos, M. J. (2007). Hot spots—a review of the protein–protein interface determinant amino-acid residues. *Proteins Struct. Funct. bioinform.* 68, 803–812. doi:10.1002/prot.21396

Mueller, A., Dekan, Z., Kaas, Q., Agwa, A. J., Starobova, H., Alewood, P. F., et al. (2020). Mapping the molecular surface of the analgesic $Na_V1.7$-selective peptide Pn3a reveals residues essential for membrane and channel interactions. *ACS Pharmacol. Transl. Sci.* 3, 535–546. doi:10.1021/acsptsci.0c00002

Murray, J. K., Ligutti, J., Liu, D., Zou, A., Poppe, L., Li, H., et al. (2015). Engineering potent and selective analogues of GpTx-1, a tarantula venom peptide antagonist of the $Na_V1.7$ sodium channel. *J. Med. Chem.* 58, 2299–2314. doi:10.1021/jm501765v

Murray, J. K., Long, J., Zou, A., Ligutti, J., Andrews, K. L., Poppe, L., et al. (2016). Single residue substitutions that confer voltage-gated sodium ion channel subtype selectivity in the $Na_V1.7$ inhibitory peptide GpTx-1. *J. Med. Chem.* 59, 2704–2717. doi:10.1021/acs.jmedchem.5b01947

Neff, R. A., Flinspach, M., Gibbs, A., Shih, A. Y., Minassian, N. A., Liu, Y., et al. (2020). Comprehensive engineering of the tarantula venom peptide Huwentoxin-IV to inhibit the human voltage-gated sodium channel $hNa_V1.7$. *J. Biol. Chem.* 295, 1315–1327. doi:10.1074/jbc.RA119.011318

Osteen, J. D., Herzig, V., Gilchrist, J., Emrick, J. J., Zhang, C., Wang, X., et al. (2016). Selective spider toxins reveal a role for the $Na_V1.1$ channel in mechanical pain. *Nature* 534, 494–499. doi:10.1038/nature17976

Pineda, S. S., Undheim, E. A., Rupasinghe, D. B., Ikonomopoulou, M. P., and King, G. F. (2014). Spider venomics: implications for drug discovery. *Future Med. Chem.* 6, 1699–1714. doi:10.4155/fmc.14.103

Rahnama, S., Deuis, J. R., Cardoso, F. C., Ramanujam, V., Lewis, R. J., Rash, L. D., et al. (2017). The structure, dynamics and selectivity profile of a $Na_V1.7$ potency-optimised Huwentoxin-IV variant. *PLoS One* 12, e0173551. doi:10.1371/journal.pone.0173551

Revell, J. D., Lund, P.-E., Linley, J. E., Metcalfe, J., Burmeister, N., Sridharan, S., et al. (2013). Potency optimization of Huwentoxin-IV on $hNa_V1.7$: a neurotoxin TTX-S sodium-channel antagonist from the venom of the Chinese bird-eating spider *Selenocosmia huwena*. *Peptides* 44, 40–46. doi:10.1016/j.peptides.2013.03.011

Rodrigues, J. P., and Bonvin, A. M. (2014). Integrative computational modeling of protein interactions. *FEBS J.* 281, 1988–2003. doi:10.1111/febs.12771

Rong, M., Duan, Z., Chen, J., Li, J., Xiao, Y., and Liang, S. (2013). Native pyroglutamation of Huwentoxin-IV: a post-translational modification that increases the trapping ability to the sodium channel. *PLoS One* 8, e65984. doi:10.1371/journal.pone.0065984

Rupasinghe, D. B., Herzig, V., Vetter, I., Dekan, Z., Gilchrist, J., Bosmans, F., et al. (2020). Mutational analysis of ProTx-I and the novel venom peptide Pe1b provide insight into residues responsible for selective inhibition of the analgesic drug target $Na_V1.7$. *Biochem. Pharmacol.* 181, 114080. doi:10.1016/j.bcp.2020.114080

Russell, R. B., Alber, F., Aloy, P., Davis, F. P., Korkin, D., Pichaud, M., et al. (2004). A structural perspective on protein–protein interactions. *Curr. Opin. Struct. Biol.* 14, 313–324. doi:10.1016/j.sbi.2004.04.006

Saez, N. J., and Herzig, V. (2019). Versatile spider venom peptides and their medical and agricultural applications. *Toxicon* 158, 109–126. doi:10.1016/j.toxicon.2018.11.298

Saez, N. J., Senff, S., Jensen, J. E., Er, S. Y., Herzig, V., Rash, L. D., et al. (2010). Spider-venom peptides as therapeutics. *Toxins (Basel)* 2, 2851–2871. doi:10.3390/toxins2122851

Salvatierra, J., Castro, J., Erickson, A., Li, Q., Braz, J., Gilchrist, J., et al. (2018). $Na_V1.1$ inhibition can reduce visceral hypersensitivity. *JCI Insight* 3, e121000. doi:10.1172/jci.insight.121000

Schmalhofer, W., Calhoun, J., Burrows, R., Bailey, T., Kohler, M. G., Weinglass, A. B., et al. (2008). ProTx-II, a selective inhibitor of Na_V1. 7 sodium channels, blocks action potential propagation in nociceptors. *Mol. Pharmacol.* 74, 1476–1484. doi:10.1124/mol.108.047670

Schrodinger (2018). *The PyMOL molecular graphics system*.

Shcherbatko, A., Rossi, A., Foletti, D., Zhu, G., Bogin, O., Galindo Casas, M., et al. (2016). Engineering highly potent and selective microproteins against $Na_V1.7$ sodium channel for treatment of pain. *J. Biol. Chem.* 291, 13974–13986. doi:10.1074/jbc.M116.725978

Shen, H., Zhou, Q., Pan, X., Li, Z., Wu, J., and Yan, N. (2017). Structure of a eukaryotic voltage-gated sodium channel at near-atomic resolution. *Science* 355, eaal4326. doi:10.1126/science.aal4326

Stevens, M., Peigneur, S., and Tytgat, J. (2011). Neurotoxins and their binding areas on voltage-gated sodium channels. *Front. Pharmacol.* 2, 71. doi:10.3389/fphar.2011.00071

Su, S., Shao, J., Zhao, Q., Ren, X., Cai, W., Li, L., et al. (2017). MiR-30b attenuates neuropathic pain by regulating voltage-gated sodium channel Nav1.3 in rats. *Front. Mol. Neurosci.* 10, 126. doi:10.3389/fnmol.2017.00126

Tan, A. M., Samad, O. A., Dib-Hajj, S. D., and Waxman, S. G. (2015). Virus-mediated knockdown of $Na_V1.3$ in dorsal root ganglia of STZ-induced diabetic rats alleviates tactile allodynia. *Mol. Med.* 21, 544–552. doi:10.2119/molmed.2015.00063

Tuncbag, N., Gursoy, A., and Keskin, O. (2011). Prediction of protein-protein interactions: unifying evolution and structure at protein interfaces. *Phys. Biol.* 8, 035006. doi:10.1088/1478-3975/8/3/035006

Van Zundert, G., Rodrigues, J., Trellet, M., Schmitz, C., Kastritis, P., Karaca, E., et al. (2016). The HADDOCK2.2 web server: user-friendly integrative modeling of biomolecular complexes. *J. Mol. Biol.* 428, 720–725. doi:10.1016/j.jmb.2015.09.014

Vetter, I., Deuis, J. R., Mueller, A., Israel, M. R., Starobova, H., Zhang, A., et al. (2017). $Na_V1.7$ as a pain target–from gene to pharmacology. *Pharmacol. Ther.* 172, 73–100. doi:10.1016/j.pharmthera.2016.11.015

Waterhouse, A., Bertoni, M., Bienert, S., Studer, G., Tauriello, G., Gumienny, R., et al. (2018). SWISS-MODEL: homology modelling of protein structures and complexes. *Nucleic Acids Res.* 46, W296–W303. doi:10.1093/nar/gky427

Wisedchaisri, G., Tonggu, L., Gamal El-Din, T. M., McCord, E., Zheng, N., and Catterall, W. A. (2021). Structural basis for high-affinity trapping of the $Na_V1.7$ channel in its resting state by tarantula toxin. *Mol. Cell* 81, 38–48.e4. doi:10.1016/j.molcel.2020.10.039

Wishart, D. S., Bigam, C. G., Holm, A., Hodges, R. S., and Sykes, B. D. (1995). 1H, 13C and 15N random coil NMR chemical shifts of the common amino acids. I. Investigations of nearest-neighbor effects. *J. Biomol. NMR* 5, 67–81. doi:10.1007/BF00227471

Wu, Y., Ma, H., Zhang, F., Zhang, C., Zou, X., and Cao, Z. (2018). Selective voltage-gated sodium channel peptide toxins from animal venom: pharmacological probes and analgesic drug development. *ACS Chem. Neurosci.* 9, 187–197. doi:10.1021/acschemneuro.7b00406

Wüthrich, K. (1983). Sequential individual resonance assignments in the 1H-NMR spectra of polypeptides and proteins. *Biopolymers* 22, 131–138. doi:10.1002/bip.360220121

Xiao, Y., Bingham, J.-P., Zhu, W., Moczydlowski, E., Liang, S., and Cummins, T. R. (2008). Tarantula Huwentoxin-IV inhibits neuronal sodium channels by binding to receptor site 4 and trapping the domain II voltage sensor in the closed configuration. *J. Biol. Chem.* 283, 27300–27313. doi:10.1074/jbc.M708447200

Xiao, Y., Blumenthal, K. M., Jackson, J. O., Liang, S., and Cummins, T. R. (2010). The tarantula toxins ProTx-II and HwTx-IV differentially interact with human $Na_V1.7$ voltage-sensors to inhibit channel activation and inactivation. *Mol. Pharmacol.* 78, 1124–1134. doi:10.1124/mol.110.066332

Xiao, Y., Jackson, J. O., Liang, S., and Cummins, T. R. (2011). Common molecular determinants of tarantula Huwentoxin-IV inhibition of Na^+ channel voltage-sensors in domains II and IV. *J. Biol. Chem.* 286, 27301–27310. doi:10.1074/jbc.M111.246876

Xie, W., Strong, J. A., and Zhang, J. M. (2015). Local knockdown of the $Na_V1.6$ sodium channel reduces pain behaviors, sensory neuron excitability, and sympathetic sprouting in rat models of neuropathic pain. *Neuroscience* 291, 317–330. doi:10.1016/j.neuroscience.2015.02.010

Xu, H., Li, T., Rohou, A., Arthur, C. P., Tzakoniati, F., Wong, E., et al. (2019). Structural basis of $Na_V1.7$ inhibition by a gating-modifier spider toxin. *Cell* 176, 702–715. doi:10.1016/j.cell.2018.12.018

Xu, W., Zhang, J., Wang, Y., Wang, L., and Wang, X. (2016). Changes in the expression of voltage-gated sodium channels $Na_V1.3$, $Na_V1.7$, $Na_V1.8$, and $Na_V1.9$ in rat trigeminal ganglia following chronic constriction injury. *Neuroreport* 27, 929–934. doi:10.1097/wnr.0000000000000632

Zeng, X., Li, P., Chen, B., Huang, J., Lai, R., Liu, J., et al. (2018). Selective closed-state $Na_V1.7$ blocker JzTx-34 exhibits analgesic effects against pain. *Toxins (Basel)* 10, E64. doi:10.3390/toxins10020064

Zhang, F., Liu, Y., Zhang, C., Li, J., Yang, Z., Gong, X., et al. (2015). Natural mutations change the affinity of μ-theraphotoxin-Hhn2a to voltage-gated sodium channels. *Toxicon* 93, 24–30. doi:10.1016/j.toxicon.2014.11.220

Zhang, J., Chen, X., Eaton, M., Wu, J., Ma, Z., Lai, S., et al. (2021). Severe deficiency of the voltage-gated sodium channel $Na_V1.2$ elevates neuronal excitability in adult mice. *Cell Rep.* 36, 109495. doi:10.1016/j.celrep.2021.109495

Zhang, Y., Yang, Q., Zhang, Q., Peng, D., Chen, M., Liang, S., et al. (2018). Engineering gain-of-function analogues of the spider venom peptide HnTx-I, a potent blocker of the $hNa_V1.7$ sodium channel. *Toxins (Basel)* 10, 358. doi:10.3390/toxins10090358

frontiers | Frontiers in Pharmacology

TYPE Original Research
PUBLISHED 11 January 2024
DOI 10.3389/fphar.2023.1328950

OPEN ACCESS

EDITED BY
Michelle Yap,
Monash University Malaysia, Malaysia

REVIEWED BY
Manuela Berto Pucca,
Sao Paulo State University, Brazil
Kae Yi Tan,
University of Malaya, Malaysia

*CORRESPONDENCE
Rachel H. Clare,
rachel.clare@lstmed.ac.uk
Nicholas R. Casewell,
Nicholas.Casewell@lstmed.ac.uk

†These authors have contributed equally to this work

RECEIVED 27 October 2023
ACCEPTED 21 December 2023
PUBLISHED 11 January 2024

CITATION
Clare RH, Dawson CA, Westhorpe A, Albulescu L-O, Woodley CM, Mosallam N, Chong DJW, Kool J, Berry NG, O'Neill PM and Casewell NR (2024), Snakebite drug discovery: high-throughput screening to identify novel snake venom metalloproteinase toxin inhibitors.
Front. Pharmacol. 14:1328950.
doi: 10.3389/fphar.2023.1328950

Snakebite drug discovery: high-throughput screening to identify novel snake venom metalloproteinase toxin inhibitors

Rachel H. Clare[1,2*†], Charlotte A. Dawson[1,2†], Adam Westhorpe[1,2], Laura-Oana Albulescu[1,2], Christopher M. Woodley[3], Nada Mosallam[3], Daniel J. W. Chong[3], Jeroen Kool[4], Neil G. Berry[3], Paul M. O'Neill[3] and Nicholas R. Casewell[1,2*]

[1]Department of Tropical Disease Biology, Centre for Snakebite Research and Interventions, Liverpool School of Tropical Medicine, Liverpool, United Kingdom, [2]Department of Tropical Disease Biology, Centre for Drugs and Diagnostics, Liverpool School of Tropical Medicine, Liverpool, United Kingdom, [3]Department of Chemistry, University of Liverpool, Liverpool, United Kingdom, [4]Division of BioAnalytical Chemistry, Department of Chemistry and Pharmaceutical Sciences, Faculty of Science, Amsterdam Institute of Molecular and Life Sciences, Vrije Universiteit Amsterdam, Amsterdam, Netherlands

Snakebite envenoming results in ~100,000 deaths per year, with close to four times as many victims left with life-long sequelae. Current antivenom therapies have several limitations including high cost, variable cross-snake species efficacy and a requirement for intravenous administration in a clinical setting. Next-generation snakebite therapies are being widely investigated with the aim to improve cost, efficacy, and safety. In recent years several small molecule drugs have shown considerable promise for snakebite indication, with oral bioavailability particularly promising for community delivery rapidly after a snakebite. However, only two such drugs have entered clinical development for snakebite. To offset the risk of attrition during clinical trials and to better explore the chemical space for small molecule venom toxin inhibitors, here we describe the first high throughput drug screen against snake venom metalloproteinases (SVMPs)—a pathogenic toxin family responsible for causing haemorrhage and coagulopathy. Following validation of a 384-well fluorescent enzymatic assay, we screened a repurposed drug library of 3,547 compounds against five geographically distinct and toxin variable snake venoms. Our drug screen resulted in the identification of 14 compounds with pan-species inhibitory activity. Following secondary potency testing, four SVMP inhibitors were identified with nanomolar EC_{50}s comparable to the previously identified matrix metalloproteinase inhibitor marimastat and superior to the metal chelator dimercaprol, doubling the current global portfolio of SVMP inhibitors. Following analysis of their chemical structure and ADME properties, two hit-to-lead compounds were identified. These clear starting points for the initiation of medicinal chemistry campaigns provide the basis for the first ever designer snakebite specific small molecules.

KEYWORDS

venom, toxin, snakebite envenoming, SVMP, small molecule drugs, neglected tropical diseases

1 Introduction

Snakebite envenoming is responsible for perhaps as many as 138,000 deaths annually, while the extensive morbidity burden of sequalae is estimated to represent around 6 million disability adjusted life years (DALYs) (Gutiérrez et al., 2017). Snakebite predominately affects rural populations of the tropics, and consequently the World Health Organization (WHO) recently classified snakebite envenoming as a priority neglected tropical disease (NTD) (Chippaux, 2017). Snakebite can result in catastrophic healthcare expenditure, as well as subsequent loss of livelihood, due to the loss or incapacitation of the primary earner in a household (Herzel et al., 2018; Harrison et al., 2019). In addition, the psychological impact of surviving a snakebite and related socio-economic implications (e.g., social stigma, ostracization and loss of time in education) can cause substantial long-term impacts on individuals and their families (Williams et al., 2011a; Harrison et al., 2019; Kasturiratne et al., 2021; Oliveira et al., 2022).

One of the major challenges that snakebite victims face is restricted access to effective treatment, since current antivenom therapies are often unavailable in the remote rural and indigenous communities that are most vulnerable to snakebite (Gutiérrez et al., 2017; Longbottom et al., 2018; Harrison et al., 2019; Beck et al., 2022). This challenge with antivenom availability is largely attributed to the need for cold chain storage and high costs associated with provision (Williams et al., 2011b). However, despite antivenom currently being the only approved therapeutic for the treatment of snakebite, these animal-derived polyclonal antibody-based therapies have several other limitations associated with them. Antivenom can only be given in a healthcare setting due to the high risk of adverse reactions and the need for intravenous administration (Williams et al., 2011a; de Silva et al., 2016) and their mode of production, i.e., raising animal polyclonal antibodies against a specific venom or venoms, results in products that are restricted in terms of the snake species they are effective against (Harrison et al., 2017; Laxme et al., 2019; Ainsworth et al., 2020).

Snake venoms are a complex mix of several protein families, peptides, and small molecules, which have evolved over millions of years to facilitate prey capture (Tasoulis and Isbister, 2017; Tasoulis et al., 2021). Snake venoms often display compositional variation, and while this is most commonly observed between snake species, there are also several examples of extensive intraspecific and ontogenetic venom variation reported in the literature (Chippaux et al., 1991; Currier et al., 2010; Casewell et al., 2020; 2014; Amazonas et al., 2018; Laxme et al., 2019; Oliveira et al., 2019). Venom variation results in variation in toxin functionality, with associated human snakebite pathologies being equally diverse; the most prominent being neurotoxicity (neuromuscular paralysis), cytotoxicity (local swelling, blistering and tissue necrosis) and haemotoxicity (haemorrhage and coagulopathy) (Warrell, 2010; Gutiérrez et al., 2017; Slagboom et al., 2017; Longbottom et al., 2018). Of the many venom components found across medically important venomous snakes (i.e., families Viperidae and Elapidae), four toxin families are considered amongst the most important therapeutic targets due to their role contributing to these pathologies: three finger toxins (3FTx), snake venom serine proteases (SVSP), phospholipases A_2 (PLA_2) and snake venom metalloproteinases (SVMP) (Ferraz et al., 2019).

Snake venom metalloproteinases (SVMPs) are zinc-dependent endoproteolytic toxins that evolved from ADAM genes (Moura-da-Silva et al., 1996; Casewell et al., 2012). These toxins are found in the venoms of almost all medically important snakes, though they are most abundant in viperids, where they can account for up to 74% of total venom composition (average, 36%) (Tasoulis and Isbister, 2017; Dawson et al., 2021). SVMPs can be broadly divided into three classes based on their tertiary structure (P-I, P-II, and P-III), with each being progressively larger and more structurally complex due to the presence of additional domains (Fox and Serrano, 2008; 2005). Haemorrhage is the most pathologically serious complication resulting from SVMP activity and can occur both systemically and locally. The degradation of collagen and other key extracellular matrix proteins by SVMPs weakens the vascular endothelium, with the impact of haemodynamic forces on this weakened endothelium then enabling blood to escape from the vessels (Gutiérrez et al., 2016; Asega et al., 2020). In addition, several SVMPs also target different points in the coagulation cascade, particularly the common pathway components, fibrinogen, prothrombin and factor X (Kini and Koh, 2016; Asega et al., 2020). These key clotting factors are then consumed, either by their activation or degradation, ultimately leading to the depletion of fibrinogen and, in severe cases, venom induced consumption coagulopathy (Maduwage and Isbister, 2014; Kini and Koh, 2016).

Recent innovations in snakebite therapeutics have centred around the use of monoclonal antibodies or small molecule toxin inhibitors (i.e., drugs), with the latter focusing on their potential application against PLA_2 and SVMP rich venoms (Lewin et al., 2016; Knudsen and Laustsen, 2018; Albulescu et al., 2020b; Clare et al., 2021; Hall et al., 2022; Menzies et al., 2022). So far, two groups of molecules with differing modes of action have been found to inhibit SVMP activity. The first are metal chelators that bind Zn^{2+}; the leading candidate from this class is 2, 3-Dimercapto-1-propanesulfonic acid (DMPS: Unithiol), a drug licensed for the treatment of heavy metal poisoning, marketed under the name Dimaval®, and available in both oral and parenteral forms (Drisko, 2018). DMPS exhibits efficacy in *in vivo* models of snakebite envenoming against venoms rich in SVMP toxins (Albulescu et al., 2020a; Menzies et al., 2022), and recently completed Phase I dose optimisation studies for snakebite indication (Abouyannis et al., 2022). The second drug group are the matrix metalloproteinase inhibitors (MMPi); these compounds include a zinc-binding motif and directly interact with the active site of these enzymes (Gutiérrez et al., 2021). Marimastat has emerged as an exciting early candidate from this group; initially developed as an anti-cancer drug, marimastat passed into Phase III clinical trials, where ultimately development was halted due to lack of efficacy (Winer et al., 2018). Marimastat exhibits broad and potent inhibition of SVMP toxins *in vitro* (Xie et al., 2020; Menzies et al., 2022) and exerts promising preclinical efficacy against the local and systemic haemotoxic effects of several snake venoms in small animal models (Albulescu et al., 2020b; Hall et al., 2022; Menzies et al., 2022). Like DMPS, marimastat exhibits desirable oral bioavailability (Millar et al., 1998), which is an exciting characteristic for future snakebite therapeutics, as drugs could potentially be rapidly administered in rural communities soon after a bite. Reducing current delays to snakebite treatment is likely to substantially improve patient outcomes (Gutiérrez et al., 2017).

One of the other major potential benefits of drugs like DMPS and marimastat is the opportunity to prioritise those with existing clinical data or regulatory approvals, which could result in major reductions in the time and costs associated with translating drugs to market (Ashburn and Thor, 2004).

Although both DMPS and the PLA_2 inhibiting drug varespladib have moved into clinical development for snakebite indication (Abouyannis et al., 2022; Carter et al., 2022), the snakebite drug portfolio remains extremely limited, with attrition a major risk. There is a strong need to develop a broad portfolio of potential snakebite drugs in the early hit discovery stage to allow the selection of candidates with the highest chance of success, and to provide multiple back-up compounds should a primary hit series fail during hit-to-lead optimisation.

Consequently, in this study we performed a repurposed drug screen to identify novel SVMP toxin-inhibiting drugs. We first report on the validation of a high-throughput primary screen capable of assessing SVMP inhibition and processing ~3,500 compounds per day. Next, we performed a drug discovery campaign by screening a commercial human pharmacopoeia library consisting of 3,547 post-Phase I drugs, with the aim of identifying hits for direct repurposing or as starting points for future medicinal chemistry campaigns. The results of our screening campaign, the first of its kind applied in the context of snakebite, yielded four novel compounds with promise for downstream development.

2 Materials and methods

2.1 Venoms

Venoms were extracted from specimens of *Echis ocellatus* (likely *Echis romani* following recent taxonomic reclassification (Trape, 2018), and awaiting molecular confirmation) (Nigeria), *Crotalus atrox* (United States), and *Bitis arietans* (Nigeria) maintained within the herpetarium at the Centre for Snakebite Research and Interventions (CSRI) at the Liverpool School of Tropical Medicine (LSTM). Crude venoms were pooled by species and lyophilised for long term storage at 2°C–8°C. Venoms from *Calloselasma rhodostoma* (Thailand) and *Bothrops jararaca* (Brazil) were sourced from the historical collection of lyophilised venoms at LSTM. Venoms were reconstituted to 10 mg/mL in sterile Phosphate Buffered Saline (PBS) (Cat no: 20012027, ThermoFisher) prior to use.

2.2 Drug stocks

Several matrix metalloproteinase inhibitors were commercially sourced, namely, marimastat ((2*S*,3*R*)-*N*4-[(1*S*)-2,2-Dimethyl-1-[(methylamino)carbonyl]propyl]-*N*1,2-dihydroxy-3-(2-methylpropyl) butanediamide, ≥99%, Cat no: 2631, Tocris Bioscience), prinomastat hydrochloride (AG3340 hydrochloride, ≥98%, Cat no: HY-12170A, MedChemExpress), tanomastat (4′-chloro-γ-oxo-αS-[(henylthiol) methyl]-[1,1′-biphenyl]-4-butanoic acid, ≥98%, Cat no: 19258, Cayman chemicals), batimastat ((2R,3S)-N4-Hydroxy-N1-[(1S)-2-(methylamino)-2-oxo-1-(phenylmethyl)ethyl]-2-(2-methylpropyl)-3-[(2-thienylthio)methyl]butanediamide, ≥98%, Cat no: SML0041, Sigma) and doxycycline (6-Desoxy-5-hydroxytetracycline hydrochloride hemihydrate hemiethanolate, ≥93.5%, Cat no: D9891, Sigma). The metal chelators dimercaprol (2,3-dimercapto-1-propanol, ≥98% iodometric, Cat no: 64046, Sigma) and DMPS (2,3-dimercapto-1-propane-sulfonic acid sodium salt monohydrate, 95%, Cat no: H56578, Alfa Aesar) were also commercially sourced. Small molecules with alternative toxin targets were tested as negative drug controls; varespladib (2-[[3-(2-Amino-2-oxoacetyl)-2-ethyl-1-(phenylmethyl)-1H-indol-4-yl]oxy]-acetic acid, ≥98%, Cat no: SML1100, Sigma) and nafamostat mesylate ((6-Carbamimidoylnaphthalen-2-yl)4-(diaminomethylideneamino) benzoate methanesulfonic acid, > 97%, Cat no: ab141432, Abcam).

For the primary high-throughput screen (HTS) a bespoke repurposed drug library (a combination of the HY-L035 and HY-L026 libraries with overlaps removed) was purchased from MedChemExpress. The library was curated by MedChemExpress to contain a diverse chemical panel of 3,547 post-Phase I and approved drugs that have completed preclinical and clinical studies for a wide range of diseases, as well as having well-characterised bioactivity, safety, and bioavailability properties, making them suitable for drug repurposing (Supplementary Datasheet).

2.3 Drug preparations

Drugs were either supplied at 10 mM or reconstituted in dimethyl sulfoxide (DMSO) (≥99.7%, Cat no: D2650, Sigma) to the same concentration and stored at −20°C. Daughter plates were created with 40 µL per well of 1 mM stocks on V-bottomed 384-well plates (Cat no: 781280, Greiner) to allow the creation of assay-ready plates using a VIAFLO 384 electronic pipette (Integra), excluding columns 1 and 24. Daughter plates and assay-ready plates were stored at −20°C, with the latter used within a month of creation. For SVMP assay-ready plates, 0.91 µL of each drug from the respective daughter plate was plated, such that in the final assay volume of 91 µL, a final concentration of 10 µM was reached. Controls were processed in a similar manner into columns 1 and 24 of each plate; DMSO, PBS, 10 µM marimastat, and 50 nM marimastat, with each condition repeated 4 times within each control column. In secondary screening, dose response curves were created, with a top final assay concentration of 10 µM and reaching sub-nanomolar concentrations (concentration range was dependent on specific plate layout), with each concentration tested in duplicate. For DMPS and dimercaprol, dose response curves started at a concentration of 160 µM to account for reduced inhibitory potency compared to other compounds, with each concentration tested in duplicate.

2.4 *In vitro* drug screening—neutralisation of venom SVMP activity

The SVMP activity of crude venom in the presence of inhibitors or vehicle control (DMSO) was measured using a quenched fluorogenic substrate (substrate for MMPs, ADAMs and Cathepsins, Cat no: ES010, Bio-Techne). The substrate was diluted in reaction buffer (150 mM NaCl, 50 mM Tris-HCl pH 7.5) and used at a final assay concentration of 7.5 µM

(supplied as a 6.2 mM stock). Reactions consisted of 1 µg of venom in 15 µL PBS co-incubated with 0.91 µL of inhibitor at a concentration of 1 mM. The 384-well plate (Cat no: 781101, Greiner) was briefly centrifuged in a Platefuge (Benchmark Scientific) and incubated at 37°C for 25 min. Following incubation, the plate was acclimatised to room temperature for 5 min, before the addition of freshly prepared fluorogenic substrate (75 µL of 9.2 µM). The plates were read on a CLARIOstar microplate reader (BMG Labtech), at an excitation wavelength of 320–10 nm and emission wavelength of 420–10 nm with 10 flashes per well at 25°C, at a pre-defined end read time. The end-read times were selected independently for each venom, as the plateau point for the venom + vehicle control (maximum fluorescence) identified in an initial 1-h kinetic read.

The SVMP activity for the end-read data was calculated for each test condition as a percentage of the mean of the venom + vehicle wells (100% activity), with a baseline of the marimastat 10 µM controls representing 0% activity (Supplementary Equation S1). For the dose response screens, absolute half maximal effective concentration (EC_{50}) values were calculated from the percentage inhibition values by fitting a nonlinear regression curve for the normalised response (variable slope) for each compound using GraphPad Prism 9.0 (GraphPad Software, San Diego, United States).

In addition, these controls were used to calculate the Z prime (Z′) as a quality control measure for each screening plate (Supplementary Equation S2).

2.5 Chemistry prioritisation

The repurposed HTS library was screened for common Pan-Assay Interference compoundS (PAINS) substructures (Baell and Holloway, 2010) using the in-built PAINS filter in the RDKIT cheminformatics package version 2022.03.5 as implemented in Python (Landrum, 2006). Tree Manifold Approximation Projection (TMAP) visualisation was performed using the TMAP python module version 1.0.6. (Probst and Reymond, 2020). ADME properties of hit molecules and radar plots were obtained using the SwissADME web server (Daina et al., 2017). Compounds were hand-picked based on their predicted ADME properties and potential further optimisation.

3 Results

3.1 Optimisation for high-throughput capability

The SVMP assay implemented here has previously been used for quantifying venom activity and toxin inhibition and is based on the adapted use of a commercial assay designed for human MMPs (Albulescu et al., 2020b; Hou et al., 2021; Menzies et al., 2022; Nguyen et al., 2022). The fluorescence-quenched peptide substrate measures the activity of peptidases such as SVMPs which cleave the amide bond between the fluorescent group and the quencher group, resulting in an increase in fluorescence. When metalloproteinase activity is inhibited, the quencher is undisturbed, resulting in only background fluorescence. To increase the throughput of this assay, we implemented the use of robotics and associated adaptation of the method described by Albulescu et al., 2020b, including reducing the substrate concentration from 10 µM to 7.5 µM to minimise the cost of completing a high-throughput screen. The 384-well assay was semi-automated by utilising a VIAFLO 384-channel pipette which allowed single-step addition of both the venom and substrate to the assay-ready drug plates. This two-step protocol, in conjunction with assay ready drug plates, could be utilised to test a panel of venoms in a single batch run. The capacity to create assay-ready plates was provided by the VIAFLO 384-channel pipette's ability to stamp out multiple plates from manually created master drug plates, enabling creation of either single-dose primary screening or downstream dose-response plates. The finalised high-throughput-compatible method is demonstrated in Figure 1.

Through the adaptation to using end-point measurements rather than the original 1-h kinetic measurement, the time required to read a single plate was reduced to less than 100 s. The endpoint was selected as the plateau point of substrate cleavage, measured in triplicate. This endpoint was dependent on the SVMP activity profile of the individual venoms selected; for example, the endpoint for *E. ocellatus* venom was selected as 20 min post substrate addition (drug vehicle control, DMSO in Figure 2A). This provided the capacity to stagger multiple plate batches when working with large drug libraries, thus increasing the throughput capacity of the assay from a maximum of seven plates/day for a kinetic read to a maximum of 21 plates/day with this endpoint read, whilst maintaining a strong assay window.

The aim of this screening campaign was to identify novel molecules with activity at <10 µM in the primary screen and, ideally, exhibiting low nanomolar activity EC_{50} in secondary screening comparable to marimastat's EC_{50} demonstrated in Figure 2B (Clare et al., 2019). Based on this, positive (10 µM marimastat) and negative (vehicle) controls were included on all screening plates as a quality control assessment. For *E. ocellatus* there was a 16-fold assay window between the fluorescence of the controls at the selected 20-min endpoint (351,812 and 21,354 for vehicle control and marimastat, respectively) (Figure 2A). Furthermore, to align with industry practice for drug discovery campaigns, the controls were used to calculate Z′ for each plate to monitor the assay window and variation in the data as an additional quality control step (Zhang et al., 1999). The Z′ is indicative of how discrete each control is; the closer the Z′ value is to 1, the less likely there is to be overlap between the positive and negative control values. Therefore, the Z′ of 0.93 emphasises the robust nature of this readout due to a combination of large assay window and minor variation in the data from 96 samples per control (Figure 2A).

3.2 Validation of the high throughput screen

To ensure that the optimised methodology was robust for HTS, we assessed intra- and inter-plate signal uniformity across triplicate 384-well plates containing either the negative control (vehicle control; plates 1–3) or the positive control (10 µM marimastat; plates 4–6). As seen in Supplementary Figure S1A, there was signal uniformity both horizontally and vertically across each plate (coefficient of variation [CV%] between 2.42 and 3.93), though there was a degree of inter-plate variance in raw signal values between repeated experiments, as best

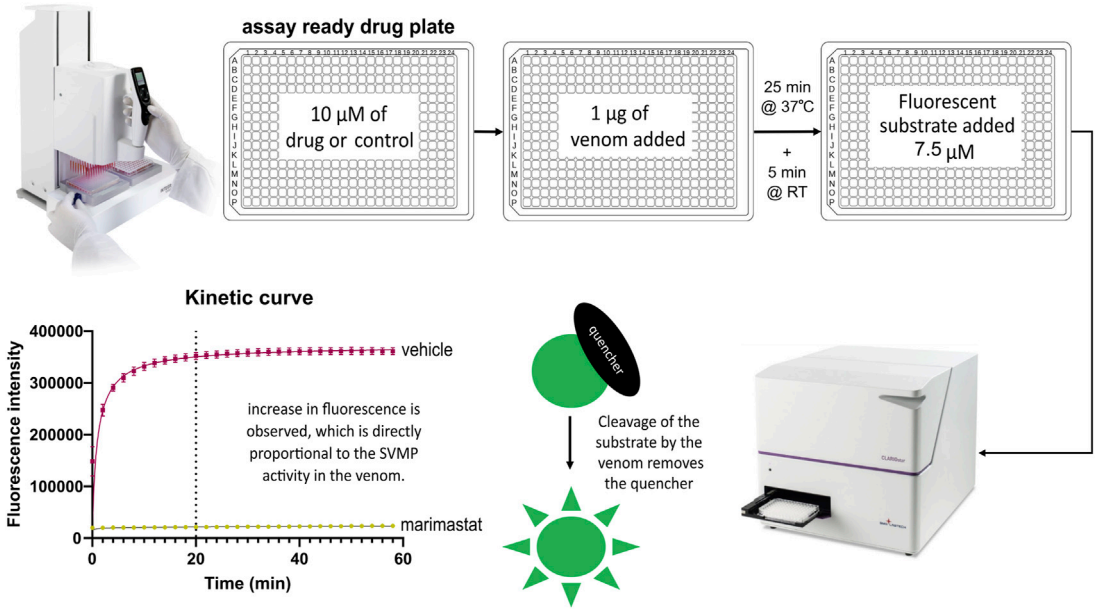

FIGURE 1
High-throughput SVMP screening workflow. This three-step screen is completed within 2 hours. Master drug plates are created with selected drugs of interest and control samples including negative vehicle controls (DMSO) and positive controls (the SVMP inhibiting MMPi marimastat). Using the VIAFLO 384 handheld electronic pipette (Integra), assay-ready drug plates are created by adding 0.91 µL of compound from a master plate. To initiate the assay, 1 µg of venom is added and the plate is incubated for 25 min at 37°C, followed by a 5 min acclimatisation to room temperature (RT). The fluorescence-quenched peptide substrate is added to all wells at a final concentration of 7.5 µM with a final assay volume of 91 µL including 10 µM of drug. Following an incubation time selected based on the plateau point previously determined by a kinetic read (e.g., 20 min for *Echis ocellatus* in this figure) the plate is read with triplicate endreads. Active drugs inhibit the ability of the venom to cleave the quencher off the fluorescent substrate, resulting in a low fluorescent read out, whereas inactive drugs will give a high fluorescence read due to uninhibited venom activity.

evidenced by reduced signal in plate 1 compared to plates 2 and 3 (mean 270,148 vs. 360,521 and 391,484 fluorescence AU, respectively). However, the assay window was still greater than 11-fold between the lowest vehicle control signal (plate 1) and the highest marimastat signal (plate 5). Normalising the data to percentage of inhibition based on the positive and negative controls, with 10 µM marimastat representing 100% inhibition, corrected this variance (Supplementary Figure S1B) and allowed for inter-plate consistency across a HTS for identifying drug hits.

Following validation of positive and negative controls, we then determined whether there was any inter-well interference when control wells were interleaved; as this is a fluorescence-based assay, there is potential for a high-signal well to bleed over into low-signal wells and be erroneously detected. Consequently, full rows of wells in duplicate (i.e., rows A + B, C + D, etc.) were plated containing PBS, DMSO, or marimastat at either 10 µM or a suboptimal 50 nM concentration (Supplementary Figure S2). Minimal variance was observed between the positive (raw signal range from 275,763–409,939 across all plates) and negative (raw signal range from 18,037–27,605 across all plates) controls, confirmed by a CV% from the raw data of 3.24% or lower across all conditions from all plates, and resulting in Z′ of 0.89–0.94. Although there is variation in the 50 nM control (percentage inhibition ranges from 21.7% to 78.7%), the condition is clearly discrete from the positive and negative readings. In addition, no spill-over into the previously defined strong hit classification was detected (>80% inhibition) (Supplementary Figure S2).

As a validation screen, we tested a panel of drugs known to inhibit the activity of snake venom toxins. These included metal chelators (DMPS and dimercaprol) and a broad range of MMPis (marimastat, prinomastat, batimastat, tanomastat and doxycycline). In addition, we included the drugs varespladib and nafamostat which are known to target other snake venom toxins (PLA_2 and SVSP, respectively), but not SVMPs, as negative controls. The observed EC_{50}s were as expected based on prior experience, with marimastat, prinomastat and batimastat all having strong SVMP inhibitory activity into the low nanomolar range while the metal chelators, which are known to have lower potency in this assay, displayed EC_{50}s in the low micromolar range (Figure 3). As expected, the negative control drugs exhibited no activity at the top 10 µM dose tested, and therefore EC_{50} curves were not created (Figure 3).

The strong, consistent Z′ results and clear signal windows from these validation experiments provided confidence to expand this approach to four other medically important viper venoms. These came from four distinct viper genera (family *Viperidae*) found on four different continents, and were selected to account for well-known variations in venom composition among snakes (Tasoulis and Isbister, 2017; Casewell et al., 2020), including variable SVMP content (Table 1). All venoms were initially measured using the original kinetic read method of the assay, and their fluorescence profile examined to determine the plateau point of their respective fluorescence signals (Figure 4A). Upon interrogation of these profiles, the following time points were selected for endpoint read data collection: *Echis ocellatus* and *Calloselasma rhodostoma,* 20 min; *Crotalus atrox* and *Bothrops jararaca*, 30 min; *Bitis arietans,* 40 min.

The same inhibitors that were used to validate the initial experiments with *E. ocellatus* venom were then applied to these

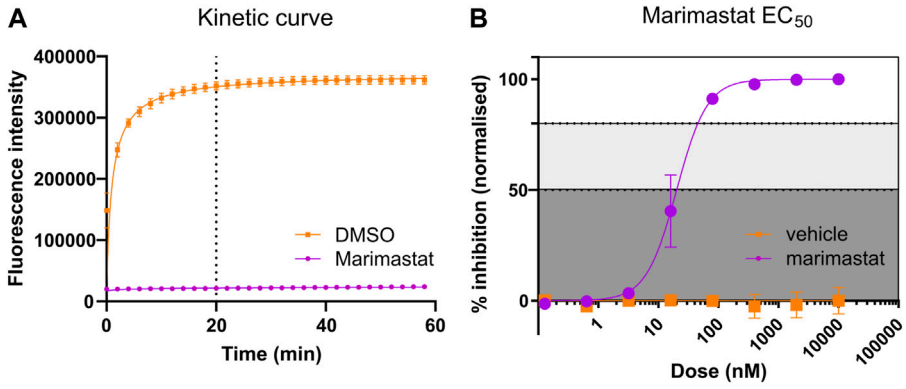

	AUC		Endpoint (20 min)		EC_{50} (based on endpoint)
	fluorescence	Z'	fluorescence	Z'	
marimastat	1274497	0.94	21354	0.93	20.18
vehicle	19926226		351812		

FIGURE 2
Comparison of kinetic Area Under Curve (AUC) measurement and endpoint measurement. **(A)** Kinetic curve measurement of positive (10 μM marimastat + venom) and negative (DMSO vehicle + venom) controls. Following the protocol outlined in Figure 1, kinetic measurement was taken for 60 min, and the AUC measurement calculated (n = 96). Dotted line indicates timepoint at which comparative endpoint reads were taken (20 min). **(B)** EC_{50} curve generated from positive and negative controls ran as a dose response plate created, starting at 10 μM and diluting 1:5 down to 128 pM. Raw data from the 20-min timepoint was normalised to a percentage inhibition based on the positive (100%) and negative (0%) controls and plotted in a dose-dependent manner (n = 2). The table demonstrates the raw values and Z′ values for both methods of response calculation. Z′ values were calculated by comparison of positive and negative raw values across the respective test plates. Z′ values range from 0 to 1, with values closer to 1 indicating clearly defined positive and negative controls, with little to no overlap in values between controls. The EC_{50} of marimastat was calculated through nonlinear trendline fit ([inhibitor] vs. normalized response—Variable slope) using Graphpad Prism version 9.

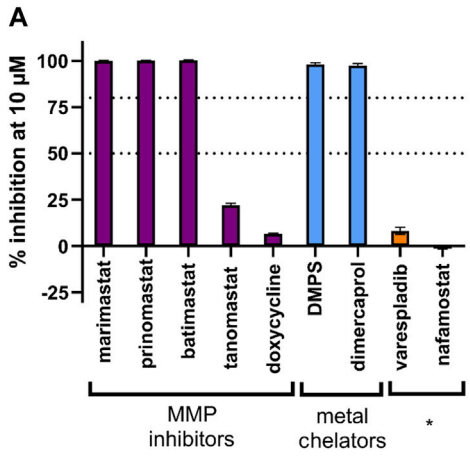

B

Drug	EC_{50} (nM)
marimastat	4.99
prinomastat	4.35
batimastat	6.23
tanomastat	N/A
doxycycline	N/A
DMPS	959
dimercaprol	1125
varespladib	N/A
nafamostat	N/A

FIGURE 3
The inhibitory potency of various drugs against the SVMP activity of *E. ocellatus* venom using the validated HTS assay. **(A)** Bar graph demonstrating the percentage inhibition (when normalised to positive and negative controls) of compounds tested through the screening method. These include chemical groups broadly known to inhibit SVMPs, namely, matrix metalloproteinase inhibitors (MMPi) and metal chelators. * indicates known inhibitors of other snake venom toxin families (PLA_2 and serine proteases) used as negative controls. Dotted lines are present at the cutoff values for mediocre (50% inhibition) and strong (80% inhibition) hit identification. **(B)** EC_{50} data calculated for each compound from the 20-min endpoint read data. Compounds with an EC_{50} displaying N/A did not cross the 50% inhibition threshold at any dose and therefore EC_{50}s could not be calculated.

additional venoms (Figure 4B). The same potency differences between the metal chelators and the MMPis were observed with the four new venoms with EC_{50}s of >500 nM maintained for the metal chelators compared to <50 nM for the MMPis. This potency difference between the two drug classes is likely due to their distinct mechanism of action (Albulescu et al., 2020b; Xie et al., 2020). There were also differences between drugs of the same class; across all venoms, DMPS produced lower EC_{50} values relative to dimercaprol (DMPS = 527–5,284 nM range across all venoms, average 2,248 nM; dimercaprol = 558–6,860 nM, average 3,144 nM). Between the

TABLE 1 Details of the venoms tested in the HTS and statistics on the resulting primary screen.

Snake species	Geographical range	SVMP % content	Z prime range	Hit rate (%)	
				Strong hits	Mediocre hits
*Echis ocellatus**	West Africa	37.5% (Nigeria)	0.74–0.94	23 (0.6)	4 (0.1)
Crotalus atrox	South United States and Mexico	49.7% (United States)	0.76–0.94	19 (0.5)	5 (0.1)
Calloselasma rhodostoma	South-east Asia	41.2% (Indonesia, Malaysia)	0.78–0.96	17 (0.5)	5 (0.1)
Bothrops jararaca	Central South America	10.3–35.6 (Brazil)	0.71–0.88	35 (1.0)	37 (1.0)
Bitis arietans	Throughout sub-Saharan Africa	21.1% (Nigeria)	0.74–0.91	21 (0.6)	22 (0.6)

Geographical range is taken from the IUCN, redlist. SVMP content sourced from Casewell et al., 2014 (*E. ocellatus*), Calvete et al., 2009 (*C. atrox*), Tang et al., 2016 (*C. rhodostoma*), Gonçalves-Machado et al., 2016 (*B. jararaca*), and Dingwoke et al., 2021 (*B. arietans*). *species likely to be *E. romani* following recent taxonomic reclassification (Trape, 2018).

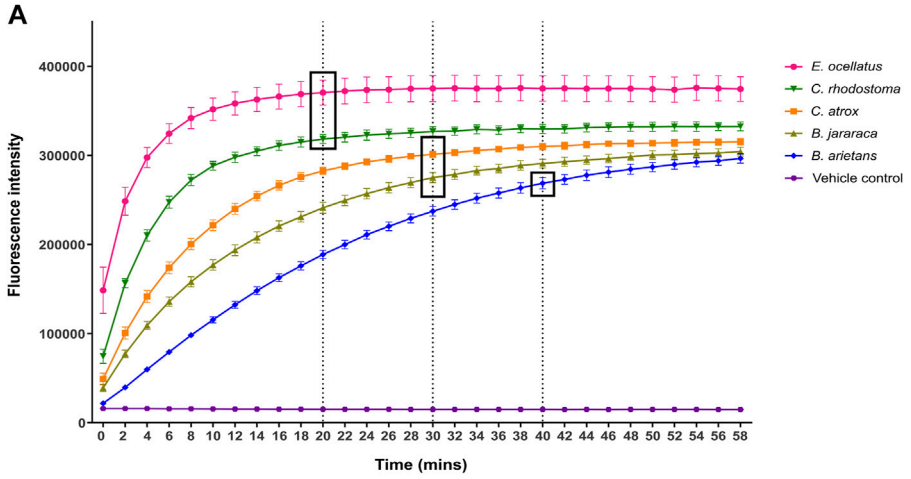

B

	EC_{50} (nM)				
Drug	*B. arietans*	*B. jararaca*	*C. atrox*	*C. rhodostoma*	*E. ocellatus*
marimastat	2.36	7.46	12.0	27.7	4.99
prinomastat	2.42	9.53	19.8	36.7	4.35
batimastat	2.49	5.57	15.4	42.0	6.23
dimercaprol	2290	558	4890	6860	1130
DMPS	1210	527	3260	5280	959

FIGURE 4
Identification of endpoint read times for each venom in the panel, and example EC_{50}s for each venom from the panel of known inhibitors. **(A)** Kinetic read of venom-only activity in the SVMP assay to identify endpoint read times. Timepoint selection was based on the time at which quencher cleaving had predominantly ceased, as indicated by a plateau in fluorescence values. Venoms with greater SVMP activity generally demonstrated earlier plateau (*E. ocellatus, C. rhodostoma*) when compared to other venoms. Dotted lines and boxes indicate selected timepoint for the respective venoms. **(B)** Table showing EC_{50} values of SVMP inhibitors from the known inhibitors when screened against the panel of five viper venoms as a dilution series.

MMPis, minimal difference was observed between the drugs for each of the venoms tested, with all EC_{50} values lower than 50 nM against all venoms. However, for all drug classes, the EC_{50}s were higher (~2–20 fold) against *C. rhodostoma* and *C. atrox* venoms compared to those obtained for *B. arietans*, *B. jararaca* and *E. ocellatus* venom.

3.3 Larger-scale screening of a repurposed drug library

Following the full validation of the assay, we next embarked on a HTS of a repurposed drug library consisting of 3,547 post-Phase I compounds. Screening of the 11-plate library at 10 µM against a single venom was possible in approximately 2 hours, depending on the venom being used for screening (20-min plateau time required 2 hours, 40-min plateau time required 2 hours and 20 min). This throughput meant that the full screen of the library against all five venoms was completed within 5 days. Consistent Z′ of between 0.71–0.96 across all 11 screening plates for each venom (total of 55 × 384 well plates) indicated that the robustness of the assay was retained during the screening campaign (Table 1).

Normalised screening results were characterised into three discrete groups; non-hits (≤50% inhibition compared to control), mediocre hits (50%–80% inhibition), and strong hits (>80%

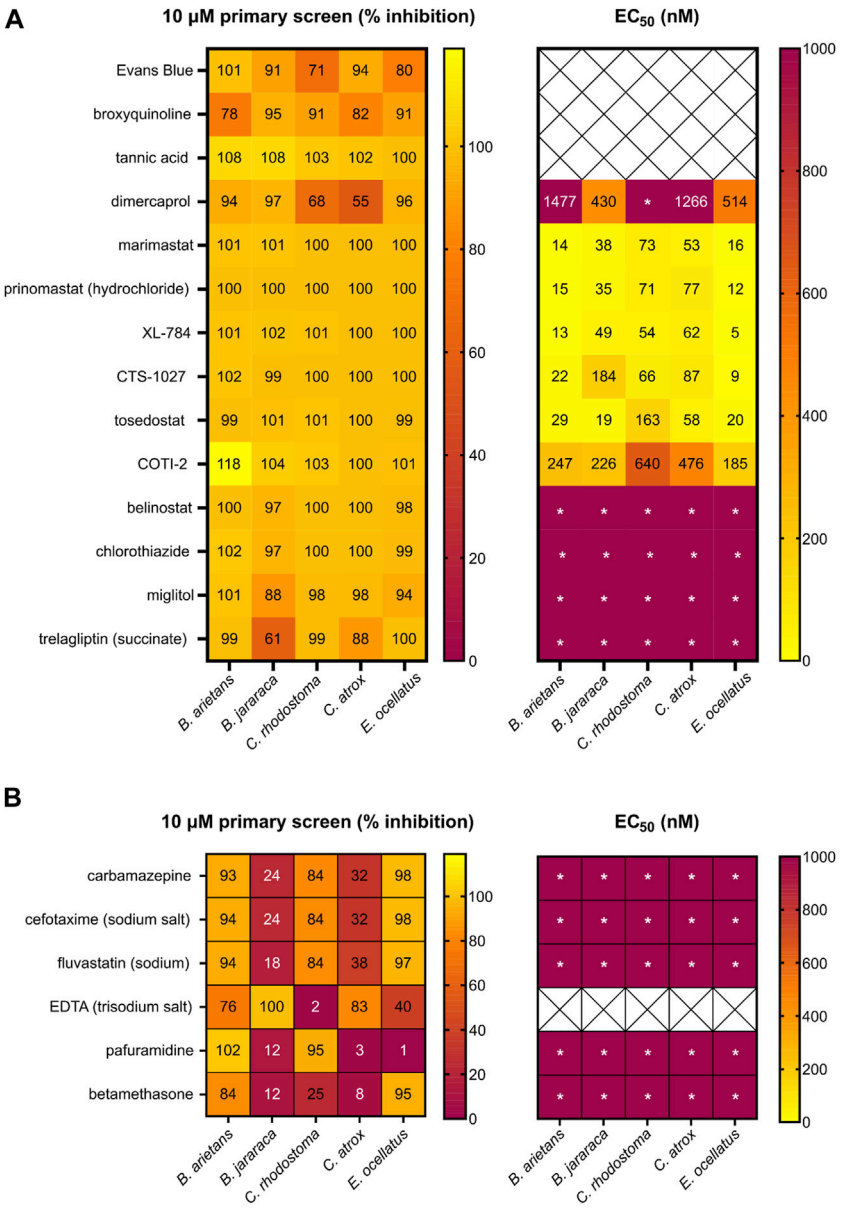

FIGURE 5
Heatmap of the hits from the primary and secondary EC_{50} screen of the repurposed compound library. Left panels present the primary screen at 10 μM and right panels present the secondary dose response screen. **(A)** Percentage inhibition of 14 compounds identified as strong hits in three or more venoms during the primary screening of the repurposed library (left) and EC_{50} data of 11 compounds progressed into the secondary screen (right). **(B)** Percentage inhibition for six strong hits in the primary screen against at least two venoms (left) and EC_{50} (right). Wells demonstrating * indicate an EC_{50} was not calculated due to low activity at the highest doses.

inhibition). The hit rate for strong hits (>80% inhibition) ranged from 0.5% to 1.0% depending on the venom screened, with the highest rate of strong hits observed against *B. jararaca* venom (35 hits, 1.0%) (Table 1). The lowest hit rates were observed against *C. rhodostoma* and *C. atrox* venoms (17 and 19 hits respectively; both ~0.5%). A greater disparity was observed in the number of mediocre hits recovered (>50% < 80% inhibition), with the highest number of hits observed against *B. jararaca* venom (37 hits, 1.0%), followed by *B. arietans* (22 hits, 0.6%). Far fewer mediocre hits were observed against the remaining venoms (*E. ocellatus,* 4; *C. atrox,* 5; *C. rhodostoma*, 5), each representing only 0.1% of the library. It is worth noting that this order of hit rate correlates with the rank ordering of EC_{50} potencies described earlier for known SVMP inhibitors, with *C. rhodostoma* and *C. atrox* venom seemingly being more challenging to inhibit.

To prioritise hits for progression into secondary EC_{50} screening, recovered hits were assessed for their consistent activity across all five venoms (Figure 5). In total, we had 109 compounds that were either a mediocre or strong hit in at least one venom, but of these, only 10 were strong hits in all five venoms. A further four were strong hits in at least three venoms and mediocre in the additional two venoms. These 14 lead hits are presented in Figure 5A. There

were a further six compounds with strong activity in two or three venoms, but lacking activity (<50% inhibition) in the additional venoms (apart from ethylenediamine tetracetic acid (EDTA), which displayed strong activity in two venoms and mediocre in a third) (Figure 5B). Of the remaining 89 compounds, inhibitory activity varied between venoms, with 32 compounds (36%) identified as strong hits against one venom (mainly *B. jararaca*) but lacking activity in the remaining four venoms. This emphasises the value in testing several venoms to maximise the chance of identifying pan-species inhibitory activities.

Of the 14 hits with pan-species activity (Figure 5A), all except three were progressed into secondary EC_{50} testing. Evans Blue and tannic acid were not considered further due to their high molecular weights coupled with known polypharmacology, while broxyquinoline was considered an intractable starting point due to previously reported toxic side effects (Strandvik and Zetterström, 1968; Baumgartner et al., 1979). The remaining 11 pan-species hits included the known and previously described SVMP inhibitors dimercaprol, marimastat and prinomastat (Rucavado et al., 2000; Ainsworth et al., 2018; Albulescu et al., 2020b; Chowdhury et al., 2021). These were progressed as additional controls in the EC_{50} screen and exhibited inhibitory potencies as anticipated (i.e., Figure 5A in comparison with Figure 4B).

The remaining eight novel hits fell into three broad inhibitory categories when tested against the five venoms in this secondary screen (Figure 5A). Three drugs (XL-784, CTS-1027 and tosedostat) had comparable EC_{50} activity (5–184 nM) to marimastat and prinomastat across all venoms. COTI-2 was slightly less active, producing EC_{50}s that were approximately 10-fold lower, though these were still superior (>2 fold) to dimercaprol across all venoms (EC_{50}s, 185–640 nM). The four remaining drugs (belinostat, chlorothiazide, miglitol and trelagliptin) were less active than dimercaprol, with EC_{50}s greater than 1 μM against each of the venoms.

Although discovery of drug compounds with pan-species activity was the overarching goal of this project, hits with strong activity against two or more venoms were also progressed to EC_{50} testing (Figure 5B) to ensure valuable hits had not been excluded (e.g., false negatives against certain venoms). We still excluded EDTA since it has been investigated previously as a potential snakebite therapy and was found to be inferior to other metal chelators (DMPS and dimercaprol), whilst having poor therapeutic characteristics; high affinity for calcium, poor safety profile, and requirement for slow intravenous administration (Flora and Pachauri, 2010; Ainsworth et al., 2018; Albulescu et al., 2020a). Of the remaining six hits in this category (Figure 5B), when tested in the EC_{50} screen, all displayed poor activity against all venoms (EC_{50}s > 1 μM), thus further validating the focus on hits with pan-species activity in the primary screen.

3.4 Chemical space visualisation of the hit compounds

To scrutinise this repurposed library from a structural activity relationship (SAR) perspective, we used Tree Manifold Approximation Projection (TMAP) to visualise the HTS chemical

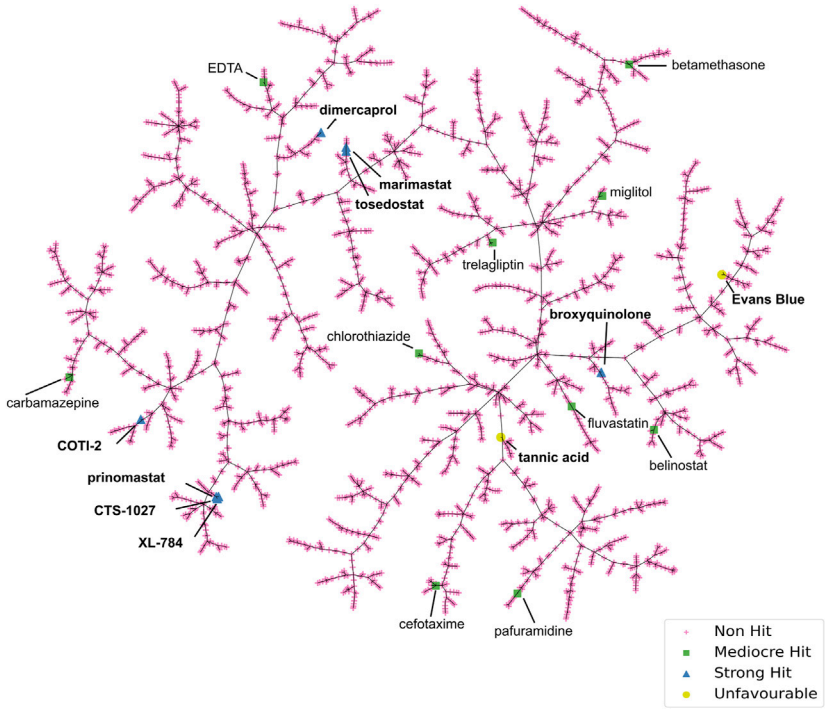

FIGURE 6
Tree Manifold Approximation Projection (TMAP) representation of the chemical space covered by the HTS library. Non-hits are shown as pink crosses, mediocre hits are shown as green squares, and strong hits are shown as blue triangles. Unfavourable hits are shown as yellow circles.

space explored and to identify trends among closely related scaffolds (Probst and Reymond, 2020). Briefly, TMAP displays chemical space as a tree manifold displaying similar groups of compounds as branches while the distance between each compound represents similarity–we would therefore expect similar compounds to exist within the same sub-branches. TMAP representation of our dataset showed that the majority of the mediocre hits detected were structurally distinct from other hits (Figure 6). However, for the lead compounds, which included the four novel hits with nanomolar EC_{50}s (XL-784, CTS-1027, COTI-2 and tosedostat) and the known SVMP inhibitors (marimastat, prinomastat and dimercaprol), this approach allowed identification of two distinct groups: i) CTS-1027, XL-784 and prinomastat—all lipophilic non-peptidomimetic hydroxamate MMPis (Johnson et al., 2006; Kahraman et al., 2009) and ii) marimastat and tosedostat—an established peptidomimetic SVMP inhibitor and a structurally similar compound, respectively. Dimercaprol and COTI-2 are visibly isolated from the other hits in separate branches and exist as singletons. This reduces confidence in the latter compounds as starting points for optimisation due to lack of evidence of an SVMP-inhibitory scaffold, with their closest neighbours in the HTS showing no SVMP-inhibitory activity. This hypothesis is further supported by the poorer performance of COTI-2 and dimercaprol in secondary EC_{50} screens compared to other hits. The structures of the lead compounds are presented in Figure 7.

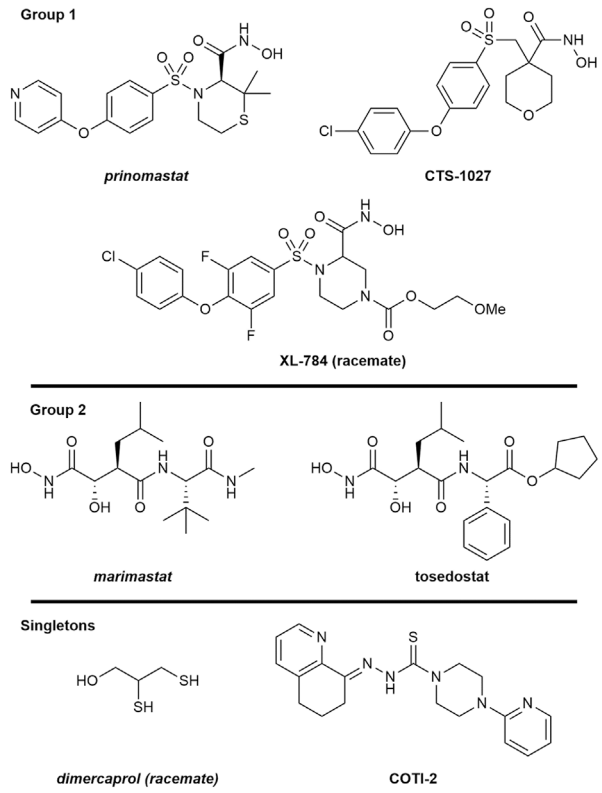

FIGURE 7
Structures of the seven lead SVMP compounds including three known inhibitors (italics) and four novel hits with nanomolar EC_{50}s grouped by structural similarity determined by TMAP. Structures are drawn by ChemDraw based on SMILES provided by the source of the drug screening library.

3.5 Assessment of absorption, distribution, metabolism and elimination (ADME) properties of the hit compounds

We used SwissADME to evaluate the predicted physicochemical properties and drug-likeness of the seven lead compounds (Figure 7) using their validated machine-learning models (Daina et al., 2017). Predicted values indicating lipophilicity (XLOGP3), molecular weight (MW), polarity (topological polar surface area, TPSA), non-planarity (fraction of carbons in the sp3 hybridisation state, Fsp3), molecular flexibility (number of rotatable bonds, RotB) and solubility are provided in Table 2, alongside radar plots for visualisation in Figure 8.

SwissADME assesses drug-likeness through design rules as determined by Lipinski, Ghose, Veber, and Egan (Ghose et al., 1999; Egan et al., 2000; Lipinski et al., 2001; Veber et al., 2002). These rules use the predicted ADME properties and defined thresholds to determine whether a compound violates a rule. The number of violations of these rules is summarised in Table 2. All compounds possess no greater than 2 violations to any rule with the exception of dimercaprol which possesses three Ghose violations due to molecular weight < 160 Da, molar refractivity < 40 and total number of atoms < 20 (Ghose et al., 1999). CTS-1027 and COTI-2 have no violations across all 4 rules, whilst marimastat and tosedostat have a single violation in Veber's rule due to having the number of rotatable bonds as > 9 (molecular flexibility). Prinomastat has one violation in both Veber and Ghose design rules due to its polarity (TPSA = 142.5 $Å^2$), though considering the thresholds of these rules (TPSA > 140 $Å^2$ and 131.6 $Å^2$, respectively) these violations are minor. XL-784 is the only compound to have violations across all four rules. This is due to its high molecular weight and number of hydrogen bond donors (Lipinski and Ghose), as well as its polarity and flexibility (Veber and Egan).

Outside the parameters used to determine rule violations, SwissADME also profiles solubility by three methods; an implementation of the ESOL method (Delaney, 2004), a model adapted from (Ali et al., 2012), and a method developed by SILICOS-IT (Daina et al., 2017). Low solubility of molecules may cause issues with absorption. No hit compounds were found to be poorly soluble (Table 2) supporting the insight from design rules that the majority of hits are unlikely to experience issues with absorption. Overall, assessment of predicted ADME properties suggests that the novel hits CTS-1027, COTI-2 and tosedostat are the most promising hits for optimisation, while XL-784 would require more extensive optimisation of its ADME properties.

4 Discussion

SVMPs are a major snake venom toxin family responsible for causing substantial pathology in snakebite patients, while conventional antivenom therapies are often associated with a high incidence of adverse effects, as well as financial and logistical constraints. Consequently, efforts are being made to find alternative therapies that could overcome these existing barriers for victims of snakebite. Through validated miniaturisation of an existing fluorometric assay and the application of liquid handling instruments, we have developed a high-throughput screening platform with the

TABLE 2 Selected SwissADME predicted properties of the seven lead SVMP compounds including three known inhibitors (italics) and four novel inhibitors. Properties of concern based on violations of drug-likeness rules are indicated in bold.

Drug	Lipophilicity	MW	Polarity	Non-planarity	Molecular flexibility	Drug likeness rule violations				Solubility
						Lipinski	Ghose	Veber	Egan	
Prinomastat	2.26	460.0	**142.5**	0.33	6	0	0	1	1	Moderate
CTS-1027	2.27	425.9	110.3	0.32	7	0	0	0	0	Soluble
XL-784	1.85	**548.9**	**145.9**	0.33	**11**	2	1	2	1	Soluble
Marimastat	0.51	331.4	127.8	0.80	**11**	0	0	1	0	Very soluble
Tosedostat	2.29	406.5	125.0	0.57	**12**	0	0	1	0	Soluble
Dimercaprol	0.19	**124.2**	97.8	1.00	2	0	3	0	0	Very soluble
COTI-2	2.54	366.5	88.7	0.37	4	0	0	0	0	Soluble

Lipophilicity: XLOGP3 is a method of LogP calculation based on the number of heteroatoms and number of carbon atoms. MW: molecular weight. Polarity: measured as the topological polar surface area (TPSA). Non-planarity: the fraction of carbons with sp3 hybridisation. Molecular flexibility: the number of rotatable bonds. Drug-likeness rule violations: the values represent the number of rule violations. Lipinski's rule: MW ≤ 500 g/mol, LogP ≤ 4.15, hydrogen bond acceptors ≤ 10 and hydrogen bond donors ≤ 5. Ghose filter: 160 ≤ MW ≤ 480, LogP ≤ 5.6, and 40 ≤ molar refractivity ≤ 130 and 20 ≤ number of atoms ≤ 70. Veber's rule: RotB ≤ 10 and TPSA ≤ 140. Egan's filter LogP≤ 5.88 and TPSA ≤ 131.6. Solubility: calculated using the widely used ESOL, dataset and model. log S scale: insoluble (<−10), poorly soluble (−10 to −6), moderately soluble (−6 to −4), soluble (−4 to −2), very soluble -(-2 to 0) and highly soluble (>0).

capacity to screen ~7,000 individual compounds against a venom of interest in a single day. Utilising this HTS platform, we screened 3,547 post-Phase I compounds in singleton at 10 μM against five medically important viper venoms of diverse taxonomy, geographic location and SVMP content. The robust nature of this HTS is quantified by consistently high Z′ across assay plates (0.71–0.96), providing confidence in the results obtained. Out of the 0.4% hit rate from the primary screen (14 strong pan-species inhibitors), after secondary testing and assessment of physiochemical properties, four discrete clusters of structurally similar strong (nM EC_{50}s) hit compounds were identified (Figures 6, 7). Three hit compounds (XL-784, CTS-1027 and tosedostat) shared structural similarities with MMP inhibitors previously shown to also inhibit SVMPs (marimastat and prinomastat (Howes et al., 2007; Arias et al., 2017; Albulescu et al., 2020b; Menzies et al., 2022)). XL-784, first prepared by Exelixis, and CTS-1027 (also known as RS-130830), originally prepared by Roche Bio-Science, are both known MMP inhibitors, while both tosedostat and COTI-2 have unknown MMP inhibitory activity. Due to the less favourable EC_{50} performance in the secondary screen, COTI-2 was deprioritised as a backup compound.

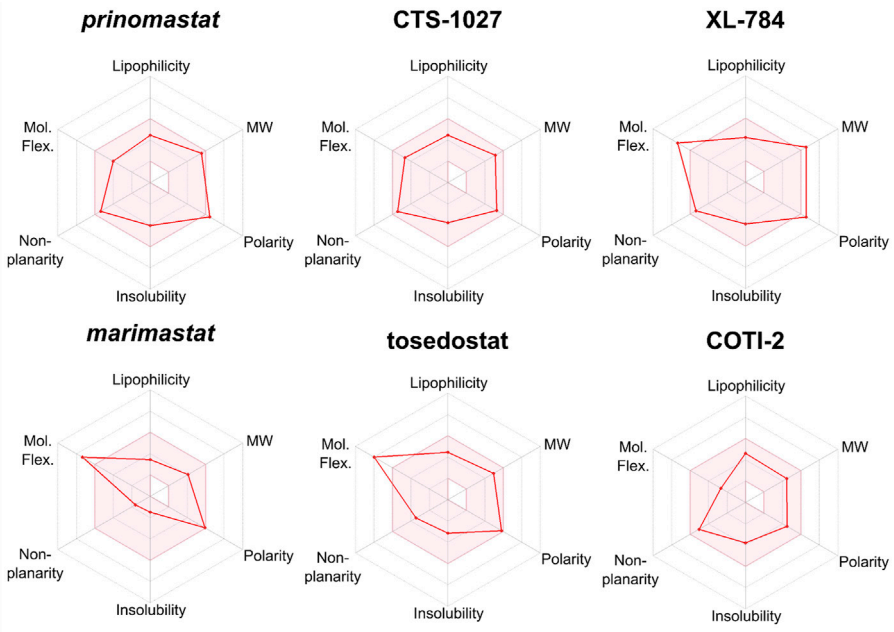

FIGURE 8
Radar plots generated by SwissADME for lead compounds of interest. The shaded area represents the ideal range for oral bioavailability. Thresholds: Lipophilicity: XLOGP3 between −0.7 and 5.0, Molecular Weight (MW): 150 < MW < 500 g/mol; Polarity: 20 < TPSA 130 Å^2, Insolubility: −log *S* < 6, non-planarity: fraction of carbons in the sp3 hybridization not less than 0.25, and Molecular Flexibility (Mol.Flex.): no more than 9 rotatable bonds.

Despite promising inhibitory potencies and ADME properties, tosedostat retains a major limitation as a future SVMP inhibiting drug. Tosedostat is a pro-drug that is metabolised into its active form, which is an aminopeptidase inhibitor investigated for cancer indications. This transformation involves cleavage of a labile ester linkage by serum esterases to reveal a carboxylic acid necessary for its aminopeptidase inhibitory function (Krige et al., 2008). As our HTS was not carried out under the appropriate metabolic conditions to generate tosedostat's active metabolite, it can be assumed that the anti-SVMP activity of this drug is mediated by its ester form. For our purposes, hydrolysis to the free acid would add unnecessary polar functionality which may have negative implications on absorption, metabolism, and overall exposure at the target SVMPs *in vivo*. For these reasons, we have deprioritised tosedostat for onward development.

The ADME properties described in Table 2 and Figures 7, 8 suggest that XL-784 is perhaps less attractive due to its high molecular weight, polarity, molecular flexibility, and number of hydrogen bond acceptors—all of which are associated with poor bioavailability, and XL-784 also has a reported low aqueous solubility of 20 μg/mL (Williams et al., 2011b). For these reasons, analogues of XL-784 with improved pharmacokinetic properties are being evaluated in our medicinal chemistry program. CTS-1027 and prinomastat provide the best medicinal chemistry starting points for future SVMP inhibitor discovery due to their desirable physicochemical and structural properties and minor violations of drug-likeness rules. However, it should be noted that CTS-1027 and prinomastat were flagged in SwissADME as having toxicity and pharmacokinetic (PK) concerns. Prinomastat previously progressed into Phase III trials where musculoskeletal toxicity was observed in a significant proportion of patients that received a treatment course of 15 mg bi-daily dosing for 3–36 months, as well as an increased risk of venous thromboembolic disease in cancer patients receiving combination chemotherapy (Bissett et al., 2005). It is anticipated that these side effects were due to inhibition of MMP-1. Consequently, a more selective MMP/SVMP inhibitor will be pursued in our drug discovery campaign to avoid joint toxicities. CTS-1027 previously entered Phase II clinical trials for the treatment of hepatitis C, and a range of serious adverse events were associated with the administration of 30 mg per day for up to 24 weeks (e.g., single incidences of anaemia, hematemesis, upper GI haemorrhage, chest pain, staphylococcal abscess, prostate cancer and chronic obstructive pulmonary disease) (Conatus Pharmaceuticals Inc, 2012). It should be noted that these toxicity concerns were associated with a long-term treatment course and high drug dosage, whereas projected snakebite therapy would likely only involve short course dosing for perhaps up to 72 h. Additionally, these side effects are reversible following treatment termination, thereby avoiding permanent pathologies (Scatena, 2000).

The HTS assay described here identifies compounds that directly inhibit the enzymatic activity of SVMP toxins (Neumann et al., 2004; Gutiérrez et al., 2021). One limitation of this assay is that compounds that inhibit SVMP activity through metal chelation will not be observed as highly potent in our HTS and thus may not be selected as hits for progression. This is important to note as the metal chelator dimercaprol has been shown to successfully inhibit SVMP activity *in vivo,* with the derivative DMPS currently being planned for progression into Phase II clinical trials for snakebite (Abouyannis et al., 2022). Therefore, screening to identify compounds with similar mode of action would require an alternative screening model that better represents the phenotypic nature of snakebite envenoming. Another caveat to consider is that fluorescence-based drug screens are vulnerable to interference from compounds that are either fluorescent quenchers (false positives) or auto-fluorescent (false negatives) (Yang et al., 2020). Diversity based screening libraries often contain compounds with several aromatic rings in their structure which are inherently fluorescent in the lower-blue range of the spectrum (excitation ~ 350 nm and emission of 450–495 nm) (Thorne et al., 2010). The emission wavelength of this assay is 410–420 nm, therefore such false negatives are likely to be minimal. Chemical scrutiny of hits prior to chemical selection can be used to identify quenching moieties and deprioritised for onward progression, while false negatives with auto-fluorescent characteristics could be progressed into secondary assays if they possessed promising structural similarities to known inhibitors or demonstrate inhibitory activity in orthogonal, non-fluorescent assays.

Prior to the initiation of medicinal chemistry campaigns around the two hit-to-lead compounds described here (CTS-1027 and prinomastat), traction along a defined drug discovery pipeline would be essential, inclusive of activity confirmation in additional *in vitro* assays and critical evaluation PK/PD properties prior to progression into *in vivo* testing. Although we do not anticipate dropouts in *in vivo* experiments (MMPis such as marimastat and metal chelators such as DMPS have previously displayed activity in murine envenoming models (Albulescu et al., 2020a; 2020b; Menzies et al., 2022)), discrepancies between *in vitro* enzymatic screening and results from *in vivo* testing could occur due to the increased degree of complexity of venom pathology in a biological system rather than an enzymatic *in vitro* setting. For example, SVMPs directly target the coagulation cascade through the activation of factor X and/or prothrombin, which are effects that this current enzymatic HTS platform cannot determine. Marimastat and prinomastat are known to inhibit SVMP activation of the clotting cascade, so a further set of experiments to confirm that hits identified in this assay show similar inhibition of coagulopathy would be beneficial as a tertiary screen (Mackessy and Stephen, 2009; Cabral-Pacheco et al., 2020). In addition to tertiary *in vitro* testing, the pharmacokinetic and pharmacodynamic (PK/PD) properties of the lead compounds need to be considered to allow for rational dose design prior to progression into preclinical *in vivo* models. One benefit of screening repurposed compound libraries, such as in this HTS study, is that many of the compounds involved will have already been subjected to human safety and efficacy testing, which will provide data of value for considering human dose prediction.

As described above, we have identified two novel lead candidates which are poised for progression along our drug discovery pipeline (tertiary screening and PK/PD evaluation inclusive of informed dose selection). Prinomastat and CTS-1027 are viable as parent compounds for the establishment of medicinal chemistry campaigns to develop the first designer toxin-specific small molecule for the treatment of snakebite. To our knowledge, this is the first time a validated, scalable HTS platform has been demonstrated for the investigation of small molecule inhibitors against medically relevant snake venom toxins. We hope that this work will help to overcome barriers of throughput and accelerate the

future identification of alternative snakebite therapeutics. In addition to small molecules, this platform is amenable to use to discover monoclonal antibody-based therapeutics (Knudsen and Laustsen, 2018; Laustsen, 2018; Harrison and Gutiérrez, 2019; Knudsen et al., 2019), as well as for high-throughput profiling of SVMP activity from a diversity of venoms (e.g., macroevolutionary or population-level analyses). The platform can also be utilised for libraries of any size; smaller, rationally selected libraries can be screened rapidly (e.g., analogues from a medicinal chemistry campaign) and progressed directly to secondary EC_{50} screening, whilst the scalability of this platform makes it equally applicable to larger, more diverse libraries such as the ReFRAME collection (12,000 small molecules which have reached clinical development or undergone significant preclinical development (Janes et al., 2018)) and AstraZeneca's open innovation programme (AstraZeneca, 2022). Furthermore, it is feasible this HTS could be scaled up further based on the precedence for ultra-HTS discovery programmes which use the same fluorescent substrate (Madoux et al., 2016; Hou et al., 2021).

Our ongoing work aims to develop and validate a drug discovery pipeline from primary *in vitro* HTS through to preclinical testing, paving the way for the discovery and development of novel snakebite therapeutics against pathogenically important snake venom toxins. The automated set up of this HTS platform has also been applied in parallel to other toxin families, such as the PLA_2s (Albulescu et al., 2020b). Collectively, these studies have the potential to vastly broaden the portfolio of preclinical stage small molecules for snakebite with options for novel drug combinations directed at distinct snake venom components. Following the long-term goal of successful progression through snakebite targeted clinical development regulatory approved oral drugs that can be rapidly delivered in the community soon after a bite to alleviate the severe, often life-threatening effects would provide a paradigm shift in snakebite envenoming therapeutics (Clare et al., 2021; Gutiérrez et al., 2021; Abouyannis et al., 2022; Carter et al., 2022).

Data availability statement

The original contributions presented in the study are included in the article/Supplementary Material, further inquiries can be directed to the corresponding author.

Author contributions

RC: Conceptualization, Data curation, Formal Analysis, Funding acquisition, Methodology, Writing–original draft. CD: Data curation, Formal Analysis, Methodology, Validation, Writing–original draft. AW: Data curation, Formal Analysis, Methodology, Validation, Writing–original draft. L-OA: Methodology, Validation, Writing–review and editing. CW: Data curation, Formal Analysis, Methodology, Writing–original draft. NM: Data curation, Methodology, Writing–original draft. DC: Data curation, Methodology, Writing–original draft. JK: Funding acquisition, Writing–review and editing, Conceptualization. NB: Funding acquisition, Writing–review and editing, Conceptualization, Methodology. PO'N: Funding acquisition, Writing–review and editing, Conceptualization, Methodology. NC: Funding acquisition, Conceptualization, Methodology, Writing–original draft.

Funding

The author(s) declare financial support was received for the research, authorship, and/or publication of this article. This study was funded by: i) A Director's Catalyst Fund from LSTM [supported by Wellcome Institutional Strategic Support Fund 3 (204806/Z/16/Z) and LSTM Internal Funding] awarded to RC, ii) a UK Medical Research Council-funded Confidence in Concept Award (MC_PC_15040) to NC, and iii) a Wellcome Trust grant awarded to JK, NB, PO'N and NC (221712/Z/20/Z). This research was funded in part by the Wellcome Trust. For the purpose of open access, the authors have applied a CC BY public copyright licence to any Author Accepted Manuscript version arising from this submission.

Acknowledgments

We thank Paul Rowley and Edouard Crittenden for maintenance and husbandry of the snake collection and provision of venom samples at LSTM.

Conflict of interest

The authors declare that the research was conducted in the absence of any commercial or financial relationships that could be construed as a potential conflict of interest.

Publisher's note

Supplementary material

The Supplementary Material for this article can be found online at: https://www.frontiersin.org/articles/10.3389/fphar.2023.1328950/full#supplementary-material

SUPPLEMENTARY FIGURE S1

Full-plate control data separated by column and row to demonstrate inter- and intra-plate consistency. **(A)** Graphs demonstrating the raw data from three independently-ran control plates, containing either full maximum signal (vehicle: DMSO) or full baseline signal (10 μM marimastat), with values split by row (left) or column (right). Consistently high vehicle values and consistently baseline marimastat values can be seen irrespective of where on the plate they are located. **(B)** Normalised data from the same experiments as shown in **(A)**. Normalisation of this data reduces inter-plate variation, as can be seen with plate 1 compared to plates 2 and 3 in **(A)**, without affecting the separation of the positive and negative control signal windows.

SUPPLEMENTARY FIGURE S2
Interleaved control data separated by column and row to demonstrate inter- and intra-plate consistency. Graphs demonstrating the normalised results from three independently-ran control plates, containing alternating rows of maximum signal (vehicle: DMSO), baseline signal (10 μM marimastat), venom vehicle (PBS) or a suboptimal dose of marimastat (50 nM). Values ordered by row (top) or column (bottom). As with Supplementary Figure S1, consistency can be seen in matched conditions regardless of the location of the well on the plate, as well as between independently repeated plates. The suboptimal dose of marimastat selected demonstrates that it inhibits at around 50% that of the baseline concentration.

SUPPLEMENTARY DATASHEET S1
Repurposed Drug library—The details provided by MedChemExpress of the bespoke 3,547 repurposed drug library created for snakebite drug discovery screening are displayed. This is inclusive of chemical structural data through simplified molecular-input line-entry system (SMILES) keys (column K) and CAS number.

References

Abouyannis, M., FitzGerald, R., Ngama, M., Mwangudzah, H., Nyambura, Y. K., Ngome, S., et al. (2022). TRUE-1: trial of Repurposed Unithiol for snakebite Envenoming phase 1 (safety, tolerability, pharmacokinetics and pharmacodynamics in healthy Kenyan adults). *Wellcome Open Res.* 7, 90. doi:10.12688/wellcomeopenres.17682.1

Ainsworth, S., Menzies, S. K., Casewell, N. R., and Harrison, R. A. (2020). An analysis of preclinical efficacy testing of antivenoms for sub-Saharan Africa: inadequate independent scrutiny and poor-quality reporting are barriers to improving snakebite treatment and management. *PLoS Negl. Trop. Dis.* 14, e0008579. doi:10.1371/journal.pntd.0008579

Ainsworth, S., Slagboom, J., Alomran, N., Pla, D., Alhamdi, Y., King, S. I., et al. (2018). The paraspecific neutralisation of snake venom induced coagulopathy by antivenoms. *Commun. Biol.* 1, 34. doi:10.1038/s42003-018-0039-1

Albulescu, L.-O., Hale, M. S., Ainsworth, S., Alsolaiss, J., Crittenden, E., Calvete, J. J., et al. (2020a). Preclinical validation of a repurposed metal chelator as an early-intervention therapeutic for hemotoxic snakebite. *Sci. Transl. Med.* 12, eaay8314. doi:10.1126/scitranslmed.aay8314

Albulescu, L.-O., Xie, C., Ainsworth, S., Alsolaiss, J., Crittenden, E., Dawson, C. A., et al. (2020b). A therapeutic combination of two small molecule toxin inhibitors provides broad preclinical efficacy against viper snakebite. *Nat. Commun.* 11, 6094. doi:10.1038/s41467-020-19981-6

Ali, J., Camilleri, P., Brown, M. B., Hutt, A. J., and Kirton, S. B. (2012). Revisiting the general solubility equation: *in silico* prediction of aqueous solubility incorporating the effect of topographical polar surface area. *J. Chem. Inf. Model.* 52, 420–428. doi:10.1021/ci200387c

Amazonas, D. R., Portes-Junior, J. A., Nishiyama-, M. Y., Jr, Nicolau, C. A., Chalkidis, H. M., Mourão, R. H. V., et al. (2018). Molecular mechanisms underlying intraspecific variation in snake venom. *J. Proteomics* 181, 60–72. doi:10.1016/j.jprot.2018.03.032

Arias, A. S., Rucavado, A., and Gutiérrez, J. M. (2017). Peptidomimetic hydroxamate metalloproteinase inhibitors abrogate local and systemic toxicity induced by Echis ocellatus (saw-scaled) snake venom. *Toxicon* 132, 40–49. doi:10.1016/j.toxicon.2017.04.001

Asega, A. F., Menezes, M. C., Trevisan-Silva, D., Cajado-Carvalho, D., Bertholim, L., Oliveira, A. K., et al. (2020). Cleavage of proteoglycans, plasma proteins and the platelet-derived growth factor receptor in the hemorrhagic process induced by snake venom metalloproteinases. *Sci. Rep.* 10, 12912. doi:10.1038/s41598-020-69396-y

Ashburn, T. T., and Thor, K. B. (2004). Drug repositioning: identifying and developing new uses for existing drugs. *Nat. Rev. Drug Discov.* 3, 673–683. doi:10.1038/nrd1468

AstraZeneca (2022). AstraZeneca open innovation. Available at: https://openinnovation.astrazeneca.com.

Baell, J. B., and Holloway, G. A. (2010). New substructure filters for removal of pan assay interference compounds (PAINS) from screening libraries and for their exclusion in bioassays. *J. Med. Chem.* 53, 2719–2740. doi:10.1021/jm901137j

Baumgartner, G., Gawel, M. J., Kaeser, H. E., Pallis, C. A., Rose, F. C., Schaumburg, H. H., et al. (1979). Neurotoxicity of halogenated hydroxyquinolines: clinical analysis of cases reported outside Japan. *J. Neurol. Neurosurg. Psychiatry* 42, 1073–1083. doi:10.1136/jnnp.42.12.1073

Beck, T. P., Tupetz, A., Farias, A. S., Silva-Neto, A., Rocha, T., Smith, E. R., et al. (2022). Mapping of clinical management resources for snakebites and other animal envenomings in the Brazilian Amazon. *Toxicon X* 16, 100137. doi:10.1016/j.toxcx.2022.100137

Bissett, D., O'Byrne, K. J., von Pawel, J., Gatzemeier, U., Price, A., Nicolson, M., et al. (2005). Phase III study of matrix metalloproteinase inhibitor prinomastat in non-small-cell lung cancer. *J. Clin. Oncol. Off. J. Am. Soc. Clin. Oncol.* 23, 842–849. doi:10.1200/JCO.2005.03.170

Cabral-Pacheco, G. A., Garza-Veloz, I., Castruita-De la Rosa, C., Ramirez-Acuña, J. M., Perez-Romero, B. A., Guerrero-Rodriguez, J. F., et al. (2020). The roles of matrix metalloproteinases and their inhibitors in human diseases. *Int. J. Mol. Sci.* 21, 9739. doi:10.3390/ijms21249739

Calvete, J. J., Fasoli, E., Sanz, L., Boschetti, E., and Righetti, P. G. (2009). Exploring the venom proteome of the western diamondback rattlesnake, Crotalus atrox, via snake venomics and combinatorial peptide ligand library approaches. *J. Proteome Res.* 8, 3055–3067. doi:10.1021/pr900249q

Carter, R. W., Gerardo, C. J., Samuel, S. P., Kumar, S., Kotehal, S. D., Mukherjee, P. P., et al. (2022). The BRAVO clinical study protocol: oral varespladib for inhibition of secretory phospholipase A2 in the treatment of snakebite envenoming. *Toxins* 15, 22. doi:10.3390/toxins15010022

Casewell, N. R., Huttley, G. A., and Wüster, W. (2012). Dynamic evolution of venom proteins in squamate reptiles. *Nat. Commun.* 3, 1066. doi:10.1038/ncomms2065

Casewell, N. R., Jackson, T. N. W., Laustsen, A. H., and Sunagar, K. (2020). Causes and consequences of snake venom variation. *Trends Pharmacol. Sci.* 41, 570–581. doi:10.1016/j.tips.2020.05.006

Casewell, N. R., Wagstaff, S. C., Wüster, W., Cook, D. A. N., Bolton, F. M. S., King, S. I., et al. (2014). Medically important differences in snake venom composition are dictated by distinct postgenomic mechanisms. *Proc. Natl. Acad. Sci. U. S. A.* 111, 9205–9210. doi:10.1073/pnas.1405484111

Chippaux, J.-P. (2017). Snakebite envenomation turns again into a neglected tropical disease. *J. Venom. Anim. Toxins Trop. Dis.* 23, 38. doi:10.1186/s40409-017-0127-6

Chippaux, J. P., Williams, V., and White, J. (1991). Snake venom variability: methods of study, results and interpretation. *Toxicon Off. J. Int. Soc. Toxinology* 29, 1279–1303. doi:10.1016/0041-0101(91)90116-9

Chowdhury, A., Zdenek, C. N., Lewin, M. R., Carter, R., Jagar, T., Ostanek, E., et al. (2021). Venom-induced blood disturbances by palearctic viperid snakes, and their relative neutralization by antivenoms and enzyme-inhibitors. *Front. Immunol.* 12, 688802. doi:10.3389/fimmu.2021.688802

Clare, R. H., Clark, R., Bardelle, C., Harper, P., Collier, M., Johnston, K. L., et al. (2019). Development of a high-throughput cytometric screen to identify anti-wolbachia compounds: the power of public–private partnership. *SLAS Discov. Adv. Sci. Drug Discov.* 24, 537–547. doi:10.1177/2472555219838341

Clare, R. H., Hall, S. R., Patel, R. N., and Casewell, N. R. (2021). Small molecule drug discovery for neglected tropical snakebite. *Trends Pharmacol. Sci.* 42, 340–353. doi:10.1016/j.tips.2021.02.005

Conatus Pharmaceuticals Inc. (2012). A trial of CTS-1027 in interferon-naive hepatitis C patients (clinical trial registration No. NCT00925990). Available at: https://clinicaltrials.gov/study/NCT00925990.

Currier, R. B., Harrison, R. A., Rowley, P. D., Laing, G. D., and Wagstaff, S. C. (2010). Intra-specific variation in venom of the African Puff Adder (Bitis arietans): differential expression and activity of snake venom metalloproteinases (SVMPs). *Toxicon Off. J. Int. Soc. Toxinology* 55, 864–873. doi:10.1016/j.toxicon.2009.12.009

Daina, A., Michielin, O., and Zoete, V. (2017). SwissADME: a free web tool to evaluate pharmacokinetics, drug-likeness and medicinal chemistry friendliness of small molecules. *Sci. Rep.* 7, 42717. doi:10.1038/srep42717

Dawson, C. A., Ainsworth, S., Albulescu, L.-O., and Casewell, N. R. (2021). "Snake venom metalloproteinases," in *Handbook of venoms and toxins of reptiles* (USA: CRC Press), 363–379.

Delaney, J. S. (2004). ESOL: estimating aqueous solubility directly from molecular structure. *J. Chem. Inf. Comput. Sci.* 44, 1000–1005. doi:10.1021/ci034243x

de Silva, H. A., Ryan, N. M., and de Silva, H. J. (2016). Adverse reactions to snake antivenom, and their prevention and treatment. *Br. J. Clin. Pharmacol.* 81, 446–452. doi:10.1111/bcp.12739

Dingwoke, E. J., Adamude, F. A., Mohamed, G., Klein, A., Salihu, A., Abubakar, M. S., et al. (2021). Venom proteomic analysis of medically important Nigerian viper Echis ocellatus and Bitis arietans snake species. *Biochem. Biophys. Rep.* 28, 101164. doi:10.1016/j.bbrep.2021.101164

Drisko, J. A. (2018). "Chapter 107 - chelation therapy," in *Integrative medicine* Editor D. Rakel Fourth Edition (Germany: Elsevier), 1004–1015.e3. doi:10.1016/B978-0-323-35868-2.00107-9

Egan, W. J., Merz, K. M., and Baldwin, J. J. (2000). Prediction of drug absorption using multivariate statistics. *J. Med. Chem.* 43, 3867–3877. doi:10.1021/jm000292e

Ferraz, C. R., Arrahman, A., Xie, C., Casewell, N. R., Lewis, R. J., Kool, J., et al. (2019). Multifunctional toxins in snake venoms and therapeutic implications: from pain to hemorrhage and necrosis. *Front. Ecol. Evol.* 7. doi:10.3389/fevo.2019.00218

Flora, S. J. S., and Pachauri, V. (2010). Chelation in metal intoxication. *Int. J. Environ. Res. Public. Health* 7, 2745–2788. doi:10.3390/ijerph7072745

Fox, J. W., and Serrano, S. M. T. (2005). Structural considerations of the snake venom metalloproteinases, key members of the M12 reprolysin family of metalloproteinases. *Toxicon Off. J. Int. Soc. Toxinology* 45, 969–985. doi:10.1016/j.toxicon.2005.02.012

Fox, J. W., and Serrano, S. M. T. (2008). Insights into and speculations about snake venom metalloproteinase (SVMP) synthesis, folding and disulfide bond formation and their contribution to venom complexity. *FEBS J.* 275, 3016–3030. doi:10.1111/j.1742-4658.2008.06466.x

Ghose, A. K., Viswanadhan, V. N., and Wendoloski, J. J. (1999). A knowledge-based approach in designing combinatorial or medicinal chemistry libraries for drug discovery. 1. A qualitative and quantitative characterization of known drug databases. *J. Comb. Chem.* 1, 55–68. doi:10.1021/cc9800071

Gonçalves-Machado, L., Pla, D., Sanz, L., Jorge, R. J. B., Leitão-De-Araújo, M., Alves, M. L. M., et al. (2016). Combined venomics, venom gland transcriptomics, bioactivities, and antivenomics of two *Bothrops jararaca* populations from geographic isolated regions within the Brazilian Atlantic rainforest. *J. Proteomics, Proteomics Evol. Ecol.* 135, 73–89. doi:10.1016/j.jprot.2015.04.029

Gutiérrez, J. M., Albulescu, L.-O., Clare, R. H., Casewell, N. R., Abd El-Aziz, T. M., Escalante, T., et al. (2021). The search for natural and synthetic inhibitors that would complement antivenoms as therapeutics for snakebite envenoming. *Toxins* 13, 451. doi:10.3390/toxins13070451

Gutiérrez, J. M., Calvete, J. J., Habib, A. G., Harrison, R. A., Williams, D. J., and Warrell, D. A. (2017). Snakebite envenoming. *Nat. Rev. Dis. Primer* 3, 17063–17121. doi:10.1038/nrdp.2017.63

Gutiérrez, J. M., Escalante, T., Rucavado, A., and Herrera, C. (2016). Hemorrhage caused by snake venom metalloproteinases: a journey of discovery and understanding. *Toxins* 8, 93. doi:10.3390/toxins8040093

Hall, S. R., Rasmussen, S. A., Crittenden, E., Dawson, C. A., Bartlett, K. E., Westhorpe, A. P., et al. 2022. Repurposed drugs and their combinations prevent morbidity-inducing dermonecrosis caused by diverse cytotoxic snake venoms. doi:10.1101/2022.05.20.492855

Harrison, R. A., Casewell, N. R., Ainsworth, S. A., and Lalloo, D. G. (2019). The time is now: a call for action to translate recent momentum on tackling tropical snakebite into sustained benefit for victims. *Trans. R. Soc. Trop. Med. Hyg.* 113, 835–838. doi:10.1093/trstmh/try134

Harrison, R. A., Gutiérrez, J. M., Suntravat, M., Rodriguez-Acosta, A., Galan, J. A., and Salazar, E. (2019). The neutralization efficacy of expired polyvalent antivenoms: an alternative option. *Toxicon Off. J. Int. Soc. Toxinology* 168, 32–39. doi:10.1016/j.toxicon.2019.06.216

Harrison, R. A., Oluoch, G. O., Ainsworth, S., Alsolaiss, J., Bolton, F., Arias, A.-S., et al. (2017). Preclinical antivenom-efficacy testing reveals potentially disturbing deficiencies of snakebite treatment capability in East Africa. *PLoS Negl. Trop. Dis.* 11, e0005969. doi:10.1371/journal.pntd.0005969

Herzel, B. J., Samuel, S. P., Bulfone, T. C., Raj, C. S., Lewin, M., and Kahn, J. G. (2018). Snakebite: an exploratory cost-effectiveness analysis of adjunct treatment strategies. *Am. J. Trop. Med. Hyg.* 99, 404–412. doi:10.4269/ajtmh.17-0922

Hou, S., Diez, J., Wang, C., Becker-Pauly, C., Fields, G. B., Bannister, T., et al. (2021). Discovery and optimization of selective inhibitors of meprin α (Part I). *Pharmaceuticals* 14, 203. doi:10.3390/ph14030203

Howes, J.-M., Theakston, R. D. G., and Laing, G. D. (2007). Neutralization of the haemorrhagic activities of viperine snake venoms and venom metalloproteinases using synthetic peptide inhibitors and chelators. *Toxicon* 49, 734–739. doi:10.1016/j.toxicon.2006.11.020

Janes, J., Young, M. E., Chen, E., Rogers, N. H., Burgstaller-Muehlbacher, S., Hughes, L. D., et al. (2018). The ReFRAME library as a comprehensive drug repurposing library and its application to the treatment of cryptosporidiosis. *Proc. Natl. Acad. Sci.* 115, 10750–10755. doi:10.1073/pnas.1810137115

Johnson, J. L., Fritsche-Danielson, R., Behrendt, M., Westin-Eriksson, A., Wennbo, H., Herslof, M., et al. (2006). Effect of broad-spectrum matrix metalloproteinase inhibition on atherosclerotic plaque stability. *Cardiovasc. Res.* 71, 586–595. doi:10.1016/j.cardiores.2006.05.009

Kahraman, A., Bronk, S. F., Cazanave, S., Werneburg, N. W., Mott, J. L., Contreras, P. C., et al. (2009). Matrix metalloproteinase inhibitor, CTS-1027, attenuates liver injury and fibrosis in the bile duct-ligated mouse. *Hepatol. Res. Off. J. Jpn. Soc. Hepatol.* 39, 805–813. doi:10.1111/j.1872-034X.2009.00541.x

Kasturiratne, A., Lalloo, D. G., and Janaka de Silva, H. (2021). Chronic health effects and cost of snakebite. *Toxicon X* 9, 100074. –10. doi:10.1016/j.toxcx.2021.100074

Kini, R. M., and Koh, C. Y. (2016). Metalloproteases affecting blood coagulation, fibrinolysis and platelet aggregation from snake venoms: definition and nomenclature of interaction sites. *Toxins* 8, 284. doi:10.3390/toxins8100284

Knudsen, C., and Laustsen, A. H. (2018). Recent advances in next generation snakebite antivenoms. *Trop. Med. Infect. Dis.* 3, 42. doi:10.3390/tropicalmed3020042

Knudsen, C., Ledsgaard, L., Dehli, R. I., Ahmadi, S., Sørensen, C. V., and Laustsen, A. H. (2019). Engineering and design considerations for next-generation snakebite antivenoms. *Toxicon* 167, 67–75. doi:10.1016/j.toxicon.2019.06.005

Krige, D., Needham, L. A., Bawden, L. J., Flores, N., Farmer, H., Miles, L. E. C., et al. (2008). CHR-2797: an antiproliferative aminopeptidase inhibitor that leads to amino acid deprivation in human leukemic cells. *Cancer Res.* 68, 6669–6679. doi:10.1158/0008-5472.CAN-07-6627

Landrum, G. (2006). *RDKit: open-source cheminformatics software*.

Laustsen, A. H. (2018). Toxin-centric development approach for next-generation antivenoms. *Toxicon* 150, 195–197. doi:10.1016/j.toxicon.2018.05.021

Laxme, R. R. S., Khochare, S., Souza, H.F. de, Ahuja, B., Suranse, V., Martin, G., et al. (2019). Beyond the 'big four': venom profiling of the medically important yet neglected Indian snakes reveals disturbing antivenom deficiencies. *PLoS Negl. Trop. Dis.* 13, e0007899. doi:10.1371/journal.pntd.0007899

Lewin, M., Samuel, S., Merkel, J., and Bickler, P. (2016). Varespladib (LY315920) appears to Be a potent, broad-spectrum, inhibitor of snake venom phospholipase A2 and a possible pre-referral treatment for envenomation. *Toxins* 8, 248. doi:10.3390/toxins8090248

Lipinski, C. A., Lombardo, F., Dominy, B. W., and Feeney, P. J. (2001). Experimental and computational approaches to estimate solubility and permeability in drug discovery and development settings. *Adv. Drug Deliv. Rev.* 46, 3–26. doi:10.1016/S0169-409X(00)00129-0

Longbottom, J., Shearer, F. M., Devine, M., Alcoba, G., Chappuis, F., Weiss, D. J., et al. (2018). Vulnerability to snakebite envenoming: a global mapping of hotspots. *Lancet* 392, 673–684. doi:10.1016/S0140-6736(18)31224-8

Mackessy S. P. M. and Stephen P. (2009). *Handbook of venoms and toxins of reptiles* (Boca Raton: CRC Press). doi:10.1201/9781420008661

Madoux, F., Dreymuller, D., Pettiloud, J.-P., Santos, R., Becker-Pauly, C., Ludwig, A., et al. (2016). Discovery of an enzyme and substrate selective inhibitor of ADAM10 using an exosite-binding glycosylated substrate. *Sci. Rep.* 6, 11. doi:10.1038/s41598-016-0013-4

Maduwage, K., and Isbister, G. K. (2014). Current treatment for venom-induced consumption coagulopathy resulting from snakebite. *PLoS Negl. Trop. Dis.* 8, e3220. doi:10.1371/journal.pntd.0003220

Menzies, S. K., Clare, R. H., Xie, C., Westhorpe, A., Hall, S. R., Edge, R. J., et al. (2022). *In vitro* and *in vivo* preclinical venom inhibition assays identify metalloproteinase inhibiting drugs as potential future treatments for snakebite envenoming by Dispholidus typus. *Toxicon X* 14, 100118. doi:10.1016/j.toxcx.2022.100118

Millar, A. W., Brown, P. D., Moore, J., Galloway, W. A., Cornish, A. G., Lenehan, T. J., et al. (1998). Results of single and repeat dose studies of the oral matrix metalloproteinase inhibitor marimastat in healthy male volunteers. *Br. J. Clin. Pharmacol.* 45, 21–26. doi:10.1046/j.1365-2125.1998.00639.x

Moura-da-Silva, A. M., Theakston, R. D., and Crampton, J. M. (1996). Evolution of disintegrin cysteine-rich and mammalian matrix-degrading metalloproteinases: gene duplication and divergence of a common ancestor rather than convergent evolution. *J. Mol. Evol.* 43, 263–269. doi:10.1007/BF02338834

Neumann, U., Kubota, H., Frei, K., Ganu, V., and Leppert, D. (2004). Characterization of Mca-Lys-Pro-Leu-Gly-Leu-Dpa-Ala-Arg-NH2, a fluorogenic substrate with increased specificity constants for collagenases and tumor necrosis factor converting enzyme. *Anal. Biochem.* 328, 166–173. doi:10.1016/j.ab.2003.12.035

Nguyen, G. T. T., O'Brien, C., Wouters, Y., Seneci, L., Gallissà-Calzado, A., Campos-Pinto, I., et al. (2022). High-throughput proteomics and *in vitro* functional characterization of the 26 medically most important elapids and vipers from sub-Saharan Africa. *GigaScience* 11, giac121. doi:10.1093/gigascience/giac121

Oliveira, I. S., Ananias, C. B., Medeiros, J. M., Franco, M. V. S., Ferreira, I. G., Cerni, F. A., et al. (2022). Medical management after lancehead snakebite in north amazon: a case report of long-term disability. *Toxins* 14, 494. doi:10.3390/toxins14070494

Oliveira, I.S. de, Cardoso, I. A., Bordon, K. de C. F., Carone, S. E. I., Boldrini-França, J., Pucca, M. B., et al. (2019). Global proteomic and functional analysis of *Crotalus durissus* collilineatus individual venom variation and its impact on envenoming. *J. Proteomics, V. ICAP Proteogenomics* 191, 153–165. doi:10.1016/j.jprot.2018.02.020

Probst, D., and Reymond, J.-L. (2020). Visualization of very large high-dimensional data sets as minimum spanning trees. *J. Cheminformatics* 12, 12. doi:10.1186/s13321-020-0416-x

Rucavado, A., Escalante, T., Franceschi, A., Chaves, F., León, G., Cury, Y., et al. (2000). Inhibition of local hemorrhage and dermonecrosis induced by *Bothrops asper* snake venom: effectiveness of early *in situ* administration of the peptidomimetic metalloproteinase inhibitor batimastat and the chelating agent CaNa2EDTA. *Am. J. Trop. Med. Hyg.* 63, 313–319. doi:10.4269/ajtmh.2000.63.313

Scatena, R. (2000). Prinomastat, a hydroxamate-based matrix metalloproteinase inhibitor. A novel pharmacological approach for tissue remodelling-related diseases. *Expert Opin. Investig. Drugs* 9, 2159–2165. doi:10.1517/13543784.9.9.2159

Slagboom, J., Kool, J., Harrison, R. A., and Casewell, N. R. (2017). Haemotoxic snake venoms: their functional activity, impact on snakebite victims and pharmaceutical promise. *Br. J. Haematol.* 177, 947–959. doi:10.1111/bjh.14591

Strandvik, B., and Zetterström, R. (1968). Amaurosis after broxyquinoline. *Lancet* Issue 7548 291, 922–923. Originally published as Volume 1. doi:10.1016/S0140-6736(68)90280-8

Tang, E. L. H., Tan, C. H., Fung, S. Y., and Tan, N. H. (2016). Venomics of Calloselasma rhodostoma, the Malayan pit viper: a complex toxin arsenal unraveled. *J. Proteomics* 148, 44–56. doi:10.1016/j.jprot.2016.07.006

Tasoulis, T., and Isbister, G. K. (2017). A review and database of snake venom proteomes. *Toxins* 9, 290. doi:10.3390/toxins9090290

Tasoulis, T., Pukala, T. L., and Isbister, G. K. (2021). Investigating toxin diversity and abundance in snake venom proteomes. *Front. Pharmacol.* 12, 768015. doi:10.3389/fphar.2021.768015

Thorne, N., Auld, D. S., and Inglese, J. (2010). Apparent activity in high-throughput screening: origins of compound-dependent assay interference. *Curr. Opin. Chem. Biol.* 14, 315–324. doi:10.1016/j.cbpa.2010.03.020

Trape, J.-F. (2018). Partition d'Echis ocellatus Stemmler, 1970 (Squamata, Viperidae), avec la description d'une espèce nouvelle. *Bull. Société Herpétologique Fr.* 167, 13–34.

Veber, D. F., Johnson, S. R., Cheng, H.-Y., Smith, B. R., Ward, K. W., and Kopple, K. D. (2002). Molecular properties that influence the oral bioavailability of drug candidates. *J. Med. Chem.* 45, 2615–2623. doi:10.1021/jm020017n

Warrell, D. A. (2010). Snake bite. *Lancet lond. Engl.* 375, 77–88. doi:10.1016/S0140-6736(09)61754-2

Williams, D. J., Gutiérrez, J.-M., Calvete, J. J., Wüster, W., Ratanabanangkoon, K., Paiva, O., et al. (2011a). Ending the drought: new strategies for improving the flow of affordable, effective antivenoms in Asia and Africa. *J. Proteomics* 74, 1735–1767. doi:10.1016/j.jprot.2011.05.027

Williams, J. M., Zhang, J., North, P., Lacy, S., Yakes, M., Dahly-Vernon, A., et al. (2011b). Evaluation of metalloprotease inhibitors on hypertension and diabetic nephropathy. *Am. J. Physiol.-Ren. Physiol.* 300, F983–F998. doi:10.1152/ajprenal.00262.2010

Winer, A., Adams, S., and Mignatti, P. (2018). Matrix metalloproteinase inhibitors in cancer therapy: turning past failures into future Successes. *Mol. Cancer Ther.* 17, 1147–1155. doi:10.1158/1535-7163.MCT-17-0646

Xie, C., Albulescu, L., Bittenbinder, M. A., Somsen, G., Vonk, F., Casewell, N. R., et al. (2020). Neutralizing effects of small molecule inhibitors and metal chelators on coagulopathic *Viperinae* snake venom toxins (preprint). *Pharmacol. Toxicol.* doi:10.1101/2020.06.02.129643

Yang, Z.-Y., He, J.-H., Lu, A.-P., Hou, T.-J., and Cao, D.-S. (2020). Frequent hitters: nuisance artifacts in high-throughput screening. *Drug Discov. Today* 25, 657–667. doi:10.1016/j.drudis.2020.01.014

Zhang, J. H., Chung, T. D., and Oldenburg, K. R. (1999). A simple statistical parameter for use in evaluation and validation of high throughput screening assays. *J. Biomol. Screen.* 4, 67–73. doi:10.1177/108705719900400206

frontiers | Frontiers in Pharmacology

TYPE Original Research
PUBLISHED 11 January 2024
DOI 10.3389/fphar.2023.1331224

OPEN ACCESS

EDITED BY
Michelle Yap,
Monash University Malaysia, Malaysia

REVIEWED BY
Manuela Berto Pucca,
Sao Paulo State University, Brazil
Marco Aurelio Sartim,
Universidade Nilton Lins, Brazil
Isadora Sousa de Oliveira,
University of São Paulo, Brazil

*CORRESPONDENCE
Nicholas R. Casewell,
nicholas.casewell@lstmed.ac.uk

RECEIVED 31 October 2023
ACCEPTED 19 December 2023
PUBLISHED 11 January 2024

CITATION
Albulescu L-O, Westhorpe A, Clare RH, Woodley CM, James N, Kool J, Berry NG, O'Neill PM and Casewell NR (2024), Optimizing drug discovery for snakebite envenoming via a high-throughput phospholipase A2 screening platform. *Front. Pharmacol.* 14:1331224. doi: 10.3389/fphar.2023.1331224

Optimizing drug discovery for snakebite envenoming via a high-throughput phospholipase A2 screening platform

Laura-Oana Albulescu[1,2], Adam Westhorpe[1,2], Rachel H. Clare[1,2], Christopher M. Woodley[3], Nivya James[3], Jeroen Kool[4], Neil G. Berry[3], Paul M. O'Neill[3] and Nicholas R. Casewell[1,2]*

[1]Centre for Snakebite Research and Interventions, Department of Tropical Disease Biology, Liverpool School of Tropical Medicine, Liverpool, United Kingdom, [2]Centre for Drugs and Diagnostics, Department of Tropical Disease Biology, Liverpool School of Tropical Medicine, Liverpool, United Kingdom, [3]Department of Chemistry, University of Liverpool, Liverpool, United Kingdom, [4]Division of BioAnalytical Chemistry, Department of Chemistry and Pharmaceutical Sciences, Faculty of Science, Amsterdam Institute of Molecular and Life Sciences, Vrije Universiteit Amsterdam, Amsterdam, Netherlands

Snakebite envenoming is a neglected tropical disease that causes as many as 1.8 million envenomings and 140,000 deaths annually. To address treatment limitations that exist with current antivenoms, the search for small molecule drug-based inhibitors that can be administered as early interventions has recently gained traction. Snake venoms are complex mixtures of proteins, peptides and small molecules and their composition varies substantially between and within snake species. The phospholipases A2 (PLA_2) are one of the main pathogenic toxin classes found in medically important viper and elapid snake venoms, yet varespladib, a drug originally developed for the treatment of acute coronary syndrome, remains the only PLA_2 inhibitor shown to effectively neutralise venom toxicity *in vitro* and *in vivo*, resulting in an extremely limited drug portfolio. Here, we describe a high-throughput drug screen to identify novel PLA_2 inhibitors for repurposing as snakebite treatments. We present method optimisation of a 384-well plate, colorimetric, high-throughput screening assay that allowed for a throughput of ~2,800 drugs per day, and report on the screening of a ~3,500 post-phase I repurposed drug library against the venom of the Russell's viper, *Daboia russelii*. We further explore the broad-spectrum inhibitory potential and efficacy of the resulting top hits against a range of medically important snake venoms and demonstrate the utility of our method in determining drug EC_{50}s. Collectively, our findings support the future application of this method to fully explore the chemical space to discover novel PLA_2-inhibiting drugs of value for preventing severe pathology caused by snakebite envenoming.

KEYWORDS

high-throughput screening, drug discovery, toxin inhibitors, snake venom, snakebite envenoming, neglected tropical disease

Introduction

Snakebite envenoming is a neglected tropical disease (NTD) that results in ~140,000 deaths and 400,000 disabilities globally each year (Gutiérrez et al., 2017). It disproportionately affects the low and middle income countries (LMIC) of Asia, Africa, the Americas and Oceania, and predominantly impacts isolated rural communities (Harrison et al., 2009) for whom transportation to a clinic to receive treatment can take >6 h (Sharma et al., 2004; Ogunfowokan, 2012; Longbottom et al., 2018; Mise et al., 2018). The only approved treatment for snakebite is antivenom - animal derived, polyclonal antibody-based products generated via immunisation of equines or ovines. Despite saving thousands of lives annually, antivenom comes with several limitations, including risk of severe adverse reactions such as anaphylaxis (de Silva et al., 2016), high cost, lack of availability in many remote areas, and reliance on the cold chain (Williams et al., 2011). Because of its requirement for intravenous delivery, coupled with the need to manage potentially life-threatening adverse reactions, antivenom can only be administered under medical supervision in a clinical environment, which causes treatment delays and poor patient outcomes. Finally, antivenom is highly species-specific due to snake venom variation, meaning that an antivenom will typically only be efficacious against those venoms included in the immunising mixture (Chippaux et al., 1991; Gutiérrez et al., 2017).

The diversity of snake venoms, each of which can consist of a variable mixture of over >200 peptide and/or protein components (Casewell et al., 2013), also complicates the clinical picture of envenoming. Medically important venomous snakes fall into two main families: Viperidae (vipers) whose bites are typically characterised by causing haemotoxic and/or tissue destructive effects, and Elapidae (elapids) whose venoms are typically neurotoxic (Gutiérrez et al., 2017). This divergence in pathology is driven by differences in the main toxin classes present, with viper venoms often dominated by enzymatic toxins such as snake venom metalloproteinases (SVMPs), group II phospholipase A_2 (PLA_2), and snake venom serine proteases (SVSPs), whereas non-enzymatic three-finger toxins (3FTxs) and group I PLA_2s are often the most abundant in elapid venoms (Tasoulis and Isbister, 2017).

Since PLA_2s are major contributors to the snakebite pathology caused by most venomous snakes, understanding their mechanisms of action can help us devise new treatments to mitigate their pathological effects. Enzymatic PLA_2s hydrolyse the sn-2 ester bonds of cell membrane phospholipids, contain a catalytic Asp49 residue and utilise Ca^{2+} as a cofactor. In contrast, non-enzymatic PLA_2s are Ca-independent and lack a negative charge at position 49, with aspartic acid replaced by either a positive (typically lysine) or non-charged amino acid (Kini, 2003; Gutiérrez and Lomonte, 2013). Anticoagulant enzymatic PLA_2s are monomeric and have been described in both viper {RVV-PFIIc from *Daboia russelii* (Chakraborty et al., 2002) and elapid [e.g., *Naja nigricollis* (Kerns et al., 1999; Kini, 2005)]} venoms. On the other hand, multimeric (including homo- or hetero-dimeric) PLA_2s are present in various venoms and can include both enzymatic and non-enzymatic PLA_2 subunits, or can be formed of complexes with other toxins which facilitate targeting of the PLA_2s to their site of action. For example, *Oxyuranus scutellatus* venom contains the trimeric catalytically active (Asp49) PLA_2 taipoxin (Fohlman et al., 1976; Cendron et al., 2012), while members of the pitviper genus *Crotalus* have heterodimeric PLA_2s which either have [e.g., crotoxin (Sampaio et al., 2010)] or lack (e.g., CoaTX-II (Almeida et al., 2016)) enzymatic activity. Additionally, β-bungarotoxin from the elapid *Bungarus multicinctus* consists of an enzymatic PLA_2 and a Kunitz-type peptide heterodimer and exerts presynaptic neurotoxicity (Kwong et al., 1995). Intriguingly, enzymatic and non-enzymatic PLA_2s can also coexist in the same venom. One such example is the venom of the pitviper *Bothrops asper* (terciopelo) which contains two types of monomeric myotoxins: the enzymatic myotoxin-I and the non-enzymatic myotoxin II, both of which destabilise the sarcolemma before being internalised in the cell nucleus (Vargas-Valerio et al., 2021). Given this diverse range of pathological effects, and the near ubiquity of PLA_2 toxins across the variable venoms of medically important snakes (Tasoulis and Isbister, 2017), broad-spectrum neutralisation of the toxic effects of PLA_2s would represent a major step in the treatment of snakebite envenoming.

The concept of broadly targeting and neutralising a whole venom toxin class, rather than focusing on species-specific treatments, has recently gained traction in the snakebite community (Bulfone et al., 2018; Clare et al., 2021; Gutiérrez et al., 2021). Small molecule toxin inhibitors capable of neutralising SVMP or PLA_2 toxins (Rucavado et al., 2004; Lewin et al., 2016; Arias et al., 2017; Lewin et al., 2018a; Lewin et al., 2018b; Bryan-Quirós et al., 2019; Albulescu et al., 2020a; Albulescu et al., 2020b; Menzies et al., 2022), and which can be formulated as oral drugs, have been proposed as rapid interventions to be given to snakebite patients in the field soon after a snakebite. Such treatments could possess several advantages over conventional antivenoms, such as their potential for cross-species neutralisation through generic inhibition of the active site of a class of toxins, improved safety profiles, reduced cost over antibodies, and potential ease of administration (Clare et al., 2021). The efficacy of such drugs has been investigated in the context of both systemic (Rucavado et al., 2004; Arias et al., 2017; Lewin et al., 2018a; Lewin et al., 2018b; Albulescu et al., 2020a; Albulescu et al., 2020b) and local (Bryan-Quirós et al., 2019; Albulescu et al., 2020a; Hall et al., 2023) envenoming in *in vivo* preclinical models, and in the context of both single drug treatments and combinations of inhibitors targeting different toxin families. Among these, varespladib and its orally bioavailable analogue methyl varespladib have been shown to be highly effective in neutralizing the toxicity of both several viper and elapid venoms *in vitro* and *in vivo* (Lewin et al., 2016; Lewin et al., 2018a; Lewin et al., 2018b). Importantly, varespladib appears to target both enzymatic and non-enzymatic PLA_2s and leads to a conformational change upon binding which renders the toxin unable to access and act upon its substrate (Salvador et al., 2019). Although varespladib was originally developed for the treatment of acute coronary syndrome (Chiara Ricci, 2015), it has recently progressed into human clinical trials (phase II) in India and United States for snakebite indication, in a drug repurposing approach (Lewin et al., 2022). While this is a highly promising development, the snakebite drug portfolio remains limited, with no robust backup PLA_2-inhibiting molecules in place to offset the risk of attrition or failure during clinical development. This is predominately because no concerted drug

discovery screening efforts to identify novel PLA_2 inhibiting compounds have been described to date.

Here, we present the first high-throughput screen (HTS) for novel inhibitors capable of neutralising the PLA_2-activity of snake venoms. We describe the methodology and optimisation steps leading to the validation of a 384-well plate colorimetric assay capable of screening ~2,800 drugs/day, and report our findings from the primary screening of a model ~3,500 compound, post-phase I, commercial drug library. To account for the potential influence of venom variation and varying inhibitory drug potencies against distinct PLA_2 isoforms, we further explored our hits for their broad-spectrum efficacy against a panel of diverse snake venoms. We hope that the described methodology will prove valuable to the snakebite community in its search for novel broad-spectrum small molecule inhibitors directed against venom PLA_2 toxins.

Methods

Venoms

Venoms were sourced from either wild-caught specimens maintained in, or donated historical venom samples stored in, the herpetarium of the Liverpool School of Tropical Medicine. The venom pools selected encompassed vipers and elapids from diverse geographical localities and were from: *D. russelii* (Sri Lanka), *B. arietans* (Nigeria), *N. nigricollis* (Tanzania), *C. atrox* (United States), *N. naja* (captive bred) and *C. durissus terrificus* (Brazil). Crude venoms were lyophilized and stored at 4 °C to ensure long term stability. Prior to use, venoms were resuspended to 10 mg/mL in PBS (pH 7.4, Cat no: 10010023, Gibco) and then further diluted to 1 mg/mL stock solutions in PBS for the described experiments.

PLA_2 assay optimisation

The Abcam $sPLA_2$ assay (Cat No: ab 133089, Abcam) functions by measuring the rate of hydrolysis of the sn-2 bond of a phosphatidylcholine analogue, diheptanoyl-thio-phosphatidylcholine, by secretory PLA_2s ($sPLA_2$s). Once hydrolysed, this substrate yields a free thiol group that interacts with 5,5′-dithio-bis-(2-nitrobenzoic acid) (DTNB), which is then converted into 2-nitro-5-thiobenzoic acid, causing a change in colour which is measurable at 405 nm. This conversion is measured kinetically and occurs at a linear rate until the substrate is exhausted, at which point the absorbance plateaus. Appropriate PLA_2 concentrations are determined to fit within the linear range of the assay and a bee venom positive control is included with the kit. The assay is designed for 96-well plates and is quite costly at GBP£440/96 tests at the time of writing. We wanted to adapt and miniaturise this methodology for high-throughput screening of PLA_2 activity and inhibition in 384-well plates to decrease cost and increase output, without compromising assay robustness.

To this end we miniaturised the assay 5-fold to a working volume of 45 µL, decreased the stock concentration of the substrate from 1.66 to 1.33 mM, and modified the reaction volumes to enable the use of robotics. The final reaction consisted of 10 µL of snake venom diluted in assay buffer (25 mM Tris-HCl, pH 7.5, 10 mM $CaCl_2$, 100 mM KCl, 0.3 mM Triton X-100), 5 µL of 4 mM DTNB in 0.4 M Tris-HCl, pH 8.0 and 30 µL of 1.33 mM substrate stock in assay buffer. The final concentrations of DTNB and that of the substrate in the assay were 0.44 and 0.88 mM, respectively.

To determine PLA_2 inhibition, 0.5 µL of 1 mM drugs in DMSO (≥99.7%, Cat No: D2650, Sigma) were printed onto 384-well plates using a VIAFLO384 384-channel electronic pipette (Integra). Then, 10 µL of snake venom at a concentration appropriate for the venom being screened was added to the plates using the VIAFLO384 and the plates were sealed with adhesive plate seals (Greiner BioOne), spun down and incubated for 25 min at 37°C. To prevent the degradation of any potential photolabile compounds, the plates were wrapped in aluminium foil prior to the incubation step. The plates were then taken out of the incubator and left to acclimatise at room temperature for 5 min. Five microliters of 4 mM DTNB and 30 µL of 1.33 mM substrate were then added sequentially to the plates using the VIAFLO384, after which the plates were immediately read kinetically on a CLARIOstar plate reader (BMG Labtech) at 405 nm for 15 min (settings for a full 384-well plate were 11 flashes, 161 s cycle time).

Range finding for venoms

To determine working ranges for the various PLA_2-rich venoms, serial dilutions were performed for each venom. Initially, for venoms such as *D. russelii* and *N. nigricollis* a large concentration interval was tested ranging from 200 pg to 2 µg, but it was quickly determined that the 1–100 ng interval is usually sufficient to identify an appropriate venom activity that falls within the linear range of the assay. Therefore, for other venoms used for breadth of inhibition tests a smaller concentration window was used.

Assay validation

Prior to conducting drug library screens, it was important to assess whether any drift or edge effects occurred in our setup. To this end, interleaved plates containing DMSO, assay buffer, 10 µM varespladib (≥98%, Cat no: SML1100, Sigma) and 10 µM marimastat [a matrix metalloproteinase (MMP) inhibitor previously used to inhibit snake venom metalloproteinase venom toxins *in vitro* (Albulescu et al., 2020b); ≥99%, Cat No: M2699, Sigma] were set up. These consisted of full rows of these compounds in a repeating pattern (e.g., DMSO was in rows A, E, I, M, buffer was in rows B, F, J, N, etc.) on a 384-well plate. The assay was conducted as previously described using 20 ng/well of *D. russelii* venom across the plate. This was repeated three times on different days. To determine PLA_2 activity under each of these conditions, the slope of each reaction was calculated by dividing the difference in absorbance at 405 nm between the first two time points in the linear range (t_n–t_0) by time (in min) where t_n was 2 min 41 s in this case. These values were then inputted into the following equation:

$$A\left(\frac{\mu mol}{min \times mL}\right) = \frac{slope \times 0.045}{(4.6 \times 0.01)}$$

where A represents venom activity, 0.045 is a factor representing the total volume of the assay (45 µL), 4.6 is the extinction coefficient of DTNB in 384-well plates, and 0.01 represents the sample size of 10 µL. This activity is then converted into specific activity by dividing the overall activity to the amount of venom in the reaction in micrograms.

To assess the quality of the assay, we calculated Z prime values across the plate by using the following formula:

$$Z' = 1 - \frac{3(\sigma\ (pos) - \sigma\ (neg))}{|\mu\ (pos) - \mu\ (neg)|}$$

where σ and µ represent the standard deviations and means of the positive (varespladib containing wells) and negative controls (DMSO only containing wells), respectively. Acceptable assay Z′s are ≥ 0.4, with increased values up to 1 representing highly robust datasets. Plate means and coefficients of variation for the positive and negative controls were also calculated.

Primary screening of the drug library

Following assay validation in 384-well format, a bespoke repurposed drug library of 3,547 compounds was purchased from MedChemExpress. This library (a combination of the HY-L035 and HY-L026 libraries with overlaps removed) was curated by MedChemExpress to contain a diverse chemical panel of post-phase I and approved drugs that have completed preclinical and clinical studies for a wide range of diseases. All drugs have well-characterised bioactivity, safety, and bioavailability properties, making them suitable for drug repurposing. Once in house this library was formatted as 11 × 384-well stock plates containing drugs at a concentration of 1 mM in DMSO. These were screened against 2 ng/µL (20 ng/well) of *D. russelii* (Sri Lanka) snake venom, as determined earlier. In addition to the blinded compounds on the plates, control compounds were added to confirm that the assay had performed appropriately. These controls included 10 µM varespladib as a positive control (100% inhibition) and vehicle (DMSO) as a negative control (0% inhibition). Assay-ready plates (ARPs) were made by transferring 0.5 µL from each well of the stock plates onto new 384-well plates, so that the layout of the ARP matched that of the stock plate. Venom was added at 10 µL per well (20 ng venom/well) across the plate, except for column 24 which received 10 µL of assay buffer. These latter wells containing control drugs and assay buffer served as the blank. The plates were incubated for 25 min at 37°C, then left to reach room temperature for 5 min. Next, 5 µL of DTNB, followed by 30 µL of substrate were added sequentially to the wells, and the plate was immediately read kinetically on a CLARIOstar multiwell plate reader at 405 nm (temperature set to 25°C, 15 min total read time, 161 s/read cycle). The data were analysed as above by calculating the slopes of all reactions on the plate. The average of the slopes of the blanks was then subtracted from each of these values, and specific activity calculated as described and expressed as µmol/min/mL/µg of venom.

To determine percentage inhibition relative to the positive and negative controls we applied the following formula:

$$\%\ inhibition = \left(\frac{A - \mu\ (pos)}{\mu\ (neg) - \mu\ (pos)}\right) \times 100$$

where A represents specific activity as determined for each sample, and µ (pos) and µ (neg) represent the means of the specific activity in the positive and negative controls, respectively.

Compounds that demonstrated inhibitory PLA_2 activity of at least 60% compared to varespladib and venom alone were progressed to allow retesting for confirmation of their activity.

Rescreening hits from the drug library

Thirty-six compounds from the MedChemExpress library were identified as hits in the primary screen (9 strong at >80% and 27 mediocre between 60% and 80% inhibition of venom PLA_2 activity). However, considering the primary screen was run in singleton, we wanted to confirm whether 60% inhibition was an appropriate threshold to allow us to identify true positives. These compounds were thus selected and transferred onto one plate for retesting together against *D. russelii* venom (20 ng/well). These experiments were conducted and analysed as above, with n = 4 repeats per compound.

Retesting of top hits

To further confirm our top hits and assess breadth of inhibition across venoms, the following compounds were ordered in from commercial sources: (*R*)-(-)-Gossypol acetic acid (≥98%, Cat No: HY-15464A, MedChemExpress), DL-Borneol (Cat No: 23468, Cayman Chemical), punicalagin (Cat No: 13069, Cayman Chemical), quercetin dihydrate (≥96%, Cat No: HY-N0146, MedChemExpress) and prasugrel hydrochloride (≥98%, Cat No: HY-15284A, MedChemExpress). Drugs were made into 1 mM working stocks in DMSO, after which they were tested at a final concentration of 10 µM against a variety of PLA_2-rich venoms (*D. russelli*, *N. nigricollis*, *N. naja*, *B. arietans*, *C. atrox* and *C. durissus terrificus*. The amount of venom used in each case has been described above in the "*Range finding for venoms*" section.

EC_{50} testing

To further explore the capabilities of the assay, EC_{50} curves were generated for drug hits that displayed the best broad-spectrum venom inhibition (gossypol, punicalagin and varespladib) against three venoms: *D. russelii*, *N. nigricollis* and *C. durissus terrificus*. Drugs were plated as before, starting at 10 µM followed by 2-fold dilutions down to 5 pM, with each dilution series plated in quadruplicate. The data were analysed and expressed as described above and the percentage PLA_2 inhibition values were used to generate EC_{50}s in Graphpad Prism 9 using a nonlinear regression to fit the dose-response inhibition curve.

Computational chemistry

The HTS library was screened for common Pan-Assay INterference compoundS (PAINS) substructures (Baell and Holloway, 2010) using the in-built PAINS filter in the RDKIT

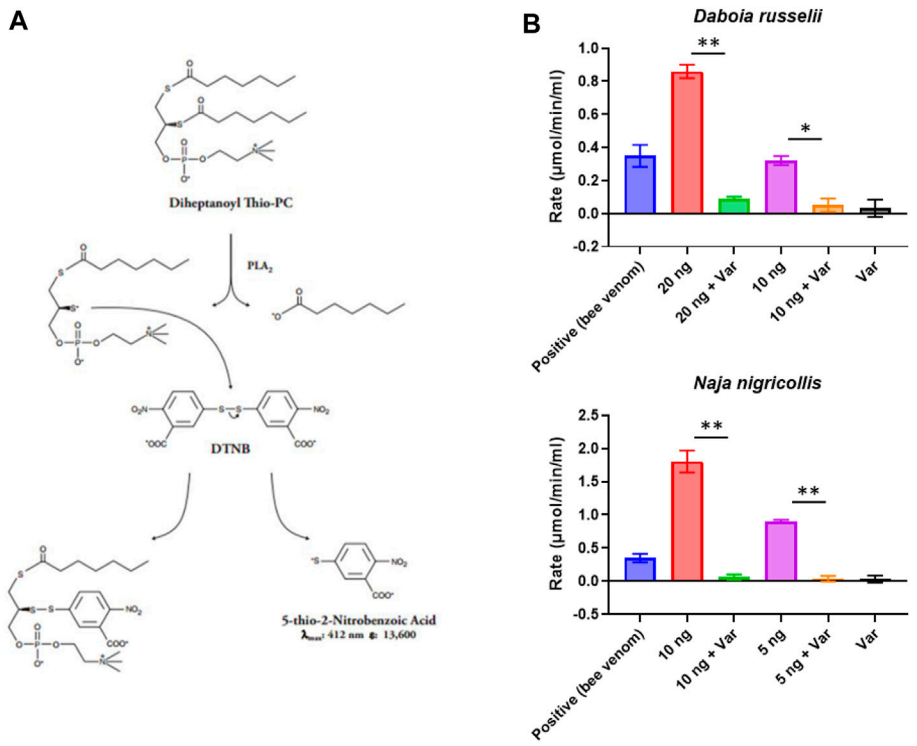

FIGURE 1
Assay setup and miniaturisation. **(A)** Assay reaction principle. **(B)** Examples of venoms optimised for work under HTS conditions. Various venom concentrations were explored to ensure they were within the linear range of the assay (20, 10 or 5 ng shown here), and then inhibition of PLA_2 activity by 10 µM varespladib (var) was tested. Data shown represents the reaction rate, with bars showing the mean of duplicate readings and error bars representing standard error. Significance is displayed above the graphs with *p*-values $p < 0.05$ (**) and $p < 0.5$ (*) shown.

cheminformatics package version 2022.03.5 as implemented in Python (Landrum et al., 2020). Tree Manifold Approximation Projection (TMAP) visualisation was performed using the TMAP python module version 1.0.6 (Probst and Reymond, 2020). The DataWarrior open source program was used to calculate the Ligand efficiency metrics (Sander et al., 2015). LogP and heavy atom counts were calculated using StarDrop™ ADME QSAR module (Version 7.3, Optibrium, Ltd., Cambridge, United Kingdom).

Results

Optimising a commercial $sPLA_2$ assay for HTS screening of drug libraries

To best utilise commercial drug libraries as a source for novel PLA_2 inhibitors, we first needed to identify and optimise a screening method that would allow us to fully explore the chemical space. To this end, we took advantage of the commercially available Abcam secretory PLA_2 kit (ab133089), which we miniaturised and adapted for use in 384-well format using robotics (see Methods, Figure 1A). This resulted in a 5-fold scale-down of the assay volume and decreased substrate concentrations to allow increased sample throughput while reducing the cost. Using the kit-supplied bee venom as a positive control, we determined working concentration ranges for a representative viper (*D. russelii*) and elapid (*N. nigricollis*) snake venom, with 10-fold dilutions ranging from 200 pg to 2 µg of venom tested. Our findings demonstrated that 20 ng of *D. russelli* and 5 ng of *N. nigricollis* venom were sufficient to display at least equivalent activity to the positive bee venom control, while still falling within the linear range of the assay (Supplementary Figure S1). We next demonstrated that 10 µM of the gold standard PLA_2 inhibitor, varespladib, inhibited venom activity to baseline readings for both viper and elapid venoms (Figure 1B).

To further test the applicability of our adapted assay for large scale screening we next investigated assay reproducibility across the 384-well plate and replicability between different batches of 384-well plates. To determine intra-plate and inter-plate variability, we ran three identical interleaved plates containing *D. russelii* venom on different days. The plate setup (Figure 2A) accounted for all drugs being dissolved in DMSO; as such the DMSO-only control is a proxy for venom alone (negative control), whereas the varespladib control represents a positive control (100% inhibition). Marimastat, a peptidomimetic inhibitor of a different class of venom toxins (the snake venom metalloproteinases), and assay buffer, both of which are not expected to neutralise PLA_2 activity, were also included in the panel as additional controls (marimastat at a concentration of 10 µM). The signals across the plate after blank subtraction were expressed as activity (µmol/min/mL/µg venom) and are displayed in Figures 2B–D. The venom only controls (labelled "DMSO") and the two controls, which do not inhibit PLA_2 activity, displayed values of 6–8 µmol/min/mL/µg venom, which are venom-dependent. When PLA_2 activity was inhibited with varespladib this dropped sharply,

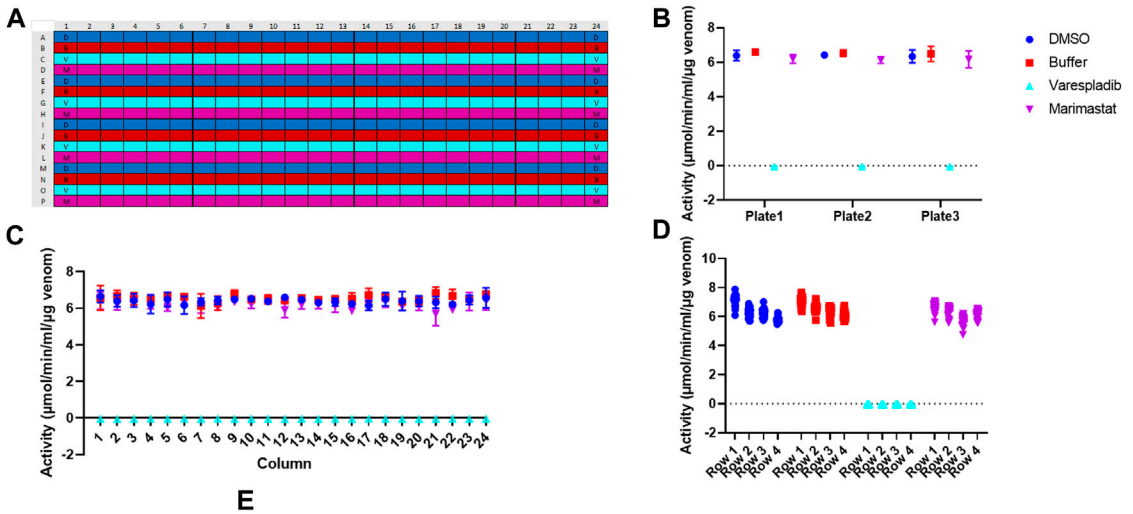

E

	Interleaved (DMSO)		Interleaved (Var 10 µM)		
QC Plate	Mean	CV	Mean	CV	Z prime
1	1.828	6.54	0.153	5.04	0.6
2	1.832	4.02	0.152	5.36	0.73
3	1.823	11.32	0.137	4.40	0.61

FIGURE 2
Assay optimisation for high throughput screening. **(A)** Plate map showing interleaved controls across the 384-well plate. D - DMSO (dark blue), B - buffer (red), V - varespladib (light blue), M - marimastat (magenta). **(B)** Signal variability across runs (n = 3) expressed as the average activity across each 384-well plate with standard deviation (SD) represented by error bars. **(C)** Signal consistency (n = 3) expressed as the average activity for each column across all 384-well plates with corresponding SD shown by error bars. No drift is observed from column 1 to 24. **(D)** The signal variability for each row containing the same control (DMSO, buffer, 10 µM varespladib or 10 µM marimastat). The average of all 24-data points/row across 3 plates is displayed for each condition—e.g., for DMSO/venom only, rows 1–4 indicate rows A, E, I and M. A minimal decrease in activity is noted from A to M, but this still allows for a significant window of detection between the positive and negative controls. **(E)** Quality control statistics for each interleaved plate tested including mean values, coefficients of variation (CVs) of controls and Z′ values.

allowing us to establish a baseline (100% inhibition). No differences were noted between the average signal values on each of the three plates, suggesting good reproducibility of the method (Figure 2B). Similarly, when variability was assessed on a column or row basis, we noted no drift across columns (1–24) and only a minimal change in activity from the top to bottom rows – a reflection of the time it takes the instrument to read the plate in real time (Figures 2C, D). Our data suggest that under these conditions we can obtain a reliable assay window between our positive and negative controls in which to measure PLA_2 inhibition by various drugs. The full plate by plate data is provided in Supplementary Figure S2. We calculated resulting Z-primes, which represents a measure of assay quality (Zhang et al., 1999), where the threshold routinely set for such assays is indicated by a $Z' > 0.5$. Values from each of our three runs were ≥0.6, thereby confirming the robustness of our method (Figure 2E).

Screening a commercial drug library for novel PLA_2 inhibitors

Following method validation, we next wanted to test the ability of our assay to identify novel PLA_2 inhibitors by screening a commercial drug library. To this end, we purchased a bespoke library sourced from MedChemExpress, which we screened against the medically important and PLA_2-rich venom of *D. russelii* (Faisal et al., 2021; Laxme et al., 2021). The library was curated to contain diverse chemistry of 3,547 approved or post-phase I clinically trialled drugs (i.e., diversity of those that have previously completed preclinical and clinical studies for a wide range of diseases), as well as having well-characterised bioactivity, safety and bioavailability properties, making them amenable for drug repurposing. The drugs were plated at a final assay concentration of 10 µM in 384-well format with controls on either side of the plate. As our assay setup allows for a throughput of ~2,800 drugs/day/venom, we were able to complete the screen for this library in under 2 days using single point measurements. The percentage inhibition of PLA_2 activity was calculated relative to the positive (varespladib, set at 100%) and negative (DMSO, venom-only, 0%) controls and resulted in nine strong hits (percentage inhibition >80%, 0.25% hit rate) and 27 mediocre hits (percentage inhibition 60% < x < 80%, 0.76% hit rate). The majority of drugs are not significant inhibitors of PLA_2 activity and fall within the −10% to 30% inhibition interval, with the data following a gaussian distribution as confirmed by the Shapiro-Wilks test for normally distributed data ($W = 0.97$, p-value = 2.13e−26) (Figure 3A).

We next selected all hits displaying >60% inhibition and independently rescreened them in the assay (Figures 3B, C). With one exception (salvianolic acid A), strong hits were consistently confirmed as PLA_2 inhibitors in the subsequent independent runs (Figure 3B), with average inhibition values of at least 60% in eight of the nine hits, and at least 80% in five of the nine hits. Varespladib, which is

10.3389/fphar.2023.1331224

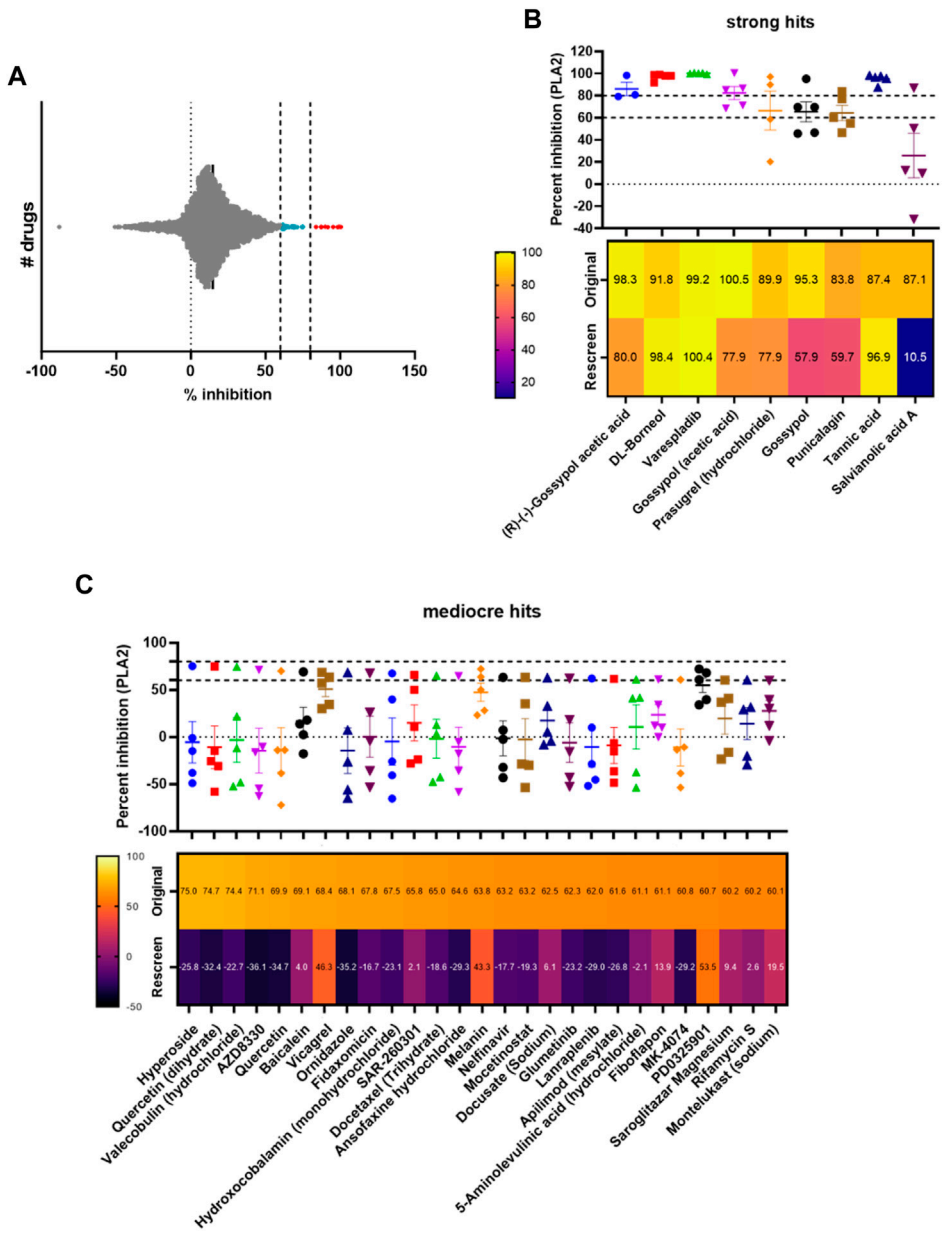

FIGURE 3
Screening of a commercial library and assessing hit reproducibility for strong and mediocre hits. **(A)** Visualisation of the distribution of hits, with strong hits highlighted in red (>80%) and mediocre hits in light blue (60% < x < 80%). **(B)** Percentage PLA_2 inhibition for strong hits. The original data from the screen and rescreens are presented, and the median value ($3 \leq n \leq 5$) across all datasets is displayed with SDs. Below, a heat map displaying the values identified in the original screen versus the average values in the rescreen ($2 \leq n \leq 4$) is presented. **(C)** Percentage PLA_2 inhibition for mediocre hits with SDs, with heat map below showing the original screen value versus the average value in the rescreen (bottom). Drug names are presented underneath each heat map.

also part of the MedChemExpress commercial drug library, was also detected as a hit with >99% inhibition of PLA_2 activity. Conversely, mediocre hits were much more variable and, when retesting, the majority were revealed as false positives; only three of the 27 originally detected mediocre hits displayed average inhibition values of >40% upon rescreen (between 43% and 53% inhibition, Figure 3C). This suggests the need to implement a stringent cut-off—in this case the application of the "strong hit" threshold of 80% inhibition appears appropriate—and reconfirm hits before progressing any drugs into downstream analyses.

Of the strong hits recovered, gossypol, a phenolic compound derived from the cotton plant, appeared three times as an independent hit (mean inhibition between screen and rescreen of 89.2%, 89.2% and 76.6% for *R*-(-)-gossypol acetic acid, gossypol acetic acid and gossypol, respectively). Other plant compounds we recovered were punicalagin (mean inhibition of 71.7%), a compound found in pomegranates, tannic acid (92.1%), a polyphenol found in various woody plant species, and DL-borneol (95.1%), a terpene derivative from the teak family. Additionally, prasugrel hydrochloride, a platelet aggregation

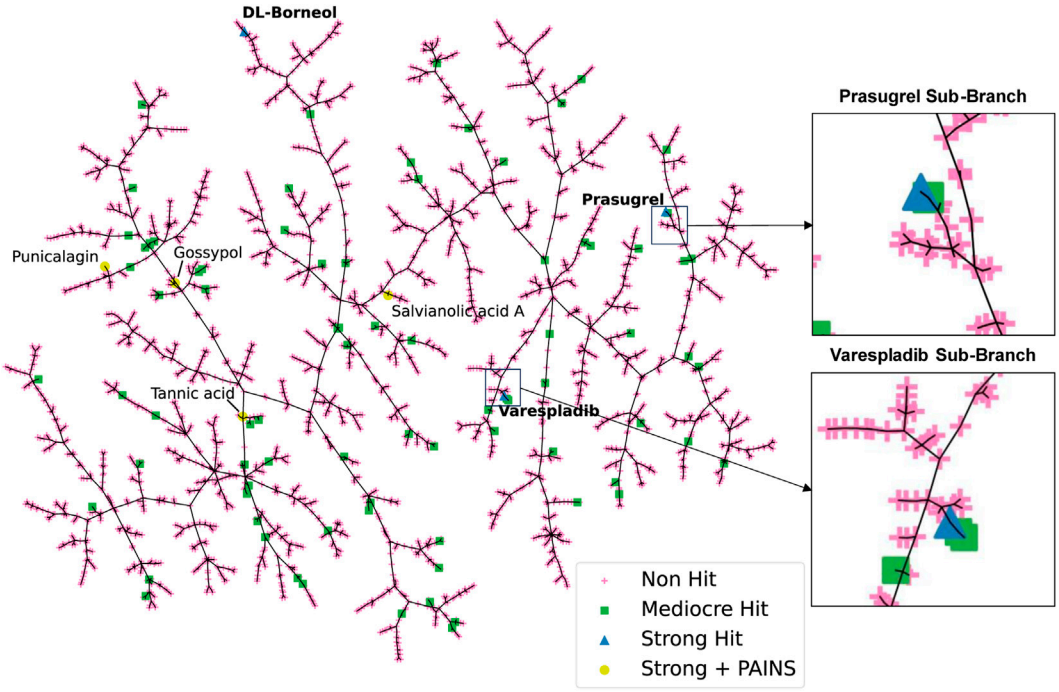

FIGURE 4
TMAP representation of the chemical space covered by our HTS library. Non-hits are shown as pink crosses, mediocre hits are shown as green squares, and strong hits are shown as blue triangles. Strong hits containing PAINS fragments are shown as yellow circles.

inhibitor, was also among our top hits (mean inhibition of 83.9%). We decided to pursue all strong hits with average inhibition values of >70%, including *R*-(-)-gossypol acetic acid, DL-Borneol, punicalagin, and prasugrel hydrochloride. Tannic acid was excluded from this selection as it is a likely false positive since it is known to react with the exposed -SH group present in the substrate and prevent the reaction between the latter and DTNB (Chen et al., 2022).

PAINS filtering of drug hits

All compounds were virtually screened for substructures common to Pan-Assay INterference compoundS (PAINS) (Baell and Holloway, 2010). In our approach we screened the structures of all compounds for known PAINS substructures and flagged compounds containing these structures as being more likely to represent a false positive result. Out of all the strong and mediocre hits identified in the primary HTS, we identified 15 PAINS flagged structures (Supplementary Figure S3) of which four were strong hits. Gossypol, punicalagin, tannic acid and salvianolic acid were all flagged as PAINS positive due to containing catechol moieties—a moiety known to be have promiscuous reactivity, redox activity and to chelate metal ions (Matlock et al., 2018).

As previously mentioned, tannic acid was excluded due to documented reactivity with free thiols (Chen et al., 2022). Gossypol was also flagged due to containing the catechol moiety, but also for containing reactive aldehyde groups which have been documented to form Schiff bases with primary amines (Kovacic, 2023). This is supported by the identification of gossypol as a promiscuous compound using data-mining and deep-learning approaches (Yu et al., 1997; Bisson et al., 2016). Despite this limitation, owing to its documented inactivation of PLA_2 in prior biochemical assays, we carried gossypol forward for further inhibitory profiling (B.-Z. Yu et al., 1997).

While lacking any reports of promiscuous behaviour in HTS, punicalagin, like tannic acid, is a naturally occurring tannin and contains many catechol moieties which may lead to false positives in our assay. This is supported by single-digit micromolar potency or less in 17 separate reported bioassays on the Chembl database (https://www.ebi.ac.uk/chembl/compound_report_card/CHEMBL416615/, accessed September 2023). Nevertheless, punicalagin was further shown via rescreening to inhibit PLA_2 activity and was taken forward for further characterisation.

Visualisation of the HTS dataset

To visualise the HTS chemical space and to identify trends among closely related scaffolds identified as PLA_2 inhibitory molecules we employed Tree Manifold Approximation Projection (TMAP) (Probst and Reymond, 2020). TMAP visually represents chemical space as a tree-like manifold, grouping similar compounds into branches based on their proximity, revealing meaningful patterns and relationships within chemical space.

Visualisation of our dataset (Figure 4) shows that mediocre and strong hits are well distributed across the manifold with most mediocre hits isolated from other compounds. Most strong hits, including those flagged for containing PAINS related substructures, are similarly isolated on sub-branches, with the exception of varespladib and prasugrel, which share their sub-branches with mediocre hits fiboflapon and vicagrel, respectively. Fiboflapon is

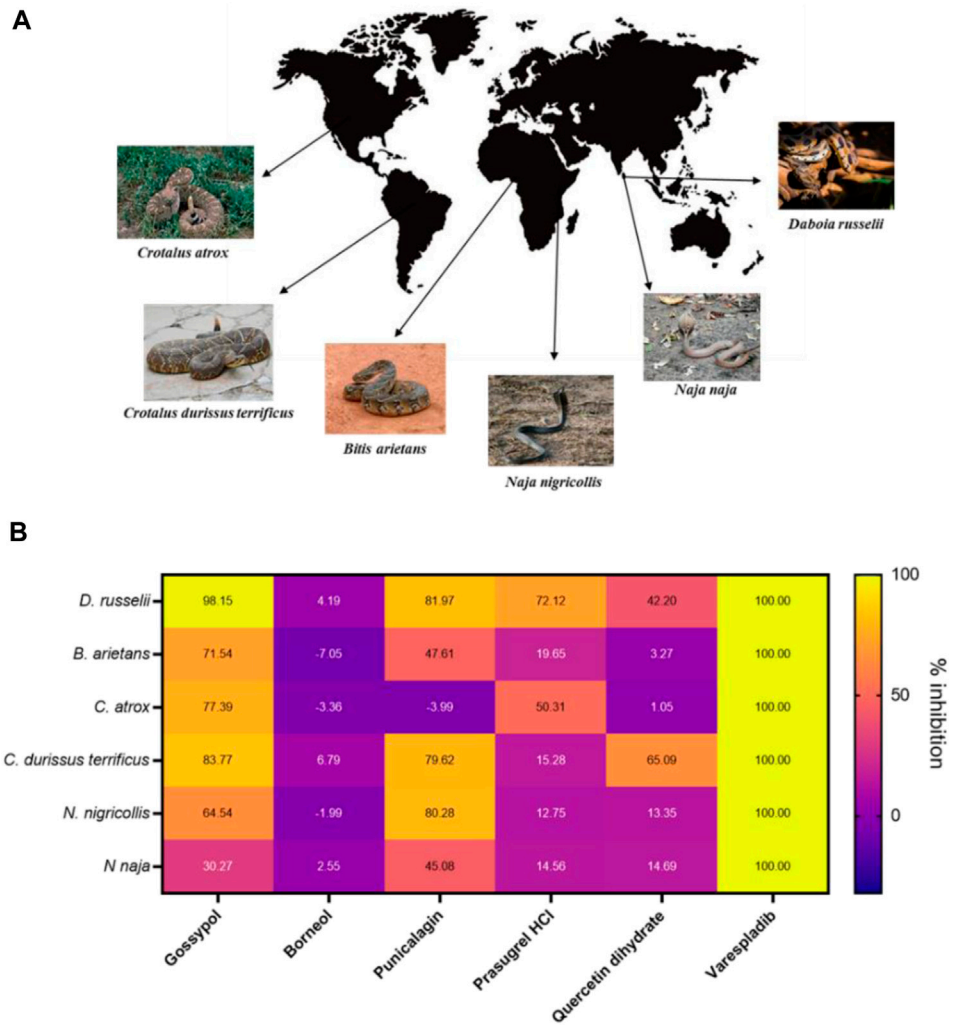

FIGURE 5
The PLA_2 inhibitory capability of selected strong hits against different snake venoms. **(A)** Geographical distribution of a selection of PLA_2-rich venoms spanning both viper and elapid snakes. Images either belong in the public domain or are displayed under a creative commons license; photographers Gary Stolz (*C. atrox*), Leandro Avelar (*C. durissus terrificus*), Kelly Abram (*B. arietans*), Lucy Keith-Diagne (*N. nigricollis*), Dr. Raju Kasambe (*N. naja*) and Tushar Mone (*D. russelli*). **(B)** Heat map displaying PLA_2 inhibition values (in percentages) of selected drugs against those six venoms. Drugs were assayed at a top dose of 10 μM against an optimised venom amount which elicited a strong signal in the assay: *D. russelii* (30 ng), *N. naja* (40 ng), *B arietans* (40 ng), *C. atrox* (30 ng), *N. nigricollis* (5 ng) and *C. durissus terrificus* (12.5 ng). Varespladib was used as the positive control and was normalised as 100% inhibition.

a potent inhibitor of 5-lipoxygenase-activating protein which shares a common *N*-aryl-2,3-disubstituted indole core with varespladib. Similarly, vicagrel, a closely related analogue of prasugrel, is an antiplatelet prodrug based on clopidogrel and which is converted sequentially by esterases and cytochrome P450 enzymes into an active metabolite common to both prasugrel and clopidogrel. The close proximity of these two strong hits to closely related moderate hits is suggestive of common inhibitory scaffolds.

Exploring the breadth of inhibition and potency of selected strong hits

As our original screen only assessed PLA_2 inhibition for *D. russelii* venom, we wanted to understand whether our remaining hits were able to inhibit the PLA_2 activity of a variety of PLA_2-rich venoms at a top dose of 10 μM. As such, we chose venoms spanning a wide spectrum of geographical locations from Asia, Africa, South and North America, including both vipers (*Crotalus atrox* and *Crotalus durissus terrificus* from the *Crotalinae* subfamily and *Bitis arietans* from *Viperinae*) and elapids (*Naja naja* and *N. nigricollis*) (Figure 5A). This is important, because while both vipers and elapids have PLA_2 toxins in their venoms, these evolved independently via the duplication of different genes encoding different PLA_2 subclasses (IIA and IB, respectively) (Lynch, 2007; Fry et al., 2008). Following approved industry practices, we commercially sourced re-synthesised versions of our top hits to ensure their inhibitory activity was maintained independent of the material present in the commercial drug screening library. In addition to our selection of remaining

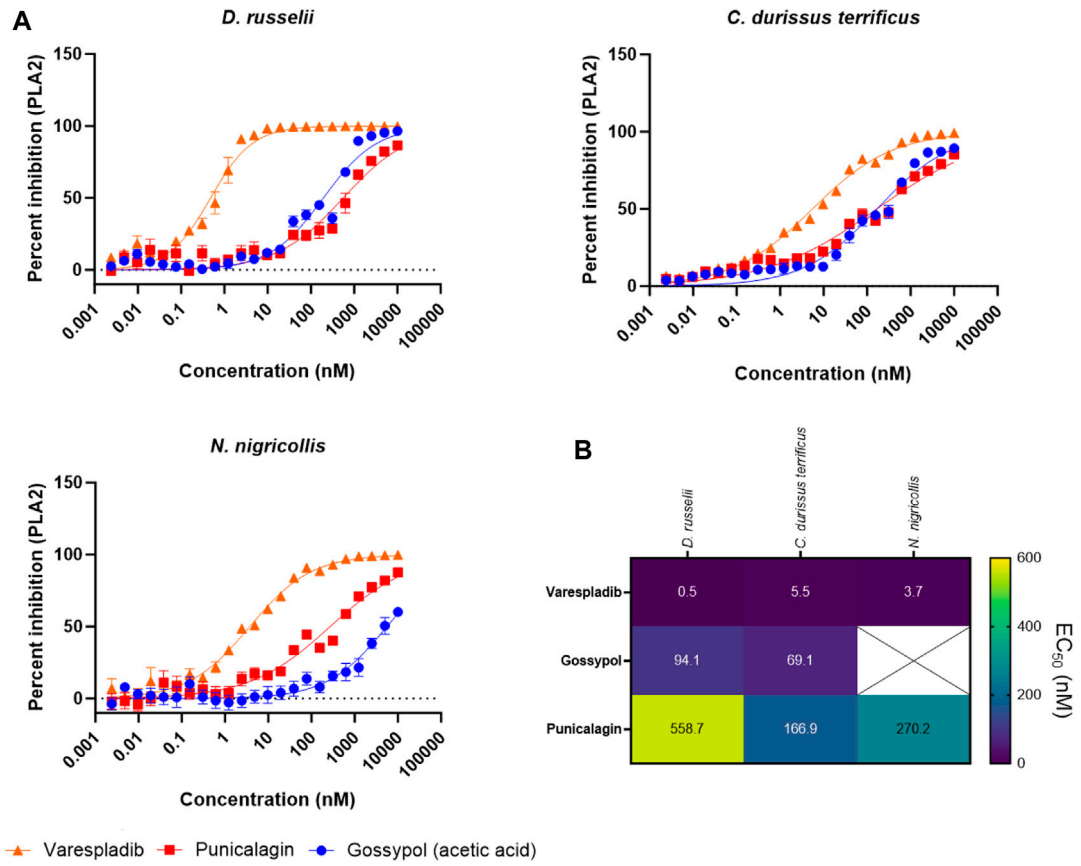

FIGURE 6
Testing the PLA_2 inhibitory potency of the top three drug hits against diverse snake venoms. **(A)** EC_{50} curves of venom PLA_2 inhibition for *R*-(-)-gossypol acetic acid, punicalagin and varespladib against three snake venoms (*D. russelii*, *C. durissus terrificus* and *N. nigricollis*). Curves were generated using 2-fold drug dilutions (n = 4), which spanned the 5 pM - 10 μM concentration range. **(B)**. EC_{50} values for the drugs against the three venoms. The crossed-out space denotes that the EC_{50} was not reported as the top inhibitory dose (10 μM) did not yield >80% inhibition of PLA_2 activity.

strong hits, we also chose to test quercetin dihydrate, a compound which was previously shown to inhibit enzymatic PLA_2s from *C. durissus terrificus* venom (Cotrim et al., 2011), and was initially recovered as a mediocre hit (inhibition value >70%) but failed to inhibit *D. russelii* venom in the rescreen (Figure 3C).

Gossypol, punicalagin and prasugrel hydrochloride all displayed PLA_2 inhibition values above 72% against the venom of *D. russelii*, with gossypol and punicalagin exhibiting considerable breadth of inhibition against a selection of viper and elapid venoms (>70% inhibition against four venoms for gossypol and >80% inhibition against three venoms for punicalagin, Figure 5B). Interestingly, the new stock of quercetin dihydrate led to 42% inhibition of the PLA_2 activity of *D. russelii* venom, and also partly inhibited the PLA_2 activity of *C. durissus terrificus* venom (~65%), in line with previous reports (Cotrim et al., 2011). However, the ineffectiveness of quercetin at inhibiting the PLA_2 activities of the other four venoms tested (all <15% inhibition), coupled with its known promiscuity (Giannetti et al., 2008), likely limit its translational potential. Despite being a strong hit in both the primary and rescreen of the library, DL-borneol did not re-test as a hit against any of our six venoms, perhaps indicating issues with compound resynthesis. Contrastingly, the known PLA_2 inhibitor varespladib (also our positive control) displayed the best cross-species effectiveness, with potent PLA_2 inhibitory activity observed against all six diverse snake venoms, reducing readings to control levels. These findings highlight that this previously described drug remains the standout inhibitory molecule for inhibiting PLA_2 venom toxins, despite the increased chemical space explored in this commercial drug library screen.

To better explore the potency of our broad-spectrum hits, we next decided to generate EC_{50} curves for our three top performing drugs (varespladib, gossypol, and punicalagin) against three venoms. We chose the venoms of *D. russelii*, *C. durissus terrificus* and *N. nigricollis* because, with one exception (gossypol against *N. nigricollis* venom), all venoms were effectively inhibited by all three drugs at the top dose of 10 μM (Figure 5B, at least 71% inhibition). Our range of drug serial dilutions covered a concentration interval from 5 pM to 10 μM (Figure 6A). Varespladib was consistently the most potent PLA_2 inhibitor with EC_{50}s ranging from 500 pM against *D. russelii* venom to 5.5 nM against *C. durissus terrificus*. Gossypol was slightly more effective than punicalagin for the two viper venoms tested (Figure 6B) with EC_{50}s in the low nanomolar range (94.1 and 69.1 nM for *D. russelii* and *C. durissus terrificus* respectively), but

provided only partial inhibition for *N. nigricollis* venom at the top dose tested (10 μM). Similarly, punicalagin was most effective against the venom of *C. durissus terrificus* (EC_{50} of 166.9 nM), but its potency decreased to intermediate levels for the other two tested venoms (558.7 and 270.2 nM for *D. russelii* and *N. nigricollis* venoms respectively). Overall, these data demonstrate that the validated screening assay enables the identification of novel inhibitors that display strong to moderate inhibition against snake venom PLA_2s and that our methodology is appropriate for broad-spectrum efficacy and EC_{50} testing.

Discussion

Here we present the miniaturisation of a colorimetric assay which allowed us to assess PLA_2 activity in snake venoms in a high throughput manner. We show that this methodology allows for a throughput of ~2,800 drugs/day/venom and is therefore suitable for determining broad-spectrum inhibitory activities and potencies of novel PLA_2 inhibitors of value for snakebite drug discovery. We have optimised the assay to ensure reproducibility within and between 384-well plates, and which resulted in Z′ values of >0.5. Using the commercially sourced MedChemExpress repurposed drug library we demonstrated the applicability of the assay for snakebite drug screening, and identified novel compounds capable of neutralising venom PLA_2 activities. Our screening activities further contextualised varespladib as a potent and broad inhibitor of snake venom phospholipase toxins.

One important consideration for identifying hits was the stringency of our self-imposed cut-offs, with more stringent cut-offs ultimately required to ensure reproducibility given the relatively narrow assay window. As such, we defined strong hits as those exhibiting >80% PLA_2 inhibition and these were validated in follow-up experiments to possess a true positive rate of 88.9% (8 out of 9). Contrastingly, false positives were abundant in the inhibitory interval initially assigned as mediocre hits (60% < x < 80%; 24 out of 27 initial mediocre hits; 88.9% FPR), leading us to largely exclude these from follow-up studies. One exception was quercetin, a compound retained because it was previously shown to inhibit the enzymatic PLA_2 activity of *C. durissus terrificus* venom (Cotrim et al., 2011). Although we confirmed this activity against this same venom in our assay (Figure 5), this compound was not effective against other venoms, and thus appears not be a potent broad spectrum PLA_2 inhibitor.

Among the nine strong hits identified from the primary screen, we noted an abundance of plant-derived compounds such as gossypol (isolated from cottonseed), punicalagin (a compound found in pomegranates), salvianolic acid A (from *Salvia miltiorrhiza* which is used in traditional Chinese medicine) and tannic acid (a polyphenol found in many plant species). Tannic acid likely represents a false positive as it is known to react with the exposed -SH group present in the assay substrate, thereby preventing its reaction with DTNB (Chen et al., 2022), and thus was excluded from follow up studies. Further, while salvianolic acid A failed to reproducibly inhibit *D. russelii* venom in the rescreen and was dropped from downstream experiments, both gossypol and punicalagin consistently displayed inhibition of at least >59% of the PLA_2 activity of this venom. Gossypol was a hit in our library in three different instances (*R*-(-)-gossypol acetic acid, gossypol acetic acid and gossypol) and displayed inhibitory values between 95% and 100% against *D. russelii* venom (Figure 3B).

Gossypol is an orally active polyphenolic aldehyde which was trialled as a male contraceptive in the 1970s in China and shown to be efficacious and well tolerated at a dose of up to 20 mg/day (Liu et al., 1987; Coutinho et al., 2000). It is non-teratogenic (Beaudoin, 1985) and was shown to induce G0/G1 cell cycle arrest, inhibit DNA replication and lead to apoptosis (Zhang et al., 2003). In addition, gossypol inhibited proliferation in non-small cell lung carcinoma cells (Wang et al., 2018). While gossypol is flagged for PAINS associated substructures, and is documented as being a promiscuously reactive compound (Bisson et al., 2016; Matlock et al., 2018; Kovacic, 2023), we carried gossypol forward for further characterisation owing to reported inhibition of secreted PLA_2 activity (B. Z. Yu et al., 1997). In our assay, gossypol showed broad-spectrum PLA_2 inhibition across various viper and elapid venoms (Figure 5B), with at least 64% neutralisation of PLA_2 activity across four other venoms when tested at 10 μM. However, gossypol appears to more effectively inhibit viper venom PLA_2s (type IIA), with 71%–98% inhibition observed against the four viper species, compared with only 30% and 64% inhibition against the two elapid venoms (type IB PLA_2) (Figure 5B). This was also the case based on calculated EC_{50}s, which were in the nanomolar range for the two viper venoms (*C. durissus terrificus*, 69.1 nM; *D. russelii* at 94.1 nM), while an EC_{50} could not be precisely estimated for the elapid *N. nigricollis* due to a lack of complete inhibition at the highest dose tested.

One other plant-derived hit displaying >79% PLA_2 inhibition across three snake venoms was punicalagin, one of the largest phenolic compounds known to date. Punicalagin was shown to possess antioxidant, anticancer and anti-inflammatory activity (Seeram et al., 2005; Danesi and Ferguson, 2017; Berdowska et al., 2021) while being non-toxic at high doses in rodents (Cerdá et al., 2003). Punicalagin was also flagged as containing PAINS related substructures in our virtual screen, however promiscuous biological activity has not been reported. While showing a more reduced spectrum of inhibition against the different snake venoms when compared to gossypol, punicalagin did display higher nanomolar EC_{50}s against both viper and elapid venoms, with a value of 166.9 nM against *C. durissus terrificus* and 270.2 nM against *N. nigricollis* venom, though reduced potency was observed against *D. russelii* venom (558.7 nM) (Figure 6). In contrast to these plant-derived compounds, the platelet aggregator inhibitor prasugrel failed to provide more than mediocre inhibition against any of the other snake venoms tested (>50% inhibition observed for only two venoms). While prasugrel was found to possess poor broad-spectrum activity, visualisation of HTS chemical space brought the closely related platelet inhibitor vicagrel as a mediocre hit—this suggests that their common scaffold may have inherent, albeit weak, PLA_2 inhibitory activities.

Despite the application of the optimised PLA_2 inhibition assay for the discovery of novel venom toxin inhibitors via a high throughput screening approach, none of the hits identified exhibited equivalent or superior PLA_2 inhibitory potencies to that of varespladib (potent inhibition against the six diverse venoms at

10 μM and EC_{50}s in the 0.5–5.5 nM range across all three venoms tested) (Figures 5, 6), which represents the current "gold standard" PLA_2 inhibitor in snake venom research (Lewin et al., 2016; 2022; Clare et al., 2021). Moreover, in addition to the limitations associated with reduced potency and inhibitory breadth, the phenolic compounds identified in our screen are relatively large molecules possessing several structural characteristics (Supplementary Figure S3; Supplementary Table S1), which render them suboptimal for progression for drug development purposes.

To be considered for lead development, a compound requires suitable physicochemical properties in addition to specific target affinity. Beyond the rule of five (Lipinski, 2000), ligand efficiency (LE) and ligand lipophilicity efficiency (LLE) are two metrics in modern early drug discovery that predict the affinity and quality of screened hits against a target (Hevener et al., 2018). The LE metric calculates ligand affinity using activity values (percentage inhibition values in this case) and the number of heavy atoms (Hopkins et al., 2004) and as such the values depend on their molecular weight. On the other hand, LLE accounts for the lipophilic properties of the molecules (LogP). Candidate drugs possessing higher LE and LLE metrics should be preferred during target-based drug discovery programs when compared to active ligands against that target (Leeson and Springthorpe, 2007). In addition, Gleeson (Gleeson, 2008), suggested that along with good activity profiles, lower molecular weight and LogP values must be emphasized in hit compounds for improved ADMET properties. Amongst our hits, LE values decreased with an increase in molecular weight/heavy atoms. When compared to varespladib, gossypol and punicalagin both displayed decreased LE metrics (Supplementary Table S1) due to their larger heavy atom count. In addition, while salvianolic acid and punicalagin presented similar LLE metrics to varespladib (accounted by their lower logP approximations), they had some of the lowest LE metrics among our strong hits. Together, these characteristics make gossypol and punicalagin suboptimal molecules for further progression.

Although varespladib retains exciting promise pending forthcoming snakebite clinical trial outcomes (Lewin et al., 2022), the high attrition rate of drug development provides a strong rationale to continue the search for novel PLA_2 inhibiting compounds. To that end, we are currently utilising the methodology described herein to explore the wider chemical space covered by several other drug libraries. We believe this approach will be useful for identifying novel repurposed drugs in the field of snakebite envenoming, as well as allowing for the initiation of medicinal chemistry campaigns to rationally optimise hits by improving DMPK characteristics amenable to snakebite indication.

Despite our success in miniaturising this assay and markedly reducing cost, we are aware that research kits for determining PLA_2 activity remain scarce and expensive, especially for researchers based in LMIC where snakebite is prevalent. This could be addressed by companies either producing cost-effective detection kits in line with demand as the use of these kits expands, or by exploring the use of alternative, more affordable, PLA_2 substrates, which could then be incorporated into newly validated laboratory methodologies alongside use of appropriate home-made buffers.

In conclusion, we have successfully miniaturised a commercial PLA_2 assay for high throughput screening and validated it for snakebite drug discovery purposes using snake venom. We show that the method is robust and applicable for screening of PLA_2 inhibitors across various distinct snake venoms, but that it also has the potential for wider applications, including exploring the inhibitory potential of other therapeutic molecules for snakebite (i.e., monoclonal antibodies) and those outside this specific field (i.e., in the context of other venoms, and/or human or bacterial phospholipases). In addition, the HTS approach and platform have also been successfully used in our lab to screen for inhibitors of other toxin families (SVMPs, Clare et al., 2024). Overall, we hope that this will prove to be a valuable approach that will enable the development of improved therapeutics for treating the world's tropical snakebite victims.

Data availability statement

The raw data supporting the conclusion of this article will be made available by the authors, without undue reservation.

Author contributions

L-OA: Methodology, Writing–original draft, Investigation. AW: Investigation, Methodology, Writing–original draft. RC: Methodology, Funding acquisition, Writing–review and editing. CW: Methodology, Writing–review and editing, Investigation. NJ: Investigation, Methodology, Writing–review and editing. JK: Writing–review and editing, Conceptualization, Funding acquisition. NB: Conceptualization, Funding acquisition, Writing–review and editing, Methodology. PO'N: Conceptualization, Funding acquisition, Methodology, Writing–review and editing. NC: Conceptualization, Funding acquisition, Methodology, Writing–original draft.

Funding

The author(s) declare financial support was received for the research, authorship, and/or publication of this article. This study was funded by a UK Medical Research Council-funded Confidence in Concept Award (MC_PC_15040) to NC, and a Wellcome Trust grant (221712/Z/20/Z) awarded to JK, NB, PO'N, and NC. This research was funded in part by the Wellcome Trust. For the purpose of open access, the authors have applied a CC BY public copyright license to any Author Accepted Manuscript version arising from this submission.

Acknowledgments

We thank Paul Rowley and Edouard Crittenden for maintenance and husbandry of the snake collection at LSTM and for performing venom extractions.

Conflict of interest

The authors declare that the research was conducted in the absence of any commercial or financial relationships that could be construed as a potential conflict of interest.

Publisher's note

All claims expressed in this article are solely those of the authors and do not necessarily represent those of their affiliated organizations, or those of the publisher, the editors and the reviewers. Any product that may be evaluated in this article, or claim that may be made by its manufacturer, is not guaranteed or endorsed by the publisher.

Supplementary material

The Supplementary Material for this article can be found online at: https://www.frontiersin.org/articles/10.3389/fphar.2023.1331224/full#supplementary-material

References

Albulescu, L. O., Hale, M. S., Ainsworth, S., Alsolaiss, J., Crittenden, E., Calvete, J. J., et al. (2020b). Preclinical validation of a repurposed metal chelator as an early-intervention therapeutic for hemotoxic snakebite. *Sci. Transl. Med.* 12 (542), eaay8314. doi:10.1126/SCITRANSLMED.AAY8314

Albulescu, L. O., Xie, C., Ainsworth, S., Alsolaiss, J., Crittenden, E., Dawson, C. A., et al. (2020a). A therapeutic combination of two small molecule toxin inhibitors provides broad preclinical efficacy against viper snakebite. *Nat. Commun.* 11 (1), 6094. doi:10.1038/S41467-020-19981-6

Almeida, J. R., Lancellotti, M., Soares, A. M., Calderon, L. A., Ramírez, D., González, W., et al. (2016). CoaTx-II, a new dimeric Lys49 phospholipase A2 from Crotalus oreganus abyssus snake venom with bactericidal potential: insights into its structure and biological roles. *Toxicon* 120, 147–158. doi:10.1016/j.toxicon.2016.08.007

Arias, A. S., Rucavado, A., and Gutiérrez, J. M. (2017). Peptidomimetic hydroxamate metalloproteinase inhibitors abrogate local and systemic toxicity induced by Echis ocellatus (saw-scaled) snake venom. *Toxicon* 132, 40–49. doi:10.1016/j.toxicon.2017.04.001

Baell, J. B., and Holloway, G. A. (2010). New substructure filters for removal of Pan assay interference compounds (PAINS) from screening libraries and for their exclusion in bioassays. *J. Med. Chem.* 53 (7), 2719–2740. doi:10.1021/jm901137j

Beaudoin, A. R. (1985). The embryotoxicity of gossypol. *Teratology* 32 (2), 251–257. doi:10.1002/tera.1420320213

Berdowska, I., Matusiewicz, M., and Fecka, I. (2021). Punicalagin in cancer prevention—via signaling pathways targeting. *Nutrients* 13 (8), 2733. doi:10.3390/nu13082733

Bisson, J., McAlpine, J. B., Friesen, J. B., Chen, S. N., Graham, J., and Pauli, G. F. (2016). Can invalid bioactives undermine natural product-based drug discovery? *J. Med. Chem.* 59 (5), 1671–1690. doi:10.1021/acs.jmedchem.5b01009

Bryan-Quirós, W., Fernández, J., Gutiérrez, J. M., Lewin, M. R., and Lomonte, B. (2019). Neutralizing properties of LY315920 toward snake venom group I and II myotoxic phospholipases A2. *Toxicon* 157, 1–7. doi:10.1016/j.toxicon.2018.11.292

Bulfone, T. C., Samuel, S. P., Bickler, P. E., and Lewin, M. R. (2018). Developing small molecule therapeutics for the initial and adjunctive treatment of snakebite. *J. Trop. Med.* 2018, 4320175–4320214. doi:10.1155/2018/4320175

Casewell, N. R., Wüster, W., Vonk, F. J., Harrison, R. A., and Fry, B. G. (2013). Complex cocktails: the evolutionary novelty of venoms. *Trends Ecol. Evol.* 28 (4), 219–229. doi:10.1016/J.TREE.2012.10.020

Cendron, L., Mičetić, I., Polverino de Laureto, P., and Paoli, M. (2012). Structural analysis of trimeric phospholipase A2 neurotoxin from the Australian taipan snake venom. *FEBS J.* 279 (17), 3121–3135. doi:10.1111/J.1742-4658.2012.08691.X

Cerdá, B., Cerón, J. J., Tomás-Barberán, F. A., and Espín, J. C. (2003). Repeated oral administration of high doses of the pomegranate ellagitannin punicalagin to rats for 37 days is not toxic. *J. Agric. Food Chem.* 51 (11), 3493–3501. doi:10.1021/jf020842c

Chakraborty, A. K., Hall, R. H., and Ghose, A. C. (2002). Purification and characterization of a potent hemolytic toxin with phospholipase A2 activity from the venom of Indian Russell's viper. *Mol. Cell. Biochem.* 237 (1–2), 95–102. doi:10.1023/A:1016591318855

Chen, C., Yang, H., Yang, X., and Ma, Q. (2022). Tannic acid: a crosslinker leading to versatile functional polymeric networks: a review. *RSC Adv.* 12 (13), 7689–7711. doi:10.1039/d1ra07657d

Chiara Ricci, N. F. (2015). Pharmacological inhibition of phosholipase A2: results from phase 3 clinical trials with darapladib and varespladib in patients with cardiovascular disease. *Cardiovasc. Pharmacol. Open Access* 04 (02), 2–6. doi:10.4172/2329-6607.1000137

Chippaux, J. P., Williams, V., and White, J. (1991). Snake venom variability: methods of study, results and interpretation. *Toxicon official J. Int. Soc. Toxinology* 29 (11), 1279–1303. doi:10.1016/0041-0101(91)90116-9

Clare, R. H., Hall, S. R., Patel, R. N., and Casewell, N. R. (2021). Small molecule drug discovery for neglected tropical snakebite. *Trends Pharmacol. Sci.* 42 (5), 340–353. doi:10.1016/j.tips.2021.02.005

Clare, R. H., Dawson, C. A., Westhorpe, A., Albulescu, L. O., Woodley, C. M., Mosallam, N., Chong, D. J., et al. (2024). Snakebite drug discovery: high-throughput screening to identify novel snake venom metalloproteinase toxin inhibitors. *Front. Pharmacol.* 14. doi:10.3389/fphar.2023.1328950

Cotrim, C. A., de Oliveira, S. C. B., Diz Filho, E. B. S., Fonseca, F. V., Baldissera, L., Antunes, E., et al. (2011). Quercetin as an inhibitor of snake venom secretory phospholipase A2. *Chemico-Biological Interact.* 189 (1–2), 9–16. doi:10.1016/j.cbi.2010.10.016

Coutinho, E. M., Athayde, C., Atta, G., Gu, Z. P., Chen, Z. W., Sang, G. W., et al. (2000). Gossypol blood levels and inhibition of spermatogenesis in men taking gossypol as a contraceptive. A multicenter, international, dose-finding study. *Contraception* 61 (1), 61–67. doi:10.1016/s0010-7824(99)00117-1

Danesi, F., and Ferguson, L. R. (2017). Could pomegranate juice help in the control of inflammatory diseases? *Nutr.* 9 (9), 958. doi:10.3390/nu9090958

de Silva, H. A., Ryan, N. M., and de Silva, H. J. (2016). Adverse reactions to snake antivenom, and their prevention and treatment. *Br. J. Clin. Pharmacol.* 81 (3), 446–452. doi:10.1111/bcp.12739

Faisal, T., Tan, K. Y., Tan, N. H., Sim, S. M., Gnanathasan, C. A., and Tan, C. H. (2021). Proteomics, toxicity and antivenom neutralization of Sri Lankan and Indian Russell's viper (*Daboia russelii*) venoms. *J. Venom. Animals Toxins Incl. Trop. Dis.* 27, e20200177. doi:10.1590/1678-9199-JVATITD-2020-0177

Fohlman, J., Eaker, D., Karlsoon, E., and Thesleff, S. (1976). Taipoxin, an extremely potent presynaptic neurotoxin from the venom of the Australian snake taipan (Oxyuranus s. scutellatus). Isolation, characterization, quaternary structure and pharmacological properties. *Eur. J. Biochem.* 68 (2), 457–469. doi:10.1111/j.1432-1033.1976.tb10833.x

Fry, B. G., Scheib, H., van der Weerd, L., Young, B., McNaughtan, J., Ramjan, S. F. R., et al. (2008). Evolution of an arsenal: structural and functional diversification of the venom system in the advanced snakes (Caenophidia). *Mol. Cell. proteomics MCP* 7 (2), 215–246. doi:10.1074/mcp.M700094-MCP200

Giannetti, A. M., Koch, B. D., and Browner, M. F. (2008). Surface plasmon resonance based assay for the detection and characterization of promiscuous inhibitors. *J. Med. Chem.* 51 (3), 574–580. doi:10.1021/jm700952v

Gleeson, M. P. (2008). Generation of a set of simple, interpretable ADMET rules of thumb. *J. Med. Chem.* 51 (4), 817–834. doi:10.1021/jm701122q

Gutiérrez, J. M., Albulescu, L. O., Clare, R. H., Casewell, N. R., Abd El-Aziz, T. M., Escalante, T., et al. (2021). The search for natural and synthetic inhibitors that would complement antivenoms as therapeutics for snakebite envenoming. *Toxins* 13 (7), 451. doi:10.3390/toxins13070451

Gutiérrez, J. M., Calvete, J. J., Habib, A. G., Harrison, R. A., Williams, D. J., and Warrell, D. A. (2017). Snakebite envenoming. *Nat. Rev. Dis. Prim.* 3, 17063. doi:10.1038/nrdp.2017.63

Gutiérrez, J. M., and Lomonte, B. (2013). Phospholipases A2: unveiling the secrets of a functionally versatile group of snake venom toxins. *Toxicon* 62, 27–39. doi:10.1016/j.toxicon.2012.09.006

Hall, S. R., et al. (2023). Repurposed drugs and their combinations prevent morbidity-inducing dermonecrosis caused by diverse cytotoxic snake venoms. *Nature Communications.* 14 (1), 7812. Available at: https://doi.org/10.1038/s41467-023-43510-w

Harrison, R. A., Hargreaves, A., Wagstaff, S. C., Faragher, B., and Lalloo, D. G. (2009). Snake envenoming: a disease of poverty. *PLoS Neglected Trop. Dis.* 3 (12), e569. doi:10.1371/journal.pntd.0000569

Hevener, K. E., Pesavento, R., Ren, J., Lee, H., Ratia, K., and Johnson, M. E. (2018). Hit-to-Lead: hit validation and assessment. *Methods Enzym.* 610, 265–309. doi:10.1016/bs.mie.2018.09.022

Hopkins, A. L., Groom, C. R., and Alex, A. (2004). Ligand efficiency: a useful metric for lead selection. *Drug Discov. Today* 9 (10), 430–431. doi:10.1016/S1359-6446(04)03069-7

Kerns, R. T., Kini, R. M., Stefansson, S., and Evans, H. J. (1999). Targeting of venom phospholipases: the strongly anticoagulant phospholipase A2 from *Naja nigricollis* venom binds to coagulation factor Xa to inhibit the prothrombinase complex. *Archives Biochem. Biophysics* 369 (1), 107–113. doi:10.1006/abbi.1999.1345

Kini, R. M. (2003). Excitement ahead: structure, function and mechanism of snake venom phospholipase A2 enzymes. *Toxicon* 42 (8), 827–840. doi:10.1016/j.toxicon.2003.11.002

Kini, R. M. (2005). Structure-function relationships and mechanism of anticoagulant phospholipase A2 enzymes from snake venoms. *Toxicon* 45 (8), 1147–1161. doi:10.1016/j.toxicon.2005.02.018

Kovacic, P. (2003). Mechanism of drug and toxic actions of gossypol: focus on reactive oxygen species and electron transfer. *Curr. Med. Chem.* 10 (24), 2711–2718. doi:10.2174/0929867033456369

Kwong, P. D., McDonald, N. Q., Sigler, P. B., and Hendrickson, W. A. (1995). Structure of beta 2-bungarotoxin: potassium channel binding by Kunitz modules and targeted phospholipase action. *Struct. Lond. Engl. 1993)* 3 (10), 1109–1119. doi:10.1016/s0969-2126(01)00246-5

Landrum, G., Tasco, P., and Kelley, B. (2020). rdkit/rdkit: 2020_03_1 (Q1 2020) Release. Zenodo. doi:10.5281/zenodo.3732262

Laxme, R. R. S., Khochare, S., Attarde, S., Suranse, V., Iyer, A., Casewell, N. R., et al. (2021). Biogeographic venom variation in Russell's viper (*Daboia russelii*) and the preclinical inefficacy of antivenom therapy in snakebite hotspots. *PLOS Neglected Trop. Dis.* 15 (3), e0009247. doi:10.1371/journal.pntd.0009247

Leeson, P. D., and Springthorpe, B. (2007). The influence of drug-like concepts on decision-making in medicinal chemistry. *Nat. Rev. Drug Discov.* 6 (11), 881–890. doi:10.1038/nrd2445

Lewin, M., Gilliam, L., Gilliam, J., Samuel, S. P., Bulfone, T. C., Bickler, P. E., et al. (2018a). Delayed LY333013 (oral) and LY315920 (intravenous) reverse severe neurotoxicity and rescue juvenile pigs from lethal doses of *Micrurus fulvius* (eastern coral snake) venom. *Toxins* 10 (11), 479. doi:10.3390/toxins10110479

Lewin, M., Gutiérrez, J., Samuel, S. P., Herrera, M., Bryan-Quirós, W., Lomonte, B., et al. (2018b). Delayed oral LY333013 rescues mice from highly neurotoxic, lethal doses of papuan taipan (Oxyuranus scutellatus) venom. *Toxins* 10 (10), 380. doi:10.3390/toxins10100380

Lewin, M., Samuel, S., Merkel, J., and Bickler, P. (2016). Varespladib (LY315920) appears to be a potent, broad-spectrum, inhibitor of snake venom phospholipase A2 and a possible pre-referral treatment for envenomation. *Toxins* 8 (9), 248. doi:10.3390/toxins8090248

Lewin, M. R., Carter, R. W., Matteo, I. A., Samuel, S. P., Rao, S., Fry, B. G., et al. (2022). Varespladib in the treatment of snakebite envenoming: development history and preclinical evidence supporting advancement to clinical trials in patients bitten by venomous snakes. *Toxins* 14 (11), 783. doi:10.3390/toxins14110783

Lipinski, C. A. (2000). Drug-like properties and the causes of poor solubility and poor permeability. *J. Pharmacol. Toxicol. Methods* 44 (1), 235–249. doi:10.1016/S1056-8719(00)00107-6

Liu, G. Z., Lyle, K. C., and Cao, J. (1987). Clinical trial of gossypol as a male contraceptive drug. Part I. Efficacy study. *Fertil. Steril.* 48 (3), 459–461. doi:10.1016/s0015-0282(16)59418-7

Longbottom, J., Shearer, F. M., Devine, M., Alcoba, G., Chappuis, F., Weiss, D. J., et al. (2018). Vulnerability to snakebite envenoming: a global mapping of hotspots. *Lancet (London, Engl.* 392, 673–684. doi:10.1016/S0140-6736(18)31224-8

Lynch, V. J. (2007). Inventing an arsenal: adaptive evolution and neofunctionalization of snake venom phospholipase A2 genes. *BMC Evol. Biol.* 7 (1), 2. doi:10.1186/1471-2148-7-2

Matlock, M. K., Hughes, T. B., Dahlin, J. L., and Swamidass, S. J. (2018). Modeling small-molecule reactivity identifies promiscuous bioactive compounds. *J. Chem. Inf. Model.* 58 (8), 1483–1500. doi:10.1021/acs.jcim.8b00104

Menzies, S. K., Clare, R. H., Xie, C., Westhorpe, A., Hall, S. R., Edge, R. J., et al. (2022). *In vitro* and *in vivo* preclinical venom inhibition assays identify metalloproteinase inhibiting drugs as potential future treatments for snakebite envenoming by Dispholidus typus. *Toxicon* 14, 100118. doi:10.1016/j.toxcx.2022.100118

Mise, Y., Lira-da-Silva, R., and Carvalho, F. (2018). Time to treatment and severity of snake envenoming in Brazil. *Rev. Panam. Salud Pública* 42, e52–e56. doi:10.26633/RPSP.2018.52

Ogunfowokan, O. (2012). Bite-to-hospital time and morbidity in victims of viper bite in a rural hospital in Nigeria. *Afr. J. Prim. Health Care Fam. Med.* 4 (1). doi:10.4102/phcfm.v4i1.371

Probst, D., and Reymond, J.-L. (2020). Visualization of very large high-dimensional data sets as minimum spanning trees. *J. Cheminformatics* 12 (1), 12. doi:10.1186/s13321-020-0416-x

Rucavado, A., Escalante, T., and Gutiérrez, J. M. (2004). Effect of the metalloproteinase inhibitor batimastat in the systemic toxicity induced by *Bothrops asper* snake venom: understanding the role of metalloproteinases in envenomation. *Toxicon* 43 (4), 417–424. doi:10.1016/j.toxicon.2004.01.016

Salvador, G. H. M., Gomes, A. A. S., Bryan-Quirós, W., Fernández, J., Lewin, M. R., Gutiérrez, J. M., et al. (2019). Structural basis for phospholipase A2-like toxin inhibition by the synthetic compound Varespladib (LY315920). *Sci. Rep.* 9 (1), 17203. doi:10.1038/s41598-019-53755-5

Sampaio, S. C., Hyslop, S., Fontes, M. R. M., Prado-Franceschi, J., Zambelli, V. O., Magro, A. J., et al. (2010). Crotoxin: novel activities for a classic β-neurotoxin. *Toxicon* 55 (6), 1045–1060. doi:10.1016/j.toxicon.2010.01.011

Sander, T., Freyss, J., von Korff, M., and Rufener, C. (2015). DataWarrior: an open-source program for chemistry aware data visualization and analysis. *J. Chem. Inf. Model.* 55 (2), 460–473. doi:10.1021/ci500588j

Seeram, N. P., Adams, L. S., Henning, S. M., Niu, Y., Zhang, Y., Nair, M. G., et al. (2005). *In vitro* antiproliferative, apoptotic and antioxidant activities of punicalagin, ellagic acid and a total pomegranate tannin extract are enhanced in combination with other polyphenols as found in pomegranate juice. *J. Nutr. Biochem.* 16 (6), 360–367. doi:10.1016/j.jnutbio.2005.01.006

Sharma, S. K., Chappuis, F., Jha, N., Bovier, P. A., Loutan, L., and Koirala, S. (2004). Impact of snake bites and determinants of fatal outcomes in southeastern Nepal. *Am. J. Trop. Med. Hyg.* 71 (2), 234–238. doi:10.4269/ajtmh.2004.71.234

Tasoulis, T., and Isbister, G. K. (2017). A review and database of snake venom proteomes. *Toxins* 9 (9), 290. doi:10.3390/toxins9090290

Vargas-Valerio, S., Robleto, J., Chaves-Araya, S., Monturiol-Gross, L., Lomonte, B., Tonello, F., et al. (2021). Localization of Myotoxin I and Myotoxin II from the venom of *Bothrops asper* in a murine model. *Toxicon* 197, 48–54. doi:10.1016/j.toxicon.2021.04.006

Wang, Y., Lai, H., Fan, X., Luo, L., Duan, F., Jiang, Z., et al. (2018). Gossypol inhibits non-small cell lung cancer cells proliferation by targeting egfrl858r/t790m. *Front. Pharmacol.* 9, 728. doi:10.3389/fphar.2018.00728

Williams, D. J., Gutiérrez, J. M., Calvete, J. J., Wüster, W., Ratanabanangkoon, K., Paiva, O., et al. (2011). Ending the drought: new strategies for improving the flow of affordable, effective antivenoms in Asia and Africa. *J. Proteomics* 74 (9), 1735–1767. doi:10.1016/j.jprot.2011.05.027

Yu, B.-Z., Rogers, J., Ranadive, G., Baker, S., Wilton, D. C., Apitz-Castro, R., et al. (1997). Gossypol modification of ala-1 of secreted phospholipase A2: a probe for the kinetic effects of sulfate glycoconjugates. *Biochemistry* 36 (41), 12400–12411. doi:10.1021/bi962972i

Zhang, J.-H., Chung, T. D. Y., and Oldenburg, K. R. (1999). A simple statistical parameter for use in evaluation and validation of high throughput screening assays. *SLAS Discov.* 4 (2), 67–73. doi:10.1177/108705719900400206

Zhang, M., Liu, H., Guo, R., Ling, Y., Wu, X., Li, B., et al. (2003). Molecular mechanism of gossypol-induced cell growth inhibition and cell death of HT-29 human colon carcinoma cells. *Biochem. Pharmacol.* 66 (1), 93–103. doi:10.1016/s0006-2952(03)00248-x

Frontiers in Pharmacology

Explores the interactions between chemicals and living beings

The most cited journal in its field, which advances access to pharmacological discoveries to prevent and treat human disease.

Discover the latest Research Topics

See more →

Frontiers

Avenue du Tribunal-Fédéral 34
1005 Lausanne, Switzerland
frontiersin.org

Contact us

+41 (0)21 510 17 00
frontiersin.org/about/contact